



Ricardo Nuno Madeira Soares Branco

FATIGUE LIFE PREDICTION OF NOTCHED COMPONENTS SUBJECTED TO COMPLEX LOADING

Dissertação de Doutoramento na área científica de Engenharia Mecânica, especialidade de Construção Mecânica, orientada pelo Senhor Professor Doutor José Domingos Moreira da Costa e Senhor Professor Doutor Fernando Jorge Ventura Antunes, apresentada no Departamento de Engenharia Mecânica da Faculdade de Ciências e Tecnologia da Universidade de Coimbra

Fevereiro de 2013



UNIVERSIDADE DE COIMBRA

Ricardo Nuno Madeira Soares Branco

FATIGUE LIFE PREDICTION OF NOTCHED COMPONENTS SUBJECTED TO COMPLEX LOADING

Dissertação de Doutoramento na área científica de Engenharia Mecânica, especialidade de Construção Mecânica, orientada pelo Senhor Professor Doutor José Domingos Moreira da Costa e Senhor Professor Doutor Fernando Jorge Ventura Antunes, apresentada no Departamento de Engenharia Mecânica da Faculdade de Ciências e Tecnologia da Universidade de Coimbra

Fevereiro de 2013



UNIVERSIDADE DE COIMBRA

Fatigue Life Prediction of Notched Components Subjected to Complex Loading

Ricardo Nuno Madeira Soares Branco

Universidade de Coimbra

Fevereiro de 2013

ISBN 978-972-8954-31-4

To my *sweethearts*

Maria João, Leonor, Maria Inês

to my *mother* and to my *grandmother*

Maria de Jesus

ACKNOWLEDGEMENTS

I would like to sincerely thank my supervisors, Prof. José Domingos and Prof. Fernando Antunes, for their excellent support and valuable guidance throughout this project. It has been a privilege to work with both of them.

I am also very thankful to Prof. Amílcar Ramalho for all the help provided in the SEM analysis as well as to Adalberto Serra for his assistance and friendliness during the in-phase combined bending-torsion tests.

I am grateful for the fruitful collaboration with Prof. FengPeng Yang and Prof. ZhengBang Kuang from Shanghai Jiaotong University as well as with Prof. Luiz Ricardo from Aalborg University.

I wish to express my thanks to Paulo Amaro and José Cruz who prepared the samples used in this research and to Prof. Luís Roseiro and Paulo Bento who helped me in the acquisition of fracture surfaces by laser scan.

I would like to acknowledge Prof. Martins Ferreira, Prof. Luís Borrego and Prof. Rui Martins their letters of recommendation for applying to the PROTEC grant program as well as to IPC/ISEC/DEM for providing me the opportunity to pursue my PhD.

Last but not least, I am very grateful to all my family for all their support, understanding and encouragement over the years.

The author is indebted to the Portuguese Foundation for the Science and Technology (FCT) and COMPETE program from FEDER (European Regional Development Fund) for the financial support (Projects PTDC/EME-PME/114892/2009 and PEst-C/EME/UI0285/2011). The author is also thankful to the PROTEC grant program (Reference SFRH/PROTEC/49844/2009).



ABSTRACT

DIN 34CrNiMo6 high strength steel is a very versatile engineering material. It combines high ductility, deep hardenability, toughness and strength. Due to the combination of these properties, it is ideal for critical components which work under severe service conditions, for instance shafts, axles, crankshafts, connecting rods, pinions, torsion bars, bolts, aircraft components, high pressure vessels for nuclear plants, among others. Besides, such components have geometric discontinuities introduced for design purposes and are often subjected to relatively complex loading. These characteristics make them susceptible to fatigue failure. In order to reduce the risk of unexpected in-service failure, accurate fatigue life prediction models are required.

The thesis has two main purposes. The first is the study of the fatigue behaviour of DIN 34CrNiMo6 high strength steel under proportional biaxial loading. The loading paths analysed are single bending, single torsion and in-phase bending-torsion. In relation to the last type, three ratios of the bending moment (B) to the torsion moment (T) are considered, namely $B=2T$, $B=T$ and $B=2T/3$. The specimen geometries used in the experiments are round bars with lateral U-shaped notches. The tests are conducted at stress ratios close to zero ($R=0$) under constant-amplitude loading. The detection of crack initiation is carried out *in situ* with a digital monitoring system. The fatigue life predictions are obtained using the Coffin-Manson (CM) and Smith-Watson-Topper (SWT) models. The notch effect is evaluated with the theory of critical distances and the strain energy density model. A very satisfactory correlation between both the experimental and the predicted lives was found either from the CM or the SWT models.

The second objective of the thesis is the development of user-friendly software to address in-plane fatigue crack growth problems. This computer application incorporates an extensive range of geometries, such as notched and unnotched rectangular cross-section bars with corner cracks, notched and unnotched round bars with surface cracks, and notched and unnotched plates with through cracks. Additionally, it is able to compute automatically the transition from corner and surface cracks to through cracks. The main independent variables affecting the calculation procedure are identified and optimised. Then, the procedure is successfully validated by comparing the numerical results obtained here with those available in the literature. After that, the software is applied to specific issues, namely the evaluation of the extent of the surface region in cracked bodies; the development of a plane strain specimen able to study different phenomena affected by the stress state, for instance those involving diffusion, plastic deformation and brittle fracture; and the determination of the Paris law constants from the analysis of crack front marks on fracture surfaces of small cross-section round bars. In all the above-mentioned situations, the software proved to be efficient and user-friendly.

Keywords: biaxial loading, in-phase combined bending-torsion, notch effect, fatigue life prediction, crack initiation, crack shape evolution, crack growth, surface region, plane strain specimen, Paris law constants.

RESUMO

O aço de alta resistência DIN 34CrNiMo6 é um material muito versátil. Este aço combina elevada ductilidade, alta temperabilidade, tenacidade e resistência. As propriedades acima referidas fazem dele um material ideal para componentes críticos, tais como cambotas, veios, eixos, bielas, pinhões, barras de torção, parafusos, componentes aeronáuticos, reservatórios sob pressão para unidades nucleares, etc., que funcionam sob a ação de condições de serviço severas. Além disso, estes componentes apresentam descontinuidades geométricas introduzidas por questões de projeto e são muitas vezes sujeitos a carregamentos relativamente complexos. Estas características tornam-nos suscetíveis a falhas por fadiga. Para que este risco seja reduzido é necessário ter modelos de previsão de vida à fadiga fiáveis.

A presente tese tem dois objetivos principais. O primeiro consiste no estudo do comportamento à fadiga do aço de alta resistência DIN 34CrNiMo6 quando sujeito a carregamentos proporcionais biaxiais. Neste trabalho são analisados carregamentos de flexão simples, torção pura e flexão-torção em fase. Em relação ao último tipo, são consideradas três relações entre o momento fletor (B) e o momento torçor (T), nomeadamente $B=2T$, $B=T$ e $B=2T/3$. As geometrias de provetes utilizadas têm uma secção circular e apresentam um entalhe lateral em forma de U. Os ensaios são efetuados para razões de tensão próximas de zero com amplitude de carga constante. A deteção da iniciação da fenda é realizada *in situ* com o auxílio de um sistema de aquisição de imagem digital. As previsões de vida à fadiga são obtidas com os modelos de Coffin-Manson (CM) e Smith-Watson-Topper (SWT). O efeito do entalhe é avaliado a partir da teoria das distâncias críticas e do modelo da densidade de energia de deformação. Os resultados previstos aproximam-se, de forma muito satisfatória, dos obtidos experimentalmente, quer no modelo de CM, quer no modelo de SWT.

O segundo objetivo da tese consiste no desenvolvimento de um *software* para análise de problemas de propagação de fendas por fadiga. A ferramenta informática desenvolvida apresenta uma considerável lista de geometrias que incluem desde barras entalhadas e não entalhadas de secção retangular com fendas de canto, barras entalhadas e não entalhadas de secção circular com fendas superficiais, e placas entalhadas e não entalhadas com fendas passantes. Além disso, esta ferramenta é capaz de efetuar a transição automática de fendas de canto e superficiais para fendas passantes. As principais variáveis independentes que afetam a exatidão do procedimento de cálculo são identificadas e otimizadas. Em seguida, o procedimento é validado com sucesso através da comparação dos resultados numéricos obtidos com os existentes na literatura. Finalmente, o *software* é aplicado a casos específicos, nomeadamente à determinação da dimensão da camada superficial em peças entalhadas; ao desenvolvimento de um provete de deformação plana para estudar fenómenos afetados pelo estado de tensão, tais como difusão, deformação plástica e fratura frágil; e à obtenção das constantes da lei de Paris a partir de frentes de fenda existentes nas superfícies de fratura de peças com secção circular de pequeno diâmetro. Nos casos acima referidos, a ferramenta informática revelou ser eficiente e simples de utilizar.

Palavras-chave: carregamento biaxial, carregamento combinado flexão-torção em fase, efeito do entalhe, previsão de vida à fadiga, iniciação de fenda, evolução da forma da fenda, propagação de fenda, região superficial, provete de deformação plana, constantes da lei de Paris.

LIST OF CONTENTS

	Page
ACKNOWLEDGEMENTS	vii
ABSTRACT	ix
RESUMO	xi
LIST OF CONTENTS	xiii
LIST OF FIGURES	xvii
LIST OF TABLES	xxxv
CHAPTER 1 - INTRODUCTION	
1.1 Introduction	3
1.2 Research objectives	4
1.3 Outline of thesis.....	5
CHAPTER 2 - LITERATURE REVIEW	
PART A - FATIGUE PHENOMENON	
2.1 Fatigue phenomenon.....	9
i) Effect of microstructure	12
ii) Effect of processing techniques.....	13
iii) Effect of environmental factors.....	14
a. Corrosive environmental.....	14
b. Temperature	16
iv) Effect of load.....	17
a. Mean stress	19
b. Type of loading	21
c. Loading sequence.....	22
d. Loading frequency	22
v) Effect of geometry.....	23
a. Stress concentration	23
b. Surface finish	24
2.2 Fatigue design philosophies.....	27
2.3 Cyclic stress-strain response.....	28
2.4 Fatigue life of notched bodies.....	36
2.4.1 Stress-based models.....	36
2.4.2 Strain-based models.....	45
2.4.3 Energy-based models.....	49
2.5 Multiaxial fatigue	53
2.5.1 Stress-based models.....	59

i) Equivalent stress methods.....	59
ii) Stress invariant methods.....	62
iii) Average stress methods.....	66
2.5.2 Strain-based models.....	68
2.5.3 Energy-based models.....	69
2.5.4 Critical plane methods.....	71
i) Stress-based models.....	72
ii) Strain-based models.....	74
iii) Energy-based models.....	77

CHAPTER 2 - LITERATURE REVIEW

PART B - CRACK GROWTH MODELLING

2.6 State-of-the-art.....	83
2.7 The automatic crack growth technique.....	88
2.7.1 Finite element method.....	90
i) Mesh topology.....	91
ii) Types of finite elements.....	92
iii) Radial size of crack front elements.....	94
iv) Orientation and refinement of layers.....	96
v) Crack front shape definition.....	98
2.7.2 Calculation of stress intensity factor with the FEM.....	99
i) Displacement matching methods.....	100
ii) Energy-based methods.....	102
2.7.3 Crack growth model.....	106
i) Crack growth increment.....	107
2.8 Effect of physical variables on crack shape and fatigue life.....	108
2.8.1 Effect of initial crack shape.....	109
2.8.2 Effect of Paris law exponent.....	111
2.8.3 Effect of loading type.....	112
2.8.4 Effect of geometry.....	113
2.8.5 Surface effects.....	114

CHAPTER 3 - EXPERIMENTAL PROCEDURE

3.1 Material.....	119
3.2 Uniaxial tensile tests.....	121
3.3 Determination of the elastic constants using a resonant technique.....	122
3.4 Low-cycle fatigue tests.....	125
3.5 High-cycle fatigue tests.....	128
3.6 Fatigue crack front marking tests.....	134
3.7 Analysis of material microstructure.....	135

3.8	Analysis of fracture surfaces	137
3.9	Three-dimensional laser scanning of fracture surfaces	138
3.10	Determination of the Paris law constants from fatigue crack front marks.....	139

CHAPTER 4 - NUMERICAL PROCEDURE

4.1	Determination of elastic constants.....	145
4.2	High-cycle fatigue tests	148
4.3	Modelling of crack shape evolution.....	153
4.4	Extent of surface region in cracked geometries.....	162
4.5	Definition of a plane strain specimen	167
4.6	Determination of the Paris law constants from fatigue crack front marks.....	170

CHAPTER 5 - EXPERIMENTAL RESULTS

5.1	Microstructure of the material	175
5.2	Uniaxial tensile tests	176
5.3	Determination of the elastic constants using a resonant technique.....	178
5.4	Low-cycle fatigue tests	181
5.4.1	Cyclic stress-strain response.....	183
5.4.2	Low-cycle fatigue life and low-cycle fatigue properties.....	189
5.4.3	Analysis of fracture surfaces.....	196
5.5	High-cycle fatigue tests	199
5.5.1	Fatigue crack paths, surface crack angles and fracture surfaces.....	200
5.5.2	Experimental fatigue life	214
5.5.3	Fatigue life predictions	222

CHAPTER 6 - NUMERICAL RESULTS

6.1	Modelling of crack shape evolution.....	237
6.1.1	Lynx: new tool to model mode I fatigue crack growth.....	237
6.1.1.i)	Pre-processing stage.....	238
6.1.1.ii)	Processing stage	240
6.1.1.iii)	Post-processing stage.....	243
6.1.2	Procedure optimisation	243
6.1.2.i)	Mesh topology.....	244
6.1.2.ii)	Type of finite elements.....	245
6.1.2.iii)	Radial size of crack front elements	246
6.1.2.iv)	Density and orientation of layers.....	248
6.1.2.v)	Crack front definition	249
6.1.2.vi)	Stress intensity factor calculation.....	250
6.1.2.vii)	Crack growth model.....	251
6.1.3	Procedure validation.....	252

6.2	Extent of the surface region in cracked bodies.....	255
6.2.1	Selection of representative crack shapes	257
6.2.2	Stress triaxiality at the crack front.....	261
6.2.3	Effects of the variables affecting crack shape on stress triaxiality	263
6.2.4	Evaluation of the extent of the surface region.....	267
6.2.5	Relations S_1-K_T and S_2-K_T	276
6.3	Definition of a plane strain specimen for fatigue and fracture studies	279
6.3.1	Selection of representative crack shapes	280
6.3.2	Stress triaxiality at the crack front.....	281
6.3.3	Definition of a plane strain specimen.....	284
6.3.4	Stress intensity factor solution	292
6.3.5	Sensitivity analysis.....	293
6.4	Determination of the Paris law constants from fatigue crack front marks	294
CHAPTER 7 - CONCLUSIONS AND FUTURE RESEARCH		
7.1	Conclusions.....	303
7.2	Future research.....	306
REFERENCES		309

LIST OF FIGURES

	Page
Figure 2.1 Main stages of fatigue failure (Farahmand, 1997)	9
Figure 2.2 Slip bands formation leading to crack initiation as a result of cyclic loading (Farahmand, 1997)	10
Figure 2.3 Schematic illustration of the three basic modes of fracture: a) mode I; b) mode II; c) mode III (Socie, 2000)	11
Figure 2.4 Schematic illustration of the two crack growth patterns in multiaxial fatigue suggested by Brown <i>et al.</i> (1973) and termed case A and case B: a) multiaxial strains; b) plane of maximum shear stress amplitude and plane and direction of stage I crack growth; d) plane and direction of stage II crack growth (Suresh, 1998)	12
Figure 2.5 Effect of steel microstructure on endurance ratio (Boyer, 1986)	13
Figure 2.6 Effect of non-metallic inclusion size on fatigue life in specimens made of DIN 34CrNiMo6 high strength steel (ASM, 2000a)	14
Figure 2.7 S-N curves of DIN 34CrNiMo6 high strength steel tested in corrosive environment and in air (Puchi-Cabrera, 2007)	15
Figure 2.8 S-N curves of DIN 34CrNiMo6 high strength steel obtained at different temperatures (MIL-HDBK-5H, 1988)	17
Figure 2.9 Types of loading: a) random; b) blocks of constant amplitude; c) constant amplitude	18
Figure 2.10 Family of S-N curves obtained at different stress ratios for DIN 34CrNiMo6 high strength steel (MIL-HDBK-5H, 1988)	19
Figure 2.11 Goodman, Gerber and Soderberg diagrams	20
Figure 2.12 S-N curves obtained under rotating bending and axial loading for DIN 34CrNiMo6 high strength steel (Socie, 1980)	21

Figure 2.13 Fatigue data showing sequence effects for two load histories (load history <i>A</i> and load history <i>B</i>) in 2024-T4 aluminium (Socie, 1980)	22
Figure 2.14 S-N curves for DIN 34CrNiMo6 high strength steel obtained using notched ($K_T = 2$) and unnotched ($K_T = 1$) specimens (MIL-HDBK-5H, 1988)	23
Figure 2.15 S-N curves of conventionally heat treated and nitrided DIN 34CrNiMo6 high strength steel for different nitriding treatment conditions (Sirin, 2008)	25
Figure 2.16 Typical S-N bands for conventionally heat treated, shot peened and nitrided crankshafts made of DIN 34CrNiMo6 high strength steel (ASM, 2000a)	25
Figure 2.17 S-N curves for conventionally heat treated and electroless Ni-P plated DIN 34CrNiMo6 high strength steel (Díaz, 2000)	26
Figure 2.18 Material response to different modes of cyclic input variables: a) cyclic strain hardening; b) cyclic strain softening; c) cyclic mean stress relaxation; d) cyclic strain ratcheting (Ellyin, 1997)	29
Figure 2.19 Schematic presentation of a saturated hysteresis loop (Ellyin, 1997)	30
Figure 2.20 Monotonic and cyclic stress-strain curves for DIN 34CrNiMo6 high strength steel (Landgraf, 1970)	31
Figure 2.21 Schematic representation of the master curve (Ellyin, 1997)	33
Figure 2.22 Elastic, plastic and total strain amplitudes versus number of reversals to failure	34
Figure 2.23 Cyclic strain energy per density for uniaxial stress state (Koh, 2002)	36
Figure 2.24 Schematic presentation of the average stress model (Yao, 1995)	38
Figure 2.25 Schematic presentation of the fracture mechanics model (Yao, 1995)	39
Figure 2.26 Schematic presentation of the stress field intensity model (Qylafku, 1999)	41
Figure 2.27 Typical elastic-plastic stress distribution versus the distance from the notch tip (Qylafku, 1999)	42
Figure 2.28 Concept of the theory of critical distances (TCD): a) point method; b) line method; c) area method (Susmel, 2011)	44

Figure 2.29	Kitagawa-Takahashi diagram describing the crack size effect on fatigue propagation of short and long cracks (Taylor, 2008)	44
Figure 2.30	Schematic illustration of the local strain approach (Ellyin, 1997)	45
Figure 2.31	Schematic illustration of the procedure used to obtain the local stress-strain response at the notch tip using a smooth specimen according to the Neuber's rule (Suresh, 1998)	47
Figure 2.32	Schematic illustration of the procedure used to obtain the stress intensity parameter and the strain intensity parameter using an elastic-plastic finite element analysis (Shang, 2001)	48
Figure 2.33	Graphical interpretation of the equivalent energy density concept (Glinka, 1985)	50
Figure 2.34	Notch with small-scale yielding at its root: a) plastic zone size; b) tractions at a radius R away from the notch root (Ellyin, 1997)	51
Figure 2.35	Typical strain energy density distribution at the notch tip plotted in a log-log scale (Bentachfine, 1999)	52
Figure 2.36	Shaft subjected to both shear and axial stresses resulting in: a) proportional multiaxial loading; b) non-proportional multiaxial loading (Socie, 2000)	54
Figure 2.37	Typical example of an: a) in-phase; b) out-of-phase strain history (Socie, 2000)	55
Figure 2.38	Non-proportional loading histories: a) phase difference; b) amplitude difference (Socie, 2000)	56
Figure 2.39	a) Definition of $x(t)$; b) polar representation of $\Delta\epsilon_I$ (Ioth, 2004)	57
Figure 2.40	Schematic representation of the minimum circumscribed circle approach and minimum circumscribed ellipse approach (Freitas, 2000)	58
Figure 2.41	Schematic illustration of the maximum normal stress, maximum shear stress and von Mises theories (Socie, 2000)	60
Figure 2.42	Fatigue limits of three different steels under combined bending-torsion loading (Socie, 2000)	61
Figure 2.43	Ellipsoid in R^m space and circumscribed rectangular prism arbitrarily oriented (Mamiya, 2002)	65

Figure 2.44	Definition of the spherical coordinates of the unit vector \mathbf{n} normal to the plane Δ (Bernasconi, 2008)	66
Figure 2.45	Normal strain and shear strain histories in the critical plane (Karolczuk, 2005)	76
Figure 2.46	Elastic and plastic strain energies (Socie, 2000)	78
Figure 2.47	Schematic presentation of the 3D-FE automatic fatigue crack growth technique: a) definition of a crack front; b) calculation of the displacement field of crack front nodes; c) calculation of stress intensity factors along the crack front; d) calculation of nodal advances of crack front nodes; e) relocation of corner and intermediate nodes (Branco, 2013)	88
Figure 2.48	Main parameters of the calculation procedure developed to predict the fatigue crack shape using the FEM (Branco, 2008)	89
Figure 2.49	Examples of a typical mesh topology used to analyse cracked bodies (Branco, 2008): a) spider web mesh; b) transition mesh; c) cracked region; d) uncracked region; e) assembled FE model	92
Figure 2.50	a) 20-node isoparametric brick element; b) quarter-point 20-node isoparametric brick element; c) collapsed 20-node isoparametric brick element; d) double collapsed 20-node isoparametric brick element; e) 15-node isoparametric wedge element (not collapsed); f) quarter-point 15-node isoparametric wedge element (not collapsed)	93
Figure 2.51	Relation between radial size of crack front elements (L_1) and singular region (r_s): a) $L_1 < r_s$; b) $L_1 \approx r_s$; c) $L_1 > r_s$ (Antunes, 1999)	95
Figure 2.52	Evolution of the optimum value of L_1 for different specimen geometries (Branco, 2008b)	96
Figure 2.53	Different degrees of mesh non-orthogonality (Lin, 1999)	97
Figure 2.54	Effect of the mesh orthogonality on the geometric factor using the quarter-point displacement method and the distance between: a) Q and A ; b) Q and A' (Lin, 1999)	97
Figure 2.55	Comparison of numerical and experimental crack shapes (Branco, 2006)	98
Figure 2.56	Crack front shape definitions: a) polygonal line; b) cubic spline curve	99

Figure 2.57	Quarter-point singular elements and coordinates for near crack-tip field description	100
Figure 2.58	Schematic representation of K calculation using the extrapolation method (Antunes, 1999)	102
Figure 2.59	a) Local virtual crack extension; b) uniform virtual crack extension	103
Figure 2.60	Evolution of W_E with ΔA (Antunes, 1999)	105
Figure 2.61	Effect of the crack growth increment on the: a) number of fatigue cycles (Lin, 1999b); b) crack shape (Branco, 2006)	107
Figure 2.62	Examples of dependent parameters used to characterise crack shape changes	109
Figure 2.63	Evolution of: a) crack aspect ratio (Lin, 1997); b) stress intensity factor (Branco, 2012d) in round bars with surface cracks subjected to tension	110
Figure 2.64	Evolution of: a) a/b with a/D for different values of m (Couroneau, 1998); b) transition depth with m for different loading types and geometries (Couroneau, 1998; Branco, 2008; Branco, 2008a)	111
Figure 2.65	Evolution of the crack aspect ratio with the dimensionless crack length in: a) round bars with surface cracks (Branco, 2009b); b) rectangular plates with surface cracks (Lin, 1999a) subjected to tension and bending	112
Figure 2.66	Evolution of the crack aspect ratio in: a) corner cracks emanating from fastener holes in plates (Lin, 1998); b) surface cracks of notched and unnotched round bars subjected to tension (Carpinteri, 2006a)	113
Figure 2.67	Evolution of the crack aspect ratio in: a) rectangular cross-section plates with surface cracks under tension (Lin, 1999a); b) round bars with surface cracks under tension (Carpinteri, 2010).	114
Figure 3.1	Comparison of lower yield strength versus lower ultimate tensile strength for various conventional and advanced high strength steels	119
Figure 3.2	Specimen geometry used in uniaxial tensile tests (in accordance with ASTM E8)	121
Figure 3.3	Scheme of electromechanical machine and experimental apparatus used in tensile tests	122

Figure 3.4	Test apparatus used in the determination of the experimental resonant frequencies by the impulse excitation technique	123
Figure 3.5	Specimen geometry used in the IET tests: a) initial geometry; b) final geometry	124
Figure 3.6	Specimen geometry used in LCF tests (in accordance with ASTM E606)	126
Figure 3.7	Scheme of experimental apparatus used in LCF tests	127
Figure 3.8	Specimens used in multiaxial fatigue tests: a) single bending and in-phase combined bending-torsion; b) single torsion	128
Figure 3.9	Proportional loading paths applied in fatigue tests: a) single bending (B); b) in-phase bending-torsion ($B=2T$); c) in-phase bending-torsion ($B=T$); d) in-phase bending-torsion ($B=2T/3$); e) single torsion (T)	129
Figure 3.10	a) Servo-hydraulic testing machine used in fatigue tests. Details of the gripping system assembled for: b) single bending; c) single torsion; d) in-phase combined bending torsion ($B=2T$) tests	131
Figure 3.11	Digital monitoring system used in detection of crack initiation and growth. Details of the: a) digital camera and optical device; b) micrometre driven translation stage	131
Figure 3.12	Relation between the force applied by the piston of the testing machine and the resultant bending and torsion moments at the specimen: a) single bending; b) single torsion; c) in-phase combined bending-torsion tests	133
Figure 3.13	Sample for OM and SEM analyses: a) material supplied; b) sample used	136
Figure 3.14	a) Optical microscope (Carl Zeiss Axiotech 100HD model); b) scanning electron microscope (Philips XL30 model)	136
Figure 3.15	Triangulation scanner principle: a) point; b) line; c) pattern	138
Figure 3.16	a) Roland Picza 3D Laser Scanner LPX-600; b) typical aspect of samples after painting	139
Figure 3.17	Mixed numerical-experimental technique proposed to calculate the constants of the Paris law	140
Figure 3.18	Specimen geometry used in crack front marking tests	140

Figure 3.19	a) Fracture surface (initial crack of 1.0mm, 25kN cyclic tension loading); b) sketch of the visible crack fronts used	141
Figure 4.1	Types of specimen geometries analysed: a) round bar; b) rectangular cross-section plate; c) disk; d) half-disk; e) half-disk with hole	146
Figure 4.2	a) Three-dimensional finite element mesh; b) first longitudinal bending resonant mode (f_1); c) first torsional resonant mode (f_2)	148
Figure 4.3	Algorithm of the iterative procedure used to calculate the elastic constants	148
Figure 4.4	Physical models of the: a) single bending test; b) single torsion test; c) in-phase combined bending-torsion test	149
Figure 4.5	Schematic presentation of finite element mesh generation: a) primary points; b) relation between primary and secondary points; c) volumes of notched region	150
Figure 4.6	Finite element mesh: a) assembled model; b) detail of the notched region; c) detail of the middle-section of the notched region	151
Figure 4.7	a) Evolution of σ_{vM}/σ_1 with the number of elements on the curve N_3 ; b) variation of σ_{vM}/σ_1 with the number of elements on the curve N_3	152
Figure 4.8	Dimensionless sensitivities of the ratio σ_{vM}/σ_1 to the number of elements on the curves N_i	153
Figure 4.9	Schematic presentation of the 3D-FE fatigue crack growth technique used: a) definition of the crack front; b) calculation of the displacement field of crack front nodes; c) calculation of stress intensity factors along the crack front; d) calculation of nodal advances along the crack front; e) relocation of corner and intermediate nodes of the crack front	154
Figure 4.10	Geometries studied: a) rectangular bar with corner crack; b) notched rectangular bar with corner crack; c) round bar with surface crack; d) notched round bar with surface crack; e) plate with surface crack; f) notched plate with surface crack; g) plate with through crack; h) notched plate with through crack	154
Figure 4.11	Physical models: a) rectangular bar with corner crack; b) notched rectangular bar with corner crack; c) round bar with surface crack; d) notched round bar with surface crack; e) plate with surface crack; f) notched plate with surface crack; g) plate with through crack; h) notched plate with through crack	155

Figure 4.12	Methodology used to create the FE meshes for crack shape modelling: a) standard 20-node isoparametric element; b) collapsed 20-node isoparametric element; c) collapsed 20-node isoparametric element with intermediate nodes at quarter-point positions; d) crack front definition; e) spider web mesh; f) spider web and transition meshes; g) assembled model	156
Figure 4.13	Definition of the: a) number of elements of the unnotched geometries; b) number of elements of the notched geometries; c) radial size of the elements of spider web and transition meshed	157
Figure 4.14	Typical FE mesh used in fatigue crack growth simulations for notched plates with through cracks ($r = 1.75\text{mm}$, $n = 2\text{mm}$, $t = 7.5\text{mm}$, $L = 200\text{mm}$, $W = 50\text{mm}$): a) general overview; b) detail of the notch; c) detail of the crack tip and the spider web mesh	158
Figure 4.15	Schematic determination of stress intensity factors along the crack front using the extrapolation method with two points; b) identification of nodes moved to quarter-point positions	159
Figure 4.16	a) Calculation of local crack increments; b) positioning the corner and intermediate nodes by using a cubic spline function	161
Figure 4.17	Methodology used to calculate the extent of the surface region: a) FCG simulation; b) creation of a refined 3D-FE mesh; c) calculation of the stress components at the crack front; d) computation of triaxiality parameters and analysis of results	163
Figure 4.18	Typical refined FE mesh used to evaluate the extent of the surface region for the notched round bar with surface crack: a) general overview; b) detail of notch; c) detail of layer refinement	165
Figure 4.19	Relation between the global and local Cartesian coordinate systems defined to calculate the stress tensors of the crack front nodes	166
Figure 4.20	a) Grooved M(T) specimen; b) U-shaped groove; c) V-shaped groove	168
Figure 4.21	Typical FE meshes used: a) general overview; b) crack tip; c) notch plane; d) refinement towards thickness ($L = 200\text{ mm}$, $2W = 50\text{ mm}$, $r = 1.5\text{mm}$, $n = 3\text{mm}$, $t = 5\text{mm}$, $\eta = 0^\circ$)	169

Figure 4.22	Simplified methodology for defining a plane strain specimen assuming straight crack shapes: a) development of a refined finite element mesh; b) calculation of stress components at the crack front; d) computation of triaxiality parameters and analysis of results	170
Figure 4.23	Mixed numerical-experimental technique proposed to determine the constants of the Paris law: a) physical model; b) finite element mesh	171
Figure 4.24	Definition of the <i>ad</i> dependent parameters used to predict the crack shape	172
Figure 5.1	Microstructure of the DIN 34CrNiMo6 high strength steel from a sample polished and etched with nital: a) optical microscopy; b) scanning electron microscopy (Branco, 2012b)	176
Figure 5.2	Monotonic stress-strain curves obtained in the tensile tests	177
Figure 5.3	Tensile fracture surfaces obtained by SEM: a) low magnification; b) high magnification	178
Figure 5.4	a) Output signal versus time; b) response in frequency domain obtained by FFT analysis for the rectangular cross-section specimen (Branco, 2009c)	179
Figure 5.5	Dimensionless sensitivities of the elastic constants to the material density, experimental resonant frequencies and specimen dimensions (Branco, 2009c)	180
Figure 5.6	Stress-strain hysteresis loops: a) $\Delta\epsilon/2 = \pm 2.0\%$; b) $\Delta\epsilon/2 = \pm 0.8\%$ (Branco, 2012e)	182
Figure 5.7	Evolution of the stress amplitude with the: a) number of cycles; b) life ratio for different strain amplitudes (Branco, 2012b)	184
Figure 5.8	Cyclic stress-strain curve obtained by connecting the tips of stable hysteresis loops for different strain amplitudes of fully-reversed strain-controlled tests (Branco, 2012e)	185
Figure 5.9	Relationship between cyclic stress amplitude and elastic strain amplitude (Branco, 2012e)	186
Figure 5.10	Monotonic and cyclic stress-strain curves of DIN 34CrNiMo6 (Branco, 2012b)	186
Figure 5.11	Degree of softening versus strain amplitude	187

Figure 5.12	Cyclic stress-strain curve obtained by connecting the compressive tips of the stable hysteresis loops of different strain amplitudes (Branco, 2012b)	188
Figure 5.13	Master curve obtained by matching the upper branches of hysteresis loops of different strain amplitudes (Branco, 2012b)	189
Figure 5.14	Stress amplitude versus number of reversals to failure	190
Figure 5.15	Plastic strain amplitude versus number of reversals to failure	191
Figure 5.16	Total strain-life, fatigue strength-life and fatigue ductility-life curves (Branco, 2012b)	192
Figure 5.17	Plastic strain energy dissipated per cycle versus number of reversals to failure (Branco, 2012b)	193
Figure 5.18	Calculated versus experimentally measured plastic strain energy dissipated per cycle	194
Figure 5.19	Strain energy density range per cycle versus number of reversals to failure	195
Figure 5.20	Macroscopic surface morphologies of low-cycle fatigue specimens: a) $\Delta\epsilon/2=0.5\%$; b) $\Delta\epsilon/2=0.8\%$; c) $\Delta\epsilon/2=1.25\%$; d) $\Delta\epsilon/2=1.5\%$ (Branco, 2012b)	196
Figure 5.21	Fracture surfaces for different values of $\Delta\epsilon/2$ (Branco, 2012b): a) $\Delta\epsilon/2 = 0.4\%$; b) $\Delta\epsilon/2 = 2.0\%$; c) $\Delta\epsilon/2 = 2.0\%$ (detail of fatigue striations combined with secondary cracks)	197
Figure 5.22	SEM micrographs of fracture surfaces near the crack initiation site for different total strain amplitudes: a) $\Delta\epsilon/2 = 0.4\%$; b) $\Delta\epsilon/2 = 1.0\%$; c) $\Delta\epsilon/2 = 2.0\%$ (Branco, 2012b)	198
Figure 5.23	Surface crack paths and initiation sites for different loading paths. Specimen reference: a) B-1; b) B2T-2; c) BT2-1; d) B2T3-2; e) T-1	201
Figure 5.24	Numerical prediction of surface crack paths and initiation sites for different loading paths: a) B; b) B=2T; c) B=T; d) B=2T/3; e) T (Branco, 2012e)	201
Figure 5.25	Surface crack orientation at the early stage of crack growth for different loading paths. Specimen reference: a) B-m; b) B2T-m; c) BT-m; d) B2T3-m; e) T-m (Branco, 2012e)	202

Figure 5.26	Experimental versus predicted crack surface angles at the initial stage of crack growth for different loading paths	203
Figure 5.27	Multi-crack initiation sequence in a single bending test (specimen B-4): a) 42010 cycles; b) 45020 cycles; c) 50007 cycles; d) 56011 cycles	204
Figure 5.28	Fracture surfaces of fatigue crack front marking tests for the different loading paths. Specimen reference: a) B-m; b) B2T-m; c) BT-m; d) B2T3-m; e) T-m	205
Figure 5.29	Crack aspect ratio (a'/b') versus dimensionless crack length (a'/D')	206
Figure 5.30	Fracture surfaces obtained by 3D scanner for the different loading paths. Specimen reference: a) B-m; b) B2T-m; c) BT-m; d) B2T3-m; e) T-m	207
Figure 5.31	SEM micrographs of fracture surfaces near the crack initiation site for a single bending test magnified: a) 750 times; b) 1000 times	208
Figure 5.32	SEM micrographs of fracture surfaces near the crack initiation site for an in-phase combined bending-torsion test ($B=2T/3$) magnified: a) 99 times; b) 750 times	209
Figure 5.33	SEM micrographs of fracture surfaces near the crack initiation site for a single torsion test magnified: a) 200 times; b) 1000 times	210
Figure 5.34	SEM micrographs of fracture surfaces containing several inclusions: a) single bending loading; b) in-phase combined bending-torsion loading ($B=2T/3$)	211
Figure 5.35	SEM micrographs of fracture surfaces revealing multi-crack initiation. Specimen reference: a) B2T3-1; b) B2T3-m; c) B2T-m	212
Figure 5.36	SEM micrographs of fracture surfaces revealing the junction of two cracks initiated at the notch surface: a) left side; b) right side of the fracture step	213
Figure 5.37	Crack length definition to obtain the 2b-N curves: a) close cracks; b) cracks overlapped	214
Figure 5.38	Crack length versus number of loading cycles for the in-phase combined bending-torsion loading tests ($B=2T$)	214
Figure 5.39	Crack length versus number of loading cycles for the in-phase combined bending-torsion loading tests ($B=T$)	215

Figure 5.40	Crack length versus number of loading cycles for the in-phase combined bending-torsion loading tests ($B=2T/3$)	215
Figure 5.41	Notch surface: a) BT-2 test ($2b \approx 3.86\text{mm}$); b) BT-1 test ($2b \approx 0.95\text{mm}$)	216
Figure 5.42	Crack length versus number of loading cycles for tests performed under the same normal stress amplitude for different loading paths	217
Figure 5.43	Normal stress amplitude versus number of cycles to failure for the in-phase combined bending-torsion tests	218
Figure 5.44	Normal stress amplitude versus number of cycles to failure for the single bending tests	219
Figure 5.45	Shear stress amplitude versus number of cycles to failure for the single torsion tests	219
Figure 5.46	Local von Mises equivalent stress amplitude versus fatigue life for the different loading paths studied	220
Figure 5.47	Local von Mises equivalent stress amplitude versus number of cycles in which at the first time the crack reached a surface length equal to 0.5mm	221
Figure 5.48	Relation between $N_{0.5}$ and N_f for the different loading paths studied	222
Figure 5.49	Range of the threshold of the stress intensity factor versus stress ratio	223
Figure 5.50	Local von Mises equivalent stress range versus distance from the notch surface for a specimen subjected to single bending	225
Figure 5.51	Dimensionless local von Mises equivalent stress range ($\Delta\sigma_{vmL}/\Delta\sigma_{vmL,max}$) versus the dimensionless distance from the notch surface (d/D_{PM}) for the different loading paths studied	225
Figure 5.52	Detail of crack front marks obtained in a test performed under in-phase combined bending-torsion loading (Specimen reference: BT-m)	226
Figure 5.53	Experimentally obtained versus predicted fatigue lives obtained by the Coffin-Manson model	228

Figure 5.54	Experimentally obtained versus predicted fatigue lives obtained by the Smith, Watson and Topper model	228
Figure 5.55	Hysteresis loops obtained for a single bending test by applying the strain energy density concept (Case B-3)	230
Figure 5.56	Experimentally obtained versus predicted fatigue lives obtained by the Coffin-Manson model	232
Figure 5.57	Experimentally obtained versus predicted fatigue lives obtained by the Smith, Watson and Topper model	232
Figure 5.58	Probability density functions of fatigue life predictions for the CM and SWT models	234
Figure 6.1	Schematic illustration of the calculation procedure (Branco, 2011a)	237
Figure 6.2	Graphical-user interface: a) specimen geometry; b) crack shape; c) material properties and loading definitions; d) FE mesh (Branco, 2011a)	239
Figure 6.3	Graphical-user interface: a) calculation of stress intensity factor; b) maximum crack front advance; c) transition options; d) output definitions (Branco, 2011a)	240
Figure 6.4	Main graphical user interface (Branco, 2011a)	241
Figure 6.5	Algorithm to carry out an automatic transition from a corner or surface crack to a through crack: a) general overview; b) identification of the main stages	242
Figure 6.6	Identification of numerical independent parameters that affect the accuracy of a numerical procedure able to study the fatigue crack growth based on the finite element method (Branco, 2013a)	243
Figure 6.7	Evolution of the stress intensity factor along the crack front in a rectangular plate with through crack ($T=5\text{mm}$, $L=200\text{mm}$, $2W=50\text{mm}$, $a=12.5\text{mm}$, $L_1=\text{constant}$) subjected to tension (Branco, 2013a)	244
Figure 6.8	Evolution of the K_I/K_{\max} ratio along the crack front in a notched round bar with a semi-circular surface crack of 1.5mm subjected to tension ($D = 24\text{mm}$, $L=200\text{mm}$, $r=1.5\text{mm}$, $n=2\text{mm}$, $a=1.5\text{mm}$, $L_1=\text{constant}$)	246

- Figure 6.9 Evolution of the K_i/K_{max} ratio along the crack front in a rectangular plate with a straight crack ($T = 5\text{mm}$, $L = 200\text{mm}$, $2W = 50\text{mm}$, $a = 12.5\text{mm}$, $L_1 = \text{constant}$) subjected to tension (Branco, 2013a) 247
- Figure 6.10 Evolution of the K_i/K_{max} ratio along the crack front in a notched plate with a through crack ($T = 10\text{mm}$, $L = 200\text{mm}$, $2W = 50\text{mm}$, $a_m = 12.47\text{mm}$, $r = 1.5\text{mm}$, $n = 2\text{mm}$) subjected to tension (Branco, 2013a) 248
- Figure 6.11 Evolution of the K_i/K_{max} ratio along the crack front in a notched round bar with a semi-circular surface crack subjected to tension ($D = 16\text{mm}$, $L = 200\text{mm}$, $a_m = 2.55\text{mm}$, $r = 0.75\text{mm}$, $n = 1.5\text{mm}$) 249
- Figure 6.12 Evolution of the K_i/K_{max} ratio along the crack front in rectangular plate with a curved crack front ($T = 10\text{mm}$, $L = 200\text{mm}$, $2W = 50\text{mm}$, $a_m = 12.53\text{mm}$) subjected to tension (Branco, 2013a) 250
- Figure 6.13 Effect of Δa_{max} on a/b in a round bar with a surface crack ($D = 16\text{mm}$, $L = 100\text{mm}$) 251
- Figure 6.14 Crack front developments in unnotched round bars ($D = 16\text{mm}$, $L = 100\text{mm}$, $m = 3$, $n = 0.30$, $E = 210\text{ GPa}$) from different initial defects subjected to tension: a) part-circular shape ($a_0/D = 0.1$, $a_0/b_0 = 1$); b) straight shape ($a_0/D = 0.1$, $a_0/b_0 = 0$) 252
- Figure 6.15 Crack front developments in notched round bars ($D = 16\text{mm}$, $L = 100\text{mm}$, $r = 0.5\text{mm}$, $n = 2\text{mm}$, $m = 3$, $\nu = 0.30$, $E = 210\text{ GPa}$) from a semi-circular crack ($a_0/D = 0.0625$, $a_0/b_0 = 1$) subjected to: a) tension; b) bending 253
- Figure 6.16 Evolution of the: a) crack aspect ratio with the dimensionless crack length; b) ratio K_{min}/K_{max} ratio with the dimensionless crack length (Branco, 2012d) 254
- Figure 6.17 Effect of the: a) notch radius; b) loading type; c) thickness; d) crack closure on the crack shape (Branco, 2012a) 257
- Figure 6.18 Evolution of the crack aspect ratio (d/t) with the dimensionless crack length (a/W) for notched ($L = 200\text{mm}$, $2W = 50\text{mm}$, $t = 5\text{mm}$, $r = 1.5\text{mm}$, $n = 2\text{mm}$) and unnotched ($L = 200\text{mm}$, $2W = 50\text{mm}$, $t = 5\text{mm}$) plates with through cracks subjected to tension (Branco, 2013) 259
- Figure 6.19 Evolution of the K_{min}/K_{max} ratio with the dimensionless crack length in notched ($L = 200\text{mm}$, $2W = 50\text{mm}$, $t = 5\text{mm}$, $r = 1.5\text{mm}$, $n = 2\text{mm}$) and unnotched ($L = 200\text{mm}$, $2W = 50\text{mm}$, $t = 5\text{mm}$) plates with through cracks subjected to tension (Branco, 2013) 260

Figure 6.20	Crack front profiles selected to compute the h stress triaxiality parameter at the crack front in: a) unnotched and notched rectangular bars with corner cracks; b) unnotched and notched round bars with surface cracks; c) unnotched and notched plates with through cracks	261
Figure 6.21	Evolution of the h stress triaxiality parameter with the dimensionless position (x/t) in a notched plate with through crack considering two mesh densities towards the thickness ($r=0.5\text{mm}$, $n=1.0\text{mm}$, $t=10\text{mm}$)	262
Figure 6.22	Evolution of Θ and h stress triaxiality parameters with the dimensionless position (x/t) in a notched plate with through crack ($r=0.5\text{mm}$, $n=1.0\text{mm}$, $t=5\text{mm}$) for two different values of ν	263
Figure 6.23	Effect of: a) specimen geometry; b) notch radius; c) specimen size; d) notch depth and crack length on the stress triaxiality (Branco, 2012a)	264
Figure 6.23	(continued). Effect of: e) crack length and exponent of the Paris law; f) crack closure; g) loading; h) Poisson's ratio on the stress triaxiality (Branco, 2012a)	265
Figure 6.24	Definitions of surface, near-surface and interior regions (Branco, 2012a)	267
Figure 6.25	Evolution of S_1 with a/W : a) notched rectangular bars with corner cracks; b) notched round bars with surface cracks; c) notched plates with through cracks (Branco, 2012a)	269
Figure 6.26	Evolution of S_1 with a/W for unstable crack shapes (Branco, 2012a)	271
Figure 6.27	Evolution of S_2 with a/W : a) notched rectangular bars with corner cracks; b) notched round bars with surface cracks; c) notched plates with through cracks (Branco, 2012a)	272
Figure 6.28	Evolution of S_2 with a/W for unstable crack shapes (Branco, 2012a)	273
Figure 6.29	Evolution of S_1 and S_2 : a) notched rectangular bars with corner cracks; b) notched round bars with surface cracks (Branco, 2012a)	275
Figure 6.29	(continued). Evolution of S_1 and S_2 : c) notched plates with through cracks (Branco, 2012a)	276

Figure 6.30	Evolution of S_1 and S_2 with K_T : a) notched rectangular bars with corner cracks; b) notched round bars with surface cracks; c) notched plates with through cracks (Branco, 2012a)	277
Figure 6.31	Effect of: a) groove; b) thickness on fatigue crack shape developments ($L = 200\text{mm}$, $2W = 50\text{mm}$, $a_0/W = 0.2$) obtained in standard M(T) and notched M(T) specimens (Branco, 2013a)	280
Figure 6.32	Effect of the: a) thickness and crack length; b) groove radius; c) groove depth and groove angle; d) exponent of the Paris law and Poisson's ratio on the h-curves (Branco, 2013)	282
Figure 6.33	Scheme of the strategy adopted to define the plane strain specimen (Branco, 2013)	284
Figure 6.34	Evolution of p_β for: a) $\beta = 0.96$; b) $\beta = 0.94$ in standard and modified M(T) specimens (Branco, 2013)	286
Figure 6.35	Different combinations of r , t and n for different plane strain state criteria (Branco, 2013)	288
Figure 6.36	Effect of: a) thickness; b) groove radius; c) groove depth; d) groove angle and crack shape on the h-curves (Branco, 2010a)	289
Figure 6.37	Evolution of p_β for: a) $\beta = 0.96$; b) $\beta = 0.94$ in an analysis based on straight crack fronts	291
Figure 6.38	Comparison of p_β values considering stable crack fronts and straight crack fronts	292
Figure 6.39	Stress intensity factor solution for the plane strain specimen	293
Figure 6.40	Sensitivity analysis of the main independent variables	294
Figure 6.41	Fatigue crack shape developments of different initial surface cracks in round bars subjected to tension and bending (Branco, 2012c)	295
Figure 6.42	Fatigue propagation paths of different initial configurations in round bars subjected to tension and bending (Branco, 2012c; Branco, 2012d)	296
Figure 6.43	Determination of the Paris law exponent (Branco, 2012d)	297

Figure 6.44 Determination of the Paris law constant (Branco, 2012d)

299

Figure 6.45 Evolution of d_i/r_i with θ_i for several experimental crack fronts (Branco, 2012d)

300

LIST OF TABLES

	Page
Table 2.1 Ratios of the fatigue limit in torsion to in rotating bending for different materials (Frost, 1999)	16
Table 2.2 Ratios of the fatigue limit in torsion to in rotating bending for different materials (Frost, 1999)	21
Table 2.3 Fatigue limit at various testing frequencies for different materials (Krouse, 1934) .	22
Table 2.4 Size effect of specimen diameter on fatigue limit (Frost, 1999)	27
Table 2.5 Different methods used to obtain a cyclic stress-strain curve (Ellyin, 1997)	30
Table 2.6 Rotation factor for different strain histories (Socie, 2000)	56
Table 2.7 Non-proportional hardening coefficient for various materials (Socie, 2000)	57
Table 3.1 Equivalent standard grades (DIN 34CrNiMo6)	120
Table 3.2 Nominal chemical composition of DIN 34CrNiMo6 (wt%)	120
Table 3.3 Total strain and total stress amplitudes defined in low-cycle fatigue tests	126
Table 3.4 Summary of loading conditions tested in single bending tests	129
Table 3.5 Summary of conditions tested in single torsion tests	129
Table 3.6 Summary of loading conditions tested in-phase combined bending-torsion tests	130
Table 3.7 Main dimensions used in the tests	133
Table 3.8 Loading used in fatigue crack front marking tests	135
Table 3.9 Details of the fatigue crack front marking process	135
Table 3.10 Summary of fracture surfaces analysed by SEM	137
Table 3.11 Scanning settings selected	139

Table 3.12	Nominal chemical composition of S45 carbon steel (wt%)	140
Table 3.13	Mechanical properties of S45 carbon steel at room temperature	140
Table 3.14	Polar coordinates of the experimental crack shapes used	141
Table 3.15	Number of cycles between the experimental crack fronts	142
Table 4.1	Sensitivities of the resonant frequencies to the Young's modulus and to the Poisson's ratio	146
Table 4.2	Initial and final densities of the finite element mesh	151
Table 4.3	Physical dimensions used in simulations of crack shape evolution	156
Table 4.4	Minimum numbers of elements and nodes used in FE meshes	159
Table 4.5	Details of FCG simulations of the unnotched and notched rectangular bars with corner cracks	163
Table 4.6	Details of FCG simulations of the unnotched and notched round bars with surface cracks	164
Table 4.7	Details of FCG simulations of the unnotched and notched plates with through cracks	164
Table 4.8	Details of FCG simulations ($L=200$ mm, $2W=50$ mm, $a_0=0.5$ mm)	169
Table 5.1	Standard heat treatments applied to DIN 34CrNiMo6 steel (ASM, 2000)	175
Table 5.2	Mechanical properties of the DIN 34CrNiMo6 high strength steel	177
Table 5.3	Calculation of the elastic constants of the DIN 34CrNiMo6 high strength steel	180
Table 5.4	Results of low-cycle fatigue tests	183
Table 5.5	Cyclic stress-strain curve parameters of DIN 34CrNiMo6 high strength steel	186
Table 5.6	Master curve parameters of DIN 34CrNiMo6 high strength steel	188
Table 5.7	Fatigue strength properties of DIN 34CrNiMo6 high strength steel	190
Table 5.8	Fatigue ductility properties of DIN 34CrNiMo6 high strength steel	191

Table 5.9	Experimental and theoretical values of ΔW_p	194
Table 5.10	Constants of Eq. 5.16 for DIN 34CrNiMo6 high strength steel	194
Table 5.11	Constants of Eq. 5.19 for DIN 34CrNiMo6 high strength steel	195
Table 5.12	Summary of results of the single bending tests	199
Table 5.13	Summary of results of the single torsion tests	199
Table 5.14	Summary of results of the in-phase combined bending-torsion tests	200
Table 5.15	Comparison between experimental and predicted surface crack orientations	203
Table 5.16	Constants of the S-N curves obtained in the present research	218
Table 5.17	Constants of Equation 5.23 for the mean curve and upper and lower bound	220
Table 5.18	Constants of Equation 5.24 for the mean curve and upper and lower bound	222
Table 5.19	Material properties for DIN 34CrNiMo6 high strength steel (Luke, 2011)	223
Table 5.20	Experimental and predicted fatigue lives for the single bending tests	227
Table 5.21	Experimental and predicted fatigue lives for the single torsion tests	227
Table 5.22	Experimental and predicted fatigue lives for the in-phase combined bending-torsion tests	227
Table 5.23	Experimental and predicted fatigue lives for the single bending tests	230
Table 5.24	Experimental and predicted fatigue lives for the single torsion tests	231
Table 5.25	Experimental and predicted fatigue lives for the in-phase combined bending-torsion tests	231
Table 5.26	Statistical data for the N_e/N_p ratios obtained from the CM model	233
Table 5.27	Statistical data for the N_e/N_p ratios obtained from the SWT model	233
Table 6.1	Sizes of the elements of spider web mesh and transition mesh	247
Table 6.2	Constants of Equation 6.5 (Branco, 2012a)	274

Table 6.3	Constants of Equation 6.6 and Equation 6.7 (Branco, 2012a)	278
Table 6.4	Constants of Equation 6.8 (Branco, 2012a)	279
Table 6.5	Main geometrical variables of the plane strain specimens (Branco, 2013)	287
Table 6.6	Predicted C and m constants for different combinations of the experimental crack shapes used (Branco, 2012d)	299

CHAPTER 1

INTRODUCTION

This chapter provides an introduction to the research topic and describes in detail the main purposes of the thesis.

NOMENCLATURE

a	crack length
FEM	finite element method
N	number of loading cycles
S	applied stress
SEM	scanning electron microscopy

1.1. Introduction

High strength steels cover a broad spectrum of applications and are being increasingly used in different areas due to both good strength-to-weight ratio and good corrosion resistance. DIN 34CrNiMo6, in particular, combines deep hardenability, high ductility, toughness and strength. These features make it ideal for critical components, such as shafts, axles, crankshafts, connecting rods, pinions, torsion bars, bolts, aircraft components, high pressure vessels for nuclear plants, among others.

In general, such components are subjected to severe service conditions and complex loading. Besides, they have geometric discontinuities introduced by design and functional purposes. These characteristics make them susceptible to fatigue failure. For the material studied in the present research, there are many cases of fatigue failure reported in the literature. In the last few years, some critical examples are drive shafts (Savković, 2012), connecting rods (Griza, 2009), diesel generator crankshafts (Espadafor, 2009), train axles (Yu, 2009), bolts and pins (Yu, 2008), wing-fuselage connectors (Witek, 2006) and cargo aircraft main landing gears (Eliaz, 2005).

Therefore, fatigue failure remains to be a major concern. Fatigue failure is a sequential process that encompasses three main stages, i.e. crack initiation, crack propagation and final fracture. It is a result of numerous factors and can cause not only a large loss of money but also loss of lives. Despite the significant progress achieved in the last decades, several factors affecting fatigue phenomenon are not completely understood. In order to reduce the risk of unexpected in-service failure, additional research on fatigue life prediction of notched components under complex loading is required.

In notched components, the highest stresses and strains are found close to the notch root. Due to stress and strain concentration phenomena, nominal elastic stresses can result in elastoplastic stress-strain fields around the notch. The fatigue damage accumulation caused by cyclic loading at the notch root is likely to lead to crack initiation and crack propagation which can culminate in fatigue failure. Therefore, a crucial task in the design of notched components is an effective evaluation of the fatigue life. Nonetheless, the complexity of the problem depends on several variables, including the notch geometry, loading type, loading magnitude, among others. The effect of a biaxial loading in notched components is a current research topic. However, there are no significant data on combined bending-torsion loading.

In certain situations, particularly in notched components, the crack propagation stage can be dominant in terms of total fatigue life. Technological processes, such as casting, welding, machining, etc., may enhance the importance of this stage, since they introduce small defects that act as local stress raisers making easier the crack initiation. In this sense, an efficient prediction of fatigue crack propagation life is fundamental for an effective design. Numerical methods have proved to be reliable tools to address fatigue crack growth problems. Nevertheless, this approach requires specific algorithms, usually not available in commercial software, implying additional programming tasks, which are time-consuming and laborious. On the other hand, the existing reliable software has been developed by research groups and is

not available commercially. Therefore, there is a need to create new software especially suited to the study of fatigue crack growth.

1.2. Research objectives

The first objective of the thesis is to contribute to a better understanding of the fatigue behaviour of DIN 34CrNiMo6 high strength steel under in-phase combined bending-torsion loading. In order to meet this aim, severely notched specimens subjected to constant amplitude loading are studied. More specifically, this investigation includes the following tasks:

- Experimental characterisation of the material in terms of microstructure, elastic constants, monotonic and cyclic properties, fatigue strength and fatigue ductility properties, and hysteresis loop shapes;
- Experimental determination of both a-N and S-N curves for notched specimens subjected to different in-phase combined bending-torsion loadings;
- Experimental analysis and numerical prediction of initiation sites, fatigue crack paths and surface crack angles at the initial stage of crack growth;
- Analysis of crack initiation sites by SEM in order to identify the damage mechanisms involved in the fatigue process and three-dimensional laser scanning of fracture topologies;
- Development of an appropriate finite element model able to evaluate the local stress and local strain fields around the notch and identification of an appropriate fatigue damage parameter;
- Prediction of fatigue life for notched specimens subjected to in-phase combined bending-torsion loading using different fatigue life prediction models available in the literature.

The second objective of the thesis is the development of user-friendly software able to address fatigue crack growth problems as well as its optimisation, validation and application to specific issues. Briefly, the main tasks are the following:

- Development and programming of an efficient calculation procedure with a user-friendly interface able to study in-plane fatigue crack growth problems;
- Systematic identification and optimisation of the independent variables affecting the accuracy of the calculation procedure;
- Validation of the calculation procedure developed here by comparing the numerical results obtained with those available in the literature;
- Application of the software to evaluate the extent of surface regions in notched specimens with different types of crack front, namely surface cracks, corner cracks and through cracks;
- Definition of a plane strain specimen to be applied in the study of different phenomena affected by the stress state, for instance those involving diffusion, plastic deformation and brittle fracture;
- Determination of the Paris law constants from the analysis of crack fronts marked on fracture surfaces of small cross-section round bars.

1.3. Outline of thesis

The present thesis is organised into seven chapters. A brief description of each one is given below:

- Chapter 1 provides an introduction to the research topic and describes in detail the main purposes of the thesis;
- Chapter 2 is devoted to the literature review. It is divided into two main parts. The first tackles the fatigue phenomenon. It identifies the main variables affecting fatigue and describes some of the models used to predict the fatigue life of notched components and to predict the fatigue life under multiaxial loading. The second is focused on the numerical modelling of fatigue crack growth using the finite element method;
- Chapter 3 outlines the experimental procedure. It describes the material, specimen geometries and testing apparatus used in the monotonic tensile tests, determination of the elastic constants, low-cycle fatigue tests, in-phase combined bending-torsion tests and fatigue crack front marking tests. The details on the procedures used to analyse the microstructure of the material and the fracture surfaces by scanning electron microscopy and optical microscopy; to acquire the fracture surfaces by three-dimensional laser scanner; and to determine the Paris law constants from fatigue crack front marks are also provided in this chapter;
- Chapter 4 describes the numerical procedure. The two first sections present the numerical models developed to calculate the elastic constants of the material and to evaluate the stress and strain fields at the notch tip for the in-phase combined bending-torsion tests. The third section is concerned with the fatigue crack growth models implemented to study the crack shape evolution in notched and unnotched rectangular bars with corner cracks, notched and unnotched round bars with surface cracks, and notched and unnotched plates with through cracks. The three last sections address the strategies used to evaluate the extent of the surface region in cracked bodies; to develop a plane strain specimen; and to determine the Paris law constants from the analysis of crack front marks on fracture surfaces of small cross-section round bars;
- Chapter 5 details the experimental findings. In the first section, the microstructure of the material is analysed. The second section presents the results of the monotonic uniaxial tests. The third section tackles the calculation of the elastic constants. The fourth section is devoted to the low-cycle fatigue tests and the analysis of the fracture surfaces by SEM. The last section is concerned with the in-phase combined bending-torsion tests. It encompasses the analysis of initiation sites, fatigue crack paths, surface crack angles, topologies of fracture, crack front profiles, among others. The determination of the fatigue life in terms of a-N and S-N curves as well as the fatigue life predictions using different methods available in the literature are also presented here;
- Chapter 6 contains the numerical findings. The first section is devoted to the presentation of the in-plane fatigue crack growth software developed in the present research. It encompasses the identification and optimisation of the main variables affecting the accuracy of the numerical procedure as well as the validation of the numerical results. The second section evaluates the extent of the surface region in notched geometries. The third section deals with the development of a plane

strain specimen. The last section concerns the determination of Paris law constants from the analysis of fatigue crack front marks on fracture surfaces of small cross-section round bars;

- Chapter 7 presents the main conclusions of the thesis and identifies some relevant topics that merit additional research.

CHAPTER 2 - LITERATURE REVIEW

PART A - FATIGUE PHENOMENON

This chapter is devoted to the literature review and contains two main parts (Part A and Part B). Part A tackles the fatigue phenomenon and is organised into four sections. The first section identifies the main variables affecting fatigue. The second and third sections address both the different fatigue design philosophies and the cyclic stress-strain response. The fourth section deals with the fatigue life prediction models for notched bodies. The last section is focused on the multiaxial fatigue damage models.

NOMENCLATURE

a_0	intrinsic crack length	$\Delta\varepsilon_p$	plastic strain range
b	fatigue strength exponent	$\Delta\varepsilon_{eq}$	equivalent normal strain
$b\gamma$	shear fatigue strength exponent	$\Delta\varepsilon$	total strain range
c	fatigue ductility exponent	$\Delta\sigma$	normal stress range
$c\gamma$	shear fatigue ductility exponent	$\Delta\sigma_1, \Delta\sigma_2, \Delta\sigma_3$	principal stress ranges
D	notch depth	$\Delta\sigma_{eq}$	equivalent stress range
D_{PM}	critical distance for the point method	$\Delta\tau$	shear stress range
D_{LM}	critical distance for the line method	ΔW_p	plastic strain energy absorbed per cycle
D_{AM}	critical distance for the area method	ΔW_e	elastic strain energy absorbed per cycle
E	Young's modulus	ΔW_{e+}	elastic strain energy associated with the tensile stress
f_0	pulse bending fatigue limit	ΔW_{eff}	effective strain energy density
f_{-1}	fully-reversed bending fatigue limit	ΔW_t	total strain energy absorbed per cycle
$f(\varepsilon_{ij})$	equivalent strain function	ΔW_{0p}	hysteresis energy of the material at the fatigue limit
$f(\sigma_{ij})$	equivalent stress function	ΔW_{0t}	tensile elastic energy of the material at the fatigue limit
F	rotation factor	$\Delta\tau$	shear stress range
FEM	finite element method	ΔK_{th}	long crack threshold stress intensity factor range
G	shear modulus	$\varepsilon_1, \varepsilon_2, \varepsilon_3$	principal strains
HCF	high-cycle fatigue	ε_f'	fatigue ductility coefficient
IST	incremental step test	ε_{FI}	strain intensity function
K_T	stress concentration factor	ε_m	mean strain
K_f	fatigue strength reduction factor	ε_{nom}	nominal strain
K_σ	stress concentration factor	ε_n^p	nominal plastic strain
K_ε	strain concentration factor	χ	relative stress gradient
k'	cyclic hardening coefficient	φ	phase angle
k	monotonic hardening coefficient	$\sigma_1, \sigma_2, \sigma_3$	principal stresses
J_1, J_2	1 st and 2 nd invariants of the stress tensor	σ_0	fatigue limit at zero mean stress
$J_{2,a}$	amplitude of the 2 nd invariant of the stress tensor	σ_a	normal stress amplitude
LCF	low-cycle fatigue	σ_{eff}	effective stress
MST	multiple step test	σ_f'	fatigue strength coefficient
n'	cyclic hardening exponent	σ_{FI}	stress intensity function
n	monotonic hardening exponent	σ_H	hydrostatic stress
N_f	number of cycles to failure	$\sigma_{H,a}$	hydrostatic stress amplitude
N_T	transition point	$\sigma_{H,m}$	mean value of the hydrostatic stress
q	notch sensitivity index	σ_m	mean normal stress
R	stress ratio	σ_n, σ_{nom}	nominal stress
R_ε	strain ratio	σ_{n+max}	maximum normal stress
R_a, R_b	axes of the circumscribed ellipse	σ_{UTS}	ultimate tensile strength
SST	single test method	σ_{YS}	yield strength
t	time	γ	shear strain
t_{-1}	fully-reversed torsion fatigue limit	γ_{max}	maximum shear strain
U_{th}	effective threshold SIF ratio for a crack length a_{th}	γ_f'	shear fatigue ductility coefficient
U_{th0}	effective threshold SIF ratio for a long crack	τ_a	shear stress amplitude
W_e	maximum strain energy density	τ_f'	shear fatigue strength coefficient
W_n	nominal strain energy density	τ_m	mean shear stress
W_p	strain energy density due to elastic-plastic stress	ρ	notch radius
x_{eff}	effective distance	ν	Poisson's ratio
$Y(a_{th})$	geometric factor		
$\Delta\gamma$	shear strain range		
$\Delta\varepsilon_1, \Delta\varepsilon_2, \Delta\varepsilon_3$	principal strain ranges		
$\Delta\varepsilon_e$	elastic strain range		

2.1. Fatigue phenomenon

Fatigue is a progressive, localised and permanent change that takes place in mechanical components subjected to repeated or fluctuating strain fields caused by nominal stresses considerably below the tensile strength of the materials involved. Fatigue failure can occur due to load fluctuations but also due to the synergy of several damaging factors, which are usually called creep fatigue, thermomechanical fatigue, corrosion fatigue, sliding contact fatigue, rolling contact fatigue, fretting fatigue, etc. (Suresh, 1998).

As is well-known, August Wöhler (1819-1914) was the first researcher to address fatigue failure (Wöhler, 1871) by studying the behaviour of full-scale railway axles under cyclic loading. The presentation of the test data in terms of applied stress versus number of cycles to failure, termed S-N diagram, was a major innovation and rapidly spread to other applications also subjected to fluctuating load, such as ships, aircrafts, industrial machinery, etc. (Farahmand, 1997).

Fatigue failure, as depicted in Figure 2.1, is a sequential process that encompasses three main stages. The first stage comprises the microscopic crack nucleation and crack initiation. Due to the difficulty in separating these two events, many authors divide *crack nucleation* and *crack initiation* into two independent stages. The second stage is the stable crack growth. In this period, the crack reaches a critical size at which the remaining uncracked cross-section of the mechanical component becomes too weak to carry the imposed loading. The last stage consists of a period of unstable crack propagation which culminates in a sudden fracture of the remaining cross-section of the mechanical component.

Crack initiation is, in general, a surface phenomenon. Different reasons have been suggested to explain this fact. For example, the lower restraint at the material surface has been mentioned as a favourable condition to crack initiation. Other arguments are the inhomogeneous stress distribution due to notch effects or other geometrical discontinuities which lead to peak stresses at the surface. Surface roughness and similar surface effects, such as corrosion or fretting fatigue, also promote crack initiation at the

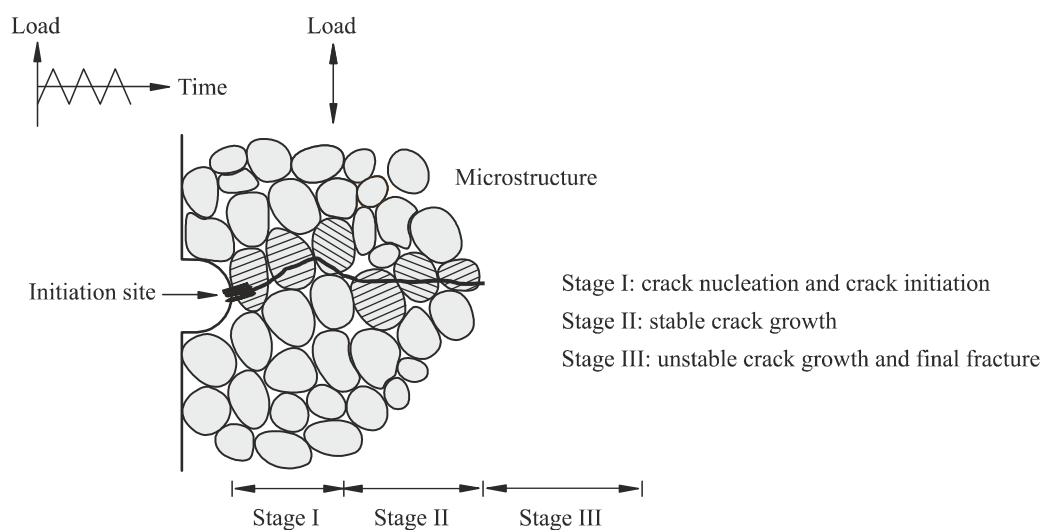


Figure 2.1. Main stages of fatigue failure (Farahmand, 1997).

surface. Therefore, crack initiation life is highly dependent on surface conditions.

Fatigue crack nucleation, as postulated by Ewing and Humfrey (1903), starts from invisible microcracks in slip bands. Further studies demonstrated that nucleation of microcracks generally occurs very early in the fatigue life. Nevertheless, microcracks remain invisible for a considerable part of the total life. Cyclic slip is caused by cyclic shear stress. However, the shear stress on crystallographic slip planes differs from grain to grain. In short, it depends on the size and shape of the grains, crystallographic orientation of the grains and anisotropy of the material. In view of this fact, some grains at the material surface are more susceptible to cyclic slip than others.

Figure 2.2 schematises the crack initiation on the surface of a ductile metal under uniaxial tensile stress. In grains favourably oriented to the applied fluctuating load, fine localised slip lines appear on the surface of material. At the early stage, the slip lines are visible on the surface for the tensile portion of the cycle and disappear in the unloading portion. After few cycles, this reversible process is interrupted and permanent slip bands are formed. These permanent slip bands, named as persistent slip bands (PSB), can result in intrusions and extrusions, which are localised stress concentration sites for the formation of a microcrack. Further continuation of cyclic loading results in stable crack growth. At the early stage of stable crack growth, the direction of the propagation is not exactly perpendicular to the applied load but depends on the orientation of the primary slip band (see Figure 2.1). In a subsequent moment, the growth direction changes and the crack tends to propagate in a direction normal to the applied load. In general, this stage is influenced by the magnitude of the alternating stress, mean stress and severity of the environment. When a critical crack length is reached, the propagation becomes unstable leading to the

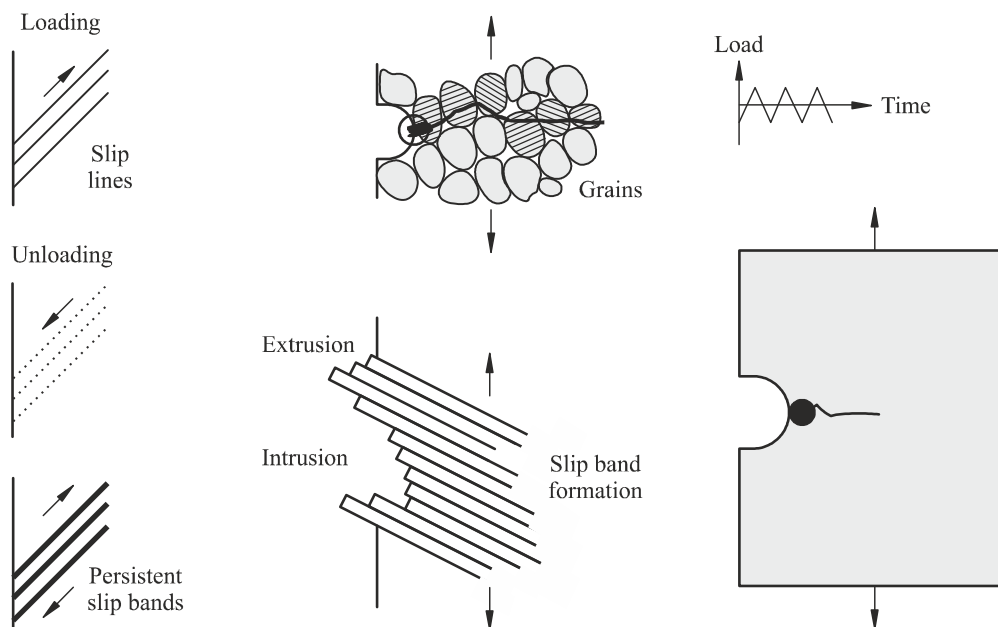


Figure 2.2. Slip bands formation leading to crack initiation as a result of cyclic loading (Farahmand, 1997).

final fracture.

With respect to polycrystalline metals, such as high strength steels or aluminium alloys, it is important to note that they have a complex nucleation process which is affected by the presence of grain boundaries, precipitates, impurities and inclusions. In this case, slip bands are the result of dislocation movements within individual grains. These movements can only occur along a slip plane determined by the crystal structure. Particularly in high strength steels, the crack nucleation from inclusions has been reported by several authors (Ransom, 1954; Costa, 2001; Puchi-Cabrera, 2007; Sirin, 2008; Branco, 2012e). It tends to occur at inclusions located at the material surface or slightly below. Although inclusions are not harmful in terms of static strength, they reduce the ductility of the material and tend to interact with cyclic slip. In practice, an inclusion acts as a micronotch leading to a local change in the stress distribution. High strength steels, due to their high yield stresses, have high notch sensitivity. In this sense, the presence of inclusions in this kind of materials must be avoided, otherwise crack nucleation can occur.

As schematised in Figure 2.1, a crack first starts in a surface grain and then grows into the next. In this stage, the overall growth path is along planes of maximum shear stress. According to the terminology of fracture mechanics, it corresponds to mode II (Figure 2.3b). In the second stage, the crack gradually turns to grow perpendicular to the tensile stress axis, i.e. under mode I (Figure 2.3a). The transition between both stages, which occurs over a few grains, is mainly controlled by the material microstructure and applied stress. In general, lower stress magnitudes increase the time associated with stage I and *vice versa*. On the other hand, the length of the stage I increases with the grain size of the material.

In materials subjected to multiaxial fatigue, as illustrated in Figure 2.4, crack growth patterns can be explained in two different ways. According to Brown *et al.* (1973), the different crack growth patterns depend on the orientations of the planes of maximum shear stress amplitudes with the free surface of the material. The first crack growth pattern (Figure 2.4a-d) is termed *case A* while the other (Figure 2.4e-h)

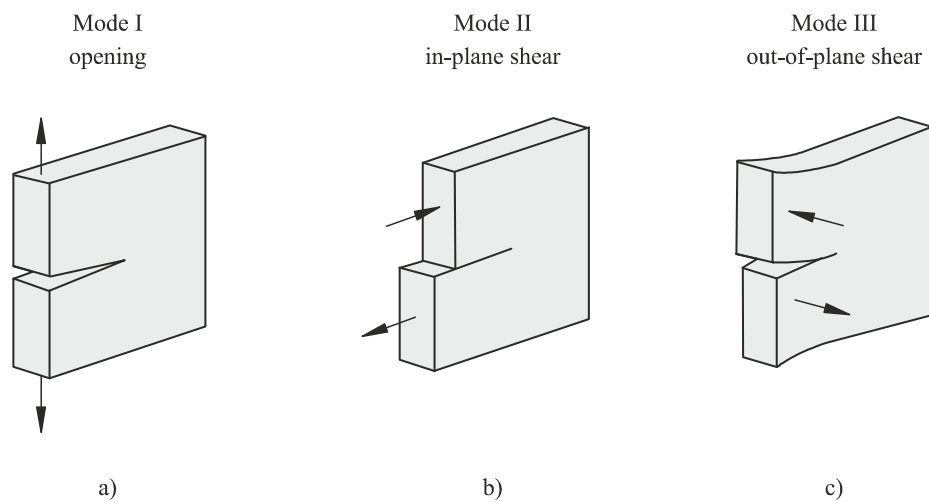


Figure 2.3. Schematic illustration of the three basic modes of fracture: a) mode I; b) mode II; c) mode III (Socie, 2000).

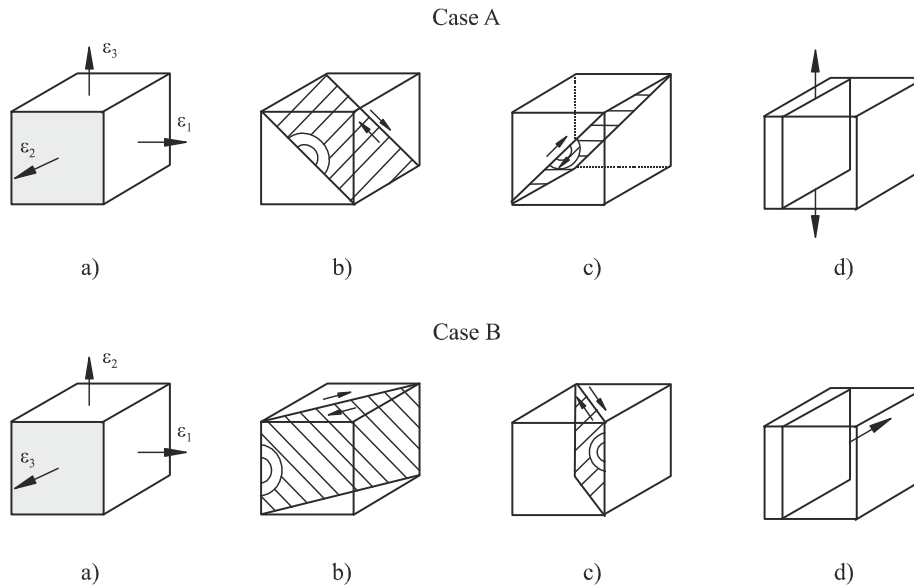


Figure 2.4. Schematic illustration of the two crack growth patterns in multiaxial fatigue suggested by Brown *et al.* (1973) and termed *case A* and *case B*: a) multiaxial strains; b) plane of maximum shear stress amplitude and plane and direction of stage I crack growth; d) plane and direction of stage II crack growth (Suresh, 1998).

is termed *case B*. The surface planes are marked in grey in Figures 2.4a. The planes of maximum shear stress amplitudes, wherein the stage I cracks initiate, are depicted in Figures 2.4b-c. In *case A*, the shear stress acts on the free surface in a direction parallel to the crack length and there is no shear stress acting perpendicular to the free surface along the crack depth. This is an in-plane stress shear. In these circumstances, the crack advances more in a direction parallel to the surface than in a direction normal to the surface, i.e. this type of crack tends to be shallow and has a small crack aspect ratio. The plane in which the stage II crack growth occurs is exhibited in Figure 2.4d and is due to simultaneous or alternating slip involving more than one slip system. In *case B*, the crack is subjected to out-of-plane shear stress. Here, the stage I crack growth initiates at the surface oriented at a 45° angle. The crack advances from the free surface to the interior of the material leading to a more critical cross-section reduction than that in the previous case. The stage II crack growth is presented in Figure 2.4d and is also from the free surface into the material. In this case, the fatigue crack growth process can be described by the intrusion-extrusion model.

Fatigue life is a result of many factors which are grouped into different categories, such as microstructure of the material, processing techniques, load spectrum, environment and geometry (Ellyin, 1997). The effects of the above-mentioned factors are briefly outlined below.

i) Effect of microstructure

As already referred, average grain size, grain structure and microstructural defects have a strong effect on fatigue life. Figure 2.5 plots typical ratios of the endurance limit to the ultimate tensile strength against

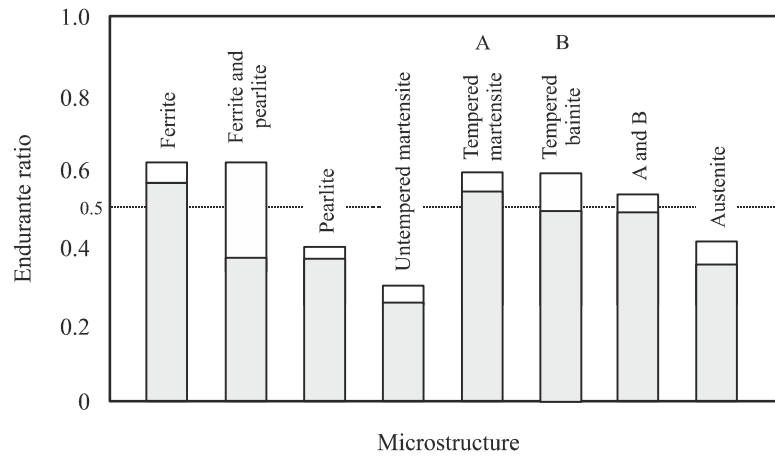


Figure 2.5. Effect of steel microstructure on endurance ratio (Boyer, 1986).

the steel microstructures. According to the figure, a tempered martensite structure provides the highest fatigue limit. Pearlitic structures, particularly those with coarse pearlite, have poor resistance to fatigue. In general, materials with large grain sizes exhibit lower fatigue limit than those with smaller grain size when subjected to cyclic loading at room temperature. On the contrary, at temperatures in the creep range, the coarse-grained materials appear to have better fatigue performance.

The damage in metallic materials is caused by plastic deformation, which is generally due to the motion of dislocations. This motion is affected by precipitates, impurities, grain boundaries, among others. As is well-known, the dislocation structure and density is influenced by the cyclic deformation. Besides, the initial dislocation structures vary considerably with the processing technique used (annealing or work hardening, etc.). Furthermore, a cyclic loading can cause phase transformation (for example, austenite-martensite transformations) which generally results in a reduced fatigue life (Ellyin, 1997).

ii) *Effect of processing techniques*

Processing techniques such as forging, rolling and extrusion have influence on the grain orientation and can produce directional properties. Generally speaking, the oriented direction has better fatigue properties than the transverse direction. For instance, the ratio of transverse to longitudinal fatigue limits in specimens made of DIN 34CrNiMo6 high strength steel was found to be about 0.7-0.8 (Ranson, 1952). On the other hand, material processing techniques, such as grinding, turning, extrusion, can also be a source of defects, i.e. cavities, inclusions, pores, etc. which act as micronotches. Figure 2.6 shows the cycles to failure for specimens of DIN 34CrNiMo6 high strength steel with large spherical inclusions (diameters of about 0.13mm) and with small spherical inclusions (no larger than 0.02mm) detected at the fracture surfaces and identified as silicate particles. As can be seen, the fatigue lives achieved were significantly affected by the size of the inclusions. In fact, inclusions cause an early strain localisation which accelerates the fatigue crack initiation process.

Fatigue life is also highly influenced by heat treatments, namely hardening, cold and hot working, surface

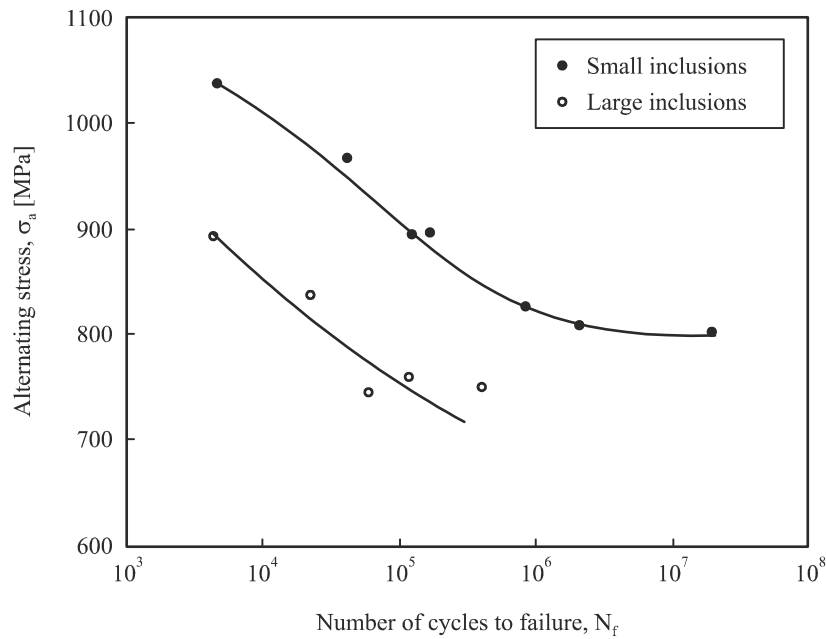


Figure 2.6. Effect of non-metallic inclusion size on fatigue life in specimens made of DIN 34CrNiMo6 high strength steel (ASM, 2000a).

coating, plating, cladding, among others. Components are generally heat treated after manufacturing to enhance several properties, in particular residual stresses. The existence of tensile residual stresses at the surface must be avoided, since it is not beneficial to fatigue behaviour. On the contrary, compressive residual stresses at the surface enhance fatigue properties. Nevertheless, heat treatments in steels can cause surface decarburisation which decreases the surface toughness and produces microcracks. Besides, it is important to note that forming, drawing, forging, extrusion, rolling, machining, etc. produce rough surfaces, microstructural changes and residual stresses. Therefore, it is expected that these rough surfaces lead to a decrease in fatigue life.

iii) Effect of environmental factors

a. Corrosive environment

The mechanical degradation of a material due to the conjoint action of cyclic stresses and harmful environments is named corrosion fatigue. The most visible effects are pitting and surface roughness. These regions act as micronotches and are potential sites of crack nucleation. In this context, the critical locations are those where fatigue slip activity occurs. The slight difference between the electromechanical potential of the outside and the inside of the slip band promotes the corrosion process. The performance against corrosion fatigue can be increased by improving the surface properties through the application of different surface treatments, for instance nitriding, shot peening, cladding, plating, among others. The effect of a corrosive environment (3% wt. NaCl solution) on fatigue behaviour of DIN 34CrNiMo6 high strength steel is presented, as an example, in Figure 2.7 (Puchi-Cabrera, 2007). The S-N curves for tests in air and in corrosive environment were obtained by fitting the experimental data to a power law function. As can be seen, the curves behave differently. In air, there is a fatigue limit. On the contrary,

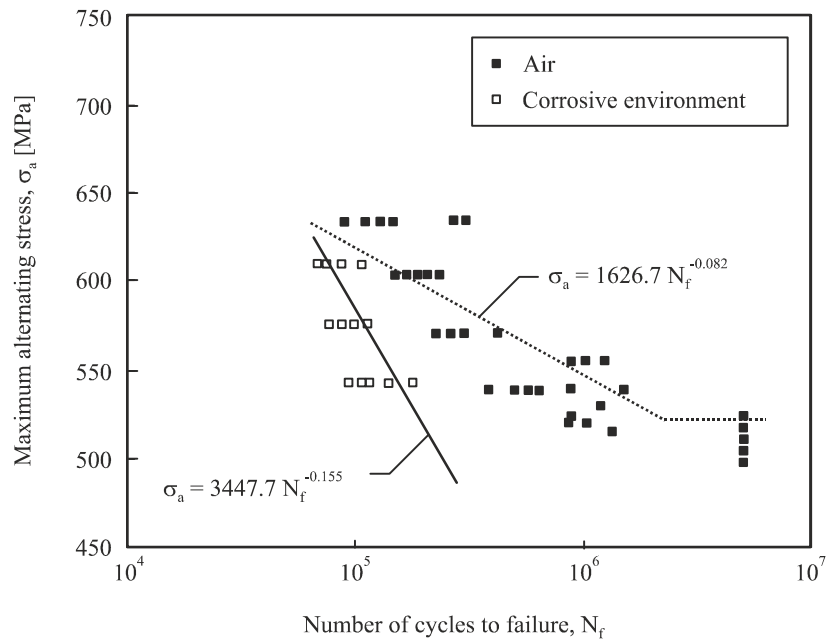


Figure 2.7. S-N curves of DIN 34CrNiMo6 high strength steel tested in corrosive environment and in air (Puchi-Cabrera, 2007).

in a corrosive environment, the fatigue limit is not observed. On the other hand, the S-N curve obtained in a corrosive environment is shifted to the left, which is clear sign of lower fatigue strength.

Different mechanisms have been proposed to explain the effect of a corrosive environment on fatigue crack growth. These mechanisms can generally be grouped into three categories (Ellyin, 1997), i.e.

- oxidation of the crack surface: it changes the properties of the material around the crack tip and additionally promotes the development of crack closure. The crack surfaces develop a brittle oxide layer due to subsequent crushing and reforming. This process tends to create a wedge-like shape at the crack tip which reduces the crack driving force (Suresh, 1982). Additionally, as postulated by Zhiqiang *et al.* (1991), crack closure simplifies the movement of the corrosive solution out of the crack tip decreasing the exposure to the corrosive medium. The combination of these two facts, i.e. the reduced driving force induced by the oxide layer and the shielding properties generated by crack closure, promotes a decrease of the crack growth rate;
- hydrogen embrittlement: it results from the migration of atomic hydrogen to regions of high stress concentration, such as the crack tip. This absorption of hydrogen ions promotes the embrittlement of the crack tip material. The embrittled area is susceptible to microcrack initiation which progressively grows and joins to the dominant crack. This accelerated crack growth mechanism has been observed in high strength steels. In lower strength steels, the hydrogen absorption enhances the nucleation and growth of microvoids at the crack tip which also results in an accelerated crack growth;
- exposure time to the corrosive environment: the time of chemical absorption at the crack tip during each loading cycle plays an important role on the fatigue crack growth rate (Bartlett, 1990). In

general, at high values of the stress intensity factor range, a higher frequency results in lower crack growth rates. This is because, at higher frequencies, the corrosive environment is not able to fully penetrate the crack tip before closing again. At lower frequencies, the corrosive environment has more time to contact with the crack tip which increases the crack growth rates. An opposite behaviour is observed at lower values of the stress intensity factor range, i.e. reduced frequencies promote lower crack growth rates because in these circumstances the higher exposure time produces larger amounts of corrosion products which lead to early crack closure and lower driving forces.

b. Temperature

Temperature is other important environmental factor that affects both the fatigue resistance and crack propagation rates. At low temperatures, i.e. room temperature or below, crack growth is frequency or time independent. In general, the fatigue strength of a material increases as the temperature decreases. Table 2.1 compiles average values of the ratio of the fatigue strength at -40°C, -78°C and -188°C to the fatigue strength at room temperature for several groups of metallic alloys (Frost, 1962). As can be observed, these ratios are essentially in the range 1.05-2.6. Besides, it is important to note that softer materials generally provide higher ratios than harder materials. The effect of the mean tensile stress on the low-temperature fatigue strength suggests that the results lie between the modified Goodman and Gerber lines (see Figure 2.11). At high temperatures, crack growth is frequency or time dependent. Increasing temperatures cause plastic flow which alters the crack front plastic zone as well as the strain and stress distributions. Cyclic loading at elevated temperature can be described as a phenomenon combining rate-independent fatigue and rate-dependent creep mechanisms. The prevalence of one mechanism over the other depends on temperature, microstructure, loading rate, loading wave form, among others. Cyclic actions and increased temperatures enhance oxidation which may have a significant influence on crack growth. On the other hand, oxidation results in weakening and embrittlement of grain boundaries, especially at the crack tip region near the surface. In general, increasing temperatures reduce fatigue strength. Figure 2.8 presents, as an example, the effect of elevated temperature on fatigue behaviour of DIN 34CrNiMo6 high strength steel (MIL-HDBK-5H, 1988). The grey and black circles represent the experimental results while the dashed and full lines correspond to the fitting functions. As can be seen, the increase in temperature reduces the fatigue resistance. This effect is much more pronounced for the highest temperature than in the other cases.

Table 2.1. Ratios of the fatigue limit in torsion to in rotating bending for different materials (Frost, 1999).

Material	Ratio of the fatigue strength at a given temperature to the fatigue strength at room temperature ^a		
	-40°C	-78°C	-188°C
Carbon steels	1.2	1.3	2.6
Alloy steels	1.05	1.1	1.6
Stainless steels	1.15	1.2	1.5
Aluminium alloys	1.15	1.2	1.7
Titanium alloys		1.1	1.4

^a Fatigue strength at 1×10^6 cycles.

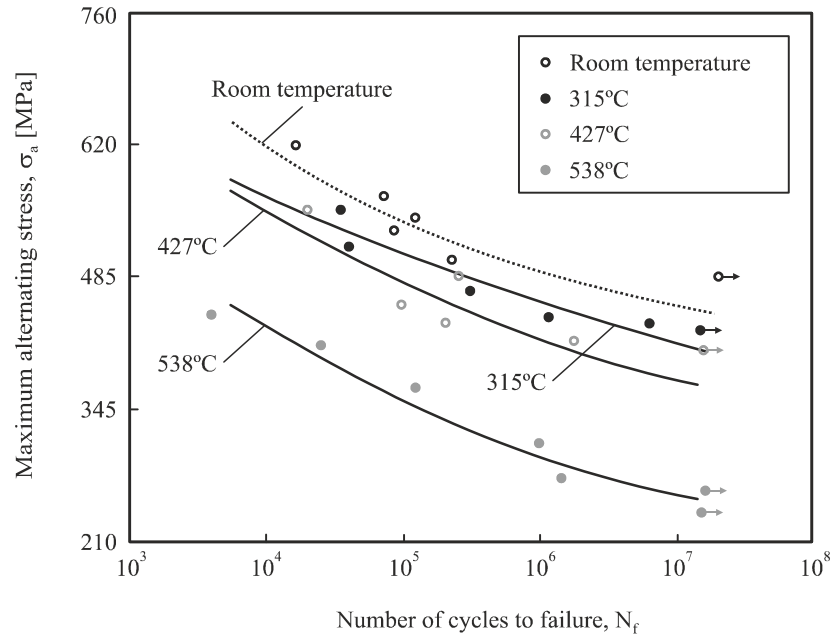


Figure 2.8. S-N curves of DIN 34CrNiMo6 high strength steel obtained at different temperatures (MIL-HDBK-5H, 1988).

iv) Effect of load

The load history experienced by a component, i.e. magnitude, sign and rate of loading, plays a major role on fatigue life. In certain cases, such as rotating shafts of stationary equipment, the load history is almost uniform with small variation from cycle to cycle. In other cases, for instance moving vehicles or aerospace components, the load history is almost random in nature during their service life (Figure 2.9a). It means that the load at a given instant cannot be predicted *a priori*. Different methods of cyclic counting have been proposed to convert irregular load histories to blocks of constant amplitude (Figure 2.9b). The *rain flow* counting method (Matsuishi, 1968) is one of the most popular approaches. Detailed information on the current practices for cycle counting can be found in the ASTM E1049 (2011) standard. In general, the counting methods can be grouped into two categories, i.e. one parameter description (e.g. level crossing count, peak count, range count) and at least two parameters description (e.g. range-mean count, etc.). The constant amplitude cyclic loading (Figure 2.9c) is used as a reasonable approximation when there are no significant deviations in the load history. According to Figure 2.9c, the stress range ($\Delta\sigma$) is given by the following expression

$$\Delta\sigma = \sigma_{\max} - \sigma_{\min} \quad (2.1)$$

being σ_{\max} and σ_{\min} the maximum stress and the minimum stress during a complete cycle. The stress amplitude (σ_a) and the mean stress (σ_m) can be written by Equation 2.2 and Equation 2.3, respectively.

$$\sigma_a = \frac{\Delta\sigma}{2} \Leftrightarrow \sigma_a = \frac{\sigma_{\max} - \sigma_{\min}}{2} \quad (2.2)$$

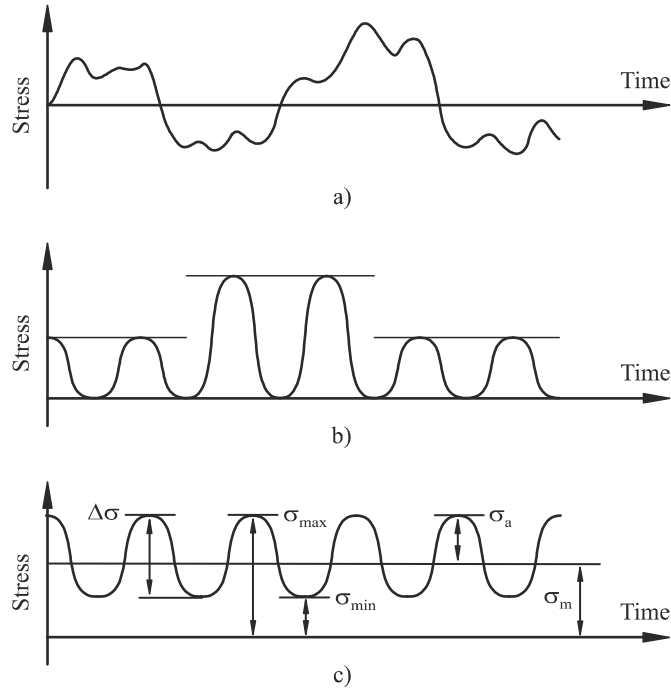


Figure 2.9. Types of loading: a) random; b) blocks of constant amplitude; c) constant amplitude.

$$\sigma_m = \frac{\sigma_{\max} + \sigma_{\min}}{2} \quad (2.3)$$

The stress ratio (R) is defined as the algebraic ratio of the minimum cyclic stress to the maximum stress cyclic stress during a complete cycle (Equation 2.4). Such a parameter is widely used to distinguish different constant amplitude loading conditions. Two common test references are $R = -1$ and $R = 0$, which are called *fully reversed* and *pulsating tension*, respectively.

$$R = \frac{\sigma_{\min}}{\sigma_{\max}} \quad (2.4)$$

The strain ratio (R_ϵ) is another parameter used in fatigue analysis and can be written in the form

$$R_\epsilon = \frac{\epsilon_{\min}}{\epsilon_{\max}} \quad (2.5)$$

being ϵ_{\min} and ϵ_{\max} the minimum strain and the maximum strain during a complete cycle, respectively. In general, this parameter is employed in strain-controlled low-cycle fatigue tests, where the total strain ($\Delta\epsilon$) is controlled throughout the cycle. As is well-known, with respect to the number of cycles to failure, fatigue is generally divided into low-cycle fatigue (LCF) and high-cycle fatigue (HCF). The former is characterised by large plastic deformation and fatigue lives usually lower than 10^4 cycles. The latter is characterised by microscopic localised plastic deformation and fatigue lives above 10^4 cycles.

The total damage induced on a given part as a result of the previous damage history and the loading order effects can be evaluated using different cumulative damage models (Fatemi, 1998). In essence, these models are based on a damage variable which controls the fatigue process (Kujawski, 1988). For example, the well-known Palmgren-Minner rule, first proposed by Palmgren (1945) and later developed by Minner (1945), is based on a linear damage accumulation law and states that the fatigue damage contribution by each individual load spectrum at a given stress level is proportional to the number of cycles applied at that stress level (n_i) divided by the total number of cycles required to fail the part at the same stress level (N_{fi}), i.e.

$$\sum \frac{n_i}{N_{fi}} = 1 \quad (2.6)$$

being i the number of loading levels. Due to its simple formulation (linear damage assumption and insensitivity to the loading sequence experienced by the component), this damage function has been criticised. However, such a rule is probably the most used damage formulation. Moreover, it is important to mention that more complex damage formulations do not necessarily provide better results than the linear damage models (Melcon, 1962; O’Neil, 1970).

a. Mean stress

The mean stress, defined by Equation 2.3, strongly affects fatigue life. In general, the effect of a positive mean stress is to reduce fatigue life whilst a negative mean stress may increase it. The influence of the mean stress on fatigue life is usually studied by establishing a set of S-N curves for different stress ratios. Figure 2.10 shows a family of S-N curves obtained at different stress ratios for DIN 34CrNiMo6 high

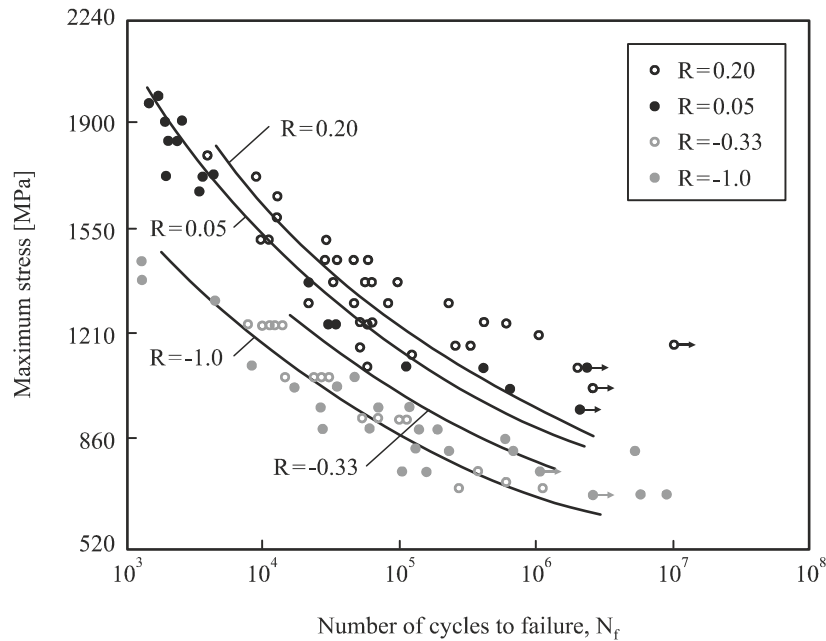


Figure 2.10. Family of S-N curves obtained at different stress ratios for DIN 34CrNiMo6 high strength steel (MIL-HDBK-5H, 1988).

strength steel (MIL-HDBK-5H, 1988). It can be noted that for a fixed maximum stress the fully-reversed condition ($R=-1$) is the most severe with the least fatigue life. Besides, for a fixed maximum stress, the higher is the stress ratio, the higher is the fatigue life. Different formulations have been proposed to predict the fatigue limit of a material under a given mean stress from the fatigue limit at zero mean stress. The two relationships generally accepted as representing the experimental data were proposed by Gerber (1874) and Goodman (1899) and can be expressed by

$$\sigma_a = \sigma_0 \left[1 - \left(\frac{\sigma_m}{\sigma_{UTS}} \right)^n \right] \quad (2.7)$$

where σ_0 is the fatigue limit at zero mean stress, σ_{UTS} is the tensile strength and n is a constant ($n = 2$ in the former and $n = 1$ in the latter). Both relationships are depicted in Figure 2.11. As can be seen, the Gerber diagram defines a parabola having as end-points the fatigue limit at zero mean stress and tensile strength of the material. The modified Goodman diagram assumes that the fatigue limit decreases linearly with increasing tensile mean stress. A diagram of similar form to the modified Goodman diagram, known as Soderberg line, is defined by the following equation

$$\sigma_a = \sigma_0 \left[1 - \left(\frac{\sigma_m}{\sigma_{YS}} \right) \right] \quad (2.8)$$

being σ_{YS} the yield strength of the material. Regardless of the relationship, loading conditions inside the lines are supposedly safe and those outside lead to failure. One the other hand, experience has shown that most data lie between the Gerber and the Goodman diagrams. In view of this fact, the Goodman line is considered as the lower bound and the Gerber line as the upper bound. It is usual to plot the Goodman and Gerber criteria in terms of dimensionless quantities, i.e. σ_a/σ_0 versus σ_m/σ_{UTS} . This approach is often

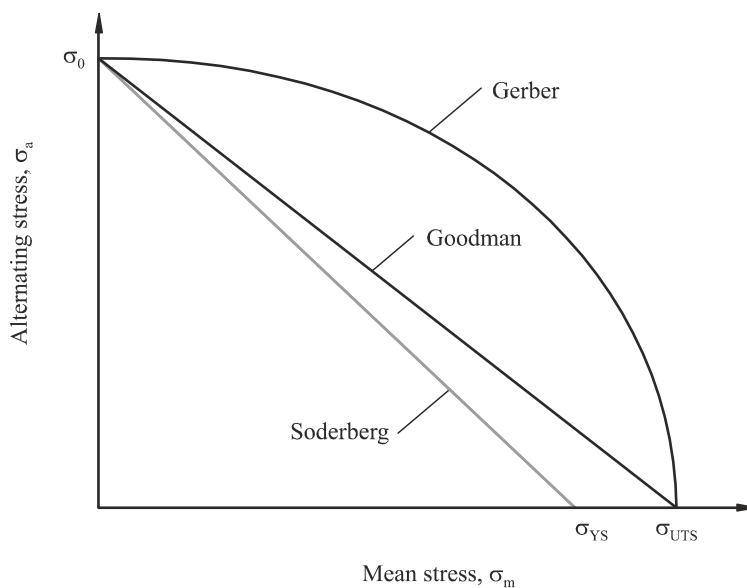


Figure 2.11. Goodman, Gerber and Soderberg diagrams.

referred to as the R-M diagram because it shows the relationship between the safe range of stress (R) and the mean stress (M).

b. Type of loading

The type of loading is also a major aspect on fatigue life. Figure 2.12 shows two S-N curves obtained for notched specimens of DIN 34CrNiMo6 high strength steel subjected to both axial and rotating bending load (Socie, 1980). As can be seen, the results have large differences. It is clear that the fatigue performance is significantly higher under rotating bending than under axial loading. The fatigue limits for torsion and rotating bending are also different. Table 2.2 lists average ratios of the fatigue limit in torsion to in rotating bending for different materials (Frost, 1999). According to the results, these ratios are typically within the range of 0.52-0.58 having an overall average equal to 0.55. For stronger wrought aluminium alloys, for instance, which do not exhibit a distinct fatigue limit, this ratio depends on the endurance at which the torsional and bending fatigue strengths are estimated. Average values of 0.64 and 0.56 have been obtained when the fatigue strengths are evaluated at 1×10^7 and 5×10^8 cycles, respectively. Besides, it appears that for those metals, in which failure is initiated at a free surface, this ratio has an average value not far from that predicted by the von Mises criterion (i.e. 0.577).

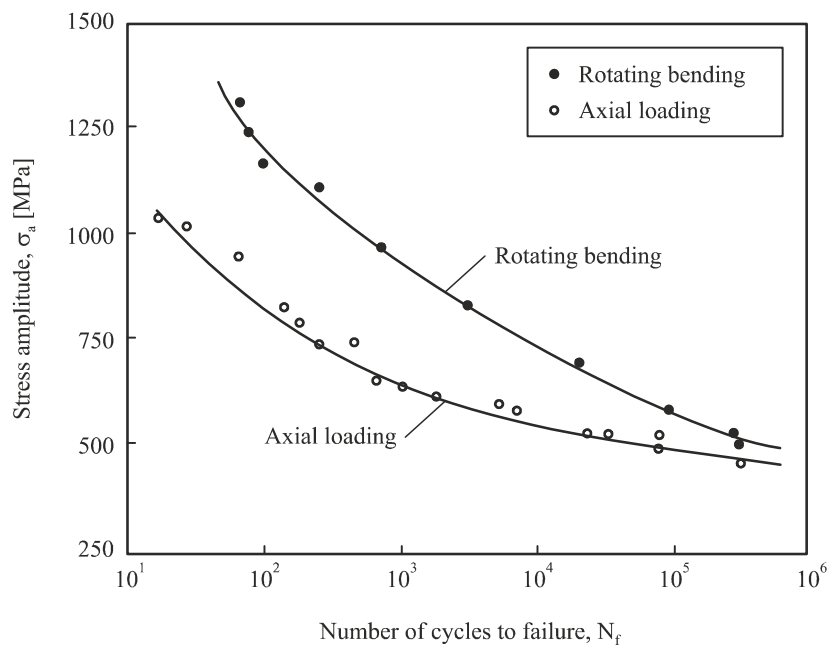


Figure 2.12. S-N curves obtained under rotating bending and axial loading for DIN 34CrNiMo6 high strength steel (Socie, 1980).

Table 2.2. Ratios of the fatigue limit in torsion to in rotating bending for different materials (Frost, 1999).

Material	Ratio of fatigue limit in torsion to in rotating bending
19 carbon steels (Moore, 1927)	0.55
14 alloy steels (Moore, 1927)	0.58
5 non-ferrous alloys (Moore, 1927)	0.52
49 wrought metallic alloys (Gough, 1924)	0.56
14 wrought metallic alloys (Cazaud, 1953)	0.575

c. Loading sequence

Loading sequence effects are also relevant parameters on fatigue performance. Take for example the fatigue data presented in Figure 2.13, which were obtained from unnotched specimens subjected to two different load histories, termed here *load history A* and *load history B* (Socie, 1980). The former has a first stress peak at $\Delta\sigma_1/2$ and the latter has a first stress peak at $-\Delta\sigma_1/2$. The remaining cyclic load pattern is identical in both cases ($\Delta\sigma_2/2$). Although both load histories have similar patterns, the resultant fatigue lives are totally different. The differences are due to the loading sequence effect. According to the results, the first negative stress peak is less damaging than the first positive stress peak. Besides, the lower is the value of $\Delta\sigma_2$, the more pronounced is the loading sequence effect on fatigue life.

d. Loading frequency

Loading frequency is another variable affecting fatigue performance. Table 2.3 presents fatigue limits obtained at various testing frequencies for different materials. The results available in the literature show

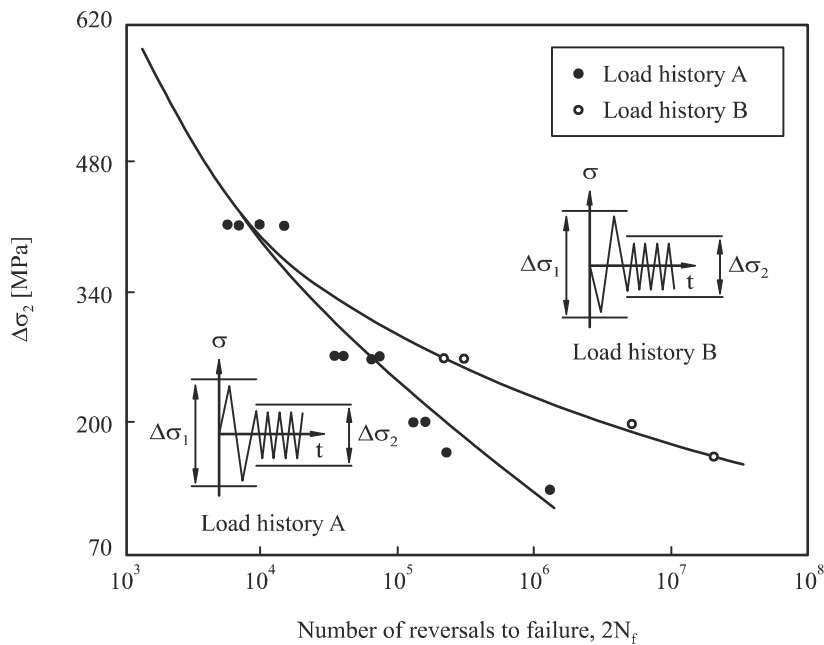


Figure 2.13. Fatigue data showing sequence effects for two load histories (*load history A* and *load history B*) in 2024-T4 aluminium (Socie, 1980).

Table 2.3. Fatigue limit at various testing frequencies for different materials (Krouse, 1934).

Material	Fatigue limit (MPa)			
	Frequency:	25Hz	167Hz	500Hz
SAE 1020 steel		215	215	230
Stainless steel		415	435	480
SAE 4140 steel		675	680	700
Grey cast iron		70	70	77
Alloy cast iron		180	180	200

that the fatigue limit or strength at long endurance of a material, which does not heat up or whose surface is not chemically attacked, remains constant or increases slightly over the frequency range of 1-200Hz. At higher testing speeds, the fatigue limit continues to increase with testing speed up to frequencies of about 2kHz. Beyond this frequency, the experimental data are not in accordance but there is evidence that after a peak frequency the fatigue strength decreases with increasing frequency.

v) *Effect of geometry*

a. *Stress concentration*

Fatigue design of a component is governed by a region of high local stress, such as an abrupt change in section, a notch or a hole. In general, these regions, termed *geometric discontinuities*, are sources of stress or strain concentration and are probable sites of crack initiation. As is well-known, at these regions, the local stress and strain are much greater than the nominal applied stress or strain. Besides, as already mentioned, the fatigue crack usually initiates at a point where the stress is highest, which often occurs at the surface. There are several reasons why stress peaks and fatigue damage often occur at the surface, such as the component may have stress raisers at the surface; the corrosion and erosion damages always roughen the smooth surface and introduce micronotches which act as local stress raisers; the microscopic plastic deformation occurs more easily at the surface due to less restraint than in the interior; and the residual stresses often reach a maximum at the surface. The fatigue life of a notched component is less than that of an unnotched component. However, it is important to highlight that the geometric discontinuities, in general, cannot be avoided due to functional requirements or connection details. The effect of stress concentration on fatigue behaviour of notched and unnotched specimens made of DIN 34CrNiMo6 high strength steel is exhibited, as an example, in Figure 2.14. In the former specimens, the

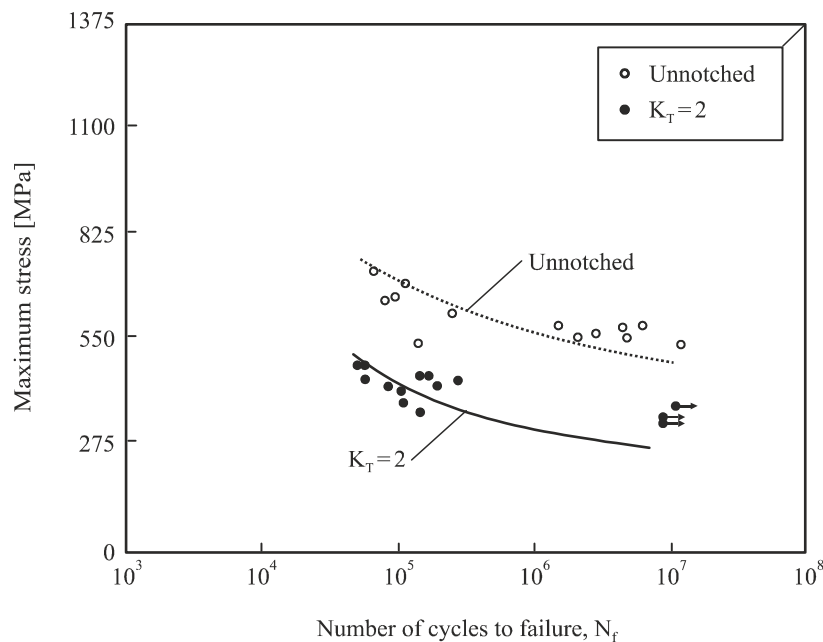


Figure 2.14. S-N curves for DIN 34CrNiMo6 high strength steel obtained using notched ($K_T=2$) and unnotched ($K_T=1$) specimens (MIL-HDBK-5H, 1988).

stress concentration factor (K_T), defined as the ratio of the peak stress in the notched specimen to that of the corresponding unnotched specimen, is equal to 2. In the latter, $K_T = 1$. As can be seen, the fatigue life is significantly reduced by the presence of the notch.

b. Surface finish

Crack initiation is associated, in general, with a free surface. Therefore, the surface characteristics resulting from the manufacturing techniques (such as grinding, turning, forging, extrusion, etc.) or surface treatments (for instance electroplating, shot peening, surface hardening, etc.) have a significant influence on fatigue properties. The influence of the manufacturing techniques as well as the additional surface treatments on fatigue strength can be explained at least by three reasons. Firstly, notch-like surface irregularities may have been created. Secondly, the condition of the material at the surface may have been changed (it may have been hardened by cold-work or softened by decarburisation). Thirdly, residual stresses may have been introduced into the surface layer. Many researchers have considered the effect of surface finishing on fatigue. In general terms, fatigue life increases as the magnitude of surface roughness decreases. Apart from the surface roughness, the fatigue properties are significantly affected by the depth and intensity of the residual stresses existing at the surface. Compressive residual stresses at the surface improve its fatigue life. Therefore, a final surface finishing process is beneficial to fatigue when it increases the depth and the intensity of the compressively stressed layer and detrimental when it decreases or removes such a layer. The compressive residual stresses can be produced by using different techniques, namely surface alloying, surface hardening, mechanical working of the surface or by a combination of these processes.

The first group includes, for example, carburising, carbonitriding and nitriding. In these processes, carbon, nitrogen or both elements are introduced into the surface layer of the component. The solute atoms strengthen the surface layer and increase its bulk relative to the material below the surface. Figure 2.15 presents, as an example, the effect of different nitriding treatment conditions on the fatigue behaviour of DIN 34CrNiMo6 high strength steel (Sirin, 2008). The S-N curve for conventionally heat treated steel is provided for comparison purposes. As can be observed, the values of the fatigue properties increase with the nitriding time. The increase in the nitriding time leads to a high case thickness, which promotes an effective movement of the fatigue crack initiation site into the core of the material. The second group includes, among others, induction, flame, laser and electron beam hardening. These processes consist of heating the surface above the critical temperature of the material and then quenching to produce a hard martensitic surface layer containing high compressive residual stresses. The last group includes, for example, shot peening, skin rolling, pre-stressing and grit blasting, among others. These processes must be carried out in the final heat-treated condition to achieve the desirable effect. The exposition of mechanically worked surfaces to elevated temperature generally results in a loss of the desirable residual gradient. In this sense, the subsequent thermal treatments must be eliminated or closely controlled when they are essential. Figure 2.16 plots, as an example, typical S-N bands for conventionally heat treated, shot peened and nitrided crankshafts made of DIN 34CrNiMo6 high strength steel (ASM,

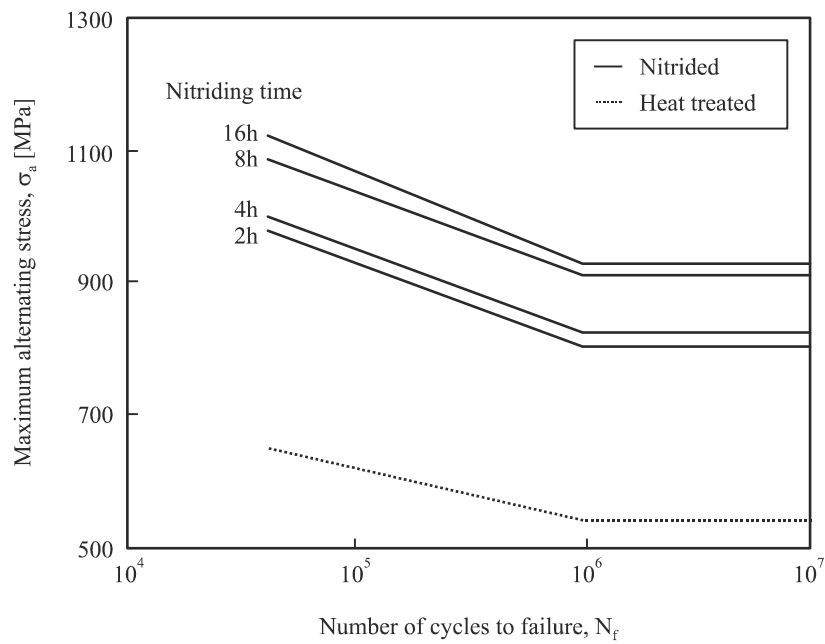


Figure 2.15. S-N curves of conventionally heat treated and nitrided DIN 34CrNiMo6 high strength steel for different nitriding treatment conditions (Sirin, 2008).

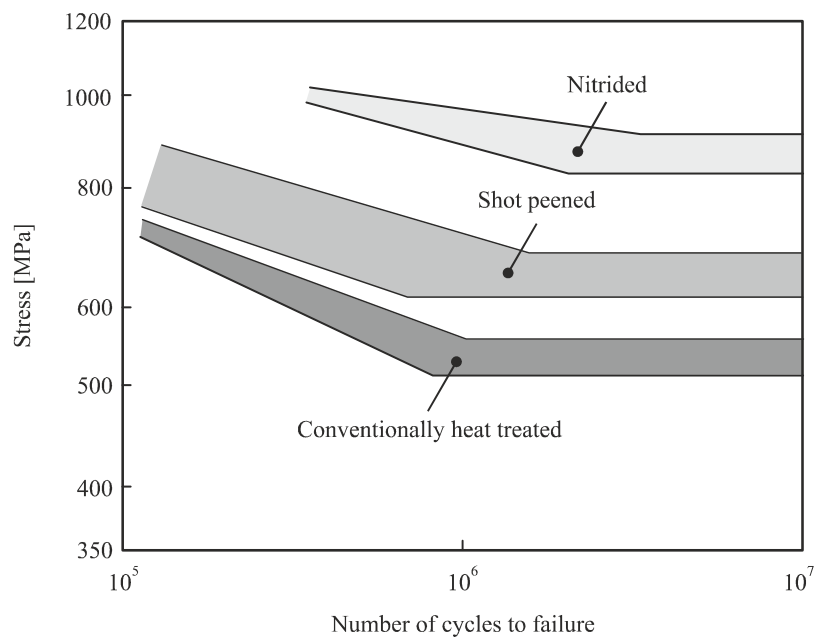


Figure 2.16. Typical S-N bands for conventionally heat treated, shot peened and nitrided crankshafts made of DIN 34CrNiMo6 high strength steel (ASM, 2000a).

2000a). The improvements in fatigue properties either due to shot peening or nitriding are unequivocal. Besides, it is also clear that the nitrided crankshafts lead to greater fatigue lives than the shot peened crankshafts. In certain conditions, various surface treatments are applied to the components to improve their corrosion resistance, appearance and wear resistance. Metal plating generally decreases the fatigue

resistance. At least, three effects can explain this behaviour, namely the notch effect of fissures in the plating; induced residual tensile stresses in the substrate; and hydrogen embrittlement. Figure 2.17 compares, as an example, the S-N curves obtained from unplated and plated DIN 34CrNiMo6 high strength steel (Díaz, 2000). The as-deposited samples were coated with an electroless nickel layer. As can be observed, the plating material leads to a significant reduction in fatigue life and in fatigue limits relatively to the unplated material. Identical conclusions have been reported in similar studies conducted with high strength steel substrates coated with different types of deposits (Garcés, 1999; Guzmán, 2000). Anodising is also used to enhance corrosion protection and wear resistance. In general, this technique produces a reduction in fatigue life ranging from a negligible amount up to 10-15% of the fatigue endurance. This reduction is attributed to one or a combination of the following factors: increased surface roughness, cracking in the coating and induced residual tensile stresses in the material immediately beneath the coating.

c. Size

As already mentioned, the fatigue results vary with the loading type. However, it is important to refer that even when the same load type is defined, the fatigue limit depends on the size of the component. The experimental results available in the literature based on laboratory tests show that the fatigue limit tends to decrease with increasing specimen diameters. Table 2.4 summarises various experimental results obtained from rotating bending tests on batches of mechanically polished specimens of different diameters cut from nominally similar material. The results confirm that, in general, the fatigue limits of these steels decrease as the specimen diameter increases. Besides, the experimental results available in the literature indicate that size-effects are more pronounced in rotating bending than in tensile tests. The

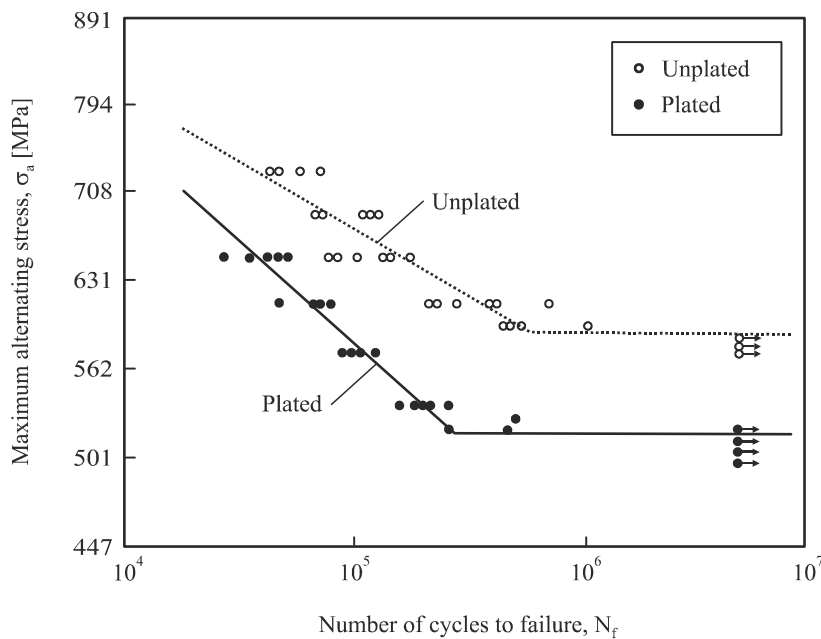


Figure 2.17. S-N curves for conventionally heat treated and electroless Ni-P plated DIN 34CrNiMo6 high strength steel (Díaz, 2000).

Table 2.4. Size effect of specimen diameter on fatigue limit (Frost, 1999).

Material	Specimen diameter (mm):	Fatigue limit (MPa)				
		3.2	6.3	12.5	25	50
SAE 1020 steel (Morkovin, 1944)		240	220	193	200	200
SAE 1020 steel, stress-relieved (Moore, 1939)		200	200	193	193	
SAE 1035 steel (Morkovin, 1944)		260	260	240	240	240
SAE 2345 steel (Moore, 1939)		480	460	460		
SAE 4130 steel (Morkovin, 1944)		520	475	450		
SAE 4340 steel (Gadd, 1945)			550		500	500

change in fatigue limit with size appear to be most marked in specimens having a worked finish, such as those created by mechanical polishing or surface-rolling (Frost, 1999).

2.2. Fatigue design philosophies

Fatigue design philosophies have evolved over the years from the simple concept of infinite life to the more sophisticated concept of damage tolerance (Kirkby, 1980). Nowadays, the four basic fatigue design philosophies are termed *infinite-life*, *safe-life*, *fail-safe* and *damage-tolerance*. These philosophies are briefly outlined below.

- *Infinite-life*: this method is based on the assumption that the maximum stress is lower than the endurance limit, below which no fatigue failures occur and therefore infinite life is expected. It is appropriate for the design of components that experience very high number of cycles and are subjected to uniform or preferably close to constant amplitude loading in non-corrosive environment, such as rotating components of machinery, engine valve springs, among others. In practice, only an endurance limit, and not a complete S-N curve, is required. Nevertheless, this design method is not economical or practical in many design situations, since it results in heavy and inefficient parts. Due to the scatter inherent to the fatigue tests, a suitable safety factor must be applied regarding the calculated endurance limit or the allowable stress.
- *Safe-life*: in this method, the allowable fatigue or strain is related to that which would be expected to cause failure at the required lifetime. This strategy is most suited to parts and structures that are subjected to limited number of load repetitions during their lifetime, so proportioning them for infinite life would be neither practical nor economically viable. For example, several spacecraft components are subjected to few hundred of loading cycles, or less, during their lifetime. In these cases, the fatigue strength should be based on the required life in order to provide an efficient design. In this design method, the allowable fatigue stress is defined from an appropriate S-N curve. The S-N curves can be obtained in different ways, i.e. using laboratory specimens, geometric details, prototypes or full-scale components. A suitable factor of safety is recommended with respect to either the life or the stress or possibly both.
- *Fail-safe*: in this method, a fatigue crack is allowed to grow but the component is designed in a way that the presence of a crack will not lead to failure before it is detected. In other words, the design includes alternative load-carrying members and therefore the failure of one of them can be tolerated

by load redistribution to the remaining members which avoids complete or catastrophic failure. The failure causes a small increase in displacement and the integrity of the component or structure is ensured by the crack stoppers. Generally, this design method requires information about the fracture toughness and crack propagation properties of the material. For example, the aircraft industry commonly uses structural details in wings or fuselages which serve as crack stoppers and prevent cracks from growing to a dangerous length between their scheduled inspections. However, it is important to note that the fail-safe concept is not economically viable for all structures.

- *Damage-tolerance*: this method is based on the assumption that manufacturing flaws can exist in any structure and that these flaws can propagate with usage. The fracture mechanics is used to analyse the crack growth and to define a critical size from which a rapid fracture can occur. An adequate selection of materials with high fracture toughness is crucial to attain an efficient design. Periodic inspections are scheduled to detect cracks of a certain size which is an important aspect either in terms of preventive maintenance or in terms of safety. For example, aircraft maintenance comprises periodic inspections done at intervals determined by a program of testing which can be redefined at any time as a result of the damage detected. The frequency of re-inspection is a critical issue for the aircraft industry since the safety margins are very small. On the contrary, in the maintenance of nuclear reactors, the safety margins are much greater and consequently the frequency of re-inspection is less important. However, the hostile radiation environment is a serious problem. It makes each inspection much more difficult and time-consuming.

2.3. Cyclic stress-strain response

The material response as a result of reversed plastic deformation can differ depending on the controlled variable. Figure 2.18 exhibits several typical stress-strain responses and the corresponding cyclic input variables. In the case of fully-reversed strain-controlled tests, the material response is characterised by strain hardening behaviour (Figure 2.18a), i.e. the uncontrolled stress increases with the number of cycles; or strain softening behaviour (Figure 2.18b), i.e. the uncontrolled stress decreases with the number of cycles. The mean stress relaxation (Figure 2.18c) occurs under strain-controlled conditions with non-zero mean strain. On the other hand, if the maximum and minimum stresses are controlled, the so called cyclic strain ratcheting takes place (Figure 2.18d). Both cyclic strain ratcheting and cyclic mean stress relaxation are characterised by unclosed hysteresis loops.

The propensity for cyclic hardening or cyclic softening can be predicted on the basis of the monotonic properties. In general, materials with a ratio of the ultimate tensile strength (σ_{UTS}) to the yield strength (σ_{YS}) greater than 1.4 (Equation 2.9) cyclically harden and those with a ratio less than 1.2 (Equation 2.10)

$$\frac{\sigma_{UTS}}{\sigma_{YS}} > 1.4 \quad (2.9)$$

$$\frac{\sigma_{UTS}}{\sigma_{YS}} < 1.2 \quad (2.10)$$

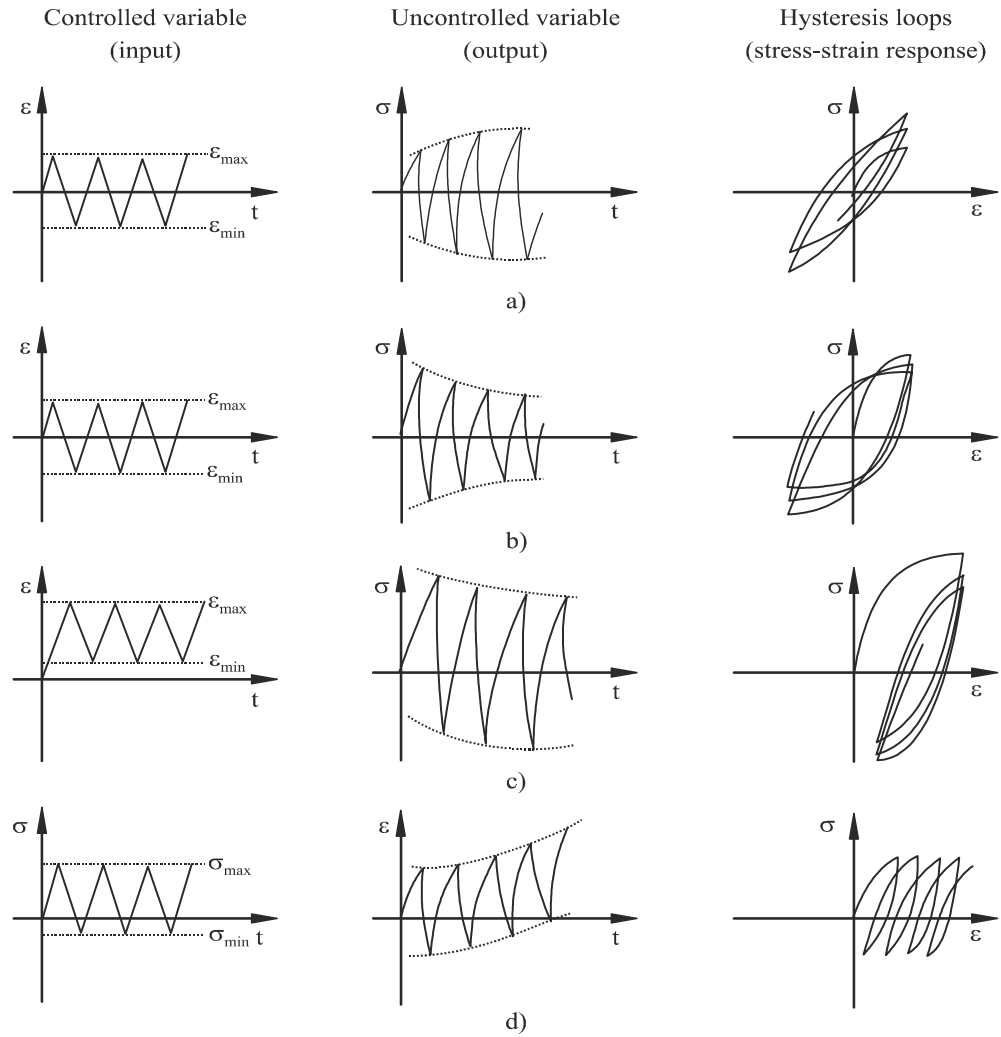


Figure 2.18. Material response to different modes of cyclic input variables: a) cyclic strain hardening; b) cyclic strain softening; c) cyclic mean stress relaxation; d) cyclic strain ratcheting (Ellyin, 1997).

cyclically soften (Smith, 1963). For ratios $1.2 < \sigma_{UTS}/\sigma_{YS} < 1.4$, hardening or softening may occur. Hard and strong materials, such as high strength steels, have a tendency to undergo cyclic softening. Soft materials, for instance aluminium alloys, exhibit cyclic hardening. In particular, the DIN 34CrNiMo6 high strength steel studied in this research agrees with this empirical rule, i.e. cyclically softens (Smith, 1963; Landgraf, 1969; Pape, 2007; Branco, 2012b).

In the majority of cyclic loading cases, the material response reaches a steady-state regime, or the variation from cycle to cycle tends to be quite small. Therefore, it is expected that the hysteresis loops do not change significantly with the number of cycles. Figure 2.19 presents an idealised saturated hysteresis loop obtained in a fully-reversed strain-controlled test conducted under constant strain rate. It is defined by saturated stress amplitude ($\Delta\sigma/2$) and saturated strain amplitude ($\Delta\varepsilon/2$). The plastic strain amplitude can be calculated using the approximate equation

$$\frac{\Delta\varepsilon_p}{2} = \frac{\Delta\varepsilon}{2} - \frac{\Delta\sigma}{2E} \quad (2.11)$$

being $\Delta\varepsilon_p/2$ the plastic strain amplitude, $\Delta\sigma/2$ the stress amplitude and E the Young's modulus.

The stable material response can be described by a cyclic stress-strain curve (Figure 2.20). Such a curve is usually obtained by connecting the tensile tips of the stabilised hysteresis loops for different strain amplitudes of fully-reversed strain-controlled tests ($R_\varepsilon = -1$). In general, a number of identical smooth highly polished samples are tested under constant amplitude until failure occurs. The hysteresis loops at the half-life are chosen as the representative stable behaviour. This method is called single step test (SST) and is rather time-consuming. Other popular methods used to obtain the cyclic stress-strain curve are summarised in Table 2.5 (Ellyin, 1997). For example, in the multiple step test (MST), the sample is

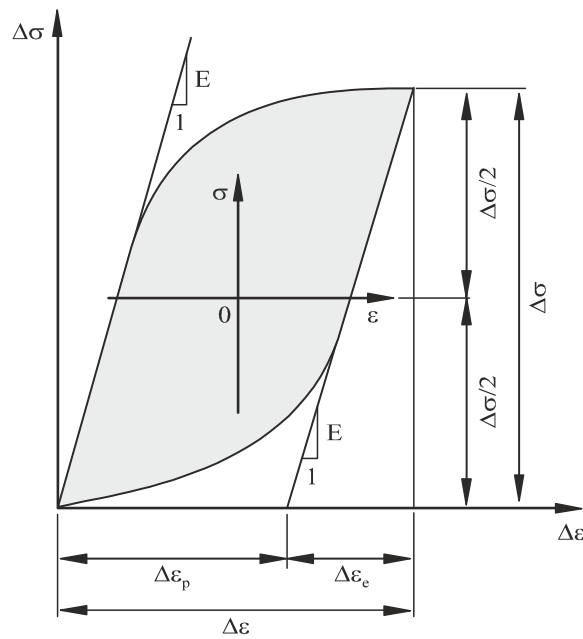


Figure 2.19. Schematic presentation of a saturated hysteresis loop (Ellyin, 1997).

Table 2.5. Different methods used to obtain a cyclic stress-strain curve (Ellyin, 1997).

Test method	Scheme of strain cycles
Single step test	
Multiple step test (low-to-high sequence)	
Multiple step test with (high-to-low sequence)	
Incremental step test	

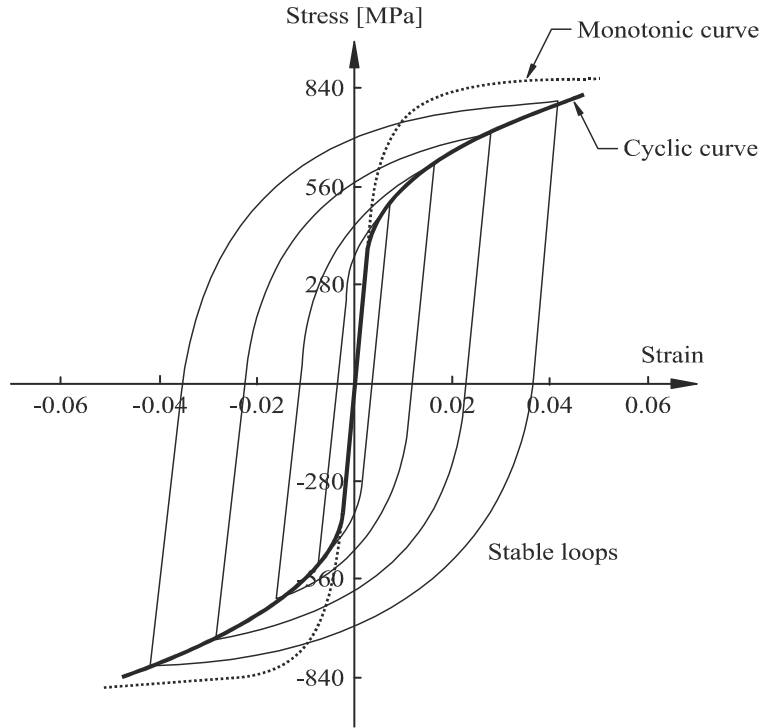


Figure 2.20. Monotonic and cyclic stress-strain curves for DIN 34CrNiMo6 high strength steel (Landgraf, 1970).

subjected to various strain blocks. A low-to-high sequence is often used, but to avoid a mean-stress effect, a high-to-low strain sequence is preferable. The incremental step test (IST) comprises the application of blocks of increasing and decreasing strain amplitudes. After several blocks, the cyclic stable state is achieved. At this point, it is only necessary to draw a line through the tips of each hysteresis loop, from the smallest strain range to the largest. Nevertheless, it is important to note that the SST method is the norm and the others are viewed as an approximation to the above.

The relative position of the monotonic and the cyclic stress-strain curves can be used to characterise the initial material behaviour in cyclic straining. Briefly, when the cyclic stress-strain curve lies above the monotonic stress-strain curve, the material cyclically hardens; when the cyclic stress-strain curve lies below the monotonic stress-strain curve, the material cyclically softens. The latter case is presented, as an example, in Figure 2.20 which compares both the monotonic and cyclically stabilised stress-strain curves for DIN 34CrNiMo6 high strength steel (Landgraf, 1970).

The stabilised stress-strain response can be described mathematically by a power law (Morrow, 1965), i.e.

$$\frac{\Delta\sigma}{2} = k' \left(\frac{\Delta\varepsilon_p}{2} \right)^{n'} \quad (2.12)$$

being n' the cyclic hardening exponent and k' the cyclic hardening coefficient. The unknowns are usually determined from the test data by a best fit procedure. Using Equation 2.11 and Equation 2.12, the

cyclically stabilised stress-strain curve can be expressed in terms of total strain amplitude versus stress amplitude as follows (Ramberg, 1943)

$$\frac{\Delta\epsilon}{2} = \frac{\Delta\epsilon_e}{2} + \frac{\Delta\epsilon_p}{2} \Leftrightarrow \frac{\Delta\epsilon}{2} = \frac{\Delta\sigma}{2E} + \left(\frac{\Delta\sigma}{2k'}\right)^{1/n'} \quad (2.13)$$

where $\Delta\epsilon_e/2$ is the elastic strain amplitude. Although this equation describes the relationship between the stable stress and strain amplitudes, it does not give any information about the shape of the hysteresis loop branches. This description, in an analytical form, is important to explain several phenomena in cyclic behaviour. The first studies on the shape of the hysteresis loops were conducted by Masing (1926). A material is said to exhibit Masing-type behaviour if the hysteresis loop branches can be described by the cyclically stabilised stress-strain curve magnified by a factor of two (Equation 2.14). Thus, the upper branches form a unique curve when the compressive tips of the stable hysteresis loops of different strain amplitudes are moved to a common origin defined by the maximum compressive stress. On the contrary, non-Masing materials are those whose behaviour differs from the above description. According to the experimental data available in the literature, the hysteresis loop branches of DIN 34CrNiMo6 high strength steel can be satisfactorily predicted by assuming Masing-type behaviour (Branco, 2012b).

$$\Delta\epsilon = \frac{\Delta\sigma}{E} + 2\left(\frac{\Delta\sigma}{2k'}\right)^{1/n'} \quad (2.14)$$

The master curve is an alternative form to measure the deviation from the Masing-type description. This curve, as depicted in Figure 2.21, can be obtained by matching the linear response of the upper branches obtained at different strain amplitudes. With respect to an auxiliary coordinate system $(\Delta\sigma^*, \Delta\epsilon^*)$, it is defined as follows

$$\Delta\epsilon^* = \frac{\Delta\sigma^*}{E} + 2\left(\frac{\Delta\sigma^*}{2k^*}\right)^{1/n^*} \quad (2.15)$$

being k^* and n^* the cyclic hardening coefficient and cyclic hardening exponent of the master curve measured with respect to the origin 0^* . The relationships between the two coordinate systems are given by the following equations (Ellyin, 1997)

$$\Delta\sigma = \Delta\sigma + \delta\sigma_0 \quad (2.16)$$

$$\Delta\epsilon_p = \Delta\epsilon_p^* \quad (2.17)$$

$$\Delta\epsilon_e = \Delta\epsilon_e^* + \frac{\delta\sigma_0}{E} \quad (2.18)$$

$$\delta\sigma_0 = \Delta\sigma - 2k^* \left(\frac{\Delta\epsilon_p}{2}\right)^{n^*} \quad (2.19)$$

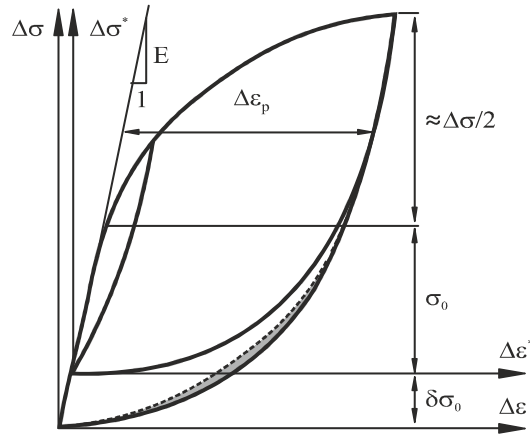


Figure 2.21. Schematic representation of a master curve (Ellyin, 1997).

where $\delta\sigma_0$ is the increase in the proportional stress limit, i.e. a measure of cyclic expansion of the elastic range. The deviation from the Masing-type behaviour for a given stable hysteresis loop can be evaluated by the area contained within the original lower branch and a symmetric lower branch. The larger the area, the greater the deviation. An example of this deviation is presented in Figure 2.21 by the grey area. The dashed line corresponds to the symmetric lower branch.

The cyclically stabilised material properties can be used to predict the fatigue life. The elastic strain component is often described in terms of a relation between stress amplitude and number of reversals to failure (Basquin, 1910), i.e.

$$\frac{\Delta\sigma}{2} = \sigma_f' (2N_f)^b \Leftrightarrow \frac{\Delta\epsilon_e E}{2} = \sigma_f' (2N_f)^b \Leftrightarrow \frac{\Delta\epsilon_e}{2} = \frac{\sigma_f' (2N_f)^b}{E} \quad (2.20)$$

where σ_f' is the fatigue strength coefficient, b is the fatigue strength exponent and $2N_f$ is the number of reversals to failure. This relation is exhibited in Figure 2.22. As can be seen, in a log-log scale, it leads to a straight line. Increased fatigue life is expected with a decreasing fatigue strength exponent and an increasing fatigue strength coefficient. The mean stress effect (σ_m) can be accounted for in Equation 2.21.

$$\frac{\Delta\sigma}{2} = (\sigma_f' - \sigma_m) (2N_f)^b \quad (2.21)$$

The plastic strain component is described by the Coffin-Manson relationship (Coffin, 1954; Manson, 1954) which can be written in the form

$$\frac{\Delta\epsilon_p}{2} = \epsilon_f' (2N_f)^c \quad (2.22)$$

being ϵ_f' the fatigue ductility coefficient and c the fatigue ductility exponent. As exhibited in Figure 2.22, the previous formula represents a straight line in a log-log scale. Increased fatigue life is expected with a decreasing fatigue ductility exponent and an increasing fatigue ductility coefficient. The mean strain

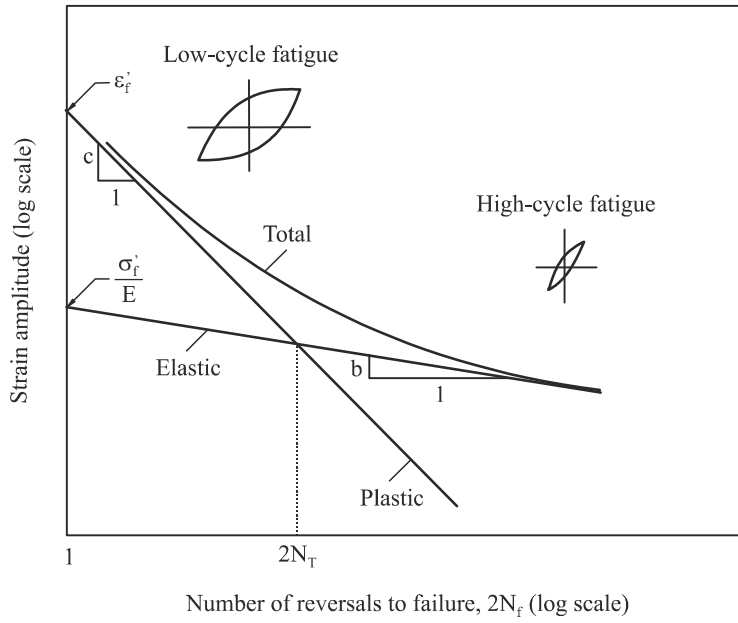


Figure 2.22. Elastic, plastic and total strain amplitudes versus number of reversals to failure.

effect can be accounted for in Equation 2.23. Unlike the mean stress effect, the mean strain effect is very small and is, in general, negligible for $N_f > 1000$ cycles (Ellyin, 1985).

$$\frac{\Delta \epsilon_p}{2} = (\epsilon_f' - \epsilon_m) (2N_f)^c \quad (2.23)$$

The total strain-life curve (Equation 2.24) can be obtained by summing both the elastic and plastic strain components. This expression can only be used to predict the fatigue life at zero mean stress and therefore it must be modified to include the mean stress effect.

$$\frac{\Delta \epsilon}{2} = \frac{\Delta \epsilon_e}{2} + \frac{\Delta \epsilon_p}{2} = \frac{\sigma_f'}{E} (2N_f)^b + \epsilon_f' (2N_f)^c \quad (2.24)$$

The Coffin-Manson (CM) model (Equation 2.25) includes a mean stress correction into the elastic term of the strain-life curve. This model is based on the premise that the mean stress has significant effect on longer lives and *vice versa*. It is consistent with observations that the mean stress has greater impact at longer lives. Manson *et al.* (1981) suggested that both the elastic and the plastic terms should be modified to account for the mean stress effect. Their model, given by Equation 2.26, maintains the independence of the elastic to plastic ratio from the mean stress but tends to overestimate the mean stress effect on short lives, where plastic strain dominates (Ince, 2011). The Smith, Watson and Topper model, defined by Equation 2.27, controls the influence of both the mean stress and the strain amplitude. Such a formulation gives, in general, good estimation of mean stress effect in the long life regime, but it is conservative in the low-cycle fatigue region (Koh, 1991).

$$\frac{\Delta \epsilon}{2} = \frac{(\sigma_f' - \sigma_m)}{E} (2N_f)^b + \epsilon_f' (2N_f)^c \quad (2.25)$$

$$\frac{\Delta \varepsilon}{2} = \frac{(\sigma'_f - \sigma_m)}{E} (2N_f)^b + \varepsilon'_f \left(\frac{\sigma'_f - \sigma_m}{\sigma'_f} \right)^{c/b} (2N_f)^c \quad (2.26)$$

$$\sigma_{\max} \frac{\Delta \varepsilon}{2} = \frac{(\sigma'_f)^2}{E} (2N_f)^{2b} + \varepsilon'_f \sigma'_f (2N_f)^{b+c} \quad (2.27)$$

The transition point ($2N_T$), as depicted in Figure 2.22, represents the life at which both the elastic and plastic strain components are equal. This condition, replacing N_f by N_T , leads to Equation 2.28. For a number of cycles longer than the transition point, the elastic component dominates over the plastic component and *vice versa*. For most materials, the number of cycles to failure associated with the transition point is within the range 10^3 - 10^4 .

$$\frac{\sigma'_f}{E} (2N_T)^b = \varepsilon'_f (2N_T)^c \Leftrightarrow 2N_T = \left(\frac{\varepsilon'_f E}{\sigma'_f} \right)^{-\frac{1}{c-b}} \quad (2.28)$$

During a cyclic loading, part of the supplied energy is stored in the material and emitted as heat. The stored energy is generally divided into a recoverable part and an unrecoverable part. The hysteresis loop is taken to represent the latter. The importance of the hysteresis energy to the fatigue phenomenon was first reported by Bairstow (1910). Under strain-controlled conditions, the area of the hysteresis loop is almost constant during the life. This area represents the plastic strain energy absorbed per cycle (ΔW_p) and is depicted in Figure 2.23 by the dark grey region.

The cyclically stabilised hysteresis loop can be used as a damage parameter to formulate a fatigue criterion for the entire range of the fatigue life. The fatigue criterion assumes the form (Ellyin, 1997)

$$\Delta W_p = \kappa_p (2N_f)^{\alpha_p} + \Delta W_{0p} \quad (2.29)$$

being κ_p and α_p two material constants determined from the best fit to the experimental data and ΔW_{0p} is the hysteresis energy of the material at the fatigue limit. For most metals, the value of ΔW_{0p} is very small and can be omitted for lives up to 5×10^5 reversals ($2N_f < 5 \times 10^5$). For lives close to the fatigue limit, the total strain energy can be used to advantage, since ΔW_p is difficult to measure accurately. The expression to calculate the total strain energy (ΔW_t) includes the sum of both the elastic and plastic strain energies per reversal which correspond, respectively, to the light grey and dark grey regions of Figure 2.23, i.e.

$$\Delta W_t = \Delta W_p + \Delta W_e \quad (2.30)$$

where ΔW_p and ΔW_e are the plastic and elastic strain energies, respectively. In this approach, the fatigue failure criterion can be written as follows (Ellyin, 1997)

$$\Delta W_t = \kappa (2N_f)^\alpha + \Delta W_0 \quad (2.31)$$

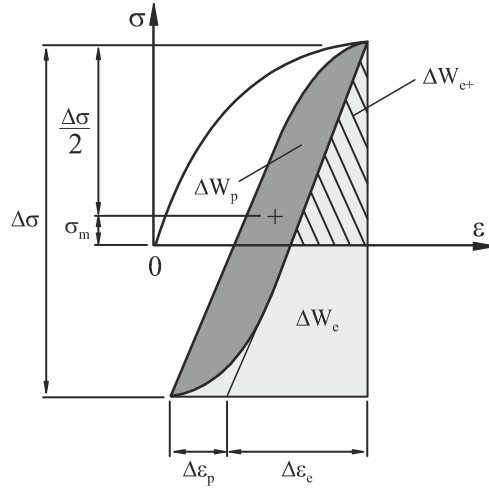


Figure 2.23. Cyclic strain energy per density for uniaxial stress state (Koh, 2002).

being κ and α two material constants obtained from the best fit to the experimental data and ΔW_0 approximately equal to the elastic energy range at the fatigue limit. The two previous approaches are not sensitive to the mean stress effect and therefore are suitable for fully-reversed or almost fully-reversed tests. In order to overcome this drawback, Golos *et al.* (1987; 1988) proposed a different approach, defined by Equation 2.32, which consists of the sum of both the plastic strain energy and elastic strain energy associated with the tensile stress (ΔW_{e+}), i.e. the dark grey and dashed regions of Figure 2.23.

$$\Delta W_t = \Delta W_p + \Delta W_{e+} \quad (2.32)$$

The fatigue failure criterion is given by (Golos, 1987)

$$\Delta W_t = \kappa t (2N_f)^\alpha + \Delta W_{0t} \quad (2.33)$$

where κt and αt are two material constants obtained from the best fit to the experimental data and ΔW_{0t} is the tensile elastic energy range at the fatigue limit.

2.4. Fatigue life of notched bodies

Fatigue life of notched components can be analysed using different models. In the following subsections, some of the models that have gained a widespread acceptance are briefly outlined.

2.4.1 Stress-based models

Stress-based approaches to high-cycle fatigue are based on empirical relationships between applied stress and number of cycles to failure, the so-called S-N curves. The presence of a discontinuity, hereafter referred to as *notch*, causes a stress concentration phenomenon. At and near the notch, the local stress is higher than the remote nominal stress. The intensity of the stress concentration on the notch root is often characterised by the elastic stress concentration factor (K_T), which is defined by the ratio of the maximum

local elastic stress to the remote nominal stress, i.e.

$$K_T = \frac{\sigma_{\max}}{\sigma_{\text{nom}}} \quad (2.34)$$

being σ_{\max} the maximum local elastic stress at the notch tip and σ_{nom} the nominal stress distant from the notch. This factor is influenced by the specimen geometry and the loading mode but is not affected by the mechanical properties of the material. The notch effect is very strong on fatigue behaviour and is usually evaluated by the *fatigue strength reduction factor* (K_f). The most accepted definition of the fatigue strength reduction factor is the ratio of the fatigue strength of an unnotched part to the fatigue strength of a notched part, i.e.

$$K_f = \frac{\Delta\sigma_0}{\Delta\sigma_{0n}} \quad (2.35)$$

being $\Delta\sigma_0$ the fatigue strength of the unnotched part and $\Delta\sigma_{0n}$ the fatigue strength of the notched part. The fatigue strength reduction factor, also called *fatigue notch factor* or *fatigue stress concentration factor*, is a function of different parameters, such as material properties, material inherent defects, notch size, notch shape, stress gradient, loading type and number of loading cycles. The relation between the fatigue strength reduction factor and the elastic stress concentration factor is often expressed in terms of the notch sensitivity index (q), which can be expressed by Equation. 2.36. A material is said to be fully notch sensitive when $K_f = K_T$, i.e. $q = 1$; and it is said to be notch insensitive when $K_f = 1$, i.e. $q = 0$.

$$q = \frac{K_f - 1}{K_T - 1} \quad (2.36)$$

The experimental determination of K_f is probably the most reliable approach. However, it is relatively expensive and time-consuming. Due to this fact, alternative approaches have been proposed to obtain the fatigue strength reduction factor. In general, these approaches can be grouped into *average stress*, *fracture mechanics* and *stress field intensity* methods. Several systematic reviews on the topic are available in the literature (Yao, 1995; Pluvinae, 1998; Qylafku, 1999; Ostash, 2001). Among the previous methods, the average stress method has been extensively used. It is based on the assumption that the controlling parameter for fatigue failure should be stress averaged over a critically stressed line, area or volume surrounding the stress concentration. The model formulated by Kuhn *et al.* (1952) is considered the basis of the average stress models and is defined by

$$K_f = 1 + \frac{K_T - 1}{1 + \frac{\pi}{\pi - \omega} \sqrt{\frac{A}{\rho}}} \quad (2.37)$$

being ρ the radius of the notch root, ω the open angle of the notch and A a material constant which is a function of the material tensile strength limit. It assumes, as schematised in Figure 2.24, that the fatigue

failure occurs when the average stress over a length d , measured from the notch root, is equal to or greater than the fatigue strength of a smooth specimen. Neuber (1958) proposed an alternative formulation

$$K_f = 1 + \frac{K_T - 1}{1 + \sqrt{\frac{a}{\rho}}} \quad (2.38)$$

where a is a material constant defined from the tensile strength limit of the material. The model proposed by Peterson (1959) is a special case of the average stress model since it assumes that the stress near the notch decreases linearly. It can be written as

$$K_f = 1 + \frac{K_T - 1}{1 + \left(\frac{a}{\rho}\right)} \quad (2.39)$$

where a is a constant defined from the yield tensile strength of the material. Siebel *et al.* (1955), based on the same assumption, obtained the expression given by the following equation

$$K_f = \frac{K_T - 1}{1 + \sqrt{a\chi}} \quad (2.40)$$

being a a material constant and χ the relative stress gradient at the notch root. Using the concept of intrinsic defects, Heywood (1962) found the expression

$$K_f = \frac{K_T - 1}{1 + 2\sqrt{\frac{a}{\rho}}} \quad (2.41)$$

where a is a constant that depends on the material and specimen. Applying the relative stress gradient,

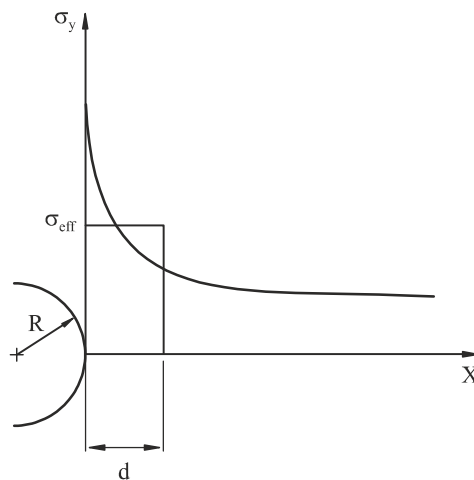


Figure 2.24. Schematic presentation of the average stress model (Yao, 1995).

Buch (1974) deduced the following relationship

$$K_f = K_T \frac{\left(1 - \frac{2.1h}{\rho_0 + \rho}\right)}{A} \quad (2.42)$$

being A and h constants that depend on the material and specimen and ρ_0 a function of the two previous constants. Wang *et al.* (1992) developed another expression based on the relative stress gradient, which can be written in the form

$$K_f = \frac{K_T}{0.88 + A\chi^b} \quad (2.43)$$

being A and b material constants and χ the relative stress gradient at the notch root. Alternative models obtained from the average stress method can be found elsewhere (Schijve, 1980; Hardy, 1992).

The fatigue strength reduction factor can also be calculated using fracture mechanics models. The fracture mechanics model proposed by Ting *et al.* (1993), as depicted in Figure 2.25, is based on the concept of a non-propagating crack of length a_{th} . In this approach, the fatigue strength reduction factor is defined by

$$K_f = \frac{U_{th} Y(a_{th})}{U_{th0}} \sqrt{\frac{D + a_{th}}{a_0}} \quad (2.44)$$

where U_{th0} is the effective threshold stress intensity ratio for a long crack, U_{th} is the effective threshold stress intensity ratio for a crack length a_{th} , $Y(a_{th})$ is the geometric factor, D is the notch depth and a_0 is the

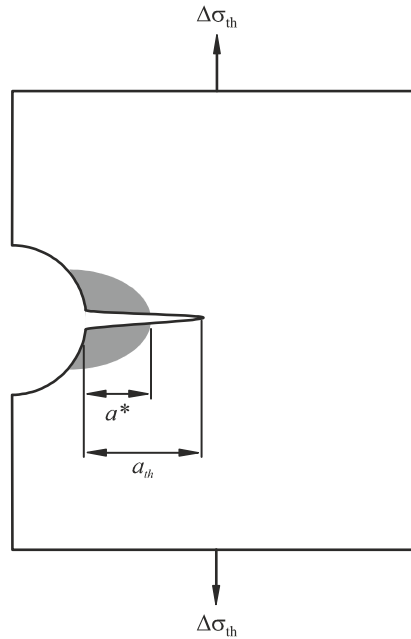


Figure 2.25. Schematic presentation of the fracture mechanics model (Yao, 1995).

intrinsic crack length. The value of a_0 can be calculated from the following equation

$$a_0 = \frac{1}{\pi} \left(\frac{\Delta K_{th}}{\Delta \sigma_0} \right)^2 \quad (2.45)$$

being ΔK_{th} the long crack threshold stress intensity factor range, which is a material constant for a given stress ratio. If $a_{th} > a^*$, Equation 2.44 assumes the form

$$K_f = Y(a_{th}) \left(1 + \sqrt{\frac{D_{eff}}{a_0}} \right) \quad (2.46)$$

where D_{eff} is the effective notch depth. If $a_{th} < a^*$, Equation 2.44 can be written as follows

$$K_f = \frac{U_{th^*} Y(a^*)}{U_{th0}} \sqrt{\frac{D + a^*}{a_0}} \quad (2.47)$$

being U_{th0} and U_{th^*} the effective threshold stress intensity factor ratio for a long crack and for a crack with length a^* , respectively. Alternative expressions for K_f obtained from fracture mechanics models were proposed by Smith *et al.* (1977) and Yu *et al.* (1988).

The stress field intensity method, as illustrated in Figure 2.26, assumes that fatigue failure is caused by damage accumulation in a region surrounding the notch with size of several grains. In this approach, the damage accumulation is not only a function of the peak stress but also of the stress field intensity of the damage zone. If the history of the local stress field intensity function in the failure region near the notch is the same as that of the smooth specimen, the notched and the smooth specimens have the same fatigue life (Yao, 1993; Shang, 2001). The stress field intensity function (σ_{FI}) can be defined by

$$\sigma_{FI} = \frac{1}{V} \int_{\Omega} f(\sigma_{ij}) \varphi(\vec{r}) dv \quad (2.48)$$

being Ω the fatigue failure region, V the volume of the fatigue failure region, $\varphi(\vec{r})$ the weight function and $f(\sigma_{ij})$ is the equivalent stress function. The equivalent stress function can be the von Mises equivalent stress, major stress, or another magnitude related to the stress, supposed to play a major role in the fatigue failure process. The weight function accounts for the contribution of the equivalent stress at a point P to the peak stress at $\vec{r} = 0$. It can be obtained either analytically or numerically. Besides, it should have the following characteristics:

- $0 \leq \varphi(\vec{r}) \leq 1$ and $\varphi(\vec{r})$ is a generalised monotonically decreasing function about $|\vec{r}|$;
- $\varphi(0) \equiv 1$, which means that the contribution of the stress at the notch root is maximum;
- when stress gradient $\chi = 0$, $\varphi(\vec{r}) \equiv 1$, which is consistent with the condition of smooth specimens.

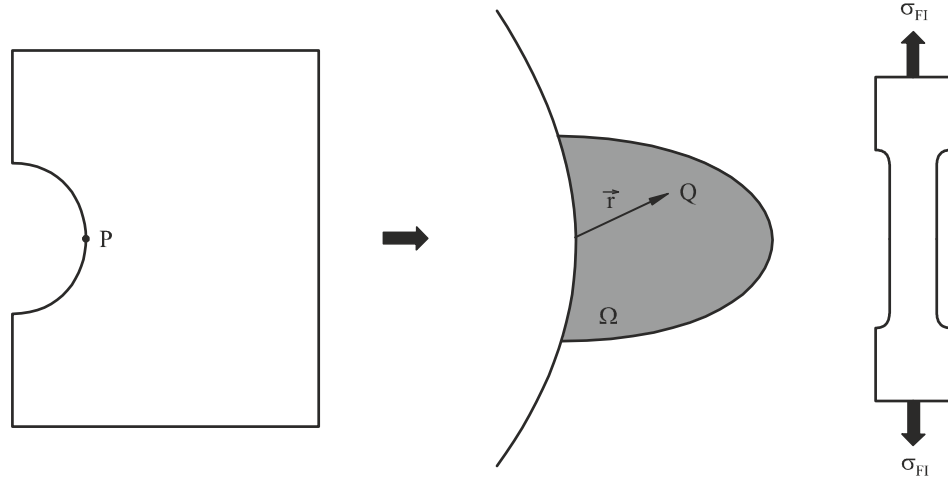


Figure 2.26. Schematic presentation of the stress field intensity model (Qylafku, 1999).

The above-mentioned conditions can be fulfilled through the following function

$$\varphi(\vec{r}) = 1 - \chi|\vec{r}| \quad (2.49)$$

where χ is the relative stress gradient. For a notched specimen, the fatigue strength reduction factor is defined by

$$K_f = \frac{1}{V} \int_{\Omega} f(\bar{\sigma}_{ij}) \varphi(\vec{r}) dv \quad (2.50)$$

being the stress equivalent function given by

$$f(\bar{\sigma}_{ij}) = f(\sigma_{ij}) \sigma_n \quad (2.51)$$

where σ_n is the applied net stress. For a plane damage zone D and for a linear damage zone E , the previous equation leads, respectively, to

$$K_f = \frac{1}{S} \int_D f(\bar{\sigma}_{ij}) \varphi(\vec{r}) dv \quad (2.52)$$

$$K_f = \frac{1}{L} \int_E f(\bar{\sigma}_{ij}) \varphi(\vec{r}) dv \quad (2.53)$$

being S and L their respective sizes. In a second stage, the original approach based on elastic stress distributions (Pluvinage, 1997; Pluvinage, 1997a) was improved to evaluate the real elastic-plastic stress distribution near the notch tip (Qylafku, 1999; Shang, 2001). Figure 2.27 exhibits a typical elastic-plastic stress distribution near the notch tip in a log-log scale and the corresponding relative stress gradient in

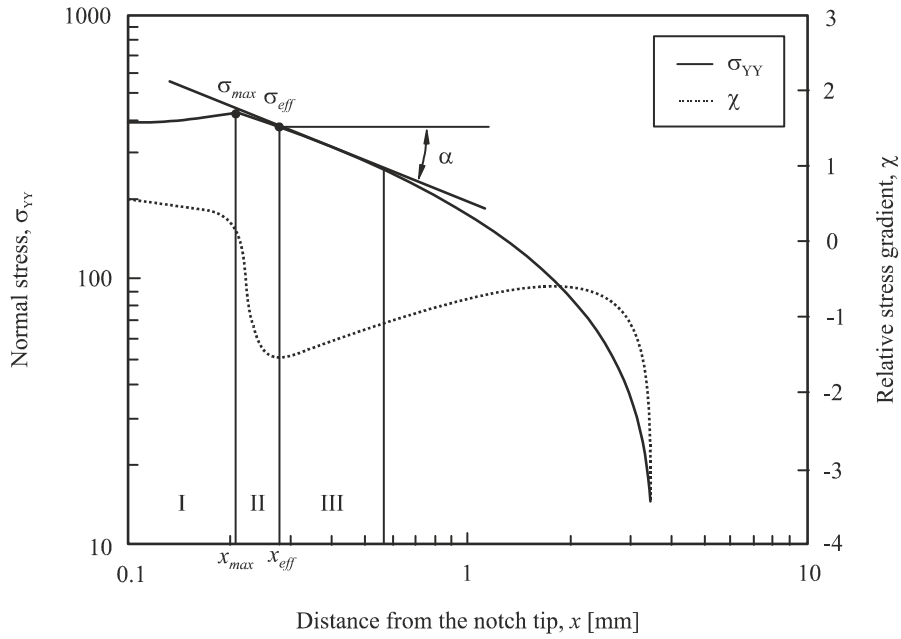


Figure 2.27. Typical elastic-plastic stress distribution versus the distance from the notch tip (Qylafku, 1999).

normal coordinates. This stress distribution encompasses three main regions:

- the *first region* includes the maximum stress ($x > 0$) which is defined by the coordinates x_{max} , σ_{max} . In elastic analyses, the maximum stress occurs at the notch tip ($x = 0$) and then the stress gradually decreases with the distance from the notch root;
- the *second region* is an intermediate between the other two regions;
- the *third region* is characterised by a stress distribution which can be fitted by a power function. In this region, the stress distribution can be considered a straight line. The abscissa of the first point of this region is named effective distance (x_{eff}) and the resultant stress is called effective stress (σ_{eff}). It is supposed to be the boundary of the fatigue process zone and it is simultaneously the boundary of the stress relaxation. The stress distribution of the third region, as referred to above, can be defined by a power law (Equation 2.54) where α and C are constants depending on loading and geometry.

$$\sigma_{YY} = \frac{C}{x^\alpha} \quad (2.54)$$

The relative stress gradient (χ), exhibited in Figure 2.27, can be written in the form

$$\chi = \frac{1}{\sigma_{YY}(x)} \frac{d\sigma_{YY}(x)}{dx} \quad (2.55)$$

being $\sigma_{YY}(x)$ the normal stress distribution in the loading direction. This expression evaluates the ratio of the first derivative of the stress distribution to the value of stress at the corresponding point. As can be

seen in Figure 2.27, at the effective distance, the relative stress gradient has its minimum value. Based on this approach, the stress field intensity can be expressed in the following form

$$\sigma_{FI}^* = \frac{1}{x_{eff}} \int_0^{x_{eff}} \sigma_{YY} (1 - \chi x) dx \quad (2.56)$$

and the fatigue strength reduction factor is given by

$$K_f = \frac{1}{x_{eff} \sigma_n} \int_0^{x_{eff}} \sigma_{YY} (1 - \chi x) dx \quad (2.57)$$

being x_{eff} the effective distance schematised in Figure 2.27.

As earlier mentioned, the average stress methods are based on the idea that fatigue failure takes place if a critical volume of material is subjected to a critical stress. The formulation proposed by Neuber (Equation 2.38) uses a reference stress obtained by averaging the elastic stress over a certain distance from the notch root and is named line method (LM). The Peterson's model (Equation 2.39) considers the stress at a specific distance from the notch apex and is called point method (PM). These two methods have been revisited by different authors (Tanaka, 1983; Lazzarin, 1997; Taylor, 1999). This approach was extended to more complex methods, such as the area method (AM) or volume method (VM) and is called the theory of critical distances (TCD). A common feature of this theory is the use of elastic stress distributions in front of the notch. Another common feature is the use of a material characteristic length, termed critical distance.

The critical distance can be obtained using the El Haddad (1980) parameter (a_0) presented in Equation 2.45. The critical distances for the point method (D_{PM}), line method (D_{LM}) and area method (D_{AM}) are schematised in Figure 2.28 and can be defined as follows

$$D_{PM} = \frac{a_0}{2} \quad (2.58)$$

$$D_{LM} = 2a_0 \quad (2.59)$$

$$D_{AM} = a_0 \quad (2.60)$$

being D_{PM} , D_{LM} and D_{AM} the critical distances for the point method, line method and area method, respectively. The calculation of a_0 is identical to that for an intrinsic crack size, which is usually described by the Kitagawa-Takahashi (1976) diagram. The intrinsic crack size (a_0) indicates the crack length below which a small crack defect exists and linear elastic fracture mechanics (LEFM) is not valid. Figure 2.29 presents a typical Kitagawa-Takahashi diagram. As can be seen, the fatigue limit changes with the length

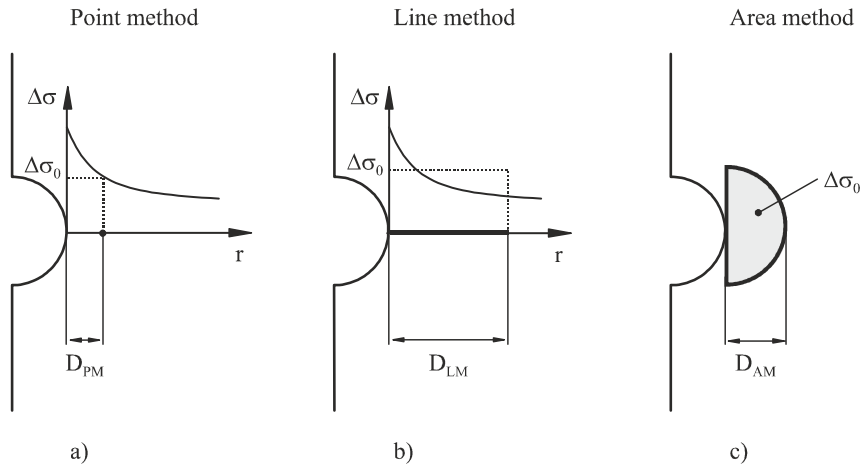


Figure 2.28. Concept of the theory of critical distances (TCD): a) point method; b) line method; c) area method (Susmel, 2011).

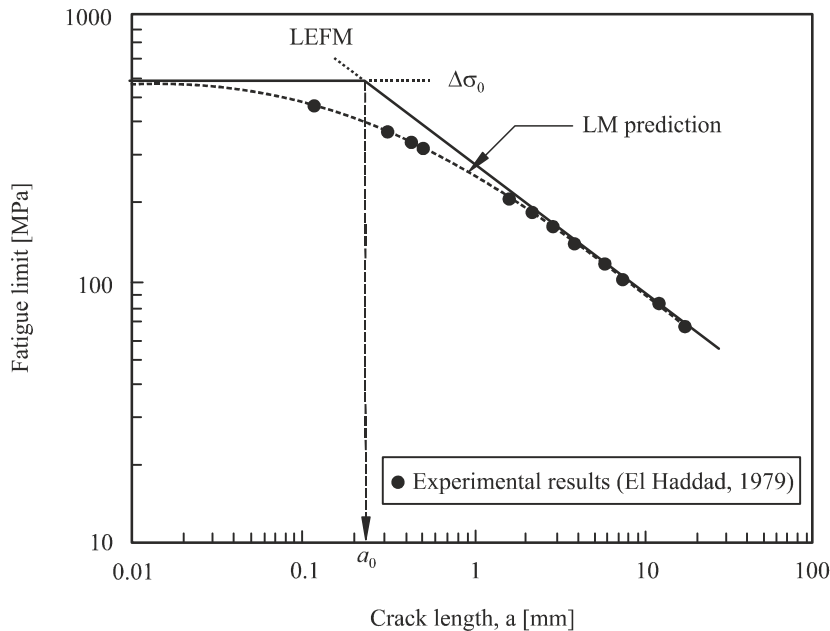


Figure 2.29. Kitagawa-Takahashi diagram describing the crack size effect on fatigue propagation of short and long cracks (Taylor, 2008).

of a pre-existing crack. For large cracks, the results lie on a line corresponding to the prediction of the LEFM and are controlled by the threshold stress intensity factor range for crack growth (ΔK_{th}). For very small cracks, the crack size has no effect on fatigue limit which is given by $\Delta\sigma_0$. For intermediate crack lengths, the data are between these two types of behaviour. General speaking, in the case of crack lengths much smaller than a_0 , the presence of a crack is harmless; in the case of crack lengths much greater than a_0 , the LEFM procedures are applied; in the case of crack lengths similar to a_0 , the analysis is carried out using the TCD.

2.4.2 Strain-based models

The strain-based models attempt to account directly for the plasticity at the notch root. This approach, as depicted in Figure 2.30, is based on the assumption that both smooth and notched specimens have the same life and accumulate the same damage if their stress-strain histories, at the crack initiation sites, are similar. In this sense, an accurate determination of the local stress-strain history experienced by the material at the notch root is essential. The available methods used to determine the local stress and strain fields at the notch root encompass experimental techniques, such as the strain gauges, X-ray diffraction, among others; analytical approximations methods, for instance the approaches proposed by Hardrath and Ohman (1953), Neuber (1968), Molski and Glinka (1981), etc.; and the application of the finite element method (FEM).

The degree of stress concentration depends on the notch geometry and can be characterised by introducing the stress concentration factor (K_σ) and the strain concentration factor (K_ϵ). These two factors can be expressed, respectively, as follows

$$K_\sigma = \frac{\sigma_{\max}}{\sigma_{\text{nom}}} \quad (2.61)$$

$$K_\epsilon = \frac{\epsilon_{\max}}{\epsilon_{\text{nom}}} \quad (2.62)$$

where σ_{\max} and ϵ_{\max} are, respectively, the maximum stress and strain at the notch root and σ_{nom} and ϵ_{nom} are, respectively, the nominal stress and strain calculated at a region remote from the stress concentration. Although there are some circumstances in which both the nominal stress and nominal strain are defined with respect to a reduced cross-section at the notch location, the former approach is preferable from a physical point of view (Ellyin, 1997). In unidirectional or cyclic straining is valid the relationship

$$K_\sigma \leq K_T \leq K_\epsilon \quad (2.63)$$

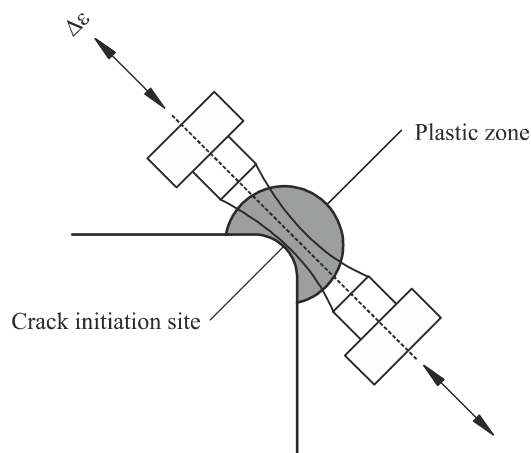


Figure 2.30. Schematic illustration of the local strain approach (Ellyin, 1997).

being K_T the elastic stress concentration factor (see Equation 2.34). In the case of elastic behaviour, the three factors are similar.

Several researchers have tried to correlate the elastic stress concentration factor to the stress and strain concentration factors. The formulation developed by Hardrath and Ohman (1953) is given by Equation 2.64. The Neuber's rule (1968) assumes that the elastic stress concentration factor is equal to the geometric mean of the stress and strain concentration factors (Equation 2.65).

$$K_\varepsilon = \frac{K_T - 1}{K_\sigma - 1} K_\sigma \quad (2.64)$$

$$K_T^2 = K_\sigma K_\varepsilon \quad (2.65)$$

Assuming a stress-strain relationship given by a power law, i.e.

$$\varepsilon = \frac{\sigma}{E} + \left(\frac{\sigma}{k} \right)^{1/n} \quad (2.66)$$

and that the nominal stress and the nominal strain are in the elastic range, Equation 2.65 can be written in the form

$$\frac{(K_T \sigma_n)^2}{E} = \frac{\sigma^2}{E} + \sigma \left(\frac{\sigma}{k} \right)^{1/n} \quad (2.67)$$

being k the monotonic hardening coefficient, n the monotonic hardening exponent, σ the local stress and σ_n the nominal stress. For cyclic loading applications, Topper *et al.* (1969) replaced K_T by the fatigue strength reduction factor (K_f), i.e.

$$\frac{(K_f \Delta \sigma_n)^2}{4E} = \frac{\Delta \sigma^2}{4E} + \frac{\Delta \sigma^2}{2} \left(\frac{\Delta \sigma}{2k'} \right)^{1/n'} \quad (2.68)$$

where k' and n' are the parameters of the appropriate cyclic stress-strain curve and $\Delta \sigma_n$ is the nominal stress range. As exhibited in Figure 2.31, the stress-strain behaviour at the notch root can be determined from the intersection of the stress-strain curve and the Neuber's hyperbolas, which occurs at points Q and R . The stress and strain amplitudes of the stabilised hysteresis loop can be calculated using the following relationship

$$\left(\frac{\Delta \sigma}{2} \frac{\Delta \varepsilon}{2} E \right)^{1/2} = K_f \left(\frac{\Delta \sigma_n}{2} \frac{\Delta \varepsilon_n}{2} E \right)^{1/2} \quad (2.69)$$

being $\Delta \sigma/2$ the local stress amplitude, $\Delta \varepsilon/2$ the local strain amplitude, $\Delta \sigma_n/2$ the nominal stress amplitude

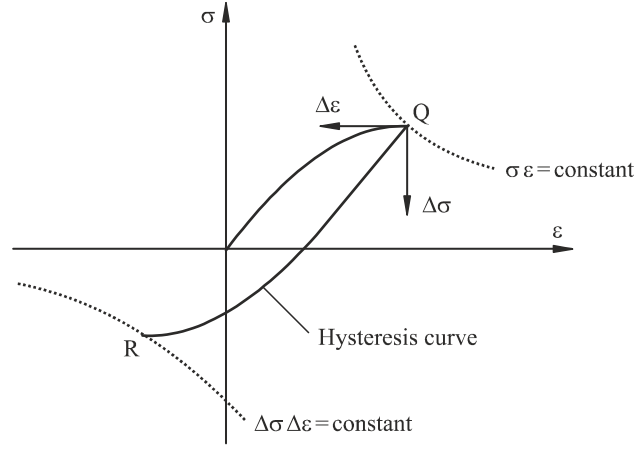


Figure 2.31. Schematic illustration of the procedure used to obtain the local stress-strain response at the notch tip using a smooth specimen according to the Neuber's rule (Suresh, 1998).

and $\Delta\epsilon_n/2$ the nominal strain amplitude. The number of cycles required to produce a crack at the notch can be determined from the fatigue life curves obtained under strain-controlled conditions using smooth specimens. Therefore, inserting both Equation 2.20 and Equation 2.22 into Equation 2.69, the number of cycles to initiate a macroscopic crack (N_i) can be expressed as follows

$$(\sigma_a \epsilon_a E)^{1/2} = \frac{1}{K_f} \left[\sigma_f'^2 (2N_i)^{2b} + E \sigma_f' \epsilon_f' (2N_i)^{b+c} \right] \quad (2.70)$$

where b and c are, respectively, the fatigue strength and the fatigue ductility exponents. The mean stress effect can be accounted for using a mean stress correction formula.

Shang *et al.* (2001) proposed a local stress-strain field intensity model (SSFI) which was developed on the basis of the local stress field intensity (SFI) approach (Yao, 1993; Qylafku; 1998). This new model assumes that the damage cumulative process at the notch depends not only on the local stress field intensity but also on the local strain intensity field. Thus, two field intensity parameters are used to describe the fatigue damage at the notch, i.e. the stress field intensity parameter (σ_{FI}) given by Equation 2.48 and the strain intensity field parameter (ϵ_{FI}) given by

$$\epsilon_{FI} = \frac{1}{V} \int_{\Omega} f(\epsilon_{ij}) \varphi(\vec{r}) dv \quad (2.71)$$

being Ω the fatigue failure region, V the volume of the fatigue failure region, $\varphi(\vec{r})$ the weight function and $f(\epsilon_{ij})$ the equivalent strain function. These weight functions, as already referred to in Section 2.4.1, are generally monotonically decreasing functions of \vec{r} . The three typical characteristics are:

- $0 \leq \varphi(\vec{r}) \leq 1$;

- $\varphi(0) \equiv 1$;
- when $\chi = 0$, $\varphi(\vec{r}) \equiv 1$.

For an isotropic material, appropriate functions are (Shang, 2001):

$$\varphi(\vec{r}) = 1 - \left(1 - \frac{\sigma_{eqQ}}{\sigma_{peak}} \right) r (1 + \sin \theta) \quad (2.72)$$

$$\varphi(\vec{r}) = 1 - \left(1 - \frac{\varepsilon_{eqQ}}{\varepsilon_{peak}} \right) r (1 + \sin \theta) \quad (2.73)$$

where σ_{eqQ} is the equivalent stress at point Q , ε_{eqQ} is the equivalent strain at point Q , σ_{peak} is the maximum stress, ε_{peak} is the maximum strain, and θ and r are schematised in Figure 2.32. The parameters $(1 - \sigma_{eqQ}/\sigma_{peak})$ and $(1 - \varepsilon_{eqQ}/\varepsilon_{peak})$ account for the effect of stress and strain gradients, respectively. The stress field intensity and the strain field intensity parameters can be determined by means of the elastic-plastic finite element method. Figure 2.32 illustrates, as an example, the calculation of the main parameters for a ductile material under plane stress state. For the i^{th} element in the fatigue failure region Ω , the equivalent stress and strain functions are defined, respectively, as follows

$$f(\sigma_{ij}) = (\sigma_{xx}^2 + \sigma_{yy}^2 - \sigma_{xx}\sigma_{yy} + 3\tau_{xy}^2)^{1/2} = \sigma_{eq}^i \quad (2.74)$$

$$f(\varepsilon_{ij}) = \frac{1}{1+\nu} \left[\frac{1-\nu+\nu^2}{(1-\nu)^2} (\varepsilon_{xx}^2 + \varepsilon_{yy}^2) - 3\varepsilon_{xx}\varepsilon_{yy} + \frac{3}{4}\gamma_{xy}^2 \right]^{1/2} = \varepsilon_{eq}^i \quad (2.75)$$

where σ_{xx} , σ_{yy} , τ_{xy} are the stress components, ε_{xx} , ε_{yy} , γ_{xy} are the strain components and ν is the Poisson's ratio. For a point Q located in the i^{th} element of the finite element mesh, the weight functions

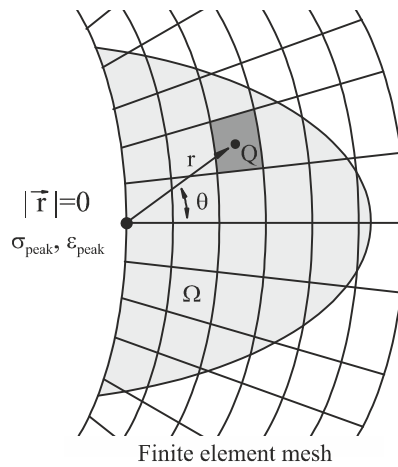


Figure 2.32. Schematic illustration of the procedure used to obtain the stress intensity parameter and the strain intensity parameter using an elastic-plastic finite element analysis (Shang, 2001).

presented in Equations 2.72 and 2.73, can be rewritten in the form

$$\varphi(r_i) = 1 - \left(1 - \frac{\sigma_{eq}^i}{\sigma_{peak}} \right) r(1 + \sin \theta) \quad (2.76)$$

$$\varphi(r_i) = 1 - \left(1 - \frac{\varepsilon_{eq}^i}{\varepsilon_{peak}} \right) r(1 + \sin \theta) \quad (2.77)$$

where σ_{eq}^i and ε_{eq}^i are, respectively, the equivalent stress and strain functions computed by means of elastic-plastic finite element analysis for the i^{th} element. Repeating this analysis for all elements in the fatigue damage failure region Ω , the stress field intensity and strain field intensity values are approximately given by

$$\sigma_{FI} = \frac{1}{S} \sum_{i=1}^n \sigma_{eq}^i \varphi(r_i) \Delta S_i \quad (2.78)$$

$$\varepsilon_{FI} = \frac{1}{S} \sum_{i=1}^n \varepsilon_{eq}^i \varphi(r_i) \Delta S_i \quad (2.79)$$

being S the area of the fatigue damage failure region.

2.4.3 Energy-based models

Hutchinson (1968) demonstrated that the strain energy density distribution in the plastic zone ahead of a crack tip for a material with bilinear stress-strain behaviour is equal to that calculated from a linear elastic stress-strain analysis. Molski and Glinka (1981) assumed the same behaviour for notched components and materials with nonlinear stress-strain distributions. In view of this point, the strain energy density can be calculated using an elastic stress distribution, even in the presence of localised plastic yielding at the notch tip. Then, the strain energy density calculated is converted into equivalent elastic-plastic strains and stresses existing at the notch tip by using the nonlinear stress-strain curve of the material under analysis.

The equivalent strain energy density concept states that the ratio of the maximum strain energy density in the notch tip to the nominal strain energy density is the same in elastic and elastic-plastic straining. This concept is depicted in Figure 2.33. If the straining at the notch root is in the elastic regime, this ratio under uniaxial stress state is equal to

$$W_e = \int_0^{\varepsilon_e} \sigma d\varepsilon \Leftrightarrow W_e = \frac{\sigma_e \varepsilon_e}{2} \Leftrightarrow W_e = \frac{\sigma_n^2 K_T^2}{2E} \Leftrightarrow W_e = W_n K_T^2 \quad (2.80)$$

where W_e is the maximum strain energy density at the notch root, W_n is the nominal strain energy density and K_T is the elastic stress concentration factor. Molski and Glinka (1981) assumed that the previous

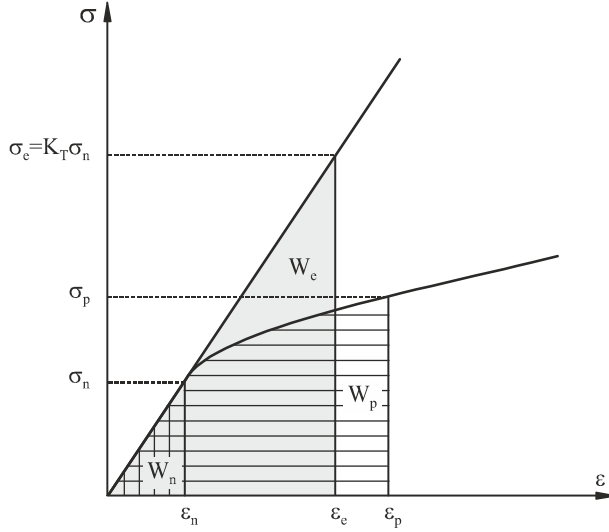


Figure 2.33. Graphical interpretation of the equivalent energy density concept (Glinka, 1985).

relationship is also applicable when localised plastic yielding occurs ahead of the notch tip, i.e.

$$W_p = W_e = W_n K_T^2 \quad (2.81)$$

being W_p the strain energy density due to the elastic-plastic stress. Using the nonlinear stress-strain curve given by Equation 2.66, the previous relationship can be written in the form

$$\frac{\sigma^2}{2E} + \frac{\sigma}{n+1} \left(\frac{\sigma}{k} \right)^{1/n} = K_T^2 \frac{\sigma_n^2}{2E} \quad (2.82)$$

where k is the monotonic hardening coefficient, n is the monotonic hardening exponent, σ is the local stress and σ_n is the nominal stress. The previous equation can be extended to account for the small non-linearity just below the yield limit. In such a case, it is given by Equation 2.83 (Glinka, 1985).

$$\frac{\sigma^2}{2E} + \frac{\sigma}{n+1} \left(\frac{\sigma}{k} \right)^{1/n} = K_T^2 \left[\frac{\sigma_n^2}{2E} + \frac{\sigma_n}{n+1} \left(\frac{\sigma_n}{k} \right)^{1/n} \right] \quad (2.83)$$

Ellyin and Kujawski (1987) obtained a similar formulation (Equation 2.84) for the strain energy density along a smooth notch boundary using the Rice's J-integral, which can be written as follows

$$\frac{\sigma^2}{2E} + \frac{1}{n+1} \sigma \varepsilon^p = K_T^2 \left[\frac{\sigma_n^2}{2E} \right] + \frac{1}{n+1} \sigma_n \varepsilon_n^p \quad (2.84)$$

being ε^p the plastic strain at the notch root and ε_n^p the nominal plastic strain. This expression reduces to the Molski-Glinka's model (Equation 2.82) when the nominal strain values are below the yield limit of the material ($\varepsilon_n^p = 0$) and reduces to the Neuber's model (Equation 2.65) when the material has a high

strain hardening slope, i.e. $2/(n+1) \approx 1$ (Ellyin, 1987).

In the case of cyclic loading, the nominal and local stresses are replaced by the nominal and local stress ranges. The stress-strain behaviour can be defined by the cyclic stress-strain curve (Equation 2.13). In this way, Equation 2.82 assumes the form

$$\frac{\Delta\sigma^2}{4E} + \frac{\Delta\sigma}{n+1} \left(\frac{\Delta\sigma}{2k'} \right)^{1/n'} = K_T^2 \frac{\Delta\sigma_n^2}{4E} \quad (2.85)$$

while Equation 2.83 can be written as follows

$$\frac{\Delta\sigma^2}{4E} + \frac{\Delta\sigma}{n+1} \left(\frac{\Delta\sigma}{2k'} \right)^{1/n'} = K_T^2 \left[\frac{\Delta\sigma_n^2}{4E} + \frac{\Delta\sigma_n}{n+1} \left(\frac{\Delta\sigma_n}{2k'} \right)^{1/n'} \right] \quad (2.86)$$

where k' is the cyclic hardening coefficient and n' is the cyclic hardening exponent.

A more general approach to analyse the elastic-plastic deformation existing at the notch root was proposed by Ellyin and Kujawski (1989). For a body subjected to small-scale yielding near the notch, as depicted in Figure 2.34, there is a relationship between the actual elastic-plastic material and a linear elastic material which can be expressed as

$$\int_{V_R} \sigma_{ij}^a \varepsilon_{ij}^a dV = \int_{V_R} \sigma_{ij}^e \varepsilon_{ij}^e dV \quad (2.87)$$

being σ_{ij}^a and ε_{ij}^a the actual stress and strain fields, σ_{ij}^e and ε_{ij}^e the stress and strain fields obtained from a linear elastic analysis, and V_R is the volume enclosed by R which is a far-field boundary where the

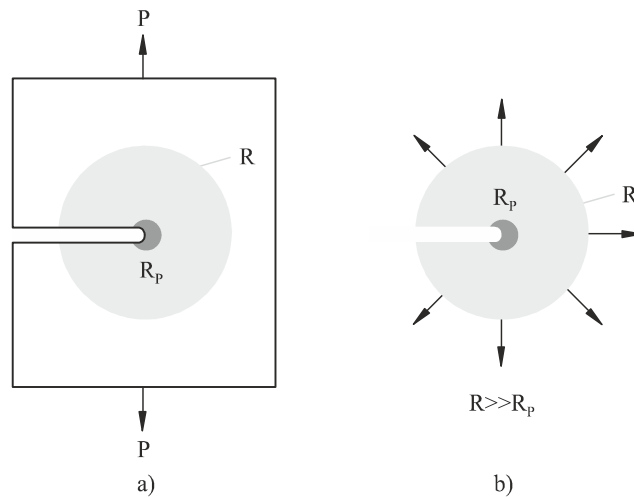


Figure 2.34. Notch with small-scale yielding at its root: a) plastic zone size; b) tractions at a radius R away from the notch root (Ellyin, 1997).

effect of the plastic zone R_p is negligible, i.e. $R \gg R_p$. For an elastic-plastic material under constant amplitude cyclic loading, the above energy approach leads to

$$K_T^2 \left[\frac{1}{2} \Delta \sigma_n \Delta \varepsilon_n \right] = \Delta W_p + \Delta W_e \quad (2.88)$$

being ΔW_p the plastic strain energy per cycle and ΔW_e the elastic strain energy per cycle. In addition, the number of cycles to failure ($2N_f$) can be related to the total strain energy per cycle (ΔW) by Equation 2.31. Therefore, the number of cycles to initiate a crack at the notch root can be estimated by solving both Equations 2.88 and 2.31. One advantage of this formulation is that it can be applied to uniaxial and multiaxial states under constant amplitude cyclic loading (Ellyin, 1989).

Bentachfine *et al.* (1999) developed a volumetric approach based on the total strain energy density per cycle. As in other volumetric approaches, this method assumes that the fatigue process requires a critical volume to take place. It can be used in both uniaxial and multiaxial fatigue problems, either in low-cycle or high-cycle regimes. The total strain energy density range (ΔW) can be obtained with the finite element method. A typical distribution of ΔW versus the distance from the notch tip is exhibited in Figure 2.35. This distribution can be divided into three main parts:

- a *first region* where the strain energy density is nearly constant and has its maximum value;
- a *second region* which is an intermediate region between the first and the third regions;
- a *third region* where the strain energy density exhibits a power law dependence on the distance from

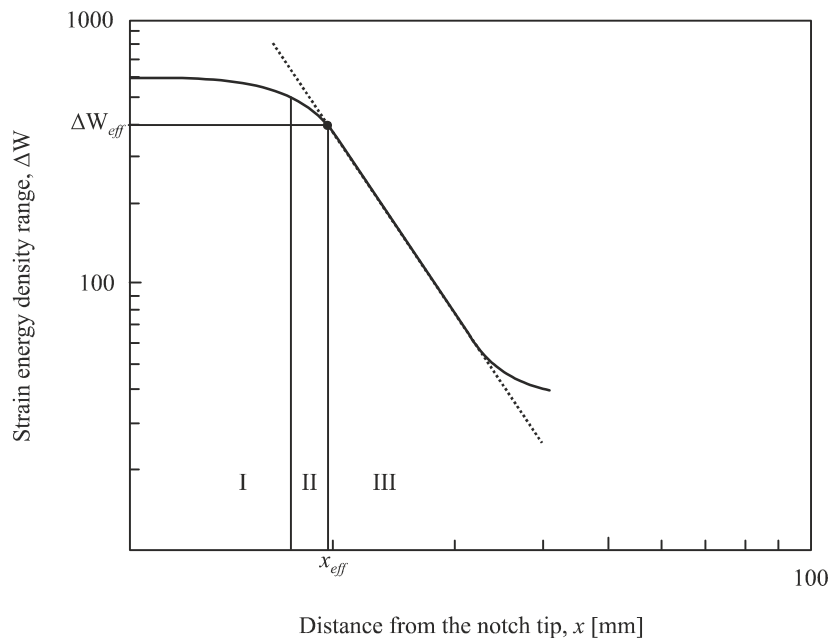


Figure 2.35. Typical strain energy density distribution at the notch tip plotted in a log-log scale (Bentachfine, 1999).

the notch tip which can be expressed mathematically as follows

$$\Delta W = \varphi r^{-\gamma} \quad (2.89)$$

where φ and γ are constants.

The critical volume, in which the fatigue process takes place, is assumed to be cylindrical and has a diameter equal to the effective distance (x_{eff}). According to the authors (Bentachfine, 1999), the effective distance must be higher than the plastic zone diameter since the effective stress is lower than the yield stress; and it must be located in the high stressed region where the stress gradient is not too high. As depicted in Figure 2.53, the strain energy density at the effective distance (x_{eff}) is termed effective strain energy density (ΔW_{eff}). The number of cycles to initiate a crack at the notch can be estimated by using the average strain energy density which is defined by

$$\overline{\Delta W} = A (2N_f)^a \quad (2.90)$$

being $\overline{\Delta W}$ the average strain energy density and A and a are parameters which depend on the notch radius. The fatigue strength reduction factor can be obtained from Equation 2.91.

$$K_f = \left(\frac{\Delta W_{eff}}{\overline{\Delta W}} \right)^{1/2} \quad (2.91)$$

2.5. Multiaxial fatigue

Many critical mechanical components and structures experience a multiaxial stress state during their service life. The fatigue process under multiaxial loading is, in general, complex because it usually involves three-dimensional stress or strain histories. In this sense, the ability to accurately predict the fatigue behaviour under complex loading states is of great practical significance. Several attempts have been made to develop a universal multiaxial damage model. Nevertheless, the efficiency of a specific model depends on different aspects, such as materials, fracture and fatigue mechanisms, loading conditions, etc. (Kim, 1999; Liu, 2005). Accordingly, no single multiaxial fatigue damage model has been universally accepted yet (Socie, 1987).

The first research on multiaxial fatigue was published by Lanza (1886) in the nineteenth century and was performed under combined bending-torsion loading. In the beginning of the twentieth century, various empirical models obtained from experimental results were proposed (Manson, 1917; Haigh, 1923; Nishiara, 1941; Gough, 1951). The first theories to predict fatigue failure under multiaxial loading were basically an extension of the failure theories for static multiaxial stress states to cyclic multiaxial stress states. The main purpose of these theories was to reduce complex multiaxial stress states to an equivalent uniaxial stress state and then use it to predict the fatigue life from conventional fatigue tests. However,

these models may work for proportional or in-phase loadings but often lead to significant errors for non-proportional or out-of-phase loadings (Garud, 1981; Zenner, 2004).

The definitions of *proportional* and *non-proportional* loadings are important concepts in multiaxial fatigue. Proportional loading is assumed to exist when the orientation of the principal stress axes remains fixed with respect to the axes of the component. Non-proportional loading is assumed to occur when the orientation of the principal stress axes changes with respect to the axes of the component. Two representative examples of proportional and non-proportional loading are illustrated in Figures 2.36a and 2.36b, respectively. The shaft is subjected to both shear and axial stresses. In the former example, the size of the Mohr's circle changes over the time but X' coincides with the principal normal stress axis. On the contrary, in the latter example, X' does not always coincide with the principal normal stress axis (Socie, 2000). The terms *in-phase* and *out-of-phase* are used to describe particular loading cases involving periodic histories, such as *sine* or *triangular* waveforms. In-phase loading results always in proportional paths while out-of-phase loading can result in proportional or non-proportional paths. For example, out-of-phase tension-torsion is always a non-proportional loading. Figure 2.37 exhibits, as an example, a typical in-phase strain history (Figure 2.37a) and a typical out-of-phase strain history (Figure 2.37b).

One of the most complicated characteristics of non-proportional loading is the additional cyclic hardening which is not observed under proportional cyclic loading. The additional cyclic hardening depends on loading conditions, temperature, material hardness and microstructure. This phenomenon was explained

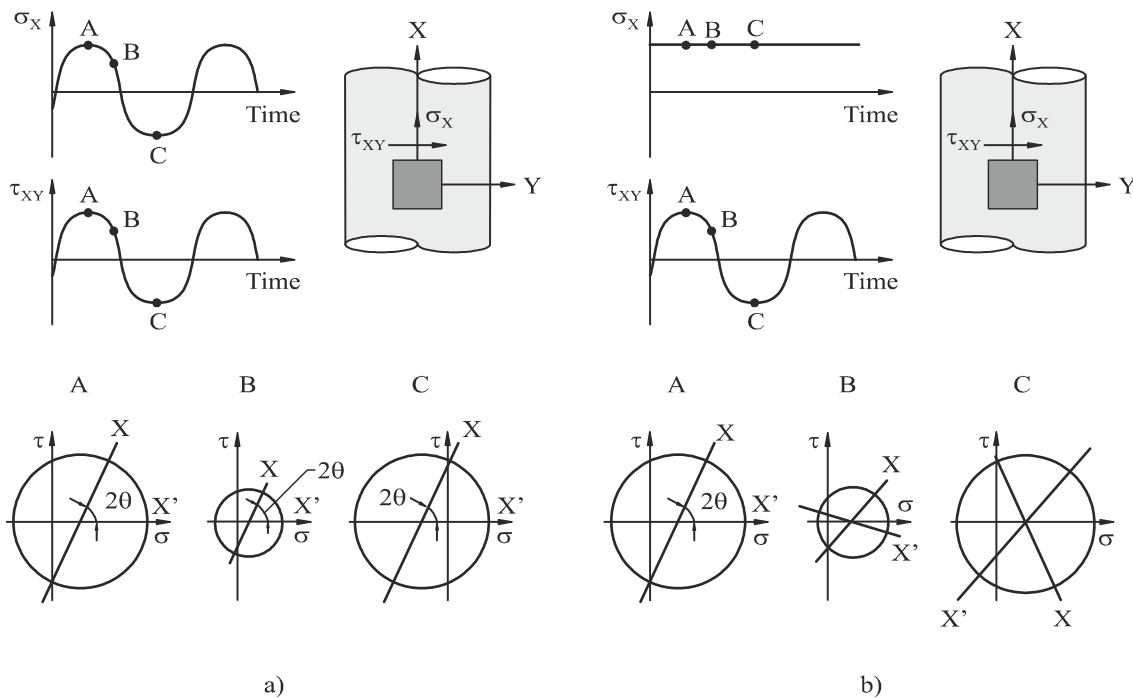


Figure 2.36. Shaft subjected to both shear and axial stresses resulting in: a) proportional multiaxial loading; b) non-proportional multiaxial loading (Socie, 2000).

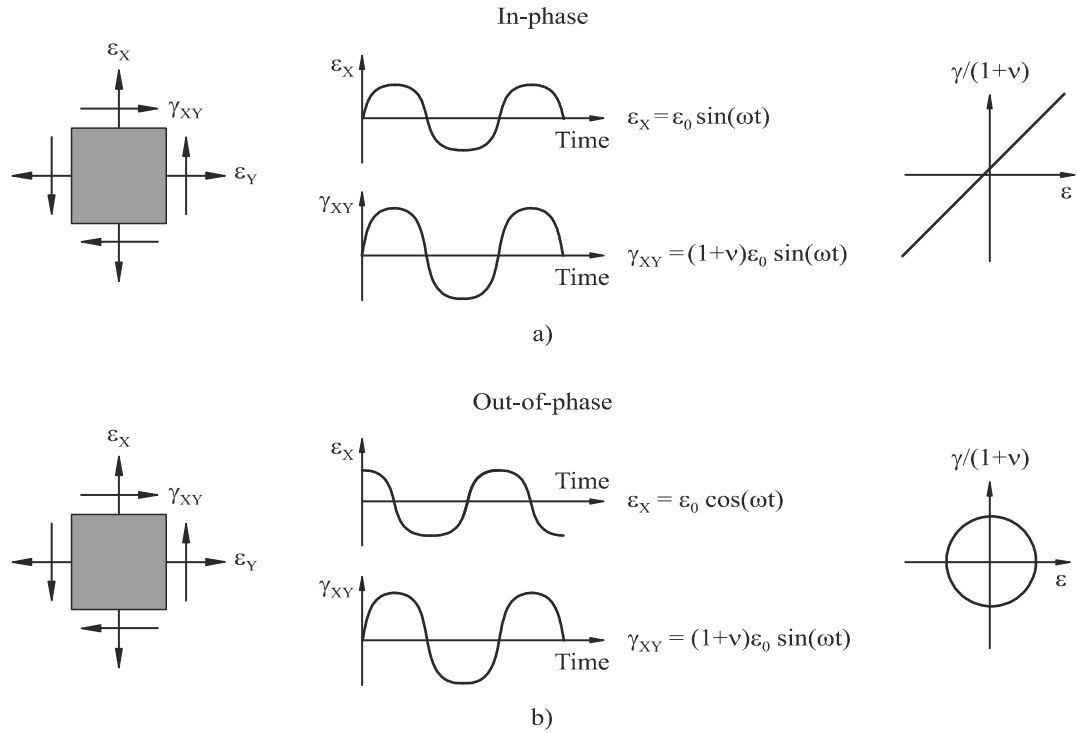


Figure 2.37. Typical example of an: a) in-phase; b) out-of-phase strain history (Socie, 2000).

by a change in the slip plane from one crystallographic slip system to another which can be produced by the rotation of maximum shear plane (Kanazawa, 1979). This may prevent the development of stable dislocation structures associated with proportional loading. Kanazawa *et al.* (1977) also reported shorter fatigue life due to the additional hardening under non-proportional loading when compared to the proportional loading with the same amplitude level. Due to this fact, the analysis of non-proportional cyclic loading has been a topic of interest in the last decades (McDowell, 1985; Benallal, 1987; Socie, 1987; Fan, 1991; Jiang, 1997).

The analysis of the non-proportional hardening effect can be carried out from three different perspectives, i.e. experimental studies, constitutive modelling or empirical methods. With respect to the first group, a considerable number of studies about the effect of the strain shape, load amplitude and load sequence on the additional non-proportional hardening behaviour can be found in the literature (Ohno, 1982; Ohashi, 1985; Tanaka, 1985a; Tanaka, 1985b; Krempl, 1984; Taleb, 2009). Regarding the second group, different constitutive models relating stress to strain or plastic strain by means of continuum mechanics were developed (Chaboche, 1979; McDowell, 1985; Doong, 1991; Tanaka, 1994). In essence, these models are based on the Mroz multiple surface (1967) and the Armstrong-Frederick (1966) plasticity formulations. A comprehensive review on plasticity theories can be found elsewhere (Chaboche, 2008). The last group quantifies the effect of non-proportional hardening from the strain amplitude path using a phenomenological approach. An example is the method proposed by Kanazawa (1979). In this case, the degree of non-proportionality is accounted for by a rotation factor (F) defined by the ratio of the maximum shear strain range at 45° to the maximum shear strain range, i.e.

$$F = \frac{\text{Maximum shear strain range at } 45^\circ}{\text{Maximum shear strain range}} \quad (2.92)$$

and depends on both phase angle and amplitude. This factor is a measure of the ellipticity of the strain path in a plot of the shear strain amplitude ($\gamma/2$) versus the normal strain (ϵ), as shown in Figure 2.38, or the ratio of the minor to the major axis of the circumscribed ellipse (Socie, 2000). Figure 2.38a shows a set of sinusoidal loadings with the same shear strain amplitude ($\gamma=2\epsilon$) and different phase angles, while Figure 2.38b exhibits a set of sinusoidal loadings with 90° phase angle and different shear strain amplitudes. The corresponding values of the rotation factor (F) are listed in Table 2.6. The additional non-proportional cyclic hardening can be modelled using the following expression

$$\frac{\Delta\sigma^e}{2} = k'(1 + \alpha F) \left(\frac{\Delta\epsilon_p^e}{2} \right)^{n'} \quad (2.93)$$

where $\Delta\sigma^e/2$ is the equivalent stress amplitude, $\Delta\epsilon_p^e/2$ is the equivalent plastic strain amplitude, k' is the proportional cyclic hardening coefficient, n' is the proportional cyclic hardening exponent, F is the rotation factor and α is the material dependent non-proportional hardening coefficient. Typical values of

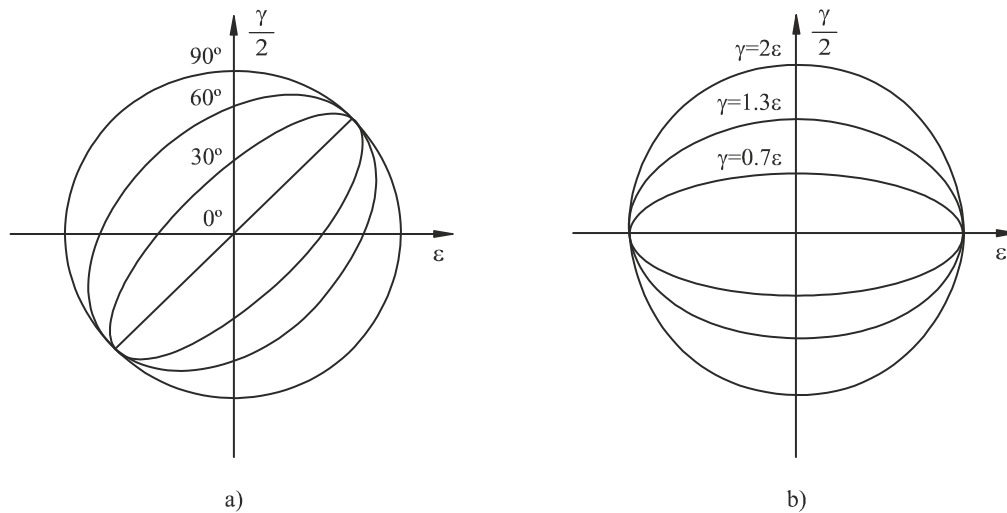


Figure 2.38. Non-proportional loading histories: a) phase difference: b) amplitude difference (Socie, 2000).

Table 2.6. Rotation factor for different strain histories (Socie, 2000).

Strain history	Rotation factor, F
$0^\circ, \gamma=2\epsilon$	0
$30^\circ, \gamma=2\epsilon$	0.27
$60^\circ, \gamma=2\epsilon$	0.57
$90^\circ, \gamma=2\epsilon$	1.0
$90^\circ, \gamma=1.3\epsilon$	0.67
$90^\circ, \gamma=0.7\epsilon$	0.33

the non-proportional hardening coefficient for different materials are compiled in Table 2.7. As can be seen, this constant depends on both material and temperature. From the two previous tables, it is possible to infer that α and F are within the range 0-1.

The formulation of the non-proportionality factor proposed by Ioth *et al.* (1995) allows evaluating the stress response from the strain history and can be expressed as

$$F = \frac{0.5\pi}{T \varepsilon_{I\max}} \int_0^T (|\sin \xi(t)| \varepsilon_I(t)) dt \quad (2.94)$$

being $\varepsilon_I(t)$ the principal stress at time t , $\varepsilon_{I\max}$ the maximum principal stress, $\xi(t)$ the angle between $\varepsilon_I(t)$ and $\varepsilon_{I\max}$ and T is the time for a cycle. The main variables are identified in Figure 2.39. This factor

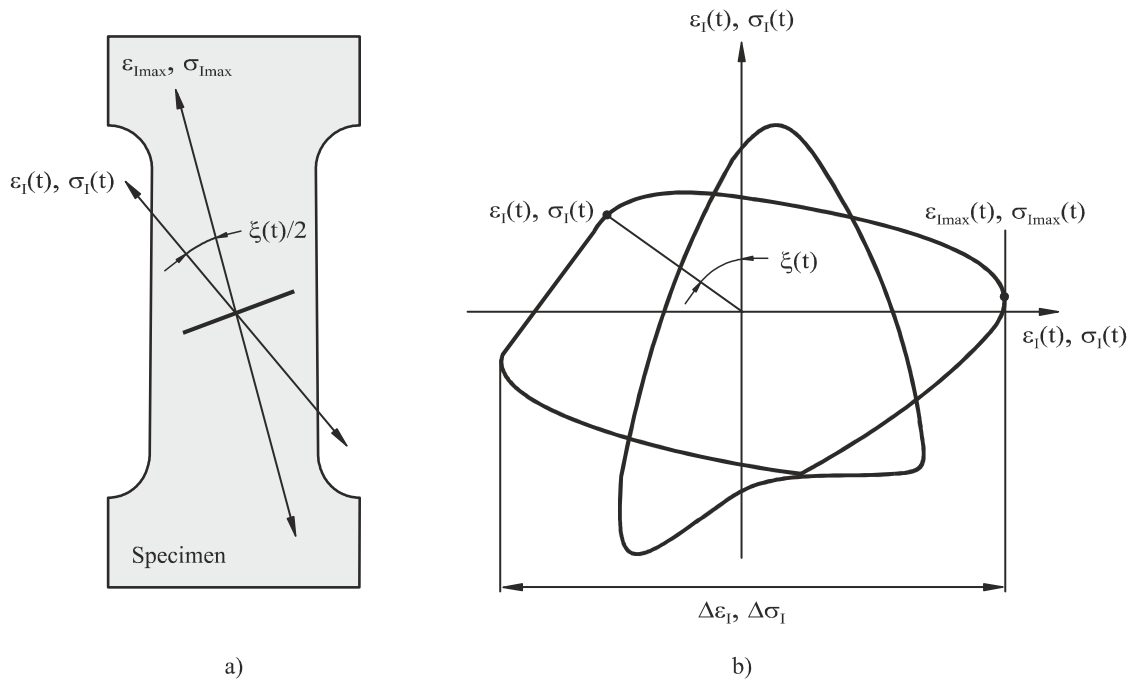


Figure 2.39. a) Definition of $\xi(t)$; b) polar representation of $\Delta\varepsilon_I$ (Ioth, 2004).

Table 2.7. Non-proportional hardening coefficient for various materials (Socie, 2000).

Material	α
316 stainless steel (Cailletaud, 1991)	1.0
304 stainless steel (Socie, 1987; Doong, 1990; Ioth, 1995)	0.5-1.0
316 stainless steel at 550°C (Andrews, 1989)	0.37
1045 steel (Fatemi, 1989)	0.3
304 stainless steel at 650°C (Hamada, 1997)	0.3
6061-T6 aluminium (Ioth, 1997)	0.2
42 Cr-Mo Steel (Chen, 1996)	0.15
1% Cr-Mo-V steel (Kanazawa, 1977)	0.14
1100 aluminium (Cailletaud, 1991)	0

evaluates the severity of non-proportional straining in a cycle. The non-proportional strain range ($\Delta\epsilon_{NP}$) can be defined by the following equation

$$\Delta\epsilon_{NP} = (1 + \alpha F) \Delta\epsilon_I \quad (2.95)$$

where F is the factor of non-proportionality, α is the material dependent non-proportional hardening coefficient and $\Delta\epsilon_I$ is the principal strain range. This factor of non-proportionality was incorporated by Ioth *et al.* (2004) into an incremental multiple surface plasticity model with six material properties. The predictions obtained for 304 stainless steel and 6061 aluminium subjected to various loading paths were satisfactory.

Another method which directly estimates the maximum shear stress amplitude from the loading path is the *minimum circumstantial circle* (Dang Van, 1989; Papadopoulos, 1997). The shear stress amplitude, as represented in Figure 2.40, is defined as the radius of the minimum circle circumscribing the load path in a deviatoric stress space. Later, Li *et al.* (2000) and Freitas *et al.* (2000) proposed a new method termed *minimum circumscribed ellipse*. In this case, the shear stress amplitude (τ_a) is defined by

$$\tau_a = (R_a^2 + R_b^2)^{1/2} \quad (2.96)$$

where R_a and R_b are, respectively, the length of the major and minor axes of the minimum circumscribed ellipse in a deviatoric stress space around the whole loading path. The graphical interpretation of this method is also presented in Figure 2.40. As can be seen, the shear stress amplitude for the rectilinear loading (load path 2) is equal to R_a , since R_b is zero. The main advantage of the minimum circumscribed ellipse method relatively to the minimum circumscribed circle method is that it can evaluate the effect of non-proportional loading in an easier manner (Li, 2000; Freitas, 2000).

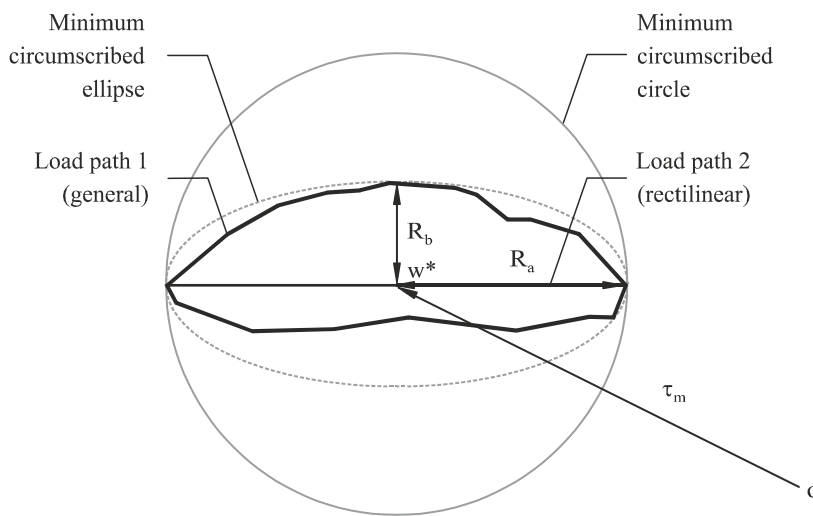


Figure 2.40. Schematic representation of the minimum circumscribed circle approach and minimum circumscribed ellipse approach (Freitas, 2000).

Multiaxial fatigue problems can be analysed using different models. In general, these models can be classified into three main categories, namely *stress-based*, *strain-based* and *energy-based* models (Garud, 1981; Wang, 2004). The stress-based models are suitable for the high-cycle fatigue regime where the behaviour is mainly elastic. The strain-based models are appropriate for the low-cycle fatigue regime where the behaviour is mainly inelastic. Energy-based models can be formulated using elastic energy for high-cycle fatigue; plastic energy for low-cycle fatigue; or the sum of elastic and plastic energies (Macha, 2001). In the last decades, numerous attempts have been made to develop a universally accepted multiaxial fatigue criterion. However, this has not yet been achieved. The accuracy of the existing criteria depends essentially on the material, loading and fatigue and fracture mechanisms (Kim, 1999).

Several review papers on multiaxial fatigue criteria are presently available in the literature. Some examples are the papers of Garud (1981), Brown and Miller (1982), Krempl and Lu (1984), Ellyin and Valaire (1982), You and Lee (1996), Papadopoulos *et al.* (1997), Macha and Sonsino (1999), Wang and Yao (2004), Karolczuk and Macha (2005), Ding *et al.* (2007), Balthazar and Malcher (2007), Meggiolaro and Castro (2009), Li *et al.* (2009), Fatemi and Shamsaei (2011), Kenmeugne *et al.* (2012). In the next subsections, various models that have gained a widespread acceptance are briefly outlined. The first subsection (Subsection 2.5.1) is devoted to the stress-based models which can be divided into equivalent stress methods, stress invariant methods and average stress methods. Subsection 2.5.2 is focused on the strain-based models. Subsection 2.5.3 tackles the energy-based models. The last subsection (Subsection 2.5.4) covers the critical plane models which comprise stress-based, strain-based and energy-based approaches.

2.5.1 *Stress-based models*

i) Equivalent stress methods

Equivalent stress methods attempt to predict the fatigue limit under a combined stress loading from usually accepted criteria for static yield under complex stress states. In this way, simple uniaxial tests could be used to describe the fatigue behaviour of components subjected to complex loading. The most usual yield criteria encompass the *maximum normal stress*, *maximum shear stress* and *von Mises* theories. Such theories applied to cyclic loading can be written, respectively, as follows (Socie, 2000)

$$\Delta\sigma_{eq} = \Delta\sigma_1 \quad (2.97)$$

$$\frac{\Delta\sigma_{eq}}{2} = \frac{\Delta\sigma_1 - \Delta\sigma_3}{2} \quad (2.98)$$

$$\Delta\sigma_{eq} = \frac{1}{\sqrt{2}} \left[(\Delta\sigma_1 - \Delta\sigma_2)^2 + (\Delta\sigma_2 - \Delta\sigma_3)^2 + (\Delta\sigma_3 - \Delta\sigma_1)^2 \right]^{1/2} \quad (2.99)$$

being $\Delta\sigma_{eq}$ the equivalent stress range and $\Delta\sigma_i$ the principal stress ranges. The three above-mentioned criteria are depicted in Figure 2.41. Typical experimental test data are also plotted for comparison

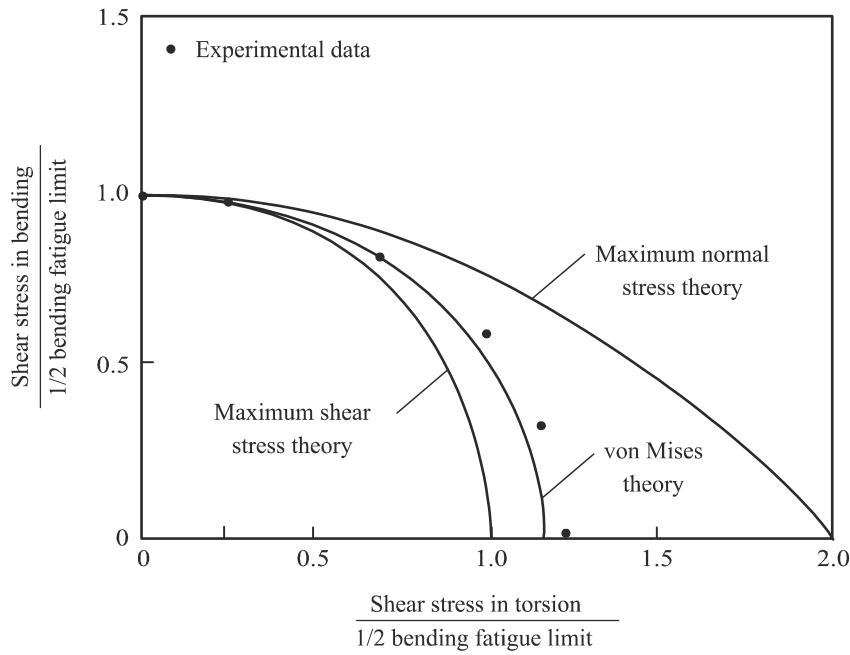


Figure 2.41. Schematic illustration of the maximum normal stress, maximum shear stress and von Mises theories (Socie, 2000).

purposes. As can be seen, the von Mises theory, sometimes called octahedral shear stress theory, better fits the experimental results than the others. These three criteria are only applicable to proportional or in-phase loading and can be combined with the Goodman diagram to incorporate the mean stress effect in in-phase problems.

Based on an extensive set of experimental results, obtained under combined in-phase bending-torsion conditions, Gough and Pollard (1935; 1937) proposed an ellipse quadrant equation for ductile materials

$$\left(\frac{\Delta\sigma}{f_{-1}}\right)^2 + \left(\frac{\Delta\tau}{t_{-1}}\right)^2 = 1 \tag{2.100}$$

and an ellipse arc equation for brittle materials

$$\left(\frac{\Delta\tau}{t_{-1}}\right)^2 + \left(\frac{f_{-1}}{t_{-1}} - 1\right)\left(\frac{\Delta\sigma}{f_{-1}}\right)^2 + \left(2 - \frac{f_{-1}}{t_{-1}}\right)\left(\frac{\Delta\sigma}{f_{-1}}\right) = 1 \tag{2.101}$$

where $\Delta\sigma$ is the normal stress range, $\Delta\tau$ is the shear stress range, f_{-1} is the fully-reversed bending fatigue limit and t_{-1} is the fully-reversed torsion fatigue limit. These formulations, though empirical in nature, correlate excellently data of combined in-phase bending-torsion and account for anisotropy effects (Lee, 1985). Figure 2.42 compares the two previous equations with experimental data obtained for various

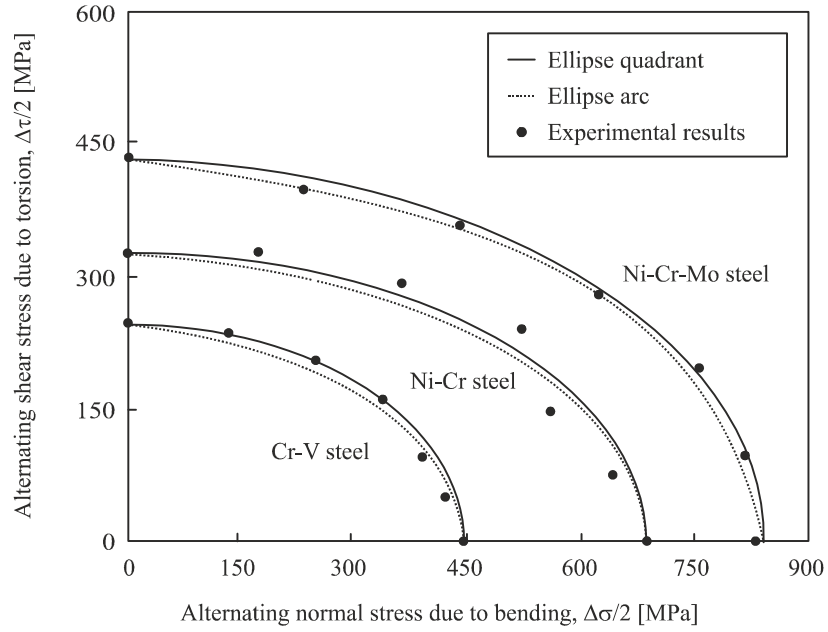


Figure 2.42. Fatigue limits of three different steels under combined bending-torsion loading (Socie, 2000).

materials. Ellipse arc and ellipse quadrant equations are represented by the full lines and dashed lines, respectively. The black circles refer to experimental results. As can be seen, the proposed equations fit well the experimental results.

More recently, Lee (1985) proposed an alternative formulation of the ellipse quadrant of Gough in order to incorporate phase difference between loadings which assumes the form

$$\frac{\Delta\sigma_{eq}}{2} = \frac{\Delta\sigma}{2} \left[1 + \left(\frac{f_{-1}K}{2t_{-1}} \right)^{\xi} \right]^{1/\xi} \quad (2.102)$$

where ξ and K are defined, respectively, by

$$\xi = 2(1 + \beta \sin\varphi) \quad (2.103)$$

$$K = 2 \frac{\Delta\sigma}{\Delta\tau} \quad (2.104)$$

being $\Delta\sigma_{eq}$ the equivalent stress range, $\Delta\sigma$ the normal stress range, $\Delta\tau$ the shear stress range, φ the phase difference between the applied bending and torsion loading and β a material constant. Lee (1989) modified Equation 2.102 to include the bending mean stress. The expression proposed was successfully applied to SM45C structural steel subjected to multiaxial bending-torsion loading and is given by

$$\frac{\Delta\sigma_{\text{eq}}}{2} = \frac{\frac{\Delta\sigma}{2} \left[1 + \left(\frac{f_{-1}K}{2t_{-1}} \right)^{\xi} \right]^{1/\xi}}{\left[1 - \left(\frac{\sigma_m}{\sigma_{UTS}} \right)^n \right]} \quad (2.105)$$

where σ_m is the bending mean stress, σ_{UTS} is the ultimate tensile strength and n is an empirical constant within the range of 1-2. Lee's equations (Equations 2.102 and 2.105) have a material constant and therefore require extra experimental work which limits the application of the method.

ii) Stress invariant methods

The basic idea of the stress invariant approaches is to directly relate the fatigue strength to the invariants of the stress tensor and or the deviator tensor. The formulation proposed by Sines (1959) relates the fatigue strength to the second invariant of the stress deviator and the first invariant of the stress tensor. It can be written as follows

$$\sqrt{J_{2,a}} + \nu\sigma_{H,m} \leq \beta \quad (2.106)$$

where $J_{2,a}$ is the amplitude of the second invariant of the stress deviator, $\sigma_{H,m}$ is the mean value of the hydrostatic stress, and ν and β are two material constants. The second invariant of the stress deviator (J_2) and the hydrostatic stress (σ_H) are defined by

$$J_2 = \frac{1}{6} [(\sigma_1 - \sigma_2)^2 + (\sigma_2 - \sigma_3)^2 + (\sigma_3 - \sigma_1)^2] \quad (2.107)$$

$$\sigma_H = \frac{J_1}{3} = \frac{1}{3}(\sigma_1 + \sigma_2 + \sigma_3) \quad (2.108)$$

being σ_1 , σ_2 and σ_3 the principal stresses and J_1 the first invariant of the stress deviator. The α and β constants can be obtained from torsion and repeated bending tests using the following relationships

$$\nu = \frac{3t_{-1}}{f_0} - \sqrt{3} \quad (2.109)$$

$$\beta = t_{-1} \quad (2.110)$$

where f_0 is the pulse bending fatigue limit and t_{-1} is the fully-reversed torsion fatigue limit. This criterion is suitable for high-cycle fatigue under multiaxial proportional loading. Furthermore, it reproduces the uniqueness of the torsion fatigue limit. In addition, it establishes a linear relationship between the bending limit and a superimposed static normal stress (Papadopoulos, 1997). In fully-reversed bending problems, the ratio of the fully-reversed torsion fatigue limit to the fully-reversed bending fatigue limit (t_{-1}/f_{-1}) is

equal to $1/\sqrt{3}$. However, this value is not in agreement with the experimental results which indicate that this ratio varies from 0.5 for mild metals to 1.0 for brittle metals. When the pulse bending fatigue limit is not available, the Goodman line (see Figure 2.11) can be applied to obtain f_0 which is given by

$$f_0 = f_{-1} \left(\frac{\sigma_{UTS}}{1 + f_{-1}} \right) \quad (2.111)$$

being f_{-1} the fully-reversed bending fatigue limit and σ_{UTS} the ultimate tensile strength. Based on this assumption, this criterion is given by Equation 2.112 (Papadopoulos, 1997).

$$\sqrt{J_{2,a}} + \left(\frac{\sqrt{3}f_{-1}}{\sigma_{UTS}} \right) \sigma_{H,m} \leq t_{-1} \quad (2.112)$$

The formulation proposed by Crossland (1956) assumes that the fatigue criterion should consider the maximum value of the hydrostatic stress, i.e.

$$\sqrt{J_{2,a}} + \alpha \sigma_{H,max} \leq \beta \quad (2.113)$$

where $\sigma_{H,max}$ is the maximum value of the hydrostatic stress and α and β are two material constants given by Equation 2.114 and Equation 2.110, respectively. As can be seen, the material constants depend on both the bending and torsion fatigue limits.

$$\alpha = \frac{3t_{-1}}{f_{-1}} - \sqrt{3} \quad (2.114)$$

The formulation proposed by Kakuno and Kawada (1979) states that the contribution of the amplitude and mean value of the hydrostatic stress must be separated, i.e.

$$\sqrt{J_{2,a}} + \alpha \sigma_{H,a} + \lambda \sigma_{H,m} \leq \beta \quad (2.115)$$

where $\sigma_{H,a}$ is the amplitude of the hydrostatic stress, $\sigma_{H,m}$ is the mean value of the hydrostatic stress, α and β are, respectively, given by Equations 2.114 and 2.110, and λ is defined by (Papadopoulos, 1997)

$$\lambda = \frac{3t_{-1}}{f_0} - \sqrt{3} \quad (2.116)$$

being t_{-1} the fully-reversed torsion fatigue limit and f_0 the pulse bending fatigue limit.

The criterion proposed by Deperrois (1991) is defined by the following expression

$$\frac{\sqrt{2}}{2} \sqrt{\sum_1^5 D_i^2} + \alpha \sigma_{H,m} \leq \beta \quad (2.117)$$

where D_1 to D_5 are values computed in a five-dimensional Euclidean space (E_5). Firstly, the longest chord D_5 between the two distinct points of the stress path in a deviatoric space is obtained. Then, it is considered a sub-space orthogonal to the direction of D_5 and the loading path is projected onto this sub-space named E_4 . After that, a new longest chord D_4 is computed. The process is repeated successively for the other sub-spaces. In some circumstances, there is a lack of uniqueness of the longest chord which makes difficult the definition of the orthogonal sub-space (Papadopoulos, 1997). Nevertheless, when the maximum chord of the loading path in E_5 is unique, this criterion provides satisfactory results (Ballard, 1995).

The stress invariant methods based on the shear stress amplitude require complex mathematical calculations when the applied cyclic loading is out-of-phase. As referred to above, different methods to calculate the shear stress amplitude have been proposed. Papadopoulos and Dang Van (1988) proposed that the shear stress amplitude is the radius of the minimum circle circumscribing the loading path. In order to simplify the calculations, the stress deviator tensor is mapped onto a vector of a five-dimensional Euclidean space (Papadopoulos, 1997). The mean value of the shear stress $(J_{2,m})^{1/2}$ is defined by the vector pointing from the origin to the centre of the minimum circumscribed circle whilst the alternating value of the shear stress amplitude $(J_{2,a})^{1/2}$ is equal to the radius R of the circle (see Figure 2.40). The centre w^* can be found by solving the min-max problem (Equation 2.118) and the radius can be determined from Equation 2.119. This method can lead to inconsistent results. Take for example the two loading paths depicted in Figure 2.40 (the first is a non-proportional loading and the second is a proportional loading). Although they produce the same equivalent shear stress amplitude, the fatigue damage is certainly different.

$$w^*: \min_w \left(\max \| S(t) - w \| \right) \quad (2.118)$$

$$\sqrt{J_{2,a}} = R = \max_t \| S(t) - w^* \| \quad (2.119)$$

Freitas *et al.* (2000) proposed a different approach to calculate the shear stress amplitude. The main difference relatively to the previous approach is that the loading path is circumscribed by an ellipse (see Figure 2.40). The equivalent shear stress amplitude, as already mentioned, is obtained by

$$\sqrt{J_{2,a}} = \sqrt{R_a^2 + R_b^2} \quad (2.120)$$

where R_a and R_b are the semi-axes of an ellipse circumscribing the whole loading path. The computational algorithm proposed comprises two main steps (Li, 2000). Firstly, the minimum circumscribed circle of

radius R_a which is equal to the major semi-axis of the ellipse is computed. This step is performed according to the minimum circumscribed circle method, i.e. by solving the min-max problem. Then, the minor semi-axis of the ellipse R_b is determined from the minimum ellipse contained both in the circle and in the loading path. This approach accounts for the effect of non-proportional loading on fatigue life and has presented good results of multiaxial fatigue strength when assessed in confrontation with experimental results reported in the literature (Li, 2000).

The approach proposed by Mamiya and Araújo (2002) suggests, as schematised in Figure 2.43, the construction of a prismatic envelope containing the loading path projected onto the deviatoric plane to calculate the equivalent shear stress amplitude. Based on this assumption, the equivalent shear stress amplitude can be written in the form

$$\sqrt{J_{2,a}} = \left(\sum_{i=1}^5 a_i^2 \right)^{1/2} \quad (2.121)$$

where a_i are the amplitudes of the components $x_i(t)$ of the microscopic deviatoric stresses defined by Equation 2.122.

$$a_i = \max_t |x_i(t)| \quad (2.122)$$

The experimental validation revealed better results than the Crossland (1956) criterion and results as good as the ones provided by Papadopoulos (1997) and Li *et al.* (2000) criteria. On the other hand, the computational algorithm required to compute the equivalent shear stress amplitude is simpler. However,

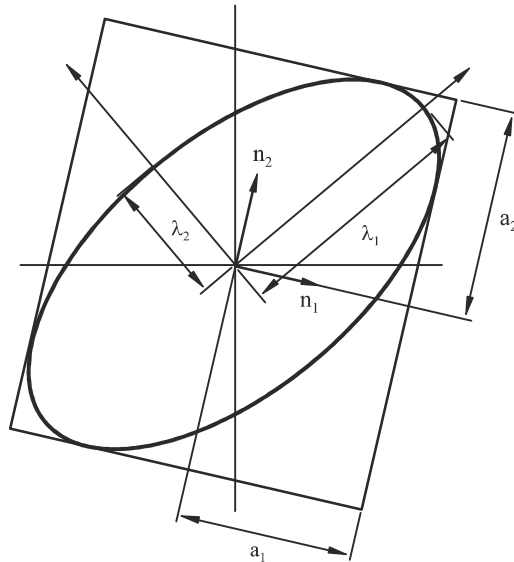


Figure 2.43. Ellipsoid in R^m space and circumscribed rectangular prism arbitrarily oriented (Mamiya, 2002).

this criterion is limited to cases in which the shape of the convex hull circumscribing the microscopic loading path is close to an ellipsoid (Mamiya, 2002).

iii) Average stress methods

Average stress methods attempt to predict the fatigue damage from average normal and shear stresses acting on a generic material plane within an elementary volume (Papadopoulos, 1997). The model proposed by Grubisic and Simbürger (1976) divides the materials into three categories, depending on the ratio of the fully-reversed torsion fatigue limit to the fully-reversed bending fatigue limit (t_{-1}/f_{-1}). For the range $0.577 \leq t_{-1}/f_{-1} \leq 0.8$, its formulation can be expressed by the following formula

$$\sqrt{\frac{15}{2}} \sqrt{\frac{1}{4\pi} \int_{\theta=0}^{2\pi} \int_{\varphi=0}^{\pi} A_n^2 \sin \theta \, d\theta \, d\varphi} \leq 1 \quad (2.123)$$

where A_n is the effective straining of a material plane Δ , and θ and φ are, as depicted in Figure 2.44, the spherical coordinates of the unit vector \mathbf{n} normal to the plane Δ . The application of this criterion in cyclic torsion with a mean shear stress is given by

$$\frac{2\tau_a}{f_{-1}} - \left(\frac{2}{f_{-1}} - \frac{2}{f_0} \right) \tau_m \leq 1 \quad (2.124)$$

being τ_a the shear stress amplitude, f_{-1} the fully-reversed bending fatigue limit and f_0 the pulse bending fatigue limit.

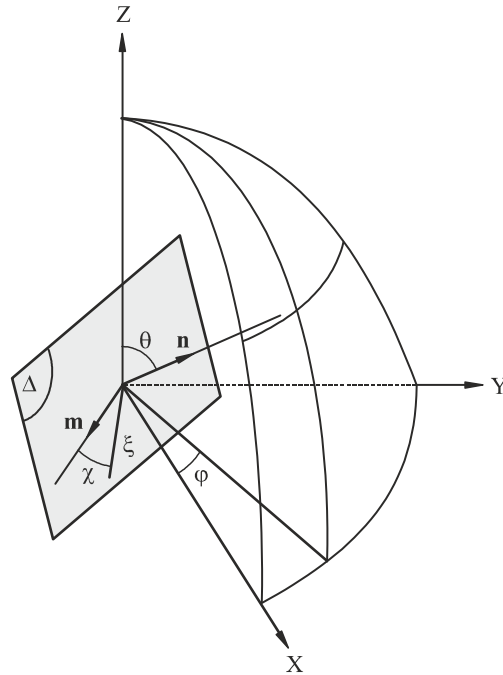


Figure 2.44. Definition of the spherical coordinates of the unit vector \mathbf{n} normal to the plane Δ (Bernasconi, 2008).

The model formulated by Liu (1993) can be condensed in the following formula

$$\sqrt{\frac{15}{8\pi} \int_{\varphi=0}^{2\pi} \int_{\theta=0}^{\pi} [a\tau_a^2(1+m\tau_m^2)+b\sigma_a^2(1+n\sigma_m)] \sin\theta d\theta d\varphi} \leq f_{-1} \quad (2.125)$$

where a , m , b and n are material parameters defined, respectively, by (Zenner, 2000)

$$a = \frac{1}{5} \left[3 \left(\frac{f_{-1}}{t_{-1}} \right)^2 - 4 \right] \quad (2.126)$$

$$a \cdot m = \frac{f_{-1}^2 - \left(\frac{f_{-1}}{t_{-1}} \right)^2 \left(\frac{t_0}{2} \right)^2}{\frac{12}{7} \left(\frac{t_0}{2} \right)^4} \quad (2.127)$$

$$b = \frac{1}{5} \left[6 - 2 \left(\frac{f_{-1}}{t_{-1}} \right)^2 \right] \quad (2.128)$$

$$b \cdot n = \frac{f_{-1}^2 - \left(\frac{f_0}{2} \right)^2 - \frac{4}{21} \left(\frac{f_0}{2} \right)^2}{\frac{15}{14} \left(\frac{f_0}{2} \right)^3} \quad (2.129)$$

being f_{-1} the fully-reversed bending fatigue limit, t_{-1} the fully-reversed torsion fatigue limit, f_0 the pulse bending fatigue limit and t_0 the pulse torsion fatigue limit. In order to reduce the number of constants, the value of t_0 can be obtained using Equation 2.130 (Zenner, 2000). This criterion can be only applied to ductile materials in the range $0.577 \leq t_{-1}/f_{-1} \leq 0.866$, otherwise a and b are negative. On the other hand, it suggests that the torsion fatigue limit is a function of a superimposed static shear stress, which does not corroborate the experimental results available in the literature (Papadopoulos, 1997).

$$t_0 = \frac{4t_{-1}}{\frac{2f_{-1}}{f_0} + 1} \quad (2.130)$$

The approach proposed by Papadopoulos (1987; 1995) is based on a mesoscopic scale introduced by Dang Van (1973). The mesoscopic scale is an intermediate scale between a macro-level and a micro-level and corresponds to the scale of the metal grains of a metallic aggregate. The fatigue criterion is defined from an average measure of the shear stress amplitude within the elementary volume, i.e.

$$\sqrt{\langle T_a^2 \rangle} = \sqrt{\frac{5}{8\pi^2} \int_{\varphi=0}^{2\pi} \int_{\theta=0}^{\pi} \int_{\chi=0}^{2\pi} (T_a^2(\varphi, \theta, \chi))^2 d\chi \sin\theta d\theta d\varphi} \quad (2.131)$$

where χ varies between 0 to 2π to cover all the gliding directions on a plane Δ . The normal stresses acting normal to the eventually existing embryo cracks are taken into account by the average measure

$$\langle N \rangle = \frac{1}{4\pi} \int_{\varphi=0}^{2\pi} \int_{\theta=0}^{\pi} N(\varphi, \theta) \sin \theta \, d\theta \, d\varphi \quad (2.132)$$

being N the normal stresses acting in the planes with orientations φ and θ . The above volumetric quantity, as demonstrated by Sines *et al.* (1981), is equal to the hydrostatic stress (σ_H). Based on these two average quantities defined in Equations 2.131 and 2.132, the fatigue criterion can be written as follows

$$\sqrt{\langle T_a^2 \rangle} + \alpha \sigma_{H, \max} \leq \beta \quad (2.133)$$

where $\sigma_{H, \max}$ is the maximum value of the hydrostatic stress. This expression is similar to the one obtained by Crossland (1956), except the second invariant of the stress deviator, which is replaced by the average stress quantity. According to the author, this criterion is confined to hard metals for which is valid the inequality $0.577 \leq t_1/f_1 \leq 0.8$. Although this model seems to be complicated, when applied to out-of-phase loading, it results in a very simple form, i.e.

$$\sqrt{\frac{\sigma_a}{3} + \tau_a} + \alpha \frac{\sigma_a + \sigma_m}{3} \leq \beta \quad (2.134)$$

being σ_a the normal stress amplitude, τ_a the shear stress amplitude, σ_m the mean normal stress, and α and β two material constants defined, respectively, by Equation 2.114 and Equation 2.110.

2.5.2 Strain-based models

After the studies of Coffin (1954) and Manson (1954), several attempts were made to correlate low-cycle multiaxial fatigue results from strain-based versions of the static yield criteria. The strain-based equations are replicas of the stress-based expressions presented in the previous subsection. The most usual strain criteria are the *maximum normal strain*, the *maximum shear strain* and the *von Mises* theories, which can be written, respectively, as follows (Karolczuk, 2005)

$$\Delta \varepsilon_{eq} = \Delta \varepsilon_1 \quad (2.135)$$

$$\frac{\Delta \varepsilon_{eq}}{2} = \frac{\Delta \varepsilon_1 - \Delta \varepsilon_3}{2} \quad (2.136)$$

$$\Delta \varepsilon_{eq} = \frac{\sqrt{2}}{2(1+\nu)} \left[(\Delta \varepsilon_1 - \Delta \varepsilon_2)^2 + (\Delta \varepsilon_2 - \Delta \varepsilon_3)^2 + (\Delta \varepsilon_3 - \Delta \varepsilon_1)^2 \right]^{1/2} \quad (2.137)$$

where $\Delta\varepsilon_{eq}$ is the equivalent strain range, $\Delta\varepsilon_1$, $\Delta\varepsilon_2$ and $\Delta\varepsilon_3$ are the principal strain ranges. The equivalent strain approach is not able to explain the nucleation and propagation of cracks on specific planes. Besides, it cannot account for the differences in the ratio of the tension fatigue limit to the torsion fatigue limit for a wide range of materials and it is not suitable for non-proportional loading. The inadequacy to correlate data from tension and torsion tests was first reported by Yokobori *et al.* (1965).

The model proposed by Mowbray (1980) is based on a Coffin-Manson type equation (You, 1996)

$$\frac{\Delta\varepsilon_1}{2} = \frac{\sigma_f'}{E} f(\lambda_\sigma, \nu) (2N_f)^b + \left(\frac{3}{3-A} \right) g(\lambda_\sigma, A) \varepsilon_f' (2N_f)^c \quad (2.138)$$

where

$$f(\lambda_\sigma, \nu) = \frac{(1 - \nu\lambda_\sigma)}{\sqrt{(1 - \lambda_\sigma + \lambda_\sigma^2)}} \quad (2.139)$$

$$g(\lambda_\sigma, A) = (2 - \lambda_\sigma) \left[3\sqrt{(1 - \lambda_\sigma + \lambda_\sigma^2)} - \frac{A(1 + \lambda_\sigma)}{6(1 - \lambda_\sigma + \lambda_\sigma^2)} \right] \quad (2.140)$$

being A an empirical constant, ν the Poisson's ratio, λ_σ the hydrostatic stress ratio. Both $f(\lambda_\sigma, \nu)$ and $g(\lambda_\sigma, A)$ functions were developed to evaluate the variation of σ_f' and ε_f' fatigue properties, which depend on the type of multiaxial loading and on the value of the hydrostatic stress. However, $\Delta\varepsilon_1/2$ is not a proper parameter in multiaxial fatigue due to its non-conservativeness (You, 1996).

Andrews and Ellison (1973) and later Sines and Ohgi (1981) modified the Coffin-Manson equation using the maximum shear strain as the damage parameter. This model is expressed mathematically by

$$\frac{\Delta\gamma_{\max}}{2} = (1 + \nu_e) \frac{\sigma_f'}{E} (2N_f)^b + (1 + \nu_p) \varepsilon_f' (2N_f)^c \quad (2.141)$$

where $\Delta\gamma_{\max}$ is the maximum shear strain range, and ν_e and ν_p are the Poisson's ratios in the elastic and plastic regions, respectively. Under proportional loading, the fatigue behaviour is well modelled. On the contrary, under non-proportional loading, the predictions are non-conservative. Therefore, without further modifications, it is not suitable for multiaxial fatigue under non-proportional loading (Ding, 2007).

2.5.3 Energy-based models

Energy-based models assume that the accumulation of plastic work is the main cause for irreversible damage and eventual fatigue failure. The model proposed by Morrow (1965) relates the hysteresis energy per cycle (ΔW_p) to the fatigue life by the following relationship

$$\Delta W_p = 4 \sigma_f' \varepsilon_f' \left(\frac{c-b}{c+b} \right) (2N_f)^{b+c} \quad (2.142)$$

where σ_f' is the fatigue strength coefficient, b is the fatigue strength exponent, ε_f' is the fatigue ductility coefficient and c is the fatigue ductility exponent. Thus, it is possible to conclude that the total work to failure is not constant since $b+c$ is not equal to unity. For long life tests, it is not reliable because the hysteresis energy per cycle is difficult to measure due to the small values of plastic strain (Socie, 2000).

Garud (1981b) extended the uniaxial hysteresis loop energy concept proposed by Morrow to multiaxial fatigue. For multiaxial loading conditions, the plastic work for a cycle (ΔW_C) is defined by

$$\Delta W_C = \int_{cycle} \sigma_{ij} d\varepsilon_{ij}^p \quad (2.143)$$

where σ_{ij} and ε_{ij}^p are the stress and plastic strain tensors. For proportional tension-torsion loading, it can be written in the form

$$\Delta W_C = \Delta \sigma \Delta \varepsilon_p \left(\frac{1-n'}{1+n'} \right) + \Delta \tau \Delta \gamma_p \left(\frac{1-n'}{1+n'} \right) \quad (2.144)$$

being n' the cyclic hardening exponent, $\Delta \sigma$ the stress range, $\Delta \varepsilon_p$ the plastic strain range, $\Delta \tau$ the shear stress range and $\Delta \gamma$ the shear strain range. Based on experimental results conducted under in-phase and out-of-phase conditions, the author suggested the following formula

$$\Delta W_C = \Delta \sigma \Delta \varepsilon_p \left(\frac{1-n'}{1+n'} \right) + \xi \Delta \tau \Delta \gamma_p \left(\frac{1-n'}{1+n'} \right) \quad (2.145)$$

where ξ is a weighting factor applied to the shear work term. Garud (1981b) proposed a constant value for the weighting factor ($\xi = 0.5$). Thus, no additional tests are required and the model can be applied using uniaxial material tests. However, other studies have demonstrated that ξ depends on the material and loading conditions (Socie, 2000). Besides, it is difficult to apply in high-cycle fatigue due to the impossibility to accurately measure the plastic work per cycle.

The model proposed by Ellyin and Golos (1988) is based on the total strain energy per cycle (ΔW). This quantity, as defined in Equation 2.32, is given by the sum of both the plastic strain energy (ΔW_p) and elastic strain energy associated with the tensile stress (ΔW_{e+}). These two variables are depicted in Figure 2.23 for uniaxial loading. For proportional or biaxial non-proportional loading, the total strain energy per cycle can be expressed as follows

$$\Delta W_t = \int_t^{t+T} \sigma_{ij} d\varepsilon_{ij}^p + \int_t^{t+T} H(\sigma_i) H(d\varepsilon_i^e) \sigma_i d\varepsilon_i^e \quad (2.146)$$

where σ_{ij} and ε_{ij} are the stress and plastic strain tensors, σ_i are the principal stresses, ε_i are the elastic part of the principal strains, T is the period of one cycle, and $H(x)$ is the Heaviside function defined as $H(x) = 1$ for $x \geq 0$ and $H(x) = 0$ for $x < 0$. The fatigue failure criterion is defined by

$$\frac{\Delta W_t}{\bar{\rho}} - C_u = \kappa_u (N_f)^{\alpha_u} \quad (2.147)$$

being C_u , κ_u and α_u material constants determined by fitting from uniaxial test data. This formulation provides good correlation between in-phase multiaxial and uniaxial tests (Ellyin, 1991). The C_u constant is associated with the positive elastic energy. The $\bar{\rho}$ constant is a multiaxial constraint factor which depends on the magnitude of the principal stresses and the effective Poisson's ratio. In practice, it accounts for the severity of the loading type. The multiaxial constraint factor is given by (Ellyin, 1997)

$$\bar{\rho} = (1 + \bar{\nu}) \frac{\varepsilon_1}{\gamma_{\max}} \quad (2.148)$$

where

$$\bar{\nu} = \frac{\nu_p(1 - \nu_e)(\varepsilon_a + \varepsilon_t) + (\nu_e - \nu_p)(\varepsilon_{a,e} + \varepsilon_{t,e})}{(1 - \nu_e)(\varepsilon_a + \varepsilon_t) + (\nu_e - \nu_p)(\varepsilon_{a,e} + \varepsilon_{t,e})}, \varepsilon_a \neq \varepsilon_t \quad (2.149)$$

and ε_1 is the principal strain, γ_{\max} is the maximum shear strain, ε_a is the applied axial strain, and ε_t is the applied shear strain, ν_e is the Poisson's ratio in the elastic region and ν_p is the Poisson's ratio in the plastic region. Equation 2.148 demonstrates the importance of the orientation of the free surface with respect to the imposed principal strains. Besides, it is able to distinguish between states where the crack grows along the surface (Case A of Figure 2.4) and those where the crack grows into the material (Case B of Figure 2.4). Under out-of-phase conditions, the multiaxial constraint factor is calculated when the shear strain in the direction 45° to the surface reaches its maximum value ($\gamma = \gamma_{\max}$), i.e.

$$\bar{\rho} = (1 + \bar{\nu}) \left[\frac{\varepsilon_1(t)}{\gamma(t)} \right]_{\gamma = \gamma_{\max}} \quad (2.150)$$

where $\varepsilon_1(t)$ and $\gamma(t)$ are, respectively, the principal strain and shear strain at time t (Ellyin, 1993).

2.5.4 Critical plane methods

Critical plane models are based on the maximum principal plane failure mode or maximum shear plane failure mode and can be divided into three main groups, namely *stress-based models*, *strain-based models* and *energy-based models* (Karolczuk, 2005). The first group may be appropriate in high-cycle fatigue,

where plastic deformation is negligible. Several examples are the models proposed by Findley (1958), Matake (1977), McDiarmid (1991; 1994), Dang Van (1989; 1989a) and Papadopoulos (2001). The second group, such as Brown and Miller (1973; 1979), Fatemi and Socie (1988) and Macha (1988) models, may be suitable in the presence of plastic deformation but do not reflect the constitutive behaviour of material. The third group reflects the constitutive behaviour of material including mean stress effects and non-proportional loading. Representative examples are the models formulated by Smith, Watson and Topper (1970), Liu (1993), Chu *et al.* (1993) and Glinka *et al.* (1995). A comprehensive review on critical plane models in multiaxial fatigue failure can be found elsewhere (Karolczuk, 2005).

i) Stress-based models

The model proposed by Findley (1959) is based on a linear combination of the shear stress amplitude and maximum normal stress acting on the critical plane. The failure criterion is defined by

$$\frac{\Delta\tau}{2} + k\sigma_{n,\max} = f \quad (2.151)$$

where $\Delta\tau$ is the shear stress range, $\sigma_{n,\max}$ is the maximum normal stress and k and f are two material constants. The critical plane is defined as the plane experiencing the maximum value of f . In the case of zero mean stress, the orientation of the critical plane depends on both the maximum principal stress direction and the material constant k . In the case of non-zero mean stress, the orientation of the critical plane is affected by the two previous quantities (σ_1 and k) and variable and static stresses. For long-life fatigue, Equation 2.151 is often written in the form (Park, 2000; Backstrom, 2001)

$$\frac{\Delta\tau}{2} + k\sigma_{n,\max} = \tau_f^* (N_f)^{b\gamma} \quad (2.152)$$

being τ_f^* computed from the following formula

$$\tau_f^* = \sqrt{1+k^2} \tau_f' \quad (2.153)$$

where τ_f' is the shear fatigue strength coefficient, $b\gamma$ is the shear fatigue strength exponent and $\sqrt{1+k^2}$ is a correction factor (≈ 1.04).

Matake (1977) also proposed a model based on a linear combination of the shear stress amplitude and maximum normal stress acting on the critical plane. However, in this case, the critical plane is the plane on which the shear stress amplitude reaches its maximum value. The failure criterion is defined by

$$\frac{\Delta\tau}{2} + \xi\sigma_{n,\max} = \beta \quad (2.154)$$

being β and ξ two material constants. Indeed, the two previous criteria are similar. The main differences

are the material constants. In the present formulation, β is given by Equation 2.110 and ξ is equal to

$$\xi = \frac{2t_{-1}}{f_{-1}} - 1 \quad (2.155)$$

where t_{-1} is the fully-reversed torsion fatigue limit and f_{-1} is the fully-reversed bending fatigue limit. This criterion was formulated to analyse cyclic torsion, cyclic bending and proportional torsion with bending. For these cases, constant directions of the principal stresses can be assumed. Thus, Equation 2.154 can be written in the form

$$\frac{\sigma_1 - \sigma_3}{2} + \xi \sigma_{n,\max} = \beta \quad (2.156)$$

where σ_1 and σ_3 are the principal stresses.

McDiarmid (1991; 1994) proposed a model based on the maximum shear stress amplitude and the normal stress acting on the critical plane. The critical plane is assumed to be the plane of maximum shear stress range. The failure criterion is given by

$$\frac{\tau_a}{t_{A,B}} + \frac{\sigma_{n,\max}}{2\sigma_{UTS}} = 1 \quad (2.157)$$

where τ_a and $\sigma_{n,\max}$ are the shear stress and the maximum normal stress acting on the critical plane, $t_{A,B}$ is the shear fatigue strength for case *A* or case *B* of Figure 2.4, and σ_{UTS} is the ultimate tensile strength. For long-life fatigue, the previous equation leads to

$$\tau_a + \left(\frac{t_{A,B}}{2\sigma_{UTS}} \right) \sigma_{n,\max} = \tau_f' (2N_f)^{b\gamma} \quad (2.158)$$

being τ_f' the shear fatigue strength coefficient and $b\gamma$ the shear fatigue strength exponent.

The failure criterion formulated by Dang Van (1989; 1989a; 1993; 1999) arose from the observation that fatigue crack nucleation is a local process that begins in grains. As a result of plastic deformation, characteristic slip bands are formed in grains leading to the crack process. This model states that the microscopic shear stress in the grain area (τ_μ) affects crack nucleation along slipping bands and that the microscopic hydrostatic stress ($\sigma_{\mu,h}$) influences crack opening process. The failure criterion assumes a linear combination of these two fatigue quantities, i.e.

$$\tau_\mu(t) + a_1 \sigma_{\mu,h}(t) = a_2 \quad (2.159)$$

where a_1 and a_2 are constants determined from cyclic uniaxial fatigue tests. The shear stress is computed

from the microscopic principal stresses applying the Tresca maximum shear stress theory

$$\tau_{\mu}(t) = \frac{1}{2} [\sigma_{\mu,1}(t) - \sigma_{\mu,3}(t)] \quad (2.160)$$

being $\sigma_{\mu,1}(t)$ and $\sigma_{\mu,3}(t)$ the microscopic principal stresses calculated from the microscopic stress tensor $\sigma_{\mu,ij}(t)$. The microscopic stress tensor is defined as follows

$$\sigma_{\mu,ij}(t) = \sigma_{ij}(t) + dev \rho^* \quad (2.161)$$

where $\sigma_{ij}(t)$ is the macroscopic stress tensor and $dev \rho^*$ is the deviatoric part of the stabilised residual stress tensor. The critical plane position corresponds to the plane where the shear stress achieves the maximum value.

The model proposed by Papadopoulos (2001) is based on a linear combination of generalised shear stress amplitude (T_a) acting on the critical plane and the maximum value of hydrostatic stress ($\sigma_{H,max}$). The failure criterion can be expressed as

$$\max T_a + \alpha_{\infty} \sigma_{H,max} \leq \gamma_{\infty} \quad (2.162)$$

where α_{∞} and γ_{∞} are material constants and T_a is an average stress quantity which corresponds to a mean square value of the shear stress amplitude in the critical plane. The critical plane is defined as the plane where T_a achieves its maximum value.

ii) Strain-based models

Brown and Miller (1973) proposed a theory based on a physical interpretation of the mechanisms of plastic deformation and fatigue crack growth in which is suggested that fatigue life is controlled by the maximum shear strain (γ_{max})

$$\frac{\gamma_{max}}{2} = \frac{\epsilon_1 - \epsilon_3}{2} \quad (2.163)$$

or the strain normal to the plane of maximum shear (ϵ_n)

$$\epsilon_n = \frac{\epsilon_1 + \epsilon_3}{2} \quad (2.164)$$

where ϵ_1 and ϵ_3 are the principal strains. This theory can be represented mathematically by contours of constant fatigue life, called Γ plots, which can be expressed by Equation 2.165 or Equation 2.166. The critical plane is assumed to be the plane with maximum shear stress.

$$\frac{\varepsilon_1 - \varepsilon_3}{2} = f\left(\frac{\varepsilon_1 + \varepsilon_3}{2}\right) \quad (2.165)$$

$$\frac{\gamma_{13}}{2} = f(\varepsilon_n) \quad (2.166)$$

The Γ plots consist of two separate curves for any given fatigue life depending on whether the crack system is case *A* or case *B* (see Figure 2.4). For each type of crack, specific equations were subsequently developed. Case *A* and case *B* are, respectively, described by (Brown, 1979)

$$\left(\frac{\Delta\gamma_{\max}}{g}\right)^j + \left(\frac{\varepsilon_n}{h}\right)^j = 1 \quad (2.167)$$

$$\frac{\Delta\gamma_{\max}}{2} = \text{constant} \quad (2.168)$$

where g , h and j are life dependent constants and $\Delta\gamma_{\max}$ is the maximum shear strain range. The value of j varies from 2 for ductile materials to 1 for brittle materials. Later, this criterion (Equations 2.167 and 2.168) was reduced to a linear form (Kandil, 1982)

$$\frac{\Delta\hat{\gamma}}{2} = \frac{\Delta\gamma_{\max}}{2} + S\Delta\varepsilon_n \quad (2.169)$$

being $\Delta\hat{\gamma}$ the equivalent shear strain range, $\Delta\varepsilon_n$ the normal strain range acting on the plane of maximum shear strain range and S a material constant (Socie, 2000). The application of strain ranges, as in the previous equation, is justified in proportional loading when shear and normal strains are in-phase and their extremes occur at the same instant. For variable amplitude loading, Wang and Brown (1993) proposed the following formula

$$\frac{\Delta\gamma_{\max}}{2} + S\Delta\varepsilon_n^* = [1 + \nu_e + (1 - \nu_e)S] \frac{\sigma_f' - \sigma_n}{E} (2N_f)^b + [1 + \nu_p + (1 - \nu_p)S] \varepsilon_f' (2N_f)^c \quad (2.170)$$

where ε_n^* is the normal strain excursion, σ_n is the mean normal stress, ν_e is the Poisson's ratio in the elastic region and ν_p is the Poisson's ratio in the plastic region. The normal strain excursion (ε_n^*) is calculated in the plane of maximum shear strain range ($\Delta\gamma_{ns}$) for the cycle with maximum value of $\Delta\gamma_{ns}$.

Fatemi and Socie (1988) replaced the normal strain term of Equation 2.169 by the normal stress. The failure criterion is expressed mathematically as

$$\frac{\Delta\gamma_{\max}}{2} \left(1 + n \frac{\sigma_{n,\max}}{\sigma_{YS}}\right) = \frac{\tau_f'}{G} (2N_f)^{b\gamma} + \gamma_f' (2N_f)^{c\gamma} \quad (2.171)$$

where $\Delta\gamma_{\max}$ is the maximum shear strain range, $\sigma_{n,\max}$ is maximum normal stress on the plane of maximum shear strain range, σ_{YS} is the yield strength, $b\gamma$ the shear fatigue strength exponent, $c\gamma$ the shear fatigue ductility exponent and n is a constant determined experimentally from axial and torsion data. The n/σ_{YS} ratio evaluates the sensitivity of the material to the normal stress. This criterion explains the difference between tension and torsion loading as well as mean stress and non-proportional hardening effects. It is important to note that critical plane models based only on strain terms are not able to reflect the mean stress effect or strain path dependent hardening (Socie, 2000). In this case, the mean stress can be incorporated into the criterion through the maximum value of normal stress acting on the critical plane

$$\sigma_{n,\max} = \sigma_{n,a} + \sigma_{n,m} \quad (2.172)$$

being $\sigma_{n,a}$ and $\sigma_{n,m}$ the alternating and mean normal stresses. For low-cycle fatigue regime, this approach leads to Equation 2.173.

$$\begin{aligned} \frac{\Delta\gamma_{\max}}{2} \left(1 + n \frac{\sigma_{n,\max}}{\sigma_{YS}} \right) &= (1 + \nu_e) \frac{\sigma_f'}{E} (2N_f)^b + \frac{n}{2} (1 + \nu_e) \frac{\sigma_f'^2}{E \sigma_{YS}} (2N_f)^{2b} + \\ &+ (1 + \nu_p) \varepsilon_f' (2N_f)^c + \frac{n}{2} (1 + \nu_p) \frac{\varepsilon_f' \sigma_f'}{E} (2N_f)^{b+c} \end{aligned} \quad (2.173)$$

Macha (1988) formulated a generalised multiaxial random fatigue criterion based on the maximum shear strain $\varepsilon_{ns}(t)$ and the normal strain $\varepsilon_n(t)$ acting on the critical plane. For a given fatigue life, the failure criterion, defined by a linear combination of strains, can be written as

$$\max_t [b\varepsilon_{ns}(t) + c\varepsilon_n(t)] = q \quad (2.174)$$

where b , c and q are constants. The fatigue failure occurs under influence of both normal and shear strains in the direction \mathbf{s} on the fracture plane with normal \mathbf{n} , as schematised in Figure 2.45. The direction \mathbf{s} in

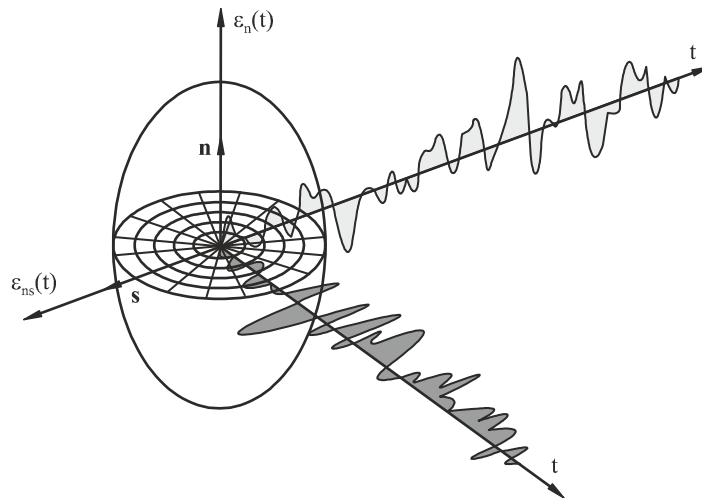


Figure 2.45. Normal strain and shear strain histories in the critical plane (Karolczuk, 2005).

the fracture plane coincides with the mean direction of the maximum shear strain. In a general case, the maximum shear strain direction rotates on the fixed plane with normal \mathbf{n} at time t . Thus, the direction \mathbf{s} is assumed to be a mean direction from all directions of maximum shear strain occurring in the analysed time (Karolczuk, 2005).

iii) Energy-based models

The model proposed by Smith, Watson and Topper (1970) assumes that fatigue failure is due to the normal strain energy density (W_n) acting on the critical plane. The damage parameter, often referred to as SWT parameter, was originally developed to incorporate the mean stress effect in uniaxial loading situations (Equation 2.27). Nevertheless, it can be used in multiaxial proportional and non-proportional loading for materials that fail primarily as a result of mode I tensile cracking. The formulation of the SWT parameter for multiaxial loading is based only on stresses and strains occurring in the critical plane and is given by (Socie, 1987)

$$W_n = \sigma_{n,\max} \frac{\Delta\varepsilon_1}{2} = \frac{\sigma_f'^2}{E} (2N_f)^{2b} + \sigma_f' \varepsilon_f' (2N_f)^{b+c} \quad (2.175)$$

being $\sigma_{n,\max}$ and $\Delta\varepsilon_1$ the maximum normal stress and the normal strain range acting on the critical plane which is defined as the plane where the normal strain range reaches its maximum value ($\Delta\varepsilon_1$). Due to the stress term, this model can be used to describe mean stress and non-proportional hardening effects.

Liu (1993) developed an energy-based method for estimating the fatigue life from the concept of virtual strain energy. In this approach, the virtual strain energy on a plane (ΔW) includes both the elastic work and the plastic work, i.e.

$$\Delta W = \Delta W_e + \Delta W_p \quad (2.176)$$

where ΔW_e is the elastic work component and ΔW_p is the plastic work component. The former is represented by the two grey areas schematised in Figure 2.46 and the latter is approximately equal to the product $\Delta\sigma\Delta\varepsilon_p$. Assuming that

$$\Delta W \cong \Delta\sigma \Delta\varepsilon \quad (2.177)$$

and applying the total strain-life relationship (Equation 2.24), the virtual strain energy can be expressed as

$$\Delta W = \frac{4\sigma_f'^2}{E} (2N_f)^{2b} + 4\sigma_f' \varepsilon_f' (2N_f)^{b+c} \quad (2.178)$$

being E the Young's modulus and σ_f' , b , ε_f' and c the fatigue strength and fatigue ductility properties. The

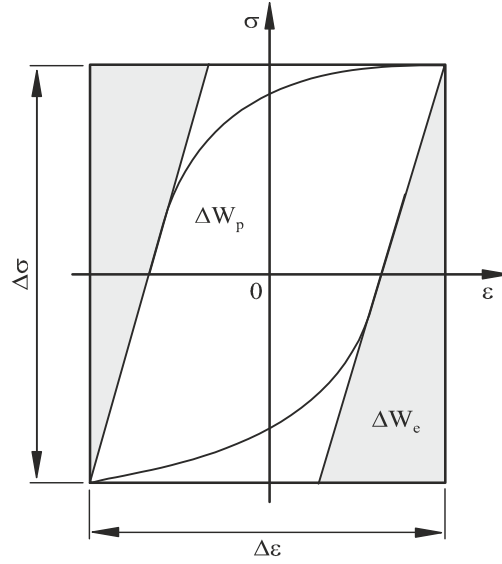


Figure 2.46. Elastic and plastic strain energies (Socie, 2000).

critical plane is the plane on which the product $\Delta\sigma\Delta\epsilon$ reaches the maximum value. In the case of shear work, it is defined as

$$\Delta W \equiv \Delta\tau \Delta\gamma \quad (2.179)$$

and Equation 2.178 is written as follows

$$\Delta W = \frac{4\tau_f'^2}{G} (2N_f)^{2b\gamma} + 4\tau_f' \gamma_f' (2N_f)^{b\gamma+c\gamma} \quad (2.180)$$

where G is the shear modulus and τ_f' , $b\gamma$, γ_f' and $c\gamma$ are the shear fatigue strength and shear fatigue ductility properties. The critical plane is the plane on which the product $\Delta\tau\Delta\gamma$ reaches the maximum value.

The virtual strain energy for multiaxial loading is associated with two possible tensile modes, i.e. a tensile failure mode, termed ΔW_I and defined by Equation 2.178, and a shear failure mode, termed ΔW_{II} and given by Equation 2.180. In the latter case, the formulation distinguishes two crack types, namely the case A ($\Delta W_{II,A}$) and case B ($\Delta W_{II,B}$) represented in Figure 2.4. For case A, the stress and strain ranges are calculated using the Mohr's circle from the first and third principal stresses (σ_1 , σ_3) and the first and third principal strains (ϵ_1 , ϵ_3). For case B, the procedure is similar but the calculations are performed using the first and second principal stresses (σ_1 , σ_2) and the first and second principal strains (ϵ_1 , ϵ_2).

The model formulated by Chu *et al.* (1993; 1995) is also based on the shear work and normal work. In order to include the mean stress effect, the stress ranges are replaced by the maximum stresses. The damage parameter (ΔW^*) is defined by

$$\Delta W^* = \left(\sigma_{n,\max} \frac{\Delta \varepsilon}{2} + \tau_{n,\max} \frac{\Delta \gamma}{2} \right)_{\max} \quad (2.181)$$

where $\Delta \varepsilon$ is the normal strain range, $\Delta \gamma$ is the shear strain range, $\sigma_{n,\max}$ is the maximum normal stress and $\tau_{n,\max}$ is the maximum shear stress. Rather than being defined on the plane of maximum normal strain or maximum shear strain, the damage parameter corresponds to the maximum value of ΔW^* . The maximum value of ΔW^* for an uniaxial test with strain amplitude ε_a and stress amplitude σ_a can be obtained by maximising the following function

$$\tau_{\theta} \gamma_{\theta} + \sigma_{\theta} \varepsilon_{\theta} = \sigma_a \varepsilon_a \left[\frac{1+\nu}{2} \sin^2(2\theta) + \frac{1-\nu}{4} + \frac{1}{2} \cos(2\theta) + \frac{1+\nu}{4} \cos^2(2\theta) \right] \quad (2.182)$$

which occurs for a plane at $\theta = 20.7^\circ$. The fatigue life expression, defined in terms of standard material constants, can be expressed as

$$\Delta W^* = A \frac{\sigma_f'^2}{E} (2N_f)^{2b} + B \sigma_f' \varepsilon_f' (2N_f)^{b+c} \quad (2.183)$$

where A and B are, respectively, defined by

$$A = \frac{1+\nu_e}{2} \sin^2(2 \times 20.7^\circ) + \frac{1-\nu_e}{4} + \frac{1}{2} \cos(2 \times 20.7^\circ) + \frac{1+\nu_e}{4} \cos^2(2 \times 20.7^\circ) \quad (2.184)$$

$$B = \frac{1+\nu_p}{2} \sin^2(2 \times 20.7^\circ) + \frac{1-\nu_p}{4} + \frac{1}{2} \cos(2 \times 20.7^\circ) + \frac{1+\nu_p}{4} \cos^2(2 \times 20.7^\circ) \quad (2.185)$$

being ν_e and ν_p the Poisson's ratio in the elastic and plastic regions. Thus, for typical values of ν_e and ν_p , i.e. 0.3 and 0.5, A and B are approximately equal to 1.02 and 1.04, respectively.

Glinka *et al.* (1995) proposed another energy-based parameter that considers only the shear work and a mean stress correction, which can be written mathematically as

$$\Delta W^* = \frac{\Delta \tau}{2} \frac{\Delta \gamma}{2} \left(\frac{\sigma_f'}{\sigma_f' - \sigma_{n,\max}} + \frac{\tau_f'}{\tau_f' - \tau_{n,\max}} \right) \quad (2.186)$$

where $\sigma_{n,\max}$ and $\tau_{n,\max}$ are the maximum absolute values of normal and shear stresses in the critical plane defined as the plane of maximum shear strain range ($\Delta \gamma$). The mean stress correction aims at evaluating crack surface sliding and crack opening. The normal mean stress is associated with crack opening and the shear mean stress is associated with crack surface sliding. The fatigue life expression, defined in terms of shear strain-life properties, is given by

$$\Delta W = \left[\frac{\tau_f'^2}{G} (2N_f)^{2b\gamma} + \tau_f' \gamma_f' (2N_f)^{b\gamma+c\gamma} \right] \left[1 + \frac{1}{1 - (2N_f)^{b\gamma}} \right] \quad (2.187)$$

where G is the shear modulus, τ_f' is the shear fatigue strength coefficient, $b\gamma$ is the shear fatigue strength exponent, γ_f' is the shear fatigue ductility coefficient and $c\gamma$ is the shear fatigue ductility exponent.

CHAPTER 2 - LITERATURE REVIEW

PART B - CRACK GROWTH MODELLING

This chapter is devoted to the literature review and contains two main parts (Part A and Part B). Part B is focused on the crack growth modelling using the finite element method and is organised into three sections. The first section presents the state-of-the-art. The second section describes in detail the main steps of the technique, namely the tasks associated with the finite element method, the tasks associated with the calculation of the stress intensity factor along the crack front, and the tasks associated with the crack growth model. The last section identifies the effects of the main physical variables on crack shape and fatigue life.

NOMENCLATURE

3D	three-dimensional
A	area
a	crack length
a/b	crack aspect ratio
a/D, a/t, a/W	dimensionless crack length
BEM	boundary element method
C	Paris law constant
C(T)	compact tension specimen
CC	corner crack specimen
dA	virtual crack area extension
da/dN	fatigue crack growth rate
dK/da	stress intensity factor gradient
D	diameter
DBEM	dual boundary element method
ESIS	European Structural Integrity Society
d _T	transition depth
E	Young's modulus
FCG	fatigue crack growth
FE	finite element
FEM	finite element method
G	energy release rate
K, K _i	stress intensity factor, stress intensity factor of the i th node
K _{IC}	fracture toughness
K _{max} , K _{min}	maximum stress intensity factor, minimum stress intensity factor
LEFM	linear elastic fracture mechanics
L ₁	radial size of crack front elements
M(T)	middle-crack tension specimen
m	Paris law exponent
N _f	fatigue life
OICC	oxide induced crack closure
PICC	plasticity induced crack closure
PPP	preferred propagation path
RICC	roughness induced crack closure
SIF	stress intensity factor
S _r	dependent parameter
t	thickness
W	width
W _E	work of external forces
Y	geometric factor
XFEM	extended finite element method
δ _i	displacement of the i th crack front node
Δa, Δa _{max}	crack growth increment, maximum crack advance
ΔK, ΔK _{max}	stress intensity factor range, maximum range of stress intensity factor
ΔK _{th}	threshold value of the stress intensity factor range
ν	Poisson's ratio
φ	stress function
Π	potential energy of a loaded body

2.6. State-of-the-art

In the last decades, the study of fatigue crack growth has received a great deal of attention. This is due to the fact that modern defect-tolerant design approaches to fatigue are based on the premise that engineering components are inherently flawed, i.e. defects are potentially present. Therefore, accurate tools to predict the crack shape and fatigue life are fundamental to increase the reliability.

Different numerical crack growth techniques have been successfully developed. One of the most efficient approaches consists of an automatic iterative procedure based on the finite element method (FEM). It comprises five main steps repeated cyclically. Firstly, an adequate three-dimensional (3D) finite element model representative of the problem is created. Secondly, the displacement field of the cracked body is obtained. Thirdly, the stress intensity factors (SIF) at the crack front are calculated. Fourthly, the crack front advances as well as the number of cycles are calculated by applying an adequate Paris law. Fifthly, the provisional crack front nodes are used to define a new crack front. The repetition of the previous steps up to the final fracture allows studying both the crack shape evolution and fatigue life.

Regarding the definition of the new crack front, two main methodologies can be distinguished. The two-degree-of-freedom model (Newman *et al.*, 1981) considers only few crack front key points (usually the surface and deepest nodes) and assumes a particular crack shape (semi-circular, part-circular, semi-elliptical, part-elliptical, etc.) throughout the propagation whose aspect ratio is allowed to change gradually as the crack grows. In the literature, there are many examples of studies conducted using this strategy. For example, Hosseini *et al.* (1985) and Mahmoud *et al.* (1986) analysed the crack shape evolution and the stress intensity factors of semi-elliptical surface cracks in plates under tension and bending. Carpinteri (1992) used the same approach to study the propagation and dimensionless SIFs of elliptical-arc surface cracks in round bars subjected to tension and bending as well as to analyse the shape change of surface cracks in round bars under cyclic axial loading (1993). In another study, Carpinteri *et al.* (1996a) studied the evolution of part-through cracks in round bars under cyclic combined axial and bending loadings. A two-parameter theoretical model that adjusts two points (the deepest point of the crack front and the point near the flaw border) to an elliptical-arc was employed. This model has been exhaustively used by the authors. They studied the fatigue growth of external surface cracks in notched and unnotched pressurised pipes (1998; 1998a; 2000; 2003; 2006) as well as in welded T-joints (2005). The crack propagation and stress intensity factors of surface cracks in semi-circular circumferential notched round bars subjected to cyclic tension and bending (2006a) were also studied. The same authors suggested an improved analysis based on a three-parameter theoretical model to predict the fatigue crack propagation of elliptical-arc surface cracks in round bars subjected to cyclic tension and bending (1996b) as well as to analyse circumferential surface flaws in pipes (2000a). In this case, the coordinates of the points along the crack front were adjusted to an ellipse by employing the least square method. The dimensionless stress intensity factors along the crack front for tension and bending were also evaluated. Shih *et al.* (1997) analysed the fatigue crack growth of round bars from two initial crack types (elliptical arc and straight-edge). A two-parameter SIF formulation which accounts for the crack aspect ratio and the crack depth ratio was developed. Burandè *et al.* (1999) studied the fatigue crack growth of a thick plate

with semi-elliptical surface cracks subjected to tension and bending. Brighenti (2000) modelled axially-cracked pipes under pulsating internal pressure by applying the two-parameter theoretical model combined with a semi-elliptical crack shape. Antunes *et al.* (2002) performed an identical approach to study the crack shape evolution, final crack length and fatigue life in notched specimens with central hole made of polymer particle composites. In this research, the crack was assumed to be quarter-elliptical. Iranpour *et al.* (2006) investigated the crack shape evolution and the stress intensity factors of pipes under bending and plates under tension considering semi-elliptical crack shapes and the two-parameter theoretical model. More recently, Carpinteri *et al.* (2009) examined the fatigue propagation of initial part-elliptical surface cracks in round bars under eccentric axial loading acting perpendicular to the crack plane. This study demonstrated that the crack paths were not remarkably affected by the values of loading eccentricity. Finally, Carpinteri *et al.* (2010) studied the effect of residual stresses due to cold-drawing processes on fatigue crack propagation in metallic cracked round bars with V-shaped circumferential notches.

The above-mentioned approach has provided acceptable results in terms of crack shape evolution and stress intensity factors. However, it is not suitable for situations containing irregular crack shapes, or for cases in which significant shape variations are expected, or even when improved predictions are required. In these cases, the multiple-degree-of-freedom model (Smith, 1989) is more suitable because each crack front node is analysed separately avoiding shape assumption. Therefore, the greater is the number of nodes along the crack front, the better are the results. A comprehensive identification and optimisation of the main parameters affecting the accuracy of the multiple-degree-of-freedom model was carried out by Lin *et al.* (1999; 1999a; 1999b). Due to its flexibility, it has been used in different contexts. Lin *et al.* (1997) studied the fatigue crack shape development of several initial surface cracks in round bars subjected to constant amplitude axial loading using nine corner nodes. Regardless of the initial crack shape, the results demonstrated that the crack always tends to preferred propagation paths. Besides, it was observed that larger values of the Paris law exponent always make the aspect ratio change more rapidly. Couroneau *et al.* (1998) proposed a simplified model to address the fatigue crack growth of surface cracks in round bars under tension and bending. It was demonstrated that once a crack has propagated up to a certain relative depth, the subsequent propagation stage is independent of its initial crack aspect ratio. In this sense, the propagation was divided into two stages. The former was influenced by the initial crack shape, loading type and Paris law exponent. The latter was a function of the loading type and Paris law exponent. On the other hand, a transition criterion between these two stages was proposed, being the transition depth a decreasing function of the Paris law exponent. In another study, the same authors discussed the validity of different simplifying hypotheses to approach the crack shape evolution in round bars under tension and bending. It was concluded that the crack front must be described by, at least, two independent parameters. Carpinteri *et al.* (2007) developed a numerical procedure to compute an approximate SIF function for surface cracks in round bars subjected to complex mode I loading. Five elementary mode I stress distributions (constant, linear, quadratic, cubic and quartic) directly applied on the crack faces were considered and the results agreed satisfactory with those found in the literature. Toribio *et al.* studied the crack shape (2009) and the compliance evolution (2011) of surface cracks in

round bars under tensile loading using a closed-form stress intensity factor solution available in the literature. This closed-form stress intensity factor was developed by Shin *et al.* (2004) and accounts for the effect of crack shape, either under tension or bending.

Particular attention has been also given to the study of fatigue crack growth in notched round bars. Lin *et al.* (1999c) tackled the shape evolution of surface cracks in fatigued round bars with semi-circular circumferential notches. The deviations of the crack profiles from the widely assumed elliptical-arc shape were examined and the results demonstrated that the shapes adopted by the crack are not always close to this crack configuration. The maximum deviations occur at the early stage of propagation. In another study, the authors (1998a) focused on surface cracks initiated from different semi-circular circumferential notches of round bars subjected to both tension and bending. Not surprisingly, the notch shape and the loading type had a significant effect on crack growth. Besides, the number of cycles required to propagate a given surface crack to a specific position was larger for bending than for tension. On the other hand, the number of cycles increases with the increase of the notch radius. The crack shape predictions were compared with those obtained from a V-notched round bar with a surface crack. In the latter case, due to the larger stress concentration along the free boundary caused by the sharp notch, the crack shape changed more rapidly. Gardin *et al.* (2007) investigated the influence of residual compressive stresses induced by roller burnishing on fatigue crack propagation in notched round bars with semi-elliptical small edge cracks. Citarella *et al.* (2010) predicted the crack paths in lateral notched round bars with initially quarter-circular cracks subjected to torsion using the dual boundary element method and the finite element method. The computational results obtained from the two methods were found to be in good agreement.

The simulation of surface and embedded cracks in plates has also been considerably studied. Gilchrist *et al.* (1991) analysed the profile adopted by semi-elliptical surface cracks under a remotely applied tension fatigue loading. The crack front was modelled assuming piecewise linear polygonal lines. It was observed that any irregular defect can attain a regular profile for which the stress intensity factor is nearly constant around the whole crack front. Besides, the ratio of the minimum SIF to the maximum SIF along the crack front was approximately unitary. This behaviour, i.e. $K_{\min}/K_{\max} \approx 1$, was termed iso-K profile. Nykänen *et al.* (1996) simulated fatigue growth of surface cracks in plates under mode I loading. The crack fronts were also modelled using piecewise linear polygonal lines with eight degrees of freedom. The predictions were in good agreement with those obtained experimentally. The improved technique optimised by Lin *et al.* (1997a) was used to simulate the growth of semi-elliptical surface cracks in plates under tension and bending. A cubic spline curve was applied to improve the crack front definition. It was observed that under tension the crack developed in an almost semi-elliptical shape and its aspect ratio did not change significantly through the thickness. However, the shape changed significantly for bending. The crack propagated much more rapidly on the free surface than at the crack depth position. In the same study, the evolution of circular and elliptical embedded defects in an infinite body under remote uniform tension was also analysed. The initially circular crack maintained its shape whilst the elliptical crack evolved to a circle due to a more rapid growth along the minor axis than along the major axis. This behaviour reflects

the tendency to equalise the crack driving force around the crack front perimeter. The studies conducted by Lazarus (1999; 2003) on fatigue growth of planar cracks loaded by remote tensile uniform loading demonstrated the same conclusions. Regardless of the initial crack shape, after a certain propagation depth, the crack reaches a circular shape. Favier *et al.* (2006) achieved identical conclusions in the analysis of various initial embedded crack shapes (circular, elliptical, rectangular, heart-shaped) in infinite bodies under mixed-mode shear loading. Nevertheless, in these simulations, the cracks evolve to almost elliptical stable shapes. Wu (2006; 2006a) proposed a new method to predict the crack shape based on a given stress intensity factor distribution for surface cracks in plates subjected to mode I loading. In essence, it consists of an iterative procedure that adjusts the SIF distribution to a function that depends on the crack geometry. Le *et al.* (2011) predicted the shape of surface cracks in plates exposed to thermal cyclic loading. The cyclic temperature gradient induced a tensile state near the surface and a compression state at the centre of the plate. As a result, the crack slowed down at the deepest point and propagated more rapidly at the surface point. Under these circumstances, the well-known iso-K profile was not reached. The interaction of coalescing surface defects in plates subjected to different remote loadings was tackled by Lin *et al.* (1997c) and by Carpinteri *et al.* (2004).

The multiple-degree-of-freedom model is a very versatile approach and has been used to address different engineering issues. Mi *et al.* (1994), using the dual boundary element method, analysed the mixed-mode crack growth of embedded elliptical cracks in cylindrical bars and quarter-elliptical corner cracks in square bars. Lin *et al.* (1997b) modelled the fatigue growth of external surface cracks in notched and unnotched pressurised pipes. The same authors (1998; 2001) simulated the fatigue crack shape for corner cracks emanating from fastener holes in plates under cyclic tension loading. Cao *et al.* (2002) developed a finite element model for studying subsurface median cracks in trilayer sandwiches due to contact loading. The crack front was constructed using a cubic spline approximation in order to represent complex crack shapes. Lee *et al.* (2004) studied fatigue crack growth in composite-repaired aluminium plates considering both linear and non-linear analyses. This study focused on several fatigue crack growth specificities, such as the crack shape evolution, the stress intensity factor variations through the thickness and the effect of the thickness on fatigue life. Sekine *et al.* (2005) investigated fatigue crack growth of cracked aluminium panels repaired with an adhesively bonded fiber-reinforced polymer composite by combining both the boundary element method and the finite element method. Spievak *et al.* (2001) focused on the analysis of the crack shape evolution and fatigue life for a spiral bevel pinion gear. The plasticity induced crack closure and moving loads were incorporated into this simulation. Branco *et al.* employed a numerical procedure to study the shape evolution of fatigue cracks in the middle-crack tension (2008) and compact tension (2008a) specimens. In both studies, the main variables affecting the crack shape were identified and the crack shape change was linked with the distribution of the stress intensity factor along the crack front. Indeed, the K distribution along the crack front was found to be the driving force for the shape variations. Branco *et al.* developed a reverse engineering technique able to determine the constants of Paris law from the analysis of fracture surfaces in double-U specimens (2009) and in small cross-section round bars (2010b; 2012d). The technique compares experimental crack shapes with numerical predictions obtained with a multiple-degree-of-freedom model. The two constants of the

Paris law are those that best fit the numerical predictions to the experimental data. Branco *et al.* (2010a) used the multiple-degree-of-freedom model to develop a grooved M(T) specimen able to obtain pure plane strain conditions. The same approach was used to study the crack shape evolution in double-U and central hole specimens with corner cracks representative of gas turbine discs with and without residual stress effects (Branco, 2011). In another study, the effect of the crack shape on plasticity induced crack closure in M(T) specimens was tackled (Branco, 2008b). The 3D fatigue crack growth technique was used to obtain stable crack shapes. Crack closure was found to produce a significant tunnelling effect, with maximum values of ΔK and K_{\max} at the surface. Hou *et al.* (2008; 2011) simulated the crack shape evolution in surface cracks considering crack closure effects. Yu *et al.* (2010; 2012) developed an equivalent thickness concept to predict the shape evolution and fatigue life in generic engineering structures from fatigue crack growth data obtained from standard specimens.

Nowadays, fatigue crack growth can be addressed using different software solutions. However, not all are available commercially. For example, ADAPCRACK3D (Schöllmann, 2003) is software focused on the determination of crack paths as well as on the evaluation of fatigue lives in arbitrary 3D geometries under complex loading. Firstly, the crack is inserted into the 3D-FE mesh of the uncracked body. Secondly, the mesh is improved since the insertion of crack, in general, entails mesh impairments. Finally, among other variables, both the crack growth and the corresponding number of load cycles are evaluated. This tool was used to analyse several unexpected in-service failures, such as fatigue crack propagation in a wheel tyre of a high speed train (Richard, 2005; Richard, 2008), in a frame of a hydraulic press (Fulland, 2008) and in real structures (Richard, 2012). FRANC3D (1999; 1999b) is alternative software able to predict complex three-dimensional crack trajectories. It comprises three main tasks. Firstly, it is developed an uncracked model. Secondly, the crack is inserted into the mesh. The insertion *a posteriori* of the crack into the model can deteriorate the mesh. Thus, several remeshing techniques are employed to improve the results. Finally, the crack propagation is performed using the boundary element method. This computer application was used by Yngvesson *et al.* (1999) to examine the fatigue crack growth of surface cracks under non-symmetric loading. Spievak *et al.* (2001) and Ural *et al.* (2005) studied fatigue crack growth of spiral bevel gears. Poursaeidi *et al.* (2009) analysed fatigue crack growth simulation in generator fan blades. Rozumek *et al.* (2010) evaluated the stress intensity factor along crack paths in cruciform specimens under out-of-phase cyclic loading. FRANC/FAM (Schöllman, 1999) was developed to predict fatigue crack growth and to evaluate fatigue lives in geometries under complex arbitrary planar loading conditions. CRACKTRACER 3D (Bremberg, 2008) is a recent tool developed based on a different approach. The cracked structure boundary is modelled as a discretised skin. Then, a tube-like domain enclosing the crack front is traced and filled with hexahedral elements while the remaining cracked structure is meshed with tetrahedral elements. Finally, the two separate meshes are connected. A former version able to address mode I loading problems was used to investigate cyclic crack propagation in corners and holes (Dhondt, 2005). ZENCRACK (2007) is commercial FE software designed for linear elastic fracture mechanics problems but it is also able to study 3D fatigue crack propagation problems. The uncracked 3D-FE mesh is created using an external FE package and consists of a pure hexahedral mesh in the complete structure. Then, the crack front is modelled by refining the mesh. It is carried out

introducing a set of special elements, named crack-blocks, in the vicinity of the crack front. In fact, although there are several types of crack-blocks, the crack region is vulnerable and potentially affected by numerical errors (Hou, 2001; Maligno, 2010). Additionally, difficulties associated with the transition from surface cracks to through cracks were also reported (Roy, 2005). NASCRAC (1989, 1989b), NASGRO (2009), AFGROW (Harter, 2002) and ESACRACK (2000) are software based on a different philosophy. In all these computer applications, fatigue life is determined from libraries of geometries and crack configurations by applying appropriate stress intensity factor solutions. In the recent years, more sophisticated algorithms able to simulate fatigue crack growth in complex three-dimensional components using structured (Kolk, 2006; Weber, 2008; Shi, 2010) and unstructured meshes (Moslemi, 2009; Ayhan, 2011) have been proposed.

2.7. The automatic crack growth technique

As referred to in the previous section, the fatigue crack growth technique can be divided into five main steps cyclically repeated. Firstly, a numerical model representative of the cracked body is created (Figure 2.47a). It includes the definition of the geometry, boundary conditions, loading, crack shape, elastic constants and fatigue crack growth rate. Secondly, the displacement field of the crack front nodes is calculated (Figure 2.47b). In general, the methods used are the finite element method (FEM), the boundary element method (BEM), the dual boundary method (DBEM), the extended finite element method (XFEM) or the two first together (FEM/BEM). Thirdly, the stress intensity factors along the crack front are computed (Figure 2.47c) using *displacement matching methods* (extrapolation method, singular elements based method, quarter-point displacement method, etc.) or *energy-based methods* (external forces work method, stiffness derivative formulation, mapping technique, J-integral method, energy domain integral, crack closure integral method, etc.). Fourthly, an adequate crack growth model is applied to calculate the crack front advances, which are used to establish a provisional crack front (Figure 2.47d)

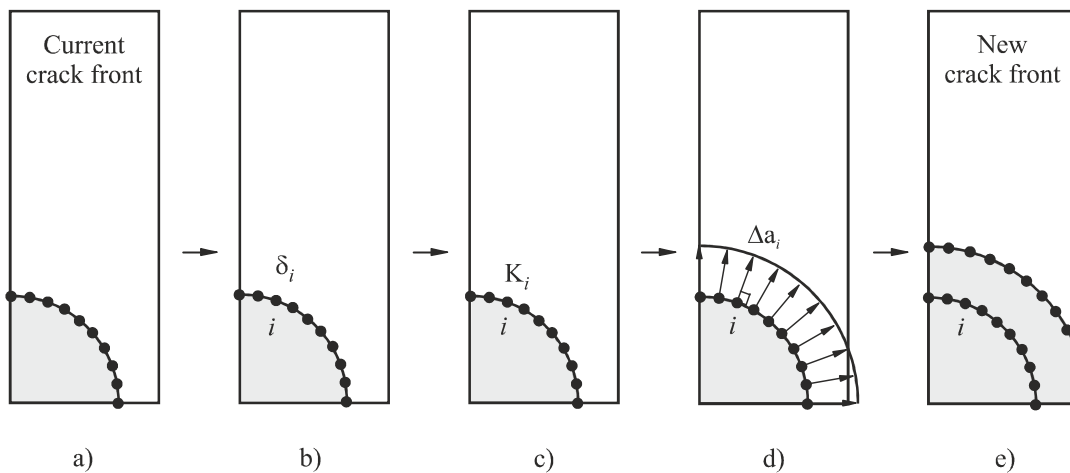


Figure 2.47. Schematic presentation of the 3D-FE automatic fatigue crack growth technique: a) definition of a crack front; b) calculation of the displacement field of crack front nodes; c) calculation of stress intensity factors along the crack front; d) calculation of nodal advances of crack front nodes; e) relocation of corner and intermediate nodes (Branco, 2013).

and to estimate the number of loading cycles. Finally, the corner nodes of the crack front are moved to their final positions (Figure 2.47e). In the models with multiple degrees of freedom, the crack front is defined using a cubic spline that passes through both the corner and intermediate nodes. In the models with two degrees of freedom, the key points (usually the surface and the deepest nodes) are used to define a theoretical crack shape, which is often assumed to be semi-circular, part-circular, semi-elliptical, part-elliptical, among others.

The above-mentioned steps are repeated many times during a simulation. According to the main variables of the calculation procedure, this automatic technique can be organised into three main tasks. As schematised in Figure 2.48, the main tasks encompass the development of a representative finite element model, the calculation of the stress intensity factors at the crack front, and the application of an adequate crack growth model. Besides, it is also clear that the output data of a given task serves directly as input data of the next step. Therefore, each calculation must be carefully studied and optimised to ensure reliable numerical results. Otherwise, errors propagate through the simulation which has a repercussion on the predicted crack fronts and fatigue lives.

Figure 2.48 identifies the main independent parameters associated with each task. The effects of some parameters are known and the adequate values can be found in the literature, such as the mesh topology, type of finite elements, crack shape definition and orientation of layers. Others require specific parametric studies that must be performed case-by-case, since there are no universal optimum values, for example the radial size of crack front elements, refinement of the layers at the crack front, crack growth increment, among others.

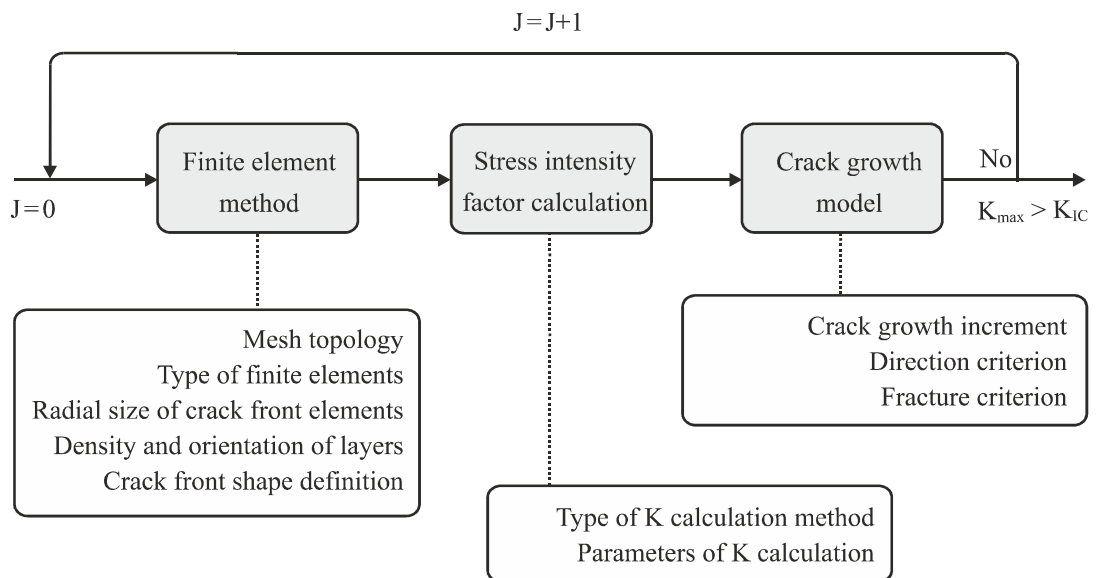


Figure 2.48. Main parameters of the calculation procedure developed to predict the fatigue crack shape using the FEM (Branco, 2008).

2.7.1 Finite element method

In an elastic body statically loaded, the stress field is obtained considering equilibrium equations, strain compatibility equations and constitutive relations. The equilibrium equations express the equilibrium of each element of volume of the body, while the strain compatibility relations guarantee that neither empty spaces nor coincidences happen when the body deforms. Finally, the constitutive relations of the material relate the stresses to the elastic strains. To simplify the mathematical formulation of the problem, a stress function ϕ can be defined, such that for a bi-dimensional problem:

$$\sigma_{xx} = \frac{\partial^2 \phi}{\partial x^2} \quad \sigma_{yy} = \frac{\partial^2 \phi}{\partial y^2} \quad \sigma_{xy} = \frac{\partial^2 \phi}{\partial x \partial y} \quad (2.188)$$

where σ_{ij} are the stress components. The stress equilibrium equations, the strain compatibility equations and the constitutive relations produce the following bi-harmonic equation:

$$\frac{\partial^4 \phi}{\partial x^4} + 2 \frac{\partial^4 \phi}{\partial x^2 \partial y^2} + \frac{\partial^4 \phi}{\partial y^4} = 0 \quad \Leftrightarrow \quad \nabla^4 \phi = 0 \quad (2.189)$$

named Airy's equation (Sokolnikoff, 1956). Thus, the study of the stress field of a body in equilibrium reduces to the calculation of ϕ that satisfies the Airy's differential equation. The solution must satisfy the boundary conditions of the problem being studied. This last requirement limits the analytical solution to bodies with simple shapes.

The FEM is a numerical procedure able to solve the Airy's equation that replaces it by a system of linear algebraic equations. Its application encompasses the following steps: i) meshing of the body under study; ii) interpolation; iii) calculation of elemental matrices; iv) assembling; v) resolution of the system of equations; and vi) calculation of displacements, stresses and strains fields from the nodal displacements. The nodal displacements are the primary variables, and the stresses and strains are calculated from them.

As is well-known, the FEM is a versatile technique with which is possible to analyse bodies with different shapes, boundary conditions, material properties and subjected to different loads. However, the solution is affected by errors because the displacement field inside each element is defined only approximately using shape functions. The accuracy of the approximation depends on the type of elements, size of elements and real displacement field. Besides, there are round-off errors which are associated with the limitations of computers to represent real numbers. In this sense, these errors propagate within the FEM affecting the final solution.

The application of the FEM to the analysis of linear elastic fracture mechanics (LEFM) problems is complicated by the stress singularity existing at the crack front. In fact, the shape functions are polynomials defined over elements of finite length, and so the strains (obtained from differentiation of

displacements), and the stresses (equal to strains multiplied by characteristic constants of the material) are also polynomials and therefore cannot reach infinite values in a finite length. Thus, the displacement field assumed by the FEM in the elements connected to the singular crack front never fits the real distribution of displacements. Accordingly, incorrect nodal displacements are obtained. Even in the elements adjacent to the crack front, the stress gradient can be too high to be simulated by them. This causes an additional difficulty when the crack front elements are small. Therefore, the order of convergence increases substantially from the crack front elements to the neighbouring ones.

In order to improve the global accuracy of the FEM analysis of cracked bodies, different solutions can be considered:

- the mesh should be refined around the crack front to capture the $r^{0.5}$ variation of the displacement field, i.e. the $r^{-0.5}$ stress variation. However, this refinement increases the computational effort. Thus, an important objective is to find an optimum mesh with which the crack tip singularity is efficiently modelled without overrunning computer storage or raising excessively computational costs;
- higher order elements, such as the isoparametric ones, are recommended. Although singularity is only approximately simulated, the solutions are substantially improved. Besides, with these elements a larger mesh can be used, not only near the crack front but in the whole body, enabling a reduction of the total number of elements for the same degree of accuracy;
- the use of singular elements at the crack front is also recommended. The order of singularity for LEFM is known for plane strain conditions. In view of this fact, such elements introduce that singularity in their formulation which reduces the error at the crack front where it is important to have accurate values. As a consequence, less refined meshes can be used near the crack front for the same degree of accuracy.

i) Mesh topology

There is a general agreement that the best mesh topology should contain, at least, two regions with different mesh schemes (Carpinteri, 1996a; Lin, 1997; Lee, 2004): a *cracked region* (Figure 2.49a) which comprises the small volume of material surrounding the crack front; and an *uncracked region* (Figure 2.49d) which corresponds to the remaining volume of the body. The former, made of several concentric rings centred at the crack tip, is automatically remeshed after each crack increment whilst the latter remains practically unchanged throughout the simulation.

This concept can be improved by including an intermediate region named *transition mesh* (Figure 2.49b) whose main aims are to decrease the total number of elements and to promote a smooth transition from a refined mesh near the crack front to a larger mesh at remote positions (Antunes, 1999). The spider web mesh (Figure 2.49a) can be created directly from the crack front coordinates in order to avoid the deterioration associated with the insertion *a posteriori* of the crack into the regular mesh. After that, it is connected to the transition mesh, which leads to the rectangular box schematised in Figure 2.49c. Finally,

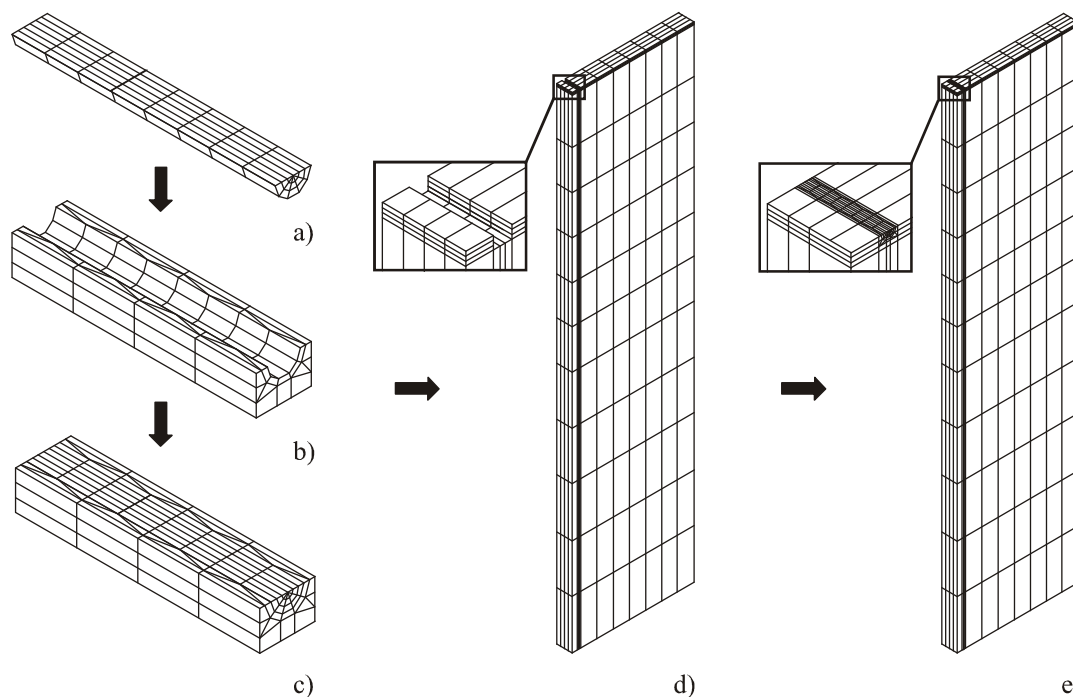


Figure 2.49. Examples of a typical mesh topology used to analyse cracked bodies (Branco, 2008): a) spider web mesh; b) transition mesh; c) cracked region; d) uncracked region; e) assembled FE model.

the regular mesh (Figure 2.49d) is added to the previous one to obtain the assembled finite element model exhibited in Figure 2.49e. This approach has been successfully used in different situations. Some examples can be found elsewhere (Branco, 2008; 2008b; 2009; 2010a; 2012d).

ii) Types of finite elements

The finite elements commonly used in fracture mechanics are the isoparametric ones. The European Structural Integrity Society (ESIS) recommendations are for isoparametric elements with quadratic shape functions (Sedmak, 1992). The isoparametric elements can represent curved shapes with a small number of elements, since they can have a distorted shape. This effect is achieved by defining the elements in local coordinates and establishing a relation between local and global coordinates. So, fewer elements can be used for modelling bodies with curved or complex boundaries. Besides, they are convergent and have a rate of convergence higher than other types of elements. On the other hand, quadratic isoparametric elements are well tested and are available in almost all general finite element packages.

Usually, the isoparametric quadrilateral 20-node element (Figure 2.50a) is employed in the uncracked region (Lin, 1999; Lee, 2004; Gardin, 2007; Carpinteri, 2009; Le, 2011). Each node has three degrees of freedom (along x , y and z axes), which means that the total number of degrees of freedom for this element is sixteen. It simulates parabolic variations of displacements and consequently linear variations of stresses and strains. A full numerical integration scheme for the calculation of rigidity matrices and nodal forces is done over $3 \times 3 \times 3$ points. Therefore, it is suitable for elastic analyses. However, the calculated stresses at

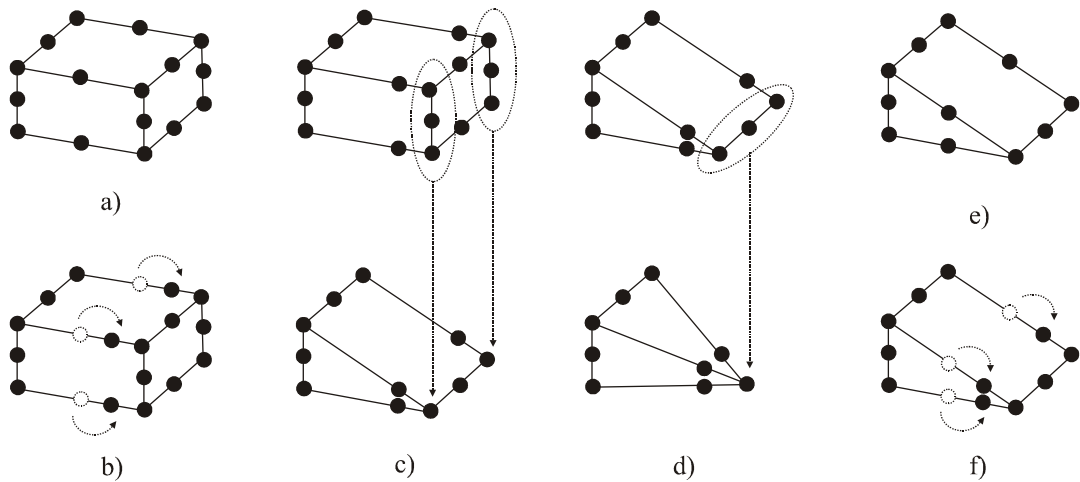


Figure 2.50. a) 20-node isoparametric brick element; b) quarter-point 20-node isoparametric brick element; c) collapsed 20-node isoparametric brick element; d) double collapsed 20-node isoparametric brick element; e) 15-node isoparametric wedge element (not collapsed); f) quarter-point 15-node isoparametric wedge element (not collapsed).

the individual integration points can show some wavy behaviour. Consequently, the presentation of stresses is often carried out using mean values, which contributes to smooth these variations (Bakker, 1992).

In the crack front, the introduction of the linear elastic $r^{-0.5}$ stress singularity in the finite element analysis can be done using analytical elements or modified isoparametric elements. The former are based on the analytical expressions of the linear elastic fracture mechanics, containing the stress intensity factor in their formulation, which avoids *posterior* calculation of SIFs. The latter are obtained from the bi-dimensional 8-node and three-dimensional 20-node isoparametric elements positioning the intermediate nodes near to the crack front at quarter-point positions (Figure 2.50b). The connection to standard elements is not a problem and there is no need for transition elements. The use of singular isoparametric elements is very interesting and simple because it only requires changing the position of nodes of the standard elements. In addition, the use of singular elements is always possible since, as referred to above, the isoparametric standard elements are present in all commercially available finite element software. Furthermore, there are different types of isoparametric singular elements. For instance, quarter-point singular elements (Figure 2.50b); quarter-point collapsed elements (Figure 2.50c); double collapsed quarter-point elements (Figure 2.50d); higher order singular elements; natural (not collapsed) quarter-point triangular or wedge elements (Figure 2.50f); and singular isoparametric elements in which not only the position of the nodes is changed but also the shape functions (Gavete, 1989). Either the quarter-point collapsed elements (Figure 2.50c) or the natural quarter-point wedge elements (Figure 2.50f) have been recurrently used by different authors (Lin, 1999; Antunes, 2002; Lee, 2004; Branco, 2008; Carpinteri, 2009; Maligno, 2010; Yu, 2012; Branco, 2012d).

The effect of different crack tip isoparametric elements on the quality of the numerical results was systematically investigated by Antunes (1999). This study encompassed the conventional 15-node isoparametric wedge element (Figure 2.50e); the quarter-point 15-node isoparametric wedge element (Figure 2.50f); and the collapsed 20-node isoparametric brick element (Figure 2.50c). The results demonstrated a high performance of the singular elements relatively to the conventional 15-node isoparametric wedge element. Besides, among the singular elements, the best was the collapsed 20-node isoparametric brick element. The good behaviour of the singular elements was expected since they incorporate the $r^{-0.5}$ crack tip singularity. However, some errors can occur at corner points (the points where the crack front intersects a free surface) because the same singularity is implicitly assumed there by the singular elements. In fact, at a corner point, there is still a $r^{-\lambda}$ singularity but usually $\lambda < 0.5$. Note that the singularity is $\lambda = 0.5$ at a corner point only when the crack front intersects the surface at the critical angle. Since most calculations are carried out for an intersection angle of 90° and a Poisson's ratio of about 0.3, $\lambda < 0.5$ for mode I (i.e., $K_I = 0$) and $\lambda > 0.5$ for mode II and mode III (i.e., K_{II} and K_{III} are infinite). In practice, values of K obtained at corner points are finite and usually of the same order as values elsewhere along the crack front (Pook, 1994) which is an indication of the inaccuracy of FEM near the surface. Bakker (1992) showed that practically only the calculated free surface value of K is affected by the mesh refinement in the direction longitudinal to the crack front. The inside values are not particularly affected by the correctness achieved at the surface. So, the finite element mesh near corner points must be refined not only in the radial direction, but also in the thickness direction. The variability of the boundary layer thickness and of the order of singularity make the mesh definition more difficult.

iii) Radial size of crack front elements

In a wide range of problems, the most efficient mesh design at the crack tip has proved to be a spider web pattern. It consists of several concentric rings focused on the crack tip (Figure 2.49a). The inner-most ring of elements is made of triangle prisms (Figure 2.50c or Figure 2.50e). Moreover, the appropriate level of mesh refinement depends on the purpose of analysis and singular elements must be included when finite element results near the crack tip are required. Guinea *et al.* (2000) concluded that the minimum angular discretisation of the elements surrounding the crack tip is 30° , which means at least six elements. Murti *et al.* (1986) recommended a minimum of five, but preferably six. Furthermore, it was demonstrated that the influence of the other rings of elements on the accuracy of the FEM results is secondary (Antunes, 1999; Guinea, 2000). On the contrary, the size of the singular elements plays a crucial role on the accuracy of results.

The optimum radial size of the singular elements (L_1) is assured when a balanced modelling of both singular and non-singular fields is achieved. The quarter-point elements can represent a radial variation of stress from the crack tip that is the sum of the $r^{-0.5}$ singular term and a constant finite stress term. Furthermore, a cracked body generally possesses, in the vicinity of the crack tip, a stress field defined by the sum of the singular term and a finite stress term which varies non-linearly with the position. If the quarter-point element is larger than the singular region (Figure 2.51c), in the domain of this element, the

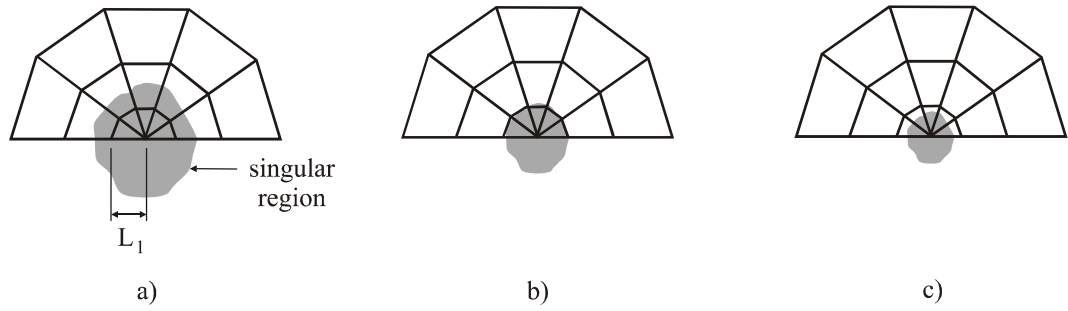


Figure 2.51. Relation between radial size of crack front elements (L_1) and singular region (r_s): a) $L_1 < r_s$; b) $L_1 \approx r_s$; c) $L_1 > r_s$ (Antunes, 1999).

finite stress term with non-linear variation has to be represented by the constant stress term (Harrop, 1982). On the other hand, if the singular elements are too small (Figure 2.51a), the elements adjacent to crack tip elements have to attempt to represent the singular term. Therefore, the singular elements cannot be smaller or bigger than the singular region (Figure 2.51b). In fact, the error introduced increases in the former case and decreases in the latter case.

An optimum singular element size should exist for each crack configuration. However, finding the optimum size in numerical fracture mechanics is not easy in virtue of the variability of the singularity dominated zone existing from one crack configuration to another. This zone is variable around a crack tip and along a crack front. Murti *et al.* (1986) analysed several crack geometries and concluded that the singularity dominated zone was different for each crack configuration. There is an optimum size of singular elements in each case, but it generally takes a different value for each crack configuration. In this way, universal optimum sizes do not exist. In addition, it is difficult to find general guidelines for proper use of singular elements for all classes of crack problems. This forces the universal optimum singular element to be defined in a weak sense under an acceptable upper bound tolerance. For instance, Antunes (1999) studied the optimum value of L_1 in a corner crack (CC) specimen. The optimum size of L_1 was found by maximising the work of the external forces, given by

$$W_E = \sum \left(\frac{1}{2} F_i \times d_i \right) \quad (2.190)$$

where F_i and d_i are the force and displacement for the i^{th} node, respectively. In fact, the discretisation error associated with the FEM produces over-rigidity, i.e. decreases W_E . Therefore, the minimisation of the error associated with a finite element discretisation corresponds to the maximisation of W_E . The results showed optimum sizes between 5-10% of the crack length. Murti *et al.* (1986) found universal optimum sizes within 15-25 % of the crack length. Nykänen (1996) found optimum values ranged from 1.25 to 2.75% of the crack length. Branco *et al.* (2008a), also based on the maximisation of W_E , studied four geometries (middle-crack tension specimen, compact tension specimen, single edge crack specimen, double edge crack specimen). As exhibited in Figure 2.62, two main trends were found: i) for the single

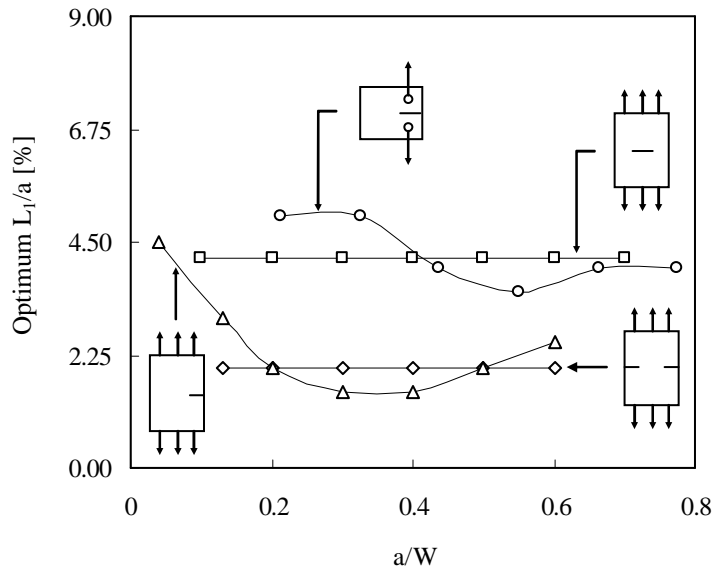


Figure 2.52. Evolution of the optimum value of L_1 for different specimen geometries (Branco, 2008a).

edge crack specimen and the compact tension specimen (two asymmetrical geometries), the optimum value of L_1/a varies with crack length; ii) for the middle-cracked tension specimen and the double edge crack specimen (symmetrical geometries), the optimum value of L_1/a appears to be constant in the range of a/W studied. Furthermore, Figure 2.52 shows that the optimum radial size of crack front elements for these cases lay in the interval 2-6% of the crack length.

iv) Orientation and refinement of layers

The degree of orthogonality of the mesh surrounding the crack front is a relevant parameter for calculating the stress intensity factor using direct methods. Lin *et al.* (1999) studied five different 2D crack plane meshes in a particular defect embedded in an infinite body under remote tension. The mesh orthogonality varied from the precisely orthogonal mesh (Figure 2.53a) to the most distorted one (Figure 2.53d). The crack fronts were defined using cubic spline functions. The geometric factor (Y) was obtained using the J-integral method (energy-based method) and the quarter-point displacement method (direct method). The results presented in Figure 2.54a show that the geometric factors found are not identical along the crack front for these meshes. Besides, it can be noted that the decrease in the degree of orthogonality is responsible for an increase in the difference of the geometric factors. Nevertheless, the geometric factors along the crack front obtained with the J-integral are nearly constant and revealed to be practically independent of the degree of non-orthogonality. However, if the QA' distance (normal to the crack front) is considered instead of the QA distance, the values of the geometric factor along the crack front become coincident for all meshes (Figure 2.54b). Therefore, applying this correction, even a mesh severely non-orthogonal can be able to achieve good results. Notwithstanding, a non-orthogonal mesh should be avoided since it introduces an extra difficulty in locating the right position of point A' which usually is not coincident with the corner node A .

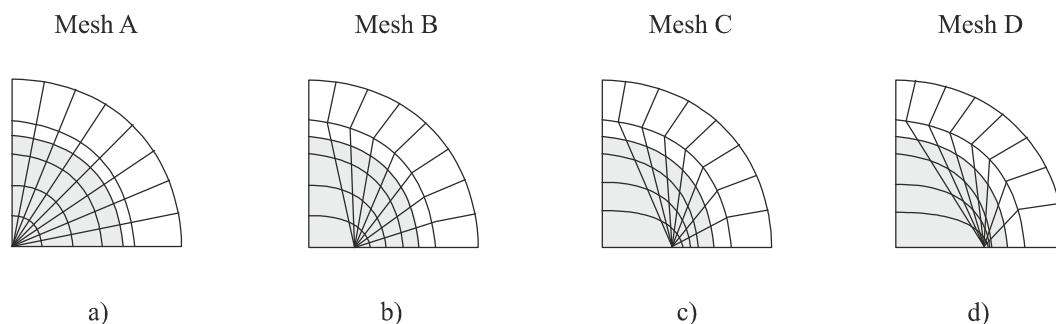


Figure 2.53. Different degrees of mesh non-orthogonality (Lin, 1999).

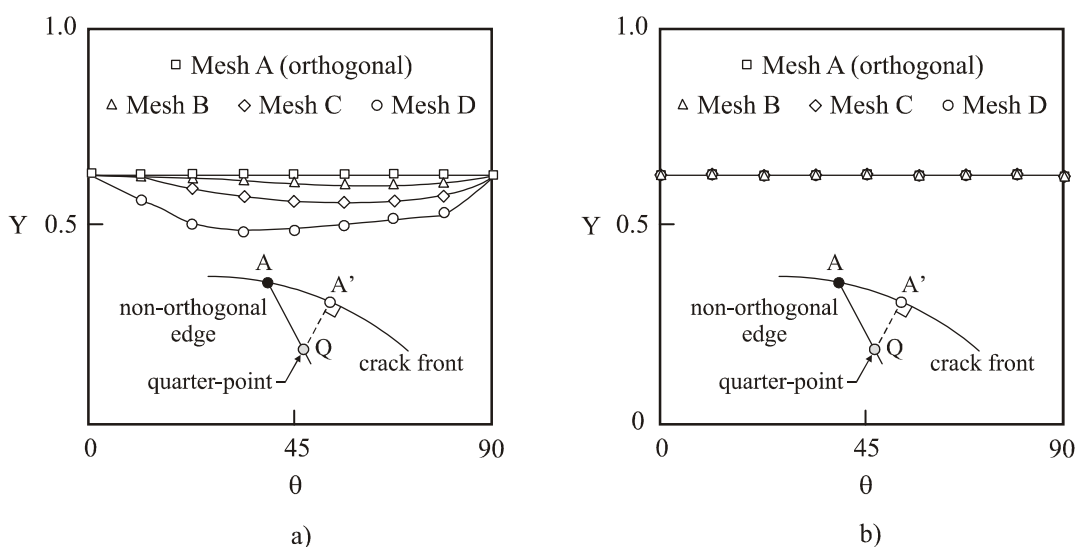


Figure 2.54. Effect of the mesh orthogonality on the geometric factor using the quarter-point displacement method and the distance between: a) Q and A ; b) Q and A' (Lin, 1999).

The quality of the numerical results is influenced by the mesh refinement along the crack front (Wu, 2006). The surface regions of the crack front are particularly important, as they involve complex singularities. The presence of lateral notches and grooves certainly affect the extent of the surface region. Besides, a relatively fast transition from plane stress state at the surface to plane strain state at interior positions can be expected. Additionally, there are surface phenomena, such as crack closure, residual stresses and even different propagation mechanisms (leading to different FCG rates) that must be properly included into the numerical models. The finite element mesh should be sufficiently refined to accommodate these near surface variations. However, a limited number of studies was found regarding the extent of the surface region. Burton *et al.* (1984) analysed through-thickness cracks and determined an extent of the surface region less than 1.5% of the crack length. Narayana *et al.* (1994) in a similar study concluded that the extent of the surface region is lower than 5% of the crack length. Antunes *et al.* (2000) studied a 5mm-quarter-circular crack in a bar with rectangular cross-section and quantified the extent of

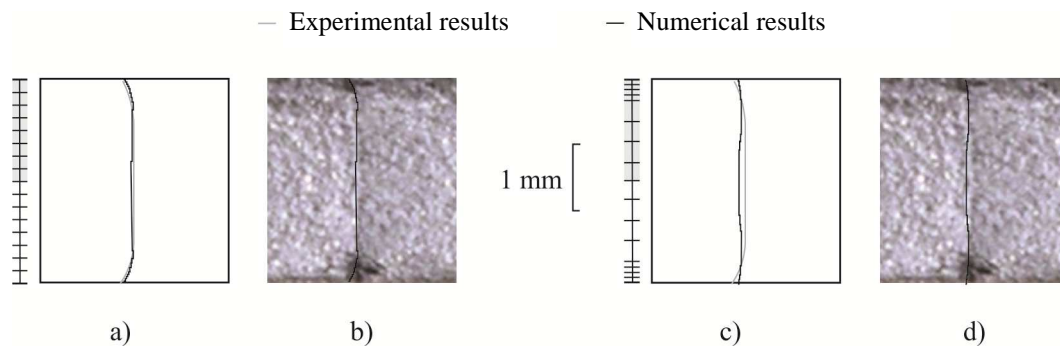


Figure 2.55. Comparison of numerical and experimental crack shapes (Branco, 2006).

the surface region in 1.5° (nearly 2.6 % of the crack length). Branco *et al.* (2006) used two different models with the same computational effort to study the crack shape evolution in middle-crack tension specimens. In the model exhibited in Figure 2.55a, the crack front had eight elements uniformly disposed, while in the model of Figure 2.55c the same number of elements was disposed non-uniformly. By comparing Figures 2.55a and 2.55c, there is no doubt that the layer refinement along the crack front is a relevant parameter. As can be seen, considerable differences between both predicted crack shapes are observed. Surprisingly, in this case, the model with more layers nearby the surface presented worse results. This fact was explained by an insufficient number of elements in depth direction, since the layers were concentrated near the surface.

v) *Crack front shape definition*

As discussed previously, the numerical prediction of crack shape is established from a set of discrete corner nodes located at the crack front. The local normal increments at these corner nodes are used to define the new crack front. The position of the intermediate nodes affects the correctness of the results. In the simplest approach (Figure 2.56a), the corner nodes are connected by straight lines and the intermediate nodes are positioned at the midpoint of both neighbouring corner nodes (Smith, 1989). Then, the SIF is calculated at these corner nodes and used to obtain the local increments. After that, a new set of points is obtained by summing the original positions and the calculated local increments. These new points are considered as the corner nodes of the new crack front and are used to define the positions of the new intermediate nodes. In certain circumstances, it is necessary to modify manually the positions of several corner nodes, especially in the cases in which large crack shape changes occur. The level of automation of the simulation technique is obviously affected which is a clear disadvantage. Besides, the numerical results have demonstrated that a crack front defined from polygonal lines leads to errors in the calculation of the stress intensity factors.

A different approach (Figure 2.56b) was proposed by Lin *et al.* (1999). Instead of using a polygonal line, the crack front is defined by a cubic spline function that passes through both the corner and intermediate nodes. In a first stage, the corner and intermediate nodes are applied to obtain a provisional crack front which serves to define a cubic spline. After that, the cubic spline is used to relocate both the corner and

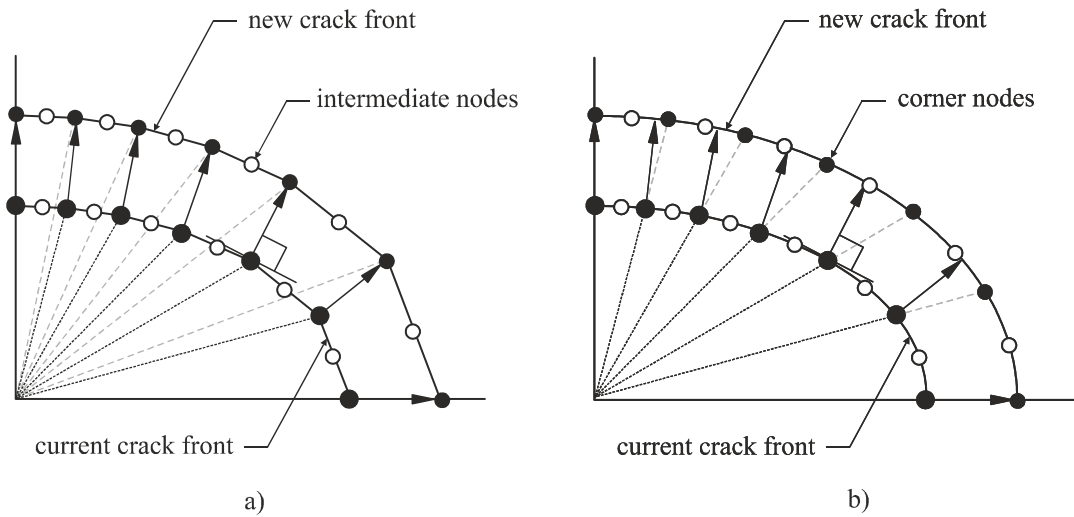


Figure 2.56. Crack front shape definitions: a) polygonal line; b) cubic spline curve.

intermediate nodes according to predefined criteria. For example, the nodes can be positioned suitably distanced along the cubic spline, as exhibited in Figure 2.55a; or can be positioned in specific locations throughout the thickness, as in the case presented in Figure 2.55b; or according to any other criterion. Besides, this procedure can be fully automated since no manual modifications of nodal positions are needed. Moreover, it is important to note that a crack front definition based on a cubic spline leads to more accurate stress intensity factors along the crack front. For example, Lin *et al.* (1999) studied the SIF values along circular defects embedded in infinite bodies subjected to remote tension. Relatively to the exact solution (Sneddon, 1946), the average of SIF values obtained with the quarter-point displacement method were inaccurate about 0.5% with the cubic spline and about 5% with the polygonal line. Such results demonstrate that the SIF values along the crack front are very sensitive to the positions of the intermediate nodes.

2.7.2 Calculation of stress intensity factor with the FEM

As referred to above, accurate stress intensity factors are decisive to obtain good fatigue life predictions. Numerically, the methods for extracting the stress intensity factors can be divided into two categories: displacement matching methods (for example, displacement extrapolation method, singular elements based method, etc.); and energy-based methods (for instance, external forces work method, stiffness derivative formulation, mapping technique, J-integral method, energy domain integral, crack closure integral method, etc.). In the first case, the form of the local solution is assumed and the value of the displacement near the crack tip is used to determine the magnitude of the coefficients in the asymptotic expansion. In the second case, the strength of the singular stress field is related to the energy release rate (G), i.e. the sensitivity of the total potential energy to the crack position. Due to the increasingly more powerful computers, these approaches have received growing attention over the past decades and are able to solve almost all the problems. However, the results obtained are only approximations of the real solutions. In the next paragraphs, the K methods used in this research are briefly outlined.

i) **Displacement matching methods**

In the displacement matching extrapolation methods, the displacement field obtained with the finite element method is compared with the analytical displacement field which contains K in its formulation. For a bi-dimensional crack under mode I loading, the analytical expression for the displacement normal to the crack plane is given by (Ingraffea, 1980)

$$v_B - v_P = K_I \frac{1+\nu}{4E} \sqrt{\frac{2r}{\pi}} \left\{ (2\kappa+1) \sin \frac{\theta}{2} - \sin \frac{3\theta}{2} \right\} + \frac{A_1(1+\nu)r}{E} (\kappa-3) \sin \theta$$

(2.191)

$$+ \frac{A_2(1+\nu)r^{3/2}}{E} \left\{ \frac{(2\kappa-1)}{3} \sin \frac{3\theta}{2} - \sin \frac{\theta}{2} \right\} + \dots$$

where E is the Young's modulus, ν is the Poisson's ratio, κ is an elastic parameter equal to $(3-4\nu)$ for plane strain and $(3-\nu)/(1+\nu)$ for plane stress, A_i are parameters depending on the geometry and load conditions, r and θ are the polar coordinates defined according to Figure 2.57, and v_B and v_P are the displacements normal to the crack plane of points P' and P , respectively. Due to the symmetry of mode I loading, the normal displacement at the crack tip is zero ($v_p=0$). The extrapolation is more accurate when evaluated along the crack faces ($\theta = \pm\pi$), as first suggested by Chan *et al.* (1970).

The simplest estimation of K_I can be made by using the first term of the previous equation. For the point A ($r=l/4$), in plane strain, under mode I loading, and $\theta=\pi$, it leads to the following equation.

$$K_I = \frac{2E}{(1+\nu)(1+\kappa)} \sqrt{\frac{2\pi}{l}} v_A$$

(2.192)

The value of K_I can be calculated by replacing the material constants, the length of the element side PB , and the displacement of point A (which can be obtained using the FEM). This K value is valid in the whole singular region because it is independent of the coordinate system.

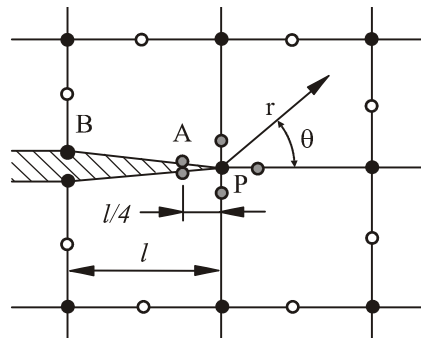


Figure 2.57. Quarter-point singular elements and coordinates for near crack-tip field description.

Considering only the two first terms and particularising Equation 2.191 for nodes A ($r = l/4$) and B ($r = l$) on the singular element at the upper face of crack ($\theta = \pi$), v_A and v_B can be written by Equation 2.193 and Equation 2.194, respectively.

$$v_A = K_I \sqrt{\frac{2}{\pi}} \frac{(1+\nu)(\kappa+1)}{4E} l^{1/2} - A_2 \frac{(1+\nu)(\kappa+1)}{12E} l^{3/2} \quad (2.193)$$

$$v_B = K_I \sqrt{\frac{2}{\pi}} \frac{(1+\nu)(\kappa+1)}{2E} l^{1/2} - 2A_2 \frac{(1+\nu)(\kappa+1)}{3E} l^{3/2} \quad (2.194)$$

By solving these equations, the stress intensity factor is given by Equation 2.195.

$$K_I = \frac{E}{3(1+\nu)(1+\kappa)} \sqrt{\frac{2\pi}{l}} (8v_A - v_B) \quad (2.195)$$

The values of stress intensity factors estimated using Equations 2.192 and 2.195 are affected by two types of errors: i) errors in the displacements obtained with the FEM. These values are more incorrect in the elements closest to the crack front, even when singular elements are used. The displacements of crack front points are particularly affected by errors (Antunes, 1993). Therefore, other points more distant from the crack front should be used in order to reduce these errors; ii) errors due to truncature of the analytical expressions of displacements since only the first term (Equation 2.192) or the two first terms (Equation 2.195) are used. The term $r^{0.5}$ is dominant near the crack tip while the other terms (r , $r^{3/2}$, r^2 , ...) become important away from the crack front. Therefore, the K values calculated from these expressions are affected by errors that increase with the distance from the crack front. In fact, a solution able to reduce this type of error would be to choose point A very close to point P . But, it is not efficient because the displacements resulting from the FEM are more incorrect in the elements closest to the crack front.

There are two solutions to overcome these errors: i) the first solution is to select point A at an optimum location, far enough from the crack front to reduce the FEM errors and close enough to reduce truncature errors. However, this optimum location is not easy to find, and even if that point is located, K values there can be too erroneous; ii) usually, the solution adopted comprises the calculation of the stress intensity factor for several points along a direction emanating from the crack tip. The calculated K values are plotted on a graph of K against r , as exemplified in Figure 2.58. Then, a curve is fitted by regression in order to extrapolate the stress intensity factor for $r=0$. This extrapolation eliminates the error associated with the analytical expressions, while the FEM errors are greatly reduced if the nodes nearest to the crack front are not used. The nodes more affected by the FEM errors can be identified in a plot of K versus r . As depicted in Figure 2.58, these nodes deviate from the dominant trend. In general, regression curves of order two or three (but not restricted to) are adequate to achieve good extrapolation.

The main advantage of this method for estimating K is its simplicity. In addition, only a FEM analysis is

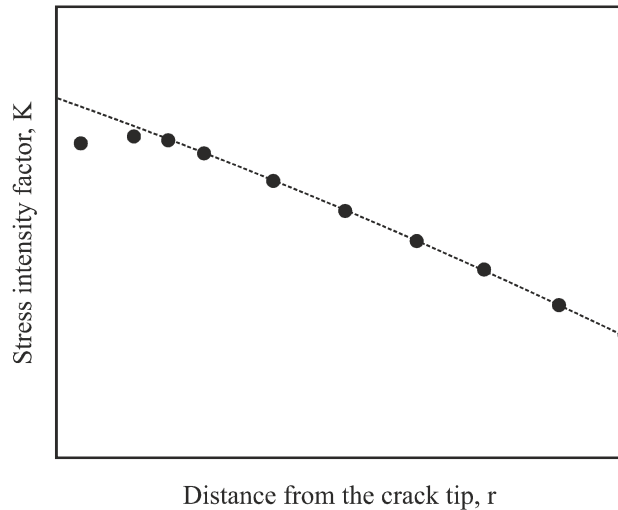


Figure 2.58. Schematic representation of K calculation using the extrapolation method (Antunes, 1999).

required to obtain a K distribution along the crack front. However, Equations 2.192 and 2.195 are only valid for plane strain conditions. It is a common practice to assume plane strain conditions for all crack front points, except for surface points where plane stress conditions prevails. Consequently, in Equations 2.192 and 2.195, E is replaced by $E/(1-\nu^2)$. Nevertheless, this is correct only if the singularity at these points is $r^{-0.5}$.

ii) Energy-based methods

In the energy-based methods, the stress intensity factor is calculated from the energy release rate (G). In the total energy method (Irwin, 1957), the total potential energy of the body is calculated for the initial and virtually extended crack using the FEM being the energy release rate obtained directly from its definition. The stiffness derivative method (Parks, 1974; Hellen, 1975) also uses a virtual crack extension technique but only the finite elements distorted by the extension are involved in the analysis. DeLorenzi (1982; 1985) improved this method by calculating G from a continuum mechanics viewpoint. But, unlike the stiffness derivative method, it is not restricted to the FEM. The J-integral method (Rice, 1968; Murakami, 1983) is an alternative technique. However, the evaluation of pointwise values is difficult in three-dimensional cracked bodies. More recent formulations of the J-integral (Li, 1985; Shih, 1986) apply a volume integration that provides better accuracy and are much easier to implement numerically. In the crack closure integral method, proposed by Irwin (1957), G is estimated considering crack extension and evaluating the work done close to the crack relatively to the original configuration. In order to avoid the need of two FEM analyses, Rybicki *et al.* (1977) used the nodal forces ahead the crack tip and the displacements behind it. Shivakumar *et al.* (1988) and Roeck *et al.* (1995) extended the formulation to three-dimensional problems. In the external forces method (Antunes, 1999), the calculation of K is done in an indirect way from the energy release rate (G) by applying the following relationship

$$K = \sqrt{\frac{EG}{1-\nu^2}} \quad (2.196)$$

where E is the Young's modulus and ν is the Poisson's ratio. This expression is valid for plane strain conditions. For plane stress conditions, it is replaced by $K = \sqrt{EG}$. In general, plane strain conditions are considered along the whole crack front, except at the free surfaces where plane stress conditions are defined. The energy release rate (G) is the derivative of the potential energy of the body with respect to the crack area for fixed load or fixed displacement, i.e.

$$G = -\frac{d\Pi}{dA} \quad (2.197)$$

where Π is the potential energy of the loaded body and dA is the virtual crack area extension. This quantity is physically meaningful and can be considered as the crack driving force. The virtual crack area extension (dA) must be in the plane of the crack and normal to the crack front, either for an infinitesimal extension (Figure 2.59a) or for a uniform extension along the whole crack front (Figure 2.59b). In the second case, G is only a mean value.

The potential energy of a cracked body statically loaded with point (\mathbf{F}_p), surface (\mathbf{F}_s) and body (\mathbf{F}_B) forces is expressed by

$$\Pi = \int_V \frac{1}{2} \boldsymbol{\sigma}^T \cdot \boldsymbol{\varepsilon} dV - \mathbf{u}^T \cdot \mathbf{F}_p - \int_S \mathbf{u}^T \cdot \mathbf{F}_s dS - \int_V \mathbf{u}^T \cdot \mathbf{F}_B dV \quad (2.198)$$

where $\boldsymbol{\sigma}$, $\boldsymbol{\varepsilon}$ and \mathbf{u} are the stress, strain and displacement vectors, respectively; V is the volume of the body; and S is the surface of the body. The surface and body forces are forces per unit of area and volume, respectively. The first term in the previous equation represents the elastic deformation energy of the body (U) and the last three terms represent the potential of the external forces. According to this expression, the

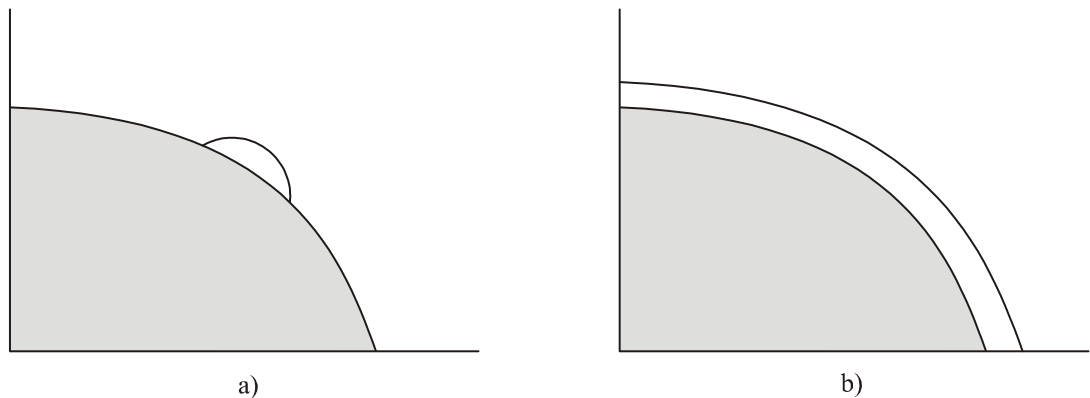


Figure 2.59. a) Local virtual crack extension; b) uniform virtual crack extension.

energy available for crack extension (energy release rate) has two sources: the work of applied external forces and the energy stored in the body.

The potential energy can be calculated in different ways. According to the principle of energy conservation (first law of thermodynamics), the work of external forces is equal to the deformation energy of the body ($W_E = U$), i.e. the work performed by the external forces in an adiabatic and reversible way is stored as deformation energy in the body. Since the work done by the external forces acting on a body is given by

$$W_E = \frac{1}{2} \mathbf{u}^T \cdot \mathbf{F}_p + \int_S \frac{1}{2} \mathbf{u}^T \cdot \mathbf{F}_s \, dS + \int_V \frac{1}{2} \mathbf{u}^T \cdot \mathbf{F}_B \, dV \quad (2.199)$$

the potential energy can be defined by Equation 2.200. Therefore, G is given by Equation 2.201.

$$\Pi = -W_E \quad (2.200)$$

$$G = \frac{dW_E}{dA} \quad (2.201)$$

This derivative can be approximately calculated considering two values of W_E for the initial and virtual crack extension areas A and $A+\Delta A$. Thus, the previous equation leads to Equation 2.202.

$$G \approx \frac{\Delta W_E}{\Delta A} \quad (2.202)$$

The error of this approximation increases with the virtual crack increment ΔA . Antunes (1993), in a 2D analysis, studied the error introduced by a finite crack extension and concluded that good results were obtained if crack increments less than 15 % of the crack length are considered. An alternative formulation to calculate G , proposed by Antunes (1993), considers the virtual crack extensions $(A-\Delta A)$ and $(A+\Delta A)$ and can be written mathematically using Equation 2.203.

$$G \approx \frac{(W_E)_{A+\Delta A} - (W_E)_{A-\Delta A}}{2\Delta A} \quad (2.203)$$

This formulation demonstrated to be clearly better than the one given by Equation 2.202. However, the best solution, presented in Figure 2.60, is obtained by calculating several values of W_E for different virtual crack increments, plot them against ΔA , fit a polynomial curve to the results by regression and evaluate the derivative of that polynomial for $\Delta A = 0$. The slope of the tangent to curve $W_E - \Delta A$ at point $\Delta A = 0$ is, therefore, the value of G . It is important to note that the accuracy of K increases with the number of

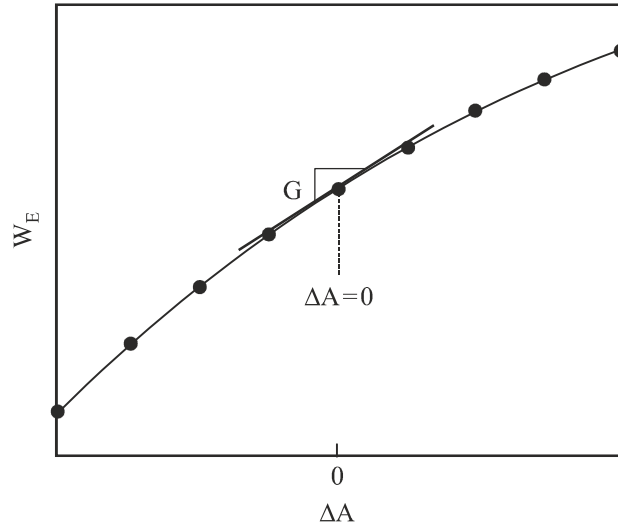


Figure 2.60. Evolution of W_E with ΔA (Antunes, 1999).

virtual crack increments considered but increases the computational effort as well.

Finally, the values of W_E can be obtained numerically using the FEM. In the FEM, the external forces are replaced by equivalent nodal forces. In view of this fact, the work of external forces can be given by

$$W_E = \sum_{i=1}^{NN} \frac{1}{2} (F_x u + F_y v + F_z w)_i = \frac{1}{2} \mathbf{F}^T \cdot \boldsymbol{\delta} \quad (2.204)$$

where NN is the number of nodes, (F_x, F_y, F_z) are the Cartesian components of the nodal force on the i^{th} node, (u, v, w) are the displacements of the i^{th} node, \mathbf{F} is the global vector of nodal forces and $\boldsymbol{\delta}$ is the global vector of nodal displacements. So, the finite element results that are necessary in the present method for K calculation are only the nodal displacements and the nodal forces.

This method is especially advantageous when loads and reactions act far from the crack front or when act close to the crack front without producing work. In these cases, the displacements close to the crack front, which are the most affected by simulation difficulties of the crack singularity, are not necessary. Therefore, a larger mesh near the crack front can be used without a significant change in the FEM results needed to calculate the stress intensity factor. Furthermore, this method uses the nodal displacements which are the primary variables of the FEM analysis and therefore are the most accurate. The main disadvantage is the need of at least two FEM analyses to calculate K . It becomes particularly important when K is necessary at several points along the crack front. Another disadvantage is the fact that the virtual crack extension technique is not suitable for the calculation of separate modes since the energy release rate is the result of the combined modes I, II and III. Besides, it is not exempt of general errors. The correctness of K remains dependent on the final accuracy of nodal displacements, number of virtual extensions, value of ΔA as well as the adequacy of the polynomial regression selected.

2.7.3 Crack growth model

The local crack front advances can be estimated using the Paris law. This expression relates the fatigue crack growth rate (da/dN) to the range of stress intensity factor (ΔK) and can be expressed by

$$\frac{da}{dN} = C(\Delta K)^m \quad (2.205)$$

where C and m are constants dependent on loading spectrum, material microstructure, environmental effects and stress state. The fatigue life (N_f) can be obtained by integrating the previous equation, i.e.

$$N_f = \int_{a_i}^{a_f} \frac{da}{C(\Delta K)^m} \quad (2.206)$$

where a_i and a_f are the lower and upper limits of integration, respectively. Since ΔK varies with the crack growth, the fatigue life can be calculated using an Euler integration algorithm (Equation 2.207).

$$N^{(j+1)} = N^{(j)} + \Delta N^{(j+1)} \Leftrightarrow N^{(j+1)} = N^{(j)} + \frac{\Delta a^{(j)}}{C[\Delta K(a^{(j)})]^m} \quad (2.207)$$

The accuracy of the numerical integration can be increased by reducing the value of Δa . If local increments along the crack front are considered, the Paris law can be used for each crack front node, i.e.

$$\frac{da_i}{dN} = C(\Delta K_i)^m \quad (2.208)$$

where da_i and ΔK_i are, respectively, the local normal crack growth increment and the range of stress intensity factor for the i^{th} node of the crack front. Making appropriate amendments in the previous equation, the local normal crack growth increment at an arbitrary node for the j^{th} iteration can be written as follows

$$\Delta a_i^{(j)} = \left(\frac{\Delta K_i^{(j)}}{\Delta K_{\max}^{(j)}} \right)^m \Delta a_{\max}^{(j)} \quad (2.209)$$

being $\Delta a_{\max}^{(j)}$ the maximum crack growth increment for the j^{th} iteration and $\Delta K_{\max}^{(j)}$ the maximum stress intensity factor range along the crack front for the j^{th} iteration. The propagation at each crack front node under mode I loading is assumed to occur in the normal direction of the crack front (Figure 2.47d). The corresponding number of fatigue cycles for the j^{th} iteration can be expressed by

$$\Delta N^{(j)} = \frac{\Delta a_{\max}^{(j)}}{C(\Delta K_{\max}^{(j)})^m} \quad (2.210)$$

where $\Delta a_{\max}^{(j)}$ is the maximum crack growth increment for the j^{th} iteration, $\Delta K_{\max}^{(j)}$ is the maximum stress intensity factor range along the crack front for the j^{th} iteration, and C and m are the Paris law constants.

As referred to above, Equations 2.209 and 2.210 can be used to estimate the local crack growth increments at each point along the crack front and the number of fatigue cycles. Nevertheless, the accurateness of these calculations depends on Δa_{\max} . In this sense, an optimum value of this parameter must be obtained to ensure feasible numerical results in terms of crack shape and fatigue life.

i) Crack growth increment

The value of Δa_{\max} plays an important role in the accuracy of the numerical procedure (Lin, 1999c; Branco, 2008a). Generally, a small constant value is used throughout the crack growth process in order to achieve more accurate results. As reported in the literature (Lin, 1999b; Branco, 2006), larger crack increments give greater number of fatigue cycles for a given crack depth. Figure 2.61a compares the number of cycles obtained using three different crack increments ($t/50$, $t/100$ and $t/167$) for a plate with surface crack subjected to tension (Lin, 1999b). As can be seen, the convergence is achieved with the decrease in crack increment. Therefore, the lower is the crack increment, the more accurate are the calculations. For example, when the crack reached the plate back, the difference between the cases of $\Delta a_{\max} = t/100$ and $\Delta a_{\max} = t/167$ is on average about 2%. Nevertheless, the difference between the cases of $\Delta a_{\max} = t/50$ and $\Delta a_{\max} = t/167$ is much higher. Besides, an oscillatory behaviour of the crack front is exhibited when higher values of Δa_{\max} are used (Courounea, 1998; Branco, 2008a). Figure 2.61b presents the evolution of d/t for three values of Δa_{\max} ($0.005a$, $0.05a$, $0.12a$) in a middle-crack tension specimen (Branco, 2006). The data show a clear convergence as the crack increment decreases. The differences between the cases of $\Delta a_{\max} = 0.005a$ and $\Delta a_{\max} = 0.05a$ are lower than 3%, whilst the differences between

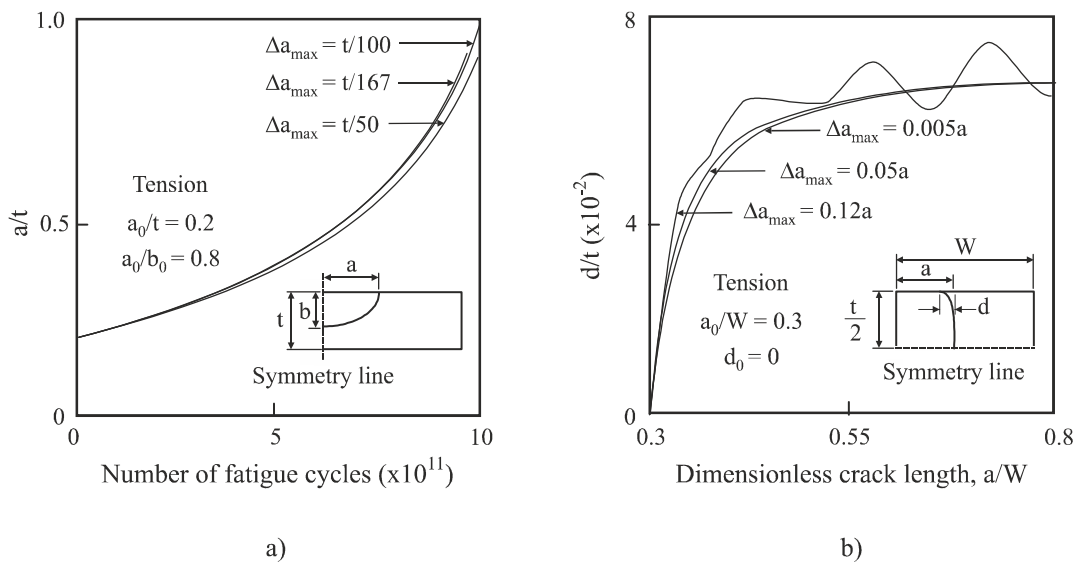


Figure 2.61. Effect of the crack growth increment on the: a) number of fatigue cycles (Lin, 1999b); b) crack shape (Branco, 2006).

the cases of $\Delta a_{\max} = 0.005a$ and $\Delta a_{\max} = 0.12a$ are greater than 10%. For the highest increment, an oscillatory behaviour is evident.

In the literature, different methodologies have been used to define the value of Δa_{\max} . Some authors consider the maximum crack increment as a relation between a geometrical variable and a constant. For example, Lin *et al.* (1999b) defined it as a fraction of the thickness ($t/167$, $t/100$, $t/50$) to examine fatigue crack growth of semi-elliptical surface cracks in rectangular plates or as a fraction of the diameter ($d/250$) in similar studies for circumferential notched round bars (1999c) and unnotched round bars (1997). Wu (2006) studied the shape of surface cracks in plates considering maximum crack increments equal to $t/200$ for tension and $t/300$ for bending. Gardin *et al.* (2007) simulated the effect of compressive residual stress fields on fatigue crack growth of notched round bars assuming a maximum crack increment equal to $d/98$. Another approach assumes that the maximum crack increment is defined as a percentage of the crack length. For example, Nykänen (1996) considered a maximum crack increment as a function of the actual crack length. Branco *et al.* studied the crack shape evolution in middle-crack tension (2008) and compact tension specimens (2008a) with maximum crack increments equal to 0.1% of the crack length. Other authors defined a constant number of load cycles per iteration. For example, Carpinteri *et al.* (2010) analysed the influence of the cold-drawing process on fatigue crack growth in V-notched round bars using a constant number of cycles equal to 250. Antunes *et al.* (2002) performed a cycle-by-cycle integration to examine the fatigue life predictions in polymer particle composites.

2.8. Effect of physical variables on crack shape and fatigue life

A detailed analysis of crack shape and fatigue life requires the use of adequate dependent parameters. The crack shape characterisation has been carried out mainly using the well-known *crack aspect ratio* and *intersection angle* parameters. The former evaluates the ratio of the surface node to the deepest node (a/b) in terms of crack length. The latter (α) quantifies the angle between the crack front and the free surface. Some examples are schematically presented in Figure 2.62. For example, Carpinteri *et al.* studied the crack shape evolution in round bars with the variables depicted in Figure 2.62a (1996a) and in Figure 2.62b (1996b). Couroneau *et al.* (1998) and Shin *et al.* (2004) used the parameters illustrated in Figure 2.62c. In another study, Couroneau *et al.* (2000) compared different models using the crack aspect ratios defined in Figures 2.62a to 2.62c in order to investigate which of those better describe the crack shape. Lin *et al.* (1997; 1999c) used the crack aspect ratio given by the variables represented in Figure 2.62d. Antunes (1999) studied high temperature fatigue crack growth in corner crack specimens using the crack aspect ratio defined through the variables a and b of Figure 2.62e. Branco *et al.* (2011) analysed the effect of residual stresses on crack shape in corner crack specimens made of nickel-base superalloys using the crack aspect ratio (a/b) of Figure 2.62f. Nykänen (1996), Lin *et al.* (1997; 1999a), Burande *et al.* (1999), Wu (2006) and Le *et al.* (2011) examined surface cracks in finite thickness plates under mode I using the variables a and b of Figure 2.62g. The crack shape developments in corner cracks emanating from fastener holes were studied by Newman *et al.* (1984), Lin *et al.* (1998) and Antunes *et al.* (2002) employing the a/b ratio defined in Figure 2.62h. Branco *et al.* investigated the crack shape evolution of

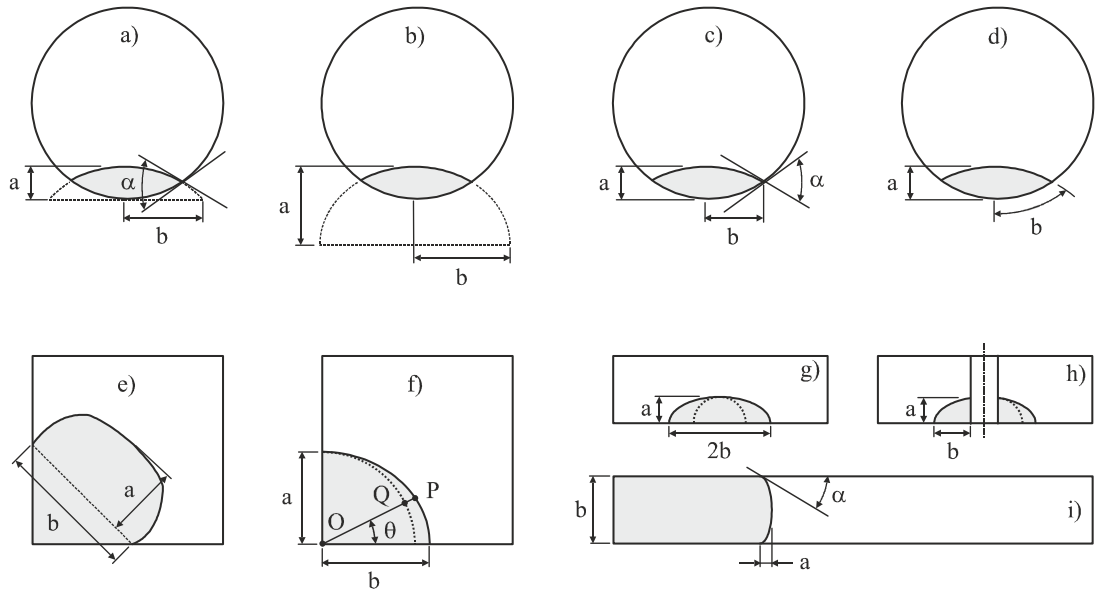


Figure 2.62. Examples of dependent parameters used to characterise crack shape changes.

through cracks in compact tension (2008a) and middle-crack tension (2008) specimens using the intersection angle and the crack aspect ratio defined in Figure 2.62i. Lin *et al.* introduced the *relative standard deviation* to examine the deviation from theoretical shapes of crack profiles obtained numerically, such as part-circular (1997), quarter-elliptical (1998, 1999c) and semi-elliptical (1997b; 1999a; 1999c) configurations. It can be written in the following form

$$S_r = \sqrt{\frac{1}{n} \sum_{i=1}^n (E_i)^2} \Leftrightarrow S_r = \sqrt{\frac{1}{n} \sum_{i=1}^n \left(\frac{\overline{OP} - \overline{OQ}}{\overline{OQ}} \right)^2} \quad (2.211)$$

where n is the number of corner nodes used to define the crack front and E_i represents the relative deviation of point P (see Figure 2.62f) from the theoretical shape (dashed line). Smaller values of S_r mean a better approximation to the theoretical shapes. Murakami *et al.* (1994) considered the crack area to characterise irregular cracks. The fatigue limit and threshold stress intensity factor range (ΔK_{th}) were related with $A^{1/2}$, being A the effective area obtained by projecting the defect or crack onto the plane perpendicular to the maximum tensile stress direction. Regarding the fatigue life, it is generally studied by analysing the crack length versus number of load cycles.

2.8.1 Effect of initial crack shape

The effect of the initial crack shape on the early propagation period has been described in the literature by several authors (Carpinteri, 1993; Lin, 1997; Couroneau, 1998; Branco, 2012d). Figure 2.63a shows the evolution of the crack aspect ratio (a/b) for several initial surface cracks in round bars subjected to tension loading (Lin, 1997). As can be seen, regardless of the initial crack configuration, the propagation tends always to a preferred propagation path (PPP). Besides, it can be noted that initial crack aspect ratios less distant from the inclined asymptote converge more rapidly to the preferred propagation path than the

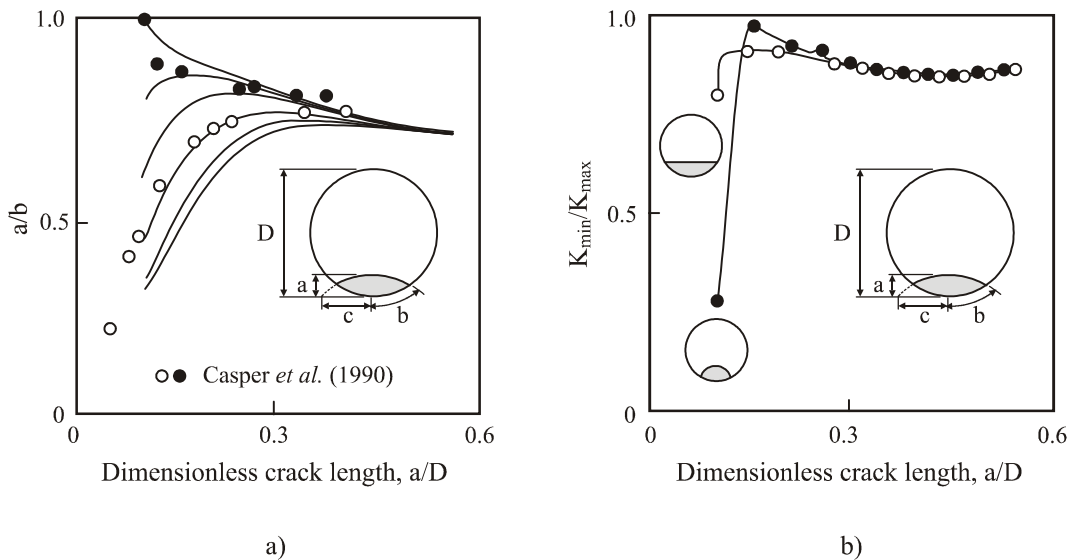


Figure 2.63. Evolution of: a) crack aspect ratio (Lin, 1997); b) stress intensity factor (Branco, 2012d) in round bars with surface cracks subjected to tension.

others. On the other hand, the influence of the initial crack shape on the crack aspect ratio weakens as the crack extends. This effect is more evident at the early propagation stage. The extent of the early propagation stage was quantified by Branco *et al.* (2008) in middle-crack tension specimens. It was given by an exponential function dependent on the initial distance to the preferred propagation path. This conclusion was subsequently extended to compact tension specimens (2008a). In the second stage of propagation, the PPP depends mainly on the loading type and Paris law exponent (Couroneau, 1998). The experimental data available in the literature (Caspers, 1990; Shin, 2004) also show a convergence towards preferred propagation paths, which is in close agreement with the numerical predictions.

As is well-known, during the fatigue crack growth process, the stress intensity factors along the crack front usually change. In addition, the SIF distribution along the crack front is quite sensitive to local shape variations, i.e. small shapes in the crack front are responsible for large changes in the stress intensity factors. Besides, the crack tends to equalise the crack driving force around its perimeter. It means that the crack attains a regular profile such that the stress intensity factor is practically constant around its front. Thus, the ratio of the minimum stress intensity factor to the maximum stress intensity factor (K_{min}/K_{max}) tends to one. This behaviour (i.e. $K_{min}/K_{max} \approx 1$), first reported by Gilchrist *et al.* (1991), is termed iso-K profile. For example, arbitrary planar defects in infinite bodies under remote uniform tension propagate into circular crack shapes which are subsequently maintained (Gilchrist, 1991; Lazarus, 1999; Lin, 1999b); arbitrary planar cracks in infinite bodies loaded in shear (Favier, 2006) grow towards stable and almost elliptical shapes. Branco *et al.* found K_{min}/K_{max} ratios approximately equal to 0.98 for the middle-crack tension specimen (2008) and for the compact tension specimen (2008a) which are close to the ideal iso-K profile. However, in other cases, it is impossible to reach the above-mentioned profile. Figure 2.63b shows the evolution of the K_{min}/K_{max} ratio for surface cracks in round bars subjected to tension (Branco, 2010b; Branco, 2012d). As can be seen, the ratio suddenly increases in the early stage of

propagation and then drops gradually to values about 0.9. Therefore, it is clear that the crack is not able to reach the iso-K profile which is justified by the presence of the free boundary (Lin, 1997). Moreover, for plates with surface cracks subjected to tension, bending and both, it is also impossible to reach and maintain the iso-K profile due to both the front and back surfaces as well as due to the bending component of load (Lin, 1999b). So, the iso-K profile depends not only on the initial crack shape and size but also on the geometry and applied load.

2.8.2 Effect of Paris law exponent

The effect of the Paris law exponent (m) on the crack aspect ratio can be anticipated by the power-law dependency of the fatigue crack growth equation (Equation 2.205). The results show that the crack aspect ratio changes more intensely for higher m values. Figure 2.64a plots the evolution of a/b against a/D in round bars with surface cracks subjected to tension and bending for three m values ($m=2$, $m=3$, $m=4$). The effect of different initial crack shape configurations is also examined. As can be seen, the increase in the Paris law exponent leads to smaller values of a/b for identical values of dimensionless crack length (a/D). Besides, a considerable effect of m on the crack aspect ratio, either in early propagation stage or in the subsequent propagation stage, is clearly observed. In the former stage, a specific propagation path is obtained for each initial crack shape. Nevertheless, in the latter stage, the propagations performed with the same values of m tend to preferred propagation paths not dependent on the initial crack shape.

The amount of crack growth needed to achieve the PPP is termed *transition depth* and depends on the Paris law exponent, loading type and specimen geometry. Figure 2.64b plots the extent of the transition depth against the exponent of the Paris law for round bars under tension and bending (Couroneau, 1998) as well as for middle-crack tension (Branco, 2008) and compact tension (Branco, 2008a) specimens. Although different transition criteria were used by these authors, the same conclusions were found, i.e.

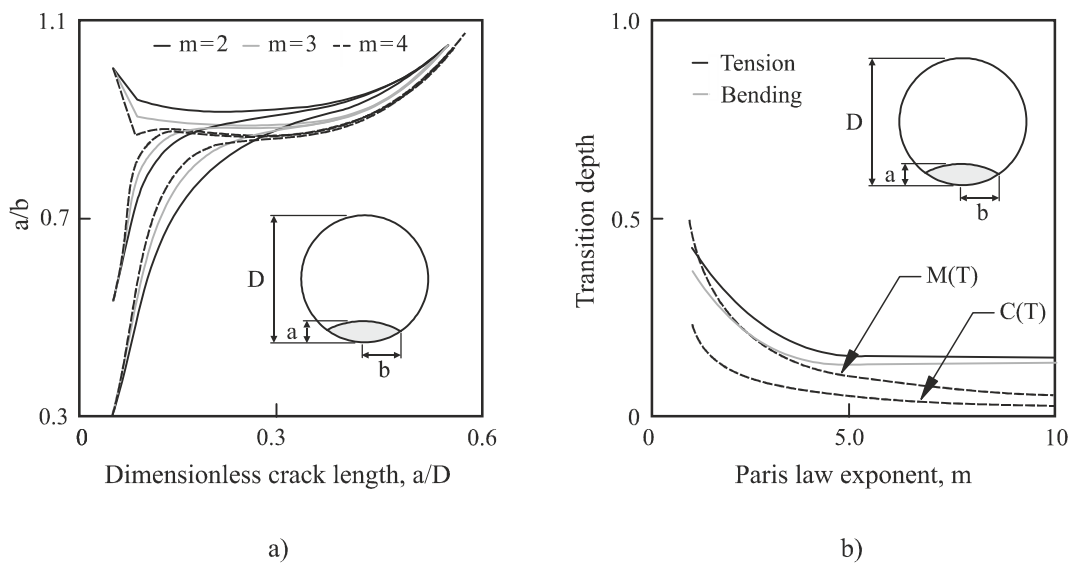


Figure 2.64. Evolution of: a) a/b with a/D for different values of m (Couroneau, 1998); b) transition depth with m for different loading types and geometries (Couroneau, 1998; Branco, 2008; Branco, 2008a).

the transition depth is a monotonously decreasing function of m . Besides, it is greater in tension than in bending. Moreover, the transition depth is greater in M(T) specimens than in C(T) specimens, which can be explained by the higher K gradients (dK/da) existing in the latter as a result of its geometrical asymmetry.

2.8.3 Effect of loading type

The role of the loading type in fatigue crack growth is known (Carpinteri, 1996a; Lin, 1999a; Branco, 2009b). Figure 2.65a shows the evolution of the crack aspect ratio (a/b) with the dimensionless crack length (a/D) for surface cracks in round bars under tension and bending (Branco, 2009b). Different initial crack fronts, namely part-circular ($a_0/b_0=1$), part-elliptical ($a_0/b_0=0.25$, $a_0/b_0=0.5$) and straight ($a_0/b_0=0$) shapes with different dimensionless crack lengths ($a_0/D = 0.05$, $a_0/D = 0.1$, $a_0/D = 0.2$) were analysed. Regardless of the loading type, all propagation paths tend to converge to inclined asymptotes. During the early growth, the process of convergence is faster for initial crack configurations closer to the preferred propagation paths. As can be observed, the convergence occurs more rapidly for bending than for tension. Besides, it is clear that the preferred propagation paths for tension and bending are different. In both cases, either the numerical or experimental results, have demonstrated that the resultant crack shapes are approximately semi-elliptical and that the a/b values are greater for tension than for bending. It means that for bending, the crack grows more rapidly along the free surface than at deepest points. A more effective loading effect on crack aspect ratio is presented in Figure 2.65b. It exhibits the evolution of a/b with a/D for surface cracks in rectangular cross-section plates subjected to tension and bending. As can be seen, the PPP are completely different which is exclusively associated with the different loading types.

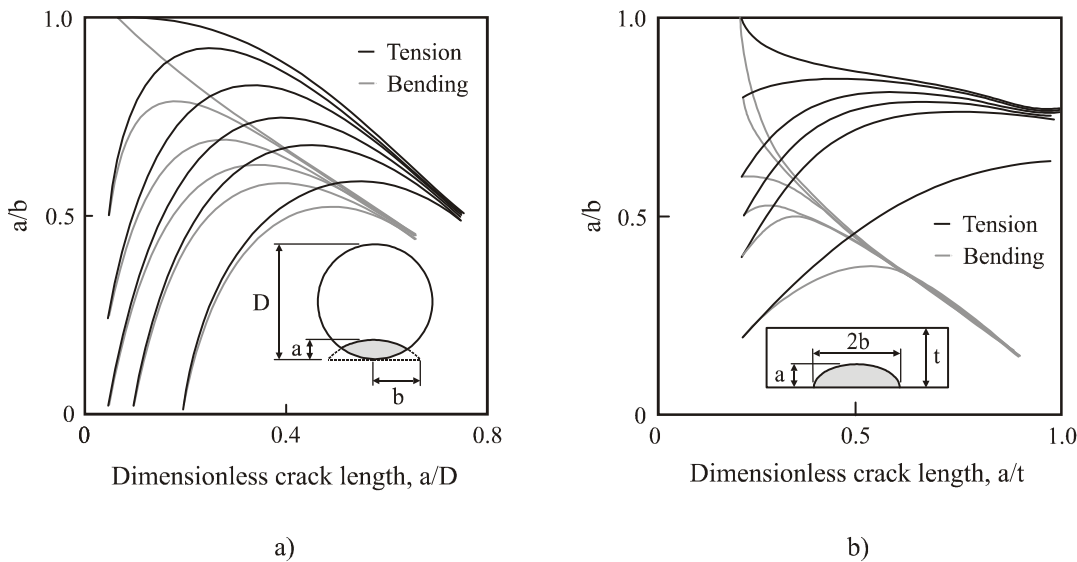


Figure 2.65. Evolution of the crack aspect ratio with the dimensionless crack length in: a) round bars with surface cracks (Branco, 2009b); b) rectangular plates with surface cracks (Lin, 1999a) subjected to tension and bending.

Besides, a slight increase in crack aspect ratio is observed as the crack approaches closely to the back surface of the plate. It is caused by the larger stress intensity factor at the depth point than that at the surface point due to the effect of the plate back surface. Similarly to the round bar, the values of a/b are lower for bending than for tension. Moreover, the convergence towards the PPP is also faster for bending than for tension.

2.8.4 Effect of geometry

The specimen geometry is another variable that affects the crack aspect ratio. These differences can be explained by specific stress gradients associated with each type of geometry. An example of the importance of stress gradients in the PPP is represented in Figure 2.66a (Lin, 1998). It plots a/b against a/t for corner cracks emanating from fastener holes in plates loaded in tension. Different ratios r/t ($r/t=0.5$, $r/t=3$) and different initial crack shapes ($a_0/b_0=1$, $a_0/b_0=1.32$, $a_0/b_0=1.72$, $a_0/b_0=2$) are analysed. The results exhibited show a strong effect of the r/t ratio on the preferred propagation paths and on the transition depth. In relation to the former effect, the increase in r/t decreases the a/b values. Regarding the latter effect, the transition depth decreases with r/t . Such trends can be explained by the relatively small gradient of the stress distribution near the hole edge for the largest r/t values. Figure 2.66b presents the evolution of the crack aspect ratio (a/b) with the dimensionless crack length (a/D) for surface cracks in circumferentially notched and unnotched round bars under tension (Carpinteri, 2006a). The presence of the notch significantly alters the a/b ratio. A considerable decrease in the crack aspect ratio is observed, regardless of the initial crack shape, which is a direct consequence of the high stress concentrations existing at the notch root. Besides, a remarkable effect of the notch on the stress intensity factor is observed along the crack front. Unlike the case of the unnotched round bars in which the maximum SIF is attained at the deepest point, for the notched round bars the maximum SIF always occurs

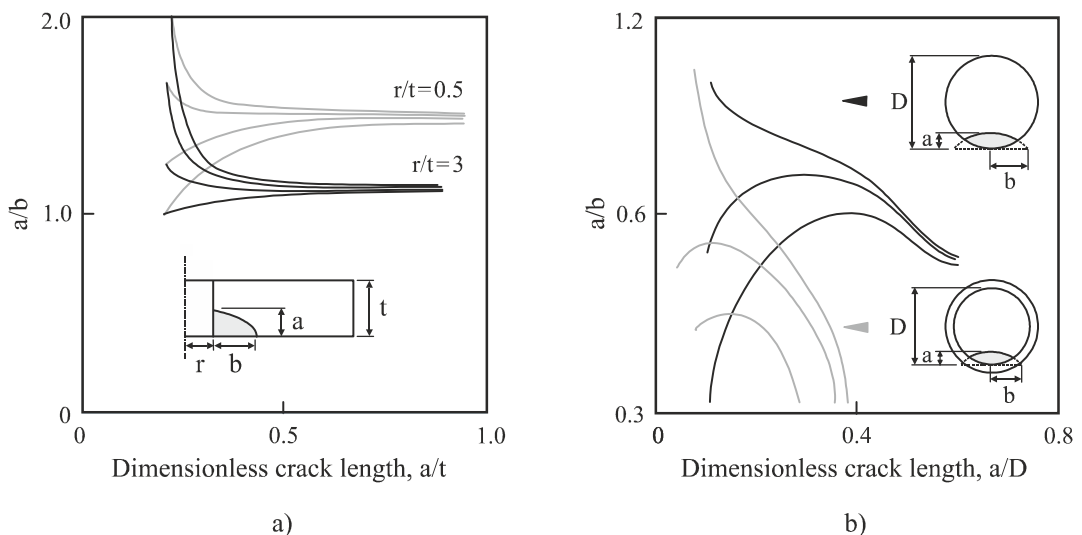


Figure 2.66. Evolution of the crack aspect ratio in: a) corner cracks emanating from fastener holes in plates (Lin, 1998); b) surface cracks of notched and unnotched round bars subjected to tension (Carpinteri, 2006a).

near the external surface of the round bar.

2.8.5 Surface effects

Surface effects, such as crack closure or residual stress, among others, have been used to explain different fatigue phenomena. The former is caused by the contact of crack flanks during a portion of the loading cycle and can be classified according to the main closure mechanisms as plasticity induced crack closure (PICC), oxide induced crack closure (OICC) and roughness induced crack closure (RICC). The latter is the result of manufacturing and processing operations from which inhomogeneous plastic deformation is introduced by mechanical, thermal or chemical phenomena.

Figure 2.67a presents the evolution of a/b with a/t in rectangular cross-section plates with surface cracks subjected to tension for a constant growth rate along the crack front and for a case with crack closure. In the second case, the constant of the Paris law at the free surface (C_S) was defined using the relationship $C_S = 0.9^m C_D$, where C_D is the Paris law constant at the deepest point of the crack surface (Newman, 1981). As can be observed, with crack closure, the crack aspect ratio slightly increases for a given dimensionless crack length. Pang (1993) further modified the previous assumption for welded joints using a constant C_S/C_D ratio equal to 0.85^m . More recently, Hou (2011) demonstrated that such a relation (i.e. $C_S = 0.9^m C_D$) for surface cracks is erroneous when is assumed a theoretical crack shape and proposed a new value approximately equal to 0.63^m . However, when the crack shape is not constrained, this relation is approximately equal to 0.8^m , which is close to the Newman's assumption. The difference is probably due to an incorrect $r^{-0.5}$ singularity used in the stress intensity factor estimation.

The effect of residual stress fields on the crack aspect ratio for round bars with surface cracks under

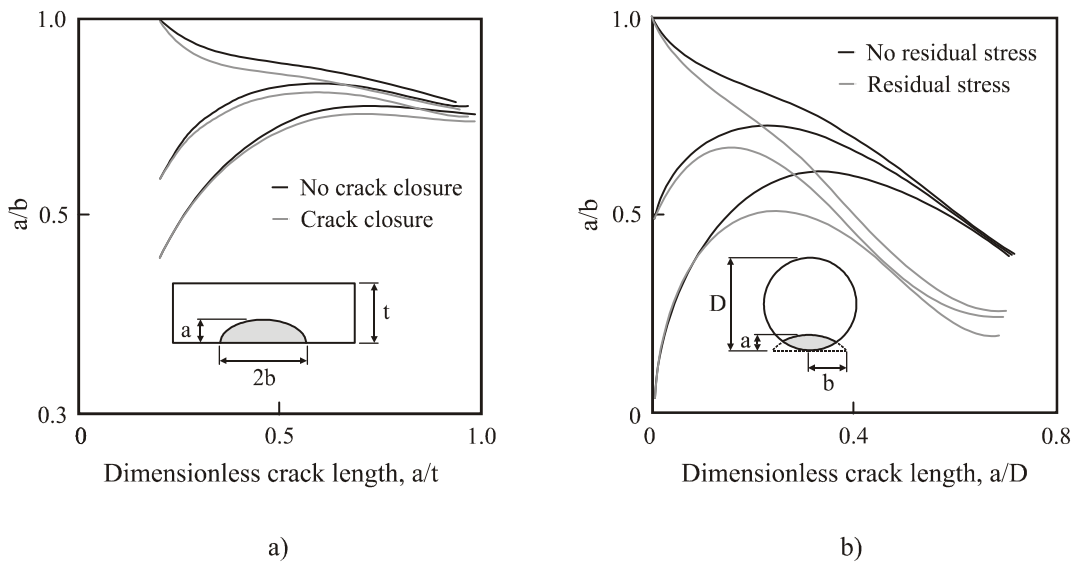


Figure 2.67. Evolution of the crack aspect ratio in: a) rectangular cross-section plates with surface cracks under tension (Lin, 1999a); b) round bars with surface cracks under tension (Carpinteri, 2010).

tension is presented in Figure 2.67b (Carpinteri, 2010). Three different initial crack shapes ($a_0/b_0 = 0$, $a_0/b_0 = 0.5$, $a_0/b_0 = 1$) with similar dimensionless crack length ($a_0/D = 0.1$) were studied. As can be seen, the introduction of residual stress fields causes lower a/b values. A similar trend was also observed for notched round bars subjected to residual stress (Gardin, 2007).

CHAPTER 3

EXPERIMENTAL PROCEDURE

This chapter outlines the experimental procedure. It describes the material, specimen geometries and testing apparatus used in the monotonic tensile tests, determination of the elastic constants, low-cycle fatigue tests, in-phase combined bending-torsion tests and fatigue crack front marking tests. The details on the procedures used to analyse the microstructure of the material and the fracture surfaces by scanning electron microscopy and optical microscopy; to acquire the fracture surfaces by three-dimensional laser scanner; and to determine the Paris law constants from fatigue crack front marks are also provided in this chapter.

NOMENCLATURE

a/D	dimensionless crack length
Acc. V	accelerating voltages
B	bending moment
B/T	ratio of the bending moment to the torsion moment
C	Paris law constant
CCD	charge-coupled device
CNC	computer numeric control
D	diameter
dε/dt	strain rate
F	force
f	frequency
FEM	finite element method
FFT	fast Fourier transformation
HSS	high strength steel
IET	impulse excitation technique
JPEG	joint photographic experts group
L ₁ -L ₄	characteristic dimensions of the gripping system
LCF	low-cycle fatigue
m	Paris law exponent
Magn	magnification
MNET	mixed numerical-experimental technique
n _B	number of cycles of overloads
OM	optical microscopy
PC	personal computer
PCI	peripheral component interconnect
Q&T	quenched and tempered
R	stress ratio
R _ε	strain ratio
SEM	scanning electron microscopy
SE	secondary electrons
Spot	spot sizes
SST	single step test
T	torsion moment
TIFF	tagged image file format
Δε	total strain range
Δσ	normal stress range
Δσ _B /Δσ	overload ratio
ΔK	stress intensity factor range
Δτ	shear stress range
σ	normal stress
σ _a	normal stress amplitude
σ _m	mean normal stress amplitude
σ/τ	ratio of the normal stress to the shear stress
τ	shear stress
τ _a	shear stress amplitude
τ _m	mean shear stress amplitude
θ _i , r _i	polar coordinates of the i th node of crack front

3.1. Material

High strength steels (HSS) cover a broad spectrum of steels and are being increasingly used in different areas due to both good strength-to-weight ratio and good corrosion resistance. With regard to the metallurgical designation, HSS can be divided into conventional high strength steels which include carbon-manganese, bake hardenable, high-strength interstitial-free and low-alloy steels; and advanced high strength steels which encompass dual phase, complex phase, transformation-induced plasticity and martensitic steels. The main difference between conventional and advanced high strength steels is their microstructure. The former are single-phase ferritic steels while the latter are primarily multi-phase steels with a microstructure containing a phase other than ferrite-perlite, such as martensite, bainite, austenite and or retained austenite in amounts enough to produce unique mechanical properties (Mejía, 2011).

Due to their diversity in terms of mechanical properties, HSS can address different demands. Figure 3.1 compares the lower yield strength and the lower ultimate tensile strength for different conventional (black contour) and advanced high strength (grey contour) steels. As can be seen, the same mechanical properties can be found for different types of material. Nevertheless, the advanced high strength steels are generically characterised by improved mechanical properties (i.e. higher yield and ultimate tensile strengths) and consequently can provide better performance (AHSS, 2009).

The material used in this research was the DIN 34CrNiMo6 high strength steel. The equivalent standard grades are listed in Table 3.1. This steel, in particular, constitutes a very important engineering material

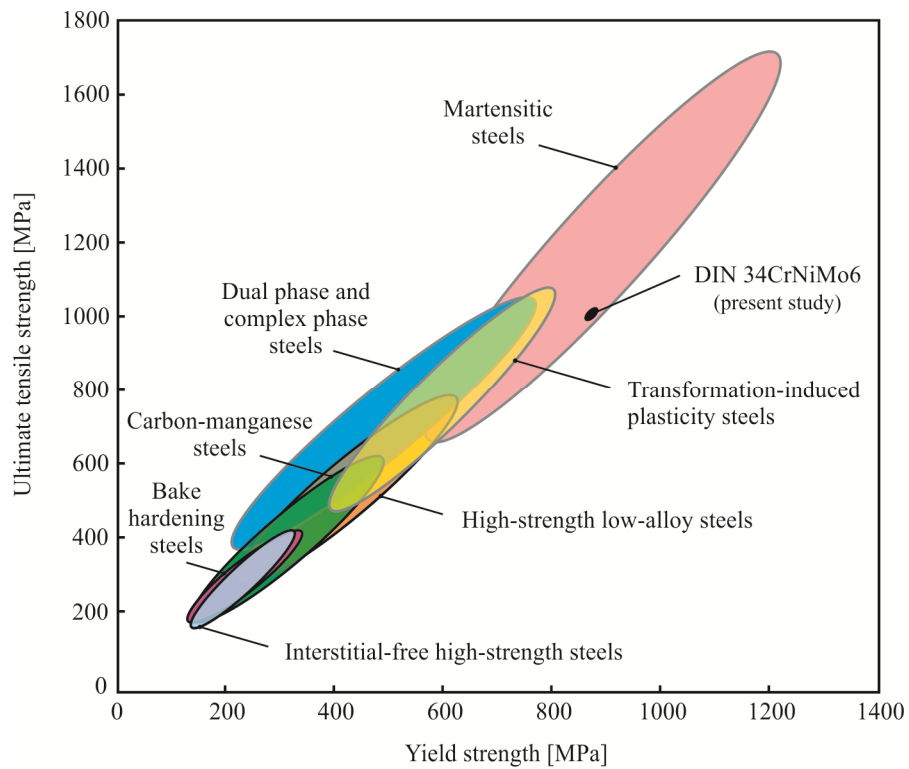


Figure 3.1. Comparison of lower yield strength versus lower ultimate tensile strength for various conventional and advanced high strength steels.

and is usually employed in the manufacture of a wide range of mechanical components that comprises axles, shafts, crankshafts, connecting rods, valves, propeller hubs, gears, couplings, torsion bars, landing gears, heavy duty parts of rock drills, among others. As can be seen in Figure 3.1, DIN 34CrNiMo6 is typically a martensitic steel (see Section 5.1). Within the group of multi-phase steels, it is the one that provides highest yield and ultimate tensile strengths. Martensitic steels are characterised by a martensitic matrix containing small amounts of ferrite and or bainite (Lee, 1999). This microstructure is the result of a rapid quenching which transforms most of the austenite into martensite. Besides, the precipitation of a fine dispersion of alloy carbides during tempering is the main process responsible for the strengthening in this steel (Huang, 1971; Lee, 1999; Tartaglia, 2008).

The material was supplied by the professional trading company of steels *F. Ramada, Aços e Indústrias S.A.* and its nominal chemical composition, in weight percentage, is presented in Table 3.2. This batch was provided by the supplier as oil quenched and tempered (Q&T). Firstly, it was austenitised at about 850-880°C for approximately 30 minutes, followed by oil cooling in order to produce a quenched martensitic structure, then tempered at about 660°C for at least 2 hours and, subsequently, air cooled. As is well-known, this low-alloy steel advantageously combines strength, ductility and toughness. However, it is extremely susceptible to the tempering conditions (Lee, 1999). For example, tempering temperatures within the range 250-450°C can cause severe embrittlement and therefore must be avoided. Additionally, the tempering temperature and the holding time also affect the mechanical properties. The increase in these variables leads to the decrease in strength and hardness. Nevertheless, the effect of tempering temperature is more significant on those properties than the holding time. Regarding the ductility, the higher are the tempering temperature and the holding time, the higher is its value. Therefore, optimum characteristics in terms of strength, ductility and toughness are achieved from different processes of heat tempering.

Table 3.1. Equivalent standard grades (DIN 34CrNiMo6).

Standard	Grade
British standards, BS 970:1991	817M40
French standards, AFNOR	35NCD6
Swedish standards, SS	2541
Italian standards, UNI	35NiCrMo6
Spanish standards, UNE	F-1272
European standards, EN	10277-5
American standards, SAE/AISI	4340
Japanese standards, JIS	SNCM447H
Russian standards, GOST	38Ch2N2MA
Indian standards, IS	40NiCrMo3

Table 3.2. Nominal chemical composition of DIN 34CrNiMo6 (wt%).

C	Si	Mn	Cr	Mo	Ni
0.34	≤ 0.40	0.65	1.50	0.22	1.50

The alloying elements have also a preponderant role in mechanical properties. The amount of carbon is the key and is deliberated higher in martensitic steels to obtain strength and hardness. Generally, the higher the alloy content, the greater the hardenability; and the higher the carbon content, the greater the available strength. Manganese contributes markedly to hardenability during quenching as well as to increase the hardness on tempering by retarding the coalescence of carbides. Nickel is similar to manganese at low alloy additions but is less potent at high alloy levels during quenching while on tempering it has a relatively small effect because it is not a carbide former. Silicon is relatively ineffective in low carbon steel but is very effective in high carbon steel during quenching; besides, it increases the hardness of tempered martensite, regardless of the tempering temperature. Molybdenum contributes to improve the hardenability during quenching; retards the softening of martensite at all tempering temperatures; and reduces the susceptibility to tempering embrittlement. Chromium behaves much like molybdenum, i.e. improves the hardenability during quenching and retards the softening of martensite at all tempering temperatures (Grange, 1977; Marder, 1986).

3.2. Uniaxial tensile tests

The uniaxial tensile tests were carried out using the specimen geometry schematised in Figure 3.2. The tests were conducted according to the procedures described in the ASTM E8 (2011) standard and aimed at obtaining the monotonic response of the high strength steel supplied as well as the main mechanical properties. The samples were machined in a high precision computer numerical control (CNC) turning centre from extruded 20mm-diameter round bars at the Department of Mechanical Engineering of the Polytechnic Institute of Coimbra (DEM/ISEC/IPC).

Two samples (references UT-1 and UT-2) were tested in a computer-controlled 100 kN Instron 4206 electromechanical tension and compression universal testing machine at the Department of Mechanical Engineering of the University of Coimbra (DEM/FCT/UC). The electromechanical machine used, depicted in Figure 3.3, is based on a variable-speed electric motor, a two-stage synchronous belt reduction system and two screws that move the crosshead up or down. The movement of the crosshead (Figure 3.3)

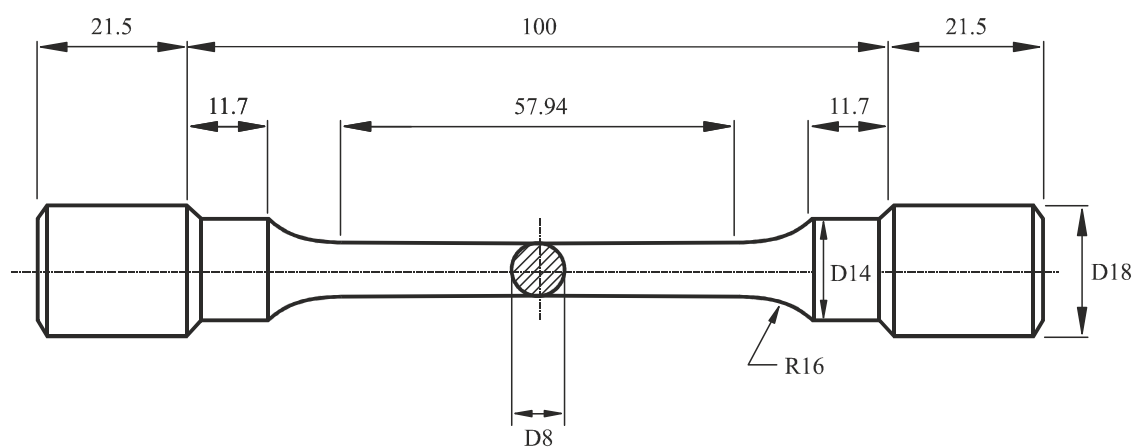


Figure 3.2. Specimen geometry used in uniaxial tensile tests (in accordance with ASTM E8).

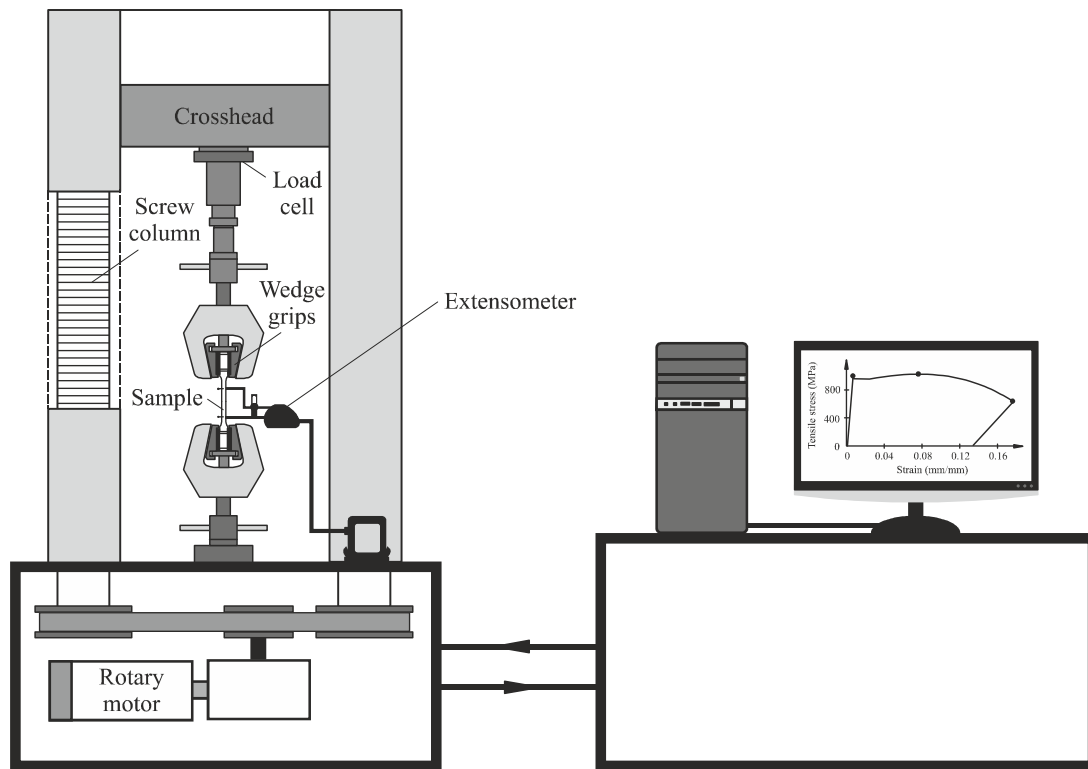


Figure 3.3. Scheme of electromechanical machine and experimental apparatus used in tensile tests.

loads the specimen in tension or in compression and can be modified by changing the speed of the motor. In general, these machines offer a wide range of test speeds and crosshead displacements.

The tests were performed at room temperature, under position control, at a displacement rate of 1 millimetre per minute, until specimen fracture occurred. The strain on specimen was measured using an axial extensometer (Instron 2630-100) with a gauge length of 50mm protected against over-extension. A multi-channel data acquisition system, able to record several variables simultaneously (such as time, extension, load, strain and displacement) was used. Data were recorded at a rate of 10 samples per second throughout the duration of the test.

The specimens were connected to the machine using mechanical wedge action grips. These grips are designed to simplify the loading, alignment and positioning of specimen. The contact between the specimen and the grip faces ensures that the gripping force increases as the pull load goes up. It makes this kind of grips particularly suitable for testing high strength materials since specimen slippage is eliminated. Besides, the attached extensometer remains at the same place after the specimen failure.

3.3. Determination of the elastic constants using a resonant technique

The knowledge of the elastic constants is fundamental to characterise the stress-strain behaviour of materials. In view of this fact, a significant number of experimental techniques have been proposed to calculate their values. Those techniques can be classified into two broad categories: *static* and *dynamic* techniques (Armstrong, 1971; Radovic, 2004; Antunes, 2008; Pantano, 2012).

The former group directly measures the stress and strain during the mechanical tests. The constants are then determined from the slope of the linear region of the stress-strain curve. Among others, mechanical tests comprise tensile, compressive, flexural or torsional tests (Pantano, 2012). An alternative static method for measuring elastic constants is nanoindentation (Radovic, 2004). In this case, a load is applied in order to make an indent which is monitored and recorded continuously as a function of displacement. From the stored data, a resultant load-displacement curve is computed. Then, the slope of the top part of the unloading curve of load-displacement is used to calculate the Young's modulus whilst the Poisson's ratio is evaluated using contact mechanics relationships.

Regarding the latter category, it encompasses *pulse* methods and *resonant* methods. Pulse methods are, generally, based on measuring the transit time, i.e. the time spent by the ultrasonic pulse through the specimen from the transmitting to the receiving transducer. In this case, the elastic constants are calculated using the dimensions and density of the sample as well as the transit time for the longitudinal and transversal ultrasonic waves. Resonant methods are based on the principle that there is an intrinsic relation between elastic constants of a sample and its vibratory behaviour. Samples are excited to vibrate and the resultant vibration is monitored in order to obtain their natural frequencies. The elastic constants are then defined from the vibration modes, natural frequencies, dimensions and mass of samples. It is important to refer that resonant methods offer remarkable advantages. For example, several constants can be calculated from one specimen; average values are measured which is suitable for numerical modelling; this method only requires small amounts of material; and as a non-destructive technique, it is suitable for quality control.

In this research, a resonant method was carried out to evaluate the elastic constants. In general, the application of a resonant method involves three main steps: i) experimental determination of resonant frequencies; ii) establishment of analytical or numerical relations between resonant frequencies and elastic properties; iii) and calculation of elastic constants.

With respect to the first step, the impulse excitation technique (IET), schematically exhibited in Figure 3.4, was used. It consists of exciting the sample by a single external mechanical impulse that induces vibrations in the sample and can be done acoustic (Radovic, 2004) or mechanically (Figure 3.4). Very

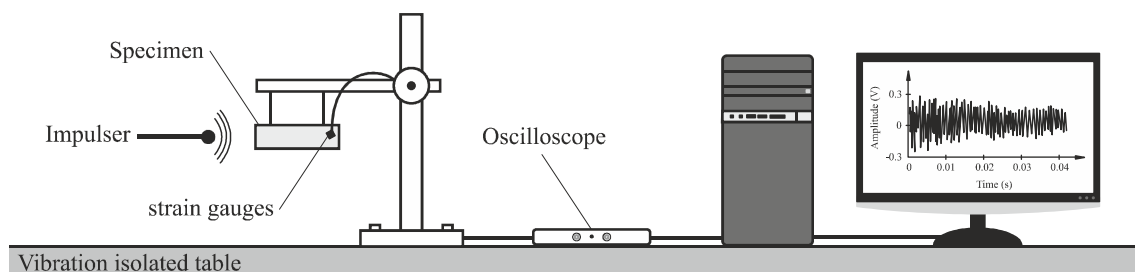


Figure 3.4. Test apparatus used in the determination of the experimental resonant frequencies by the impulse excitation technique.

little energy is required. Then, the vibration is detected and analysed in order to obtain the frequency response functions. In the present research, the dynamic response was obtained from strain gauges glued onto the sample (Figure 3.4). Finally, the resultant resonant frequencies are calculated by using a frequency analyser.

Concerning to the second step, as mentioned above, the relations between elastic properties and resonant frequencies can be established analytical and numerically. Rayleigh's (McIntyre, 1988; Ayorinde, 1993), Rayleigh-Ritz (Deobald, 1988; Frederiksen, 1995) or FE methods (Fallstrom, 1991; Antunes, 2008) are approaches often used for modelling the behaviour of a plate. The first one is easily implemented but is too inaccurate. The second one provides good accuracy but is greatly dependent on the choice of admissible functions for representing the displacement field and leads to a huge amount of calculations. The third one, due to the high calculation capacity of current computers, is a suitable option. Besides, it can be applied to 3D problems and handle with complex shapes or complex boundary conditions. In this sense, the finite element method was adopted in this study. Nevertheless, it is important to note that the procedure adopted here is not completely experimental since it combines experimental and numerical techniques. In a literal sense, it is a mixed numerical-experimental technique (MNET) being the unknown material parameters of the numerical model updated until the dynamic response numerically predicted matches the experimental observations as closely as possible.

In relation to the third step, the calculation of elastic constants with the FEM can be done in different ways. For example, optimising an objective function (Hwang, 2000); based on a sensitivity analysis of the resonant frequencies to the material properties (Lauwagie, 2004) or even using neural networks (Liu, 2002). The method based on the sensitivity analysis was implemented in this research (see Section 4.1).

The specimen geometry used in IET tests is shown in Figure 3.5b. It was machined from a small piece of material (Figure 3.5a) at the DEM/ISEC/IPC. The tests were conducted according to the procedures described in the ASTM E1876 (2009) at the DEM/FCT/UC. Firstly, the sample was cut by band saw and then was milled by a horizontal milling machine and carefully polished to obtain a perfect plate, i.e. with a uniform thickness, sharp edges and without chamfers or bevels, since accurate calculations by this

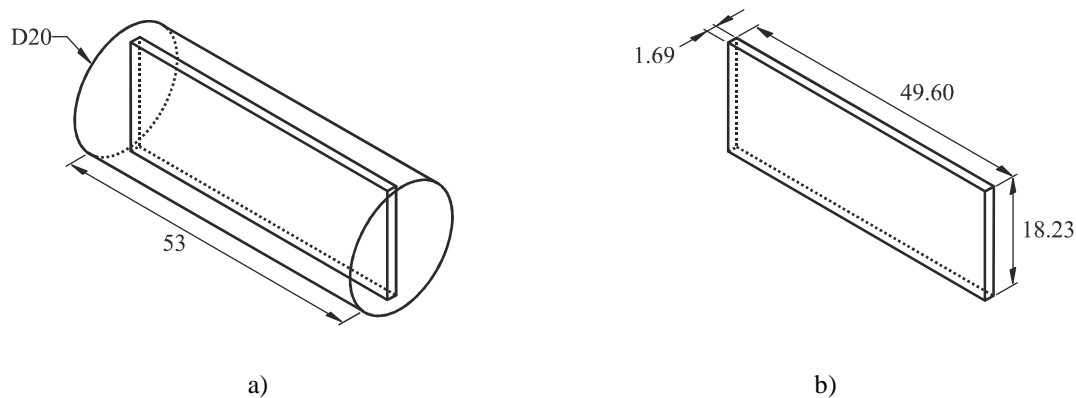


Figure 3.5. Specimen geometry used in the IET tests: a) initial geometry; b) final geometry.

methodology require similar numerical and experimental geometries (Radovic, 2004). This geometry was the outcome of a numerical study that sought to achieve the highest sensitivities to the material constants as well as to avoid superposition of distinct resonant frequencies (see Section 4.1).

Small size extensometers with electrical resistances of 120Ω and gauge factors of 2 were glued onto the specimen. These extensometers had a mass of 0.00216g and a grid size of about 2mm. Therefore, resonant frequencies were not affected. In order to measure the resonant frequencies associated with the different vibrational modes, the orientation and location of the extensometers on the specimen were meticulously selected.

The specimen was suspended with two thin cotton wires to approximate the free-free boundary conditions of the finite element model as close as possible. The impulse excitation was accomplished by a single elastic strike at anti-nodal positions. The mechanical vibration was detected by extensometers glued onto the specimen and was converted into electrical signal which was addressed to a personal computer (PC). The impulse force was not recorded.

A data acquisition system with maximum sampling rate of 20×10^6 samples per second and a vertical resolution of 12 bits was used. The sampled time functions were converted into frequency domains by a fast Fourier transformation (FFT) algorithm and then the experimental resonant frequencies were evaluated by using the software Microcal Origin (version 5.0). The density was evaluated from the mass and dimensions of the specimen which were measured using a high precision balance and a micrometre.

3.4. Low-cycle fatigue tests

The specimen geometry used in low-cycle fatigue (LCF) tests is presented in Figure 3.6. These tests were conducted according to the procedures described in ASTM E606 (2004) standard and aimed at studying the cyclic deformation behaviour as well as obtaining the fatigue ductility and fatigue strength properties of the DIN 34CrNiMo6 high strength steel studied here. The samples were machined in a high precision CNC turning centre from extruded 20mm-diameter round bars at the DEM/ISEC/IPC. Before testing, the surfaces were prepared with utmost care. A high-speed mechanical polishing with 600, 1200 and 2500 grit silicon carbide papers, and 6µm diamond paste was carried out.

Fully-reversed strain amplitude-controlled and fully-reversed stress amplitude-controlled fatigue tests were carried out at room temperature using sinusoidal waves. Table 3.3 summarises the different applied strain and stress amplitudes as well as the number of specimens used in LCF tests. The former tests were performed with total strain amplitudes ($\Delta\epsilon/2$) lying between ± 0.4 and $\pm 2.0\%$. A fixed strain ratio ($R_\epsilon = -1$) was used. Additionally, a constant strain rate ($d\epsilon/dt$) equal to $8 \times 10^{-3} \text{ s}^{-1}$ was assumed, being the testing frequency (f) calculated from Equation 3.1 as a function of the total strain amplitude. The hysteresis loops

$$f = \frac{(d\epsilon/dt)}{4(\Delta\epsilon/2)} \Leftrightarrow f = \frac{8 \times 10^{-3}}{4(\Delta\epsilon/2)} \quad (3.1)$$

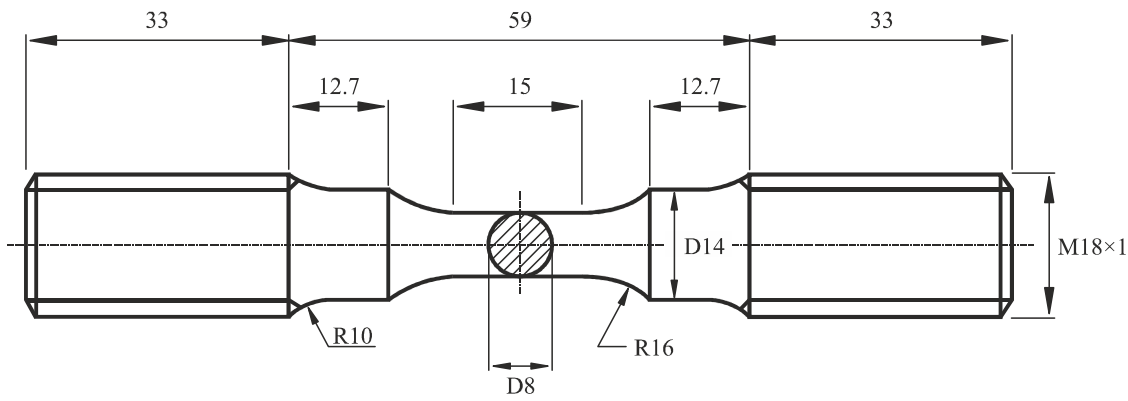


Figure 3.6. Specimen geometry used in LCF tests (in accordance with ASTM E606).

Table 3.3. Total strain and total stress amplitudes defined in low-cycle fatigue tests.

Specimen reference	Total strain amplitude, $\Delta\varepsilon/2$ [%]	Total stress amplitude, $\Delta\sigma/2$ [MPa]
D200	2.00	
D150	1.50	
D125	1.25	
D100	1.00	
D080	0.80	
D060	0.60	
D050	0.51	
D040	0.41	
T635		635.0
T600		600.0
T580		580.0
T560		560.0
T540		540.0
Total:	8 specimens	5 specimens

D_ _ _: fully-reversed strain-controlled tests

T_ _ _: fully-reversed stress-controlled tests

at the half-life were chosen as the representative of stable behaviour. Regarding the latter tests, a stress ratio (R_σ) equal to -1 was defined. The stress amplitude ($\Delta\sigma/2$) ranged from ± 540 to ± 635 MPa.

The single step test (SST) was adopted here. According to this method, identical specimens are tested under constant strain amplitude until failure occurs (see Section 2.3). Although more time-consuming than other alternative procedures, such as the multiple step test, incremental step test, monotonic tension after cyclic straining, etc., the SST is the norm. Besides, the results obtained through other test methods should be viewed as an approximation to the SST, since the plastic response, in general, is path and history dependent. Tests were interrupted when specimens separated into two pieces.

The tests were conducted at the DEM/FCT/UC on a computer-controlled 100 kN DARTEC closed-loop servo-hydraulic testing machine. As schematised in Figure 3.7, the upper grip is suspended from the

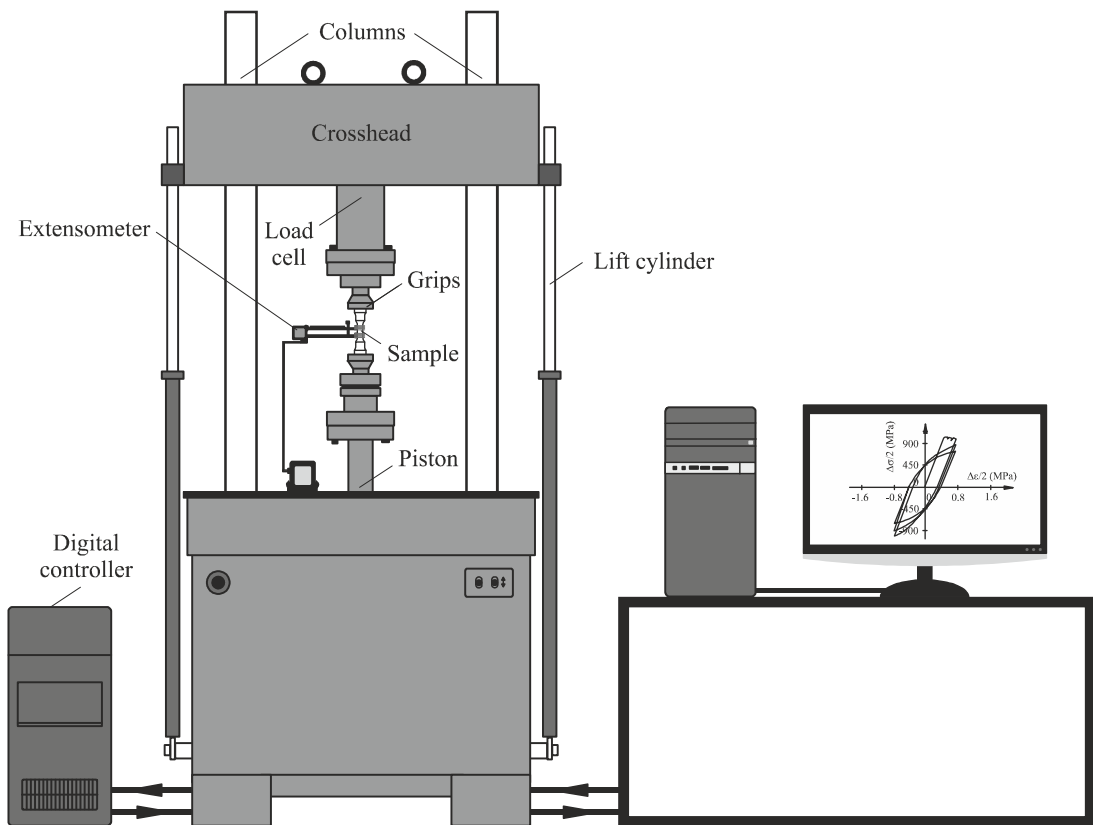


Figure 3.7. Scheme of experimental apparatus used in LCF tests.

crosshead which can slide in vertical direction using the lift cylinders. The lower grip is situated at the end of the piston of the hydraulic actuator. The system control is provided by a fully digital controller (model 8800) capable of running a broad range of static and dynamic tests. The main interface of the digital controller is windows-based software application which provides full system control, including waveform generation, limit setup and status monitoring. In alternative, hardware operator panel can also be used.

The axial load acting on the specimen is measured by a load cell mounted between the test specimen and the crosshead. A linear variable differential transformer monitors the piston position. The strain can be evaluated using an axial extensometer which is clamped to the specimen. Thus, depending on the objective, there are three alternative control modes that can be used in tests, namely *position* control, *stress* control or *strain* control. The acquisition system converts the output signals generated by the load cell, the piston position and the extensometer into digital data. Such data can be displayed in real-time on the console software in the form of line graphs and can also be recorded for further analysis using specific commercial software.

The specimens were connected to the testing machine with threaded grips which is a suitable solution to avoid misalignments in the vertical direction. A 12.5mm-gauge extensometer (model Instron 2620-601) was clamped to the specimen *via* two separated knife-edges. In strain-controlled tests, the software devoted to low-cycle fatigue (Instron LCF, version 7.02) was used. At least, 200 samples per cycle were

collected and recorded. In stress-controlled tests, data were monitored and recorded using the computer application Instron SAX (version 7.1).

3.5. High-cycle fatigue tests

The fatigue behaviour of severely notched specimens subjected to different proportional loading paths was investigated. The specimens used here are presented in Figure 3.8a and Figure 3.8b. The former was used in single bending and in-phase combined bending-torsion tests, whilst the latter was used in single-torsion tests. The geometry of Figure 3.8a consists of a 16mm-diameter round bar with a lateral notch. The notch has a U-shape with a diameter and a depth of 3mm and is placed asymmetrically with respect to the longitudinal centre of the specimen only to facilitate mounting and observation during the test. The geometry of Figure 3.8b has a smaller diameter. The notch is similar, having the same diameter, the same depth and is located at the same place. The change in geometry aimed at reducing the applied load for the same nominal stress level.

The specimens were machined in a high precision CNC turning centre from extruded 20mm-diameter round bars at the DEM/ISEC/IPC. Before testing, the surfaces were carefully polished, firstly, with a high-speed mechanical polishing using successively 600, 1200 and 2500 grit silicon carbide papers, and then using 6µm diamond paste.

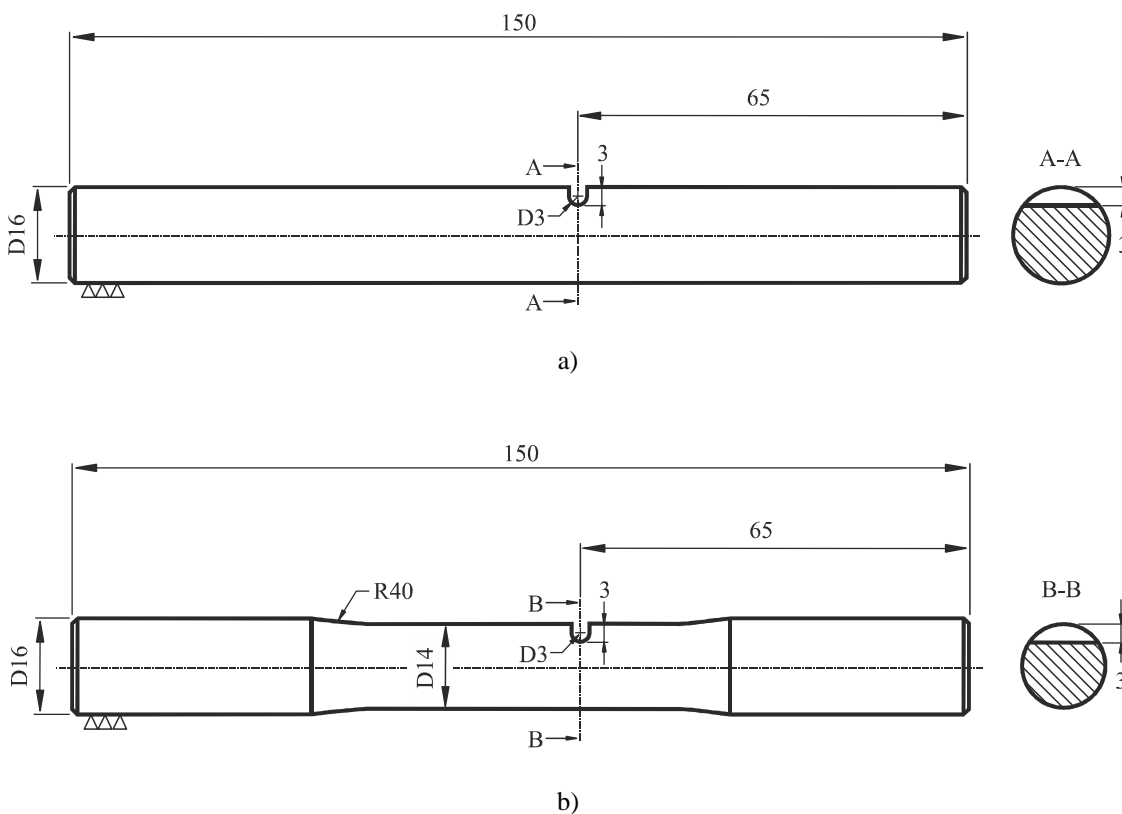


Figure 3.8. Specimens used in multiaxial fatigue tests: a) single bending and in-phase combined bending-torsion; b) single torsion.

Figure 3.9 exhibits the different loading paths applied in high-cycle fatigue tests. As can be seen, five different proportional loading paths were studied, namely single bending (Figure 3.9a), single torsion (Figure 3.9e) and in-phase combined bending-torsion (Figures 3.9b-d). With respect to the last type, three ratios of bending moment to torsion moment (ratios B/T) were adopted, which encompassed B=2T (Figure 3.9b), B=T (Figure 3.9c) and B=2T/3 (Figure 3.9d).

Tables 3.4, 3.5 and 3.6 summarise, respectively, the loading conditions studied in single bending, single torsion and in-phase combined bending-torsion tests. All loading paths were examined for three different

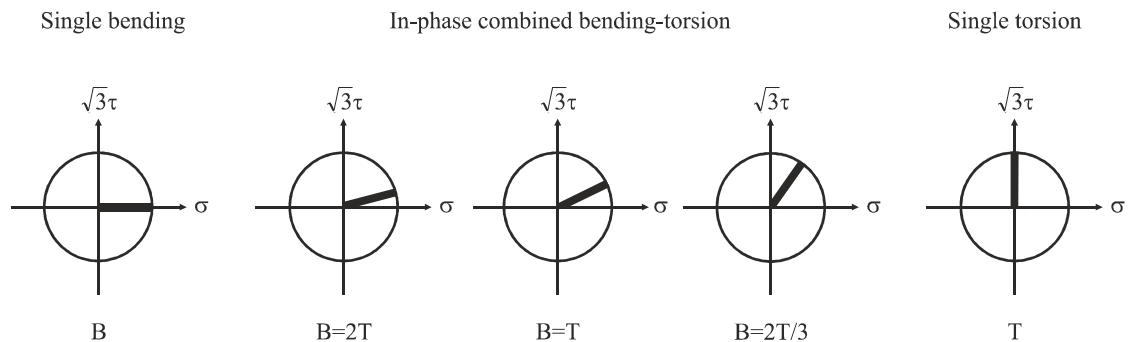


Figure 3.9. Proportional loading paths applied in fatigue tests: a) single bending (B); b) in-phase bending-torsion (B=2T); c) in-phase bending-torsion (B=T); d) in-phase bending-torsion (B=2T/3); e) single torsion (T).

Table 3.4. Summary of loading conditions tested in single bending tests.

Specimen reference	Normal stress amplitude, σ_a [MPa]	Mean normal stress, σ_m [MPa]	Normal stress range, $\Delta\sigma$ [MPa]	Stress ratio, R
B-1	195.6	206.1	401.7	0.03
B-2	195.6	206.1	401.7	0.03
B-3	218.8	229.3	448.1	0.02
B-4	218.8	229.3	448.1	0.02
B-5	295.0	304.2	599.2	0.02
B-6	295.0	304.2	599.2	0.02

Total: 6 specimens

Table 3.5. Summary of conditions tested in single torsion tests.

Specimen reference	Shear stress amplitude, τ_a [MPa]	Mean shear stress, τ_m [MPa]	Shear stress range, $\Delta\tau$ [MPa]	Stress ratio, R
T-1	334.1	167.0	334.1	0.03
T-2	334.1	167.0	334.1	0.03
T-3	400.9	200.5	400.9	0.03
T-4	400.9	200.5	400.9	0.03
T-5	445.5	222.7	445.5	0.02
T-6	490.0	245.0	490.0	0.02
T-7	490.0	245.0	490.0	0.02

Total: 7 specimens

Table 3.6. Summary of loading conditions tested in-phase combined bending-torsion tests.

Specimen reference	Normal stress amplitude, σ_a [MPa]	Mean normal stress, σ_m [MPa]	Normal stress range, $\Delta\sigma$ [MPa]	Stress ratio, R
▪ B=2T series ($\sigma_a = 4\tau_a$; $\sigma_m = 4\tau_m$; $\Delta\sigma = 4\Delta\tau$)				
B2T-1	179.1	194.0	358.1	0.04
B2T-2	223.8	238.7	447.6	0.03
B2T-3	298.4	313.3	596.8	0.02
▪ B=T series ($\sigma_a = 2\tau_a$; $\sigma_m = 2\tau_m$; $\Delta\sigma = 2\Delta\tau$)				
BT-1	179.1	194.0	358.1	0.04
BT-2	179.1	194.0	358.1	0.04
BT-3	179.1	194.0	358.1	0.04
BT-4	223.8	238.7	447.6	0.03
BT-5	223.8	238.7	447.6	0.03
BT-6	223.8	238.7	447.6	0.03
BT-7	298.4	313.3	596.8	0.02
▪ B=2T/3 series ($\sigma_a = 4/3\tau_a$; $\sigma_m = 4/3\tau_m$; $\Delta\sigma = 4/3\Delta\tau$)				
B2T3-1	179.1	189.0	358.1	0.03
B2T3-2	223.8	233.8	447.6	0.02
B2T3-3	298.4	308.4	596.8	0.02

Total: 13 specimens

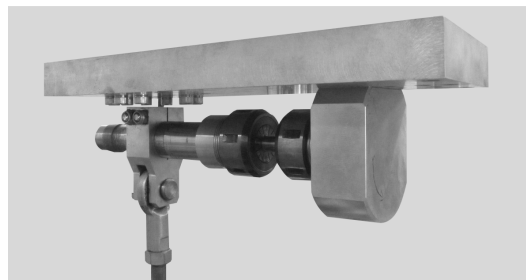
stress levels. Tests were conducted in load control, under constant amplitude loading. A stress ratio (R) very close to zero was defined in order to avoid potential fluctuations of the gripping system during the absence of loading. These loading conditions aimed at evaluating different orders of magnitude of fatigue life. Sinusoidal load waves and frequencies at about 3-6Hz were used.

Tests were performed at the DEM/FCT/UC on the servo-hydraulic testing machine described in the previous section (Figure 3.10a). A special gripping system that can be assembled in three different ways was used, as displayed in Figures 3.10b-d. In the in-phase combined bending-torsion tests, the B/T ratio can be changed by moving the screw (Figure 3.10d) in the slot. The B/T ratio can be increased by moving the screw to the left and *vice versa*. Figure 3.10d presents, as an example, the gripping system assembled for the case B=2T.

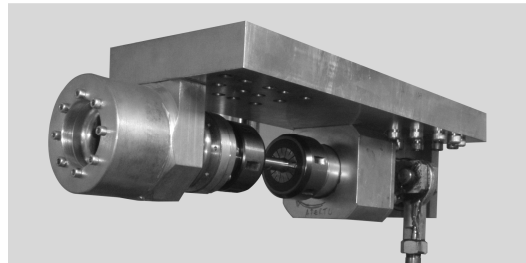
The detection of crack initiation and growth was performed *in-situ* with a digital monitoring system (Figure 3.11a-b). It consisted of a high performance 14-bit charge-coupled device (CCD) digital camera (pco.pixelfly usb) and an optical device with variable magnification (Specwell M850-S) coupled to a micrometre driven translation stage supplied by the Parker Hannifin Corporation (Model M4424). The micrometre driven translation stage was firmly fixed to the frame of the testing machine using three orthogonally-mounted aluminium profiles with independent horizontal and vertical translations (Figures 3.10a and 3.11b). The in-plane motion of the driven translation stage was done using two micrometric screws able to provide a maximum displacement in each direction of 50mm. This solution provided an easy and efficient observation of the notch. The digital camera was connected to a PC *via* a peripheral



a)



b)

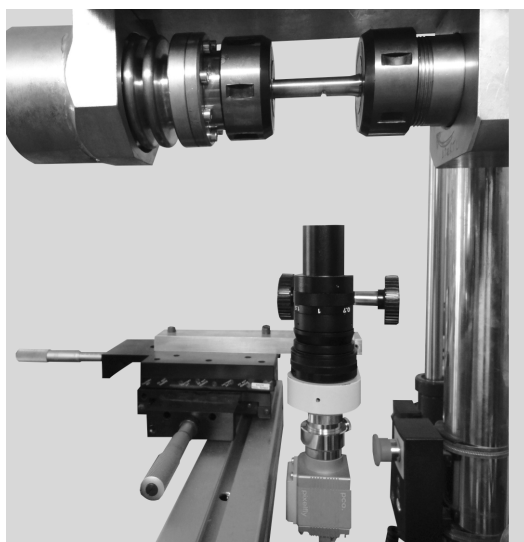


c)

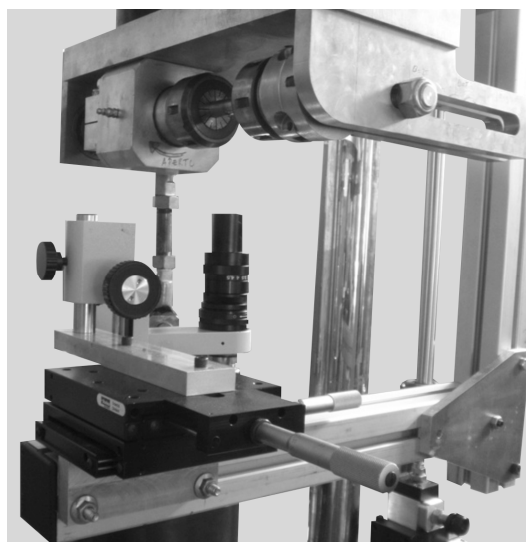


d)

Figure 3.10. a) Servo-hydraulic testing machine used in fatigue tests. Details of the gripping system assembled for: b) single bending; c) single torsion; d) in-phase combined bending-torsion ($B=2T$) tests.



a)



b)

Figure 3.11. Digital monitoring system used in the detection of crack initiation and growth. Details of the: a) digital camera and optical device; b) micrometre driven translation stage.

component interconnect (PCI) board and was controlled, in a manual mode, with the Camware 32-bit Windows software. This computer application can be used to control all camera parameters and settings as well as to save and record images in a tagged image file format (TIFF). The digital camera has a high resolution (1392×1040 pixel) and allows exposure times in the range 5μs to 60s.

In all tests, the notch was placed upside down (Figure 3.11a) and the digital monitoring system was located immediately below (Figures 3.11a-b). Therefore, the relative position of the notch with respect to the digital monitoring system was always the same, regardless of the load path applied. Apart from the software, a manual diaphragm incorporated into the optical device and a manual focus system were also used to optimise image quality. In addition, a fine layer of blue ink mixed with acetone was deposited on the surface of the notch allowing a more uniform reflection of light.

Digital images were recorded in a systematic manner using an exposure time of 1s and were captured every 5×10^3 cycles. After crack detection, usually for surface cracks having a length of 200-300μm, the interval was reduced to 2×10^3 cycles. In the final stage of testing, the images were recorded every 1×10^3 cycles. In longer tests (lives greater than about 150×10^3 cycles), during the crack initiation period, images were acquired every 10×10^3 cycles and after that were reduced successively to 5×10^3 , 2×10^3 and 1×10^3 cycles.

The notch was always observed under the maximum load applied during the test which simplified the *in situ* detection of crack initiation and growth. At the time of observation, the cyclic loading was suspended and a static load with a magnitude corresponding to the maximum applied stress was applied. As a result, the crack remained open as long as necessary which contributed to easy crack detection and an accurate measurement of surface crack length. After crack observation and image recording, the cyclic test was resumed. Tests were finished before specimen separation into two pieces, more specifically, tests were stopped automatically by the digital controller of the testing machine when a target displacement was reached during the downward movement of the piston which was fixed at 7mm. The typical uncracked ligaments observed in tests varied between 15-25% of cross-sectional area of the specimens.

The relations between the force applied by the testing machine (F) and the resultant bending (B) and torsion (T) moments in the specimen for the different types of tests are presented in Figure 3.12 (several forces and moments were intentionally omitted in those simplified free-body diagrams since they do not interfere on the specimen). Table 3.7 exhibits the values of the L_1 - L_4 variables used in this research. These values were fixed for each test. The change in L_4 was necessary to modify the ratio of the bending moment to torsion moment (B/T) which depends on the position of the screw in the slot (see Figures 3.10d and 3.11b), as explained before.

Figure 3.12 can also be used to establish a link between the force applied by the testing machine and the maximum nominal stresses acting on the specimen. In the case of the single bending tests (Figure 3.12a),

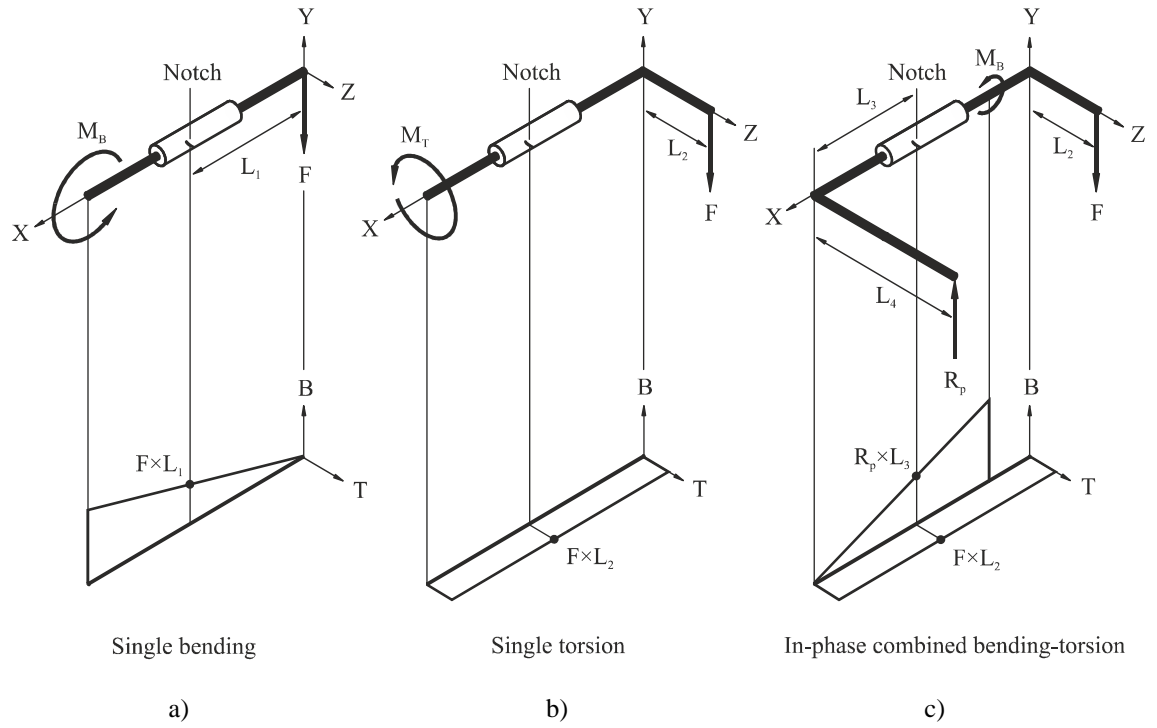


Figure 3.12. Relation between the force applied by the piston of the testing machine and the resultant bending and torsion moments at the specimen: a) single bending; b) single torsion; c) in-phase combined bending-torsion tests.

Table 3.7. Main dimensions used in the tests.

Type of test	L_1 [mm]	L_2 [mm]	L_3 [mm]	L_4 [mm]	Ratio σ/τ
Single bending	184.5				
Single torsion		60.0			
In-phase combined bending-torsion (B=2T)		60.0	125.0	62.5	4
In-phase combined bending-torsion (B=T)		60.0	125.0	125.0	2
In-phase combined bending-torsion (B=2T/3)		60.0	125.0	187.5	4/3

the maximum nominal bending stress (σ) on the cross-section of the notch root and the force applied by the testing machine (F) can be related by Equation 3.2.

$$\sigma = \frac{32B}{\pi D^3} \Leftrightarrow \sigma = \frac{32 \times (FL_1)}{\pi D^3} \Leftrightarrow F = \frac{\pi \sigma D^3}{32L_1} \quad (3.2)$$

With respect to the single torsion tests (Figure 3.12b), the relation between the maximum nominal torsion stress (τ) on the cross-section of the notch root and the force applied by the testing machine can be written according to Equation 3.3.

$$\tau = \frac{16T}{\pi D^3} \Leftrightarrow \tau = \frac{16 \times (FL_2)}{\pi D^3} \Leftrightarrow F = \frac{\pi \tau D^3}{16L_2} \quad (3.3)$$

Regarding the in-phase combined bending-torsion tests (Figure 3.12c), Equations 3.3 and 3.4 relate, respectively, the maximum nominal torsion and bending stresses acting on the cross-section of the notch root with the force applied by the testing machine. From the torsional equilibrium condition, the relation $R_p \times L_4 = F \times L_2$ can be established. In this way, the force on the screw (R_p) is given by: $R_p = F \times (L_2/L_4)$.

$$\sigma = \frac{32B}{\pi D^3} \Leftrightarrow \sigma = \frac{32 \times (R_p L_3)}{\pi D^3} \Leftrightarrow \sigma = \frac{32 \times \left(\frac{FL_2}{L_4} L_3 \right)}{\pi D^3} \Leftrightarrow \sigma = \frac{32 \times (FL_2) \times \left(\frac{L_3}{L_4} \right)}{\pi D^3} \Leftrightarrow F = \frac{\pi \sigma D^3 L_4}{32 L_2 L_3} \quad (3.4)$$

The ratio of the bending stress to the torsion stress (σ/τ), using the two previous equations, is defined by Equation 3.5. Therefore, from the values of L_3 and L_4 used in the tests, the ratios σ/τ for the cases B=2T, B=T and B=2T/3 are, respectively, equal to 4, 2 and 4/3, as listed in Table 3.7.

$$\frac{\sigma}{\tau} = \frac{\frac{32 \times (FL_2) \times \left(\frac{L_3}{L_4} \right)}{\pi D^3}}{\frac{16 \times (FL_2)}{\pi D^3}} \Leftrightarrow \frac{\sigma}{\tau} = 2 \left(\frac{L_3}{L_4} \right) \quad (3.5)$$

3.6. Fatigue crack front marking tests

Complementary to the high-cycle fatigue study, additional tests were conducted to mark the crack front on the fracture surface of the specimens. These tests were carried out using exactly the same methodology described in the previous section (i.e. included the same gripping systems, loading paths, specimens, image acquisition, etc.). Nevertheless, in this case, the main objective was to mark the crack on the fracture surface of the specimens in order to understand the effect of the loading paths studied on crack shape. In view of this fact, at least one fatigue marking test was performed for each loading path. Table 3.8 lists the loading details of each case.

The procedure adopted to mark the crack fronts on the fracture surface of the specimen was based on the *beach marking* technique (Lynch, 2007). In particular instants of the test, the applied stress level is changed for several cycles and then is resumed. The change in loading conditions affects the crack propagation resulting in particularly well-defined progression markings on the fracture surface. In this case, the perturbations were caused by overload sequences applied several times during the tests. The number of cycles of the overload sequences (n_B) was deliberately reduced throughout the test due to the increase in crack propagation velocity.

Table 3.9 summarises the criteria used to carry out the overload sequences on the specimen. In the first part of the test (when the crack was a surface crack), the overload sequences were applied for surface crack lengths multiples of approximately 2.5mm with overload ratios ($\Delta\sigma_B/\Delta\sigma$) equal to 1.75 (i.e. 75% above the nominal stress range) and values of n_B between 100-60 cycles. In the second part (when the

Table 3.8. Loading used in fatigue crack front marking tests.

Specimen reference	Stress amplitude, σ_a or τ_a [MPa]	Mean stress, σ_m or τ_m [MPa]	Stress range, $\Delta\sigma$ or $\Delta\tau$ [MPa]	Stress ratio, R
B-m	195.6	206.1	401.7	0.03
T-m	334.1	167.0	334.1	0.03
B2T-m	179.1	194.0	358.1	0.04
BT-m	179.1	194.0	358.1	0.04
B2T3-m	179.1	194.0	358.1	0.04

Table 3.9. Details of the fatigue crack front marking process.

Loading sequence and crack length details	Marking	n_B [cycles]	$\Delta\sigma_B/\Delta\sigma$	a_i [mm]	b_i [mm]
	1	100	1.75	≈ 2.5	
	2	80	1.75	≈ 5.0	
	3	60	1.75	≈ 7.5	
	4	15	1.75	≈ 10.0	
	5	10	1.50		≈ 2.0
	6	6	1.50		≈ 2.0
	7	6	1.50		≈ 2.0
	8	3	1.50		≈ 2.0

crack was a through crack), the crack length was measured laterally. The overload sequences were applied when the difference between the crack length of the last overload and the current crack length (b_i) was roughly equal to 2.0mm. In this case, the overload ratios ($\Delta\sigma_B/\Delta\sigma$) were only equal to 1.50 and the number of cycles varied between 10 and 3 cycles. Moreover, in order to better evaluate the number of cycles applied, the loading frequency was reduced to 1Hz during the overload periods.

3.7. Analysis of material microstructure

The microstructure of the material was examined by both optical microscopy (OM) and scanning electron microscopy (SEM). The sample was prepared according to the recommendations of the ASTM E3 (2011) standard. Firstly, a piece of material was cut using a band saw machine from an extruded 20mm-diameter round bar perpendicularly to the tensile axis (Figure 3.13a). Then, a preliminary polishing was carried out using a rotary disc and wet grit silicon papers with grit sizes progressively finer (600, 1200 and 2500) in order to ensure a flat surface. After that, the sample was mounted in a cylindrical mould filled with synthetic resin (Figure 3.13b). Next, the surface of the sample was carefully polished to a scratch-free condition using a rotary disc impregnated with diamond paste of different grades, namely 6 μ m and 3 μ m. The as-polished surface was successively examined with a microscope to guarantee the scratch-free condition. After final polishing, the sample surface was etched with nital ($\approx 5\%$ solution HNO₃ in ethyl alcohol).

The microstructure examination by OM was carried using a high-resolution Carl Zeiss AxioTech 100HD microscope (Figure 3.14a) connected to a digital camera (resolution: 1315 \times 1033 pixel, 12 bits per colour)

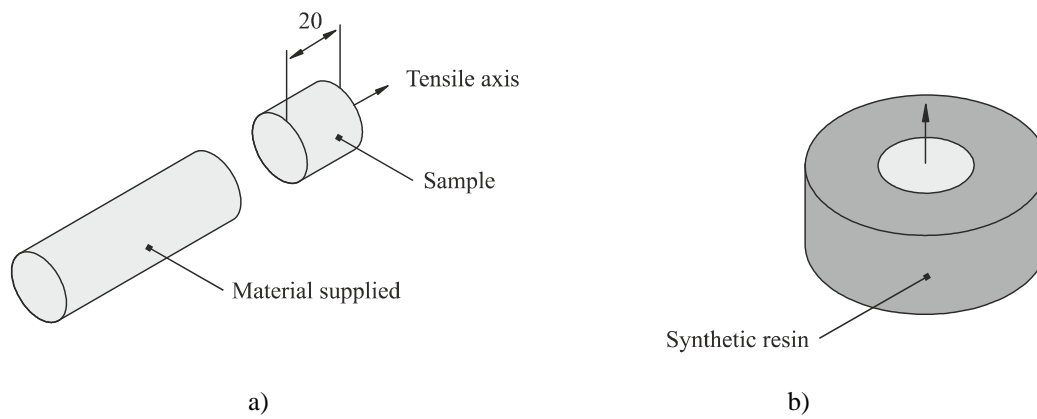


Figure 3.13. Sample for OM and SEM analyses: a) material supplied; b) sample used.

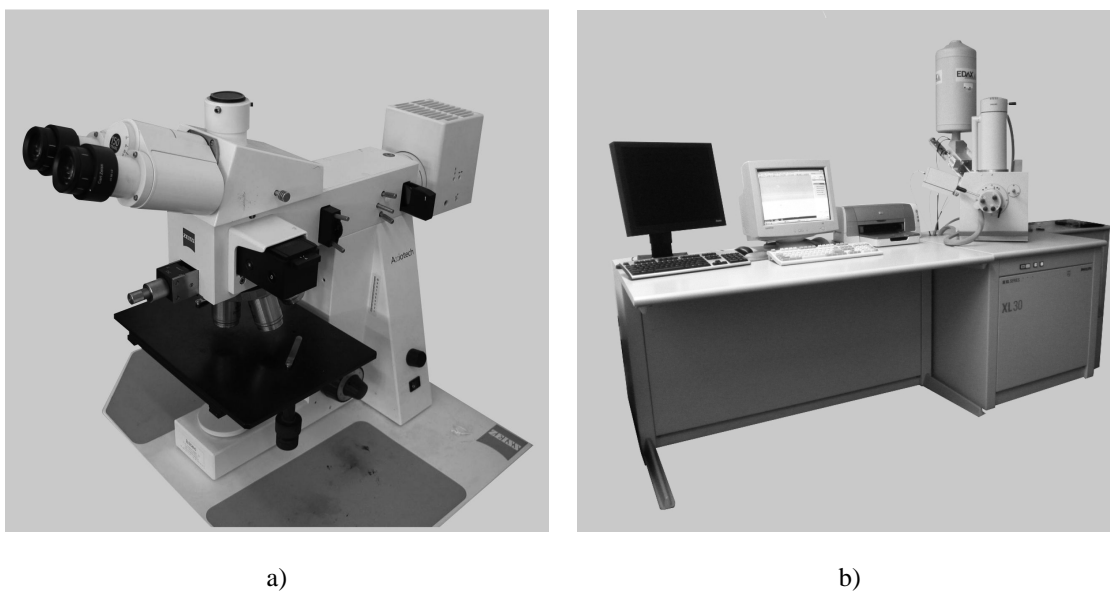


Figure 3.14. a) Optical microscope (Carl Zeiss Axiotech 100HD model); b) scanning electron microscope (Philips XL30 model).

whose output was captured by a PC equipped with the Samsung free software (version 2.0). The light source consisted of an adjustable halogen lamp. The micrographs were taken with magnifications varying between 200-1000 times and were saved in a JPEG (joint photographic experts group) file format. The grain size measurement was obtained by applying the procedure described in the ASTM E112 (2010) standard. This study was performed using the open source software package ImageJ.

The microstructure examination by SEM was performed with a Philips XL30 microscope (Figure 3.14b). The Philips XL30 is a fully computer-controlled SEM that offers a four-axis motorised stage with full manual override. Due to its fine electron source of the lanthanum hexaboride single crystal system, it is capable of very high resolutions, more specifically 3.5nm at an accelerating voltage of 30kV, which corresponds to magnifications up to 200×10^3 times. The micrographs were saved in the standard TIFF file

format. The images were formed by detection of secondary electrons (SE) with accelerating voltages (Acc. V) of 30kV, spot sizes (Spot) of 3 and magnifications (Magn) of 3×10^3 times.

3.8. Analysis of fracture surfaces

The fracture surfaces of the specimens used in uniaxial tensile tests, low-cycle fatigue tests, high-cycle fatigue tests and fatigue crack front marking tests were examined by SEM. The fracture surfaces of the two last tests were also examined by OM. The microscopes used in the former and latter observations were the ones described in the previous section which can be seen in Figure 3.14b and Figure 3.14a, respectively.

The objective of the analysis of fracture surfaces of the uniaxial tests by SEM aimed at characterising the surface morphology and the failure mechanics. Regarding the low-cycle fatigue tests, the goal was to identify the main fatigue damage mechanisms associated with the levels of strain amplitude applied. Thus, specimens covering the strain amplitudes used in tests (0.4%, 1.0% and 2.0%) were analysed. With respect to the high-cycle fatigue tests, the examination of fracture surfaces intended to understand the crack initiation behaviour caused by the different load paths applied. Therefore, a specimen from each loading path was analysed. Table 3.10 summarises the specimens examined as well as the SEM parameters defined in each case.

The main purpose of the analysis by OM was to obtain macro views of the fracture surfaces to understand the effect of the loading paths on the angles of crack initiation, topologies of fracture surfaces and

Table 3.10. Summary of fracture surfaces analysed by SEM.

Specimen reference	Accelerating voltage [kV]	Spot size	Magnification	Diffraction
▪ Uniaxial tensile tests				
UT-1	10.0, 10, 5.0	2.8, 2.0, 2.0	20, 750, 750	SE
▪ Low-cycle fatigue tests				
D200	10.0	3.3	17, 74, 500	SE
D100	10.0	3.8	19, 500	SE
D040	10.0	3.3, 3.8	18, 500	SE
▪ High-cycle fatigue tests				
B-1	5.0	2.4	21, 750	SE
T-1	5.0	2.5	300, 500	SE
B2T-1	10.0	3.8, 3.8, 3.3	20, 100, 2000	SE
BT-1	5.0	4.2	20	SE
B2T3-1	10.0	3.8	20, 99, 750	SE
▪ Fatigue crack front marking tests				
B-m	5.0	2.4, 3.3, 2.5	40, 750, 1000	SE
T-m	10.0	3.4	20, 200, 800, 2500	SE
B2T-m	10.0	3.0	25	SE
BT-m	10.0	3.8, 3.3	21, 250	SE
B2T3-m	5.0	4.2	21	SE

SE: secondary electrons

propagation planes, among others. Particularly in the case of the fatigue crack front marking tests, another objective was to observe the influence of the loading paths applied on the resultant crack shape profiles. These examinations were carried using the same methodologies described in Section 3.7 but, in this case, the magnifications defined varied between 0.8-4.5 times.

Finally, in both SEM and OM analyses, the samples were sectioned perpendicularly to their longitudinal axis using a high-speed diamond saw. Before examination, the samples were ultrasonically cleaned in trichloroethylene solution for ten minutes and then in distilled water also for ten minutes.

3.9. Three-dimensional laser scanning of fracture surfaces

Different recording techniques can be used to acquire an accurate shape of an object. Among them, laser scanning is getting great interest due to its simplicity and speed. It analyses an object by collecting a set of points which are used to construct a digital three-dimensional model. Laser scanner principles are, in essence, triangulation based, time-of-flight based and phase-difference based. In the first case, a laser point (Figure 3.15a), line (Figure 3.15b) or pattern (Figure 3.15c) is projected onto an object and the deformation of this point, line or pattern is measured by using a visible sensor. The name of the technique is due to the relative positions of the projector, the sensor and the object which are configured in a triangular shape. In the second case, the scanner computes distances by measuring the timeframe between sending a short laser pulse and receiving its reflection from an object. Since the laser pulse travels with a constant speed, the distance between the scanner and the object can be determined. In the third case, a modulated continuous laser wave is used instead of a laser pulse.

In this research, the triangulation based technique (Figure 3.15) was used to replicate the fracture surfaces of the specimens used in the fatigue crack front marking tests. This study was carried out to better understand the influence of the loading path on the topologies of fracture. The analyses were performed at the DEM/ISEC/IPC using a Roland Picza 3D Laser Scanner LPX-600 (Figure 3.16a). In order to enhance the data acquisition, the samples were painted with a thin layer of white paint (Figure 3.16b). The cloud points were determined using the plane scanning method. In this method, the object and the laser head move in synchronisation to produce parallel beams of light which are used to scan the object across its face. The precision can be controlled by increasing the number of scanned surfaces and reducing the pitches in height and width directions. Table 3.11 presents the scanning settings selected which aimed at

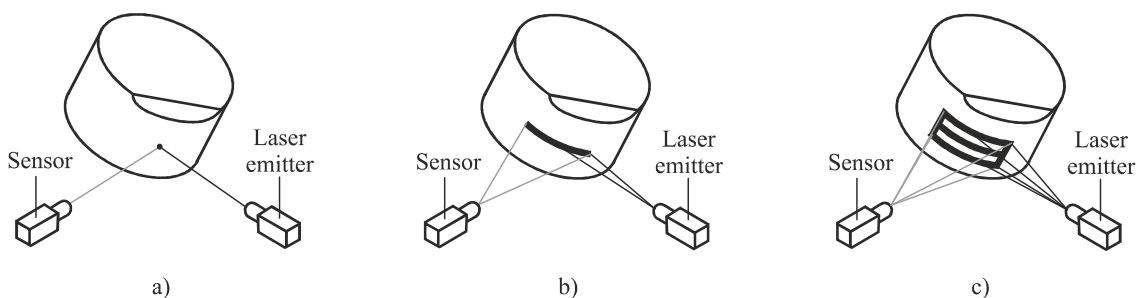


Figure 3.15. Triangulation scanner principle: a) point; b) line; c) pattern.

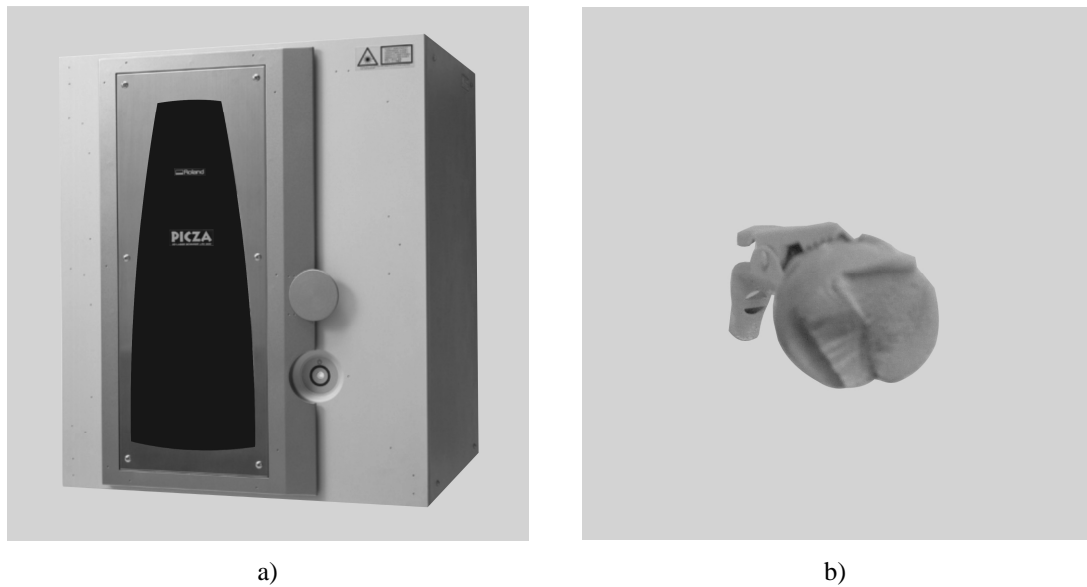


Figure 3.16. a) Roland Picza 3D Laser Scanner LPX-600; b) typical aspect of samples after painting.

Table 3.11. Scanning settings selected.

Scanned planes	Height-direction pitch [mm]	Width-direction pitch [mm]
6 (maximum)	0.2 (minimum)	0.2 (minimum)

replicating the fracture surfaces as accurately as possible. The Roland Dr.Picza 3TM software was used to control the entire process, i.e. settings definition, data acquisition, data storage and data editing.

3.10. Determination of the Paris law constants from fatigue crack front marks

The fatigue crack propagation properties are usually obtained using a well-established procedure (BS ISO 12108; ASTM E647) based on standard geometries, namely M(T) and C(T) specimens. However, these specimens cannot be easily produced when the available material has a small cross-sectional area. This is the case of circular shaped components, such as pins, bolts, wires, axles, shafts, etc. On the other hand, it is important to note that fatigue crack propagation results obtained from small cross-sectional specimens can differ considerably from standard specimens (Puigh, 1981; Sriharsha, 1999; Li, 2002). Therefore, alternative methodologies to evaluate the Paris law constants from small cross-section round bars would be interesting.

In this research, a new mixed numerical-experimental technique (MNET), able to determine the constants of the Paris law in round bars from the observation of fatigue crack marks on fracture surfaces, is proposed. As schematised in Figure 3.17, the technique encompasses three main steps. Firstly, at least two crack fronts are marked on the fracture surface of the specimen and the number of cycles between them is counted. Secondly, a representative 3D-FE fatigue crack growth model is used to predict the crack shape evolution and fatigue life. Thirdly, a comparison between the numerical and experimental results is carried out in order to find the constants that fit best the former to the latter results.

The experimental fatigue crack front marking tests were carried out by Yang *et al.* (2006). The material used was the S45 carbon steel. Its chemical composition and mechanical properties are presented in Tables 3.12 and 3.13, respectively. The tests were performed using the 12mm-diameter and 190mm-long round bar specimens presented in Figure 3.18. The initial crack shape consisted of a straight edge crack with 1mm depth and was created using a linear cutting machine. Both ends of the specimen, with diameters of 15mm and lengths of 50mm, were fixed to the grips of the testing machine through button-head connections.

A MST809 servo-hydraulic testing machine was used to apply the loading to the specimen. The tests were performed at room temperature, in load control, under a maximum cyclic tension of 25kN with 15Hz sinusoidal-wave form and stress ratio equal to 0.1. The shape and depth growth of fatigue cracks were monitored using a zoom stereomicroscope and crack front marking. The crack front marks were produced by changing the stress ratio, reducing the maximum applied load to one-half for several cycles.

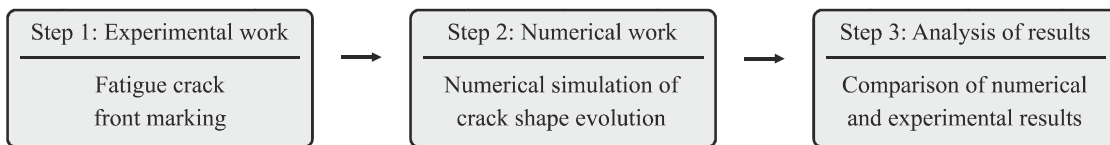


Figure 3.17. Mixed numerical-experimental technique proposed to calculate the constants of the Paris law.

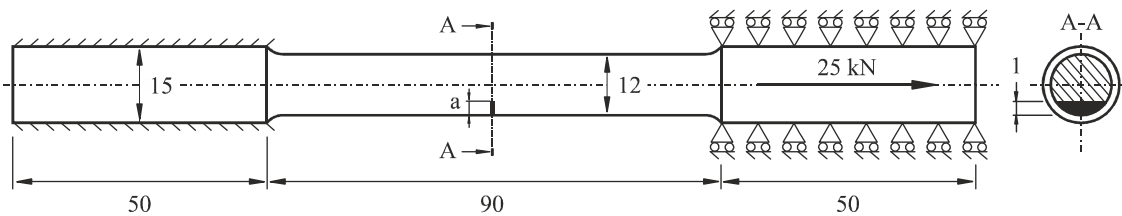


Figure 3.18. Specimen geometry used in crack front marking tests (Branco, 2012d).

Table 3.12. Nominal chemical composition of S45 carbon steel (wt%).

C	Mn	Ni	Cr	Mo	Si	P	S	Gu
0.4556	0.6490	0.0458	0.0735	0.0111	0.2310	0.0108	0.0132	0.1398

Table 3.13. Mechanical properties of S45 carbon steel at room temperature (Yang, 2006).

Property	Value
Ultimate tensile strength	775 MPa
Monotonic tensile yield strength	635 MPa
Young's modulus	206 MPa
Poisson's ratio	0.3
Fracture toughness	104 MPa·m ^{0.5}

Figure 3.19a exhibits the typical beach marks obtained in the fatigue crack marking tests. From the experimental data, several visible crack shapes, at different places of cross-section, were selected. The selection was based on a careful analysis of crack shape in terms of symmetry. The crack fronts used in the determination of C and m constants (1, 2, A and B) are presented in Figure 3.19b. Table 3.14 shows the polar coordinates (r, θ) of each one of them measured according to the referential schematised in Figure 3.19a. Only half of the crack front was analysed from which seventeen points were obtained. Table 3.15 exhibits the numbers of loading cycles applied experimentally between the different crack fronts

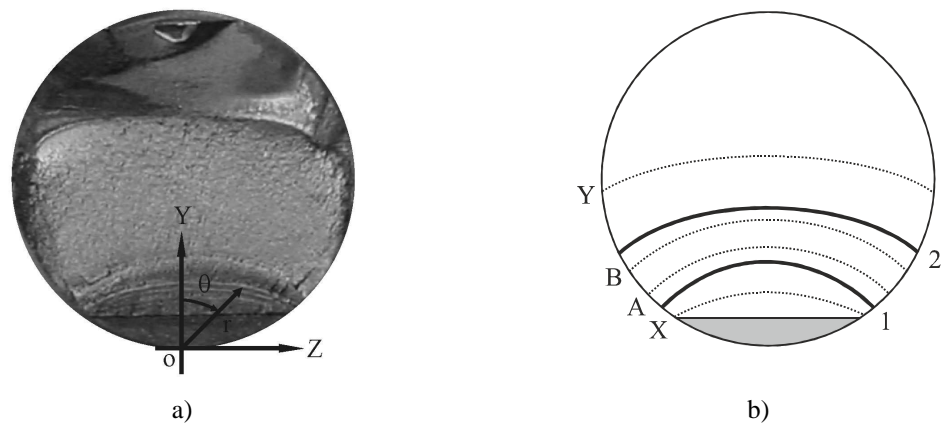


Figure 3.19. a) Fracture surface (initial crack of 1.0mm, 25kN cyclic tension loading); b) sketch of the visible crack fronts used (Branco, 2012d).

Table 3.14. Polar coordinates of the experimental crack shapes used (Branco, 2012d).

Visible crack shapes	1 ($a/D=0.253$)		2 ($a/D=0.418$)		A ($a/D=0.299$)		B ($a/D=0.383$)	
	θ [°]	r (mm)	θ [°]	r (mm)	θ [°]	r (mm)	θ [°]	r (mm)
Point, i								
1	0	3.036	0	5.020	0.000	3.597	0.000	4.598
2	5.036	3.041	4.520	5.019	4.878	3.609	4.465	4.593
3	10.081	3.065	8.642	5.054	9.666	3.635	8.857	4.615
4	15.092	3.081	12.855	5.089	14.451	3.661	13.251	4.654
5	20.065	3.121	16.951	5.133	19.235	3.700	17.644	4.694
6	25.184	3.179	21.128	5.191	24.024	3.752	22.037	4.757
7	30.103	3.235	25.287	5.279	28.809	3.813	26.429	4.819
8	35.125	3.285	29.415	5.370	33.596	3.892	30.822	4.902
9	40.068	3.364	33.558	5.469	38.382	3.978	35.215	5.004
10	45.082	3.468	37.752	5.584	43.168	4.074	39.609	5.102
11	50.019	3.569	41.873	5.717	47.954	4.196	44.002	5.213
12	55.028	3.679	46.023	5.862	52.741	4.305	48.396	5.346
13	60.008	3.809	50.116	6.024	57.525	4.448	52.788	5.482
14	62.791	3.883	52.099	6.103	59.918	4.513	54.985	5.541
15	65.000	3.949	54.234	6.199	62.312	4.581	57.182	5.602
16	67.643	4.038	56.124	6.276	64.514	4.650	59.343	5.680
17	70.060	4.109	58.068	6.381	66.717	4.718	61.505	5.752

Table 3.15. Number of cycles between the experimental crack fronts (Branco, 2012d).

Crack shape combination	Number of cycles
1-2	22953
1-B	40474
A-2	22953

analysed. Based on the experimental data, the fatigue crack growth rate calculated in depth direction was given by (Yang, 2006):

$$\frac{da}{dN} = 1.9037 \times 10^{-9} (\Delta K)^{3.256} \quad (3.6)$$

i.e., $m = 3.256$ and $C = 1.9037 \times 10^{-9}$ (da/dN [mm/cycle] and ΔK [$\text{MPa} \cdot \text{m}^{0.5}$]).

CHAPTER 4

NUMERICAL PROCEDURE

This chapter describes the numerical procedure. The two first sections present the numerical models developed to calculate the elastic constants of the material and to evaluate the stress and strain fields at the notch tip for the in-phase combined bending-torsion tests. The third section is concerned with the fatigue crack growth models implemented to study the crack shape evolution in notched and unnotched rectangular bars with corner cracks, notched and unnotched round bars with surface cracks, and notched and unnotched plates with through cracks. The three last sections address the strategies used to evaluate the extent of the surface region in cracked bodies; to develop a plane strain specimen; and to determine the Paris law constants from the analysis of crack front marks on fracture surfaces of small cross-section round bars.

NOMENCLATURE

a	crack length
a_0	initial crack length
ad	accumulated difference parameter
C	Paris law constant
D	diameter
E	Young's modulus
F_B	bending force
F_T	torsion force
FEA	finite element analysis
FEM	finite element method
f_i	resonant frequency
$f_{LB1,E}$	first experimental longitudinal bending frequency
$f_{T1,E}$	first experimental torsional frequency
$f_{LB1,N}$	first numerical longitudinal bending frequency
$f_{T1,N}$	first numerical torsional frequency
h, Θ	stress triaxiality parameters
IET	impulse excitation technique
L	length
LB1	first longitudinal bending resonant mode
L_i	radial size of the i^{th} element
MNET	mixed numerical-experimental technique
m	Paris law exponent
n	notch depth
N_i	number of elements on the i^{th} curve
N	number of loading cycles
r	notch radius
r_P	radial distance between the node P and the crack tip
S_{γ}^{ψ}	dimensionless sensitivity of the variable ψ to the parameter γ
T	original thickness
t	reduced thickness
T1	first torsional resonant mode
T_i	height of the i^{th} element
t_{pl} , t_{qm}	transformation matrixes
U	fraction of the loading cycle in which the crack remains fully open
W	width
ν	Poisson's ratio
η	notch angle
$\sigma_1, \sigma_2, \sigma_3$	principal stresses
σ_{ij}	stress tensor components
σ_H	hydrostatic stress
σ_{VM}	von Mises equivalent stress
λ	ratio of the torsion force to the bending force
$\delta_x, \delta_y, \delta_z$	displacement in the x, y and z directions
$\Delta a, \Delta a_{max}$	crack increment, maximum crack increment
$\Delta K, \Delta K_{max}$	stress intensity factor range, maximum stress intensity factor range

4.1. Determination of elastic constants

As mentioned in Section 3.3, the elastic constants were determined using a mixed numerical-experimental technique (MNET). This technique consists of three fundamental steps: firstly, the resonant frequencies are determined experimentally; secondly, a relation between the resultant experimental resonant frequencies and the values of the elastic constants is established; and thirdly, the elastic constants are calculated using an iterative procedure.

The first step was described in detail in Section 3.3. Briefly, the experimental resonant frequencies were determined by applying the impulse excitation technique (IET). A thin rectangular plate of uniform thickness was excited by a single external impulse being the vibration addressed to a personal computer and processed by a frequency analyser. The geometry used was the outcome of a preliminary numerical study carried out to obtain the highest sensitivities of the resonant frequencies to the elastic constants as well as to avoid overlapping of distinct resonant frequencies. Figure 4.1 exhibits the types of geometries analysed which were designed taking into account the shape constraint imposed by the material provided. The sensitivities of the resonant frequencies to the elastic constants were defined analytically, in a dimensionless form, to facilitate the comparison of results. The expression used is presented in Equation 4.1. In a literal sense, the sensitivity of the variable ψ to the independent parameter γ is denoted by S_{γ}^{ψ} and means that if γ is increased by 1 per cent, ψ increases by S_{γ}^{ψ} per cent.

$$S_{\gamma}^{\psi} = \frac{\partial \psi}{\partial \gamma} \cdot \frac{\gamma}{\psi} \quad (4.1)$$

Each sensitivity was calculated from three distinct finite element analyses (FEA) performed using different values of the independent variable. The pairs of points ψ - γ obtained for each independent variable were fitted to a second order polynomial function. From that function, the derivative $\partial\psi/\partial\gamma$ was calculated.

Table 4.1 presents the resonant frequencies (f_i) for the specimen geometries studied as well as the sensitivity (S_E^f) of the resonant frequency to the Young's modulus (E) and the sensitivity of the resonant frequency (S_{ν}^f) to the Poisson's ratio (ν). According to the calculations, it is possible to observe that the resonant frequencies are significantly higher for disks and round bars than for plates. However, a great resonant frequency can difficult signal acquisition since its amplitude is quite low. In view of this fact, plates are preferable than disks or round bars.

In relation to the sensitivities of the resonant frequencies to the Young's modulus, all geometries produced the same result, i.e. $S_E^f = 0.5$. Regarding the sensitivities of the resonant frequencies to the Poisson's ratio, the greatest value ($S_{\nu}^f = 0.17$) was obtained for the disk. Nevertheless, the resonant frequency is relatively high which is not suitable due to the reasons quoted above. Torsion modes ($i = 2$) of plates also have relatively high sensitivities to the Poisson's ratio ($S_{\nu}^f = -0.1105$ and $S_{\nu}^f = -0.1095$)

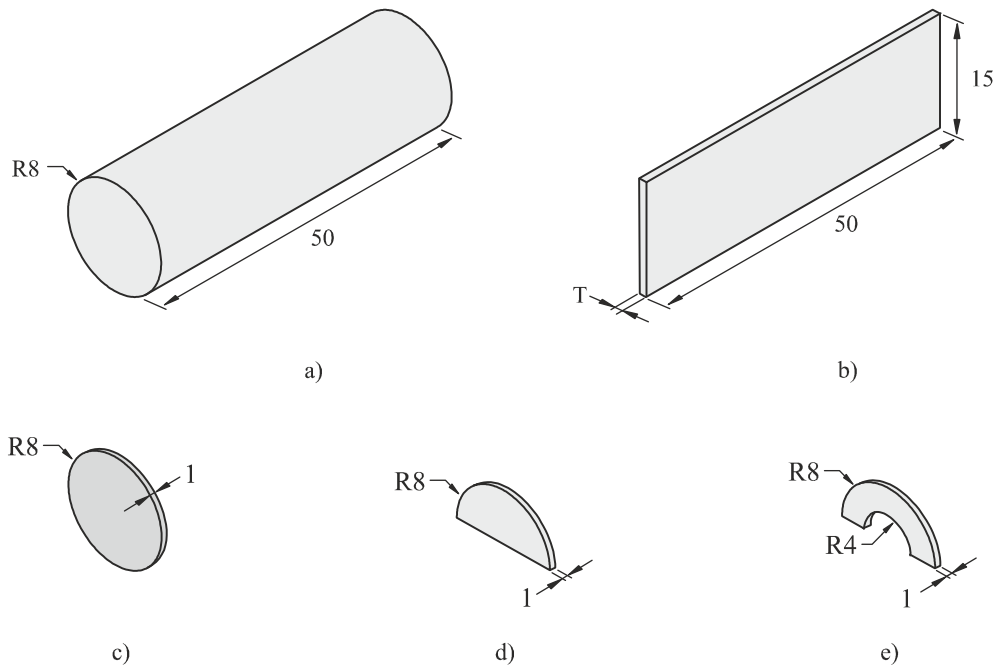


Figure 4.1. Types of specimen geometries analysed: a) round bar; b) rectangular cross-section plate; c) disk; d) half-disk; e) half-disk with hole.

Table 4.1. Sensitivities of the resonant frequencies to the Young's modulus and to the Poisson's ratio.

Resonant mode, i	$S_E^{f_i}$	$S_\nu^{f_i}$	Frequency, f_i [Hz]
Round bar			
1	0.5	-0.0093	23.938×10^3
2	0.5	-0.0257	52.120×10^3
Rectangular plate (T = 1mm)			
1	0.5	0.0067	2.131×10^3
2	0.5	-0.1095	4.258×10^3
3	0.5	0.019	5.895×10^3
Rectangular plate (T = 2mm)			
1	0.5	0.0055	4.242×10^3
2	0.5	-0.1105	8.241×10^3
3	0.5	0.015	11.631×10^3
Disk			
1	0.5	-0.0823	20.292×10^3
2	0.5	0.1700	33.894×10^3
3	0.5	-0.065	45.950×10^3
Half-disk			
1	0.5	-0.0070	26.236×10^3
2	0.5	-0.0871	34.976×10^3
3	0.5	-0.011	65.787×10^3
Half-disk with hole			
1	0.5	-0.0649	25.785×10^3
2	0.5	-0.0089	27.746×10^3
3	0.5	-0.002	44.405×10^3

along with resonant frequencies relatively low. Therefore, this kind of geometry is undoubtedly the best choice since it combines high sensitivities and low frequencies. It is important to refer that the increase in plate thickness has a reduced influence on the sensitivities but increases significantly the resonant frequencies. In order to reduce the magnitude of measurement errors, higher thicknesses are more interesting. Besides, regardless of the thickness, resonant frequencies are not overlapped.

The second step, as stated above, consists of establishing a relation between the experimental resonant frequencies and the values of the elastic constants. In a wider sense, resonant frequencies are influenced by different parameters, such as material properties, specimen geometry and boundary conditions. Assuming free-free boundary conditions, an isotropic material and a perfect rectangular plate, resonant frequencies (f_i) can be written as a function of the following variables

$$f_i = f(E, \nu, \rho, L, W, T) \quad (4.2)$$

being ρ the density, L the length, W the width and T the thickness. As is well-known, the FEM can be used to replicate the experimental tests. Nevertheless, resonant frequencies obtained numerically are affected by the type of element and by the average element size. In order to minimise these effects, sensitivity studies of the resonant frequencies to the type of element and to the average element size were done. The FE mesh used is exhibited in Figure 4.2a and was created with the pre-processor GeoStar 256K included in the commercial finite element package COSMOS/M (2001). It was developed using regularly spaced solid isoparametric elements ($50 \times 18 \times 2$ elements). The material was assumed to be homogeneous, linear elastic and isotropic. A perfect rectangular parallelepiped shape was assumed. The specimen was supported by low rigidity springs in order to simulate free-free boundary conditions. Figures 4.2b and 4.2c present, respectively, the first longitudinal bending (LB1) and the first torsional (T1) resonant modes obtained numerically using the FE model described.

Regarding the third step, the main objective is the calculation of the elastic constants. As referred to in Section 3.3, the method used here was based on a sensitivity analysis of the resonant frequencies to the material properties (Lauwagie, 2004; Antunes, 2008; Rébillat, 2011). According to the results presented in Table 4.1, the highest sensitivity of the resonant frequency to the Poisson's ratio was reached for the second resonant mode, which is the first torsional mode (Figure 4.2c). Therefore, this resonant mode was selected to determine the value of the Poisson's ratio. With respect to the Young's modulus and bearing in mind that sensitivities are not affected by the vibratory frequencies, it was evaluated from the first bending mode (Figure 4.2b).

The iterative procedure adopted to calculate the elastic constants from the resonant frequencies obtained experimentally is schematically depicted in Figure 4.3. In this procedure, the initial values of both elastic constants ($E^{(0)}$ and $\nu^{(0)}$) are defined by the user. However, it is important to note that the final values are independent of the initial ones. Then, the first numerical longitudinal bending frequency ($f_{LB1,N}$) and the sensitivity of LB1 to E ($\partial f_{LB1} / \partial E$) are calculated and subsequently used to update the value of the Young's

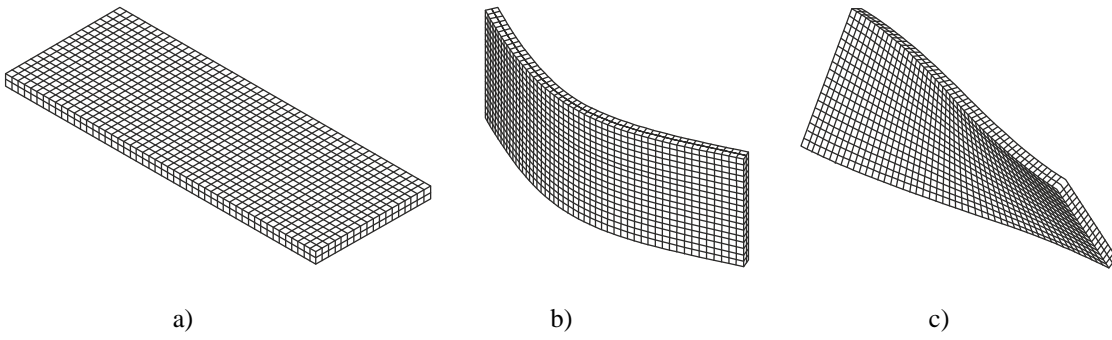


Figure 4.2. a) Three-dimensional finite element mesh; b) first longitudinal bending resonant mode (f_1); c) first torsional resonant mode (f_2).

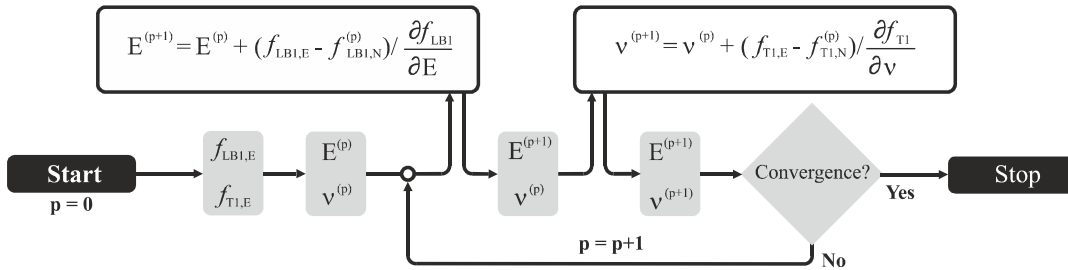


Figure 4.3. Algorithm of the iterative procedure used to calculate the elastic constants.

modulus ($E^{(p+1)}$). After that, the first numerical torsional frequency ($f_{T1,N}$) and the sensitivity of T1 to ν ($\partial f_{T1} / \partial \nu$) are calculated which allows an update of the value of the Poisson's ratio ($\nu^{(p+1)}$). These steps are repeated until convergence is achieved. One of the most interesting advantages of the present approach is the limited number of iterations required to obtain the elastic constants. The permanent and successive update of E and ν accelerates the convergence.

4.2. High-cycle fatigue tests

Fatigue failure is caused by extremely localised phenomena. This implies that the main local parameters, such as loading sequence, geometrical details, material properties, etc., must be determined as accurately as possible in order to achieve reliable fatigue life predictions. Among other methods, the FEM can provide a precise description of the local stress-strain state. As a result, it is extremely helpful to predict the region most susceptible to fatigue crack initiation. Thus, representative finite element models of the specimen geometries and loading paths studied experimentally in high-cycle fatigue tests (see Section 3.5) were developed to assess the local stress-strain states in the vicinity of the critical regions.

The physical models developed to replicate the single bending, single torsion and in-phase combined bending-torsion tests can be seen, respectively, in Figures 4.4a-c. The bending moments were applied by two forces parallel to the axis of the specimen with the same magnitude and opposite directions. The directions and points of application of this pair of forces were selected to ensure the opening of the notch,

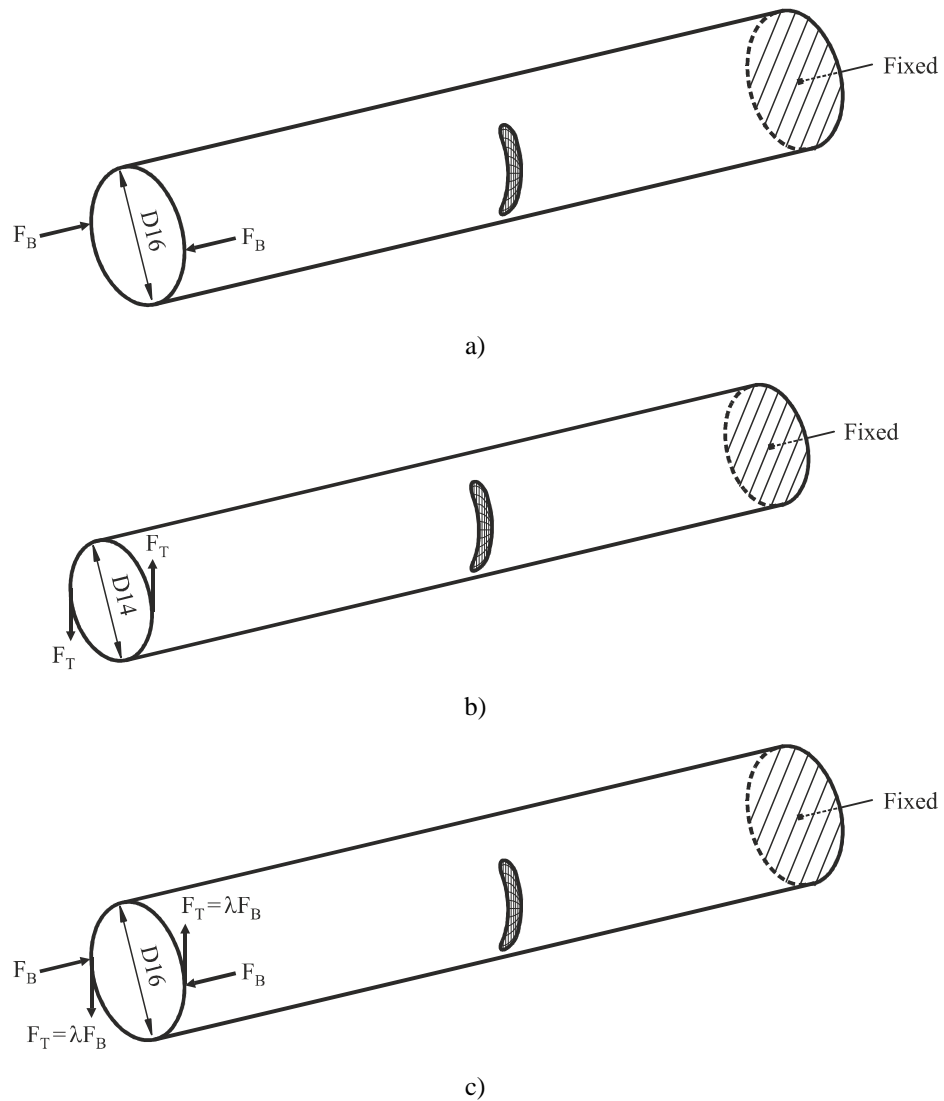


Figure 4.4. Physical models of the: a) single bending test; b) single torsion test; c) in-phase combined bending-torsion test.

i.e. the notch root was subjected to a positive bending stress. The torsion moments were created by a couple of forces with the same magnitude and opposite directions acting on a plane normal to the longitudinal axis of the specimen. The forces, in both cases, were applied at one end of the specimen while the other was fixed. The B/T ratios were defined by changing the value of λ which was equal to $1/2$, 1 and $3/2$ for the cases $B=2T$, $B=T$ and $B=2T/3$, respectively (Figure 4.4c). With respect to the specimen used in the single torsion tests, the cross-section was assumed to be constant (Figure 4.4b). The ends of the specimen were simplified due to their remote position relatively to the notch root.

Figure 4.5 schematises the procedure adopted to create the FE mesh. Firstly, a set of sixteen primary points were defined using Cartesian coordinates (Figure 4.5a). Secondly, the points were connected by straight lines. Thirdly, a new set of secondary points located at the surface of specimen was added. The geometric relation between the primary and secondary points is depicted in Figure 4.5b. In practice, as

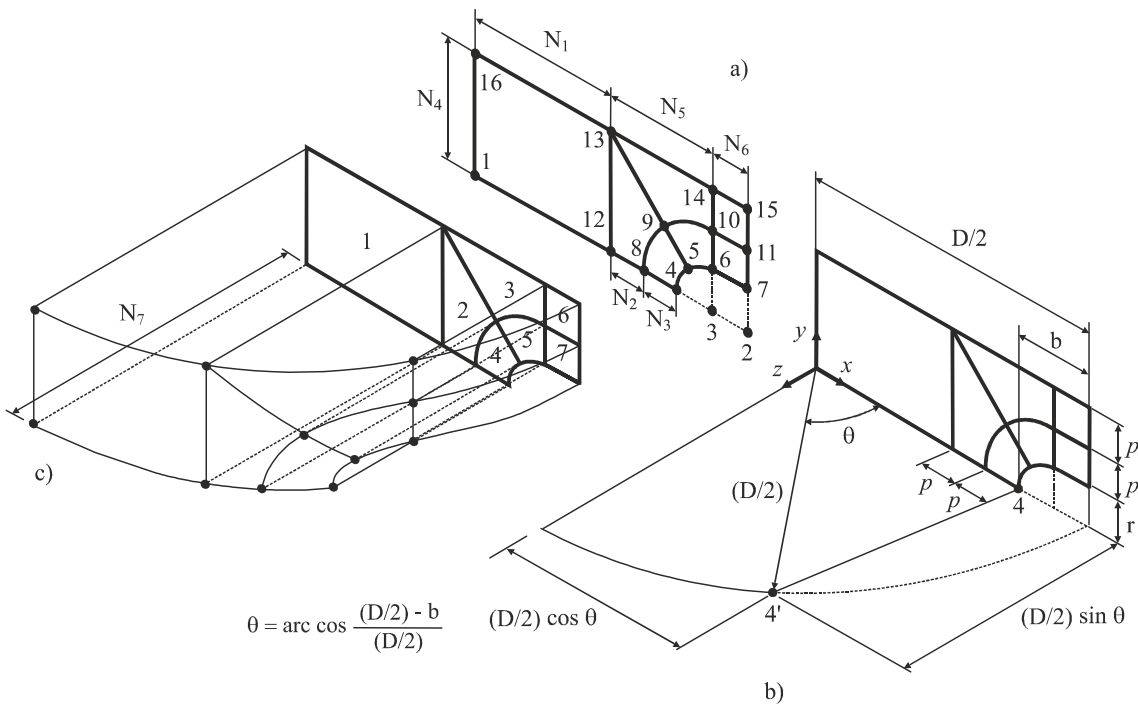


Figure 4.5. Schematic presentation of finite element mesh generation: a) primary points; b) relation between primary and secondary points; c) volumes of notched region.

illustrated to the points 4 and 4', the z-coordinates of the secondary points were placed on the surface of the specimen. Fourthly, new curves were created by joining the secondary points. Fifthly, from the straight lines and from the curves at the surface, seven volumes were defined (Figure 4.5c). Then, the three volumes above the notch, not depicted in the figure, were modelled. The following step was the generation of the unnotched part of the specimen which was done in a similar way. Next, all existing volumes were meshed. After that, the other three quarters of the specimen were generated by symmetry. Finally, the boundary conditions and loadings were defined for each case.

The FE mesh was developed parametrically which enabled the study of different notch depths (b) and notch radii (r). It was created with the pre-processor GeoStar 256K included in the commercial FEM package COSMOS/M (2001) using 3D 8-node isoparametric hexahedral elements. The assembled model, exhibited in Figure 4.6a, had 99823 nodes and 76608 elements. Figures 4.6b and 4.6c present magnifications of the notched region and of its middle-section, respectively. The mesh density resulted from a trade-off between accuracy and efficient computation. As can be seen, it is extremely refined near the notch region in order to achieve accurate results in that zone. In contrast, at remote positions, a coarser mesh was developed to reduce the computational effort.

The mesh was optimised in a systematic manner. The methodology adopted here was based on the principle that the stress field tends to stabilise with mesh refinement. In view of this fact, the starting point was a large mesh which was successively refined in the more sensitive regions. The initial mesh density is presented in Table 4.2 (N_1 to N_8 represent the number of elements on the curves identified in

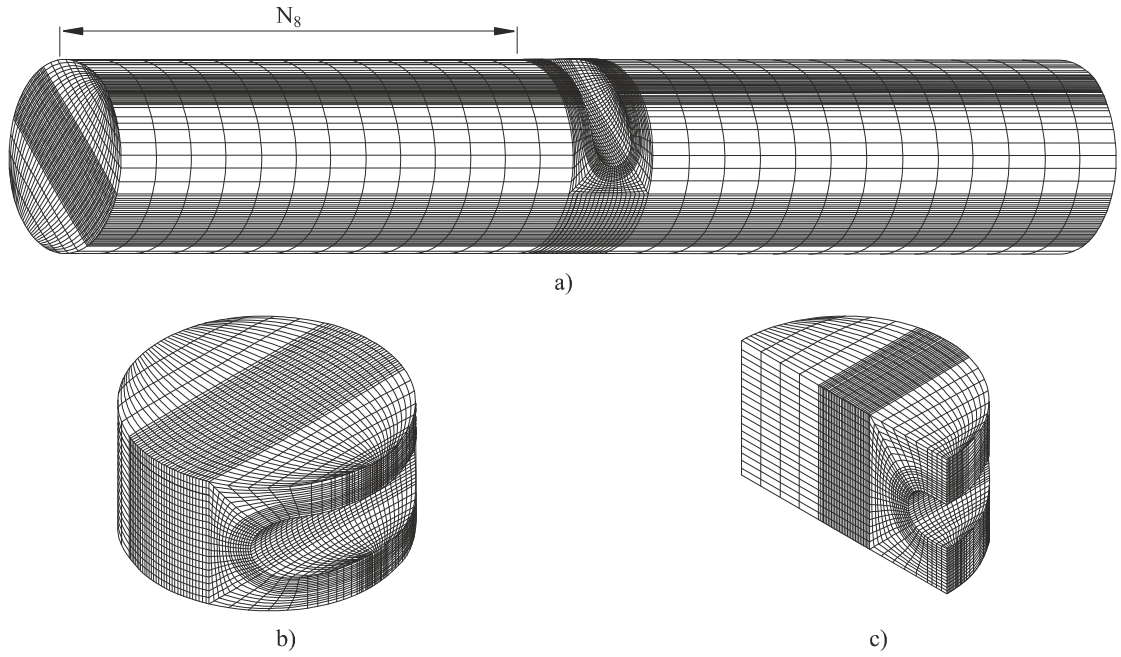


Figure 4.6. Finite element mesh: a) assembled model; b) detail of the notched region; c) detail of the middle-section of the notched region (Branco, 2012e).

Table 4.2. Initial and final densities of the finite element mesh.

Curve	N ₁	N ₂	N ₃	N ₄	N ₅	N ₆	N ₇	N ₈
Initial number of elements	6	6	12	12	6	6	12	6
Final number of elements	16	8	9	9	5	4	16	13

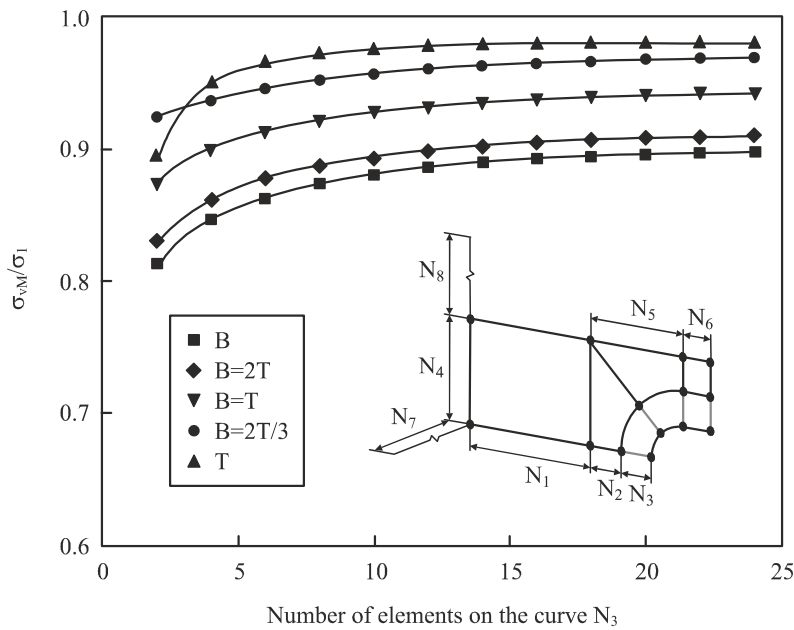
Figures 4.5a-b and 4.6a). The optimum value of elements in each curve, for the different loading paths studied, was determined by performing independent simulations. For a given curve, the number of elements varied within the interval 2-24, whilst the number of elements on the other curves remained constant. The parameter analysed, which is expected to be representative of the stress field, was the ratio of the von Mises equivalent stress (σ_{vM}) to the maximum principal stress at the notch (σ_1). The von Mises equivalent stress was computed from the following equation

$$\sigma_{vM} = \frac{1}{\sqrt{2}} \left[(\sigma_{xx} - \sigma_{yy})^2 + (\sigma_{xx} - \sigma_{zz})^2 + (\sigma_{zz} - \sigma_{yy})^2 + 6(\sigma_{xy}^2 + \sigma_{xz}^2 + \sigma_{zy}^2) \right]^{1/2} \quad (4.3)$$

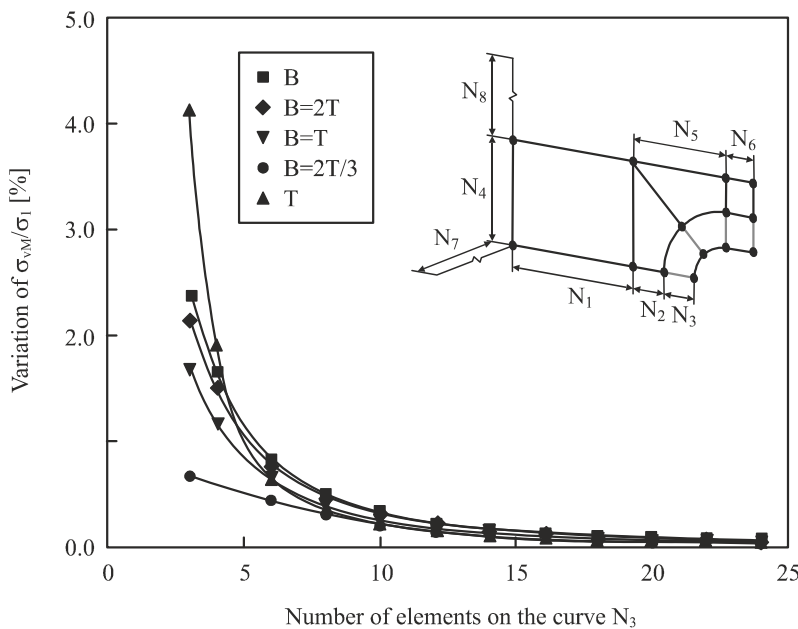
being σ_{ij} the components of the stress tensor. Figure 4.7a shows the evolution of σ_{vM}/σ_1 with the number of elements on the curve N_3 for the different loading paths studied. As observed, these ratios converge asymptotically to constant values. In view of this fact, the suitable number of elements on a given curve was calculated as the value from which the variation of the ratios for two consecutive analyses (i.e. with k and $k+1$ elements on the curve) was less than 0.35%. Figure 4.7b exhibits the variation of the σ_{vM}/σ_1 ratio with the number of elements on the curve N_3 for the different loading cases studied. From the results, it is possible to conclude that the variations decrease continuously towards zero with the number of elements;

and that the optimum value of elements on a given curve depends on the loading path. In order to simplify the numerical procedure, only a single mesh was adopted. The final number of elements is summarised in Table 4.2 and was defined as the maximum value found in the five loading situations for each curve.

The optimised mesh was subjected to a careful sensitivity analysis. Figure 4.8 presents the dimensionless sensitivities of the σ_{vM}/σ_1 ratio to the number of elements on the curves N_1 - N_8 for the different loading paths calculated using Equation 4.1. The small sensitivities obtained in the calculations, regardless of the



a)



b)

Figure 4.7. a) Evolution of σ_{vM}/σ_1 with the number of elements on the curve N_3 ; b) variation of σ_{vM}/σ_1 with the number of elements on the curve N_3 .

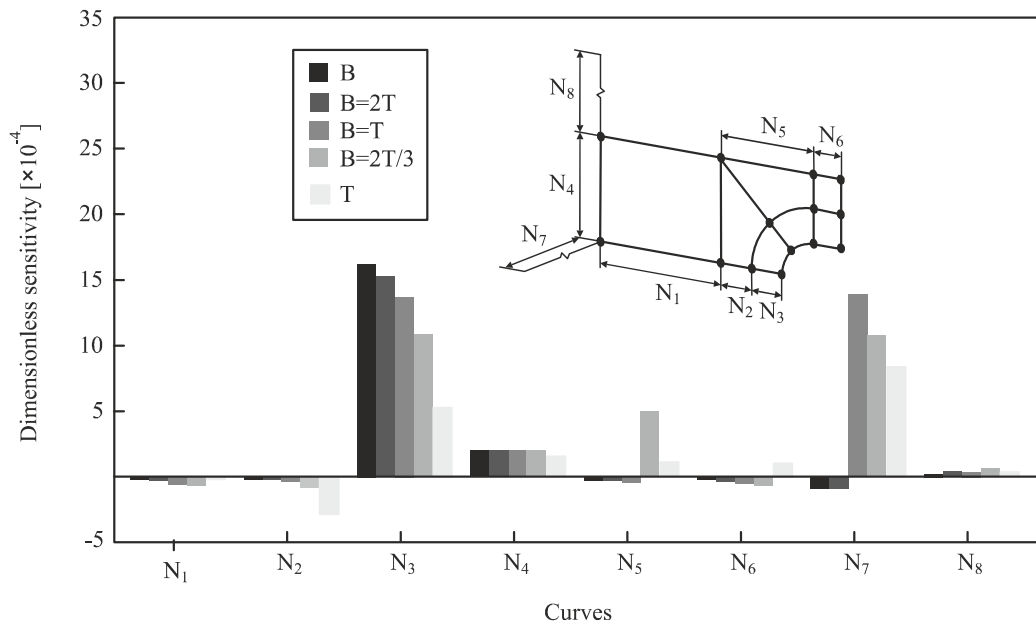


Figure 4.8. Dimensionless sensitivities of the σ_{vM}/σ_1 ratio to the number of elements on the curves N_i .

loading case, are clear indicator of an optimised mesh. Nevertheless, as expected, the curves that define the mesh density along the notch (N_3 , N_4 and N_7) are the most sensitive to the number of elements. This is reflected in greater values of dimensionless sensitivity. On the contrary, the curves away from that region are naturally less influent, as evidenced by the smaller dimensionless sensitivities.

The material was assumed to be homogeneous and isotropic with a linear regime described by its Poisson's ratio and Young's modulus. The numerical simulations were performed using the commercial FEM package COSMOS/M (2001).

4.3. Modelling of crack shape evolution

In the present study, the simulation of crack shape evolution was carried out by employing an automatic three-dimensional finite element technique (Smith, 1989; Lin, 1999). This approach, as stated in Section 2.7, comprises five main steps cyclically repeated as long as necessary. Firstly, a FE model with a representative crack shape is developed (Figure 4.9a). Secondly, the displacement field of the crack front nodes is computed (Figure 4.9b). Then, the stress intensity factors along the crack front are calculated (Figure 4.9c). After that, an adequate crack growth model is applied to define the crack front advances from which a new provisional crack front is established (Figure 4.9d). Finally, the corner and intermediate nodes are moved to their final positions using a cubic spline in order to enhance the crack front definition (Figure 4.9e). Due to the continuous repetition of the previous steps, the accuracy of each calculation must be optimised; otherwise errors propagate into the new steps leading to unreliable results.

The cracked geometries analysed here are illustrated in Figure 4.10 and encompassed unnotched and notched rectangular bars with corner cracks (Figures 4.10a-b); unnotched and notched round bars with

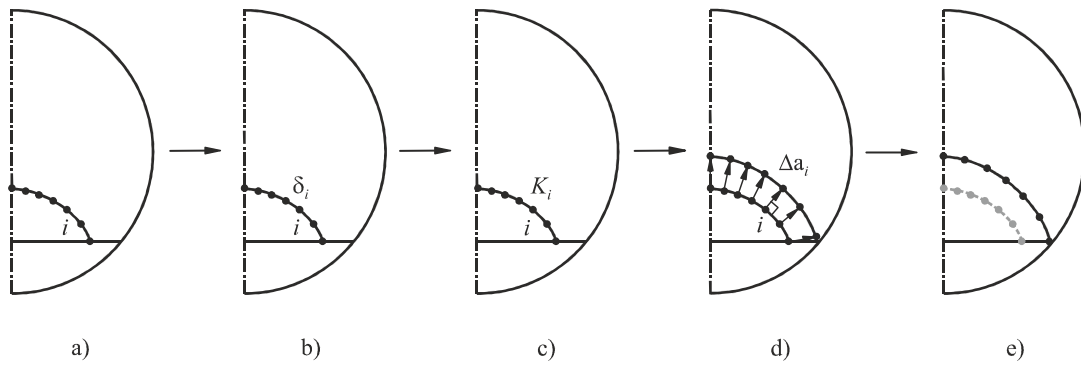


Figure 4.9. Schematic presentation of the 3D-FE fatigue crack growth technique used: a) definition of the crack front; b) calculation of the displacement field of crack front nodes; c) calculation of stress intensity factors along the crack front; d) calculation of nodal advances along the crack front; e) relocation of corner and intermediate nodes of the crack front.

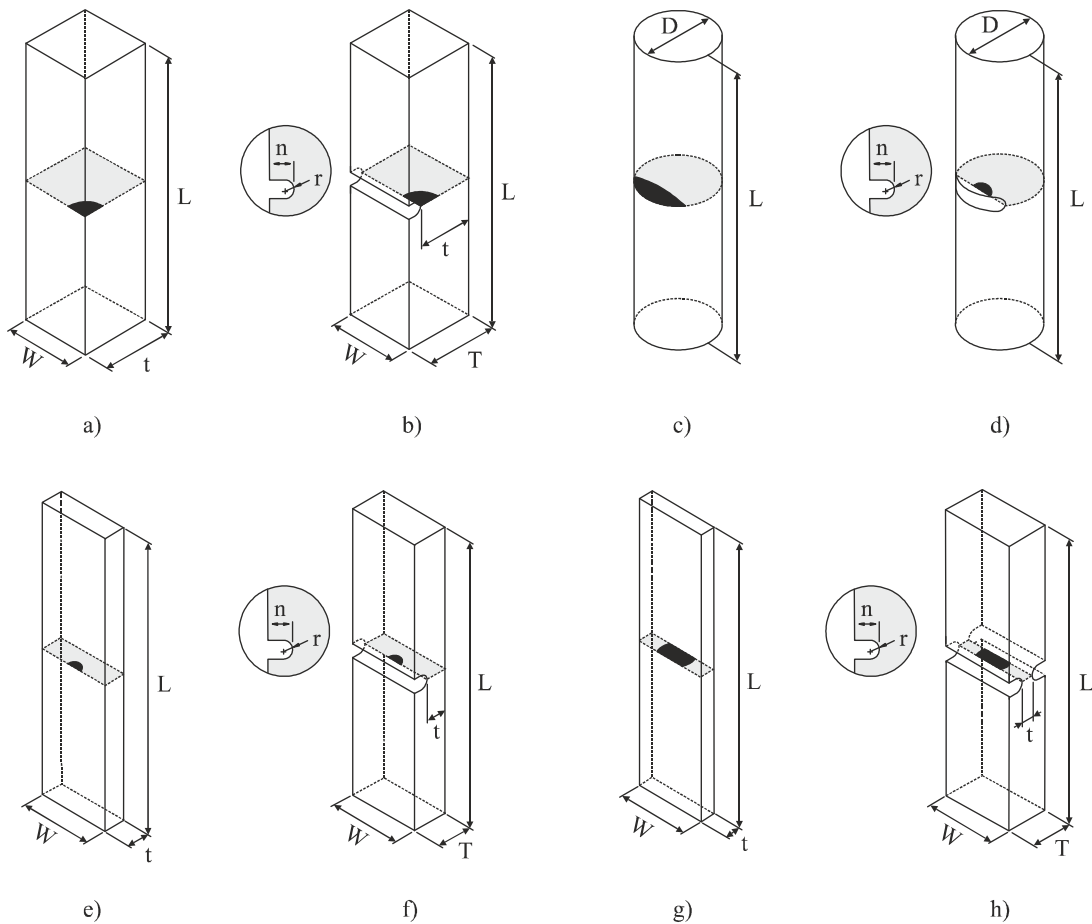


Figure 4.10. Geometries studied: a) rectangular bar with corner crack; b) notched rectangular bar with corner crack; c) round bar with surface crack; d) notched round bar with surface crack; e) plate with surface crack; f) notched plate with surface crack; g) plate with through crack; h) notched plate with through crack.

surface cracks (Figures 4.10c-d); unnotched and notched plates with surface cracks (Figures 4.10e-f); and unnotched and notched plates with through cracks (Figures 4.10g-h). The values of the physical variables used in the simulations, such as length (L), width (W), thickness at the crack plane (t), diameter (D), notch radius (r) and notch depth (n) are summarised in Table 4.3.

Figure 4.11 presents the physical models considered in the simulations. Symmetry conditions were used to reduce the computational time. For the geometries of Figures 4.10a-b, only half of the specimen was modelled (Figures 4.11a-b) by applying symmetries with respect to the y -axis ($\delta y = 0$). For the geometries of Figures 4.10c-f, only a quarter of the specimen (Figures 4.11c-f) was simulated. In these cases, symmetries with respect to the y -axis ($\delta y = 0$) and z -axis ($\delta z = 0$) were imposed. Regarding the geometries of Figures 4.10g-h, only one eighth of the specimen (Figures 4.11g-h) was modelled by defining symmetries with respect to the x -axis ($\delta x = 0$), y -axis ($\delta y = 0$) and z -axis ($\delta z = 0$). Additionally, in all cases, the movements along the x -axis ($\delta x = 0$) and along the z -axis ($\delta z = 0$) of the surfaces at the end of the specimens were restrained (from the grey line to the top) to simulate the constraint imposed by the high

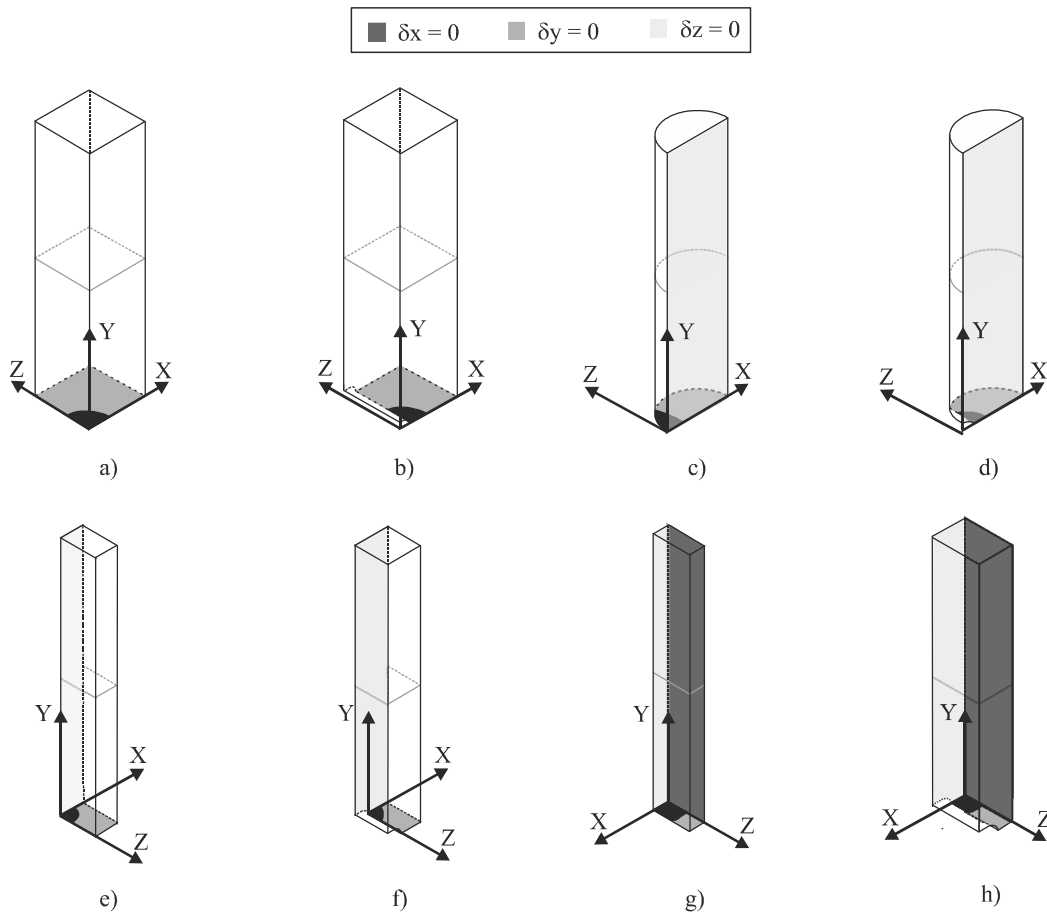


Figure 4.11. Physical models: a) rectangular bar with corner crack; b) notched rectangular bar with corner crack; c) round bar with surface crack; d) notched round bar with surface crack; e) plate with surface crack; f) notched plate with surface crack; g) plate with through crack; h) notched plate with through crack.

rigidity of the machine grips. The cracks were assumed to be planar, normal to the longitudinal axes of the specimens and existing in their middle-section. The material was defined homogeneous, isotropic and with a linear elastic behaviour. Dynamic loadings were applied at the top of the specimens. The remote tension and bending stresses were equal to 100MPa with a stress ratio $R=0.1$.

The finite element meshes were developed based on the methodology schematised in Figure 4.12. This approach, as recommended in Section 2.7.1, combines a *cracked* region and an *uncracked* region; and

Table 4.3. Physical dimensions used in simulations of crack shape evolution.

Geometry	L [mm]	W [mm]	t [mm]	D [mm]	r [mm]	n [mm]
Rectangular bar with corner crack	100-200	15	5-15			
Notched rectangular bar with corner crack	100-200	15	5-15		0.5-2	0.5-4
Round bar with surface crack	100-200			5-20		
Notched round bar with surface crack	100-200			5-20	0.5-2	0.5-4
Rectangular plate with surface crack	100-200	15	5-30			
Notched plate with surface crack	100-200	15	5-30		0.5-2	0.5-4
Plate with through crack	100-200	25	4-15			
Notched plate with through crack	100-200	25	4-15		0.5-2	0.5-4

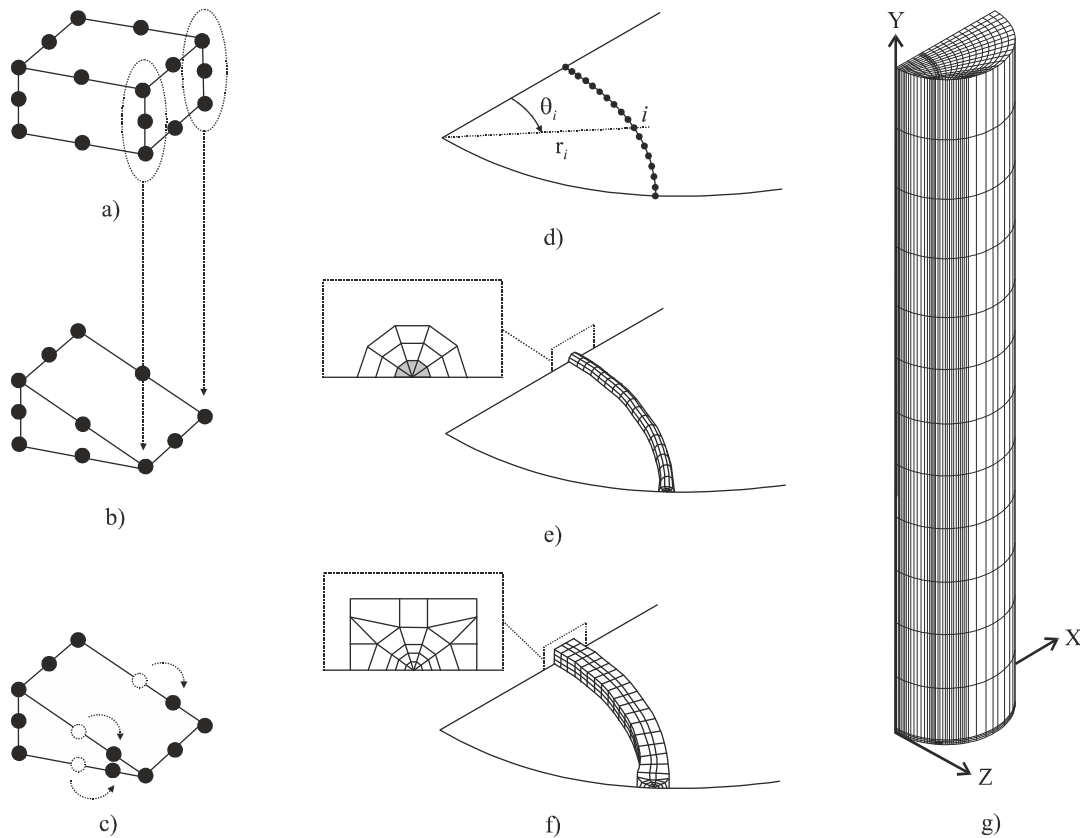


Figure 4.12. Methodology used to create the FE meshes for crack shape modelling: a) standard 20-node isoparametric element; b) collapsed 20-node isoparametric element; c) collapsed 20-node isoparametric element with intermediate nodes at quarter-point positions; d) crack front definition; e) spider web mesh; f) spider web and transition meshes; g) assembled model.

avoids the insertion of the crack *a posteriori* into the mesh of the uncracked model. The mesh was started from the crack, as depicted in Figure 4.12d. The crack front was divided into eighteen corner nodes (Figure 4.12d) and seventeen intermediate nodes. Either Cartesian or polar coordinate systems can be adopted. The spider web mesh consisted of three concentric rings with five elements arranged surrounding the crack tip (Figure 4.12e). The collapsed 20-node isoparametric element with intermediate nodes moved to quarter-positions (Figure 4.12c) was used in the first ring. The standard 20-node isoparametric element (Figure 4.12a) was employed in the other two rings. The layers of elements of the spider web mesh were oriented orthogonally to the crack front. A transition mesh aiming at promoting a smooth transition from a refined region to a relatively coarse region was added (Figure 4.12f). In general, this is achieved by creating a rectangular pattern. Here, the rectangular pattern was implemented combining standard 20-node isoparametric and collapsed 20-node isoparametric (Figure 4.12b) elements. The regular mesh (Figure 4.12g) was developed using the standard 20-node isoparametric element.

The pattern of Figure 4.13c was used to create the spider web and transition meshes. The angular discretisation of the elements surrounding the crack tip was equal to 36° . As postulated in Section 2.7.1, the minimum number of elements is five (Murti, 1986) with an angle about 30° (Guinea, 2000). The radial sizes and heights of those elements were controlled by the variables L_1-L_4 and T_1-T_3 , respectively. In the

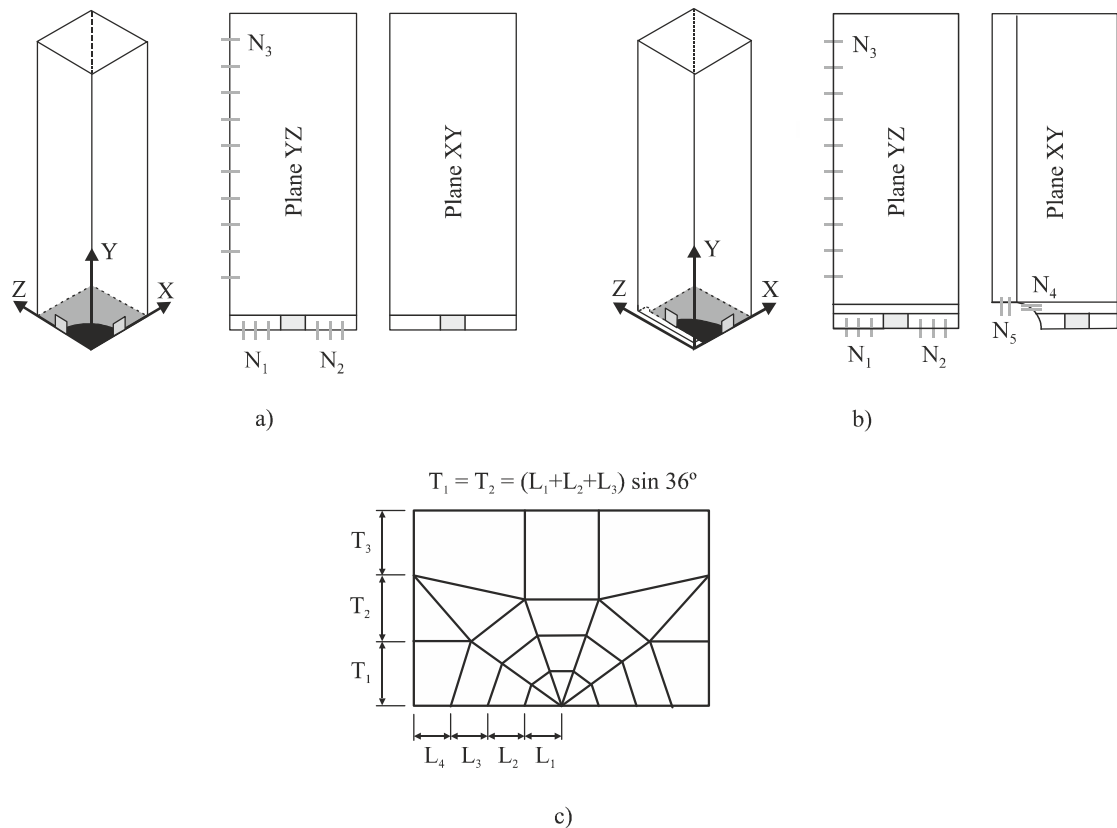


Figure 4.13. Definition of the: a) number of elements of the unnotched geometries; b) number of elements of the notched geometries; c) radial size of the elements of spider web and transition meshes.

unnotched geometries, the values of the variables T_1 - T_3 remained constant, being adopted the relation $T_1 = T_2 = T_3 = (L_1 + L_2 + L_3) \sin 36^\circ$. In the notched geometries, T_1 and T_2 were defined in the same way. However, the value of T_3 could be adjusted in order to make the mesh more flexible and adaptable to the notch size. The density of the regular mesh was specified from the variables N_1 - N_5 , which symbolise the numbers of elements on the curves (Figures 4.13a-b). The sum $N_1 + N_2$ was constant throughout each simulation. The values N_1 and N_2 were automatically calculated as a function of the crack length. For the notched geometries, the mesh was complemented by the values of N_4 and N_5 , which define the level of refinement near the notch. The former represents the number of elements between the transition mesh and the top of the notch, whilst the latter defines the number of elements in depth. These two variables change from case to case and are calculated in function of the notch radius (r) and notch depth (n).

Figure 4.14 presents a typical assembled FE mesh created for the notched plate with through crack. The values of the N_1 - N_5 variables, as well as the minimum numbers of elements and nodes used for the different geometries studied, are summarised in Table 4.4.

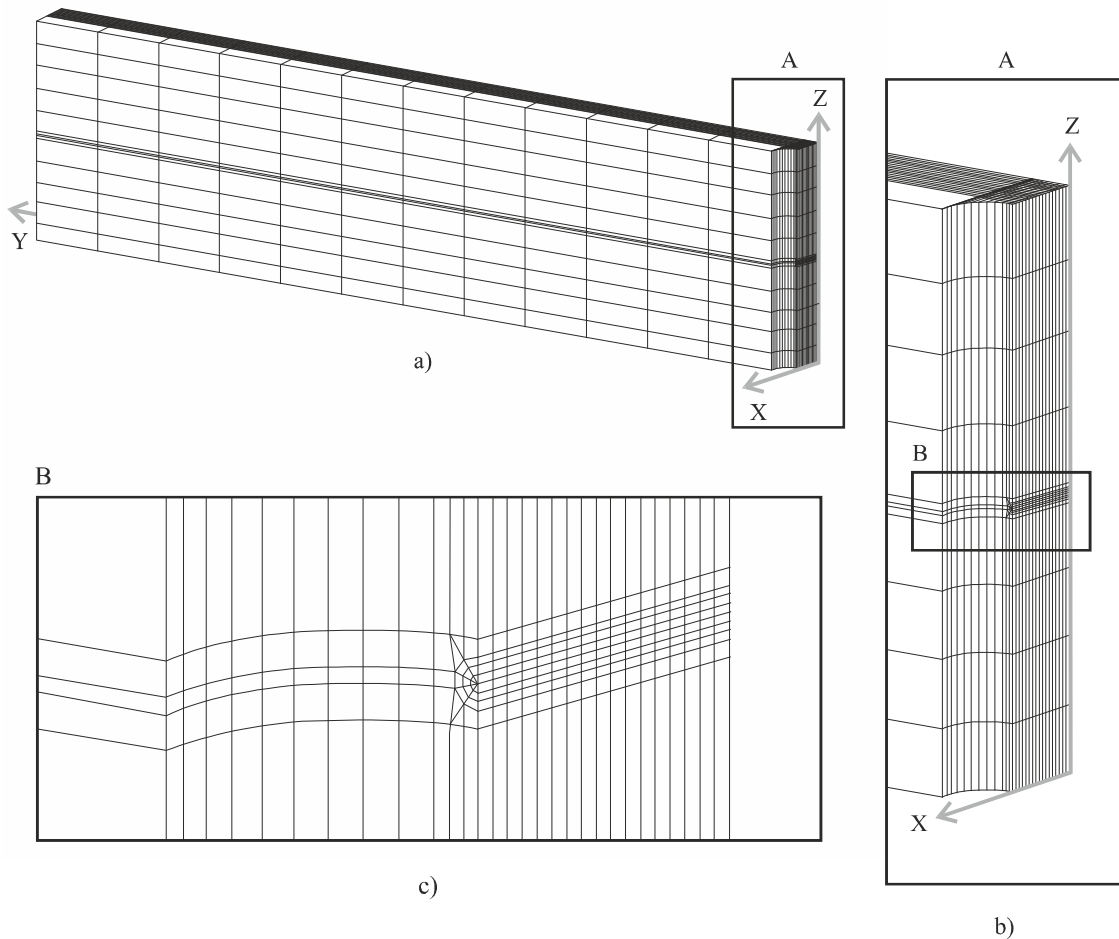


Figure 4.14. Typical FE mesh used in fatigue crack growth simulations for notched plates with through cracks ($r=1.75\text{mm}$, $n=2\text{mm}$, $t=7.5\text{mm}$, $L=200\text{mm}$, $2W=50\text{mm}$): a) general overview; b) detail of the notch; c) detail of the crack tip and the spider web mesh.

Table 4.4. Minimum numbers of elements and nodes used in FE meshes.

Geometry	$N_1 + N_2$	N_3	N_4	N_5	Elements	Nodes
Rectangular bar with corner crack	10	12			7032	68743
Notched rectangular bar with corner crack	10	12	4-10	2-10	7232	71743
Round bar with surface crack	10	12			7152	72631
Notched round bar with surface crack	10	12	4-10	2-10	7490	76210
Rectangular plate with surface crack	10	12			7032	68743
Notched plate with surface crack	10	12	4-10	2-10	7232	71743
Plate with through crack	10	12			7199	72842
Notched plate with through crack	10	12	4-10	2-10	7357	74469

The stress intensity factors along the crack front were calculated using the extrapolation method with two points. In such a method, as summarised in Figure 4.15a and explained in detail in Section 2.7.2, the K values are determined for two points (A and B) and extrapolated to the crack tip ($r=0$). In this research, the K values were estimated considering only the two first terms of the analytical expression for the displacement normal to the crack plane (see Equation 2.191). Therefore, for an arbitrary node P (Figure 4.15b), located on the upper face of the crack ($\theta = \pi$), the K value is defined by

$$K = \sqrt{\frac{\pi}{8r_p}} \times E' \times v_p \quad (4.7)$$

being r_p the radial distance between the node P and the crack tip, v_p the crack opening displacement and E' the modified Young modulus which is expressed as $E' = E/(1-\nu^2)$ in plane strain state and $E' = E$ in plane stress state. In order to simulate the linear elastic $r^{-0.5}$ stress singularity, the intermediate nodes of the elements surrounding the crack tip were moved to quarter-point positions (Figure 4.15b).

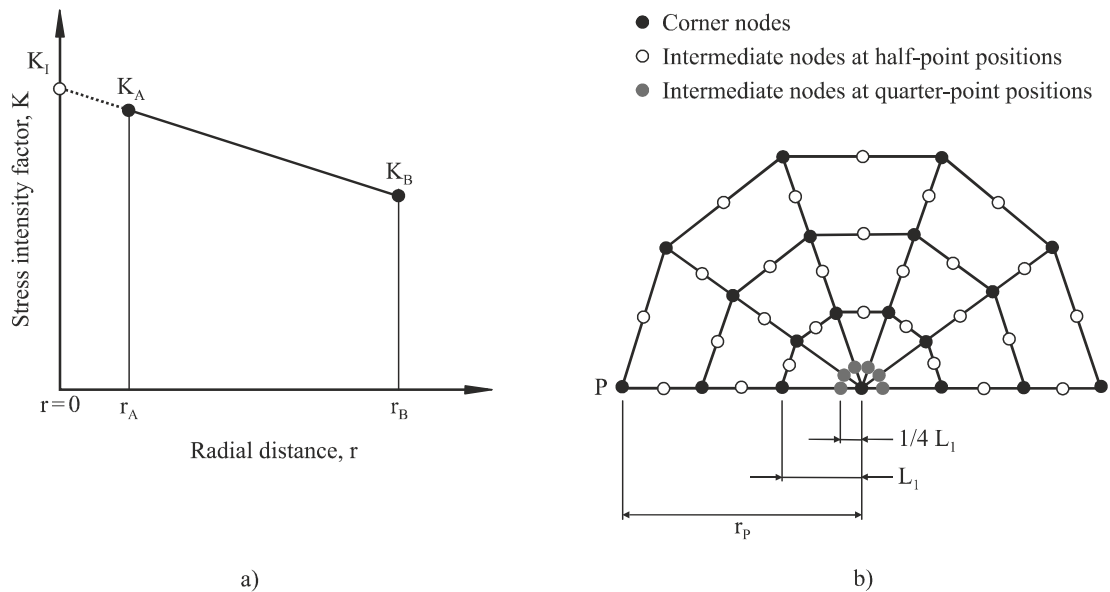


Figure 4.15. Schematic determination of stress intensity factors along the crack front using the extrapolation method with two points; b) identification of nodes moved to quarter-point positions.

The crack front was approximated by a cubic spline. In essence, it is a piecewise function that passes through a set of points (k), usually named *knots*. Therefore, for each interval, a cubic spline was established by applying the following expression

$$f_i(x_i) = \frac{f''(x_{i-1})}{6(x_i - x_{i-1})}(x_i - x)^3 + \frac{f''(x_i)}{6(x_i - x_{i-1})}(x - x_{i-1})^3 + \left[\frac{f(x_{i-1})}{x_i - x_{i-1}} - \frac{f''(x_{i-1})(x_i - x_{i-1})}{6} \right] (x_i - x) + \left[\frac{f(x_i)}{x_i - x_{i-1}} - \frac{f''(x_i)(x_i - x_{i-1})}{6} \right] (x - x_{i-1}) \quad (4.8)$$

being x_i and $f(x_i)$ the pairs of knots and $f''(x_i)$ the second order derivatives. This expression contains only two unknown variables (the second order derivatives at the end of each interval) which can be calculated by Equation 4.9. Thus, the application of the previous equation to all interior knots implies $k-1$ simultaneous equations and $k+1$ unknown second derivatives. However, because this is a natural cubic spline, the second derivatives at the end knots are zero and therefore the problem reduces to $k-1$ equations and $k-1$ unknown variables. Besides, the resulting system of equations is tridiagonal which is particularly quick and easy to solve.

$$(x_i - x_{i-1})f''(x_{i-1}) + 2(x_{i+1} - x_{i-1})f''(x_i) + (x_{i+1} - x_i)f''(x_{i+1}) = \frac{6}{(x_{i+1} - x_i)}[f(x_{i+1}) - f(x_i)] + \frac{6}{(x_i - x_{i-1})}[f(x_{i-1}) - f(x_i)] \quad (4.9)$$

The local crack increments of corner nodes for mode I loading, as schematised in Figure 4.16a, were calculated assuming that the propagation occurs along the direction normal to the crack front. For an arbitrary corner node i , the normal crack increment for the j^{th} iteration, derived from the Paris law (see Section 2.7.3), can be determined from the following equation

$$\Delta a_i^{(j)} = \left[\frac{\Delta K_i^{(j)}}{\Delta K_{\max}^{(j)}} \right]^m \Delta a_{\max}^{(j)} \quad (4.10)$$

being $\Delta a_i^{(j)}$ the crack growth increment of the i^{th} node for the j^{th} iteration, $\Delta a_{\max}^{(j)}$ the maximum crack growth increment for the j^{th} iteration, $\Delta K_i^{(j)}$ the SIF range of the i^{th} node for the j^{th} iteration, $\Delta K_{\max}^{(j)}$ the maximum SIF range for the j^{th} iteration, and m the Paris law exponent. The provisional corner nodes were used to draw a cubic spline on which both the corner and intermediate nodes were placed (Figure 4.16b). By comparing the provisional and final positions of the corner nodes, it is possible to conclude that the application of the cubic spline causes significant differences. These results were obtained for a notched circular bar with surface crack ($r = 1.98\text{mm}$, $n = 2\text{mm}$, $D = 16\text{mm}$, $L = 100\text{mm}$) using nine corner nodes uniformly disposed along the crack front and admitting a maximum crack advance $\Delta a_{\max} = D/50$. Besides, it is important to note that, as addressed in Section 2.7.1, the cubic spline promotes a smoother crack front

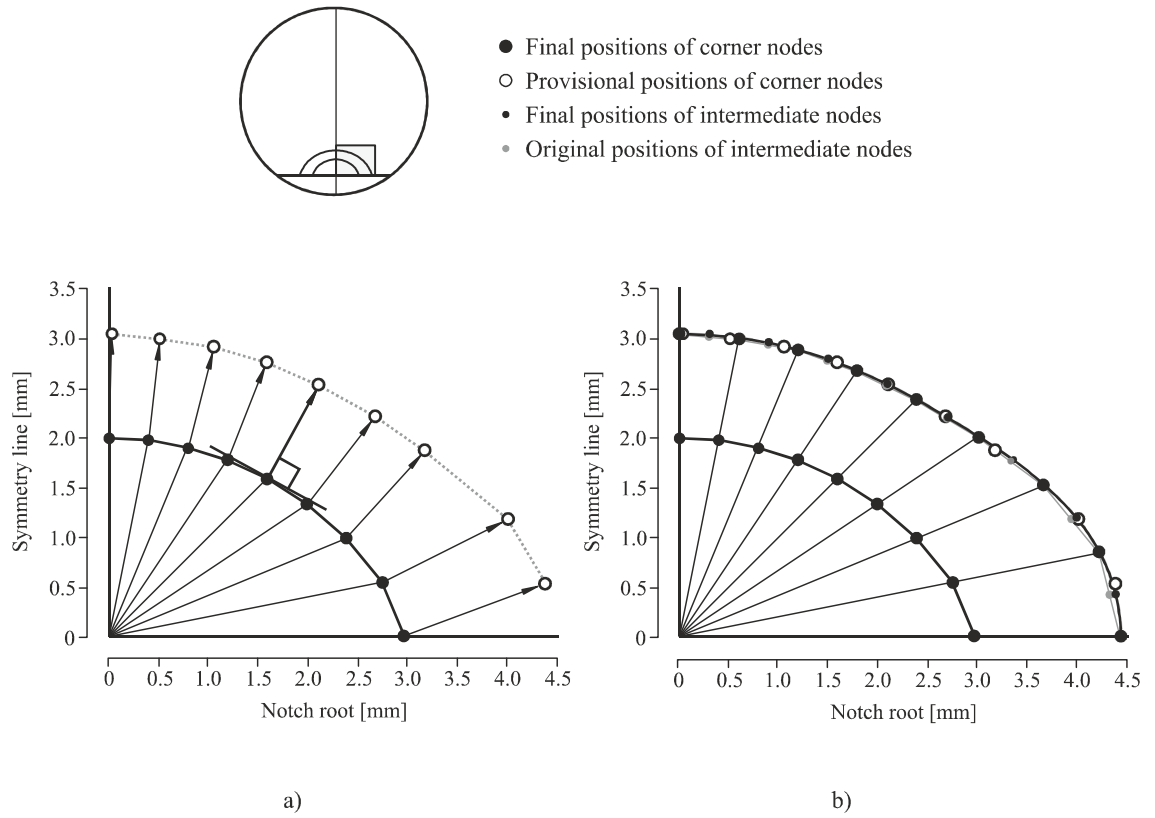


Figure 4.16. a) Calculation of local crack increments; b) positioning the corner and intermediate nodes by using a cubic spline function.

definition than the classical polygonal line (dashed line of Figure 4.16a) resulting in more accurate estimations of stress intensity factors as well as improved predictions of fatigue crack growth. Moreover, it is also important to note that the polygonal line approach is unable to ensure an automatic simulation since the end nodes are not properly located. In order to proceed, it would be essential a manual repositioning of these two nodes. On the other hand, the positions of the interior nodes cannot be controlled because each node moves freely. Contrarily, with a cubic spline, the simulation is fully automatic and the new corner nodes can be placed in any location provided that a criterion is defined. For example, in the case of Figure 4.16b, the new crack front maintains a uniform disposition of layers, i.e. the corner nodes are placed in specific locations separated from each other by $90/8^\circ$.

The number of cycles for the j^{th} iteration, derived from the Paris law and assuming a crack increment normal to the crack front, was calculated by the following equation

$$\Delta N^{(j)} = \frac{\Delta a_{\max}^{(j)}}{C(\Delta K_{\max}^{(j)})^m} \quad (4.11)$$

being C the Paris law constant. The effect of crack closure on fatigue crack growth was studied by considering an effective stress intensity range (ΔK_{eff}). For the i^{th} node of the j^{th} iteration, it was defined by Equation 4.12, where U_i represents the fraction of the load cycle for which the crack remains fully open.

$$\Delta K_{eff,i}^{(j)} = U_i \cdot \Delta K_i^{(j)} \quad (4.12)$$

Due to the variation of ΔK with the crack growth, an Euler integration algorithm was implemented in order to calculate the fatigue life. The number of cycles was computed by Equation 4.13.

$$N^{(j+1)} = N^{(j)} + \Delta N^{(j+1)} \Leftrightarrow N^{(j+1)} = N^{(j)} + \frac{\Delta a_{max}^{(j)}}{C(\Delta K_{max}^{(j)})^m} \quad (4.13)$$

4.4. Extent of surface region in cracked geometries

Finite elements meshes used in fatigue studies have a strong influence on the computational time and on the quality of the numerical results. An adequate modelling of the surface regions, among other aspects, is particularly important to perform accurate simulations. As is well-known, surface regions involve complex singularities (Bazant, 1979; Benthem, 1977). At corner points the singularity although existing is usually different from $r^{-0.5}$. Moreover, a relatively fast transition from plane stress state at the surface to plane strain state at interior positions is expected to occur. For example, the presence of lateral notches is expected to contribute to a faster transition; and surface phenomena such as crack closure, residual stresses, etc., have more intense effects near the surface. Therefore, in order to define FE models more sensitive and adjusted to the reality, it is necessary to know in advance the possible extent of the surface regions with the aim to incorporate them into the design.

The extent of the surface region was studied for unnotched and notched rectangular bars with corner cracks (Figures 4.10a-b); unnotched and notched round bars with surface cracks (Figures 4.10c-d); and unnotched and notched plates bars with through cracks (Figures 4.10g-h). This set of geometries was selected to cover a broad range of engineering situations. Note that it encompassed rectangular bars, round bars and plates as well as corner cracks, surface cracks and through cracks. The methodology adopted to carry out this study is schematised in Figure 4.17. Firstly, realistic crack shapes were obtained by employing the crack growth modelling technique described in the previous section (Figure 4.17a). After that, a representative crack front was selected (Figure 4.17b) with which a highly refined mesh was created for further analysis. Next, the stress field at the crack front (Figure 4.17c) was computed from the highly refined FE model developed. Finally, the values of triaxiality along the crack front (Figure 4.17d) were calculated and subsequently examined to quantify the extent of the surface region.

The fatigue crack growth simulations performed to obtain realistic crack shapes aimed at studying different geometrical variables, propagation conditions and loading types. Tables 4.5, 4.6 and 4.7 summarise, respectively, the various cases analysed for the unnotched and notched rectangular bars with corner cracks (Figures 4.10a-b); unnotched and notched round bars with surface cracks (Figure 4.10c-d); and unnotched and notched plates with through cracks (Figure 4.10g-h).

The refined meshes were developed in a similar way to the ones used in fatigue crack growth simulation, i.e. incorporating a spider web mesh, a transition mesh and a regular mesh. However, these new meshes were created with a high level of refinement towards the surface which was fundamental to accurately quantify the existing stress gradients in that region. Figure 4.18 shows a typical refined finite element mesh used ($r=1.5\text{mm}$, $n=2\text{mm}$, $D=16\text{mm}$, $L=200\text{mm}$). As can be seen, the crack front was divided into three main regions (Figure 4.18c). The most refined region (Region I), placed near the surface, consisted of 26 layers non-uniformly distributed. The smallest element size had $1\mu\text{m}$. The sizes of the other elements were defined from the relation $1 \times 1.1^{(i-1)} \mu\text{m}$ where i is the layer number ($i=1$ at the surface).

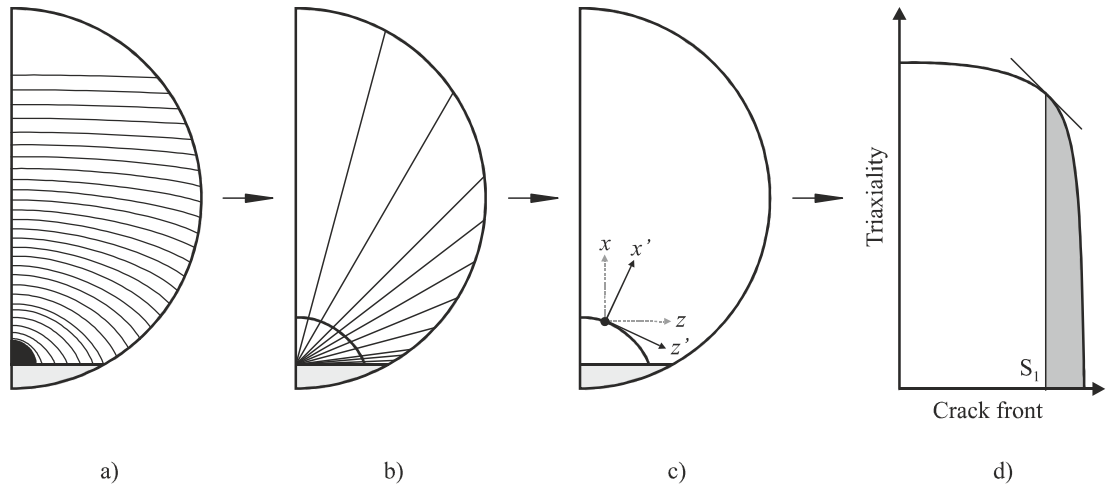


Figure 4.17. Methodology used to calculate the extent of the surface region: a) FCG simulation; b) creation of a refined 3D-FE mesh; c) calculation of the stress components at the crack front; d) computation of triaxiality parameters and analysis of results.

Table 4.5. Details of FCG simulations of the unnotched and notched rectangular bars with corner cracks.

Case	W [mm]	r [mm]	n [mm]	v	m	a_0 [mm]	Loading
Lateral notched specimen with corner crack ($L = 100\text{mm}$; $t = 12\text{mm}$; initial crack shape: quarter-circular)							
01, 02, 03	6, 7, 8	1.5	2	0.3	3	0.5	T
04, 05, 06	10	0.75, 1.0, 1.5	2	0.3	3	0.5	T
07, 08, 09, 10	10	0.5	0.75, 1, 2, 3	0.3	3	0.5	T
11, 12	8	1.5	2	0.3	2, 4	0.5	T
13, 14	6	1.5	2	0.3	3	0.5	B, B+T
15, 16	10	0.75	2	0.29, 0.31	3	0.5	T
17	10	0.5	4	0.3	3	0.5	T
18, 19, 20, 21, 22, 23, 24	5	0.5, 0.75, 1, 1.25, 1.5, 1.75, 2	2	0.3	3	0.5	T
25, 26, 27, 28, 29, 30, 31	7	0.5, 0.75, 1, 1.25, 1.5, 1.75, 2	2	0.3	3	0.5	T
32, 33, 34, 35, 36, 37, 38	10	0.5, 0.75, 1, 1.25, 1.5, 1.75, 2	2	0.3	3	0.5	T
39, 40, 41, 42, 43, 44, 45	14	0.5, 0.75, 1, 1.25, 1.5, 1.75, 2	2	0.3	3	0.5	T
Unnotched bar with corner crack ($L = 100\text{mm}$; $t = 12\text{mm}$; initial crack shape: quarter-circular)							
46, 47, 48, 49	5, 7, 10, 14			0.3	3	0.5	T

Table 4.6. Details of FCG simulations of the unnotched and notched round bars with surface cracks.

Case	t [mm]	r [mm]	n [mm]	v	m	a ₀ [mm]	Loading
Lateral U-notched round bar with surface crack (L = 100mm; initial crack shape: semi-circular)							
01, 02, 03	16	0.5, 0.65, 0.75	2	0.3	3	1	T
04, 05	8	0.5	2	0.3	3	1	B, B+T
06, 07, 08	8, 9, 10	0.75	2	0.3	3	1	T
09, 10	8	0.75	1, 1.5	0.3	3	1	T
11, 12	8	0.5	2	0.3	2, 3	1	T
13, 14, 15	12	1, 1.5, 2	2	0.3	3	1	T
16, 17	8	1.5	2	0.29, 0.31	3	1	T
18, 19, 20, 21, 22, 23, 24	6	0.5, 0.75, 1, 1.25, 1.5, 1.75, 2	2	0.3	3	0.75	T
25, 26, 27, 28, 29, 30, 31	8	0.5, 0.75, 1, 1.25, 1.5, 1.75, 2	2	0.3	3	0.75	T
32, 33, 34, 35, 36, 37, 38	12	0.5, 0.75, 1, 1.25, 1.5, 1.75, 2	2	0.3	3	0.75	T
39, 40, 41, 42, 43, 44, 45	16	0.5, 0.75, 1, 1.25, 1.5, 1.75, 2	2	0.3	3	0.75	T
Unnotched round bar with surface crack (L = 100mm; initial crack shape: part-circular)							
46, 47, 48, 49	6, 8, 12, 16			0.3	3	0.75	T

Table 4.7. Details of FCG simulations of the unnotched and notched plates with through cracks.

Case	t [mm]	r [mm]	n [mm]	v	m	a ₀ [mm]	Loading
Lateral U-notched plate with through crack (L = 100mm; 2W = 50mm; initial crack shape: straight)							
01, 02, 03	5	0.5, 1, 1.5	2	0.3	3	1	T
04, 05, 06	5, 7.5, 10	0.5	1	0.3	3	1	T
07, 08	5	0.5	2	0.3	2, 3	1	T
09, 10	5	0.5	1	0.3	3	1	B, B+T
11, 12	5	0.5	1	0.29, 0.31	3	1	T
13, 14	5	0.5	3, 4	0.3	3	1	T
15	2.5	1	4	0.3	3	1	T
16, 17, 18, 19	10	0.5, 1, 1.5, 2	2	0.3	3	0.5	T
20, 21, 22	2.5, 5, 7.5	0.5	2	0.3	3	0.5	T
23, 24, 25	5	0.5	1.5, 2.5, 4	0.3	3	0.5	T
26, 27	7.5	0.5	2	0.3	2, 4	0.5	T
28, 29	10	1.5	2	0.29, 0.31	3	0.5	T
30, 31, 32, 33, 34, 35, 36	2.5	0.5, 0.75, 1, 1.25, 1.5, 1.75, 2	2	0.3	3	0.5	T
37, 38, 39, 40, 41, 42, 43	5	0.5, 0.75, 1, 1.25, 1.5, 1.75, 2	2	0.3	3	0.5	T
44, 45, 46, 47, 48, 49, 50	7.5	0.5, 0.75, 1, 1.25, 1.5, 1.75, 2	2	0.3	3	0.5	T
51, 52, 53, 54, 55, 56, 57	10	0.5, 0.75, 1, 1.25, 1.5, 1.75, 2	2	0.3	3	0.5	T
Crack closure (U ₁ = 0.96, U ₂ = 0.98)							
58	5	0.5	1	0.3	3	1	T
Crack closure (U ₁ = 0.88, U ₂ = 0.9, U ₃ = 0.92, U ₄ = 0.94, U ₅ = 0.96, U ₆ = 0.98)							
59	5	0.5	1	0.3	3	1	T
Unnotched plate with through crack (L = 100mm; 2W = 50mm; initial crack shape: straight)							
60, 61, 62, 63	2.5, 5, 7.5, 10			0.3	3	1	T

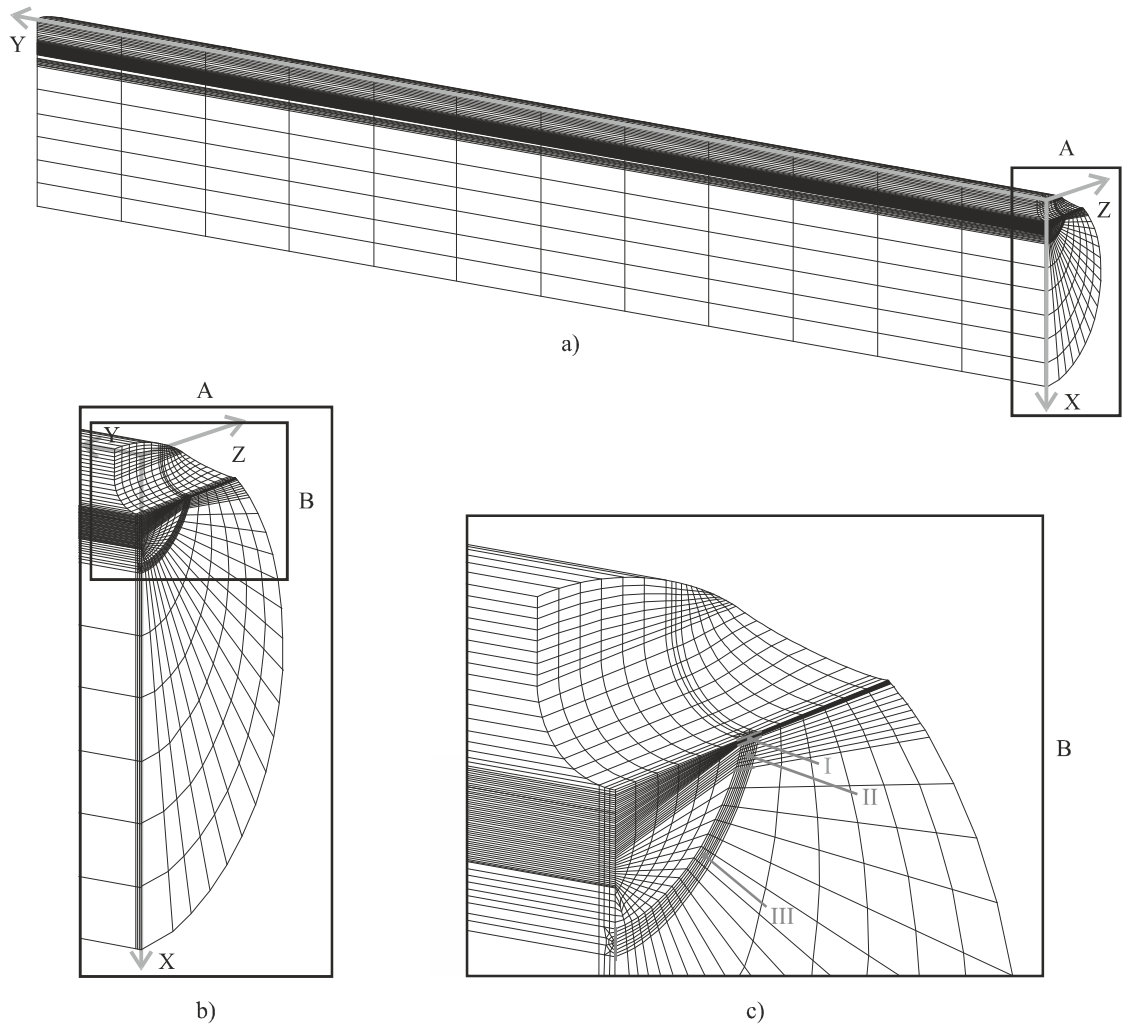


Figure 4.18. Typical refined FE mesh used to evaluate the extent of the surface region for the notched round bar with surface crack: a) general overview; b) detail of notch; c) detail of layer refinement.

The intermediate region (Region II) had 14 layers uniformly distributed with longitudinal sizes of $50\mu\text{m}$. The larger region (Region III) was created with 10 layers, also uniformly distributed, which filled the rest of the crack front.

The stress field at the crack front was computed using the application GeoStar 256K included in the commercial FEM package COSMOS/M (2001). For each crack front node (corner and intermediate), the stress tensor employed to calculate the extent of the surface region was obtained with respect to a local coordinate system ($X'Y'Z'$) whose axes X' and Y' (Figure 4.19) were normal and tangent to the crack front, respectively. The local stress tensor (σ'_{pq}) was determined by applying the transformation law for second order Cartesian tensors given by the following equation

$$\sigma'_{pq} = t_{pl} t_{qm} \sigma_{lm} \quad (4.14)$$

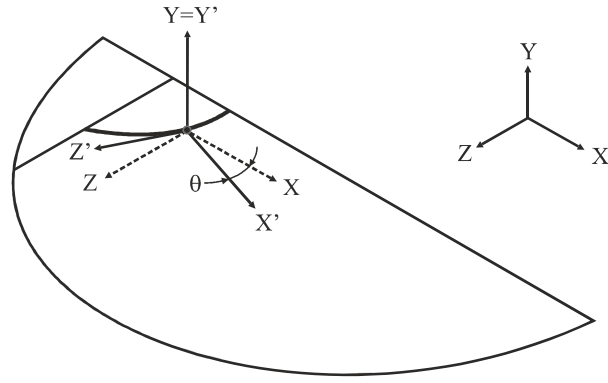


Figure 4.19. Relation between the global and local Cartesian coordinate systems defined to calculate the stress tensors of the crack front nodes.

being t_{pl} and t_{qm} transformation matrixes, σ_{lm} the stress tensor given by the software with respect to the global coordinate system (XYZ), and θ the rotation angle between the global and local Cartesian coordinate systems. The transformation matrix for a rotation about the Y-axis, as schematised in the previous figure, is given by Equation 4.15. A specific algorithm, written using the Visual Basic language, was developed to compute the rotated stress tensors and principal stresses of all corner and intermediate nodes of the crack front.

$$t_{pl} = t_{qm} = \begin{bmatrix} \cos \theta & 0 & -\sin \theta \\ 0 & 1 & 0 \\ \sin \theta & 0 & \cos \theta \end{bmatrix} \quad (4.15)$$

The extent of the surface region (Figure 4.17d) was evaluated from stress triaxiality parameters. In this study, the widely used Θ and h stress triaxiality parameters were selected. The former, probably the most used in the scientific literature, is defined as the ratio of the average hydrostatic stress (σ_H) to the equivalent von Mises stress (σ_{vM}) and can be expressed by (Chandrakanth, 1995)

$$\Theta = \frac{\sigma_H}{\sigma_{vM}} = \frac{\frac{1}{3}(\sigma_1 + \sigma_2 + \sigma_3)}{\frac{1}{\sqrt{2}}\sqrt{(\sigma_1 - \sigma_2)^2 + (\sigma_2 - \sigma_3)^2 + (\sigma_3 - \sigma_1)^2}} \quad (4.16)$$

being σ_1 , σ_2 and σ_3 the principal stresses. The latter represents the ratio of the out-of-plane stress to the sum of the in-plane normal stress components multiplied by the Poisson's ratio and can be written mathematically by (MacDonald, 1990)

$$h = \frac{\sigma_{YY}}{\nu(\sigma_{XX} + \sigma_{ZZ})} \quad (4.17)$$

where σ_{XX} , σ_{YY} and σ_{ZZ} are the normal stresses (calculated with respect to the local coordinate system).

4.5. Definition of a plane strain specimen

Stress state is a main parameter within fracture mechanics since it influences different phenomena, namely those involving diffusion (hydrogen embrittlement, high temperature fatigue crack growth), plastic deformation (ductile fracture, plasticity induced crack closure), and brittle fracture. Besides, in the near-surface regions of a crack front, the plane stress state dominates whilst at interior positions the plane strain state prevails. The isolation of the plane stress state is usually achieved with relatively thin specimens while the study of plane strain situations is performed with relatively thick specimens.

A pure plane strain specimen would be quite interesting to study all the above-mentioned phenomena. A simple way to develop such a specimen is the inclusion of lateral side grooves. This approach has been followed by different authors in order to introduce triaxial stress states. Mostovoy *et al.* (1967) developed a tapered double cantilever beam (TDCB) with lateral side grooves and the particularity of having constant K . Freed *et al.* (1966) studied side grooved specimens and proposed a modified expression to calculate fracture toughness. The specimen thickness (B) in the expression of the ASTM E399 standard, was replaced by $(B \times B_N)^{1/2}$, where B_N is the net thickness at the narrowest part of the side-groove. MacDonald *et al.* (1990) suggested the use of side grooves for fracture toughness specimens in order to meet the crack front straightness requirements. Compact tension specimens (C(T)) with lateral side grooves were used to study creep crack growth in a nickel-base superalloy at 600°C (Branco, 1999). An acceleration of crack growth was observed compared to normal C(T) specimens. Josefson *et al.* (2000) used four-point-bend specimens with V-lateral side grooves to study the effect of variable amplitude loading on crack closure level and fatigue crack growth rate under plane strain conditions. Trattnig *et al.* (2008) studied the effect of stress triaxiality ratio on fracture behaviour by using different geometries, namely C(T) specimens with lateral side grooves and circumferentially cracked cylindrical specimens. However, since there are no standards defining the lateral grooves, all of them have been fixed empirically. Therefore, the main objective here is the development of a grooved geometry able to isolate the plane strain state at a controlled level.

The geometry selected was a standard middle-crack tension specimen with lateral U-shaped (Figure 4.20b) or V-shaped (Figure 4.20c) grooves. The lateral grooves were introduced to isolate the plane strain state. Both configurations are easy to produce and ensure high reproducibility. Such features are particularly important from an experimental point of view. The main geometrical variables are identified in Figure 4.20. The reduced thickness (t) is given by the relationship $t = T - 2n$. Note that U-shaped grooves can be considered a particular case of V-shaped grooves with a notch angle (η) equal to zero.

The methodology adopted was identical to the one described in the preceding section (Figure 4.17) but conducted in the modified M(T) specimen. Firstly, realistic crack shapes were obtained by using an automatic fatigue crack growth technique. In order to achieve efficient computation, the physical model consisted of only one eighth of the specimen (Figure 4.11h). The simulations were carried out from

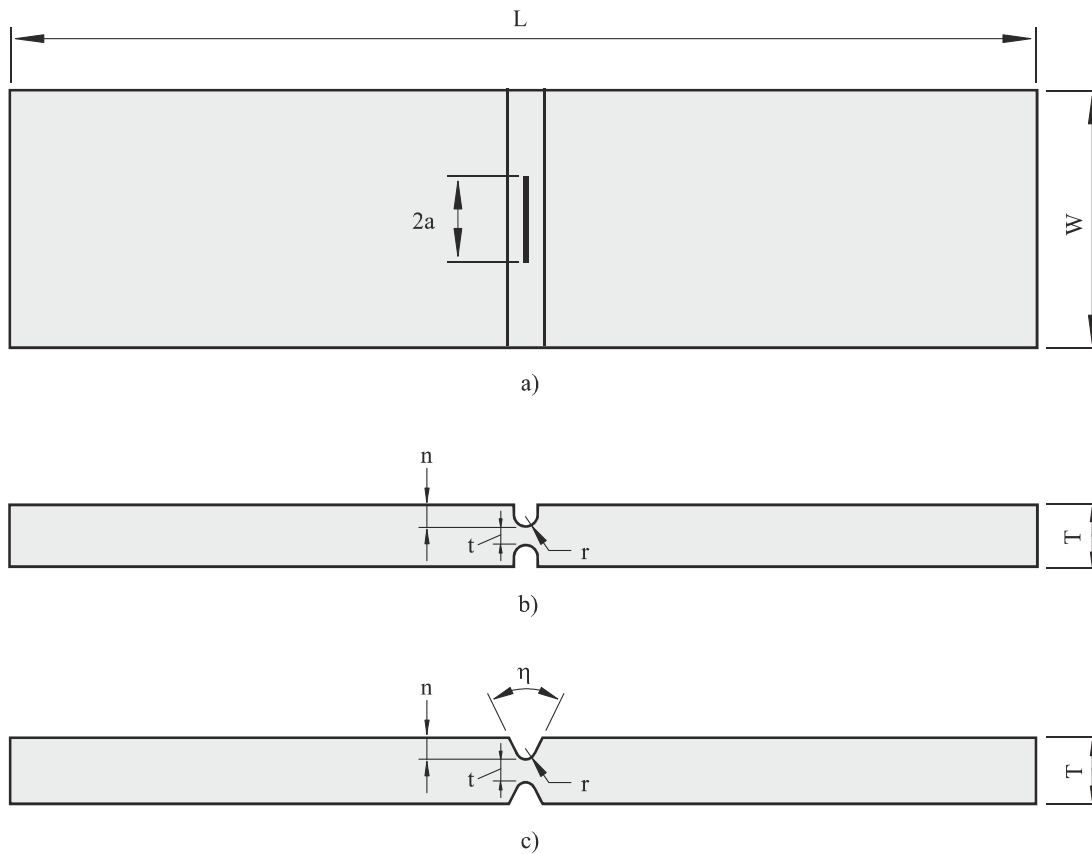


Figure 4.20. a) Grooved M(T) specimen; b) U-shaped groove; c) V-shaped groove (Branco, 2010a).

straight cracks with an initial depth (a_0) equal to 0.5mm and covered different notch geometries in terms of radius, depth and angle, different elastic constants and different fatigue crack growth rates. Table 4.8 lists the cases studied. The refined meshes, as exhibited in Figure 4.21, followed the approach set out in Section 4.4. As can be seen, the three levels of refinement towards the thickness were created (Figure 4.21d). Particularly the rather fine mesh placed at the surface was extremely important to capture the high stress gradients of that region. The stress field was computed using the application GeoStar 256K included in the commercial FEM package COSMOS/M (2001). Then, the stress components of the crack front nodes were calculated with respect to a local coordinate system (Figure 4.19) through Equation 4.14. Finally, the Θ and h stress triaxiality parameters were computed for all corner and intermediate nodes of the crack front. From the results collected, alternative specimen geometries with different levels of triaxiality were proposed.

Many studies of fatigue have been performed in M(T) specimens assuming straight crack shapes. In view of this fact, a parallel study was conducted using straight crack shapes (i.e. no fatigue crack propagation was carried out). This was important to understand the effect of the crack shape on the final dimensions of the plane strain specimen. Figure 4.22 depicts the three main steps of the simplified procedure. The first step (Figure 4.22a) consists of creating a refined mesh with a straight crack shape. After that, the stress

Table 4.8. Details of FCG simulations ($L=200\text{mm}$, $2W=50\text{mm}$, $a_0=0.5\text{mm}$).

Case	$t = T-2n$ [mm]	r [mm]	n [mm]	v	m	η [°]
1, 2, 3, 4	2.5, 5, 7.5, 10	0.75	2	0.3	3	0
5, 6, 7, 8	5	0.5, 0.75, 1, 1.5	2	0.3	3	0
9 [M(T)]	5			0.3	3	
10	5	0	2	0.3	3	90
11, 12, 13, 14	5	0.5	0.5, 0.75, 1.5, 4	0.3	3	0
15, 16, 17	5	0.5	2	0.3	3	0, 60, 90
18, 19	5	0.5	2	0.3	2, 4	0
20, 21	2.5	0.75	2	0.28, 0.32	3	0
22	1.25	1.98	2	0.3	3	0
23, 24, 25, 26, 27, 28, 29, 30	2.5, 5, 7.5, 10, 15, 20, 30, 40	0.5	1	0.3	3	0
31, 32, 33, 34, 35, 36, 37, 38	2.5, 5, 7.5, 10, 15, 20, 30, 40	0.5	2	0.3	3	0
39, 40, 41, 42, 43, 44, 45, 46	2.5, 5, 7.5, 10, 15, 20, 30, 40	0.5	4	0.3	3	0
47, 48, 49, 50, 51, 52, 53, 58	2.5, 5, 7.5, 10, 15, 20, 30, 40	0.75	1	0.3	3	0
59, 60, 61, 62, 63, 64, 65, 66	2.5, 5, 7.5, 10, 15, 20, 30, 40	0.75	2	0.3	3	0
67, 68, 69, 70, 71, 72, 73, 74	2.5, 5, 7.5, 10, 15, 20, 30, 40	0.75	4	0.3	3	0
75, 76, 77, 78, 79, 80, 81, 82	2.5, 5, 7.5, 10, 15, 20, 30, 40	1.0	1	0.3	3	0
83, 84, 85, 86, 87, 88, 89, 90	2.5, 5, 7.5, 10, 15, 20, 30, 40	1.0	2	0.3	3	0
91, 92, 93, 94, 95, 96, 97, 98	2.5, 5, 7.5, 10, 15, 20, 30, 40	1.0	4	0.3	3	0
99, 100, 101, 102, 103 M(T)	10, 15, 20, 30, 40			0.3	3	
104	14.5	0.5	2	0.3	3	0

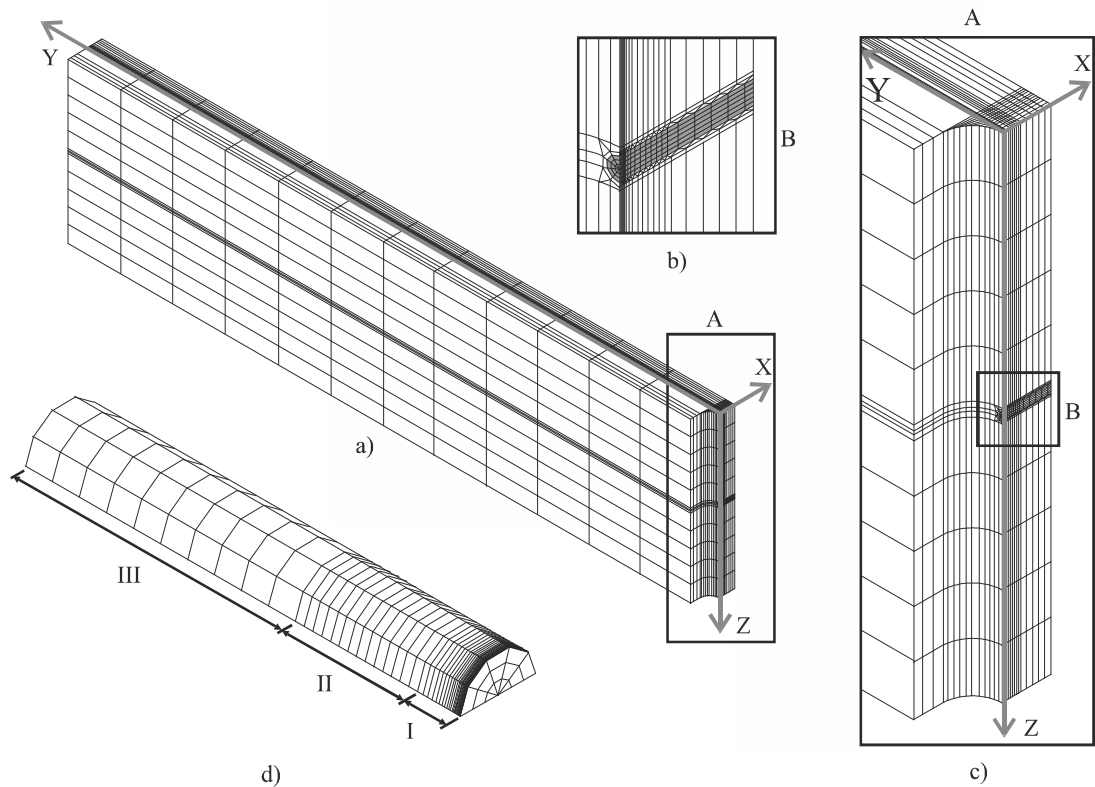


Figure 4.21. Typical FE meshes used: a) general overview; b) crack tip; c) notch plane; d) refinement towards thickness ($L=200\text{mm}$, $2W=50\text{mm}$, $r=1.5\text{mm}$, $n=3\text{mm}$, $t=5\text{mm}$, $\eta=0^\circ$).

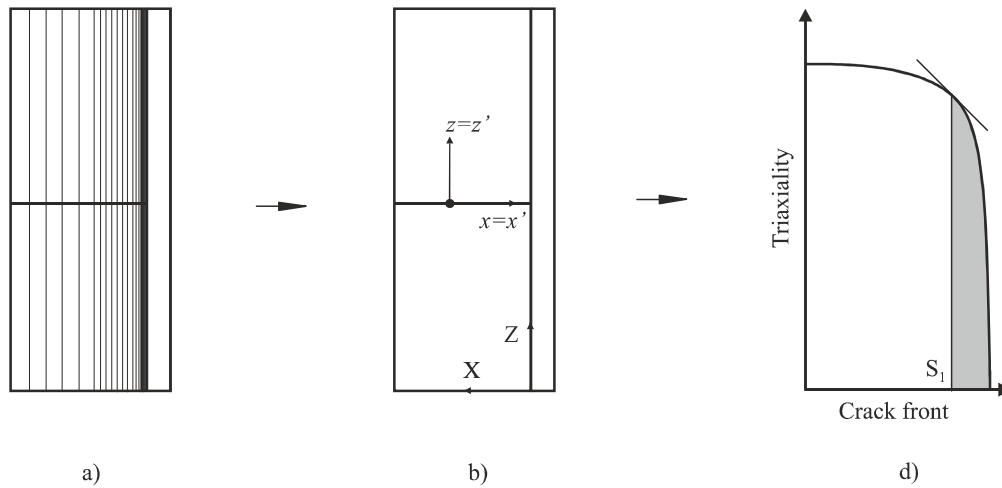


Figure 4.22. Simplified methodology for defining a plane strain specimen assuming straight crack shapes: a) development of a refined finite element mesh; b) calculation of stress components at the crack front; d) computation of triaxiality parameters and analysis of results.

components of the crack front nodes are computed (Figure 4.22b). Note that Equation 4.14 is not necessary since both global and local coordinate systems are coincident. Finally, the triaxiality parameters are calculated and analysed to propose alternative plane strain specimens (Figure 4.22c).

4.6. Determination of the Paris law constants from fatigue crack front marks

As explained in Section 3.10, the mixed numerical-experimental technique proposed to determine the Paris law constants from fatigue crack marks on fracture surfaces of small cross-section round bars encompasses three main steps (Figure 3.17). Briefly, the first step requires the marking of at least two crack fronts on the fracture surface of the specimen and the counting of the number of cycles between them. The second step aims at developing a representative numerical model able to simulate the crack shape evolution and fatigue life. Finally, the numerical results are fitted to the experimental results in order to determine the Paris law constants.

The first step, devoted to the experimental work, was described in detail in Section 3.10. The numerical simulation of crack shape evolution and fatigue life (see Figure 3.17) was carried out using the 3D-FE FCG technique described in Section 4.3. The physical model is presented in Figure 4.23a. The geometry of the ends was simplified taking into consideration their remote position relatively to the crack front. Movements along x and z ($\delta x = \delta z = 0$) were restrained to simulate the constraint imposed by the high rigidity of the machine grips (grey surface at the top of Figure 4.23a). The crack was assumed to be plane, normal to the axis of the specimen, and existing in its middle-section. Therefore, mode I loading is expected along the whole crack front. The material was defined homogeneous, isotropic and with linear elastic behaviour. Dynamic loadings created by a couple of forces applied at one end of the specimen

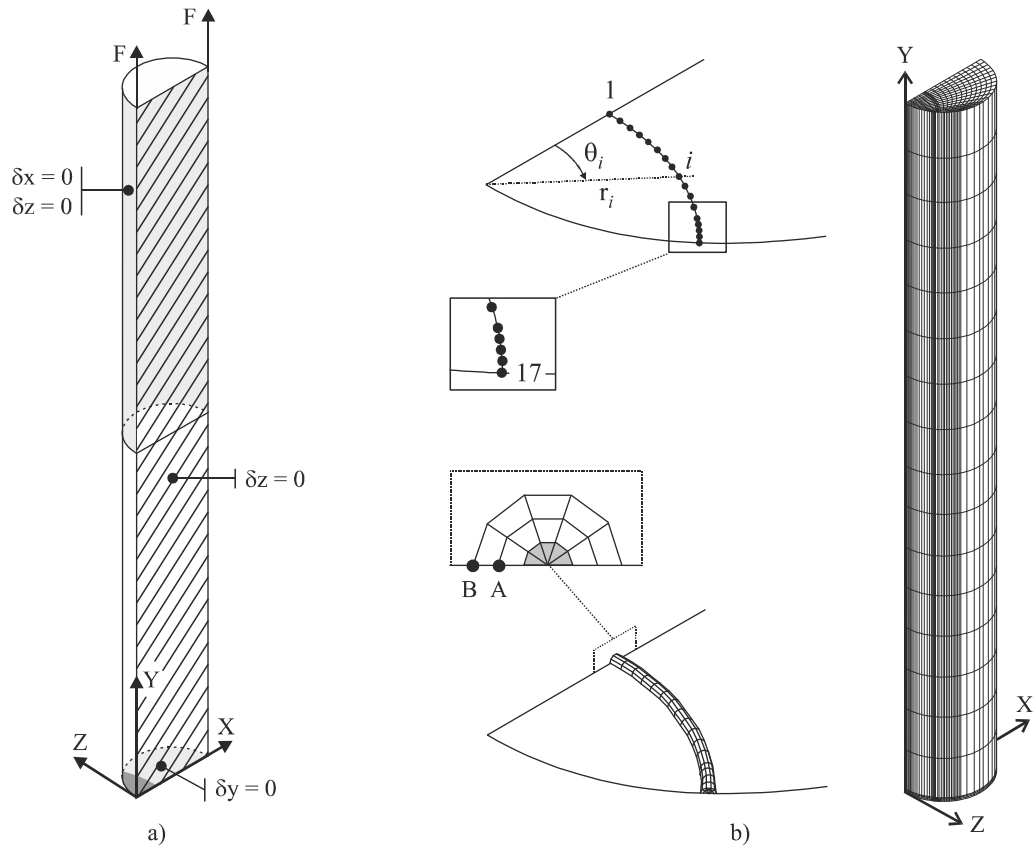


Figure 4.23. Mixed numerical-experimental technique proposed to determine the constants of the Paris law: a) physical model; b) finite element mesh (Branco, 2012d).

were defined. Figure 4.23b shows the typical finite element meshes used. The crack front was divided into seventeen corner nodes and sixteen intermediate nodes. A refined region nearby the free surface of the round bar consisting of four layers was included. The intermediate nodes of the elements surrounding the crack tip were moved to quarter-point positions. The assembled model had 71743 nodes and 7232 elements. The stress intensity factors at corner nodes were computed using the extrapolation method with two points from the points *A* and *B* depicted in Figure 4.23b. A plane strain condition was assumed for all positions, except at the free boundary where plane stress state prevailed. The local crack increments, given by Equation 4.10, were calculated assuming that the propagation occurred along the direction normal to the crack front. The crack front was approximated by a cubic spline. The fatigue cycles were evaluated with an Euler integration algorithm (Equation 4.13).

The determination of the Paris law constants (third step of Figure 3.17) was done by applying adequate dependent parameters. In this case, a new dependent parameter, named *accumulated difference* (*ad*), was proposed to predict the *m* exponent. This parameter, defined by Equation 4.18, analyses the entire crack front and is equal to zero only when all crack front nodes are overlapped with the experimental crack shape. The main variables are identified in Figure 4.24, being *d_i* the difference between the numerical and

$$ad = \sum_{i=1}^n |d_i| \quad (4.18)$$

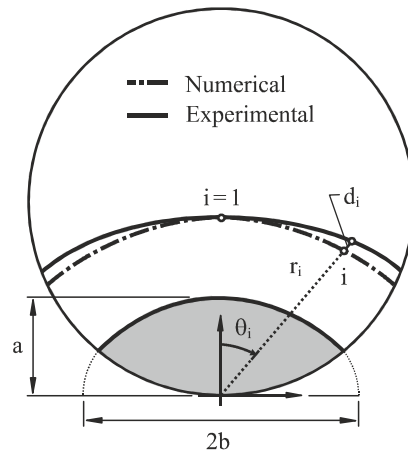


Figure 4.24. Definition of the ad dependent parameter used to predict the crack shape (Branco, 2012d).

experimental coordinates of the i^{th} node of the crack front and n the number of corner nodes at the crack front. In theory, the suitable m value is the one that minimises the ad parameter. The C constant was found by equalising the numerical and the experimental numbers of cycles.

CHAPTER 5

EXPERIMENTAL RESULTS

This chapter details the experimental findings. In the first section, the microstructure of the material is analysed. The second section presents the results of the monotonic uniaxial tests. The third section tackles the calculation of the elastic constants. The fourth section is devoted to the low-cycle fatigue tests and the analysis of the fracture surfaces by SEM. The last section is concerned with the in-phase combined bending-torsion tests. It encompasses the analysis of initiation sites, fatigue crack paths, surface crack angles, topologies of fracture and crack front profiles. The determination of the fatigue life in terms of a - N and S - N curves as well as the prediction of the fatigue life using different methods available in the literature are also presented here.

NOMENCLATURE

a	crack length
a_0	El Haddad parameter
a/b, a'/b'	crack aspect ratio
ASTM	American Society of Testing and Materials
b	fatigue strength exponent
c	fatigue ductility exponent
C	Paris law constant
d	distance from the notch root
D_{LM}	critical distance for the line method
E	Young's modulus
E_N	fatigue prediction error
FEM	finite element method
FFT	fast Fourier transformation
$f_{LB1,E}$	first experimental longitudinal bending frequency
$f_{T1,E}$	first experimental torsional frequency
$f_{LB1,N}$	first numerical longitudinal bending frequency
$f_{T1,N}$	first numerical torsional frequency
k'	cyclic hardening coefficient
LM	line method
m	Paris law exponent
n'	cyclic hardening exponent
N	number of loading cycles
N_e, N_p	experimental life, predicted life
$N_f, 2N_f$	number of cycles to failure, number of reversals to failure
$N_{0.5}$	number of cycles in which the crack reached a surface length equal to 0.5mm
PD	potential drop
R, R_σ	stress ratio
R_ϵ	strain ratio
RA	reduction area
t	time
T_σ	scatter band index
YPE	yield point elongation
$\Delta\epsilon, \Delta\epsilon/2$	strain range, strain amplitude
$\Delta\epsilon_e, \Delta\epsilon_p$	elastic strain range, plastic strain range
$\Delta\epsilon_{vML}/2$	local von Mises equivalent strain amplitude
$\Delta\sigma, \Delta\sigma/2$	stress range, stress amplitude
$\Delta\sigma_{vML}/2$	local von Mises equivalent stress amplitude
ΔK	stress intensity factor range
ΔK_{th}	range of the threshold value of the stress intensity factor
ΔK_{th0}	range of the threshold value of the stress intensity factor for R=0
ΔW_p	plastic strain energy range per cycle
ΔW_t	total strain energy range per cycle
ϵ_R	elongation
ϵ_f'	fatigue ductility coefficient
θ_p	principal direction
ν	Poisson's ratio
σ_a, σ_m	normal stress amplitude, mean normal stress
τ_a, τ_m	shear stress amplitude, mean shear stress
σ_f'	fatigue strength coefficient
σ_{ij}	stress tensor components
σ_{UTS}	ultimate tensile strength
$\sigma_{vML,max}$	maximum local von Mises equivalent stress
$\sigma_{vML,min}$	minimum local von Mises equivalent stress
$\sigma_{YS}, \sigma_{YS}'$	yield strength, cyclic yield strength

5.1. Microstructure of the material

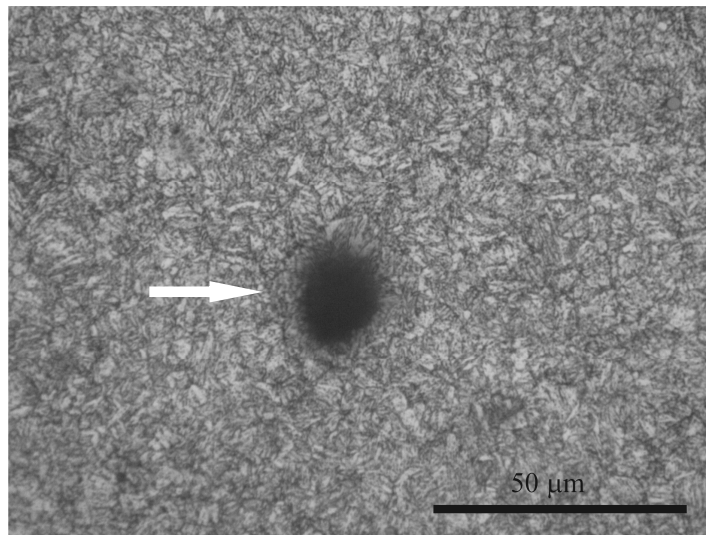
As referred to in Chapter 3, DIN 34CrNiMo6 steel combines deep hardenability, high ductility, toughness and strength. It has high fatigue and creep resistance and is often used where severe service conditions exist (ASM, 2000) and when high strength is required. These features make it ideal for critical structural applications, such as aircraft components, high pressure vessels for nuclear power plants, automobile components, among others. The optimum characteristics to address the different demands are achieved by a set of standard heat treatments which are summarised in Table 5.1.

The final microstructure has a preponderant role in mechanical properties (ASM, 2000). In essence, it primarily consists of a martensitic matrix with small amounts of ferrite, bainite and some retained austenite. A martensitic microstructure is formed when the steel cools faster than the critical cooling rate for martensitic formation. Bainite is formed through the decomposition of austenite to acicular ferrite and carbides above the martensitic start temperature. The two primary forms of bainite are upper bainite and lower bainite. In the former, the carbides are typically located between the acicular ferrite whilst in the latter the carbides tend to precipitate at an inclined angle to the major growth direction or longitudinal axis of the acicular ferrite grains (Tartaglia, 2008).

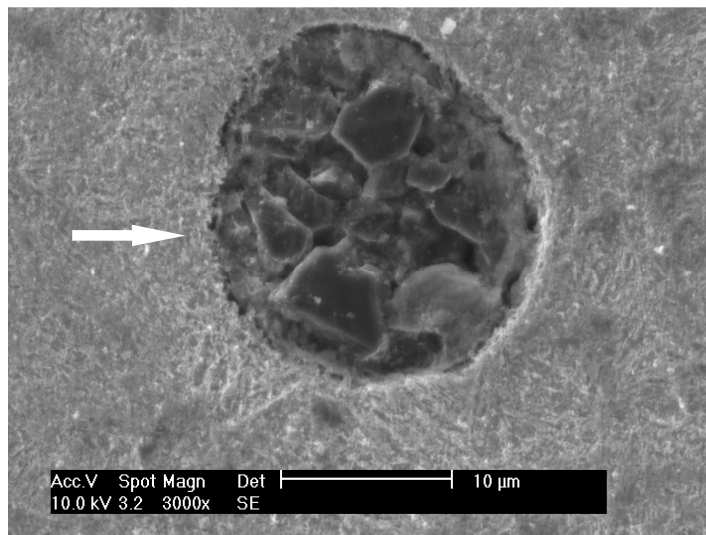
Figure 5.1a presents the microstructure of the DIN 34CrNiMo6 steel studied here, which was obtained by optical microscopy from a sample polished and etched with nital (see Section 3.7). The micrograph illustrates the grain boundaries and the non-uniform distribution of precipitates. As can be seen, the material has a fine microstructure mainly composed of martensite and lower bainite. Martensite appears lighter and bainite is etched darker in optical micrograph. The average grain size obtained using the procedure described by the ASTM E112 standard (2010) was about 8 μ m. Besides, relatively high inclusions with sizes ranging from 2-3 to 30 μ m were found. A representative example is denoted by the

Table 5.1. Standard heat treatments applied to DIN 34CrNiMo6 steel (ASM, 2000).

Heat treatment	Description
Normalise	Heat to 845-900°C and hold for a time period that depends on thickness; air cool.
Anneal	Heat to 830-860°C and hold for a time period that depends on thickness; furnace cool.
Harden	Heat to 800-845°C and hold 15 minutes for each 25mm of thickness; oil quench to below 65°C, or quench in fused salt to 200-201°C, hold 10 minutes, and then air cool to below 65°C.
Temper	Hold at least 30 minutes at 200-650°C; air cool. Temperature and time at temperature depend on desired final hardness.
Spheroidise	Preheat to 690°C and hold 2 hours, increase the temperature to 745°C and hold 2 hours, cool to 650°C and hold 6 hours, furnace cool to about 600°C, and finally air cool to room temperature. An alternative method is to heat to 730-745°C, hold several hours and then furnace cool to room temperature.
Stress relieve	After straightening, forming or machining, parts may be stress relieved at 650-675°C.
Bake	To avoid hydrogen embrittlement, plated parts must be baked at least 8 hours at 185-195°C as soon after plating as possible.



a)



b)

Figure 5.1. Microstructure of the DIN 34CrNiMo6 high strength steel from a sample polished and etched with nital: a) optical microscopy; b) scanning electron microscopy (Branco, 2012b).

white arrow. Another example is shown in Figure 5.1b, which shows a micrograph obtained by scanning electron microscopy from the same sample (see Section 3.7). The presence of inclusions in DIN 34CrNiMo6 steel is well-known and has been reported in several studies. The typical inclusions found are sulphide inclusions, globular oxides, fragmented alumina inclusions, and elongated silicate inclusions (Murty, 1975; Lee, 1999; Costa, 2001; Tartaglia, 2008). In the present research, despite several attempts, the chemical composition of the inclusions was not clearly identified.

5.2. Uniaxial tensile tests

The monotonic response of the DIN 34CrNiMo6 steel was investigated using two specimens. The tests were conducted according to the protocol described in the ASTM E8 (2011) standard (see Section 3.2). Figure 5.2 exhibits the tensile stress-strain curves of the two specimens. As can be seen, the behaviour of

the two curves is very similar, except for the non-uniform plastic deformation region ($\epsilon > 10\%$). Besides, it is also possible to observe a yield point elongation (YPE), i.e. an area in which an increase in strain occurs without an increase in stress. The difference in strain between the upper yield strength (first zero slope) and the onset of uniform strain hardening is about 1.93%.

The monotonic mechanical properties obtained are summarised in Table 5.2. These results are in good agreement with those reported in the literature (ASM, 2000a) for nearly identical conditions. However, the yield strength and the ultimate tensile strength values determined in this research are slightly higher than the reference values which can be associated with the different tempering temperatures. With regard to the elongation and reduction of area, the findings are in line with the literature.

The tensile fracture surfaces were examined by SEM (specimen UT1). Figures 5.3a-b display two micrographs taken at low and high magnifications, respectively. Figure 5.3a shows considerable plastic deformation before fracture. The plastic deformation in the centre of the plane of minimum cross-section, at the neck location, promotes the nucleation and growth of voids to a critical dimension. Necking starts

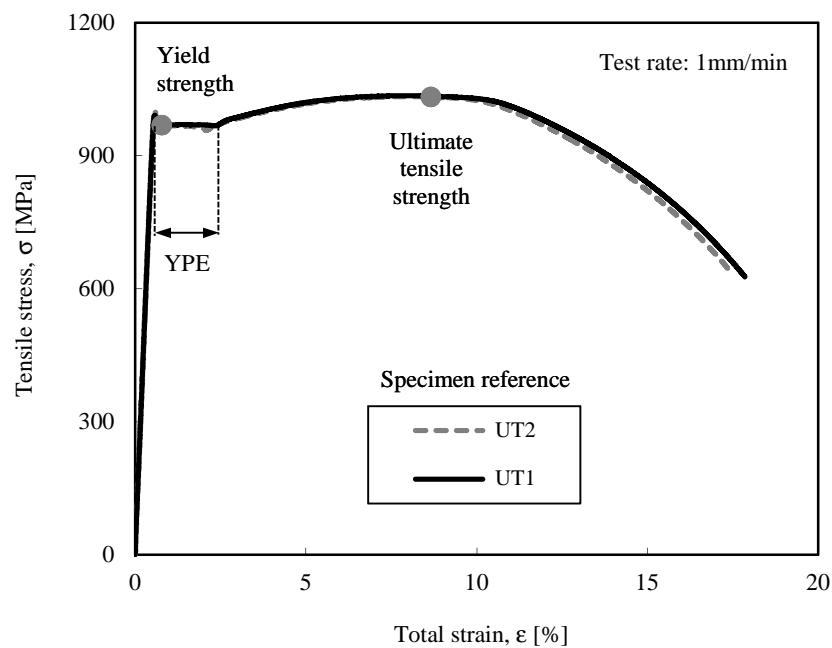


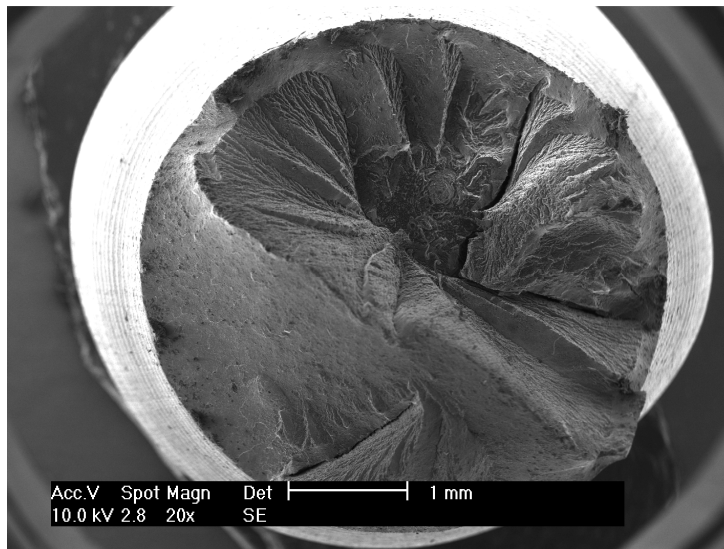
Figure 5.2. Monotonic stress-strain curves obtained in the tensile tests.

Table 5.2. Mechanical properties of the DIN 34CrNiMo6 high strength steel.

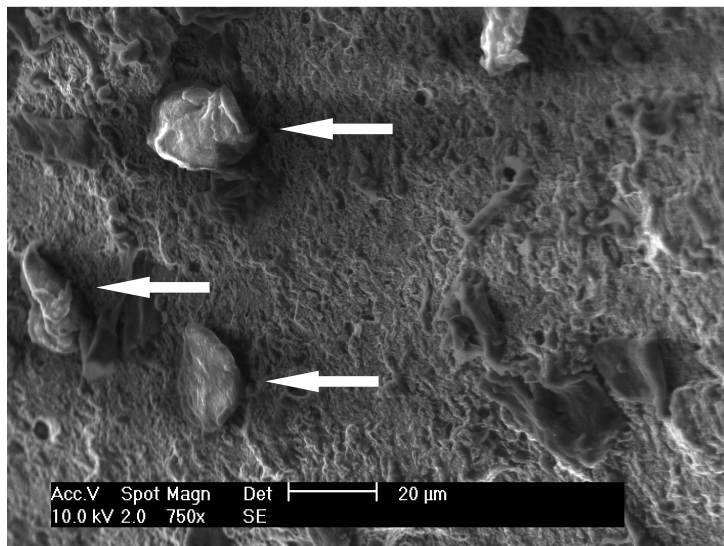
Mechanical property	Value [Experimental] ^a	Value [ASM, 2000a] ^b
Yield strength, σ_{YS} [MPa]	967	860
Ultimate tensile strength, σ_{UTS} [MPa]	1035	1020
Elongation, ϵ_R [%]	18	20
Reduction of area, RA [%]	58	60

^a Oil quenching: 850-880°C, Tempering: 660°C

^b Oil quenching: 845°C, Tempering: 650°C



a)



b)

Figure 5.3. Tensile fracture surfaces obtained by SEM: a) low magnification; b) high magnification.

when the stress-strain curve has passed the maximum point where plastic deformation is no longer uniform. Nevertheless, the typical ductile *cup-and-cone* fracture surface is not observed. In this case, the fracture is a mixed mechanism involving microvoid coalescence and cleavage. Figure 5.3b presents several inclusions found in the tensile fracture surface which are disseminated throughout the material. It has been observed that these particles, when located at the surface, came off during the polishing process. This is totally undesirable and inevitably leads to a reduction in fatigue strength.

5.3. Determination of the elastic constants using a resonant technique

The elastic constants were obtained using a mixed numerical-experimental technique that comprises the experimental determination of the resonant frequencies; the establishment of relations between resonant frequencies and elastic constants; and the calculation of the final values (see Sections 3.3 and 4.1). The

resonant frequencies were determined by applying the impulse excitation technique (see Section 3.3). The tests were conducted according to the protocol described in the ASTM E1876 (2009) standard using a rectangular cross-section specimen (see Figure 3.5).

Figure 5.4a shows a typical output signal recorded for the rectangular cross-section specimen. As can be seen, there is no evidence of damping. The frequency spectrum was obtained by fast Fourier transformation (FFT) and is presented in Figure 5.4b. The peaks represent the first longitudinal bending ($f_{LB1,E}$) and the first torsional ($f_{T1,E}$) resonant frequencies, whose values are listed in Table 5.3.

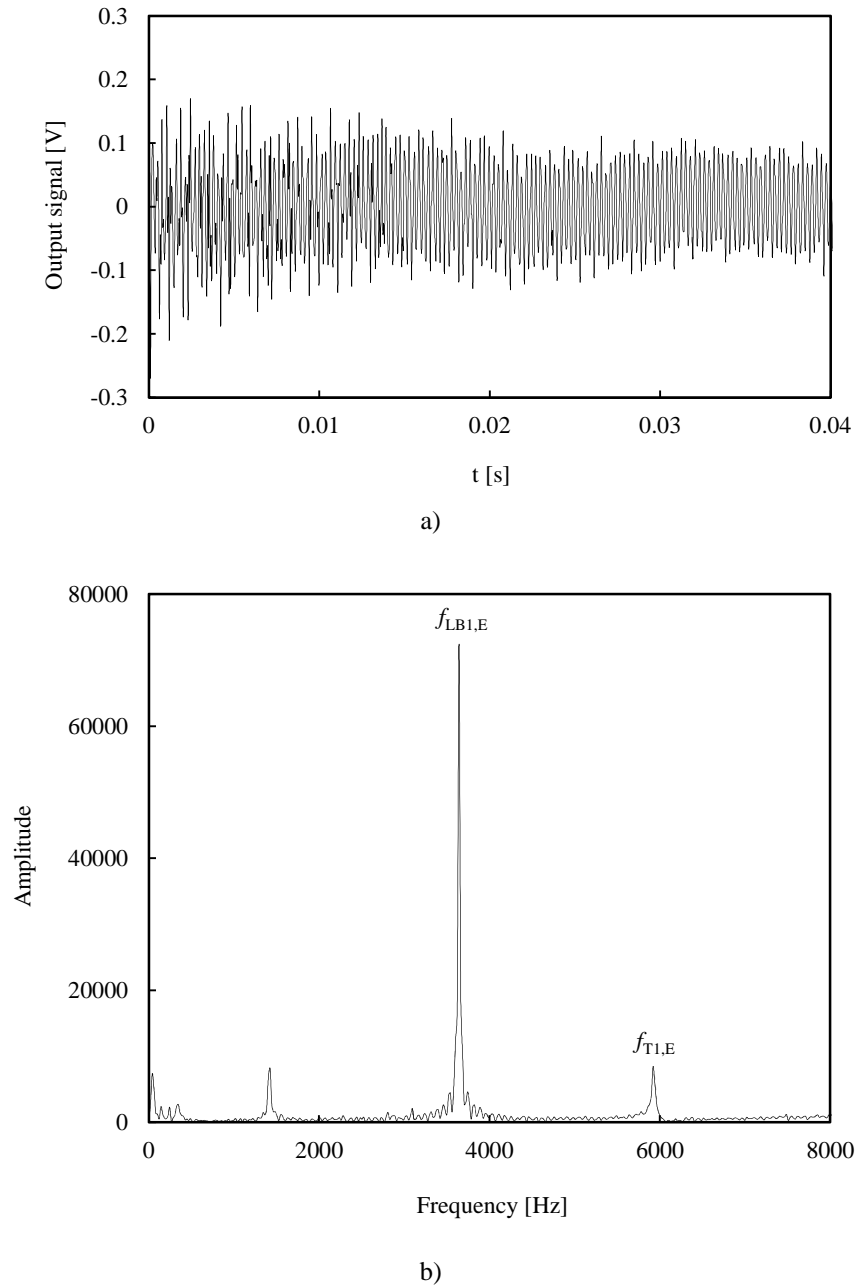


Figure 5.4. a) Output signal versus time; b) response in frequency domain obtained by FFT analysis for the rectangular cross-section specimen (Branco, 2009c).

The relation between resonant frequencies and elastic constants, as referred to in Section 4.1, was carried out using the FEM. A perfect rectangular parallelepiped shape was modelled with regularly spaced 3D isoparametric elements (see Figure 4.2a). The elastic constants were calculated using an iterative procedure based on sensitivity analyses of the resonant frequencies to the material properties (see Figure 4.3). Table 5.3 presents the evolution of elastic constants and numerical resonant frequencies ($f_{LB1,N}$ and $f_{T1,N}$) during the iterative process. As can be seen, this algorithm ensures a fast convergence to the final solution. In both cases, only three iterations were required.

A sensitivity analysis of the elastic constants to the material density, experimental resonant frequencies, and specimen dimensions was performed. The sensitivities (S_γ^ψ) were calculated analytically, in a dimensionless form, to facilitate the comparison of results (see Equation 4.1). Each value of sensitivity was obtained from three different values of the independent variable, i.e. an independent variable with no perturbation; with a perturbation of -1%; and with a perturbation of +1%. Then, the three pairs of points ψ - γ were fitted to a second order polynomial function which was used to obtain the $\partial\psi/\partial\gamma$ derivate. After that, the dimensionless sensitivity was calculated. Figure 5.5 shows the final values obtained with respect to the Young's modulus (black series) and Poisson's ratio (grey series).

Table 5.3. Calculation of the elastic constants of the DIN 34CrNiMo6 high strength steel.

Elastic constant	Iteration:	0	1	2
Young's modulus, E_{11} [GPa]		210.000	209.721	209.762
Numerical resonant frequency, $f_{LB1,N}$ [Hz]		3644.17	3641.39	3641.76
Experimental resonant frequency, $f_{LB1,E}$ [Hz]		3641.76	3641.76	3641.76
Poisson's ratio, ν_{12}		0.30000	0.29605	0.29630
Numerical resonant frequency, $f_{T1,N}$ [Hz]		5915.85	5920.38	5920.41
Experimental resonant frequency, $f_{T1,E}$ [Hz]		5920.41	5920.41	5920.41

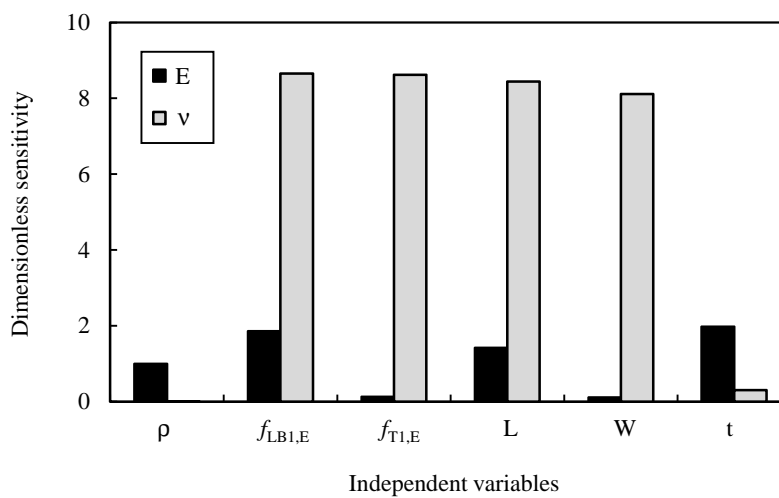


Figure 5.5. Dimensionless sensitivities of the elastic constants to the material density, experimental resonant frequencies and specimen dimensions (Branco, 2009c).

According to the figure, the greater dimensionless sensitivities of the Young's modulus are caused by the first longitudinal resonant frequency, specimen thickness, specimen length and material density. Besides, it is possible to observe that their orders of magnitude are very similar. Therefore, the accuracy of the predicted Young's modulus depends on the accuracy of these variables. The other ones, namely the first torsional resonant frequency and the specimen width, are less important in this context.

Regarding the dimensionless sensitivities of the Poisson's ratio, the greater values are produced by the experimental resonant frequencies, specimen length and specimen width. In these cases, the dimensionless sensitivities are particularly high. It means that accurate predictions of ν require an absolute control of these input variables. On the contrary, the specimen thickness and the material density play a secondary role in this calculation.

5.4. Low-cycle fatigue tests

The cyclic deformation behaviour of the DIN 34CrNiMo6 high strength steel was studied using the geometry exhibited in Figure 3.6. These tests were conducted according to the protocol described in the ASTM E606 (2004) standard (see Section 3.4). The single step test (SST) method was adopted. Eight tests were performed under fully-reversed strain-controlled conditions ($R_\epsilon = -1$) and five were carried out under fully-reversed stress-controlled conditions ($R_\sigma = -1$).

Figures 5.6a-b show the stress-strain response for two strain amplitudes ($\Delta\epsilon/2$), respectively $\Delta\epsilon/2 = \pm 2\%$ and $\Delta\epsilon/2 = \pm 0.8\%$. A strain-softening phenomenon occurs in both cases, i.e. the uncontrolled stress decreases with the increasing number of cycles until a stable state is achieved. In Figure 5.6a, the stable behaviour is observed after 40-50 cycles; in Figure 5.6b, it occurs after about 500 cycles. Therefore, in this steel, the stable cyclic state is reached generically for life ratios lower than 40% of the total number of cycles to failure. In view of this fact, the hysteresis loops at the half-life were chosen as representative of the stable behaviour.

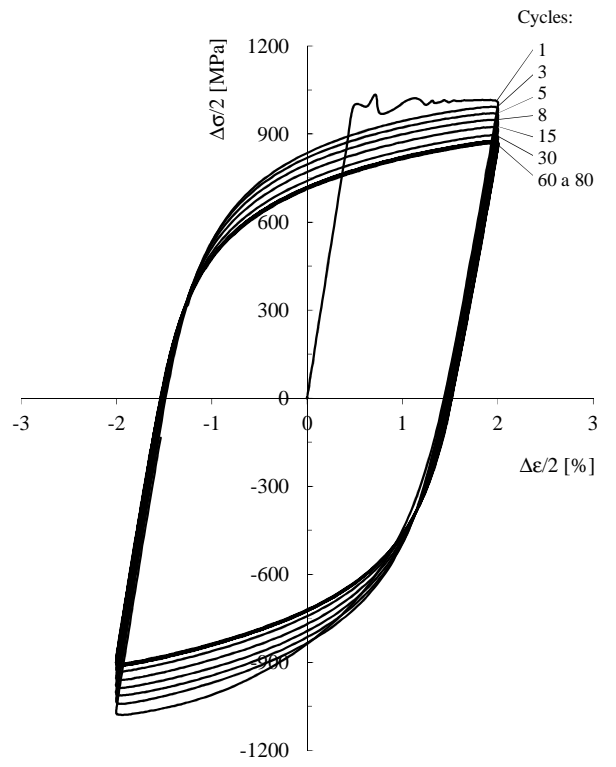
Both the stress range ($\Delta\sigma$) and the total strain range ($\Delta\epsilon$) were calculated from the hysteresis loops. The stress range was defined as ratio of the stable load range to the original circular cross-sectional area of the specimen. The total strain range was related to the elastic and plastic strain ranges by the formula

$$\Delta\epsilon = \Delta\epsilon_e + \Delta\epsilon_p \quad (5.1)$$

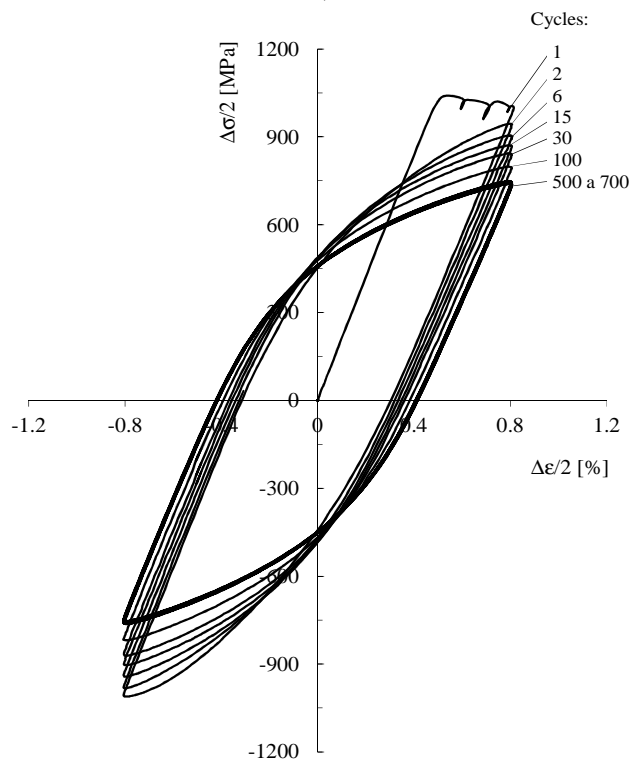
being $\Delta\epsilon_e$ and $\Delta\epsilon_p$ the elastic strain range and the plastic strain range, respectively. The former, applying the Hooke's law, is given by Eq. 5.2; the latter, replacing Eq. 5.2 in Eq. 5.1, is defined by Eq. 5.3.

$$\Delta\epsilon_e = (\Delta\sigma/E) \quad (5.2)$$

$$\Delta\epsilon_p = \Delta\epsilon - (\Delta\sigma/E) \quad (5.3)$$



a)



b)

Figure 5.6. Stress-strain hysteresis loops: a) $\Delta\epsilon/2 = \pm 2.0\%$; b) $\Delta\epsilon/2 = \pm 0.8\%$ (Branco, 2012e).

Table 5.4 summarises the main information obtained from the low-cycle fatigue tests performed in this research. In the following subsections, the cyclic deformation response, the fatigue strength and fatigue

Table 5.4. Results of low-cycle fatigue tests (Branco, 2012b).

Specimen reference	Stress amplitude, $\Delta\sigma/2$ [MPa]	Total strain amplitude, $\Delta\varepsilon/2$ [%]	Elastic strain amplitude, $\Delta\varepsilon_e/2$ [%]	Plastic strain amplitude, $\Delta\varepsilon_p/2$ [%]	Number of cycles to failure, N_f	Number of reversals to failure, $2N_f$
D200	891.8	2.003	0.425	1.578	131	262
D150	869.0	1.503	0.414	1.089	240	480
D125	831.6	1.254	0.396	0.858	321	642
D100	796.8	1.004	0.380	0.624	767	1 534
D080	750.6	0.806	0.358	0.448	1 219	2 438
D060	726.6	0.607	0.346	0.261	2 523	5 046
D050	697.5	0.512	0.332	0.180	5 140	10 280
D040	675.3	0.413	0.322	0.091	13 378	26 756
T635	635.0	0.303	0.303	-	56 181	112 362
T600	600.0	0.286	0.286	-	196 724	393 448
T580	580.0	0.277	0.277	-	138 769	277 538
T560	560.0	0.267	0.267	-	142 690	285 380
T540	540.0	0.257	0.257	-	299 787	599 574

D_ _ _: fully-reversed strain-controlled tests

T_ _ _: fully-reversed stress-controlled tests

ductility properties, the shape of the hysteresis loops, the fracture surface morphologies and the fatigue mechanisms are examined.

5.4.1 Cyclic stress-strain response

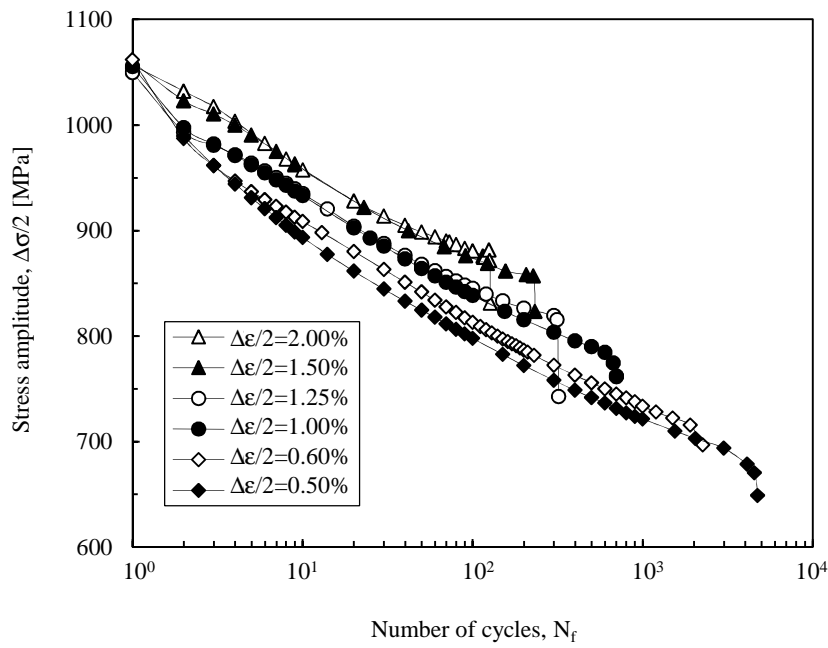
The cyclic stress curves versus the number of cycles at fixed strain amplitude, in a semi-log scale, are shown in Figure 5.7a. Regardless of the strain amplitude, a gradual cyclic softening behaviour is observed. The softening behaviour identified here agrees with the empirical rule proposed by Smith (1963), in which metals with $\sigma_{UTS}/\sigma_{YS} < 1.2$, in general, cyclically soften ($\sigma_{UTS}/\sigma_{YS} = 1.07$). Besides, it is clear that the higher is the strain amplitude, the lower is the rate of softening. On the other hand, a rapid drop in stress amplitude is observed when failure is imminent.

The cyclic stress response of the material can also be evaluated by plotting the stress amplitude against the life ratio (N/N_f). As can be seen in Figure 5.7b, this representation comprises a rapid initial softening region taking nearly 5-10% of the life ratio; followed by a region characterised by a progressive decrease in stress amplitude up to 90-95% of the life ratio; and a short region with a rapid drop in stress culminating in fatigue failure.

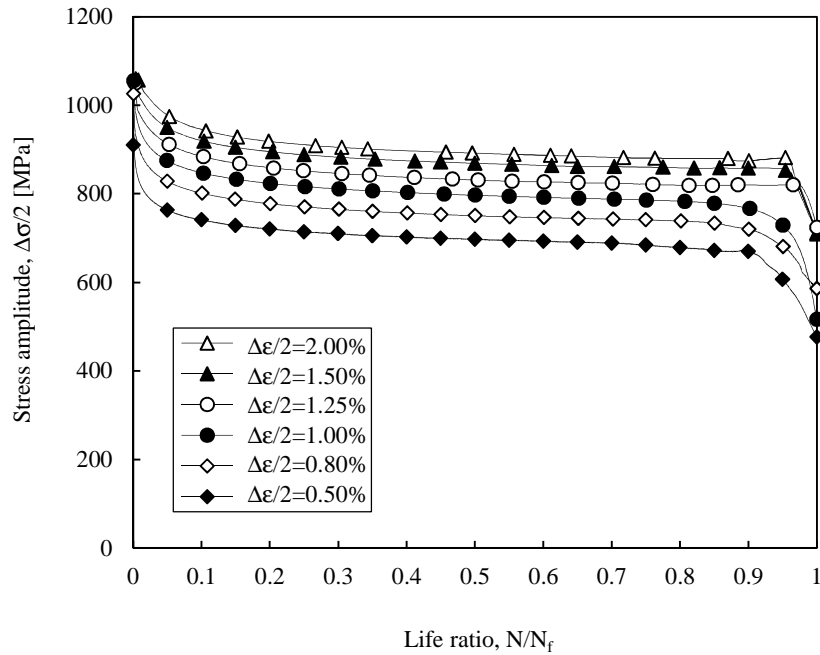
A convenient method of describing the stable material response is the cyclic stress-strain curve (Ramberg, 1943). This curve can be represented by

$$\frac{\Delta\varepsilon}{2} = \frac{\Delta\sigma}{2E} + \left(\frac{\Delta\sigma}{2k'} \right)^{1/n'} \quad (5.4)$$

being k' the cyclic hardening coefficient and n' the cyclic hardening exponent. Generally, such a curve



a)



b)

Figure 5.7. Evolution of the stress amplitude with the: a) number of cycles; b) life ratio for different strain amplitudes (Branco, 2012b).

can be drawn by connecting the tips of stable hysteresis loops for different strain amplitudes of fully-reversed strain-controlled tests. The stable hysteresis loops as well as the cyclic stress-strain curve obtained in this study are presented in Figure 5.8. As can be seen, the tips of the stable hysteresis loops are very close to the curve, either for ascending or descending branches. Nevertheless, the former are better fitted than the latter. In any cases, the Ramberg-Osgood model (Eq. 5.4) satisfactorily describes the

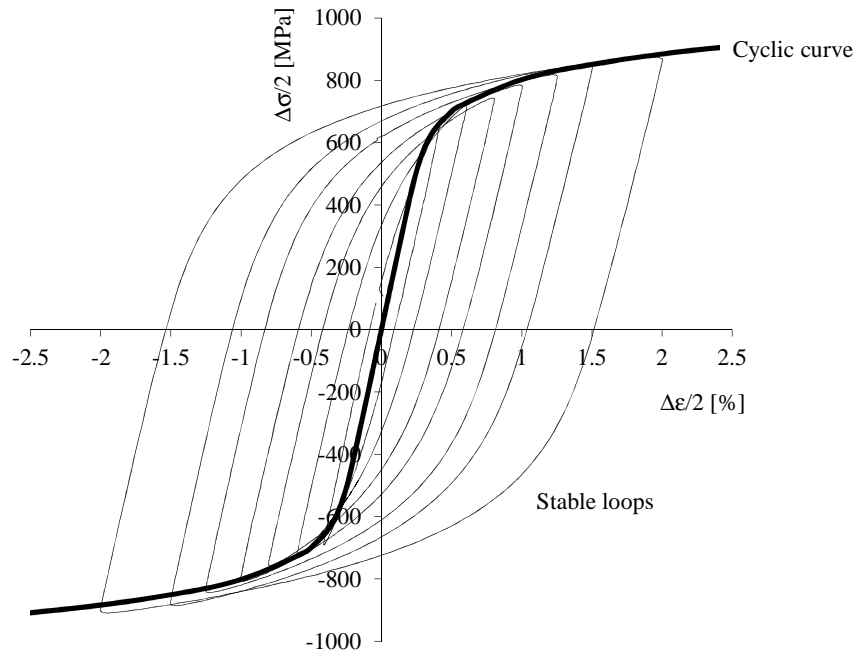


Figure 5.8. Cyclic stress-strain curve obtained by connecting the tips of stable hysteresis loops for different strain amplitudes of fully-reversed strain-controlled tests (Branco, 2012e).

stabilised hysteresis loops. The k' and n' constants, as first proposed by Morrow (1965), can be related by a power law

$$\frac{\Delta\sigma}{2} = k' \left(\frac{\Delta\varepsilon_p}{2} \right)^{n'} \quad (5.5)$$

being $\Delta\sigma/2$ the stress amplitude and $\Delta\varepsilon_p/2$ the plastic strain amplitude. Figure 5.9 plots the stress amplitude against the plastic strain amplitude in a log-log scale. As can be observed, the function is able to fit the experimental data. In this research, the unknown variables were obtained by linear regression using the least square method. A relatively high correlation coefficient was found ($r=0.982$). The k' and n' values are summarised in Table 5.5.

Figure 5.10 compares the cyclic curve and the monotonic curve (Figure 5.2) obtained here. It is evident that the cyclic curve lies above the other, which indicates cyclic softening behaviour. It is also clear that the cyclic yield strength ($\sigma_{YS'}$) is smaller than the monotonic yield strength (σ_{YS}). Regarding the monotonic curve, almost ideal elastic perfect-plastic behaviour is observed in this range. The degree of cyclic softening with respect to the monotonic stress-strain curve was defined by a simple expression

$$S = \frac{(\sigma_a^1 - \sigma_a)}{\sigma_a^1} \quad (5.6)$$

being σ_a^1 the stress amplitude in the first cycle and σ_a the stress amplitude at the half-life. The degree of cyclic softening versus the strain amplitude is plotted in Figure 5.11. According to the results presented, it

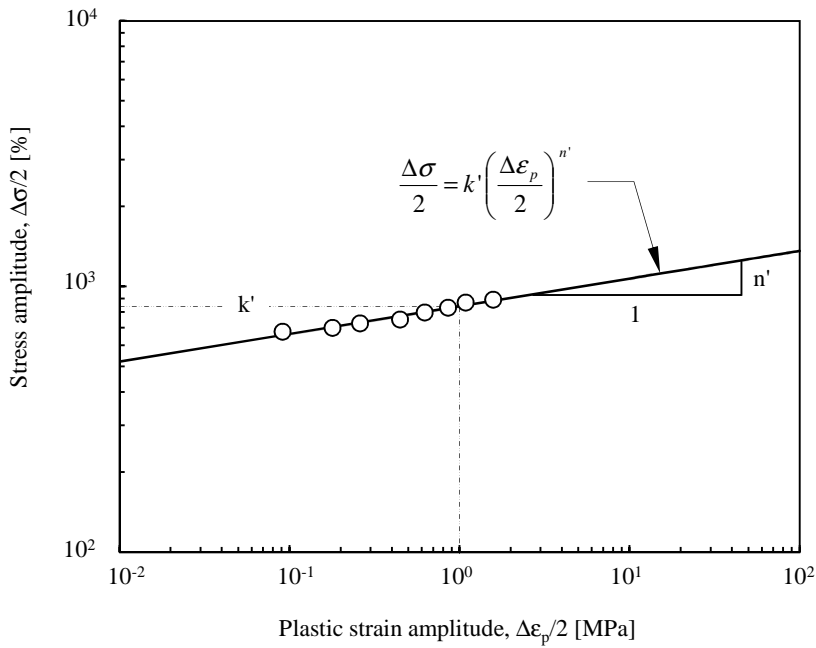


Figure 5.9. Relationship between cyclic stress amplitude and elastic strain amplitude (Branco, 2012e).

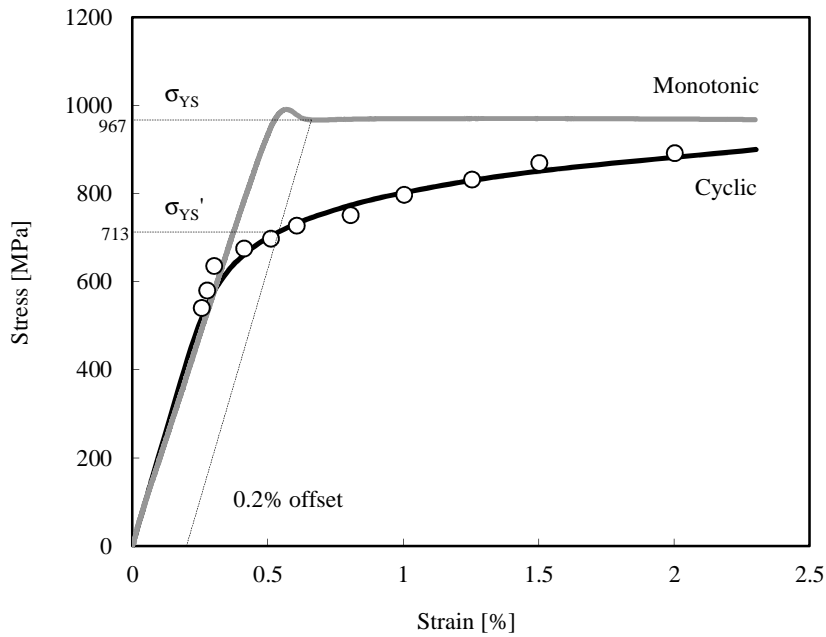


Figure 5.10. Monotonic and cyclic stress-strain curves of DIN 34CrNiMo6 (Branco, 2012b).

Table 5.5. Cyclic stress-strain curve parameters of DIN 34CrNiMo6 high strength steel.

Property	Value
Cyclic hardening coefficient, k' [MPa]	1361.6
Cyclic hardening exponent, n'	0.1041

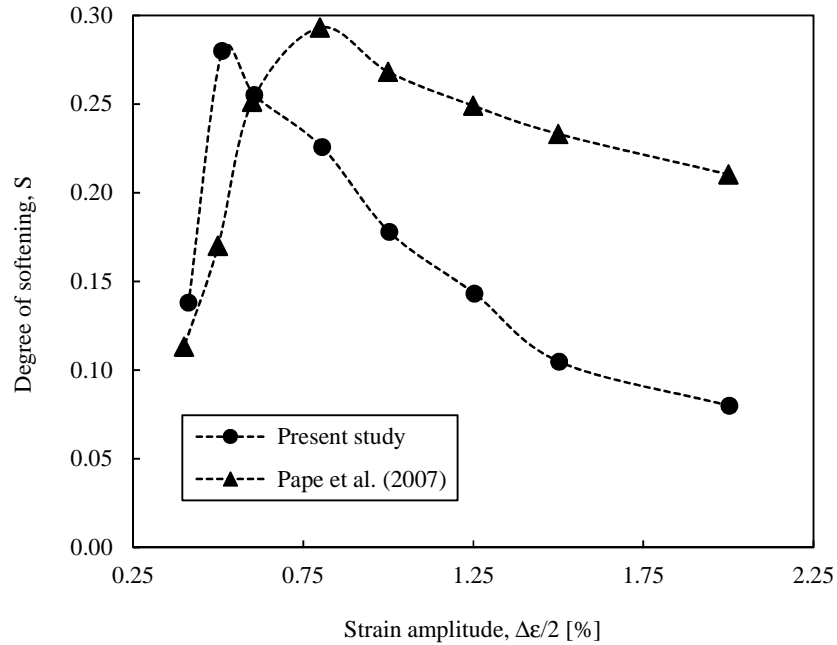


Figure 5.11. Degree of softening versus strain amplitude.

can be concluded that the degree of softening initially increases rapidly with the strain amplitude and then gradually decreases ($\Delta\epsilon > 0.52$). A similar trend was observed from the analysis of both the monotonic and cyclic curves obtained by Pape *et al.* (2007). The steep increase in the degree of softening for lower strain amplitudes occurs in both cases as well as the progressive reduction for higher amplitudes. Nevertheless, the decrease in the degree of softening is more intense in the present case.

As is well-known, the cyclic stress-strain curve describes the relation between the stable stress and stable strain amplitudes but it is not able to describe the shape of the hysteresis loops. However, several phenomena in cyclic behaviour can be explained from the analysis of the hysteresis loop shapes. The first analytical studies on hysteresis loop shapes were reported by Masing (1926). A material exhibits Masing-type behaviour when the hysteresis loop shapes can be obtained from the cyclic stress-strain curve (Equation 5.4) magnified by a factor of two (Equation 5.7). For such materials, the upper branches form a unique curve when the compressive tips of the stable hysteresis loops of different strain amplitudes are moved to a common origin defined by the maximum compressive stress. Non-Masing materials are those whose behaviour differs from the above description.

$$\Delta\epsilon = \frac{\Delta\sigma}{E} + 2\left(\frac{\Delta\sigma}{2k'}\right)^{1/n'} \quad (5.7)$$

Figure 5.12 presents the Masing curve computed from Equation 5.7 and the stable hysteresis loops for various strain amplitudes in relative coordinates (i.e. the compressive tips of the stable hysteresis loops are made to coincide). The cyclic stress-strain curve is also plotted for comparison purposes. Although the upper branches do not form a unique curve, it is possible to conclude that the Masing curve describes satisfactorily the upper branches of the stable hysteresis loops.

The master curve is an alternative way to examine the closeness of a material to the ideal Masing-type behaviour (Lefebvre, 1984). It is obtained by matching the linear response of the upper branches of the stable hysteresis loops obtained at different strain amplitudes. Its equation, regarding to an auxiliary coordinate system ($\Delta\varepsilon^*$, $\Delta\sigma^*$) with its origin at the smallest linear portion, can be written in the form

$$\Delta\varepsilon^* = \frac{\Delta\sigma^*}{E} + 2 \left(\frac{\Delta\sigma^*}{2k^*} \right)^{1/n^*} \quad (5.7)$$

where k^* and n^* are determined from the experimental data. Figure 5.13 exhibits the master curve of the material studied in this research. The unknown constants (k^* and n^*) were calculated by the least square method and are summarised in Table 5.6. A symmetric lower branch (dashed line) was also drawn for the stable hysteresis loop of $\Delta\varepsilon = 4\%$. The area between the dashed line and the corresponding full line indicates the deviation from the ideal Masing-type behaviour. As can be observed, this area is residual, which demonstrates that the Masing-type behaviour can be assumed. Besides, it tends to decrease for smaller total strain ranges.

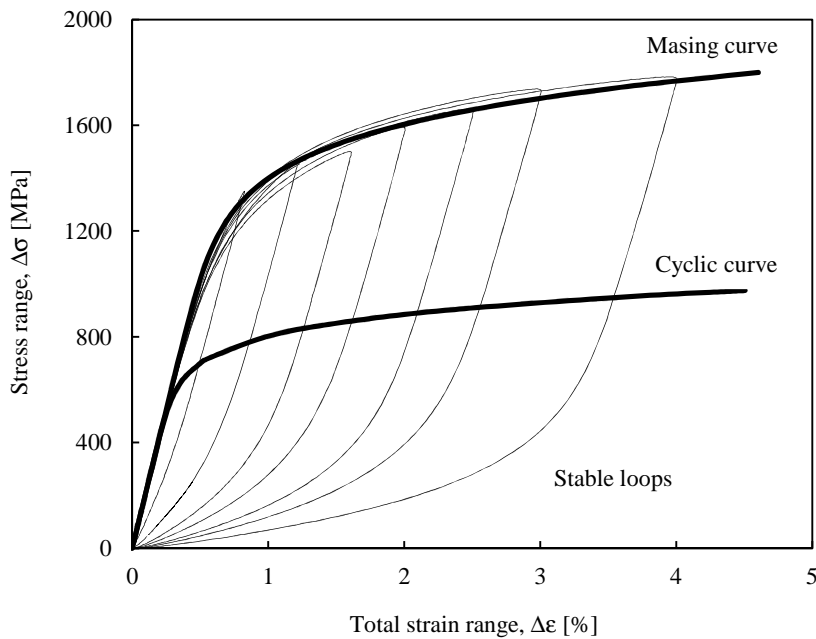


Figure 5.12. Cyclic stress-strain curve obtained by connecting the compressive tips of the stable hysteresis loops of different strain amplitudes (Branco, 2012b).

Table 5.6. Master curve parameters of DIN 34CrNiMo6 high strength steel.

Property	Value
Master curve hardening coefficient, k^* [MPa]	1384.1
Master curve hardening exponent, n^*	0.1123

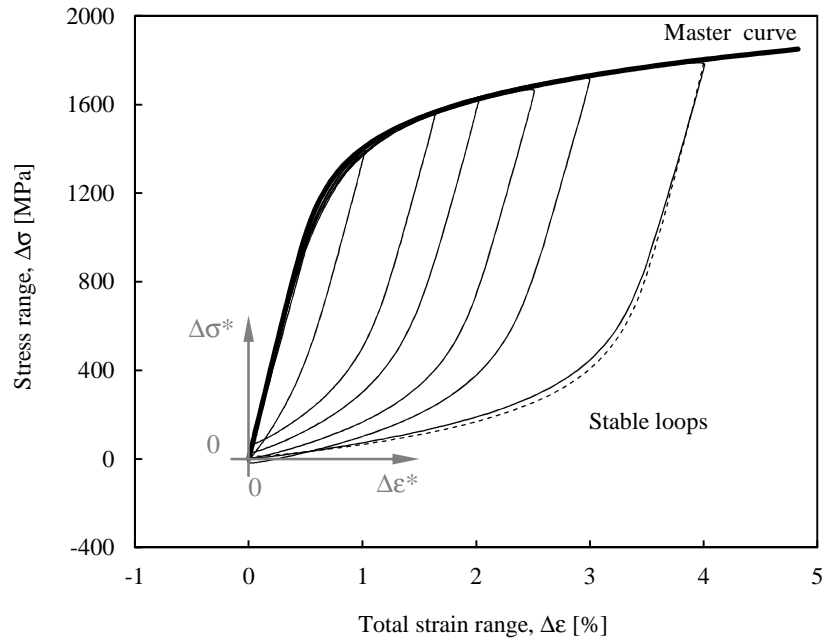


Figure 5.13. Master curve obtained by matching the upper branches of hysteresis loops of different strain amplitudes (Branco, 2012b).

5.4.2 Low-cycle fatigue life and low-cycle fatigue properties

The first stress-based approach to fatigue was carried out by Wöhler (1871). Since then, fatigue data have been presented in log-log scales. The relation between stress amplitude ($\Delta\sigma/2$) and number of reversals to failure ($2N_f$) can be written in the form (Basquin, 1910)

$$\frac{\Delta\sigma}{2} = \sigma_f' (2N_f)^b \quad (5.8)$$

being σ_f' the fatigue strength coefficient and b the fatigue strength exponent. As is well-known, Eq. 5.8 in a log-log scale leads to a straight line, as illustrated in Figure 5.14. Generally, the unknowns are evaluated by a best fit technique from the experimental data. The first constant (σ_f') is the interception of the plot at $2N_f=1$ and the other (b) is the slope of the plot. In the present research, the fatigue strength constants were obtained by linear regression using the least square method. A relatively high correlation coefficient was found ($r=0.987$). The σ_f' and b values are summarised in Table 5.7. The elastic component of strain, in uniaxial stress state, can be obtained from the Basquin relationship (Eq. 5.8) and Eq. 5.2. It leads to

$$\frac{\Delta\epsilon_e}{2} = \frac{\sigma_f'}{E} (2N_f)^b \Leftrightarrow \frac{\Delta\epsilon_e}{2} = \frac{1183.7}{E} (2N_f)^{-0.0545} \quad (5.9)$$

being $\Delta\epsilon_e/2$ the elastic strain amplitude and E the Young's modulus. Based on an energetic argument, Morrow (1965) suggested a simple rule to relate the fatigue strength exponent to the cyclic hardening

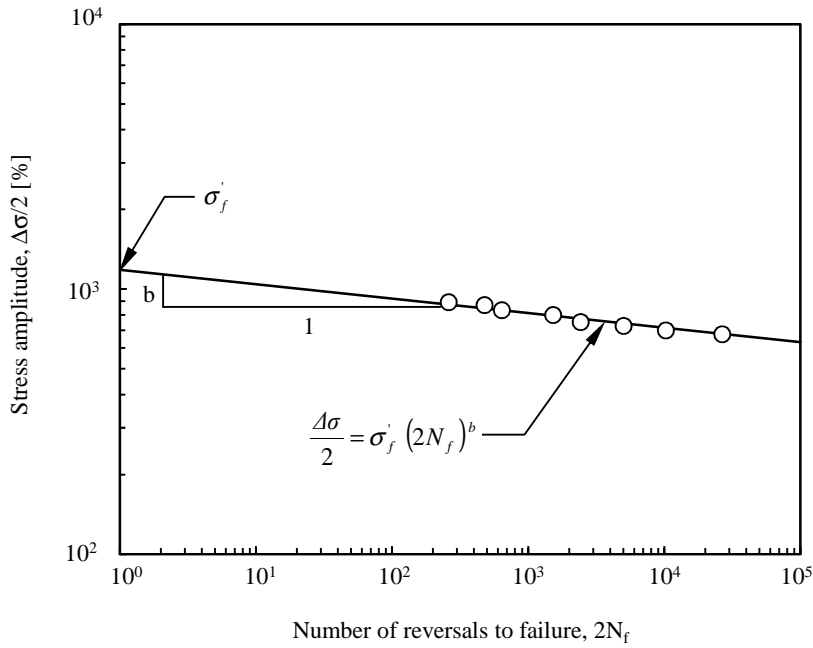


Figure 5.14. Stress amplitude versus number of reversals to failure.

Table 5.7. Fatigue strength properties of DIN 34CrNiMo6 high strength steel.

Property	Value
Fatigue strength coefficient, σ'_f [MPa]	1183.7
Fatigue strength exponent, b	-0.0545

exponent (Eq. 5.10). The prediction ($b \approx -0.06842$) is relatively close but not sufficiently precise. Note that the error is about 20%. In view of this fact, such a rule is not applicable in the case of this material.

$$b \approx \frac{-n'}{1+5n'} \quad (5.10)$$

Strain-based approaches, in essence, establish a relation between the elastic or plastic strain amplitude and fatigue life. For low-cycle fatigue ($\Delta\epsilon_p > \Delta\epsilon_e$), as first observed by Coffin and Manson (Coffin, 1954; Manson, 1954), the plastic strain amplitude ($\Delta\epsilon_p/2$) and the number of reversals to failure can be expressed in the following form

$$\frac{\Delta\epsilon_p}{2} = \epsilon'_f (2N_f)^c \quad (5.11)$$

where ϵ'_f and c are the fatigue ductility coefficient and the fatigue ductility exponent, respectively. This equation, in a log-log scale, leads to a straight line, as shown in Figure 5.15. The unknowns are evaluated by a best fit technique from the experimental data. The first constant (ϵ'_f) is the interception of the plot at $2N_f = 1$ and the other (c) is the slope of the plot. In this study, the fatigue ductility constants were obtained

by linear regression using the least square method. A relatively high correlation coefficient was found ($r=0.997$). The ϵ_f' and c values are summarised in Table 5.8. A similar relation to that of Eq. 5.10 was proposed by Morrow (1965) to relate c and n' (Eq. 5.12). The predicted value ($c \approx -0.6579$) is relatively close. The difference, in this case, is about 8%. However, in general, the correlation between experimental and predicted exponents is rather weak.

$$c \approx \frac{-1}{1+5n'} \quad (5.12)$$

The fatigue resistance relationship in terms of total strain amplitude (Eq. 5.13) can be obtained by adding the elastic and plastic components, given by Eq. 5.9 and Eq. 5.11, respectively. Figure 5.16 plots the total strain amplitude against the number of reversals to failure. The fatigue strength-life (Eq. 5.9) and fatigue ductility-life (Eq. 5.11) curves are also exhibited. The transition point (N_T), defined as the life at which both the elastic and plastic strain amplitudes are equal (see Eq. 2.28), is relatively small ($N_T = 3038$). For

$$\frac{\Delta\epsilon}{2} = \frac{\Delta\epsilon_e}{2} + \frac{\Delta\epsilon_p}{2} \Leftrightarrow \frac{\Delta\epsilon}{2} = \frac{1183.7}{E} (2N_f)^{-0.0545} + 0.4697 (2N_f)^{-0.6059} \quad (5.13)$$

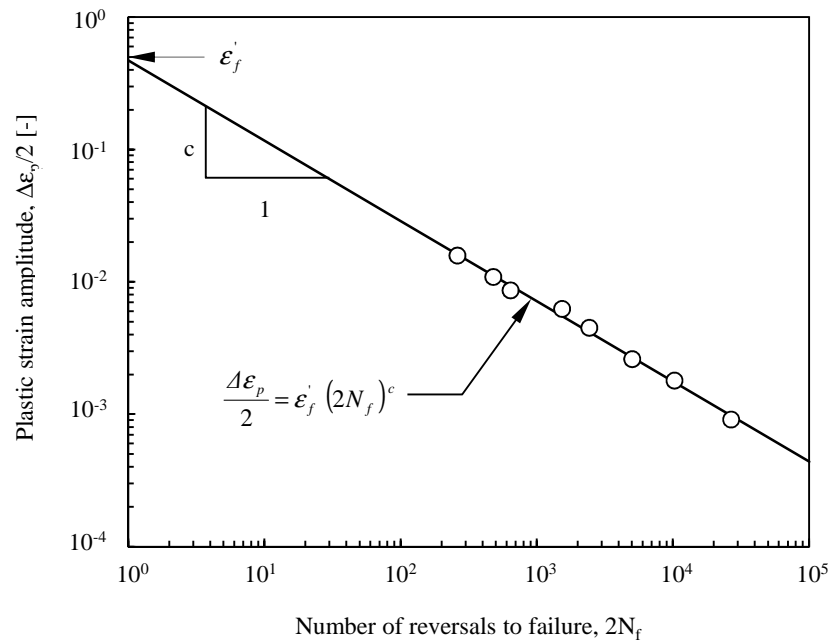


Figure 5.15. Plastic strain amplitude versus number of reversals to failure.

Table 5.8. Fatigue ductility properties of DIN 34CrNiMo6 high strength steel.

Property	Value
Fatigue ductility coefficient, ϵ_f'	0.4697
Fatigue ductility exponent, c	-0.6059

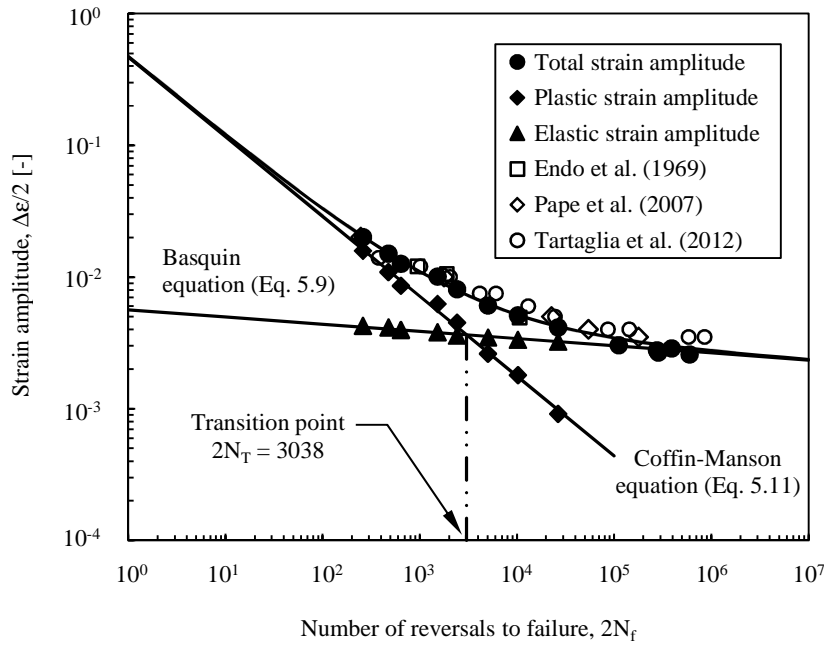


Figure 5.16. Total strain-life, fatigue strength-life and fatigue ductility-life curves (Branco, 2012b).

lives lower than N_T , the plastic strain component prevails over the elastic one and *vice versa*. Thus, it can be concluded that longer lives ($N_T > 3038$) require stress amplitudes lower than 815.8MPa (Eq. 5.8) and strain amplitudes smaller than 0.73% (Eq. 5.13). The values of the total strain-life curve obtained in this study were compared with results found in the literature for the DIN 34CrNiMo6 high strength steel (Endo, 1969; Pape, 2007; Tartaglia, 2012). Regardless of the sources and objectives of the studies, the results are all very close (see Figure 5.16).

Energy-based approaches assume that the dissipated strain energy per cycle has a main contribution to the fatigue damage process. The plastic strain energy dissipated per cycle (ΔW_p) due to plastic deformation is the area of the hysteresis loop. Under strain-controlled conditions, it is almost constant during the life, which is a clear advantage. For a Masing-type material, ΔW_p can be defined as follows (Morrow, 1965)

$$\Delta W_p = \frac{1-n'}{1+n'} \Delta\sigma \Delta\varepsilon_p \quad (5.14)$$

where $\Delta\varepsilon_p$ is the plastic strain range, $\Delta\sigma$ is the stress range and n' is the cyclic hardening exponent. For a non-Masing material, the value of ΔW_p is given by (Lefebvre, 1984)

$$\Delta W_p = \frac{1-n^*}{1+n^*} \Delta\sigma \Delta\varepsilon_p + \frac{2n^*}{1+n^*} \delta\sigma_0 \Delta\varepsilon_p \quad (5.15)$$

where n^* is the hardening exponent of the master curve and $\delta\sigma_0 = \Delta\sigma - \Delta\sigma^*$. Figure 5.17 presents a plot of the ΔW_p at the half-life versus the number of reversals to failure ($2N_f$). The ΔW_p values were obtained in three ways, namely by measuring the area of the hysteresis loops, by applying Eq. 5.14 and by applying

Eq. 5.15. Table 5.9 summarises the values of the plastic strain energy dissipated per cycle obtained for different strain amplitudes ($\Delta\varepsilon/2$). As can be seen, there are no significant differences in the three cases. For high strength steels, the plastic strain energy dissipated per cycle versus the number of reversals in a log-log scale can be satisfactorily fitted to a straight line (Ellyn, 1997), i.e.

$$\Delta W_p = \kappa p (2N_f)^{\alpha p} \quad (5.16)$$

being κp and αp two unknowns determined from the experimental data. The former (κp) is the plastic strain energy dissipated per cycle at one reversal and the latter (αp) is the slope of the straight line. The constants (κp and αp) of the experimentally measured values of ΔW_p were evaluated using the least square method and are listed in Table 5.10. The experimentally measured values of ΔW_p were compared with predictions obtained in the literature (Sih, 2004a) using the isoenergy density theory (Sih, 2004). As can be observed, the predicted values are practically superimposed on the dashed line (Eq. 5.16) and therefore are in good agreement with those measured experimentally.

The plastic strain energy per cycle measured experimentally and calculated by Eq. 5.14 (Masing-type material) and Eq. 5.15 (non-Masing material) are compared in Figure 5.18. Although not totally clear, the calculations from Eq. 5.15 are on average 1.8% more accurate than those from Eq. 5.14. However, and not surprisingly, the agreement is fairly good in both cases.

This approach, as a damage parameter, has certain limitations. For longer lives, close to the fatigue limit

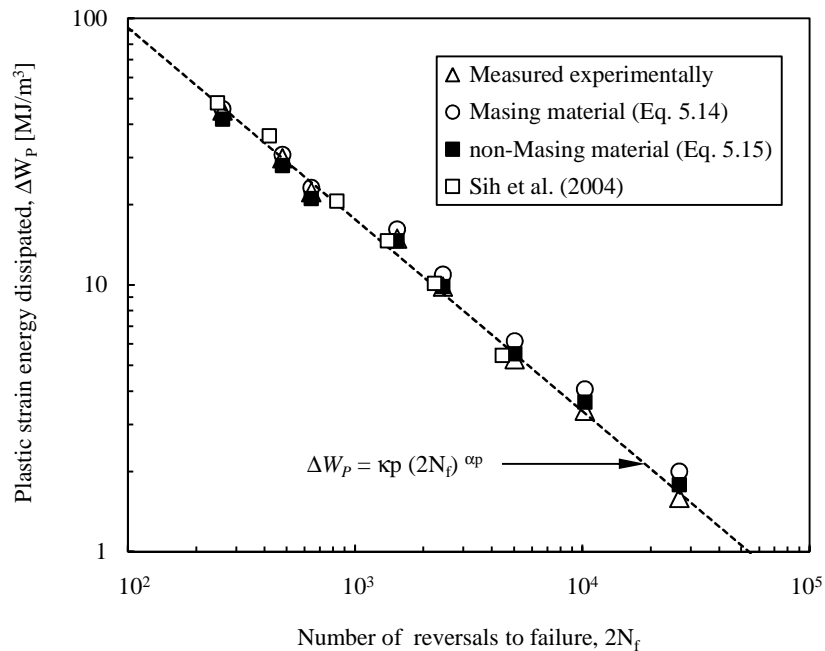


Figure 5.17. Plastic strain energy dissipated per cycle versus number of reversals to failure (Branco, 2012b).

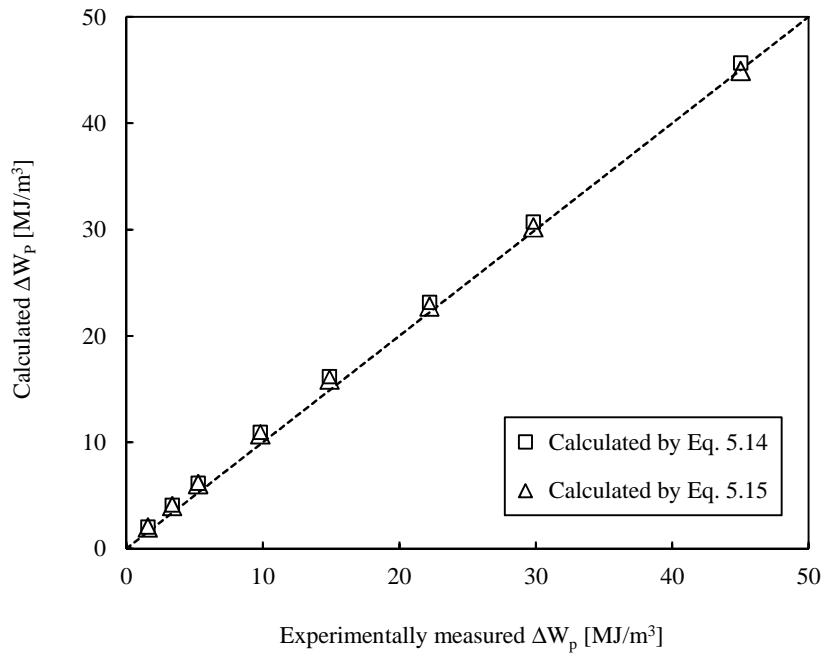


Figure 5.18. Calculated versus experimentally measured plastic strain energy dissipated per cycle.

Table 5.9. Experimental and theoretical values of ΔW_p .

Strain amplitude, $\Delta\epsilon/2$ [%]	ΔW_p measured experimentally [MJ/m ³]	ΔW_p determined by Eq. 5.14 [MJ/m ³]	ΔW_p determined by Eq. 5.15 [MJ/m ³]
2.003	45.041	45.671	41.733
1.503	29.828	30.707	28.003
1.254	22.226	23.146	21.033
1.004	14.889	16.142	14.616
0.806	9.828	10.918	9.834
0.607	5.261	6.1460	5.518
0.512	3.371	4.063	3.634
0.413	1.589	1.998	1.781

Table 5.10. Constants of Eq. 5.16 for DIN 34CrNiMo6 high strength steel.

Property	Value
Coefficient κp [MJ/m ³]	2115.84
Exponent αp	-0.6924

of the material, ΔW_p is a very small value which makes it difficult to measure. To overcome this, the total strain energy (ΔW), given by the sum of the elastic and plastic strain energies, can be used to advantage. However, both ΔW_p and ΔW approaches are more suitable for fully-reversed or almost fully-reversed tests since they are not sensitive to the mean stress. Thus, the formulation proposed by Golos *et al.* (1987) is preferable. In this case, both the sum of the hysteresis energy and elastic energy associated with the tensile stress are used. The total strain energy range per cycle (ΔW_t) can be defined by

$$\Delta W_t = \Delta W_p + \Delta W_{e+} \quad (5.17)$$

where ΔW_p is the plastic strain energy dissipated per cycle and ΔW_{e+} is the tensile elastic strain energy per cycle. For a non-Masing material under a cyclic loading with $\sigma_{\min} \leq 0$, the previous equation can be written in the form of Eq. 5.18 (Ellyin, 1987).

$$\Delta W_t = \frac{1-n^*}{1+n^*} \Delta\sigma \Delta\varepsilon_p + \frac{2n^*}{1+n^*} \delta\sigma_0 \Delta\varepsilon_p + \frac{\sigma_{\max}^2}{2E} \quad (5.18)$$

Figure 5.19 presents in a log-log scale the total strain energy range per cycle versus the number of reversals to failure for the DIN 34CrNiMo6 high strength steel studied here. The experimental data can be fitted using the following expression (Ellyin, 1987)

$$\Delta W_t = \kappa t (2N_f)^\alpha + \Delta W_{0t} \quad (5.19)$$

being $\kappa t > 0$ and $\alpha t < 0$. The constant ΔW_{0t} is the tensile elastic energy at the material fatigue limit. The κt and αt constants can be determined from the best fit to the experimental data. Table 5.11 lists the final

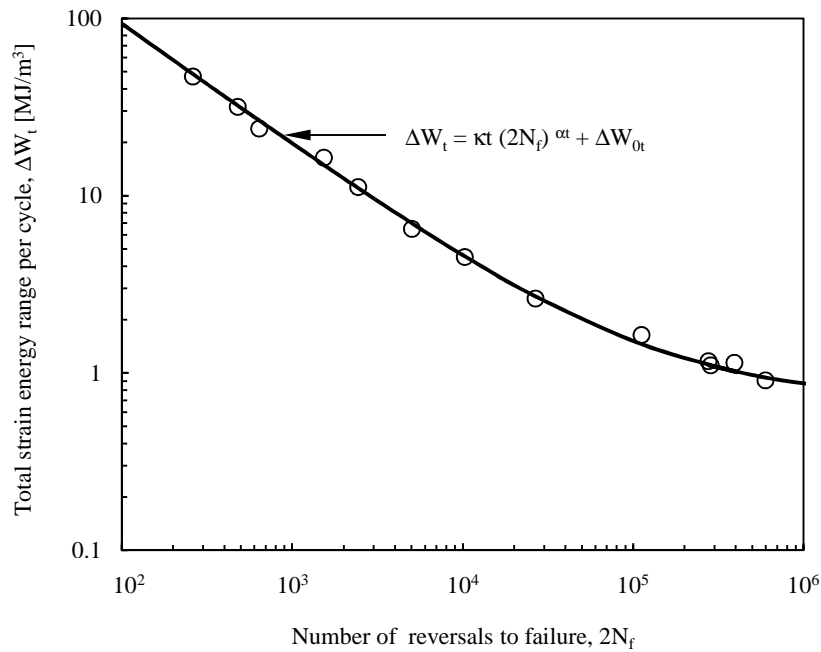


Figure 5.19. Strain energy range per cycle versus number of reversals to failure.

Table 5.11. Constants of Eq. 5.19 for DIN 34CrNiMo6 high strength steel.

Property	Value
Coefficient κt [MJ/m ³]	2165.37
Exponent αt	-0.6854
Constant ΔW_{0t} [MJ/m ³]	0.7049

values which were calculated using the least square method. As can be seen from Figure 5.19, the total strain energy range per cycle is a very good correlating parameter for the fatigue life interval studied here. All the results are very close to the proposed function (Eq. 5.19). The value of ΔW_{0r} corresponds to a fatigue limit stress amplitude of 537MPa. This is satisfactorily close to the values reported in the literature (526 ± 15 MPa) by Rabb (1996) for smooth specimens subjected to tension-compression ($R = -1$).

5.4.3 Analysis of fracture surfaces

The macroscopic surface morphologies after low-cycle fatigue tests for several total strain amplitudes are presented in Figure 5.20. Regardless of the strain amplitude, and not surprisingly, the final fracture surfaces are similar, presenting angles at about 45° in relation to the loading axes.

Figures 5.21a-c show typical SEM images of fracture surfaces taken at low magnification for different strain amplitudes. Figure 5.21a ($\Delta\epsilon/2 = 0.4\%$) exhibits a fracture surface caused by propagation of several cracks nucleated at the periphery of the specimen, leading to the formation of various steps that result from the junction of different propagation planes. However, a flat surface with practically no shear lip is observed. Figure 5.21b ($\Delta\epsilon/2 = 2.0\%$) also presents a fracture surface characterised by propagation of several cracks. Nevertheless, at this total strain amplitude, the junction of various propagation planes implies a microscopically inclined fracture. Additionally, the propagation area contains some fatigue striations combined with secondary cracks (indicated by the white arrow and exhibited in detail in Figure 5.21c). The fatigue striations denote essentially transgranular crack propagation. Moreover, as expected, the stable crack growth region is larger in Figure 5.21a due to the smaller total strain amplitude applied.

Figures 5.22a-c present typical SEM images of fracture surfaces taken at high magnification near the crack initiation site for different strain amplitudes. At lower strain amplitudes (Figure 5.22a), the initiation site is clearly dominated by cleavage-like facets whilst at higher strain amplitudes (Figure 5.22b

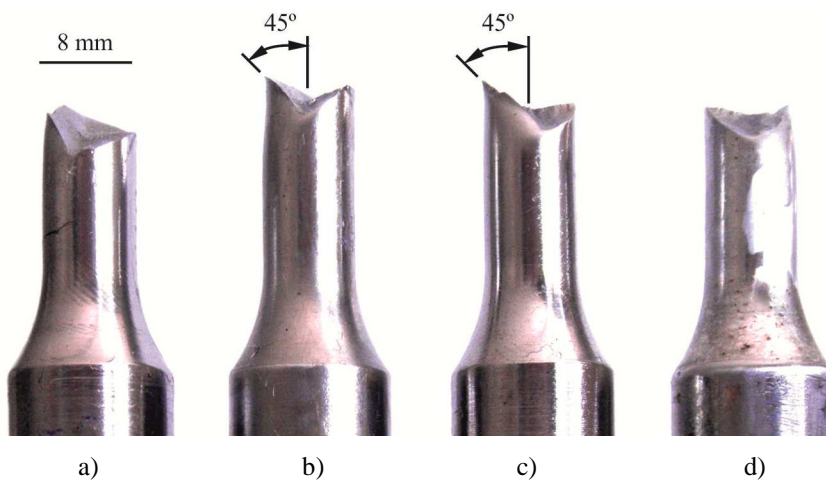
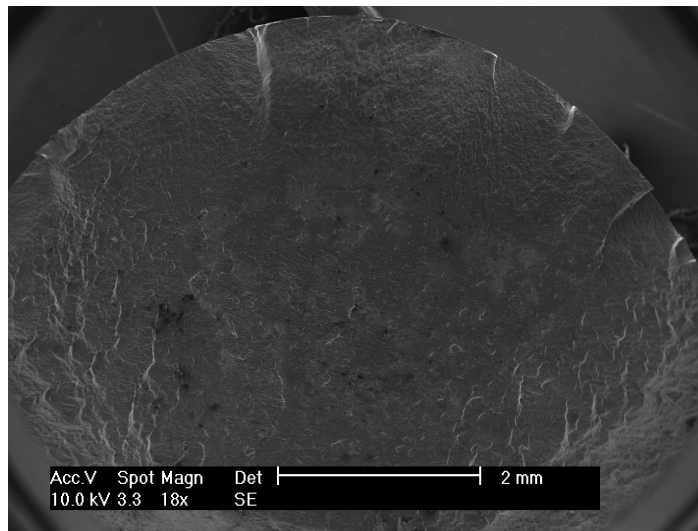
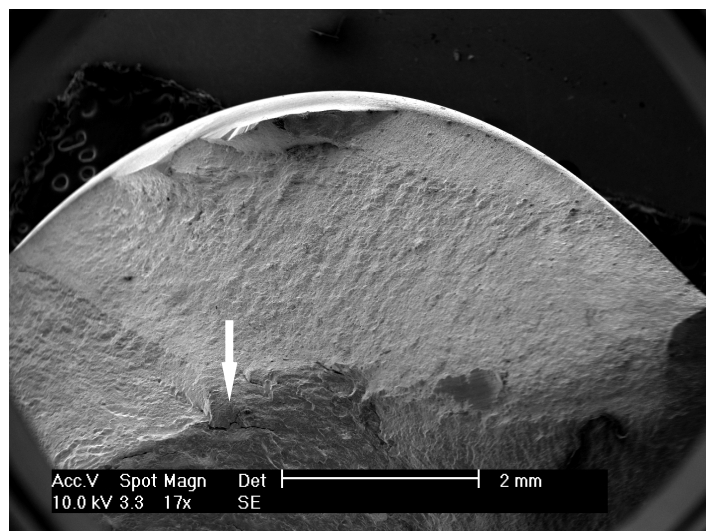


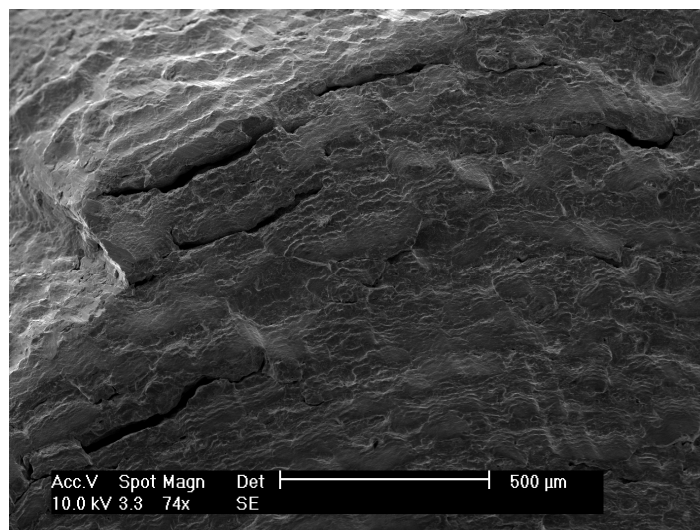
Figure 5.20. Macroscopic surface morphologies of low-cycle fatigue specimens: a) $\Delta\epsilon/2 = 0.5\%$; b) $\Delta\epsilon/2 = 0.8\%$; c) $\Delta\epsilon/2 = 1.25\%$; d) $\Delta\epsilon/2 = 1.5\%$ (Branco, 2012b).



a)

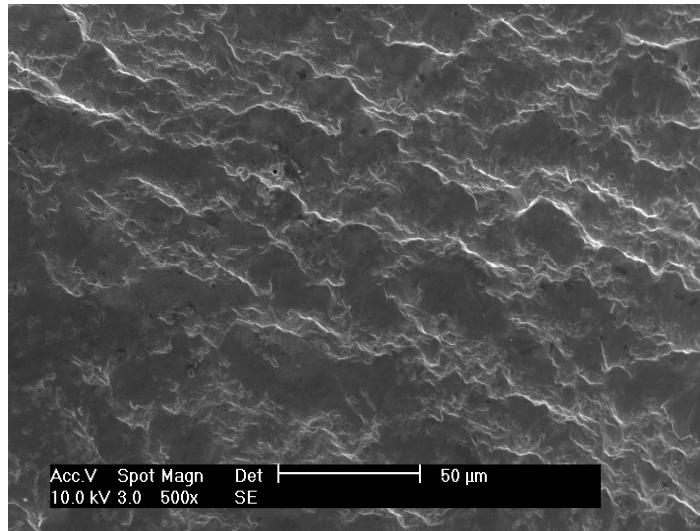


b)

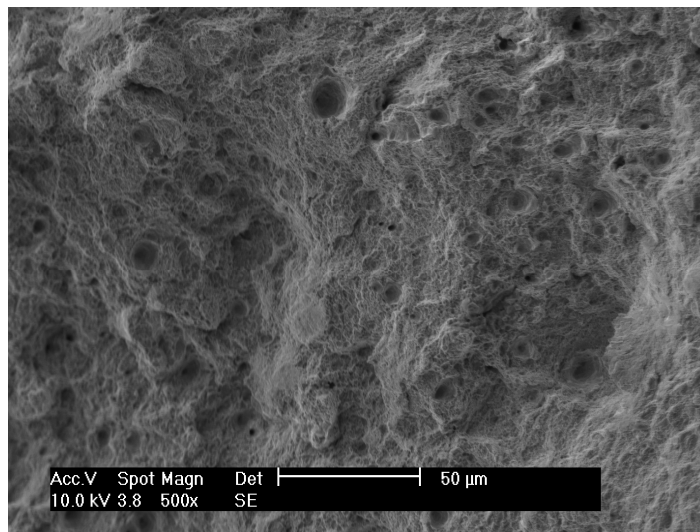


c)

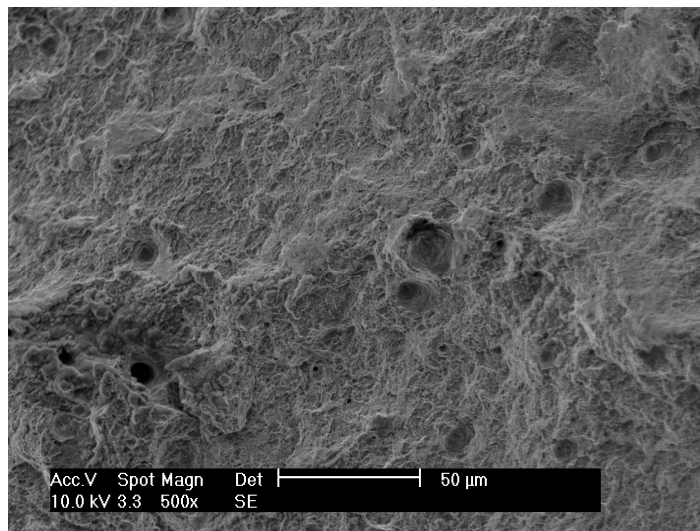
Figure 5.21. Fracture surfaces for different values of $\Delta\epsilon/2$ (Branco, 2012b): a) $\Delta\epsilon/2=0.4\%$; b) $\Delta\epsilon/2=2.0\%$; c) $\Delta\epsilon/2=2.0\%$ (detail of fatigue striations combined with secondary cracks).



a)



b)



c)

Figure 5.22. SEM micrographs of fracture surfaces near the crack initiation sites for different total strain amplitudes: a) $\Delta\epsilon/2=0.4\%$; b) $\Delta\epsilon/2=1.0\%$; c) $\Delta\epsilon/2=2.0\%$ (Branco, 2012b).

and Figure 5.22c) the initiation site is a mixed of cleavage-like facets and ductile dimples. Besides, the higher the strain amplitude is, the more numerous the ductile dimples are. The fatigue damage mechanism observed here results from the cyclic solicitations applied which cause extrusions and intrusions leading to the formation of a microcrack smaller than the grain size along the slip band at the specimen surface. Then, the microcrack grows through the grain boundaries and eventually can form, by coalescence of shorter cracks, a critical one that propagates into the bulk perpendicularly to the stress axis.

5.5. High-cycle fatigue tests

The high-cycle fatigue tests performed in this research aimed at studying the fatigue behaviour of severely notched geometries subjected to different proportional loading paths (Figure 3.9). The specimen geometries used are presented in Figure 3.8. These tests encompassed single bending (Table 3.4), single torsion (Table 3.5) and in-phase combined bending-torsion (Table 3.6). In relation to the last type, the ratios of the bending moment (B) to the torsion moment (T) analysed were B=2T, B=T and B=2T/3. The detection of crack initiation was carried out *in situ* with a digital monitoring system (Figure 3.11). Stress ratios (*R*) very close to zero (0.02-0.04) were adopted. The normal and shear stress amplitudes (σ_a and τ_m) as well as the mean normal and shear stresses (σ_m and τ_m) were calculated using Equations 3.2-3.4. Tables 5.12, 5.13 and 5.14 summarise, respectively, the main results of the single bending, single torsion and in-phase combined bending-torsion tests performed in this research.

Table 5.12. Summary of results of the single bending tests.

Specimen reference	Normal stress amplitude, σ_a [MPa]	Mean normal stress, σ_m [MPa]	Shear stress amplitude, τ_a [MPa]	Mean shear stress, τ_m [MPa]	Cycles to failure, N_f [cycles]
B-1	195.6	206.1			142052
B-2	195.6	206.1			241674
B-3	218.8	229.3			99708
B-4	218.8	229.3			71509
B-5	295.0	304.2			25410
B-6	295.0	304.2			33562

Total: 6 specimens

Table 5.13. Summary of results of the single torsion tests.

Specimen reference	Normal stress amplitude, σ_a [MPa]	Mean normal stress, σ_m [MPa]	Shear stress amplitude, τ_a [MPa]	Mean shear stress, τ_m [MPa]	Cycles to failure, N_f [cycles]
T-1			167.0	178.2	203168
T-2			167.0	178.2	234708
T-3			200.5	211.6	100857
T-4			200.5	211.6	71901
T-5			222.7	233.9	59957
T-6			245.0	256.1	55587
T-7			245.0	256.1	68199

Total: 7 specimens

Table 5.14. Summary of results of the in-phase combined bending-torsion tests.

Specimen reference	Normal stress amplitude, σ_a [MPa]	Mean normal stress, σ_m [MPa]	Shear stress amplitude, τ_a [MPa]	Mean shear stress, τ_m [MPa]	Cycles to failure, N_f [cycles]
▪ B=2T series ($\sigma_a = 4\tau_a$; $\sigma_m = 4\tau_m$; $\Delta\sigma = 4\Delta\tau$)					
B2T-1	179.1	194.0	44.8	48.5	159714
B2T-2	223.8	238.7	56.0	59.7	95383
B2T-3	298.4	313.3	74.6	78.3	39205
▪ B=T series ($\sigma_a = 2\tau_a$; $\sigma_m = 2\tau_m$; $\Delta\sigma = 2\Delta\tau$)					
BT-1	179.1	194.0	89.5	97.0	144876
BT-2	179.1	194.0	89.5	97.0	113465
BT-3	179.1	194.0	89.5	97.0	106883
BT-4	223.8	238.7	111.9	119.4	52840
BT-5	223.8	238.7	111.9	119.4	40818
BT-6	223.8	238.7	111.9	119.4	57918
BT-7	298.4	313.3	149.2	156.7	16628
▪ B=2T/3 series ($\sigma_a = 4/3\tau_a$; $\sigma_m = 4/3\tau_m$; $\Delta\sigma = 4/3\Delta\tau$)					
B2T3-1	179.1	189.0	134.3	141.8	85361
B2T3-2	223.8	233.8	167.9	175.3	30242
B2T3-3	298.4	308.4	223.8	231.3	9312

Total: 13 specimens

5.5.1 Fatigue crack paths, surface crack angles and fracture surfaces

Figures 5.23a-e show representative fatigue crack paths obtained in the experimental tests for the different loading conditions. A significant influence of the loading pattern on the crack trajectory is observed. As can be seen, in the first case (Figure 5.23a), the crack propagates in a direction approximately normal to the axis of the specimen. In the other cases (Figures 5.23b-e), the crack trajectories become more and more curved. This is due to an increase of the ratio of the shear stress to the normal stress.

Representative crack initiation sites, depicted by the white circles, are also exhibited in Figure 5.23. There is a clear effect of the loading path on the initiation process. In the two first cases (Figures 5.23a-b), due to the absence or reduced level of shear stresses, the crack initiates in the centre of the notch; in the other cases (Figures 5.23c-e), the crack initiates close to the curved edge of the notch. The closeness increases with the ratio of the shear stress to the normal stress.

The fatigue crack paths and the initiation sites seem to be controlled, in this case, by the distribution of the principal stresses along the notch surface. These stress distributions, as evidenced in Figure 5.24, vary substantially with the loading path. The combination of both the loading pattern and the notch geometry results in complex triaxial stress states. The most susceptible regions to crack initiation are identified by the white squares which correspond to the maximum principal stresses. The dashed white lines represent the most likely crack surface paths. In Figure 5.23 are also compared the numerical predictions in terms of crack initiation sites (white squares) and surface crack paths (dashed white lines) with experimental

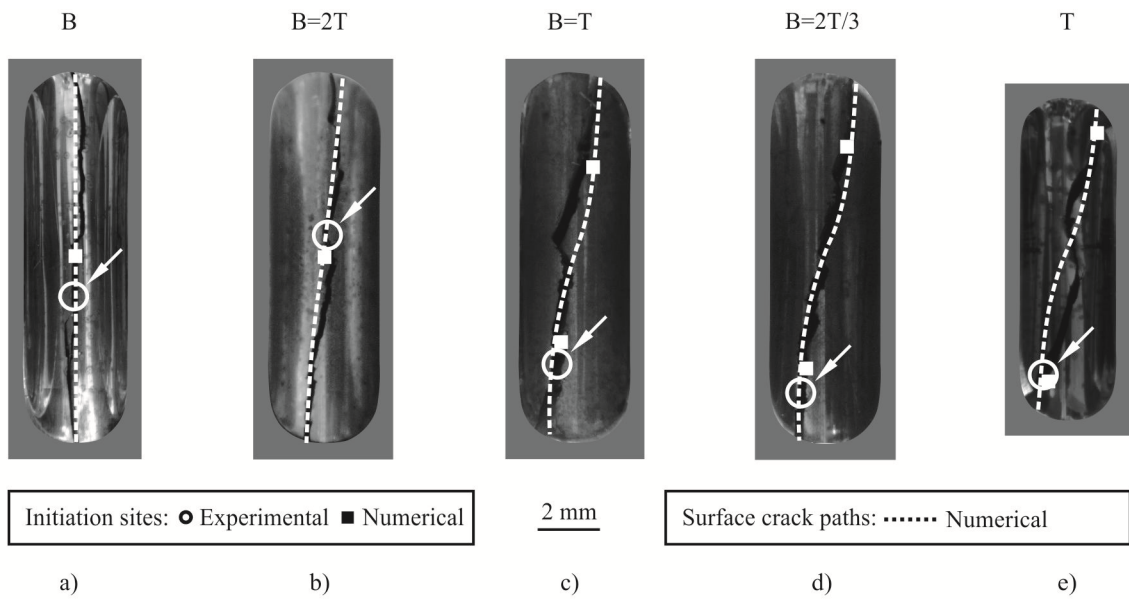


Figure 5.23. Surface crack paths and initiation sites for different loading paths. Specimen reference: a) B-1; b) B2T-2; c) BT2-1; d) B2T3-2; e) T-1 (Branco, 2012e).

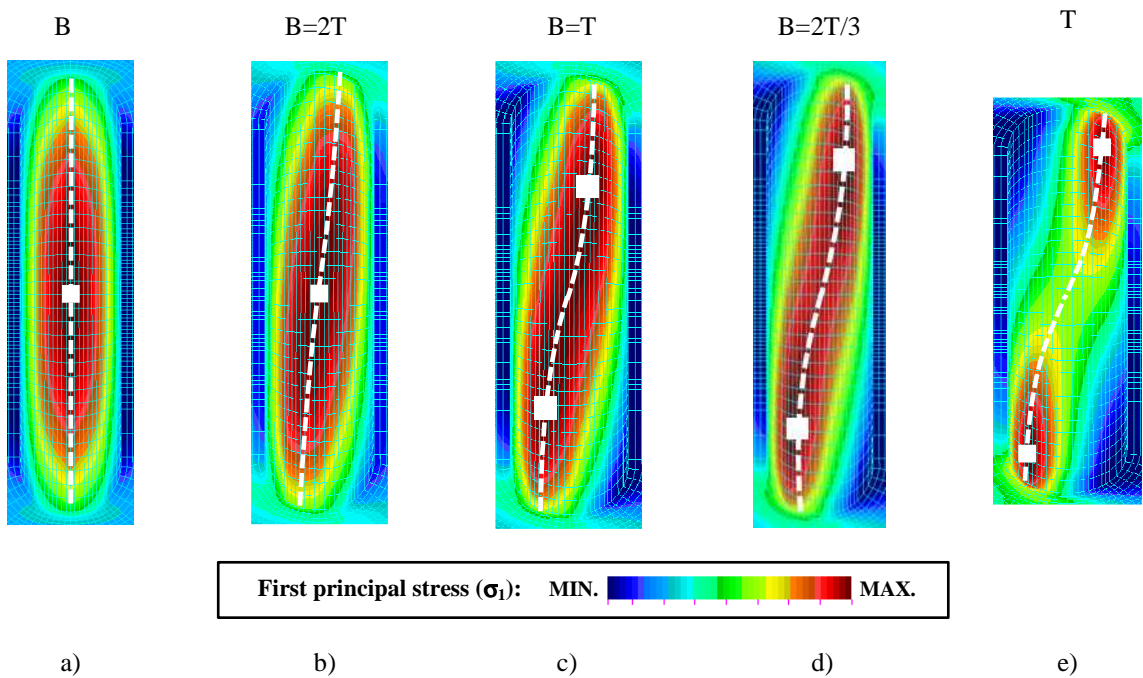


Figure 5.24. Numerical prediction of surface crack paths and initiation sites for different loading paths: a) B; b) B=2T; c) B=T; d) B=2T/3; e) T (Branco, 2012e).

results for the different loading cases studied here. As can be seen, the numerical predictions obtained from this criterion are very close to those detected experimentally.

Figures 5.25a-e exhibit representative surface crack orientations at the initial stage of crack growth with

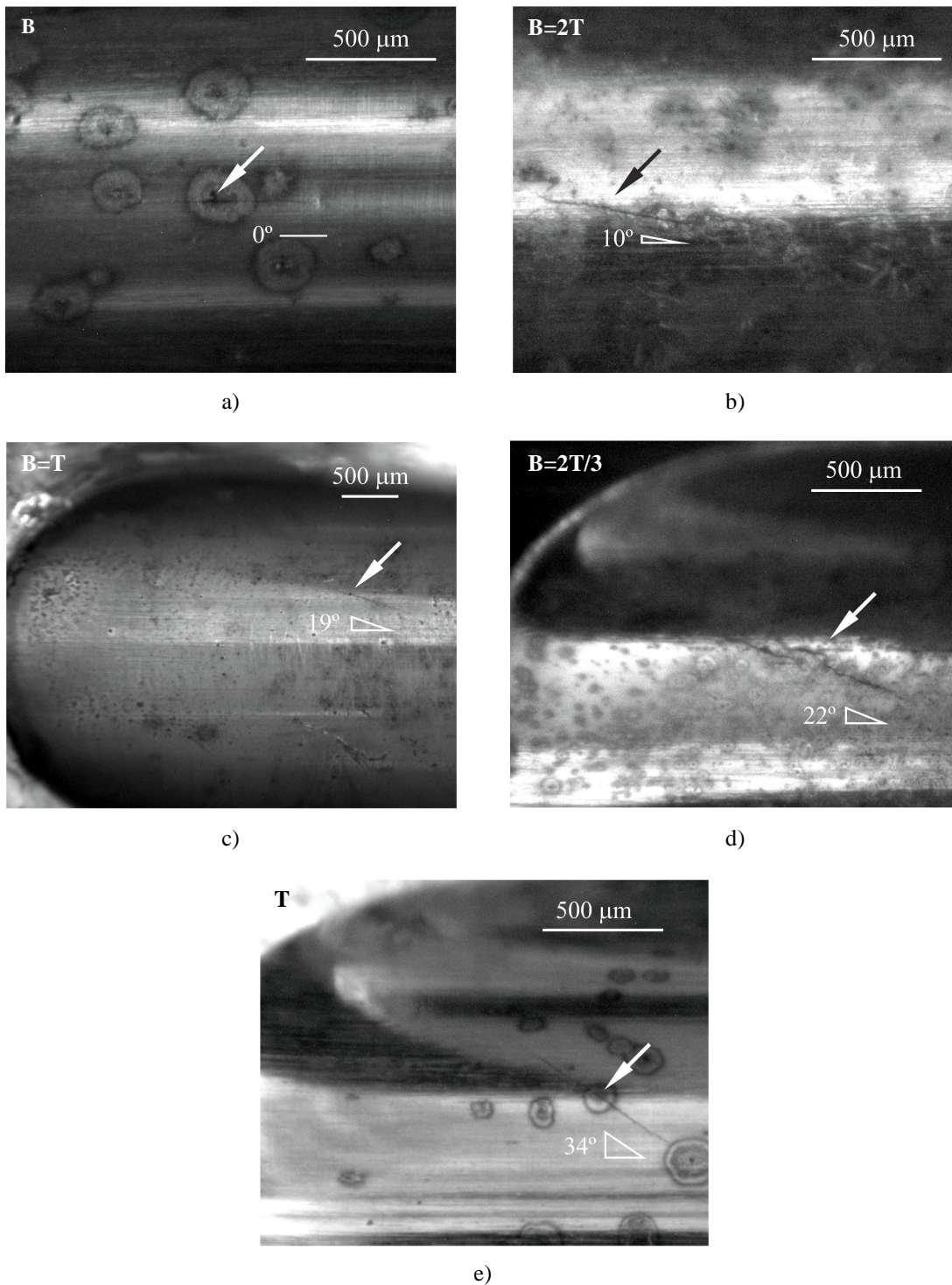


Figure 5.25. Surface crack orientation at the early stage of crack growth for different loading paths.

Specimen reference: a) B-m; b) B2T-m; c) BT-m; d) B2T3-m; e) T-m.

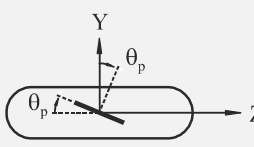
respect to the normal direction of the specimen axis for the different loading paths analysed. The angle, as schematised, varies considerably from case to case. For single bending (Figure 5.25a), the crack grows in a direction normal to the specimen axis (0°) which is expected since it is subjected to mode I loading. In the other cases (Figures 5.25b-e), the angle is increasingly greater due to the higher ratio of the shear stress to the normal stress. These cases are predominantly under mixed mode I/III loading and, therefore,

the increase in the τ/σ ratio has a direct repercussion on the surface crack orientation. These angles can be predicted by computing the principal directions (θ_p) for the nodes with maximum principal stresses, i.e. solving the following equation

$$2\theta_p = \tan^{-1} \left(\frac{\sigma_{YY} - \sigma_{ZZ}}{2\tau_{YZ}} \right) \quad (5.20)$$

being σ_{ZZ} , σ_{YY} and τ_{YZ} the stress components obtained by the FEM. Table 5.15 summarises the numerical predictions obtained by Eq. 5.20 (θ_{pn}) and the experimentally measured angles (θ_{pe}) for the different tests carried out in this research. Figure 5.26 plots the numerical predictions against the experimentally measured angles. As can be seen, numerical and experimental angles are in fairly good agreement. On the other hand, these results suggest that the propagation, at the surface, is controlled by the principal stress direction, i.e. crack paths are normal to the principal stress directions. Besides, although not perfect, the previous analysis can anticipate, in a relatively precise manner, the most likely initiation sites, surface

Table 5.15. Comparison between experimental and predicted surface crack orientations.

Referential system	Loading path	Angle predicted, θ_{pn} [°]	Angle measured, θ_{pe} [°]
	B	0	0
	B=2T	11.1	9.5-12.0
	B=T	20.8	18.0-22.5
	B=2T/3	26.1	22.0-25.1
	T	38.6	32.0-36.5

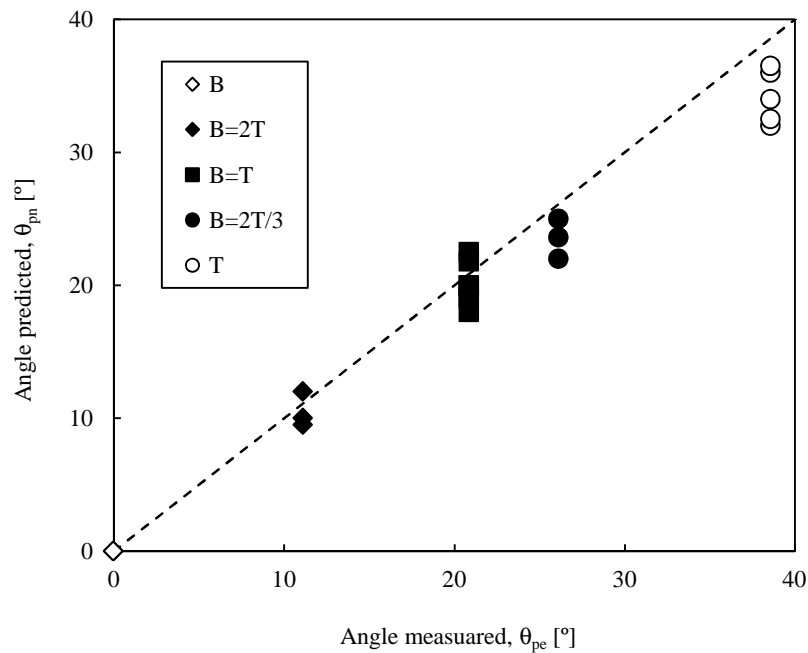


Figure 5.26. Experimental versus predicted crack surface angles at the initial stage of crack growth for different loading paths.

crack paths and surface crack orientations at the initial stage of crack growth.

Furthermore, it is important to note that crack initiation always occurred from small defects (labelled by the arrows in Figures 5.25a-e) on the notch surface, very close to the most likely initiation sites. These surface irregularities act as local stress raisers making easier the fatigue crack initiation process. Besides, due to the presence of defects throughout the notch surface, multi-crack initiation behaviour was observed in most of the cases. Take for example the image sequence exhibited in Figures 5.27a-d. In Figure 5.27a, several cracks, relatively close to each other, have initiated at different places of the notch surface. After about 3000 cycles (Figure 5.27b), the coalescence of neighbouring cracks is evident (labelled by the orange arrows). In a second stage, the cracks gradually approach each other (Figure 5.27c). In most cases, this propagation takes place in different planes. The junction of the different planes causes visible steps at the notch surface (Figure 5.27d).

Figures 5.28a-e present typical fracture surfaces obtained in the fatigue crack front marking tests for the different loading paths studied in this research. For each case, top and front views are shown. As can be

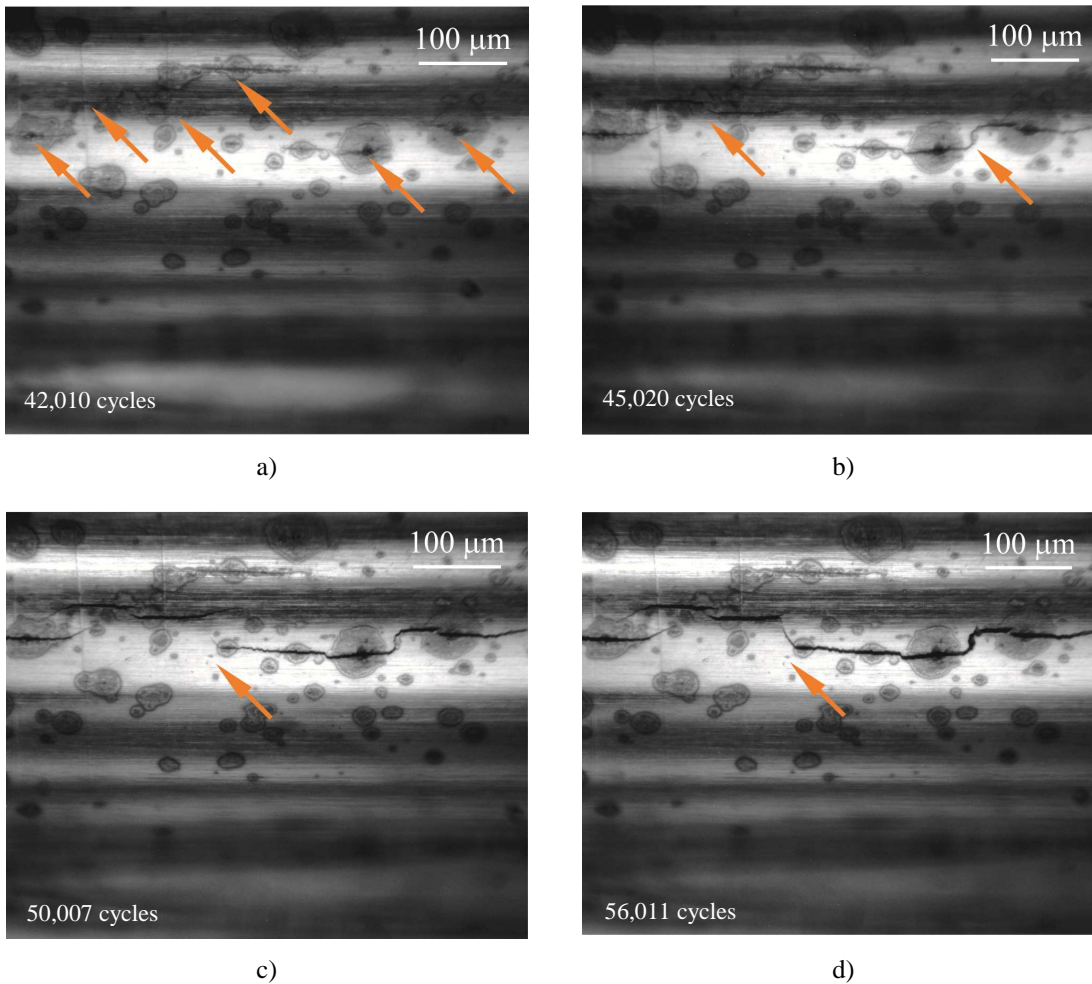


Figure 5.27. Multi-crack initiation sequence in a single bending test (specimen B-4): a) 42010 cycles; b) 45020 cycles; c) 50007 cycles; d) 56011 cycles.

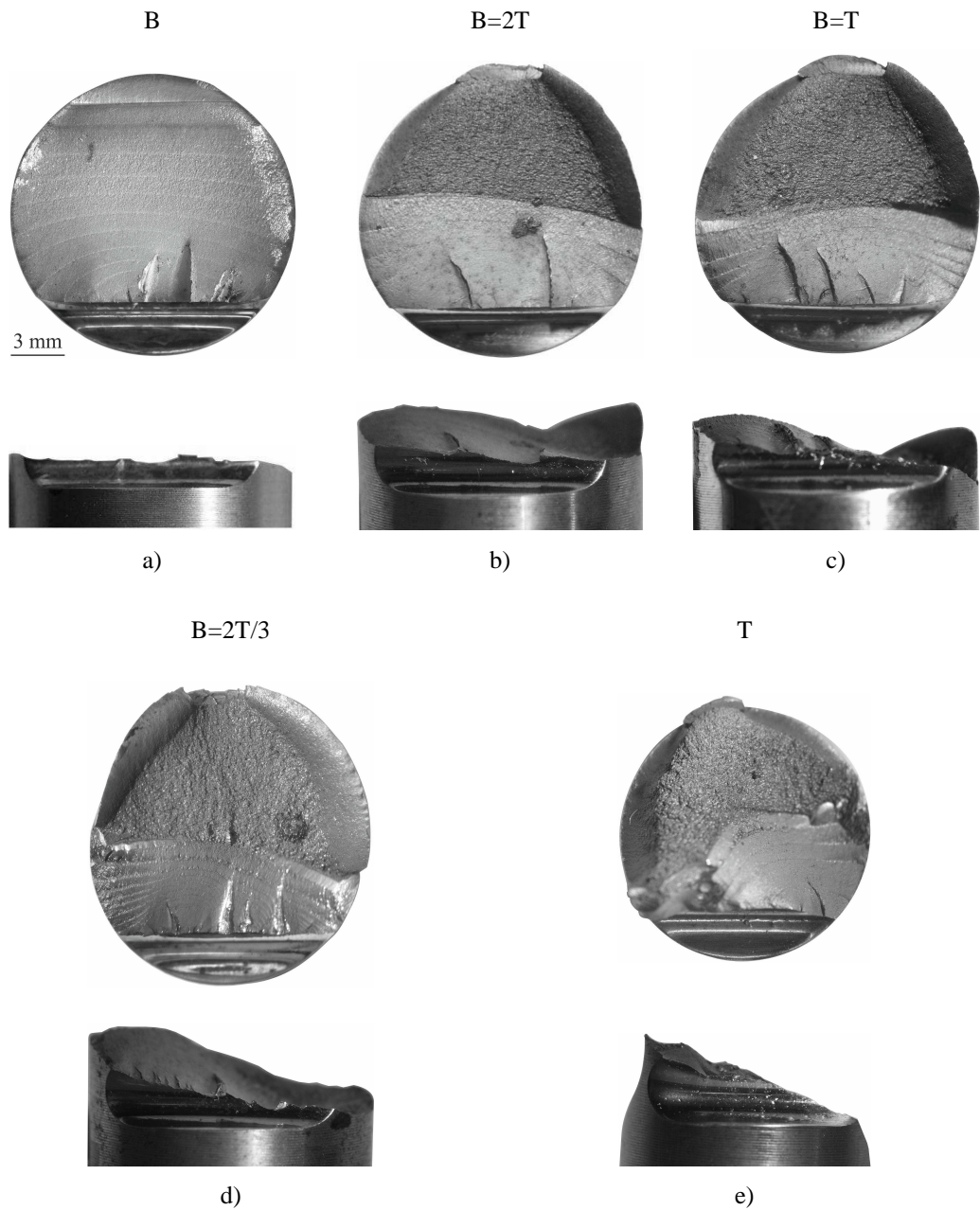


Figure 5.28. Fracture surfaces of fatigue crack front marking tests for the different loading paths.

Specimen reference: a) B-m; b) B2T-m; c) BT-m; d) B2T3-m; e) T-m (Serra, 2012).

seen, there is a considerable effect of the loading path on the fracture surfaces. For single bending (Figure 5.28a), fracture surfaces are flat and normal to the specimen axis. This is expected since these specimens are under mode I loading. The several steps observed at the surface are a reflex of the multi-crack propagation process described earlier. In the other cases (Figures 5.28b-e), the typical fracture surfaces have increasingly complex shapes due to higher ratios of the shear stress to the normal stress and are the result of out-of-plane propagation. Besides, the steps caused by the coalescence of cracks are also evident. In relation to the crack front markings, the differences are also clear. In Figure 5.28a, marks are almost semi-elliptical and progressively flatter. This fact can be confirmed in Figure 5.29, which plots the crack

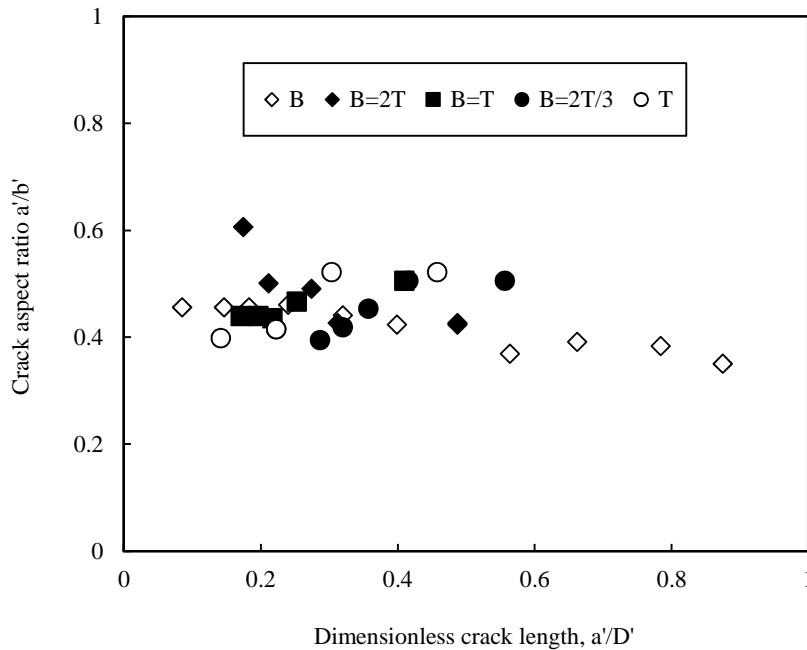
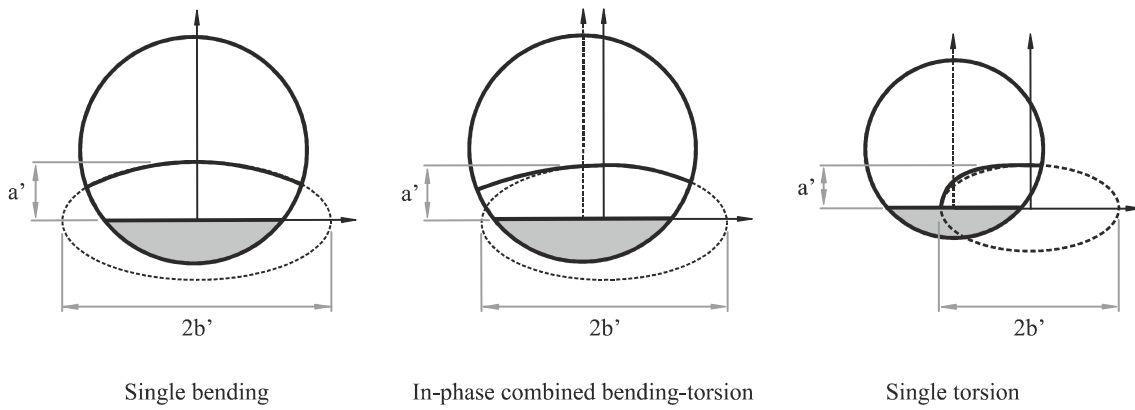


Figure 5.29. Crack aspect ratio (a'/b') versus dimensionless crack length (a'/D').

aspect ratio (a'/b') against the dimensionless crack length (a'/D'). For single bending, as schematised in the upper part of Figure 5.29, a' and b' represent the semi-axes of an ellipse whose centre is coincident with the origin of the coordinate system and $D' = D - n$ (n is the notch depth). As can be seen, a'/b' decreases with a'/D' . In the other cases (Figures 5.28b-e), marks are not symmetric in relation to the half-thickness and are increasingly curved in consequence of the higher ratios of the shear stress to the normal stress. Figure 5.29 presents the crack aspect ratio (a'/b') versus the dimensionless crack length (a'/D') for these four loading paths. The variables a' and b' , as depicted in Figure 5.29, are the semi-axes of an ellipse whose centre is on the notch root but not necessarily at the half-thickness. Therefore, such data need careful interpretation. Despite the differences in the definition of the crack aspect ratio, it is interesting to note that the a'/b' values are relatively close, regardless of the loading path.

Figures 5.30a-e show the fracture topologies obtained from the fatigue crack front marking tests by 3D laser scanning (see Section 3.9) for the different loading paths studied here. In these figures, it is possible

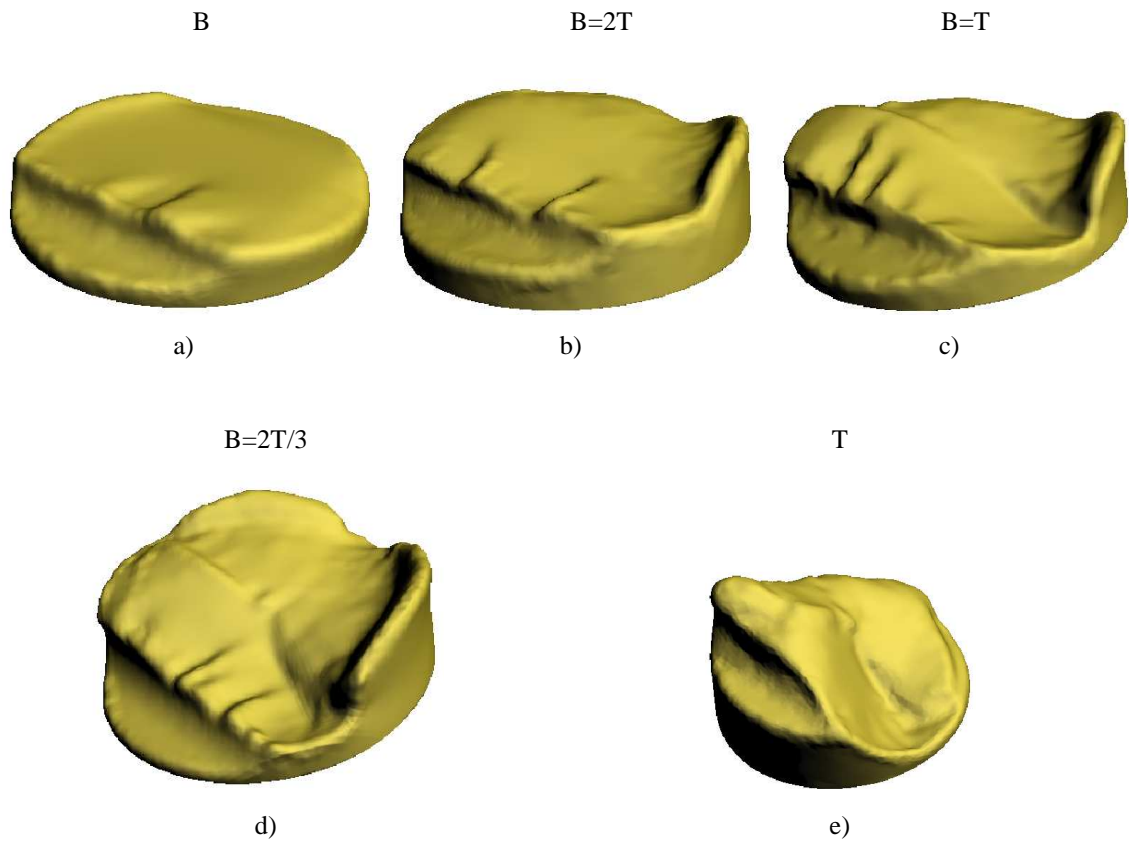
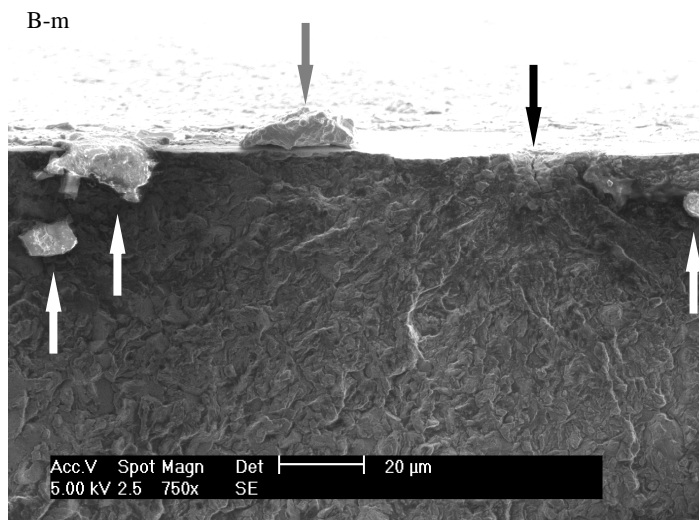


Figure 5.30. Fracture surfaces obtained by 3D scanner for the different loading paths. Specimen reference: a) B-m; b) B2T-m; c) BT-m; d) B2T3-m; e) T-m.

to better understand the surface patterns. Not surprisingly, out-of-plane propagation clearly increases with the ratio of the shear stress to the normal stress. On the other hand, the steps caused by coalescence of cracks are also evident.

The fracture surfaces were also examined by SEM in order to identify the damage mechanisms involved in the fatigue process. As mentioned before, crack initiation occurred from small defects and inclusions at the notch surface. A representative case of crack initiation from a surface defect at the notch is exhibited in Figures 5.31a-b, which was observed in the fatigue crack front marking tests for a specimen subjected to single bending. The direction of propagation is from the top to the bottom. The initiation site, either in Figure 5.31a or in Figure 5.31b, is identified by the black arrow. Particularly in the latter, due to its higher magnification, the surface defect is clearly visible. Besides, it is possible to identify the presence of several inclusions (white arrows) with different sizes and shapes. Some of them, as stated before, come off from the notch surface. A typical example is presented in Figure 5.31a (grey arrow). Unlike most cases, the particle is still attached to the specimen.

Figures 5.32a-b shows another example of crack initiation from a surface defect at the notch which occurred for an in-phase combined bending-torsion test ($B=2T/3$). In the two figures, the initiation site is



a)

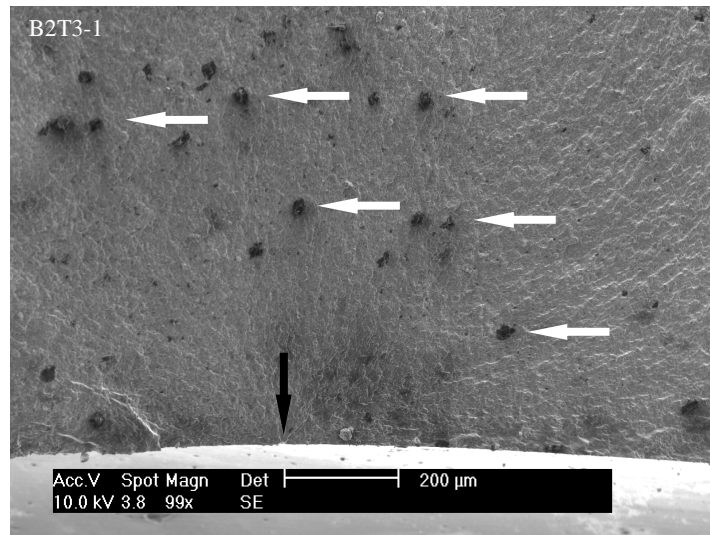


b)

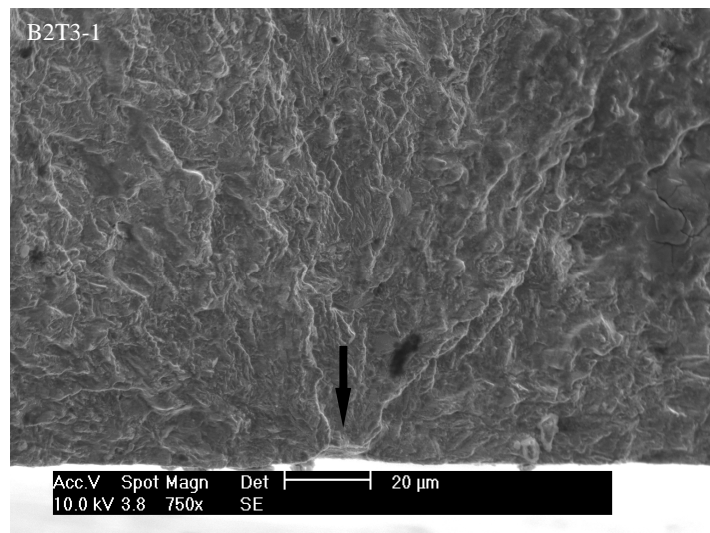
Figure 5.31. SEM micrographs of fracture surfaces near the crack initiation site for a single bending test magnified: a) 750 times; b) 1000 times.

identified by the black arrow and the direction of propagation is from the bottom to the top. Figure 5.32a was taken at low magnification whilst Figure 5.32b shows in detail the initiation site. In the latter, the surface defect is perfectly visible. Furthermore, the typical fatigue markings caused by cyclic loading are clearly observed. As can be seen, these markings are characterised by radial convergence to the initiation sites. This denotes essentially a ductile failure mode with evidence of local plastic deformation and transgranular fracture. In Figure 5.32a, it is particularly visible an area of pores (white arrows) with approximately circular shapes.

A representative example of crack initiation from an inclusion at the notch surface, occurred in a single torsion test, is shown in Figures 5.33a-b. In the two figures, the direction of propagation is identified by



a)

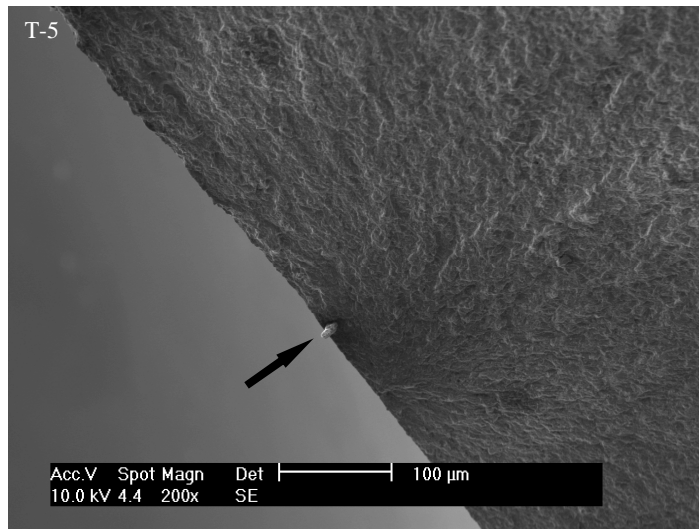


b)

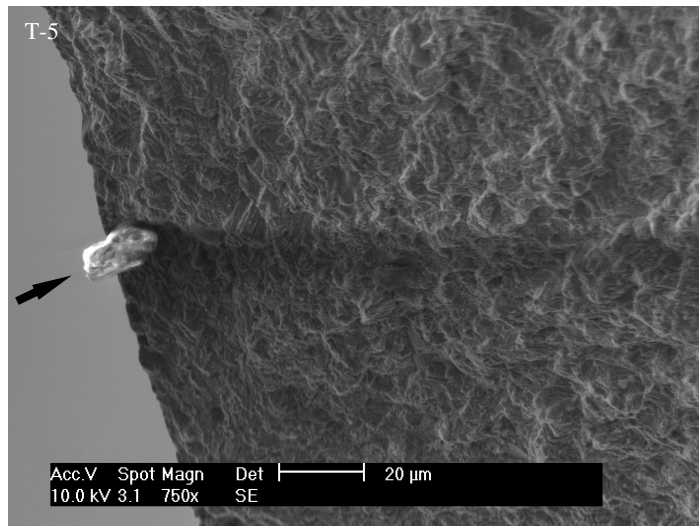
Figure 5.32. SEM micrographs of fracture surfaces near the crack initiation site for an in-phase combined bending-torsion test ($B=2T/3$) magnified: a) 99 times; b) 750 times.

the black arrow. Figures 5.33a and 5.33b were taken at low and high magnification, respectively. This particle, with maximum length of about $20\mu\text{m}$, has approximately an elliptical shape. As can be seen, the radial lines converge to the inclusion which indicates that the propagation occurred from this defect.

Figures 5.34a-b exhibit other examples of inclusions found in the analyses of fracture surfaces carried out in this research. The first image (Figure 5.34a) was obtained in the fatigue crack front marking tests for single bending loading. The inclusions of the second image (Figure 5.34b) were observed in an in-phase combined bending-torsion test ($B=2T$). The presence of inclusions and pores in DIN 34CrNiMo6 high strength steel has been reported by several authors. Costa *et al.* (2001) studied fatigue and fretting behaviour in ion-nitrided smooth specimens and concluded that crack initiation always occurred from



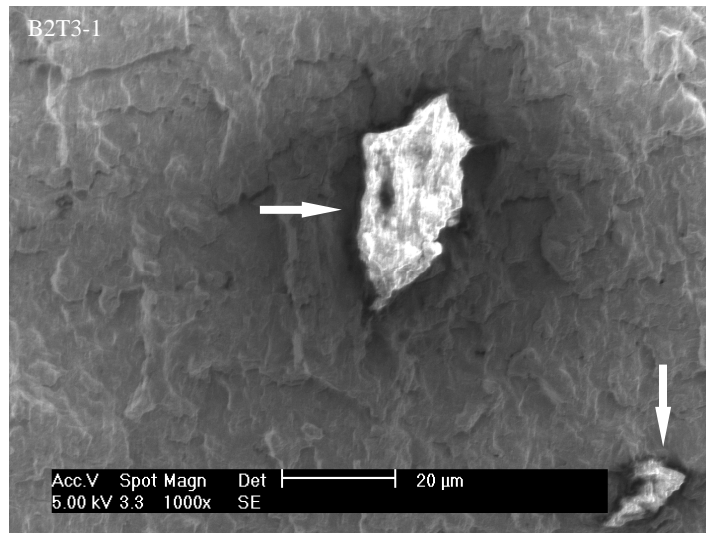
a)



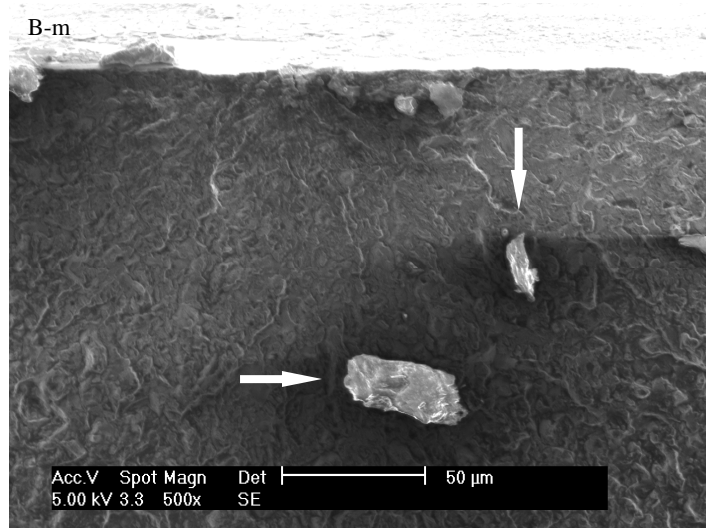
b)

Figure 5.33. SEM micrographs of fracture surfaces near the crack initiation site for a single torsion test magnified: a) 200 times; b) 1000 times.

internal defects below the surface treatment region. Sirin *et al.* (2008) also analysed the fatigue behaviour of ion-nitrided smooth specimens. The dominant fatigue crack initiation mechanism was the nucleation of cracks from non-metallic inclusions existing at the subsurface. Puchi-Cabrera *et al.* (2007) examined the fatigue performance of smooth specimens coated with 4 μm -thickness TiCN films. The fracture surfaces revealed the presence of a considerable number of unreacted particles and pores. Nevertheless, in this case, the fatigue cracks nucleated at the surface of the coating and propagated normal to the substrate-coating interface without bifurcation. Tartaglia *et al.* (2012) compared the fatigue resistance of quenched and tempered specimens with austempered specimens. The investigation of the fracture surfaces also revealed the existence of non-metallic particles on the microstructure. Among others, these



a)

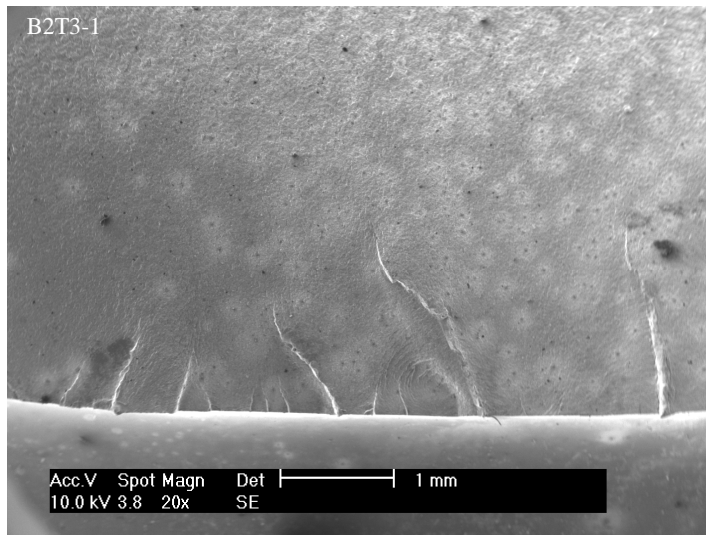


b)

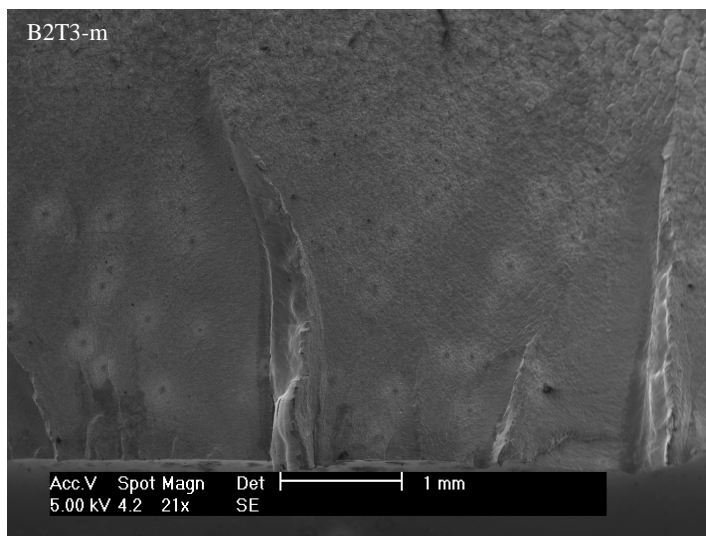
Figure 5.34. SEM micrographs of fracture surfaces containing several inclusions: a) single bending loading; b) in-phase combined bending-torsion loading ($B=2T/3$).

inclusions were identified as manganese sulphide (MnS) stringer particles. In another study on mechanical properties and hydrogen embrittlement resistance of austempered specimens and Q&T specimens, the authors found numerous types of inclusions, more specifically sulphide stringer inclusions, fragmented alumina inclusions, globular oxides and elongated silicate inclusions (Tartaglia, 2008).

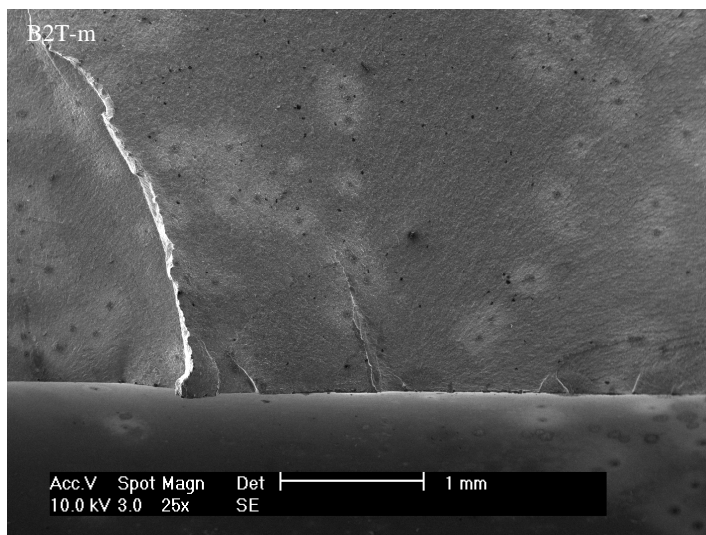
As stated before, multi-crack initiation sites were observed on the notch surfaces. Typical examples are presented in Figures 5.35a-c. In the three situations, the direction of propagation is from the bottom to the top. The first case (Figure 5.35a) results from an in-phase combined bending-torsion test ($B=2T/3$). The



a)



b)

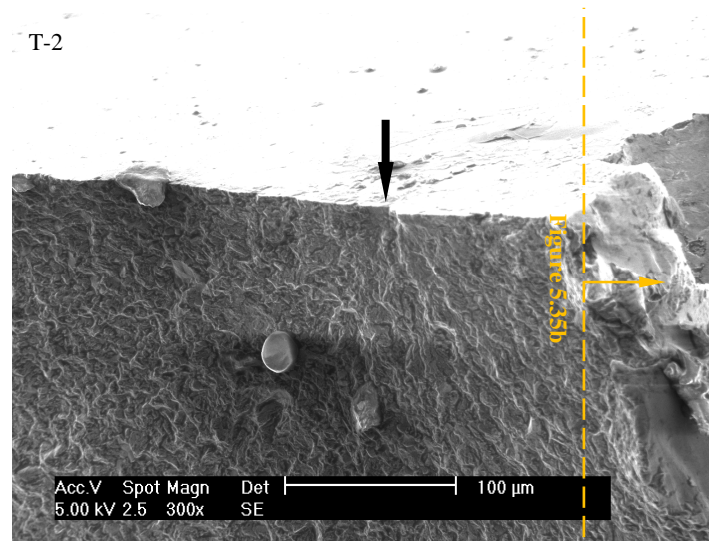


c)

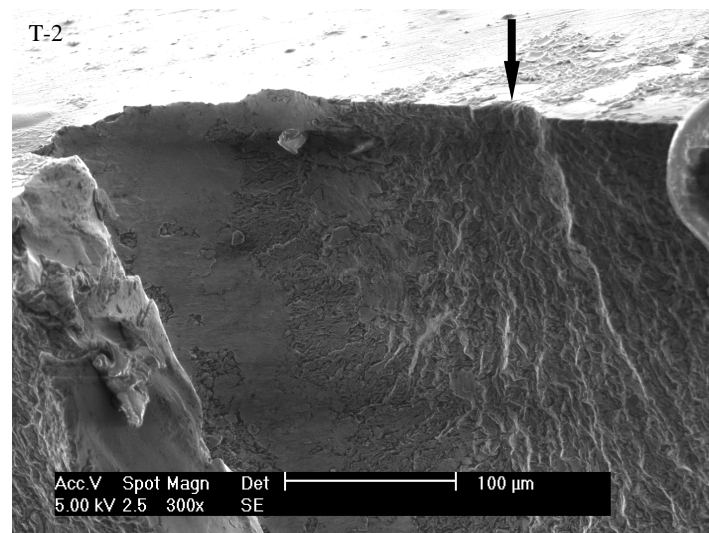
Figure 5.35. SEM micrographs of fracture surfaces revealing multi-crack initiation.
Specimen reference: a) B2T3-1; b) B2T3-m; c) B2T-m.

other two (Figures 5.35b-c) resulted from the fatigue crack front marking tests for loading paths equal to $B=2T/3$ and $B=2T$, respectively. Regardless of the case, several fracture steps are clearly observed which can be associated with the junction of different propagation planes caused by nucleation of various cracks at the periphery of the notch surface. Tartaglia *et al.* (2012) in their studies on fatigue resistance of Q&T specimens and austempered specimens reported the same behaviour.

Figures 5.36a-b show, in detail, a fracture step formed by the junction of two close cracks initiated at the notch surface of a specimen subjected to single torsion loading. The first micrograph (Figure 5.36a) presents the left side of the fracture step whilst the other (Figure 5.36b) exhibits the right side. The



a)



b)

Figure 5.36. SEM micrographs of fracture surfaces revealing the junction of two cracks initiated at the notch surface: a) left side; b) right side of the fracture step.

direction of propagation is from the top to the bottom. The two crack initiation sites, identified by the black arrows are perfectly identified by the fatigue markings. As can be seen, the nucleation of these two cracks took place at different planes which led to the formation of an accentuated fracture step.

5.5.2 Experimental fatigue life

As described in the previous subsection, fatigue failure was caused by multi-crack initiation. In order to derive the typical a-N curves, termed here 2b-N curves, for the different loading paths, it was assumed that the surface crack length, at a given instant, was equal to the sum of the individual crack lengths (see Figure 5.37a). For partially overlapped cracks, the final crack length was defined by the distance between opposite ends, as schematised in Figure 5.37b. The analysis stopped when one end of the crack surface reached the border of the notch. Figures 5.38-5.40 plot the surface crack length (2b) versus the number of loading cycles (N) for the different in-phase combined bending-torsion loading paths studied in

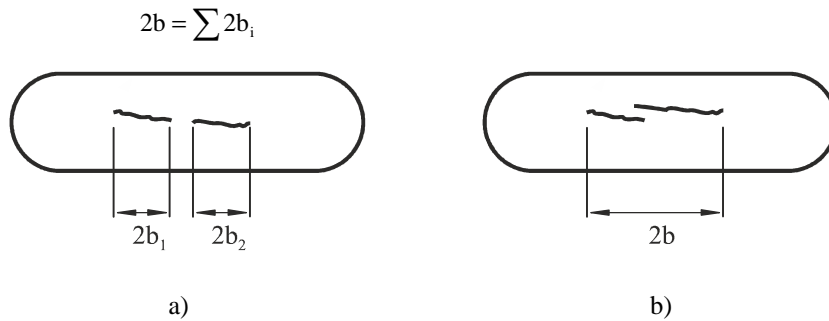


Figure 5.37. Crack length definition to obtain the 2b-N curves: a) close cracks; b) cracks overlapped.

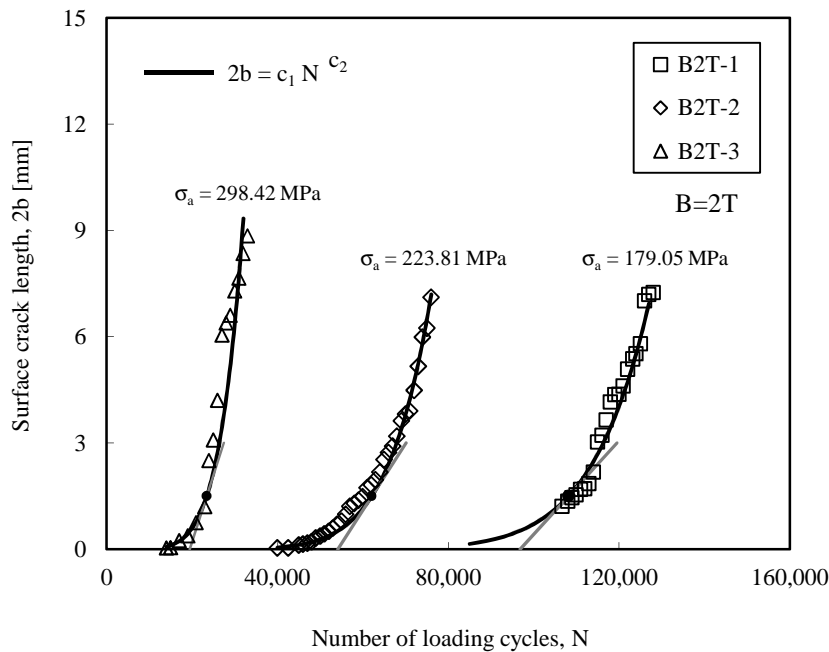


Figure 5.38. Crack length versus number of loading cycles for the in-phase combined bending-torsion loading tests (B=2T).

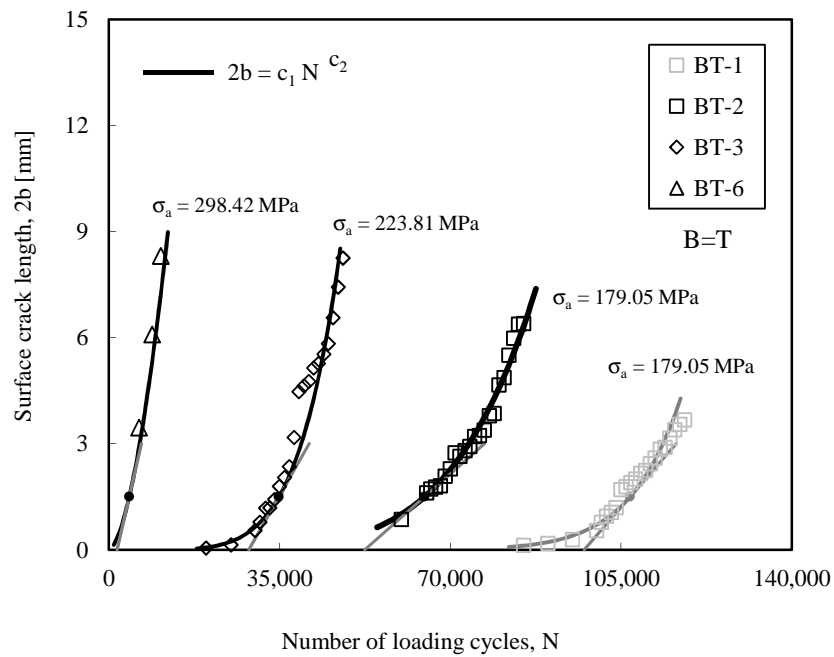


Figure 5.39. Crack length versus number of loading cycles for the in-phase combined bending-torsion loading tests (B=T).

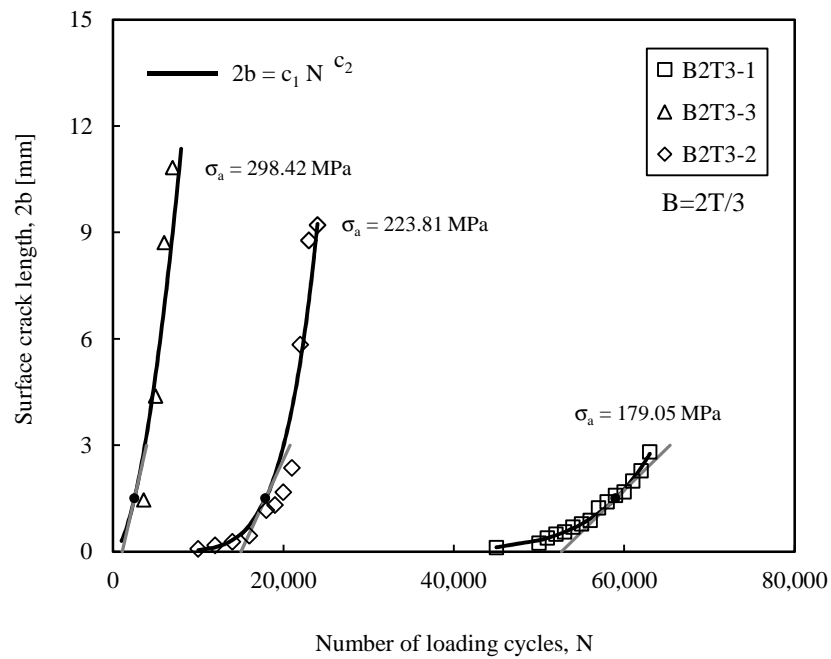
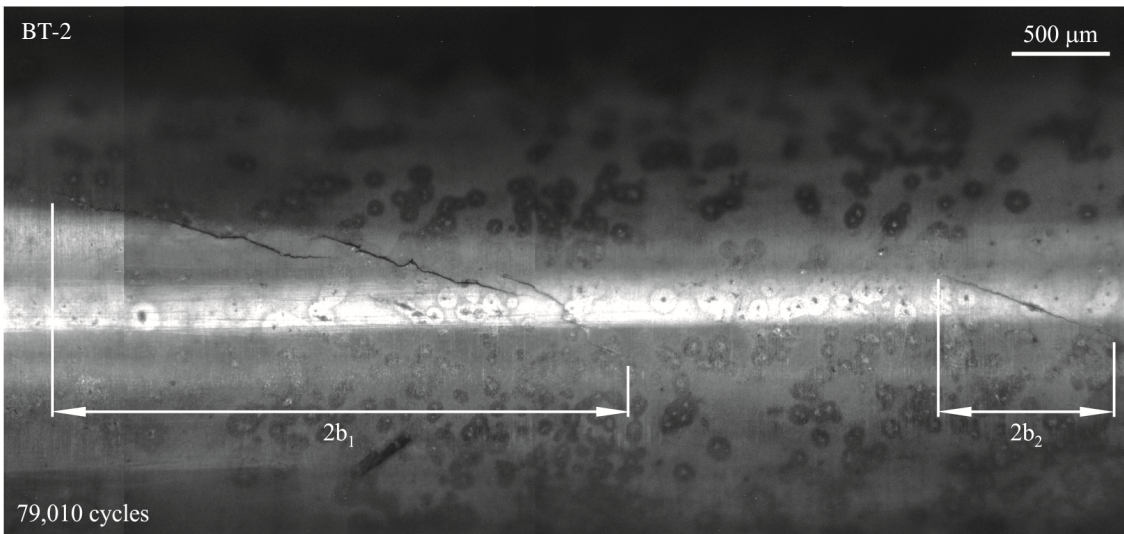


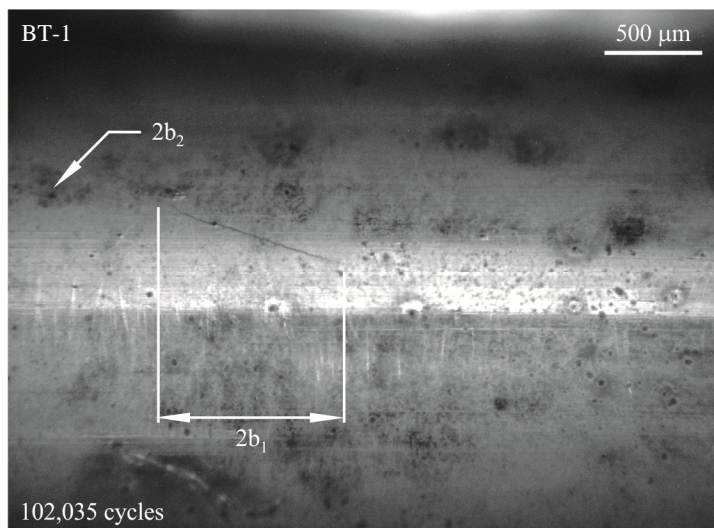
Figure 5.40. Crack length versus number of loading cycles for the in-phase combined bending-torsion loading tests (B=2T/3).

this research, respectively B=2T, B=T and B=2T/3. For each loading path, at least three different values of the normal stress amplitude (σ_a) were examined. The data were fitted to a power law. Although there are small differences, both the experimental data and the proposed expressions are relatively close. The slopes of the curves for a fixed surface crack length ($2b = 1.5\text{mm}$), obtained from the fitted functions, are

shown for illustrative purposes. The results collected are in line with the expectations. On the one hand, the higher the normal stress amplitude, the faster the surface crack growth. On the other hand, the slopes of the curve increase with the normal stress amplitude. Nevertheless, it is important to stress that, in some cases, specimens tested under identical loading conditions led to different $2b$ - N curves. This is evident by comparing the $2b$ - N curves of BT-1 and BT-2 tests (grey and black squares of Figure 5.39). As can be seen, not only the curves but also the slopes at $2b = 1.5\text{mm}$ are different. The multi-crack initiation mechanism already described is a plausible explanation for this fact. In the BT-2 test, two cracks initiated practically in simultaneous (Figure 5.41a) followed by other two. In the BT-1 test, a dominant crack arose on the notch surface (Figure 5.41b) and another one emerged only at a later stage. This is consistent with the results presented in Figure 5.39, since the $2b$ - N curve of the BT-2 test corresponds to a faster crack growth than the other, which can be associated with the multiple cracks found.



a)



b)

Figure 5.41. Notch surface: a) BT-2 test ($2b \approx 3.86\text{mm}$); b) BT-1 test ($2b \approx 0.95\text{mm}$).

The effect of the shear stress amplitude (τ_a) on the 2b-N curves is presented in Figure 5.42. It displays results of three tests carried out under the same normal stress amplitude for three different in-phase combined bending-torsion loadings ($B=2T$, $B=T$ and $B=2T/3$). Predictably, the increase in the shear stress amplitude reduces the fatigue life and increases the crack growth rate. The different crack growth rates can be inferred by comparing the slopes of the curves exhibited in the figure for $2b = 1.5\text{mm}$.

The shear stress amplitude has also a great influence on the fatigue life. Figure 5.43 plots the number of cycles to failure (N_f) against the normal stress amplitude (σ_a) for the three different in-phase combined bending-torsion tests ($B=2T$, $B=T$, $B=2T/3$) carried out in this research. As can be seen, there are clear differences between the S-N curves. Not surprisingly, the higher the shear stress amplitude, the lower the fatigue life. Additionally, the slope of the curves tends to decrease with the decrease in the shear stress amplitude. This figure also shows the 95% confidence bounds for the median curve given by the ASTM E739 (1998) standard for the case $B=T$. In the other cases ($B=2T/3$, $B=2T$), the resultant confidence bands were omitted to get a clear figure. The resultant S-N curves, as stated in the ASTM E739 (1998) standard, can be written in the following forms

$$\text{Log } N_f = c_1 + c_2 \text{Log } \sigma_a \quad (5.21)$$

$$\sigma_a = 10^{c_3} (N_f)^{c_4} \quad (5.22)$$

being c_1 to c_4 fitting constants. Table 5.16 summarises the constants found for the in-phase combined

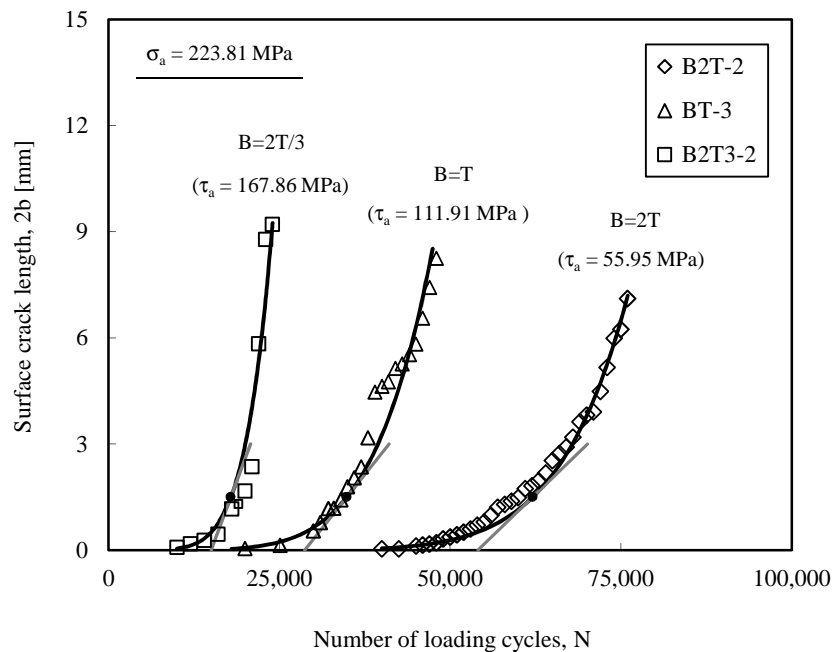


Figure 5.42. Crack length versus number of loading cycles for tests performed under the same normal stress amplitude for different loading paths.

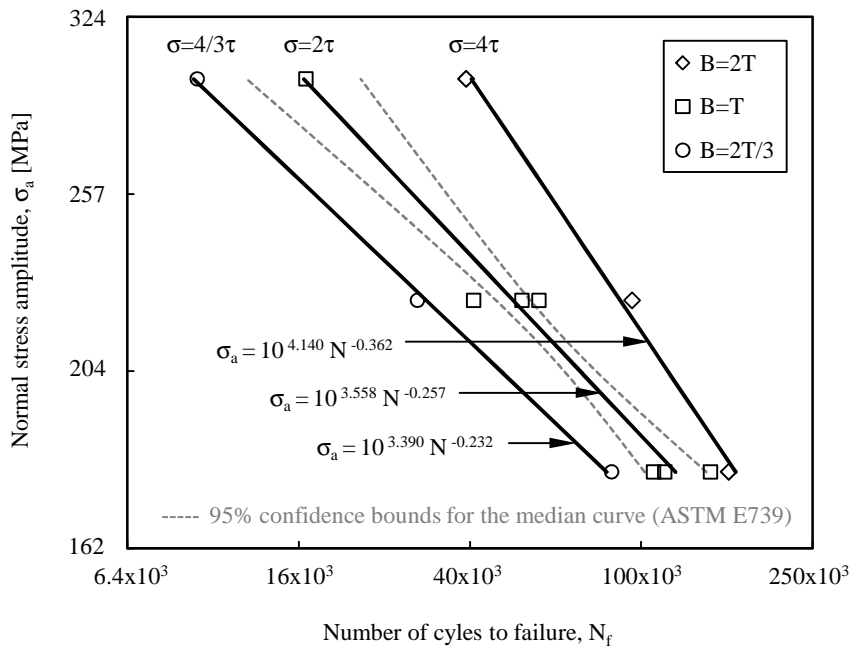


Figure 5.43. Normal stress amplitude versus number of cycles to failure for the in-phase combined bending-torsion tests.

Table 5.16. Constants of the S-N curves obtained in the present research.

Loading path	$c_1 = -\frac{c_3}{c_4}$	$c_2 = \frac{1}{c_4}$	c_3	c_4	σ^2
B	12.982	-3.435	3.779	-0.291	0.01139
B=2T	11.450	-2.766	4.140	-0.362	0.00120
B=T	13.848	-3.892	3.558	-0.257	0.00446
B=2T/3	14.666	-4.326	3.390	-0.232	0.00061
T	12.851	-3.404	3.775	-0.294	0.01076

bending-torsion tests performed in the present study. The variance of the normal distribution obtained for each case is also shown in Table 5.16.

The evolution of the normal stress amplitude with the number of cycles to failure for the single bending loading tests is exhibited in Figure 5.44. In this case, six tests were performed for three different normal stress amplitudes. As can be seen, experimental data are relatively close to the fitted S-N curve. The 95% confidence bounds for the median curve, given by the ASTM E739 (1998) standard, are also displayed in this case. The c_1 to c_4 of Equations 5.21 and 5.22 are listed in Table 5.16.

Regarding the single torsion tests, the shear stress amplitude (τ_a) was used as the representative stress, instead of σ_a since the latter is null. Figure 5.45 plots the shear stress amplitude against the number of cycles to failure for the seven tests performed in this study. As can be seen, experimental data are relatively close to the fitted stress-life curve. The 95% confidence bounds for the median curve, given by

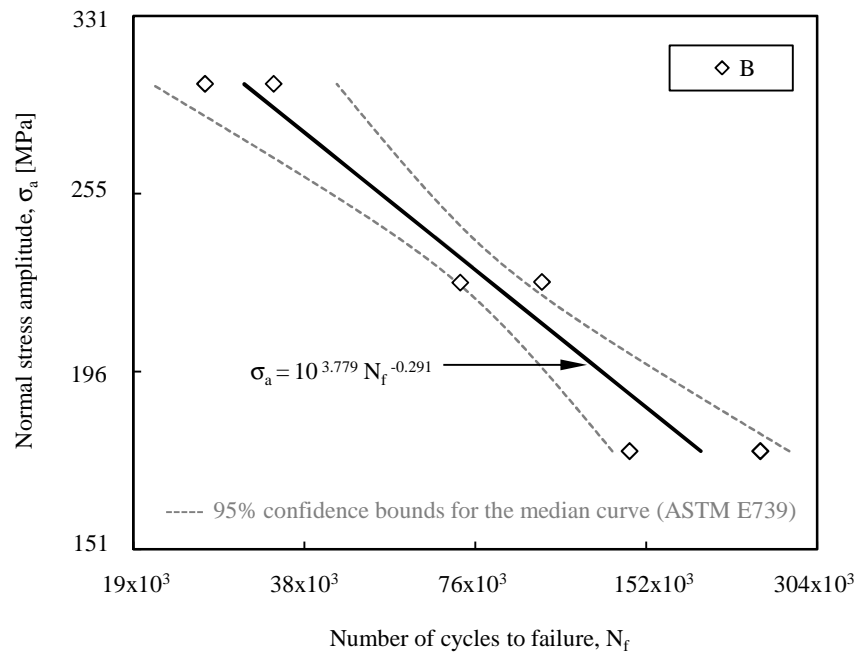


Figure 5.44. Normal stress amplitude versus number of cycles to failure for the single bending tests.

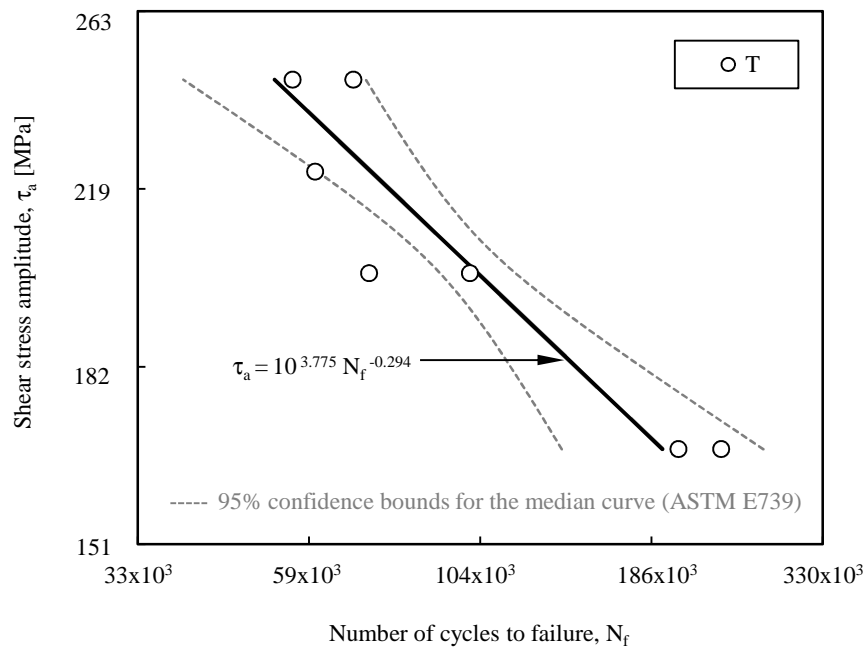


Figure 5.45. Shear stress amplitude versus number of cycles to failure for the single torsion tests.

the ASTM E739 (1998) standard, are also presented in the figure. Table 5.16 exhibits the c_1 to c_4 constants of Equations 5.21 and 5.22 calculated using the shear stress amplitude as representative stress.

The fatigue life (N_f) versus the local von Mises equivalent stress amplitude ($\Delta\sigma_{vML}/2$) for the different loading paths studied here is displayed in Figure 5.46. The local von Mises equivalent stress amplitudes

were computed from the linear elastic finite element models (see Section 4.2) at the initiation sites (see Figure 5.24). Equation 4.3 was applied to obtain both the maximum ($\sigma_{vML,max}/2$) and minimum ($\sigma_{vML,min}/2$) local stress amplitudes. In a log-log scale, as shown in the figure, a very satisfactory linear correlation between both variables was found. These data were used to obtain the design curve applying the procedure recommended by the International Institute of Welding (Hobbacher, 1996). The mean curve (dashed line) was fitted to the experimental data with a relatively high correlation coefficient ($r=0.958$). The upper and lower bounds were drawn for a 95% survival probability calculated from the mean value assuming two-sided confidence levels equal to 75%. The scatter band index (T_σ) was equal to 1.393. Table 5.17 lists the constants of Equation 5.23 for the mean curve and the upper and lower bounds.

$$\Delta\sigma_{vML}/2 = 10^{c_5} (N_f)^{c_6} \quad (5.23)$$

According to the previous results, and regardless of the loading path, the local von Mises equivalent stress amplitude seems to be able to correlate, in a satisfactory way, the resultant stress-strain states with the fatigue lives. The same conclusion was reached by Abreu *et al.* (2007) in their studies on fatigue

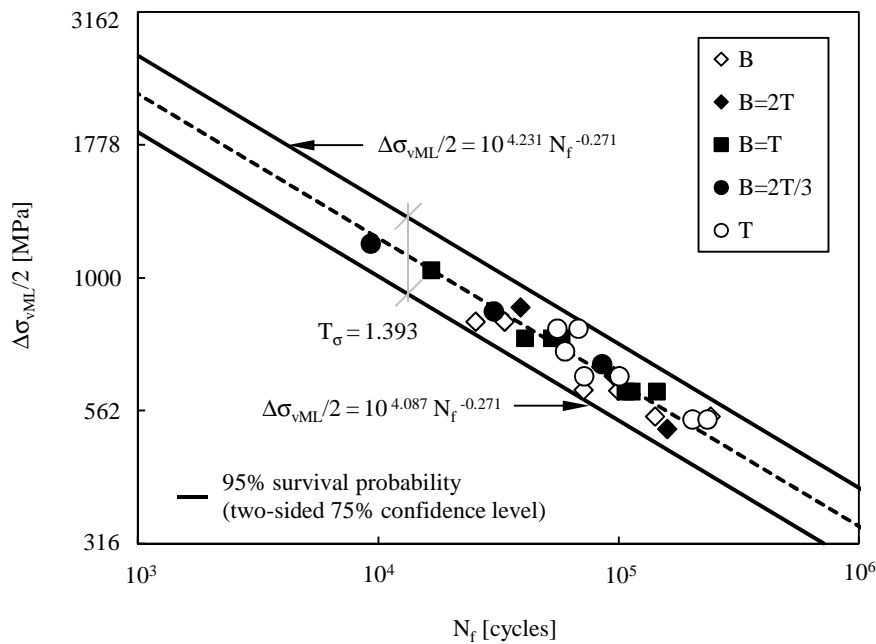


Figure 5.46. Local von Mises equivalent stress amplitude versus fatigue life for the different loading paths studied.

Table 5.17. Constants of Equation 5.23 for the mean curve and upper and lower bounds.

Curve	c_5	c_6
Upper bound	4.231	-0.271
Media curve	4.159	-0.271
Lower bound (design curve)	4.087	-0.271

behaviour of tubular specimens subjected to in-phase combined bending-torsion loading. Similar scatter band indexes equal to 1.48 and 1.62 were found for notched and welded specimens, respectively.

Figure 5.47 plots, as an example, the local von Mises equivalent stress amplitude ($\Delta\sigma_{vML}/2$) against the number of cycles in which at the first time the crack reached a surface length of 0.5mm ($N_{0.5}$). Based on the values of the crack aspect ratio (a'/b') presented in Figure 5.29, this surface crack length corresponds to crack depths clearly lower than 0.25mm, since the crack shapes are notoriously semi-elliptical. Although this is an empirical crack size, such a value is within the range typically used in aeronautical fatigue analysis. In aircraft fatigue, the value of $N_{0.5}$ is the so-called *safe-life* period, in which no visual inspection is required (Zhang, 2003). In a log-log scale, as already observed for the fatigue lives, a very satisfactory linear correlation between these two variables can be distinguished. The experimental results were fitted by linear regression with a relatively high correlation coefficient ($r=0.946$). The constants of Equation 5.24 for the mean curve and for the upper and lower bounds, obtained using the procedure recommended by the International Institute of Welding in the same conditions that those described in the previous case (i.e. 95% survival probability calculated from the mean value assuming two-sided confidence levels equal to 75%), are summarised in Table 5.18. The scatter band index (T_σ) was equal to 1.462. The increase in this parameter can be attributed to the multi-crack initiation phenomenon originated by the high concentration of defects and pores on the notch surface (see Section 5.5.1).

$$\Delta\sigma_{vML} / 2 = 10^{c_7} (N_{0.5})^{c_8} \quad (5.24)$$

Figure 5.48 exhibits the ratio of the number of cycles in which at the first time the crack reached a surface

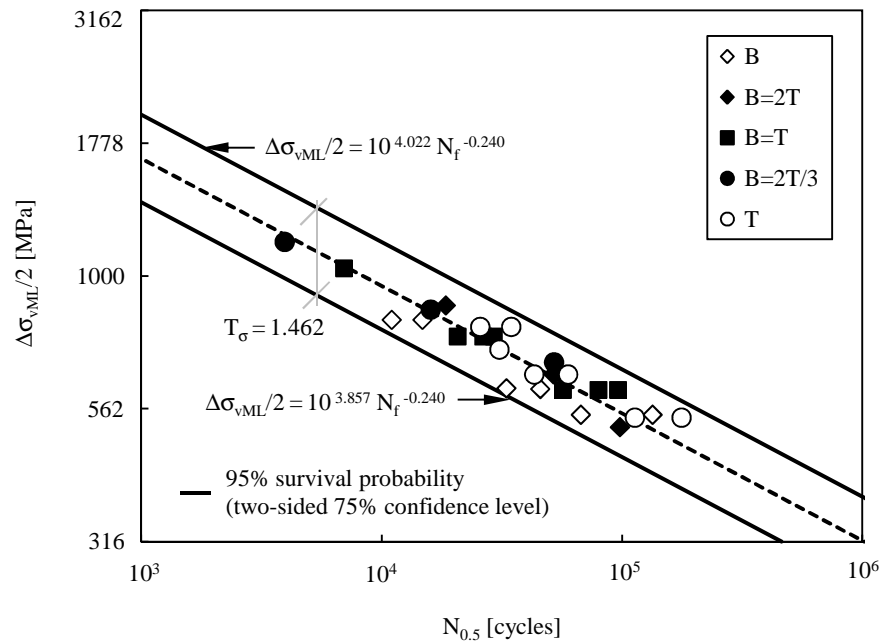


Figure 5.47. Local von Mises equivalent stress amplitude versus number of cycles in which at the first time the crack reached a surface length equal to 0.5mm.

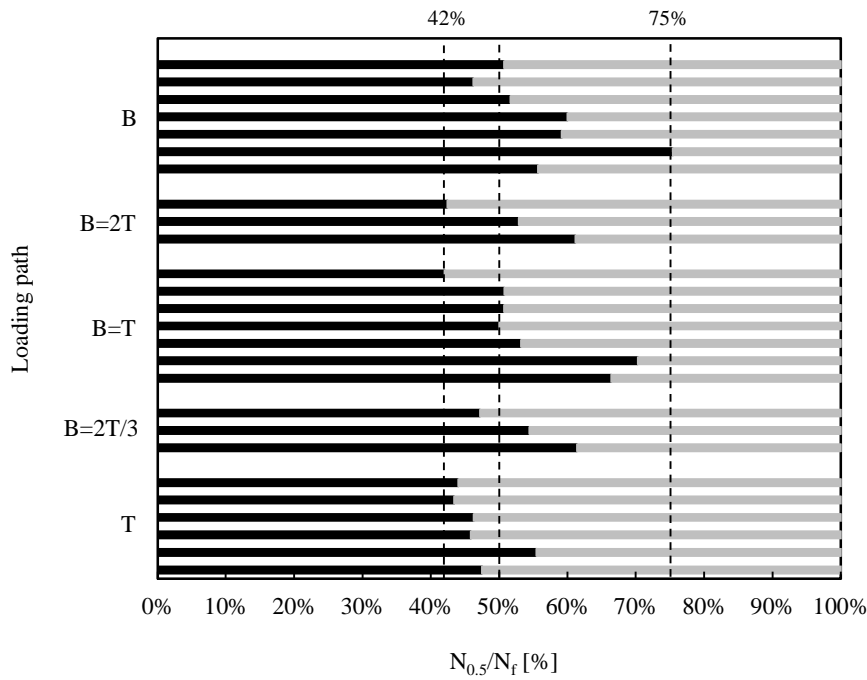


Figure 5.48. Relation between $N_{0.5}$ and N_f for the different loading paths studied.

Table 5.18. Constants of Equation 5.24 for the mean curve and upper and lower bounds.

Curve	c_7	c_8
Upper bound	4.022	-0.240
Media curve	3.939	-0.240
Lower bound (design curve)	3.857	-0.271

length of 0.5mm to the number of cycles to failure ($N_{0.5}/N_f$) for the different loading paths studied here. In each set of tests, loading increases from the top to the bottom. The $N_{0.5}/N_f$ ratio, as highlighted by the dashed lines, varies between 42-75%. Besides, it is also clear that most of these ratios are within the range 42-55%, which represents about 70% of the total number of cases. On the other hand, $N_{0.5}/N_f$ ratios are very similar for the different loading paths.

5.5.3 Fatigue life predictions

Fatigue life predictions were carried out from linear elastic finite element analyses. The notch effect on fatigue was accounted for using the theory of critical distances. The critical distance to average the stress profile can be defined using the El Haddad parameter (Equation 2.45). For $R=0$, it leads to

$$a_0 = \frac{1}{\pi} \left(\frac{\Delta K_{th}}{\Delta \sigma_0} \right)^2 \Leftrightarrow a_0 = \frac{1}{\pi} \left(\frac{7.12}{353} \right)^2 \Leftrightarrow a_0 = 129 \times 10^{-6} \text{ m} \Leftrightarrow a_0 = 129 \mu\text{m} \quad (5.25)$$

where ΔK_{th} is the range of the threshold value of the stress intensity factor and $\Delta \sigma_0$ is the fatigue limit stress range of the unnotched specimen. These two constants are determined under the same load ratio as

the mechanical component to be assessed. The value of ΔK_{th} for the DIN 34CrNiMo6 high strength steel studied here was obtained from the data available in the literature which are listed in Table 5.19 (Luke, 2011). The calculation of the range of the threshold value of the stress intensity factor for $R = 0$ (ΔK_{th0}) was performed using the formulation proposed by Klesnil and Lukas (1972)

$$\Delta K_{th} = \Delta K_{th0} (R-1)^x \quad (5.26)$$

being x a material constant obtained experimentally and ΔK_{th0} the range of the threshold value of the stress intensity factor for $R = 0$. From the above-mentioned data, the constants found were $x = 0.87$ and $\Delta K_{th0} = 7.12 \text{ MPa}\cdot\text{m}^{0.5}$. For comparison purposes, the value of ΔK_{th0} was also calculated using the model proposed by Vosikivsky (1979), i.e.

$$\Delta K_{th} = \Delta K_{th0} - BR \quad (5.27)$$

where B is a material constant. The constants obtained were $\Delta K_{th0} = 7.09 \text{ MPa}\cdot\text{m}^{0.5}$ and $B = 5.91$. Indeed, the two values of ΔK_{th0} differ only in 0.43%. As can be seen in Figure 5.49, for stress ratios close to zero,

Table 5.19. Material properties for DIN 34CrNiMo6 high strength steel (Luke, 2011).

Stress ratio	C	m	ΔK_{th}
R = -1	4.32×10^{-9}	2.5	13
R = 0.1	2.42×10^{-8}	2.5	6.5

da/dN in mm/cycle and ΔK in $\text{MPa}\cdot\text{m}^{0.5}$

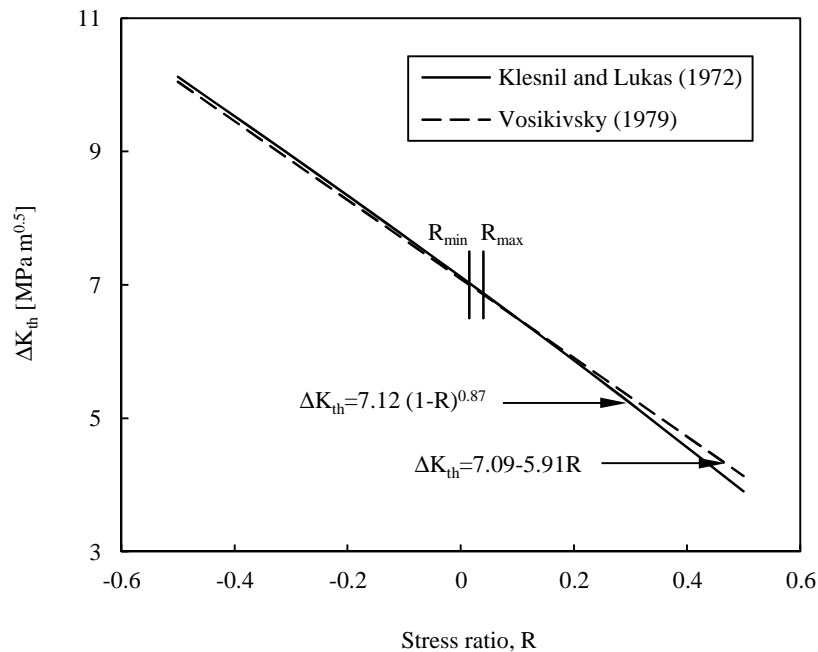


Figure 5.49. Range of the threshold of the stress intensity factor versus stress ratio.

as in the case of the present study ($R_{\min} = 0.015$ and $R_{\max} = 0.04$), both functions are almost overlapped. These formulations, although simple in nature, have been successfully used by different authors either for steels or aluminium alloys (Costa, 1991; Borrego 2001).

Regarding the fatigue limit of the notched specimen, it was calculated from the fatigue limit at zero mean stress ($R = -1$) by applying the Goodman relationship (Equation 2.7). The fatigue limit at zero mean stress was estimated from Equation 5.19 and is about 537MPa. The same value obtained from the Basquin equation (Equation 5.8) for a fatigue life equal to 1×10^6 cycles is equal to

$$\frac{\Delta\sigma}{2} = 1183.7(2N_f)^{-0.0545} \Leftrightarrow \frac{\Delta\sigma}{2} = 1183.7(2 \times 10^6)^{-0.0545} \Leftrightarrow \frac{\Delta\sigma}{2} = 536.8 \text{ MPa} \quad (5.28)$$

which is practically equivalent. Based on these values, the fatigue limit stress range of the notched specimen for $R=0$ is approximately equal to $\Delta\sigma_0 = 353\text{MPa}$.

Thus, the El Haddad parameter (El Haddad, 1979), as indicated in Equation 5.25, is equal to $129\mu\text{m}$. This calculation represents only a reference value since it was obtained for $R=0$. In practice, a specific value of a_0 was calculated for each test in order to take into account the effective stress ratio which varied from 0.015 to 0.04 (see Tables 3.4-3.6). The line method was used to average the elastic stress distribution over the critical region. In this method, the critical distance (see Equation 2.59) is given by

$$D_{LM} = 2a_0 \Leftrightarrow D_{LM} = 2 \times 129 \Leftrightarrow D_{LM} = 258 \mu\text{m} \quad (5.29)$$

where a_0 is the El Haddad parameter and D_{LM} is the critical distance for the line method.

The local von Mises equivalent stress was selected as representative of the fatigue failure process. As referred to in Section 5.5.2, it is able to correlate in a satisfactory way the resultant stress-strain states with fatigue lives. Figure 5.50 plots, as an example, the local von Mises equivalent stress (σ_{vML}) against the distance from the notch surface (d) for a specimen subjected to single bending. As can be seen, the maximum stress occurs at the notch surface and then gradually decreases to an asymptotical value. The critical stress calculated by applying the line method, as indicated in the figure, corresponds to 928MPa.

In Figure 5.51 is compared, in a dimensionless form, the stress profiles obtained for the different loading paths studied here. The local von Mises equivalent stress (σ_{vML}) was divided by its maximum value ($\sigma_{vML,\max}$) and the distance from the notch surface (d) was divided by the critical distance (D_{LM}). Looking at the resultant stress-distance curves, it is possible to observe a first stage ($d/D_{LM} \leq 1$) with similar profiles and second stage ($d/D_{LM} > 1$) in which the differences gradually increase with the dimensionless distance.

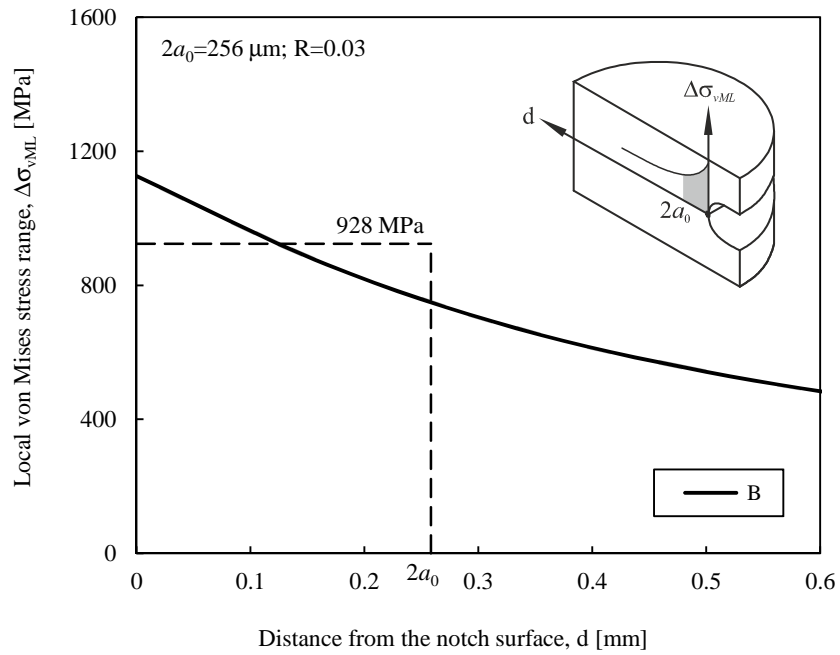


Figure 5.50. Local von Mises equivalent stress range versus distance from the notch surface for a specimen subjected to single bending.

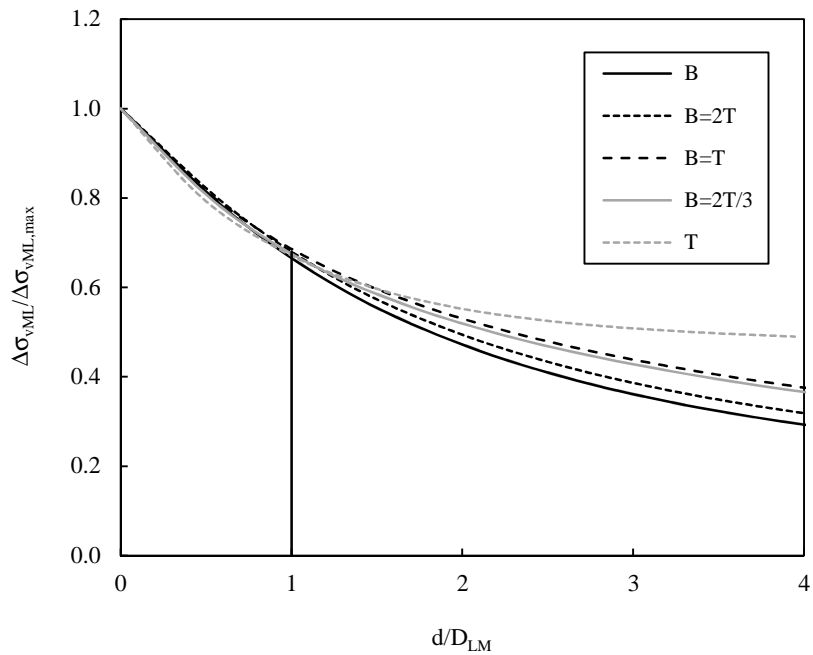


Figure 5.51. Dimensionless local von Mises equivalent stress range ($\Delta\sigma_{vML}/\Delta\sigma_{vML,max}$) versus the dimensionless distance from the notch surface (d/D_{LM}) for the different loading paths studied.

The number of cycles to crack initiation (N_e) was evaluated from the 2b-N curves. The crack length a_0 was inferred from the surface crack length ($2b_0$). Taking into consideration the crack shapes observed in the fatigue crack front marking tests, a crack aspect ratio equal to $a_0/b_0=0.8$ was assumed. As Figure 5.52 shows, such a ratio seems to be adequate. The crack front marks exhibited in the figure were obtained in a

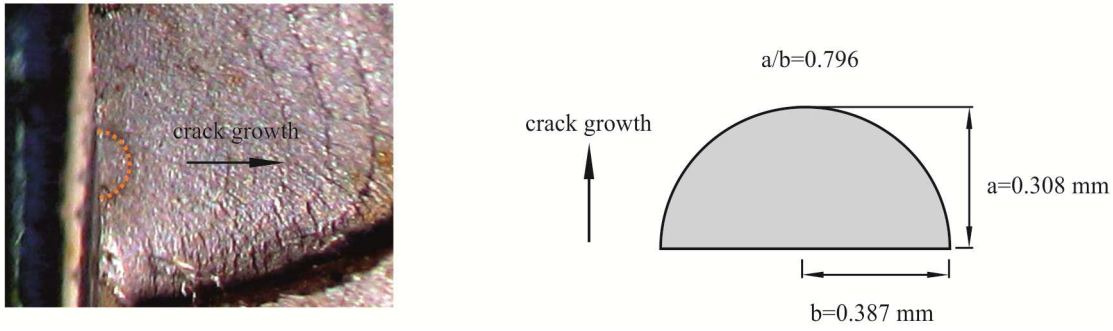


Figure 5.52. Detail of crack front marks obtained in a test performed under in-phase combined bending-torsion loading (Specimen reference: BT-m).

test conducted under in-phase combined bending-torsion loading (B=T). Based on this assumption, the initiation life was calculated when the surface crack length has reached a value equal to $2b_0$ (which corresponds to a crack depth $a_0 = 129\mu\text{m}$). For $R=0$, it leads to $2b_0 = 322\mu\text{m}$. In practice, the value of $2b_0$ was calculated for each test to account for the effective stress ratio used (see Tables 3.4-3.6) and it varied from $317\mu\text{m}$ to $321\mu\text{m}$. Tables 5.20-5.22 summarise, respectively, the crack initiation lives obtained for the single bending, single torsion and in-phase combined bending-torsion tests performed in this study.

The models of Coffin-Manson (CM) and the Smith, Watson and Topper (SWT) were used to predict the crack initiation lives. In terms of local von Mises equivalent stress, these models can be formulated, respectively, as follows

$$\frac{\Delta\varepsilon_{vML}}{2} = \frac{\sigma'_f - \sigma_{vML,m}}{E} (2N_f)^b + \varepsilon'_f (2N_f)^c \quad (5.30)$$

$$\sigma_{vML,max} \frac{\Delta\varepsilon_{vML}}{2} = \frac{(\sigma'_f)^2}{E} (2N_f)^{2b} + \varepsilon'_f \sigma'_f (2N_f)^{b+c} \quad (5.31)$$

being $\Delta\varepsilon_{vML}/2$ the averaged local von Mises equivalent strain amplitude, $\sigma_{vML,m}$ the averaged mean local von Mises equivalent stress, $\sigma_{vML,max}$ the averaged maximum local von Mises equivalent stress, E the Young's modulus, σ'_f and b the fatigue strength properties, and ε'_f and c the fatigue ductility properties.

The local stresses and strains for each test were calculated from the critical stress which was computed using the procedure described above. The elastic properties, fatigue strength properties and fatigue ductility properties used are compiled in Table 5.3, Table 5.7 and Table 5.8, respectively. The experimental fatigue lives (N_e) and the predicted fatigue lives obtained using both the CM (N_{CM}) and SWT (N_{SWT}) models for the single bending, single torsion and in-phase combined bending-torsion tests are summarised, respectively, in Tables 5.20-5.22.

The experimental lives (N_e) versus the predicted lives (N_p) calculated using the CM and SWT models for the loading paths studied here are plotted in Figures 5.53 and 5.54, respectively. As can be seen, the

Table 5.20. Experimental and predicted fatigue lives for the single bending tests.

Specimen Reference	$\sigma_{vML,max}$ [MPa]	$\sigma_{vML,m}$ [MPa]	$\Delta\varepsilon_{vML}/2$ [-]	N_e [cycles]	N_{CM} [cycles]	N_{SWT} [cycles]
B-1	919.6	471.9	2.134×10^{-3}	65765	70554	93040
B-2	919.6	471.9	2.134×10^{-3}	135085	70554	93040
B-3	1035.6	530.0	2.256×10^{-3}	53742	24300	24771
B-4	1034.8	528.0	2.263×10^{-3}	37108	24300	24771
B-5	1384.7	703.0	2.484×10^{-3}	8896	4625	2741
B-6	1384.7	703.0	2.484×10^{-3}	16956	4625	2741

Total: 6 specimens

Table 5.21. Experimental and predicted fatigue lives for the single torsion tests.

Specimen Reference	$\sigma_{vML,max}$ [MPa]	$\sigma_{vML,m}$ [MPa]	$\Delta\varepsilon_{vML}/2$ [-]	N_e [cycles]	N_{CM} [cycles]	N_{SWT} [cycles]
T-1	906.0	467.6	2.090×10^{-3}	108731	84731	116853
T-2	906.0	467.6	2.090×10^{-3}	171230	84731	116853
T-3	1087.2	558.3	2.521×10^{-3}	56636	17306	16069
T-4	1087.2	558.3	2.521×10^{-3}	43141	17306	16069
T-5	1208.0	618.7	2.809×10^{-3}	29291	9112	6862
T-6	1328.8	679.2	3.096×10^{-3}	25990	5620	3593
T-7	1328.8	679.2	3.096×10^{-3}	36424	5620	3593

Total: 7 specimens

Table 5.22. Experimental and predicted fatigue lives for the in-phase combined bending-torsion tests.

Specimen Reference	$\sigma_{vML,max}$ [MPa]	$\sigma_{vML,m}$ [MPa]	$\Delta\varepsilon_{vML}/2$ [-]	N_e [cycles]	N_{CM} [cycles]	N_{SWT} [cycles]
B=2T series						
B2T-1	873.8	454.4	1.999×10^{-3}	102386	134817	200999
B2T-2	1092.2	563.7	2.519×10^{-3}	49103	16947	15805
B2T-3	1456.3	745.9	3.386×10^{-3}	24207	3773	2111
B=T series						
BT-1	983.9	511.6	2.251×10^{-3}	92544	38305	45843
BT-2	983.9	511.6	2.251×10^{-3}	83278	38305	46026
BT-3	983.9	511.6	2.251×10^{-3}	56749	38305	46026
BT-4	1229.9	634.8	2.837×10^{-3}	26420	8365	6212
BT-5	1229.9	634.8	2.837×10^{-3}	21225	8365	6212
BT-6	1229.9	634.8	2.837×10^{-3}	31306	8365	6212
BT-7	1639.9	839.9	3.813×10^{-3}	8314	2378	1136
B=2T/3 series						
B2T3-1	1177.8	604.8	2.731×10^{-3}	50261	10539	8362
B2T3-2	1472.2	752.1	3.432×10^{-3}	17967	3594	1973
B2T3-3	1962.9	997.6	4.601×10^{-3}	4099	1295	491

Total: 13 specimens

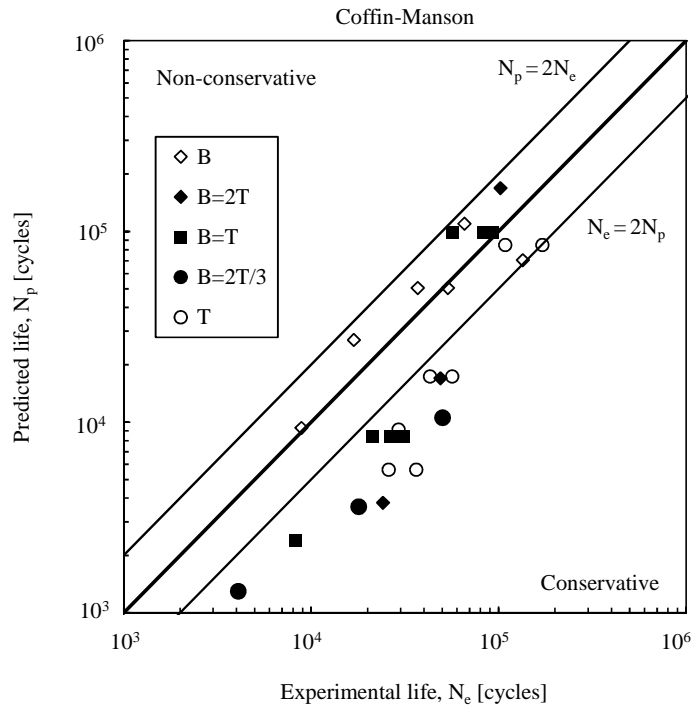


Figure 5.53. Experimentally obtained versus predicted fatigue lives obtained by the Coffin-Manson model.

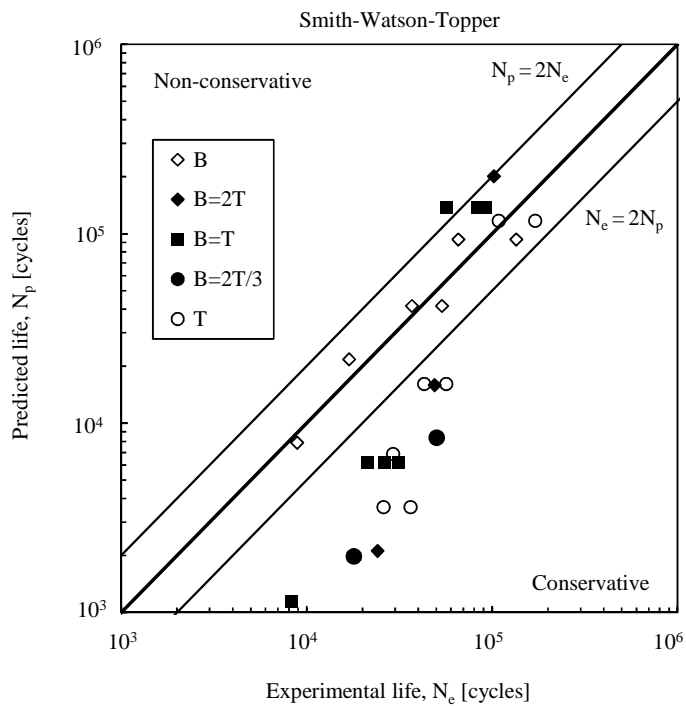


Figure 5.54. Experimentally obtained versus predicted fatigue lives obtained by the Smith, Watson and Topper model.

predictions calculated using both models are close to the experimental values for predicted lives greater than about 2×10^4 cycles. In this region, a satisfactory linear correlation is obtained in a log-log scale. On the other hand, and not surprisingly, for shorter lives the predictions tend to be increasingly conservative. This fact can be explained by an inadequate simulation of the local stress-strain field at the notch.

In order to better simulate the local stress-strain field at the notch, the equivalent strain energy density concept was applied. As stated in Section 2.4.3, this concept assumes that the ratio of the strain energy density in the notch tip to the nominal strain energy density is the same in elastic or elastic-plastic straining. A typical stress-strain curve obtained using this approach for a single bending case (Case B-3) is exhibited in Figure 5.55. Firstly, the stress and strain at the notch tip are calculated for the maximum loading (Point A). The maximum stress (σ_{\max}) can be obtained using the following equation

$$\frac{\sigma_{\max}^2}{2E} + \frac{\sigma_{\max}}{n'+1} \left(\frac{\sigma_{\max}}{k'} \right)^{1/n'} = K_T^2 \frac{\sigma_{n,\max}^2}{2E} \quad (5.32)$$

where k' is the cyclic hardening coefficient, n' is the cyclic hardening exponent, K_T is the elastic stress concentration factor, $\sigma_{n,\max}$ is the maximum nominal stress and E is the Young's modulus. In this research, the quantity $K_T \times \sigma_{\max}$ was replaced by the maximum local von Mises stress ($\sigma_{vML,\max}$) given by the FEM. The $\sigma_{vML,\max}$ values used in this research are listed in Tables 5.20-5.22. This procedure avoided the calculation of the elastic stress concentration factors. The maximum strain (ϵ_{\max}) was evaluated by substituting σ_{\max} into the cyclic stress-strain curve given by

$$\epsilon_{\max} = \frac{\sigma_{\max}}{E} + \left(\frac{\sigma_{\max}}{k'} \right)^{1/n'} \quad (5.33)$$

being k' the cyclic hardening coefficient, n' the cyclic hardening exponent and E the Young's modulus. The stress and strain ranges were obtained with respect to an auxiliary coordinate system ($\Delta\sigma$, $\Delta\epsilon$) with origin at point A (see Figure 5.55). The resultant stress range ($\Delta\sigma$) was found by solving the formula

$$\frac{\Delta\sigma^2}{4E} + \frac{\Delta\sigma}{n'+1} \left(\frac{\Delta\sigma}{2k'} \right)^{1/n'} = K_T^2 \frac{\Delta\sigma_n^2}{4E} \quad (5.34)$$

where k' is the cyclic hardening coefficient, n' is the cyclic hardening exponent, K_T is the elastic stress concentration factor, $\Delta\sigma_n$ is the nominal stress range and E is the Young's modulus. The strain range ($\Delta\epsilon$) was determined from the basic cyclic stress-strain curve by applying a factor of 2, i.e.

$$\Delta\epsilon = \frac{\Delta\sigma}{E} + 2 \left(\frac{\Delta\sigma}{2k'} \right)^{1/n'} \quad (5.35)$$

being k' the cyclic hardening coefficient, n' the cyclic hardening exponent and E the Young's modulus.

The values of $\Delta\sigma$ and $\Delta\varepsilon$ for the case B-3 are represented in Figure 5.55 and account for the difference between both point A and point B in terms of stress and strain, respectively.

The above-mentioned procedure was applied to the remaining cases of Tables 5.20 to 5.22. In all the cases, the nominal behaviour is elastic (see Tables 3.4 to 3.6) but the notch behaviour is inelastic (see Tables 5.20 to 5.22) since $\sigma_{vML,max} > \sigma_{YS}$. Therefore, this procedure can be applied in all the cases studied here. The resultant values of maximum stress (σ_{max}), mean stress (σ_m) and strain range ($\Delta\varepsilon/2$) for the different loading paths investigated are listed in Tables 5.23 to 5.25. The experimental fatigue lives (N_e) and the predicted fatigue lives obtained from both the CM (N_{CM}) and SWT (N_{SWT}) models for the single bending, single torsion and in-phase combined bending-torsion tests are summarised, respectively, in Tables 5.23-5.25.

The experimental fatigue lives (N_e) versus the predicted fatigue lives (N_p) calculated using the CM and

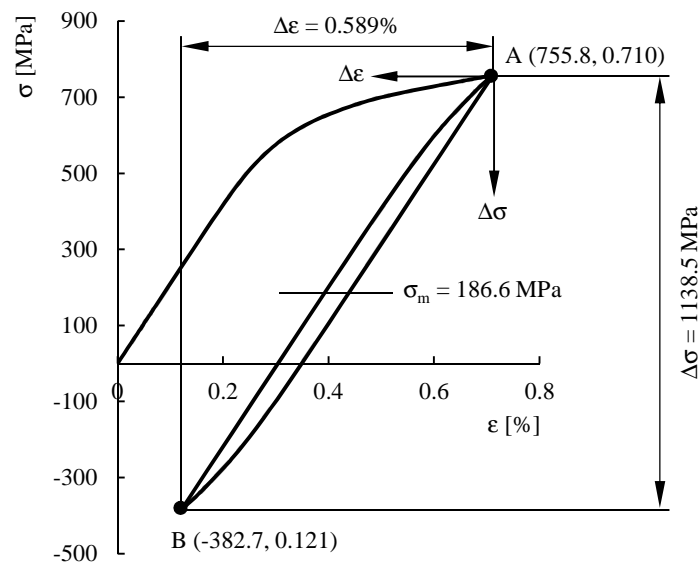


Figure 5.55. Hysteresis loops obtained for a single bending test by applying the strain energy density concept (Case B-3).

Table 5.23. Experimental and predicted fatigue lives for the single bending tests.

Specimen Reference	σ_{max} [MPa]	σ_m [MPa]	$\Delta\varepsilon/2$ [-]	N_e [cycles]	N_{CM} [cycles]	N_{SWT} [cycles]
B-1	735.4	203.9	2.652×10^{-3}	65765	113225	96656
B-2	731.3	207.8	2.598×10^{-3}	135085	132598	93040
B-3	755.8	186.6	2.943×10^{-3}	53742	54366	45320
B-4	755.8	186.6	2.943×10^{-3}	37108	54366	45320
B-5	807.1	155.1	3.972×10^{-3}	8896	10603	8470
B-6	807.1	155.1	3.972×10^{-3}	16956	10603	8470

Total: 6 specimens

Table 5.24. Experimental and predicted fatigue lives for the single torsion tests.

Specimen Reference	σ_{\max} [MPa]	σ_m [MPa]	$\Delta\varepsilon/2$ [-]	N_e [cycles]	N_{CM} [cycles]	N_{SWT} [cycles]
T-1	731.8	207.0	2.607×10^{-3}	108731	129407	111264
T-2	731.8	207.0	2.607×10^{-3}	171230	129407	111264
T-3	769.1	176.6	3.162×10^{-3}	56636	34721	28135
T-4	769.1	176.6	3.162×10^{-3}	43141	34721	28135
T-5	789.5	163.8	3.553×10^{-3}	29291	18168	14520
T-6	807.8	156.3	3.954×10^{-3}	25990	10786	8502
T-7	807.8	156.3	3.964×10^{-3}	36424	10692	8502

Total: 7 specimens

Table 5.25. Experimental and predicted fatigue lives for the in-phase combined bending-torsion tests.

Specimen Reference	σ_{\max} [MPa]	σ_m [MPa]	$\Delta\varepsilon/2$ [-]	N_e [cycles]	N_{CM} [cycles]	N_{SWT} [cycles]
B=2T series						
B2T-1	718.8	219.1	2.448×10^{-3}	102386	215775	190395
B2T-2	765.0	179.4	3.093×10^{-3}	49103	39682	32290
B2T-3	820.5	150.5	4.294×10^{-3}	24207	7554	6000
B=T series						
BT-1	745.6	194.9	2.792×10^{-3}	92544	77816	65140
BT-2	745.6	194.9	2.792×10^{-3}	83278	77816	65140
BT-3	745.6	194.9	2.792×10^{-3}	56749	77816	65140
BT-4	789.8	163.9	3.556×10^{-3}	26420	18083	14449
BT-5	789.8	163.9	3.556×10^{-3}	21225	18083	14449
BT-6	789.8	163.9	3.556×10^{-3}	31306	18083	14449
BT-7	844.2	143.8	5.024×10^{-3}	8314	4120	3273
B=2T/3 series						
B2T3-1	762.3	181.6	3.047×10^{-3}	50261	43552	35553
B2T3-2	805.6	156.2	3.911×10^{-3}	17967	11382	9054
B2T3-3	878.4	134.0	6.402×10^{-3}	4099	1868	1484

Total: 13 specimens

the SWT models for the loading paths studied here are presented in Figure 5.56 and Figure 5.57, respectively. Two scatter bands for N_e/N_p ratios equal to 0.5 (i.e. $N_p = 2N_e$) and 2 (i.e. $N_e = 2N_p$) were plotted. In general, fatigue life predictions in this range (i.e. $0.5 < N_p/N_e < 2.0$) are considered acceptable. As can be seen, in both figures, a large majority of data are inside the scatter bands (more specifically, 77% for the CM model and 65% for the SWT model). Besides, except for a single case in the CM model, the points outside the scatter bands are at the safe side (i.e. $N_e/N_p > 1$). It means that the amount of data inside the scatter bands or at the safe side is about 97% for the CM model and 100% for the SWT model. This fact suggests that the SWT model is, in general, more conservative than the CM model.

In relation to the points outside the scatter bands, they tend to occur for predicted lives lower than 10^4

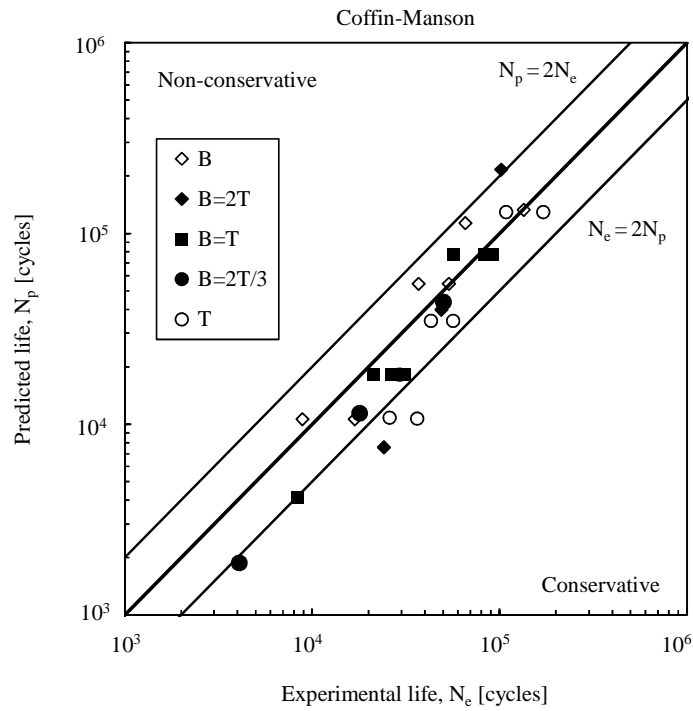


Figure 5.56. Experimentally obtained versus predicted fatigue lives obtained by the Coffin-Manson model.

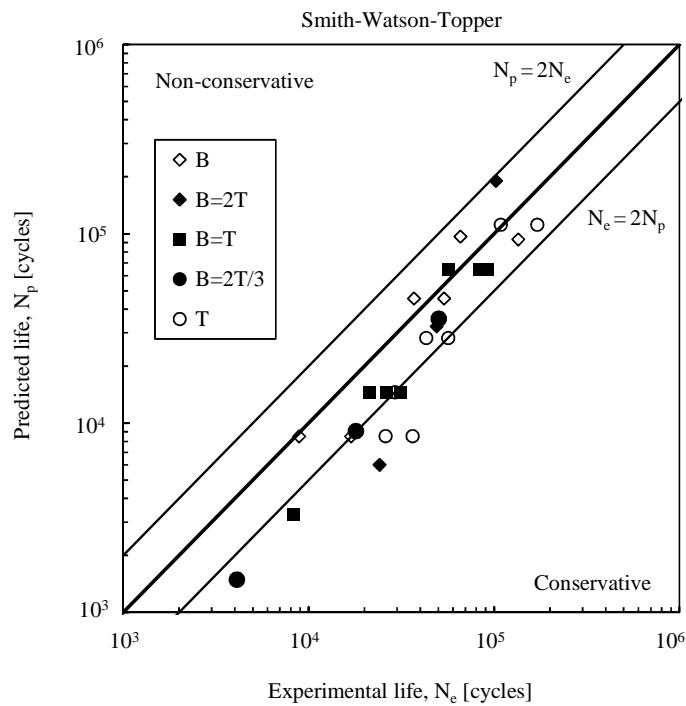


Figure 5.57. Experimentally obtained versus predicted fatigue lives obtained by the Smith, Watson and Topper model.

cycles in the cases of single torsion and in-phase combined bending-torsion loading. In this range, the SWT model is more conservative than the CM model. On the other hand, for predicted lives greater than 10^4 cycles, the data are well correlated in both models.

Tables 5.26 and 5.27 present, respectively, several statistical data obtained from the N_e/N_p ratios for the CM and SWT models, namely the minimum N_e/N_p ratio, maximum N_e/N_p ratio, mean ratio, standard deviation and mean deviation. As can be seen, the values of the N_e/N_p ratio for the CM model are within the range 0.47-3.41, with mean and standard deviation equal to 1.44 and 0.72, respectively. For the SWT model, the N_e/N_p ratios vary between 0.54-4.28 and the mean and the standard deviation are, respectively, equal to 1.79 and 0.92. Furthermore, regardless of the model, the worst results in terms of standard deviation were found for B=2T. In opposition, the best standard deviations were obtained for single bending (B).

In order to better compare the values obtained by the two models, the fatigue prediction error (E_N) defined by following expression was determined

$$E_N = \log \left(\frac{N_e}{N_p} \right) \quad (5.36)$$

where N_e is the experimental life and N_p is the corresponding predicted life. The probability density functions of the fatigue prediction error obtained for the CM and SWT models are presented in Figure 5.58. As can be seen, the CM model gives better results than the SWT model. In both cases, the errors

Table 5.26. Statistical data for the N_e/N_p ratios obtained from the CM model.

Tests	Minimum N_e/N_p	Maximum N_e/N_p	Mean	Standard deviation	Mean deviation
All tests	0.47	3.41	1.44	0.72	0.54
B	0.58	1.60	0.95	0.33	0.25
B=2T	0.47	3.20	1.64	1.15	1.04
B=T	0.73	2.02	1.34	0.40	0.34
B=2T/3	1.15	2.19	1.64	0.43	0.37
T	0.84	3.41	1.78	0.80	0.64

Table 5.27. Statistical data for the N_e/N_p ratios obtained from the SWT model.

Tests	Minimum N_e/N_p	Maximum N_e/N_p	Mean	Standard deviation	Mean deviation
All tests	0.54	4.28	1.79	0.92	0.70
B	0.68	2.00	1.20	0.44	0.35
B=2T	0.54	4.03	2.03	1.47	1.34
B=T	0.87	2.54	1.65	0.52	0.50
B=2T/3	1.41	2.76	2.05	0.55	0.47
T	0.98	4.28	2.20	1.04	0.84

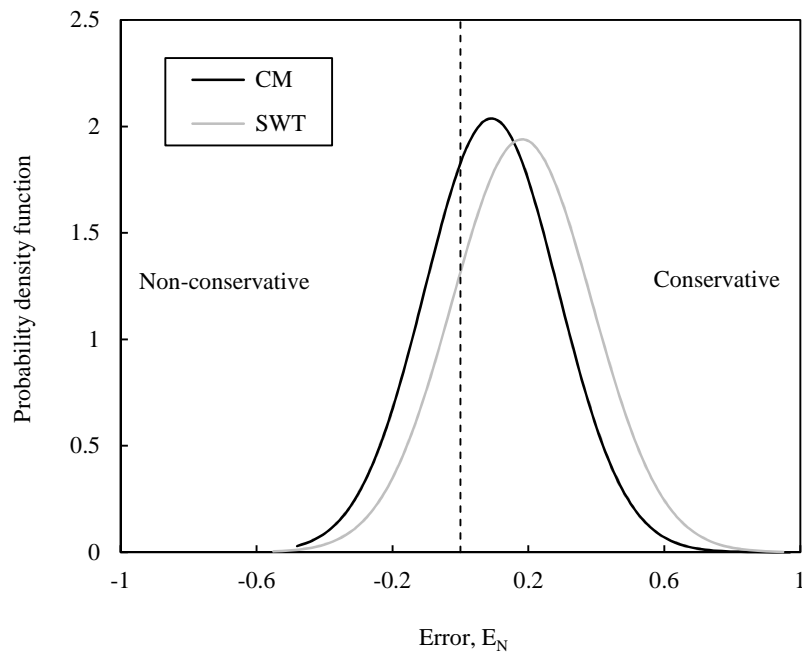


Figure 5.58. Probability density functions of fatigue life predictions for the CM and SWT models.

tend to be moved to the safe side. Nevertheless, the results obtained with the CM model are closer to a mean error equal to zero than the SWT model.

CHAPTER 6

NUMERICAL RESULTS

This chapter contains the numerical findings. The first section is devoted to the presentation of the in-plane fatigue crack growth software developed in the present research. It encompasses the identification and optimisation of the main variables affecting the accuracy of the numerical procedure as well as the validation of the numerical results. The second section evaluates the extent of the surface region in notched geometries. The third section deals with the development of a plane strain specimen. The last section concerns the determination of the Paris law constants from the analysis of fatigue crack front marks on fracture surfaces of small cross-section round bars.

NOMENCLATURE

a, a_0	crack length, initial crack length
a/b	crack aspect ratio
a/D	dimensionless crack length
ad	accumulated difference parameter
ASTM	American Society of Testing and Materials
C	Paris law constant
C(T)	compact tension specimen
D	diameter
E	Young's modulus
FEA	finite element analysis
FEM	finite element method
h, Θ , T_z , R_v	stress triaxiality parameters
K_i	stress intensity factor of the i^{th} node
K_{IC}	fracture toughness
K_{\max} , K_{\min}	maximum stress intensity factor, minimum stress intensity factor
L	length
m	Paris law exponent
M(T)	middle-crack tension specimen
MNET	mixed numerical-experimental technique
n	notch depth
N	number of loading cycles
PPP	preferred propagation path
PICC	plasticity induced crack closure
p_β	percentage of the thickness with $h \geq \beta$
r	notch radius
S_1 , S_2	extent of the surface region, extent of the near-surface region
S_γ^ψ	dimensionless sensitivity of the variable ψ to the parameter γ
SIF	stress intensity factor
T	original thickness
t	reduced thickness
T1	first torsional resonant mode
T_i	height of i^{th} element
t_{pl} , t_{qm}	transformation matrixes
U	fraction of the loading cycle in which the crack remains fully open
W	width
Y	geometric factor
ν	Poisson's ratio
η	notch angle
σ_1 , σ_2 , σ_3	principal stresses
σ_{ij}	stress tensor components
σ_H	hydrostatic stress
σ_{vM}	von Mises equivalent stress
δ_x , δ_y , δ_z	displacement in the x, y and z directions
Δa , Δa_{\max}	crack increment, maximum crack increment
ΔK , ΔK_{\max}	stress intensity factor, maximum stress intensity factor

6.1. Modelling of crack shape evolution

6.1.1. Lynx: new tool to model mode I fatigue crack growth

The modelling of fatigue crack growth (FCG) using commercial FEM packages is time-consuming and laborious. In part, this is because software is developed for general purposes. However, as stated in the preceding chapters, the numerical models used to address FCG problems are very specific and require a set of tasks usually not available. It is, therefore, necessary to create additional algorithms to perform those actions. Besides, commercial specific software is scarce and not sufficiently reliable for research purposes. On the other hand, the reliable software able to study these phenomena has been developed by research groups but is not available commercially.

In view of these facts, a new tool capable of simulating in-plane fatigue crack propagation was developed. The software, named *Lynx*, was designed in a modular manner and is very simple to use since it greatly simplifies the modelling work (Branco, 2011a). An intuitive and user-friendly interface was created to enhance its functionality. It incorporates an extensive range of situations usually studied in the context of fatigue crack propagation (Branco, 2012c), such as unnotched and notched rectangular bars with corner cracks (Figures 4.10a-b), unnotched and notched circular bars with surface cracks (Figures 4.10c-d), unnotched and notched plates with surface cracks (Figures 4.10e-f), unnotched and notched plates with through cracks (Figures 4.10g-h). Besides, due to its modular structure, other geometries can be added.

This application was developed using Visual Basic language. The flowchart of the calculation procedure is shown in Figure 6.1. As can be seen, it includes three main stages. The first one is the *pre-processing*

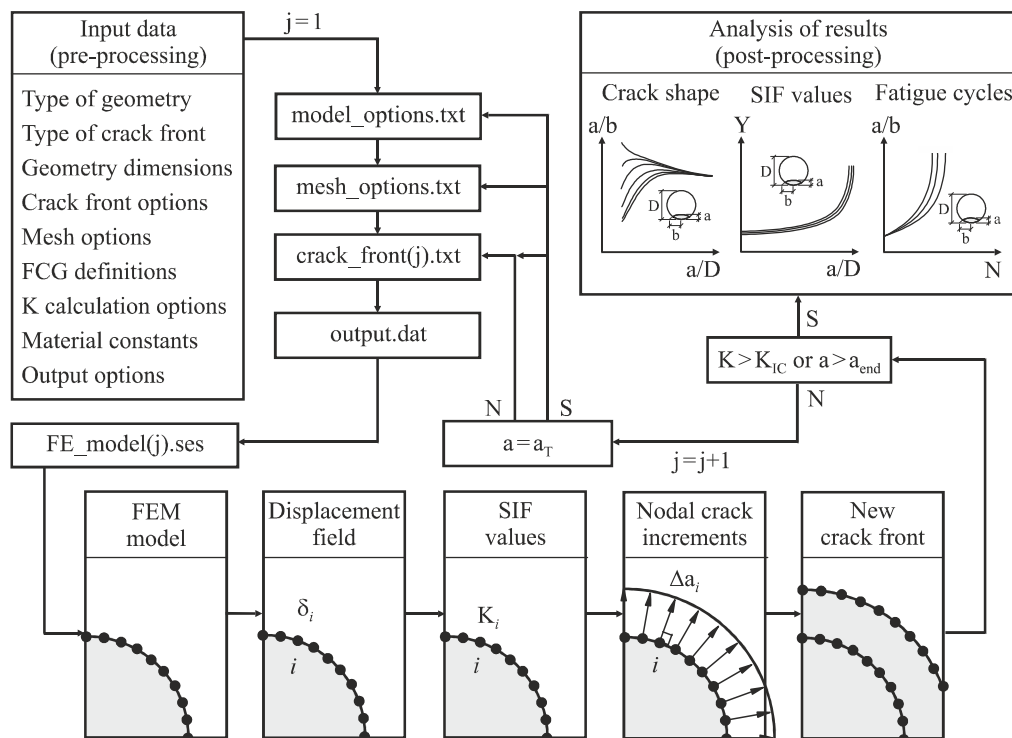


Figure 6.1. Schematic illustration of the calculation procedure (Branco, 2011a).

part in which meaningful input data are received, namely geometrical dimensions, mechanical properties and numerical variables. At this stage, the graphical user interface (GUI) is a great way to increase the user-friendliness of the program as well as to minimise human data entry errors.

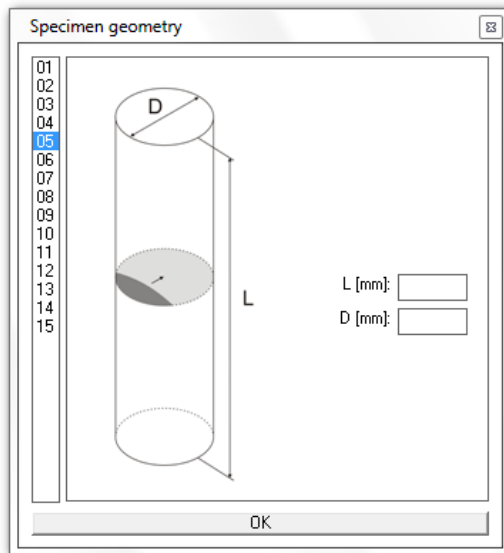
The second stage is focused on the *processing* part which is the core of the FCG simulation. Briefly, it consists of a set of subroutines repeated consecutively for hundreds of times. In such a case, there is a risk of error propagation since the final results of a subroutine are input data of the following one. Therefore, optimised variables and methods are of major importance to achieve reliable results.

Finally, the third stage refers to the *post-processing* part. In essence, the collected output data can be analysed in terms of crack shape evolution, stress intensity factors or number of fatigue cycles. Furthermore, it is also possible to provide complementary graphical and numerical results, such as displacement field, stress field, strain field, deformed shape or even animated videos using a compatible post-processor.

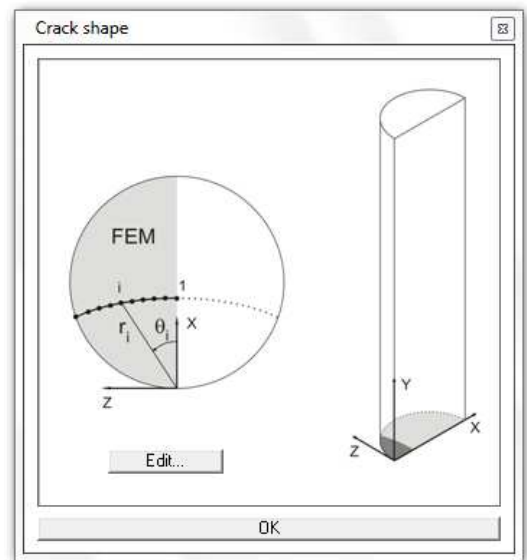
i) Pre-processing stage

In this stage, all geometrical, mechanical and numerical variables are defined using the graphical-user interface (GUI). The interface consists of eight windows, hierarchically organised according to the type of input data. This approach is more attractive to the user since it simplifies the process and ensures a clear separation of tasks. Moreover, enlightening drawings were added to the windows in order to improve the understanding of the problem. Default values are also suggested which can minimise the learning curve of less experienced users.

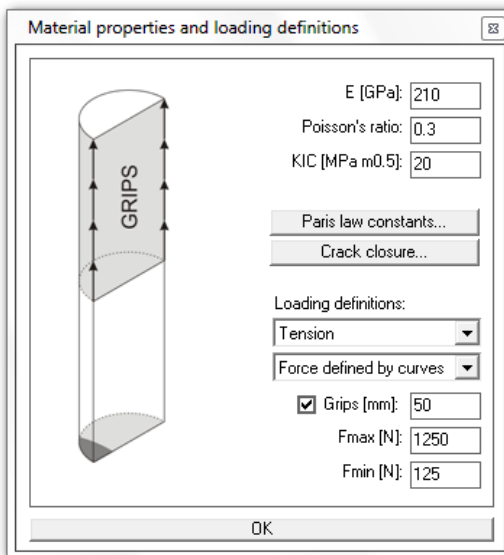
The typical windows of the graphical-user interface are exhibited in Figure 6.2 and Figure 6.3. The first window (Figure 6.2a) allows defining the specimen geometry and its main dimensions. At this moment, fifteen different situations are available but other cases can be added. The second window (Figure 6.2b) is used to define the initial crack shape. The user can set a maximum of fifty corner nodes in Cartesian or polar coordinates. The third window (Figure 6.2c) is devoted to the definition of the elastic constants, fracture toughness, fatigue crack growth rate, and type and magnitude of loading. Individual constants of the Paris law can be defined for each corner node. In the cases in which a constant fatigue crack growth rate is defined, the crack retardation at the free surface can be simulated by defining adequate crack closure levels. Besides, in situations where the crack shape changes from a corner crack (Figures 4.10a-b) or surface crack (Figures 4.10d-f) to a through crack during the propagation, it is possible to define fatigue crack growth rates for each situation (i.e. before and after the shape transition). The loadings available are tension, bending or both. The fourth window (Figure 6.2d) is related to the finite element mesh. The user can specify the number and dimension of concentric rings surrounding the crack tip as well as the total number of elements along the different curves. The fifth window (Figure 6.3a) deals with the calculation of the stress intensity factors at the crack front. Currently, only displacement matching methods are available (Section 2.7.2), namely the Zhu's method and the extrapolation method with two



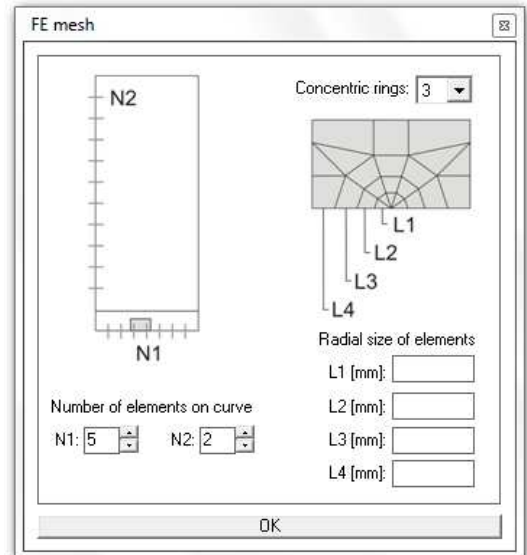
a)



b)



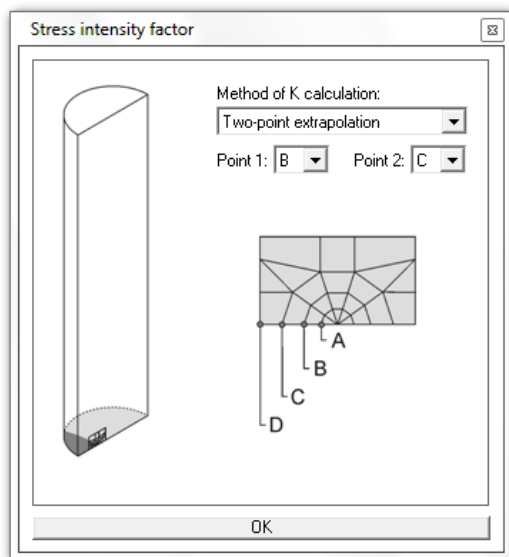
c)



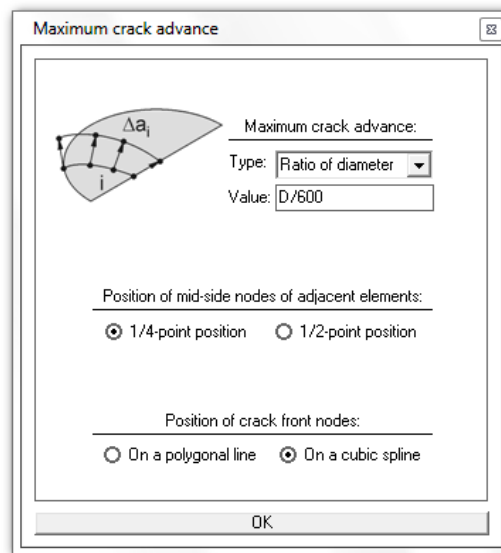
d)

Figure 6.2. Graphical-user interface: a) specimen geometry; b) crack shape; c) material properties and loading definitions; d) FE mesh (Branco, 2011a).

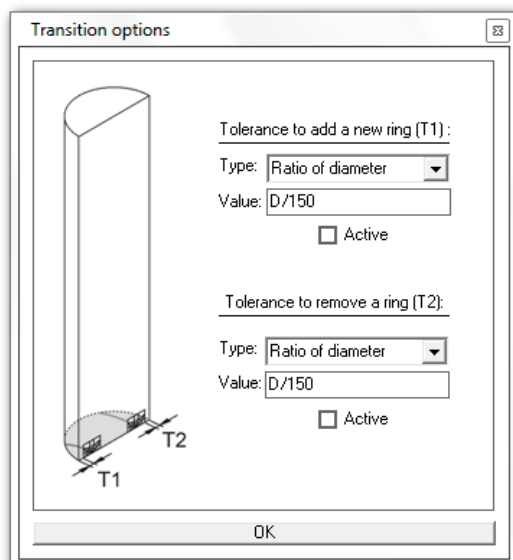
points. The sixth window (Figure 6.3b) allows the input of several numerical parameters associated with the reliability of the numerical simulation, such as the maximum crack advance (Δa_{max}), the position of the intermediate nodes of adjacent elements (quarter-point or half-point positions), and the position of the nodes at the crack front (cubic spline or polygonal line). The penultimate window (Figure 6.3c) encompasses the definition of the variables needed to carry out an automatic transition from a corner or surface crack to a through crack (cases of Figures 4.10a-b and Figures 4.10d-f). In the last window



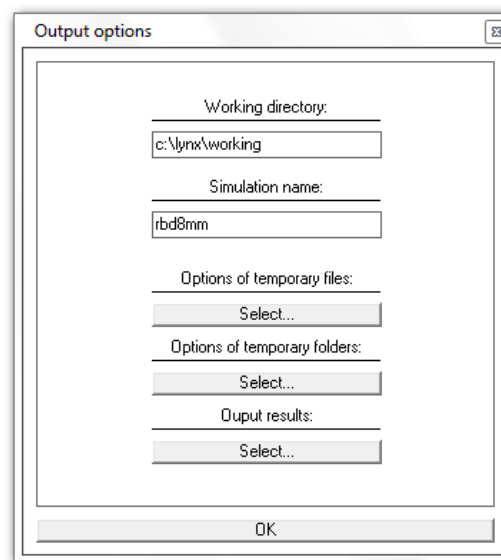
a)



b)



c)



d)

Figure 6.3. Graphical-user interface: a) calculation of stress intensity factor; b) maximum crack front advance; c) transition options; d) output definitions (Branco, 2011a).

(Figure 6.3d), several output options are taken in order to ensure a fast analysis of results as well as an adequate management of the temporary files created during the simulation.

ii) Processing stage

This stage is the core of the *Lynx* and deals with the fatigue crack growth simulation (Figure 6.1). The data entered in the preceding stage are stored in four ASCII files (*model_options.txt*, *mesh_options.txt*, *crack_front(j).txt* and *output.dat*). From the stored information, a representative finite element mesh is generated (*FE_model(j).ses*). The mesh is created from the crack front to avoid the mesh impairments

which occur when the crack is inserted *a posteriori* into the 3D-FE mesh of the uncracked body. The spider web mesh can have between one and three concentric rings. The angular discretisation of these elements is equal to 36° . The inner-most ring is based on collapsed 20-node isoparametric elements and, as a default, the intermediate nodes are placed at quarter-positions. The transition mesh is added in order to create a rectangular box which aims at promoting a faster and smoother change from a refined mesh near the crack tip to a larger mesh at remote positions. It combines both collapsed 20-node isoparametric and 20-node isoparametric quadrilateral elements. Then, the regular mesh, relatively coarse, is generated using 20-node isoparametric quadrilateral elements. As a default, the intermediate and corner nodes of the crack front are positioned on a cubic spline.

After that, the code transfers the execution control to the processor GeoStar 256K, whose main interface is exhibited in Figure 6.4, waiting for the completion of the FE analysis. In this moment, the control is recovered by the *Lynx* which reads the displacement field and calculates the stress intensity factors at the crack front. Next, an adequate crack growth model is applied in order to define the crack front advances and the corresponding number of fatigue cycles. The provisional positions are used to establish a new crack front which is the input data of the next iteration. The procedure is repeated as long as no critical values of fracture toughness or crack length are reached (i.e. $K > K_{IC}$ or $a > a_{end}$).

The transition from a corner or surface crack to a through crack ($a = a_T$) is automatically computed by the software (cases of Figures 4.10a-b and Figures 4.10d-f). The methodology developed tries to ensure that the crack front propagates as close as possible to the edge of the specimen. The algorithm implemented is

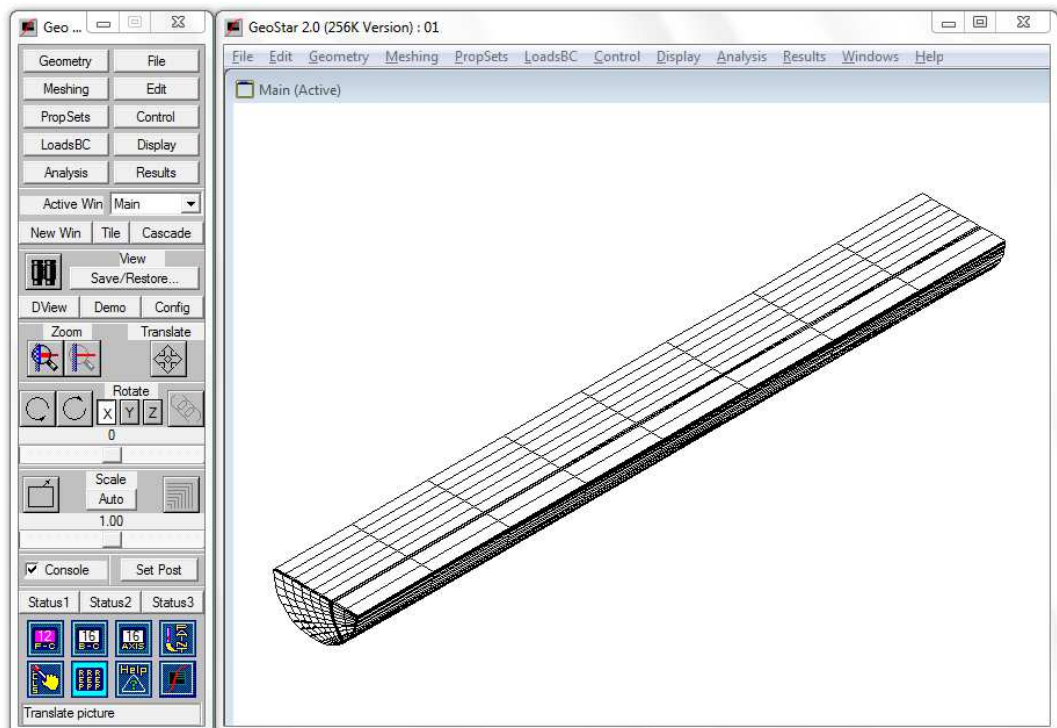


Figure 6.4. Main graphical user interface (Branco, 2011a).

presented in Figure 6.5 and, in essence, consists of a set of actions performed before the transition (B_1 - B_4); a set of actions carried out during the transition (T_R); and a set of actions conducted after the transition (A_1 - A_3). The first ones comprise a progressive reduction of the number of concentric rings, a diminution of the radial size of the crack front elements and a decrease of the maximum crack front advance. The reduction of the number of concentric rings (B_1 - B_3) occurs when the transition mesh cannot be created outside the restricted area Z_R (Figure 6.5). The decrease of the radial size of the crack front elements (L_{i^*}) and of the maximum crack front advance (Δa^*) occurs in stage B_4 in order to obtain crack fronts as close as possible to the edge of the specimen. The transition to the through crack is started when

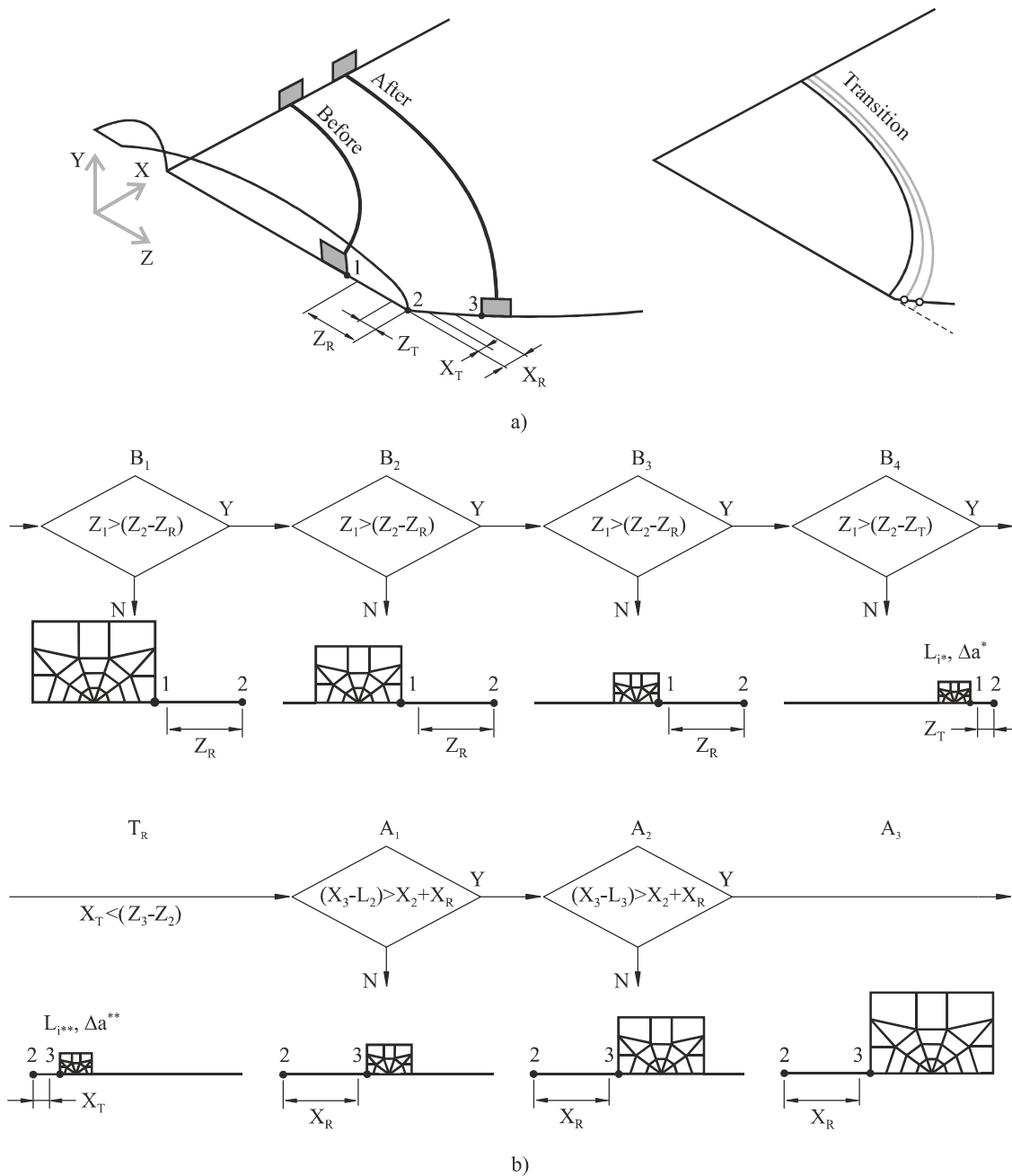


Figure 6.5. Algorithm to carry out an automatic transition from a corner or surface crack to a through crack: a) general overview; b) identification of the main stages.

the transition mesh can no longer be created outside the transition area (Z_T). At this moment, consecutive crack fronts (right-hand side of Figure 6.5a) are defined by increasing successively the crack front advance in order to reach the situation depicted in stage T_R , i.e. the transition mesh can be created out of the transition region (X_T). Then, the radial size of the crack front elements ($L_{i^{**}}$) and the maximum crack front advance (Δa^{**}) are progressively increased in order to reach their standard values. The last stages aim to increase the number of concentric rings (A_1 - A_3). A new concentric ring can be added when the free space after the restricted area (X_R) is enough to accommodate its radial size (L_2 or L_3).

In order to enhance the interactivity of the software, a *resume* option was also implemented to simplify the restart of a simulation interrupted for any reason. A specific file is created at the end of each iteration, being used when a simulation is resumed. For the same reason, a *pause* option was also added, which allows the user to observe particular moments of the simulation supported by a post-processor. Besides, the graphical-user interface (Figure 6.2 and Figure 6.3) can be used to change the input variables at any moment.

iii) *Post-processing stage*

The post-processing stage is devoted to the analysis of results (Figure 6.1). The information about the crack front profiles, stress intensity factors at the crack front and fatigue lives is exported to a spread sheet file and further analysed. Complementary, the FE meshes created during the simulation can be loaded in a compatible FE post-processor. At this moment, the original mesh files are compatible with the GeoStar 256K. Nevertheless, if necessary, other plug-in programs can be developed.

6.1.2. *Procedure optimisation*

The development of a reliable numerical procedure requires a careful identification and optimisation of the independent parameters. The identification of these parameters as well as the discussion of their effects on the simulation of fatigue crack growth were tackled in detail in Sections 2.7-2.8. Figure 6.6 summarises the independent parameters that must be considered in the study of fatigue crack growth using a numerical procedure based on the finite element method. As can be seen, the parameters are organised according to the main stages carried out in the processing part, namely the application of the finite element method (Figures 4.9a-b), calculation of the stress intensity factor at the crack front (Figure

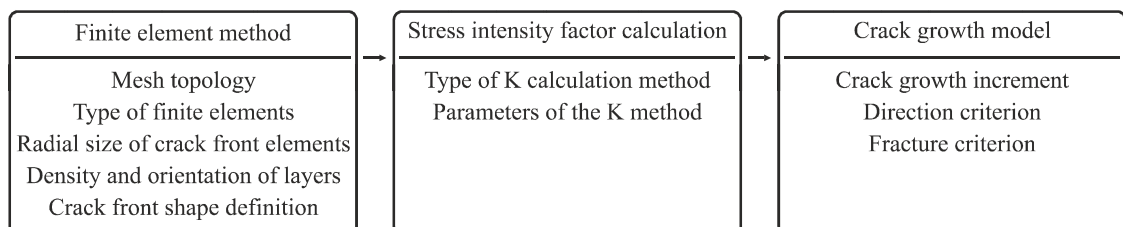


Figure 6.6. Identification of numerical independent parameters that affect the accuracy of a numerical procedure able to study the fatigue crack growth based on the finite element method (Branco, 2013a).

4.9c), and application of an appropriate crack growth model (Figures 4.9d-e). Some parameters have universal optimum values whereas others are defined parametrically.

With respect to the former group, several parameters were defined based on the literature results. It included a mesh topology that incorporated a spider web mesh centred at the crack tip; the use of singular elements able to better simulate the $r^{-0.5}$ stress singularity at the crack tip; a crack front defined by a cubic spline; and a direction criterion that assumed a local propagation normal to the crack front. These parameters have been exhaustively discussed in Sections 2.7-2.8 and Sections 4.3-4.6. Regarding the latter group, optimisation studies were performed to find the appropriate values.

i) Mesh topology

There is a broad consensus that the best topology consists of a spider web mesh with several concentric rings centred at the crack tip combined with a coarse mesh in remote positions (Figure 4.12). As referred to in the previous chapters, this topology was adopted in the present research. Besides, an intermediate mesh was added to simplify the transition between the two above-mentioned meshes.

The effect of the number of concentric rings on the stress intensity factor (SIF) along the crack front was studied in order to select an optimised pattern to the spider web mesh. Figure 6.7 presents the SIF values against the thickness for a straight crack front in rectangular plates with through cracks subjected to tension (Figure 4.10) obtained with different spider web patterns. The stress intensity factors were calculated using the extrapolation method with 2 points. The points used, as schematised in the figure, were at the same distance from the crack tip. The SIF values obtained with one concentric ring are

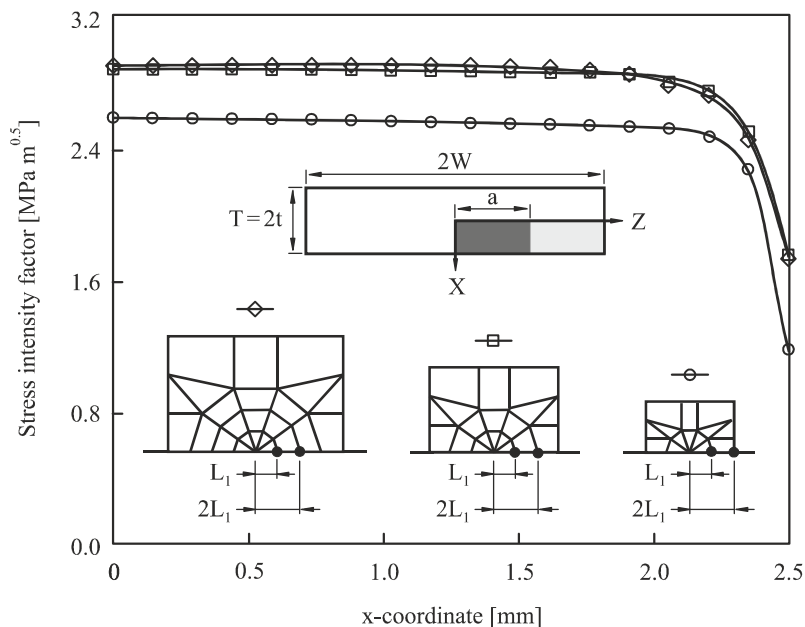


Figure 6.7. Evolution of the stress intensity factor along the crack front in rectangular plates with through cracks ($T=5\text{mm}$, $L=200\text{mm}$, $2W=50\text{mm}$, $a=12.5\text{mm}$, $L_1=\text{constant}$) subjected to tension (Branco, 2013a).

significantly lower, in general, about 10-12%. In contrast, with two or three concentric rings, the stress intensity factors are quite close and the maximum differences are smaller than 0.85%. Based on these results, a spider web mesh made with three concentric rings was implemented in this research as a default setting.

This value has been repeatedly endorsed by different authors. Lin *et al.* used three concentric rings with an angular discretisation of elements surrounding the crack tip equal to 45° to study fatigue crack growth phenomena in round bars (1997; 1998a), fastener holes (1998) and plates (1997a; 1999). Carpinteri *et al.* used exactly the same pattern in their research on FCG in pipes (2000; 2000a; 2003), round bars (2006a; 2007; 2009; 2010) and shells (2006). Antunes *et al.* (2002) also used three concentric rings but with an angular discretisation of elements surrounding the crack tip equal to 36° . Branco *et al.* used the latter pattern to simulate the crack shape evolution in compact-tension specimens (2008a); to propose a notched specimen for crack propagation studies under plane strain conditions (2010a; 2013); to determine the Paris law constants from beach marks on fracture surfaces (2009; 2012d) and to evaluate the extent of surface regions in notched cracked bodies under mode I loading (2012a). The same authors used four rings to model the crack shape evolution in middle-crack tension specimens (2008); and to study the influence of through-thickness crack shapes on plasticity induced crack closure (2008b).

ii) *Type of finite elements*

As referred to above, the finite elements were selected based on the literature results. At the crack tip, the collapsed 20-node isoparametric element with intermediate nodes at quarter-positions (Figure 4.12c) was used. In the other regions, the mesh was created using 20-node isoparametric elements (Figure 4.12a). The transition mesh was made with both 20-node isoparametric (Figure 4.12a) and collapsed 20-node isoparametric elements (Figure 4.12b). The advantage of the isoparametric elements is their natural ability to represent curved shapes because they can be distorted. Besides, they are well tested and are available in all general finite element packages.

The high performance of the singular elements relatively to the conventional elements is a fact. It was demonstrated, for instance, by Antunes (1999). In addition, it was also demonstrated that the collapsed 20-node isoparametric element with intermediate nodes at quarter-point positions (Figure 4.12c) provides better results than the 15-node isoparametric element with intermediate nodes at quarter-point positions (Figure 2.50f). The enhanced behaviour is expected since these elements incorporate the $r^{-0.5}$ crack tip singularity.

The effect of the position of the intermediate nodes on the stress intensity factor is presented in Figure 6.8. This figure exhibits the ratio of the stress intensity factor at the i^{th} node (K_i) to the maximum stress intensity factor (K_{max}) along the crack front for a notched round bar subjected to tension which was obtained using collapsed 20-node isoparametric elements with intermediate nodes at quarter-point positions and collapsed 20-node isoparametric elements with intermediate nodes at half-point positions.

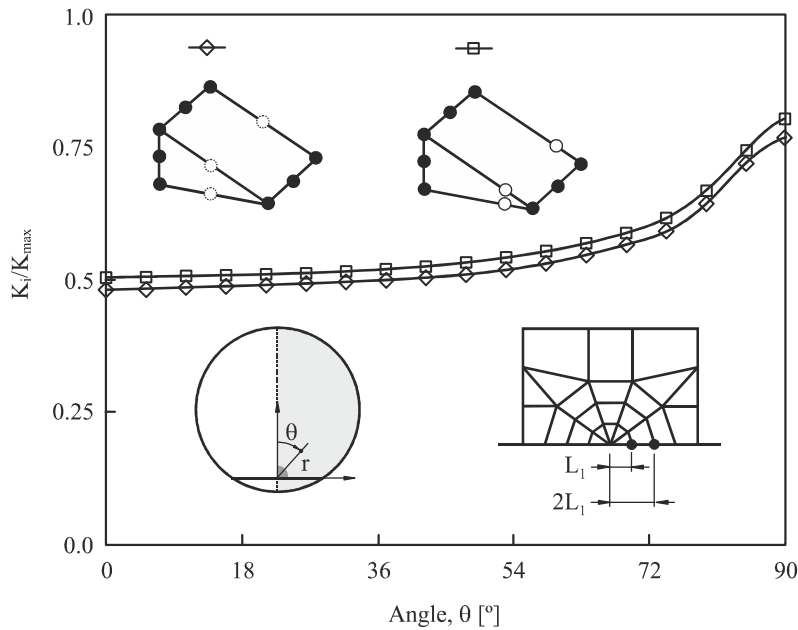


Figure 6.8. Evolution of the K_i/K_{\max} ratio along the crack front in a notched round bar with a semi-circular surface crack of 1.5mm subjected to tension ($D=24\text{mm}$, $L=200\text{mm}$, $r=1.5\text{mm}$, $n=2\text{mm}$, $a=1.5\text{mm}$, $L_1=\text{constant}$).

The SIF values were calculated using the extrapolation method with two points. The nodes selected are depicted in the figure above. Although the trends are similar, there are significant differences in the magnitudes of the K_i/K_{\max} values. Besides, it is also clear that the results for the singular element are higher, on average, about 5-6%. Naturally, these differences in the entire simulation would have implications in terms of fatigue lives and crack front profiles.

iii) Radial size of crack front elements

As stated in Section 2.7.1, the most-inner ring of the spider web mesh has a relevant role on the accuracy of the numerical results (Antunes, 1999; Guinea, 2000). In theory, the optimum radial size of the singular elements (L_1) is assured when a balanced modelling of both singular and non-singular fields is achieved. Nevertheless, in practice, this is a very complex problem because there are no universal optimum values. The optimum radial sizes of crack front elements are generally provided by individual studies (Murthi, 1986; Nykänen, 1996; Antunes, 1999; Branco, 2008; Branco, 2008a) which is computationally intensive and time-consuming. Therefore, these values are defined under an acceptable upper bound tolerance and are valid in a weak sense.

With respect to the unnotched geometries, the optimum L_1 was defined using average values available in the literature. Table 6.1 lists the range of values used here (the variables L_i and T_i were defined in Figure 4.13c). In relation to the notched geometries, the problem is more difficult to solve. On the one hand, the existing results are scarce. On the other hand, both the spider web mesh and the transition mesh must be confined to the interior of the notch (see Figure 4.14) and, therefore, the selected sizes of the finite elements are implicitly limited by the notch dimensions, particularly by its radius. In view of this fact, L_1

was defined as a fraction of the notch radius (r) and was maintained throughout the simulation. The values used for each situation are reported in Table 6.1. The relations between the radial size of crack tip elements and the values of L_2 - L_4 and T_1 - T_3 used for the unnotched and notched geometries are also summarised in the same table.

Figure 6.9 compares the evolution of the K_i/K_{\max} ratio along a straight crack front in a rectangular plate with through crack subjected to tension for two significantly different values of L_1 (1% of the crack length and 10% of the crack length). The stress intensity factors were calculated using the extrapolation method with two points, from the points A and B represented in the figure. As can be seen, the trends are similar and the differences between the K_i/K_{\max} ratios, except near the surface, are quite small. For example, for values of $x/t < 0.95$, the differences are lower than 0.4%, whilst at the surface are about 5%. Therefore, although the value of L_1 has increased one order of magnitude, the K_i/K_{\max} ratios maintained quite stable

Table 6.1. Sizes of the elements of spider web mesh and transition mesh.

Geometry	L_1	$L_2 = L_3 = L_4$	$T_1 = T_2$	T_3
Rectangular bar with corner crack	$L_1 > 0.02a \wedge L_1 > 0.1a$	$= L_1$	$= (L_1 + L_2 + L_3) \times \sin 36^\circ$	$= T_1$
Notched rectangular bar with corner crack	$L_1 < (r \sin 36^\circ) / 9$	$= L_1$	$= (L_1 + L_2 + L_3) \times \sin 36^\circ$	variable
Round bar with surface crack	$L_1 > 0.02a \wedge L_1 > 0.1a$	$= L_1$	$= (L_1 + L_2 + L_3) \times \sin 36^\circ$	$= T_1$
Notched round bar with surface crack	$L_1 < (r \sin 36^\circ) / 9$	$= L_1$	$= (L_1 + L_2 + L_3) \times \sin 36^\circ$	variable
Rectangular plate with surface crack	$L_1 > 0.02a \wedge L_1 > 0.1a$	$= L_1$	$= (L_1 + L_2 + L_3) \times \sin 36^\circ$	$= T_1$
Notched plate with surface crack	$L_1 < (r \sin 36^\circ) / 9$	$= L_1$	$= (L_1 + L_2 + L_3) \times \sin 36^\circ$	variable
Plate with through crack	$L_1 > 0.02a \wedge L_1 > 0.1a$	$= L_1$	$= (L_1 + L_2 + L_3) \times \sin 36^\circ$	$= T_1$
Notched plate with through crack	$L_1 < (r \sin 36^\circ) / 9$	$= L_1$	$= (L_1 + L_2 + L_3) \times \sin 36^\circ$	variable

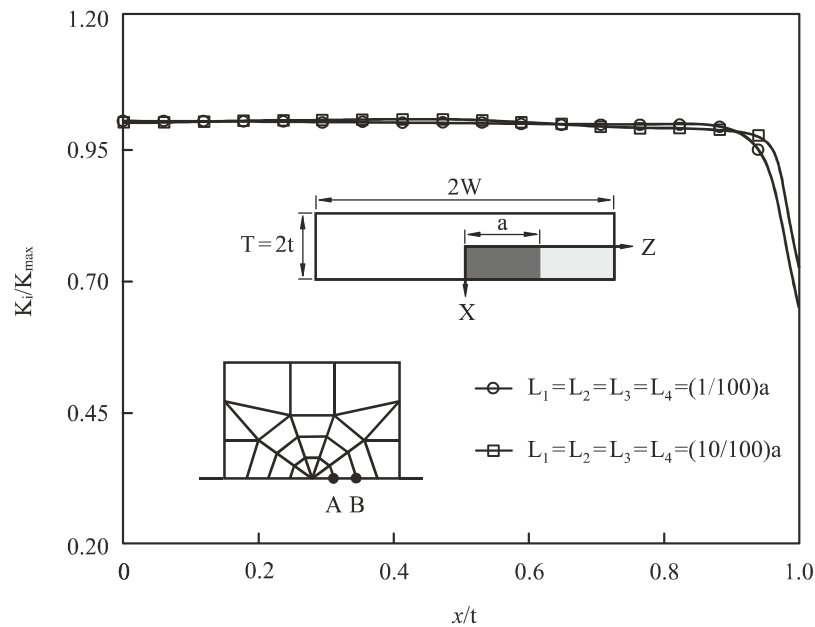


Figure 6.9. Evolution of the K_i/K_{\max} ratio along the crack front in a rectangular plate with a straight crack ($T=5\text{mm}$, $L=200\text{mm}$, $2W=50\text{mm}$, $a=12.5\text{mm}$, $L_1 = \text{constant}$) subjected to tension (Branco, 2013a).

and with no significant differences.

iv) Density and orientation of layers

Most of the numerical studies focused on fatigue crack growth assume uniform layers along the crack front. As referred to in Chapter 4, the present research follows the prevailing trend (Figures 4.12 and 4.14). The only exception was in the determination of the Paris law constants from the analysis of crack front marks on fracture surfaces of small cross-section round bars (Section 4.6). The finite element model encompassed a refined region close to the free boundary in order to provide a better description of the crack shape near that region (Figure 4.23).

Regarding the orientation of the layers surrounding the crack tip, the numerical models created to study fatigue crack growth phenomena were prepared to accommodate precisely orthogonal layers. This approach is advantageous in the calculation of stress intensity factors especially when displacement matching methods are used (Lin, 1999). The influence of the degree of non-orthogonality of the mesh surrounding the crack front on the SIF values can be seen in Figure 6.10. This figure presents the evolution of the K_i/K_{max} ratio along the crack front in a notched plate with through crack obtained from two meshes with different degrees of orthogonality. The situations studied included a precisely orthogonal mesh with layers normal to the crack front and a mesh with parallel layers to each other. The crack front selected is a stable crack shape with an average crack length of 12.47mm which is the result of a numerical simulation started from a straight crack with an initial length of 0.5mm. The SIF values were calculated using the extrapolation method with two points. The differences in the K_i/K_{max} ratios tend to increase from the half-thickness to the free surface which is a consequence of the crack curvature caused

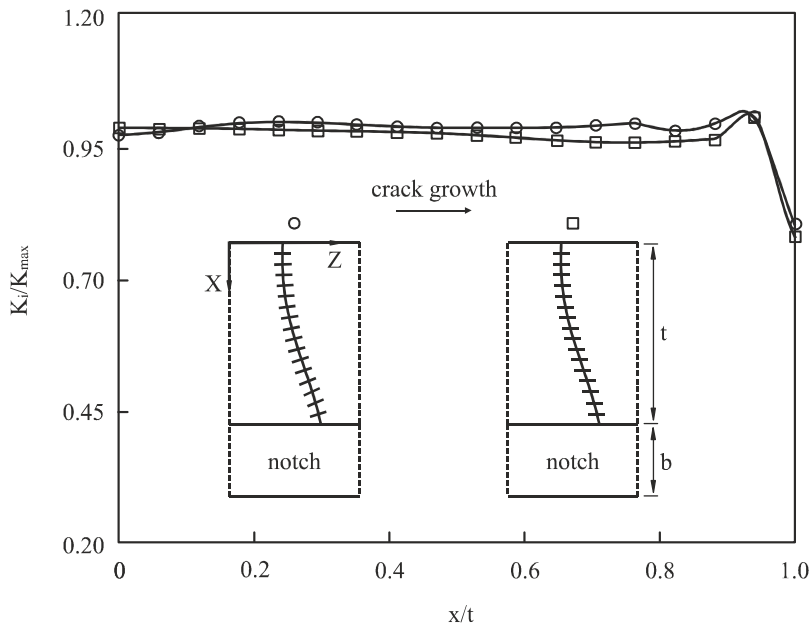


Figure 6.10. Evolution of the K_i/K_{max} ratio along the crack front in a notched plate with a through crack ($T=10\text{mm}$, $L=200\text{mm}$, $2W=50\text{mm}$, $a_m=12.47\text{mm}$, $r=1.5\text{mm}$, $n=2\text{mm}$) subjected to tension (Branco, 2013a).

by the presence of the notch. It is important to note that some layers of the precisely orthogonal model are rotated about 25° relatively to the non-orthogonal model. However, the maximum differences in the K_i/K_{\max} ratios are lower than 3.5%.

v) Crack front definition

As described in Section 2.7.1, two main approximation methods can be used to define the crack front shape, i.e. polygonal line or cubic spline. The former (Smith, 1989) consists of a simple connection of the corner nodes by straight lines, being the intermediate nodes placed at half-point positions of both neighbouring corner nodes. The latter (Lin, 1999) uses a cubic spline that passes through both the corner and intermediate nodes. In this manner, the final crack front is smoother which is associated with more accurate estimations of stress intensity factors. On the other hand, this approximation avoids the need to modify the nodal positions when large crack shape changes occur and thereby leads to a fully automatic procedure. Last but not least, the crack front profiles are more realistic than those achieved through the polygonal line.

Figure 6.11 exhibits the values of the K_i/K_{\max} ratio along the crack front in a notched round bar with surface crack obtained using a polygonal line approximation, a cubic spline approximation with both corner and intermediate nodes positioned on the curve, and a cubic spline approximation with corner nodes positioned on the curve and intermediate nodes at half-point positions. The SIF values were calculated using the extrapolation method with two points. The crack front selected was a stable crack shape with an average radius of 2.55mm which was the result of a simulation started from a semi-circular crack with radius of 0.25mm. Note that a very small crack growth increment ($\Delta a = D/800$) was adopted in

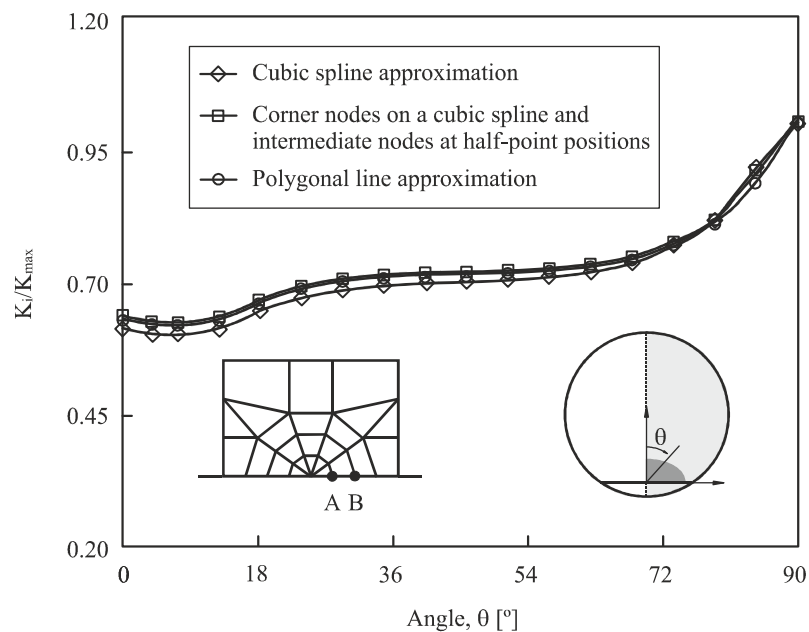


Figure 6.11. Evolution of the K_i/K_{\max} ratio along the crack front in a notched round bar with semi-circular surface crack subjected to tension ($D = 16\text{mm}$, $L = 200\text{mm}$, $a_m = 2.55\text{mm}$, $r = 0.75\text{mm}$, $n = 1.5\text{mm}$).

this simulation. This means that the provisional and final positions of the corner nodes are relatively close to each other and, therefore, the main difference between the three situations analysed is the position of the intermediate nodes. In fact, the K_i/K_{\max} ratios are highly sensitive to the positions of the intermediate nodes. As can be seen, the results are nearly the same for the polygonal line approximation and for the situation in which the corner nodes are on a cubic spline and the intermediate nodes are at half-point positions. However, the values of the K_i/K_{\max} ratios are, on average, about 3% lower when the intermediate nodes are positioned together with the corner nodes on the cubic spline curve.

vi) Stress intensity factor calculation

Numerical methods to extract the stress intensity factors, as explained in Section 2.7.2, can be divided into displacement matching methods and energy-based methods. The former group compares the predicted numerical displacement field with the analytical displacement field, which contains K in its formulation. The latter group calculates the stress intensity factor from the energy release rate. It is important to emphasise that energy-based methods are more accurate than displacement matching methods but, in general, require more computational effort. In this sense, a trade-off between accuracy and computational effort is a solution to increase the efficiency.

In this research, two direct methods (extrapolation method with two points and Zhu’s method) and an energy-based method (external forces method) were tested. The mathematical formulations were presented in detail in Section 2.7.2. Figure 6.12 exhibits typical results of the SIF values estimated along the crack front using these methods for a plate with through crack subjected to tension. An overview of the figure shows that both the external forces method and extrapolation method with two points have

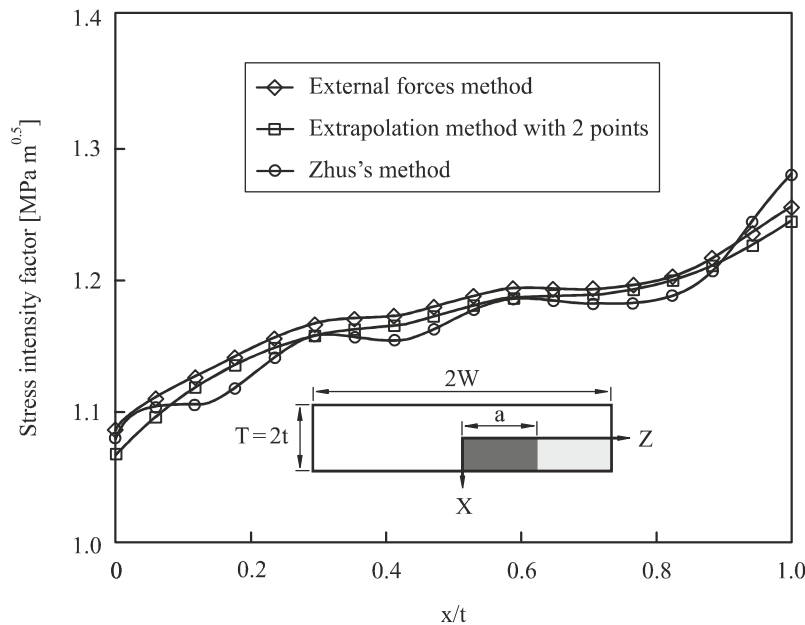


Figure 6.12. Evolution of the K_i/K_{\max} ratio along the crack front in rectangular plate with a curved crack front ($T=10\text{mm}$, $L=200\text{mm}$, $2W=50\text{mm}$, $a_m=12.53\text{mm}$) subjected to tension (Branco, 2013a).

identical trends. The SIF values obtained by the energy-based method are 1-2% higher. Regarding the Zhu's method, it can be distinguished an oscillatory behaviour in the values of the stress intensity factors which does not match with the other two methods. As a consequence, the differences relatively to the external forces method are considerably higher, between 4-6%.

The computational effort is another major issue which cannot be ignored. Although the external forces method is more accurate, it requires thirty-seven analyses to carry out an iteration (assuming a crack front divided into eighteen nodes, as mentioned in Section 4.3) whilst the direct methods only need a single analysis. On the basis of these reasons, it would be unreasonable to adopt the energy-based method. Thus, the choice has fallen on the extrapolation method with two points, since it combines accuracy and efficiency. Furthermore, this method has been successfully used in diverse situations (Antunes, 1999; Branco, 2008; 2008a; 2008b; 2009; 2011a; 2012d; 2013). Therefore, it is well established and well tested.

vii) Crack growth model

The crack growth model applied in the present research was discussed in Section 4.3. As already noted in Section 2.7.3, the maximum crack advance (Δa_{\max}) is intimately connected with the accuracy of the numerical results in terms of crack shape and fatigue life (Lin, 1999c; Branco, 2008a). In order to ensure good predictions, small values of Δa_{\max} are recommended. The inaccuracies result from the assumption that $C(\Delta K)^m$ is constant for each iteration which is not true. As is well-known, it depends on the crack length and increases continuously as the crack propagates.

Figure 6.13 shows the evolution of the crack aspect ratio (a/b) with the dimensionless crack length (a/D) for different maximum crack advances ($D/50, D/100, D/150, D/200, D/250, D/300$) in a round bar with

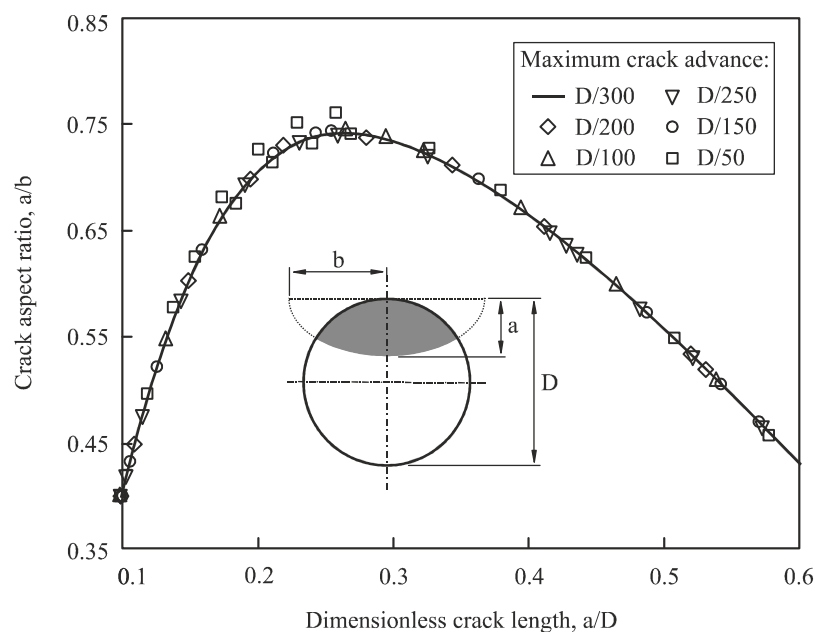


Figure 6.13. Effect of Δa_{\max} on a/b in a round bar with surface crack ($D=16\text{mm}, L=100\text{mm}$).

surface crack subjected to tension. The initial crack shape was a part-elliptical front with $a_0/b_0 = 0.4$ and $a_0/D = 0.1$. For a maximum crack advance equal to $D/50$, the typical oscillatory behaviour reported in Section 2.7.3 is clearly distinguished. The values of a/b are either above or below the full line, especially for dimensionless crack lengths (a/D) within the interval 0.15-0.30. These sudden changes in the crack shape are clear sign of unduly high crack advances. By reducing this parameter, it is possible to remove such a phenomenon. Take, for instance, the predictions obtained with values of Δa_{\max} equal to $D/200$, $D/250$ and $D/300$. In these cases, the results are perfectly superimposed and the maximum differences are lower than 1%. In view of this fact, a value of $D/300$ was defined as the recommended crack advance for round bars since it conciliates efficient computation and accuracy. Based on the same approach, the recommended values of crack advances for notched and unnotched bars with corner cracks; notched and unnotched plates with surface cracks; and for notched and unnotched plates with through cracks were found to be equal to $t/250$, $W/500$ and $W/300$, respectively.

6.1.3. Procedure validation

The typical crack front developments obtained with the fatigue crack growth technique developed here are presented in the two following figures (Figures 6.14 and 6.15). Figure 6.14 shows the shape evolution of a part-circular surface crack ($a_0/D = 0.1$, $a_0/b_0 = 1$) and a straight surface crack ($a_0/D = 0.1$, $a_0/b_0 = 0$) in a round bar subjected to tension. These results clearly demonstrate that the early propagation stage is strongly dependent on the initial crack shape. As can be seen, the initial straight shape ($a_0/b_0 = 0$) grows much more rapidly in depth direction than along the free surfaces. In contrast, the growing of the part-circular shape ($a_0/b_0 = 1$) is more balanced along the whole crack front. Nevertheless, the effect of the initial crack shape gradually weakens as the crack extends leading to a subsequent propagation stage in which the crack front profiles are very similar to each other. These stable crack shapes are often termed preferred propagation paths (PPP). The amount of crack growth needed to achieve the second stage, as

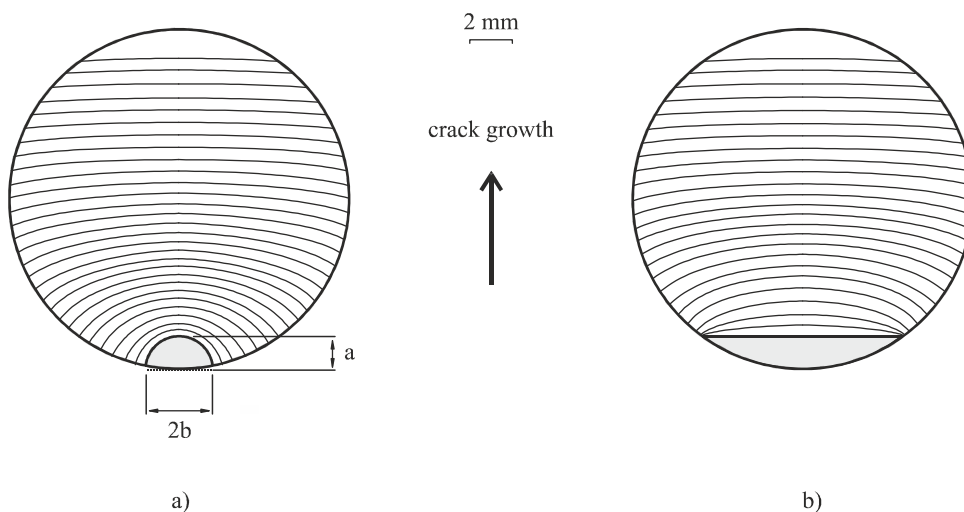


Figure 6.14. Crack front developments in unnotched round bars ($D = 16\text{mm}$, $L = 100\text{mm}$, $m = 3$, $\nu = 0.30$, $E = 210\text{ GPa}$) from different initial defects subjected to tension: a) part-circular shape ($a_0/D = 0.1$, $a_0/b_0 = 1$); b) straight shape ($a_0/D = 0.1$, $a_0/b_0 = 0$).

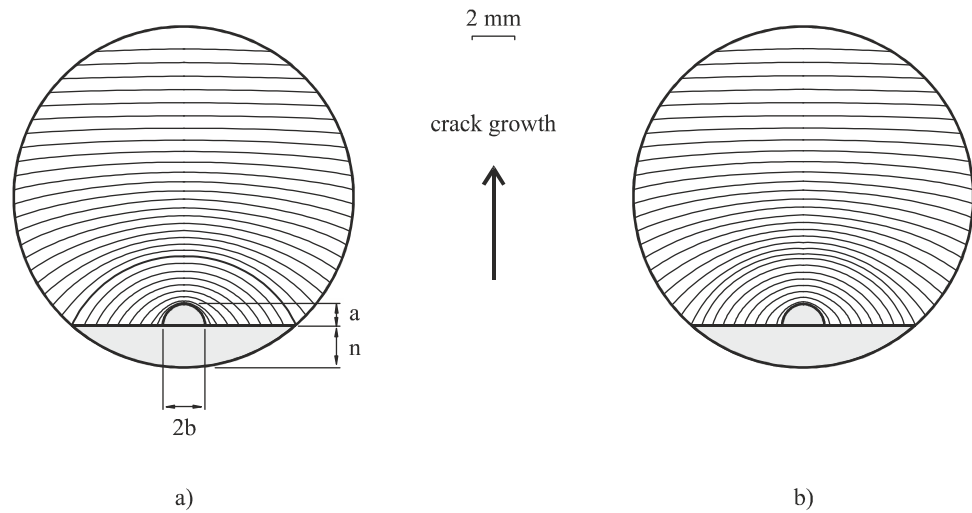
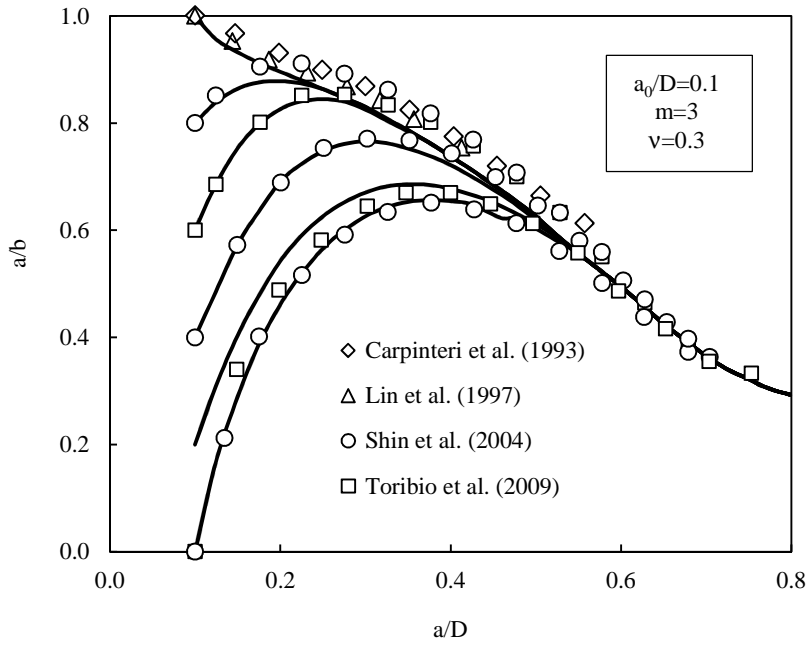


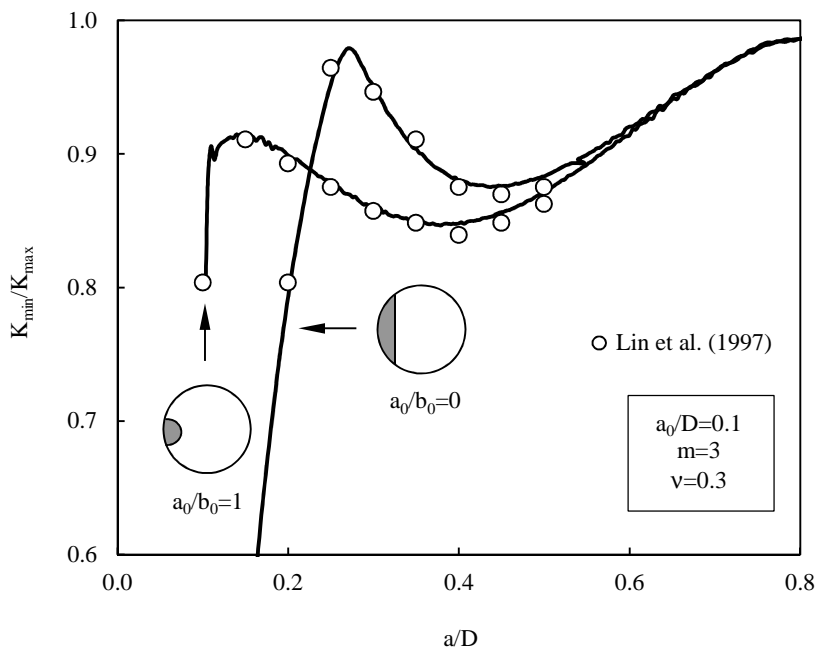
Figure 6.15. Crack front developments in notched round bars ($D=16\text{mm}$, $L=100\text{mm}$, $r=0.5\text{mm}$, $n=2\text{mm}$, $m=3$, $\nu=0.30$, $E=210\text{ GPa}$) from semi-circular cracks ($a_0/D=0.0625$, $a_0/b_0=1$) subjected to: a) tension; b) bending.

pointed out by several authors (Carpinteri, 1993; Couroneau, 1998; Lin, 1998; Branco, 2009b), depends not only on the initial crack shape but also on the loading type, fatigue crack growth rates, elastic constants and crack length. Therefore, shapes intrinsically closer to the PPP reach it faster than the others. Figure 6.15 exhibits the shape evolution of a semi-circular defect ($a_0/D=0.0625$, $a_0/b_0=1$) in a notched round bar ($r=0.5\text{mm}$, $b=2\text{mm}$) subjected to tension and bending. Although not obvious in the figure, a rigorous analysis of the results shows that all the propagation is affected by the loading effect. On the one hand, when the crack is a surface crack, it grows more rapidly in the depth direction under bending than under tension. On the other hand, the preferred propagation path, when the crack becomes a through crack, tends to be more flat than the PPP for tension (Branco, 2012a). Besides, it is notorious that the crack front profiles in this phase are not significantly affected by the notch, since the crack shape developments of Figure 6.15a are very close to those found in Figures 6.14a-b.

The crack front profiles and the values of the stress intensity factor computed using the present numerical procedure were compared with the ones found in the literature for validation. Figure 6.16a presents the evolution of the crack aspect ratio (a/b) with the dimensionless crack length (a/D) for different initial crack fronts with the same dimensionless crack length ($a_0/D=0.1$) in a round bar subjected to tension. In fact, as suggested in Figure 6.14, the trajectory drawn by the crack strongly depends on the initial crack aspect ratio. Nevertheless, this high effect weakens gradually, as the crack propagates, leading the crack shape to a preferred propagation path. Additionally, it is possible to observe a good agreement between the numerical results presented here and those found in the literature (Carpinteri, 1993; Lin, 1997; Shin, 2004; Toribio, 2009) for the same propagation conditions ($a_0/D=0.1$, $m=3$, $\nu=0.3$). Figure 6.16b shows the ratio of the minimum SIF to the maximum SIF along the crack front (K_{\min}/K_{\max}) during the crack growth for a round bar with surface crack under constant amplitude cyclic tension. Different initial crack shapes ($a_0/b_0=0$, $a_0/b_0=1$) with the same dimensionless crack length ($a_0/D=0.1$) were considered.



a)



b)

Figure 6.16. Evolution of the: a) crack aspect ratio with the dimensionless crack length; b) K_{\min}/K_{\max} ratio with the dimensionless crack length (Branco, 2012d).

This ratio (K_{\min}/K_{\max}) is interesting to characterise the SIF variations along the crack front with the crack growth. At the early stage, it suddenly increases and then goes down slightly to values about 0.85-0.88. After that, the ratio rises up slightly towards values close to one ($K_{\min}/K_{\max} \approx 0.98$). Moreover, at the early stage, the gradient of the K_{\min}/K_{\max} ratio is less intense for the part-circular crack shape ($a_0/b_0=1$) than for the straight crack shape ($a_0/b_0=0$). This explains the more significant shape changes observed in the latter

case (Figure 6.14b). The predicted values of the K_{\min}/K_{\max} ratio were compared with results found in the literature (Lin, 1997) for the same propagation conditions ($a_0/D=0.1$, $m=3$, $\nu=0.3$). As can be seen, both types of data are in excellent agreement. Note that the maximum differences are lower than 1.3%.

6.2. Extent of the surface region in cracked bodies

Reliable numerical tools for analysing two-dimensional fatigue crack growth problems are available but the transition to three-dimensional models is still taking place. Besides, the scarce software solutions developed to predict fatigue crack growth from experimental $da/dN-\Delta K$ curves (see Section 2.6) are not all available commercially; and the commercial solutions available are not sufficiently robust to perform fully automatic and error-free simulations (Hou, 2001). Therefore, more effective methods are required to improve the quality of the numerical results.

On the other hand, it must not be forgotten that the study of fatigue crack growth based on the FEM is closely related to the type of finite element meshes created, either in terms of computational time or in terms of quality of results. Among other aspects, an adequate FE mesh must be developed to accurately simulate the extent of the surface regions. Surface regions are particularly important since they involve complex singularities. At corner points, the singularity although existing, is usually different from $r^{-0.5}$.

Indeed, the order of singularity depends on the intersection angle of the crack with the free surface and on the Poisson's ratio of the material (Bazant, 1979; Benthem, 1977; Heyder, 2005). Besides, a relatively fast transition from plane stress at the surface to plane strain at interior positions is expected to occur. The presence of lateral notches certainly affects this transition and, accordingly, the extent of the surface region with or without notches is different. Moreover, surface phenomena, such as crack closure, residual stress, etc., have more intense effects near the surface and must be properly incorporated into the numerical model to enhance simulations.

The extent of the surface region can be quantified using stress triaxiality parameters. The ratio of the average hydrostatic stress to the equivalent von Mises stress (Θ) is probably the most used (see Equation 4.16). This parameter varies typically from 0 for pure shear to 5-6 for sharp notches. Among others, it was used by Wang *et al.* (2000) to study ductile failure of tubular joints; by Chen *et al.* (2005) and Anvari *et al.* (2006) to model ductile crack growth using cohesive elements; by Kim *et al.* (2004) to compile solutions of crack tip stress triaxialities for standard and non-standard fracture toughness testing specimens via detailed elastic-plastic 3D-FE analyses; and by Mirone (2007) to predict ductile failure of notched geometries subjected to different triaxiality histories. An alternative parameter (see Equation 6.1) also defined from the ratio of the average hydrostatic stress to the equivalent von Mises stress and the Poisson's ratio was proposed by Lemaitre (1996).

$$R_v = \frac{2}{3}(1-\nu) + 3(1-2\nu)\left(\frac{\sigma_H}{\sigma_{vM}}\right)^2 \quad (6.1)$$

The ratio of the out-of-plane stress component to the sum of the in-plane stresses multiplied by the Poisson's ratio (h) is an alternative stress triaxiality parameter also often used in the literature (see Equation 4.17). This parameter varies from 0 for plane stress to 1 for plane strain. It was used by Bakker (1992) to study three-dimensional constraint effects on the stress intensity factor in plates with through-thickness cracks; by Kotousov *et al.* (2002) to compute three-dimensional stress constraint effects in elastic plates with notches; by Berto *et al.* (2004) to calculate constraint factors in plates with V-shaped notches; by Kotousov *et al.* (2010) to evaluate constraint factors in plates under quasi-brittle fracture; and by Branco *et al.* (2010a; 2013) to propose grooved middle-crack tension specimens for plane strain studies.

The out-of-plane stress constraint (T_z) is another stress triaxiality parameter which can be defined by the following relationship (Guo, 1993)

$$T_z = \frac{\sigma_3}{\sigma_1 + \sigma_2} \quad (6.2)$$

being σ_1 , σ_2 , σ_3 the principal stresses in the normal plane of the crack front calculated with respect to a local coordinate system ($X'Y'Z'$) whose Z' -axis is tangential to the crack front. In a literal sense, $T_z = 0$ for plane stress state and $T_z = \nu$ for plane strain state. This parameter was used by Guo (1999) to analyse the plastic constraint for through-thickness cracked bodies; by She *et al.* (2007) to study out-of-plane constraints of cracks in thin elastic plates; by Zhao *et al.* (2007) to describe the stress field near the border of semi-elliptical surface cracks in plates; by Zhang *et al.* (2007) to characterise 3D stress states of quarter-elliptical corner cracks subjected to uniform tension; by Yang (2009) to obtain stress and strain concentration factors for notched round bars subjected to tension; and by Yu *et al.* (2010) to define equivalent thicknesses for corner cracks relatively to through-thickness specimens.

O'dowd *et al.* (1991; 1992) introduced the elastic-plastic Q-value to quantify the crack tip constraint as plastic flow progress from small scale yielding to fully yielded conditions. Henry *et al.* (1997) found a unique linear relationship between the Θ stress triaxiality factor and the Q-value which is independent of the specimen geometry, specimen size, crack depth and deformation level. Nevertheless, a limited number of studies focused on the extent of surface regions near corner points were found. This extent is expected to change with the specimen geometry, presence of notches, loading pattern, loading level and material properties. Burton *et al.* (1984) analysed through-thickness cracks and reported extents of $z/a \leq 1.5\%$ for the surface region. Narayana *et al.* (1994) estimated the thickness of the surface effect (t_s) by the following formula

$$\frac{t_s}{t} = \frac{1}{4 + 16t/a} \quad (6.3)$$

being t the thickness of the cracked body and a half of the crack length. Bakker (1992) studied the variation of the h parameter along the crack front, and the influence of thickness and crack tunnelling in

plates with through-thickness cracks. Antunes *et al.* (2000) used the variation of the stress intensity factor to quantify the extent of near-surface regions in corner crack specimens. The maximum values were observed at angular positions $\alpha=1.5^\circ$, which corresponds to an extent of the surface region $z/a \leq 2.6\%$ for a quarter-circular crack with radius of 5mm. Camas *et al.* (2011; 2012) analysed the size of the plastic zone and the stress state along the thickness direction in standard C(T) specimens using ultrafine meshes.

6.2.1. Selection of representative crack shapes

The extent of the surface region, as stated in Section 4.4, was studied using realistic crack shapes. The broad range of simulations performed are summarised in Tables 4.5-4.7 and encompassed notched and unnotched rectangular bars with corner cracks (Figures 4.10a-b); notched and unnotched round bars with surface cracks (Figures 4.10c-d); and notched and unnotched plates with through cracks (Figure 4.10g-h).

For each geometry, the set of simulations defined aimed at analysing the main parameters affecting the crack shape, namely specimen size, notch configuration, fatigue crack growth rates, loading type and elastic constants. Some of these effects are schematised in Figure 6.17. Figure 6.17a presents the effect of the notch radius on the crack shape in notched round bars ($D = 16\text{mm}$, $L = 100\text{mm}$) subjected to tension.

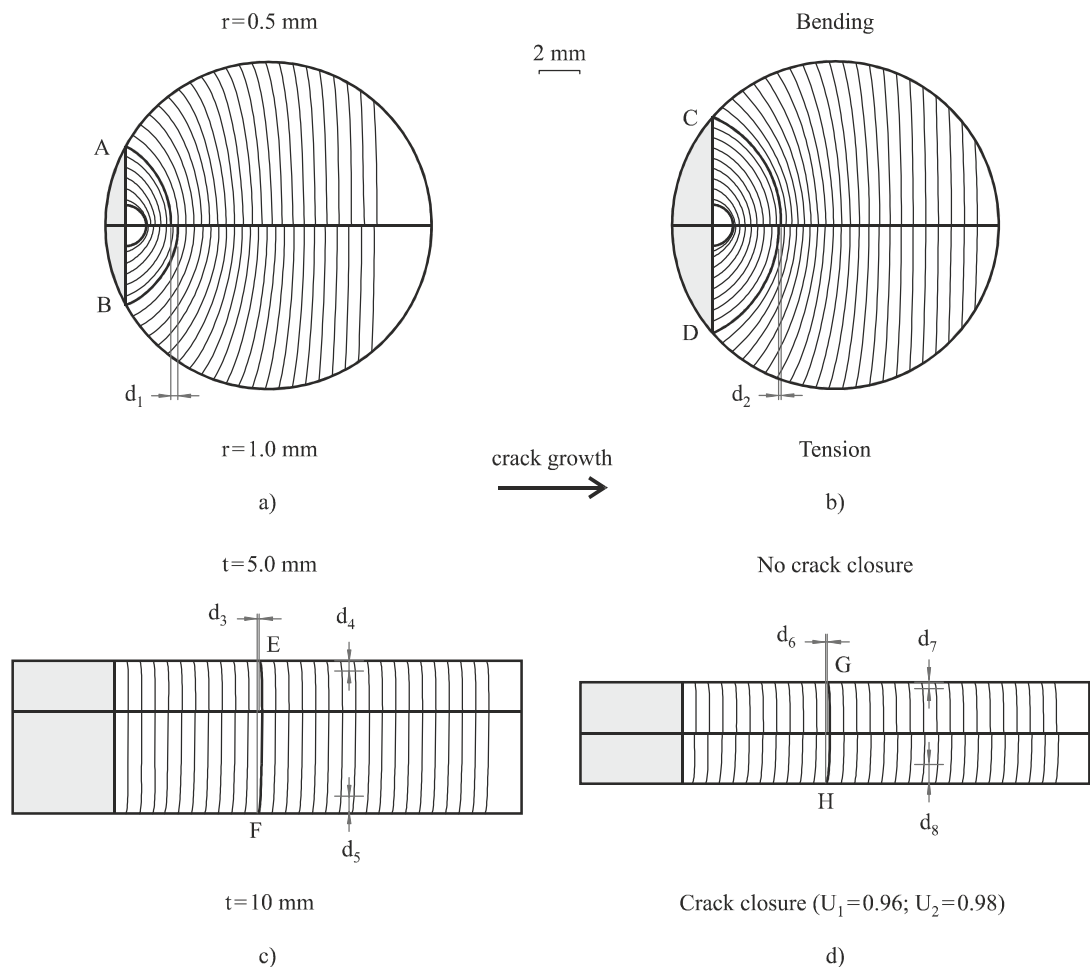


Figure 6.17. Effect of the: a) notch radius; b) loading type; c) thickness; d) crack closure on the crack shape (Branco, 2012a).

Two different notch radii ($r=0.5\text{mm}$ and $r=1.0\text{mm}$) with the same notch depth ($n=1.0\text{mm}$) were studied. As can be seen, the decrease in the notch radius leads to a faster crack growth towards the notch root which is a natural consequence of the greater stress concentration factor. The difference d_1 in the depth direction, measured when both profiles *A* and *B* became through cracks, is clear sign of this. After this moment, the notch effect decreases gradually over time, resulting in very similar profiles, regardless of the situation.

Figure 6.17b exhibits the loading effect on the crack shape in a notched round bar ($D = 16\text{mm}$, $L=100\text{mm}$, $r=0.5\text{mm}$, $n=2.0\text{mm}$) subjected to tension and bending. The crack front profiles are different throughout the propagation. Surface cracks under bending grow more rapidly in the depth direction than under tension, as indicated by the difference d_2 measured when the profiles *C* and *D* became through cracks. But even after this, the crack shape developments are different to each other. Due to a progressive attenuation of the notch effect, the profiles tend to be similar to the preferred propagation paths of the unnotched round bars which are slightly different for tension and bending (Carpinteri, 1993; Branco, 2009b) as referred to above.

The effect of the specimen size on the crack shape in a rectangular plate with through crack subjected to tension ($L=100\text{mm}$, $2W=50\text{mm}$) is visible in Figure 6.17c. Two different thickness values ($t=5\text{mm}$ and $t=10\text{mm}$) were considered in this analysis. The crack shape is almost straight in both situations, except in a small portion near the surface where a typical delay is observed (Branco, 2008). The delay increases with the thickness, as evidenced by d_3 which represents the difference between the surface coordinates of two crack fronts with the same length at the half-thickness of the specimens. Besides, the extent of the surface region in the depth direction (d_4 and d_5) is different and tends to be greater for higher values of thickness. The results clearly show that $d_5 > d_4$.

The effect of the crack closure phenomenon on the crack shape in a rectangular plate with through crack subjected to tension ($L=100\text{mm}$, $2W=50\text{mm}$, $t=5\text{mm}$) is displayed in Figure 6.17d. The case at the top has no crack closure while the other has crack closure at the surface and near-surface nodes, respectively $U_1=0.96$ and $U_2=0.98$. On the one hand, the crack curvature in both cases is substantially different; with crack closure, the tunnelling effect is greater, as demonstrates the value of d_6 . On the other hand, the extent of the delay in the depth direction is also different; it is more effective in the case of crack closure than without crack closure, as can be seen by comparing the values of d_7 and d_8 .

The FCG simulations were started intentionally from very small initial defects (see Tables 4.5-4.7). In this way, the transient part of the propagation represented a small portion of the simulation. This period of propagation is essentially affected by the initial crack shape, loading type, fatigue crack growth rates and specimen geometry (Courneau, 1998; Branco, 2008a). Branco *et al.* (2008a) compared the extent of this phase in standard C(T) and M(T) specimens (see Figure 2.46b) and observed that it is greater in the latter, which was explained by the lower da/dK gradients existing in this geometry (Schijve, 1998). Figure 6.18

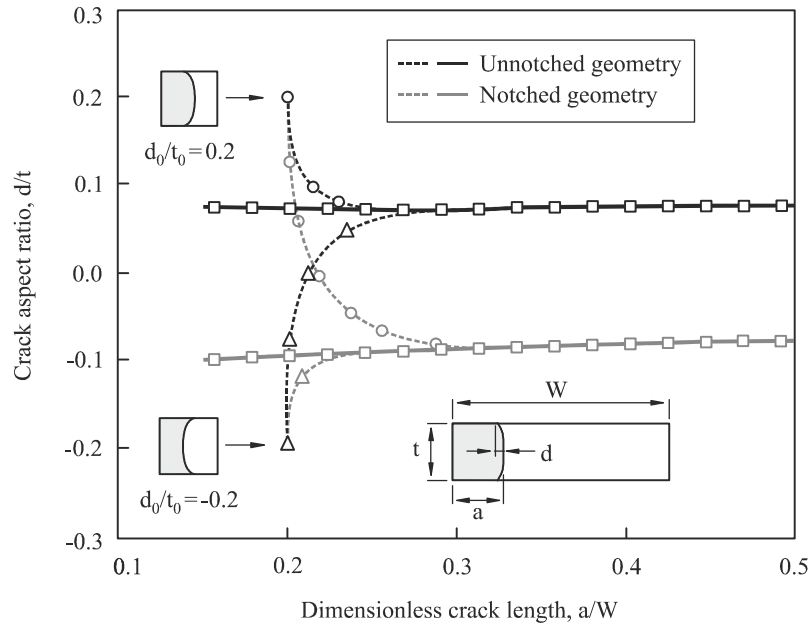


Figure 6.18. Evolution of the crack aspect ratio (d/t) with the dimensionless crack length (a/W) for notched ($L=200\text{mm}$, $2W=50\text{mm}$, $t=5\text{mm}$, $r=1.5\text{mm}$, $n=2\text{mm}$) and unnotched ($L=200\text{mm}$, $2W=50\text{mm}$, $t=5\text{mm}$) plates with through cracks subjected to tension (Branco, 2013).

plots the crack aspect ratio (d/t) versus the dimensionless crack length (a/W) for unnotched plates with through cracks ($L=200\text{mm}$, $2W=50\text{mm}$, $t=5\text{mm}$) subjected to tension. Different initial crack shapes with similar dimensionless crack length ($a_0/W=0.2$) were studied. The dashed black and grey lines correspond to the transient part of propagation. In this phase, a high sensitivity of the crack aspect ratio with regard to the initial crack configuration is observed, which results in a period of significant shape changes. The full black and grey lines represent, respectively, the stable propagations of the notched and unnotched plates. This preferred propagation paths are undoubtedly different in these two cases, but regardless of the situation, the initial crack configurations closer to the PPP reach it faster than the others. Besides, it is also unquestionable that the transient phase, in these cases, is a short period of the propagation.

Concerning with the values of stress intensity factor along the crack front, an identical behaviour was found. Figure 6.19 presents the evolution of the K_{\min}/K_{\max} ratio with the dimensionless crack length (a/W) in notched and unnotched plates with through cracks subjected to tension. The initial crack shapes of the notched and unnotched plates had crack aspect ratios equal to $d_0/t=0.2$ and $d_0/t=-0.2$, respectively. The dashed black and grey lines correspond to the transient parts of propagation. As can be distinguished, sudden changes in K_{\min}/K_{\max} ratios are visible in this phase which is clear evidence of strong shape changes. Nevertheless, the gradients of the K_{\min}/K_{\max} ratios decrease gradually as the crack tends to the stable part of propagation. These facts are in agreement with the evolution of the crack aspect ratios observed in the previous figure. The full black and grey lines represent the stable propagations of the notched and unnotched plates, respectively. The K_{\min}/K_{\max} ratios, in these cases, are almost overlapped and are relatively close to unity (≈ 0.98). Besides, it is also evident that the convergence of the K_{\min}/K_{\max}

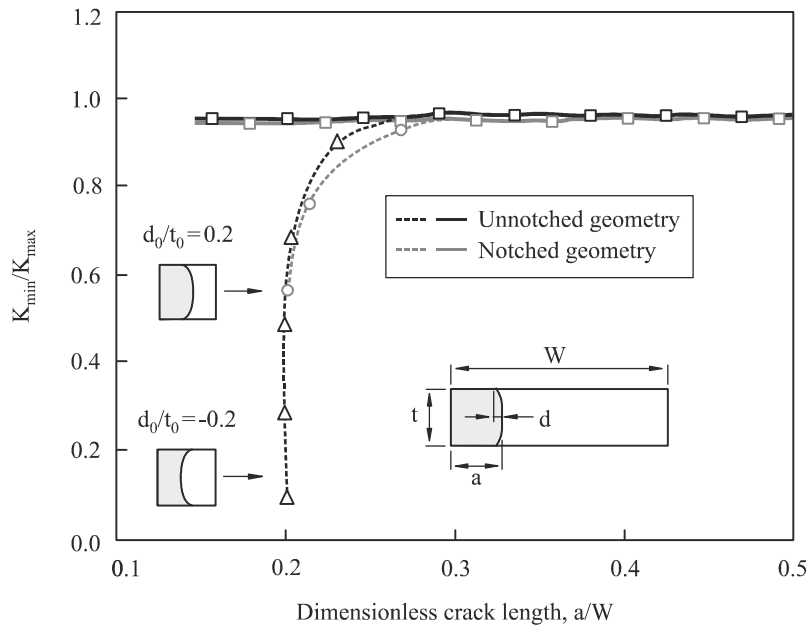


Figure 6.19. Evolution of the K_{\min}/K_{\max} ratio with the dimensionless crack length in notched ($L=200\text{mm}$, $2W=50\text{mm}$, $t=5\text{mm}$, $r=1.5\text{mm}$, $n=2\text{mm}$) and unnotched ($L=200\text{mm}$, $2W=50\text{mm}$, $t=5\text{mm}$) plates with through cracks subjected to tension (Branco, 2013).

ratios towards the stable values is fast and occupies a very limited period of propagation.

The analysis of these two figures makes clear that the transient part of propagation in M(T) specimens is relatively small; and that the crack front profiles are very similar in the stable phase. Based on these two premises, the 3D-FE refined models developed to calculate the stress triaxiality were computed from stable crack shapes. The crack front profiles selected had values of dimensionless crack length equal to $a/W=0.5$. In this region, the crack is perfectly stabilised which means that no transient crack shapes are used. Therefore, unless stated otherwise, the analysis of stress triaxiality along the crack front was performed using stable crack shapes with dimensionless crack length $a/W=0.5$. Figure 6.20a identifies the stable crack shapes selected in the course of the present investigation for the different cases studied.

The same concept was adopted with regard to the other geometries of this study, namely unnotched and notched rectangular plates with corner cracks (Figure 4.11a-b); and unnotched and notched round bars with corner cracks (Figure 4.11c-d). Figures 6.20b-c present the way used to select the representative crack shapes in these cases. Nevertheless, the propagation in these cases is relatively different. In truth, the propagation still tends to preferred propagation paths but the crack aspect ratio and the K_{\min}/K_{\max} ratio are not constant as the crack grows. This is evident, for example, in Figures 6.16a and 6.16b in which are represented, respectively, the evolutions of the crack aspect ratio and the K_{\min}/K_{\max} ratio with the dimensionless crack length for different initial crack shapes in round bars with surface cracks subjected to tension. Among other reasons, this behaviour can be explained by the nature of the free boundaries of the

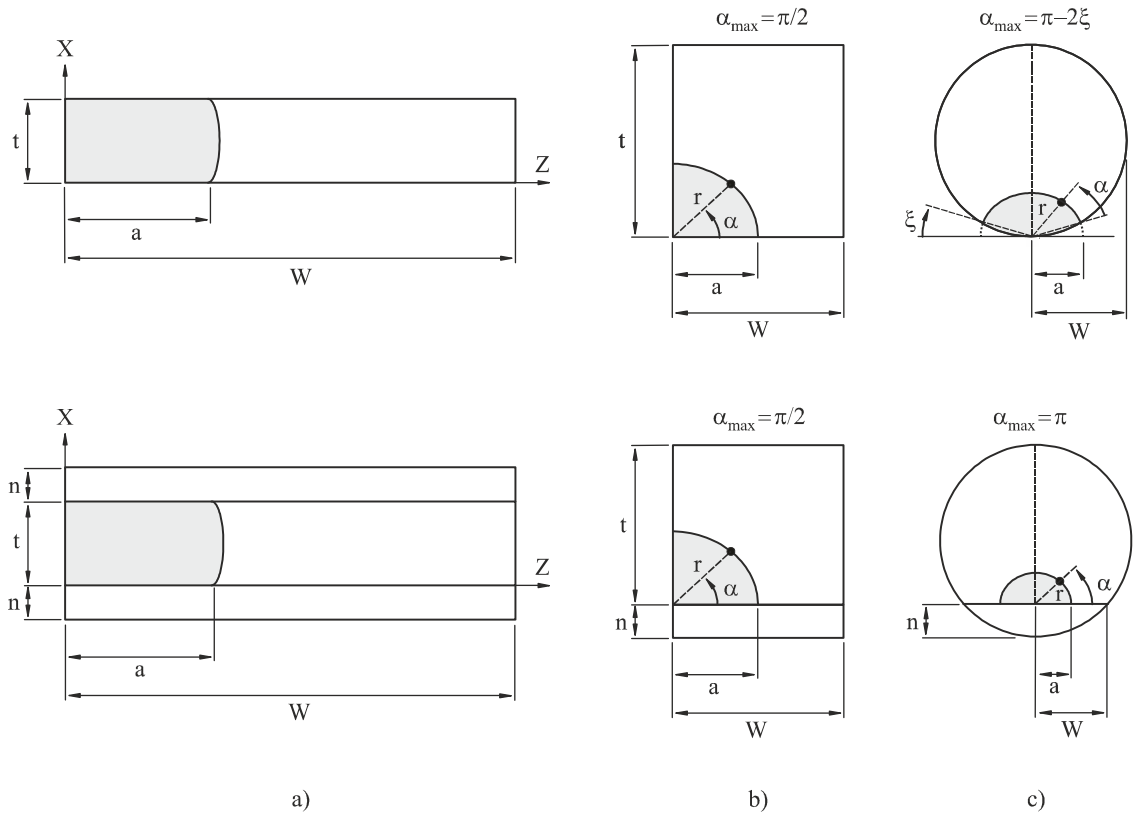


Figure 6.20. Crack front profiles selected to compute the h stress triaxiality parameter at the crack front in: a) unnotched and notched plates with through cracks; b) unnotched and notched rectangular bars with corner cracks; c) unnotched and notched round bars with surface cracks.

geometry which forces the crack perimeter to change continuously during the propagation. In the other three cases (unnotched rectangular bars with corner cracks, notched rectangular bars with corner cracks and notched round bars with surface cracks), the propagation behaves identically, i.e. the crack aspect ratios and the K_{\min}/K_{\max} ratios are not constant in the stable part of propagation. Therefore, the extent of the surface region evaluated for $a/W = 0.5$ is not valid for other ranges. In order to address this incongruence, correcting functions that take into account the effect of the crack length on the extent of the surface region were further developed (see Equation 6.8).

6.2.2. Stress triaxiality at the crack front

As referred to in Section 4.4, the stress triaxiality at the crack front was calculated using the ratio of the average hydrostatic stress to the equivalent von Mises stress (Θ) and the ratio of the out-of-plane stress to the in-plane stress components multiplied by the Poisson's ratio (h). Due to high stress gradients existing near the surface, the definition of an appropriate mesh refinement in the thickness direction was a very important aspect. The mesh must be sufficiently sensitive to detect the faster transition from plane stress state near the free boundary to plane strain state at interior positions. Figure 6.21 plots the values of the h stress triaxiality parameter against the dimensionless position (x/t) in a notched plate with through crack obtained using a numerical model with uniform layers (black line) and a numerical model with a ultrafine mesh near the surface (grey symbols). The two models have equal number of layers (49) and therefore

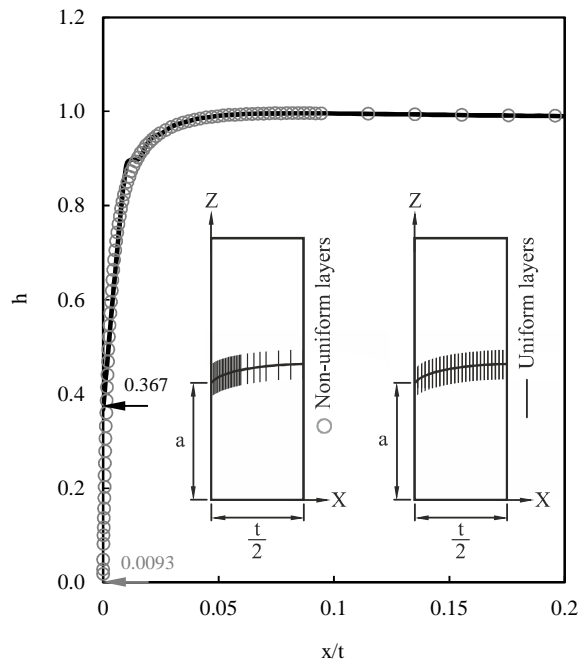


Figure 6.21. Evolution of the h stress triaxiality parameter with the dimensionless position (x/t) in a notched plate with through crack considering two mesh densities towards the thickness ($r=0.5\text{mm}$, $n=1.0\text{mm}$, $t=10\text{mm}$).

require the same computational effort. At the surface ($x/t=0$), the values of h are substantially different. The non-uniform layer model gives a value of h near to zero ($h=0.0093$), indicating that the plane stress state was achieved, as would be expected. On the contrary, in the other model, the relatively high value of h ($h=0.367$) at the surface does not suggest the existence of plane stress state, which is contradictory. This error is naturally due to the coarse mesh, not sufficiently refined to detect high stress gradients near the surface. The sudden variation in the h values, particularly in the range 0.8-0.95, is other evidence that the uniform layer model is unable to represent the real stress triaxiality state. Nevertheless, with respect to interior positions ($x/t>0.03$), the differences are imperceptible, which indicates that the high refinement here is not necessary. This fact can be explained by the lower stress gradients that occur in that zone. The final mesh density, used in the following calculations, combines these two main aspects, i.e. it is ultra-refined near the surface and relatively coarse at interior positions. The smallest element size of the ultra-refined mesh, as described in Section 4.4, is equal to $1\mu\text{m}$. The sizes of the other elements are defined from the relationship $1 \times 1.1^{(i-1)} \mu\text{m}$ where i is the layer number.

Another important decision was made regarding the stress triaxiality parameters. The h stress triaxiality parameter, unlike the Θ stress triaxiality parameter, has fixed lower and upper limits. This is a strong advantage since it simplifies the comparison of results obtained in different situations. Figure 6.22 exhibits the evolution of the Θ and h stress triaxiality parameters along the dimensionless position (x/t) in a notched plate with through crack for two different values of the Poisson's ratio ($\nu=0.29$ and $\nu=0.30$)

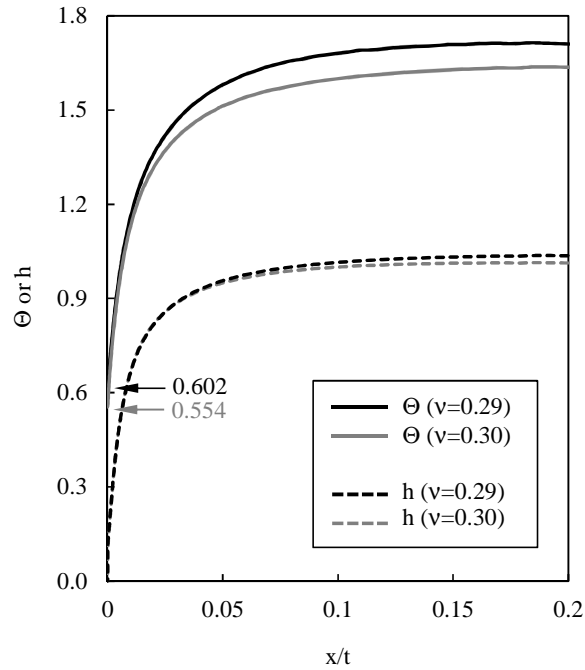


Figure 6.22. Evolution of Θ and h stress triaxiality parameters with the dimensionless position (x/t) in a notched plate with through crack ($r=0.5\text{mm}$, $n=1.0\text{mm}$, $t=5\text{mm}$) for two different values of ν .

using the non-uniform layer model. As can be seen, both h -curves (dashed lines) start from zero (nearly zero) and tend to unity. However, the Θ -curves (full lines) have different initial values (0.602 and 0.554) and converge to asymptotic values relatively different (1.707 and 1.637). This demonstrates that the comparison of results in the latter case is more complex since the upper and lower limits are not known. Besides, the range of variation changes from case to case which introduces too much unpredictability. In the former case, the situation is quite different because the upper ($h=1$) and lower ($h=0$) limits as well as the range of variation are well-defined. Besides, the upper and lower limits represent extreme states, i.e. plane strain state ($h=1$) and plane stress state ($h=0$). Based on these facts, the h stress triaxiality parameter was selected to carry out the following analysis.

6.2.3. Effects of the variables affecting crack shape on stress triaxiality

A close relationship between crack shape and stress triaxiality at the crack front was observed. Therefore, the variables affecting the crack shape, such as specimen geometry, material properties, fatigue crack growth rates, loading paths, etc., are important in terms of stress triaxiality. The understanding of these effects on the stress triaxiality is crucial to accurately examine the extent of the surface region.

Figure 6.23 presents the effect of the previous variables on the h stress triaxiality curves. In the following figure, the h -curves are plotted against the dimensionless parameters x/t or α/α_{\max} (these variables are depicted in Figure 6.20). The former is used in the cases of geometries with through cracks and the other is used in the remaining cases. An overview of Figure 6.23 shows that the h -curves start from zero near the free boundary (plane stress state) and tend to unity in the depth direction (plane strain state).

Nevertheless, the transition between these two extreme states varies considerably from case to case, in particular, the slope of the h-curves near the surface. The effect of the specimen geometry on the h-curves is exhibited in Figure 6.23a (cases 09, 01 and 07 of Tables 4.5, 4.6 and 4.7, respectively). Three different geometries with the same notch configurations ($r=0.5\text{mm}$, $n=2.0\text{mm}$) are analysed (more specifically, a

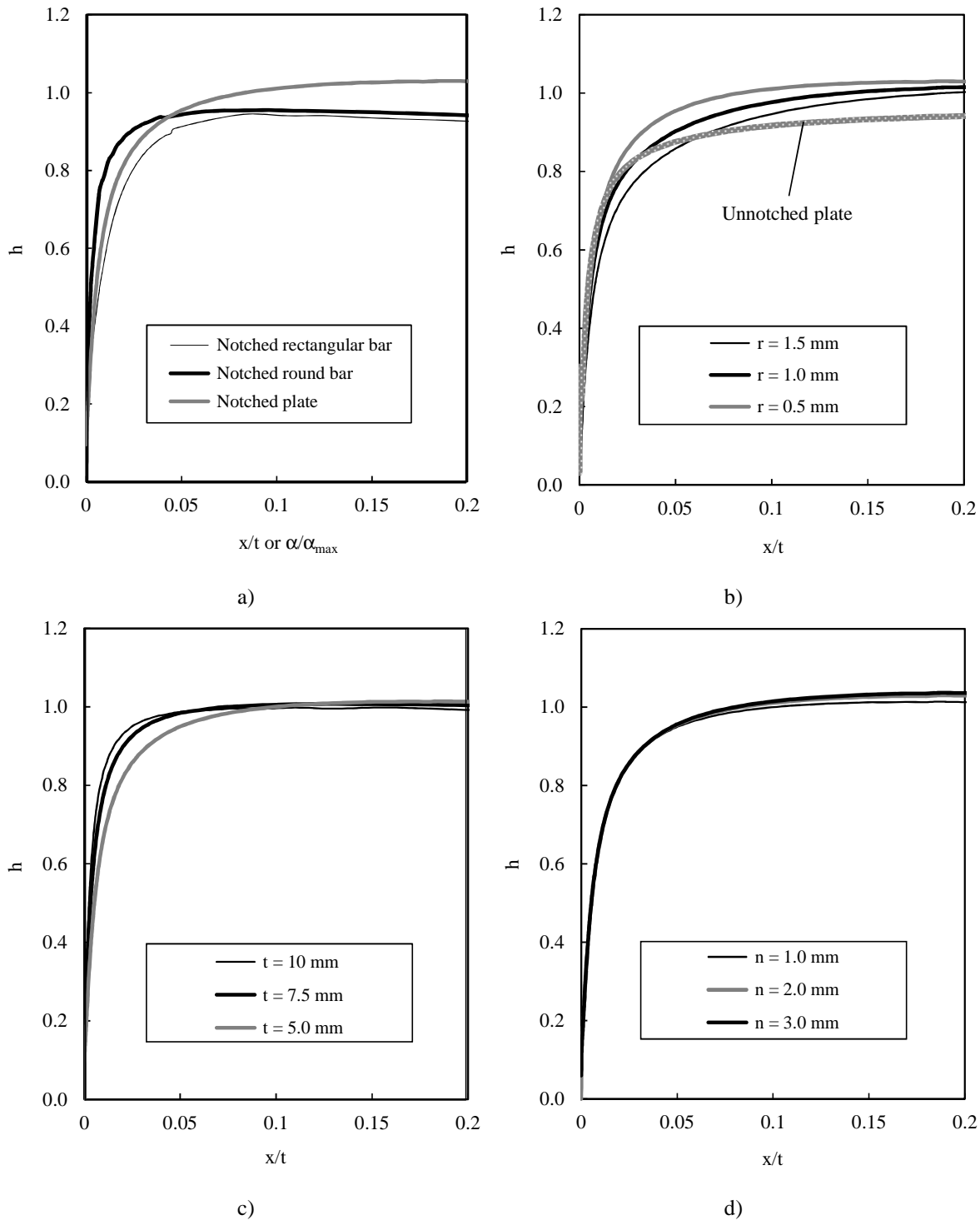


Figure 6.23. Effect of: a) specimen geometry; b) notch radius; c) specimen size; d) notch depth and crack length on the stress triaxiality (Branco, 2012a).

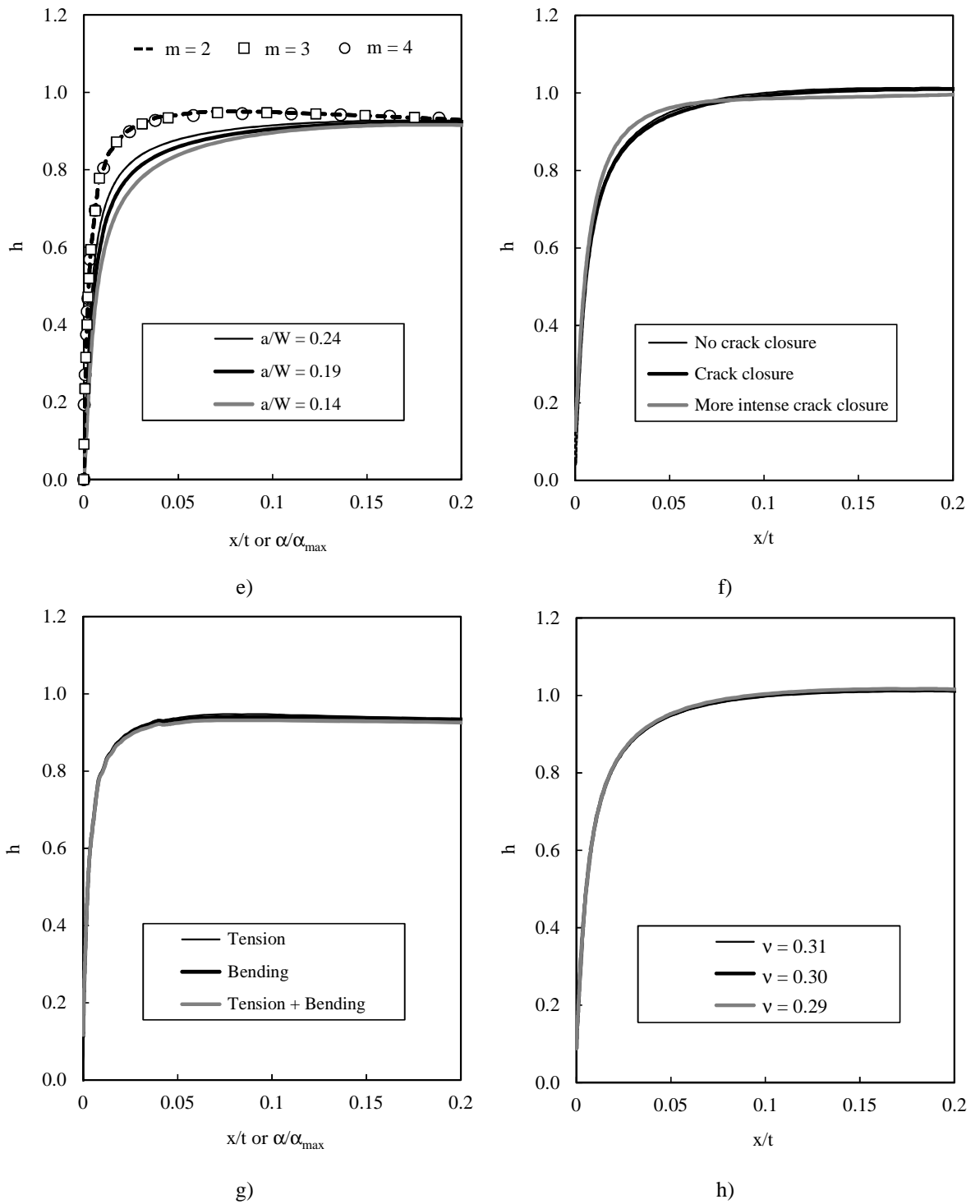


Figure 6.23 (continued). Effect of: e) crack length and exponent of the Paris law; f) crack closure; g) loading; h) Poisson's ratio on the stress triaxiality (Branco, 2012a).

notched rectangular bar with corner crack, a notched round bar with surface crack and a notched plate with through crack). As can be seen, the h -curve of the notched plate tends to higher values of stress triaxiality in the depth direction than the others. On the other hand, the slopes near the surface are clearly different in the three cases. Therefore, the results evidence that each h -curve is an intrinsic characteristic of the geometry.

The effect of the notch radius (r) on the h-curves is shown in Figure 6.23b. Three different notch radii (cases 01-03 of Table 4.7) are analysed in a notched plate with through crack. The notch radius exerts a strong influence on the h-curves that acts throughout the crack front. The h-curves computed for greater radii lay always below the others. This trend is explained by different stress concentration factors near the notch root caused by different notch radii. The increase in the stress concentration factor results in higher slopes of the h-curves near the surface. Besides, as already observed in Figure 6.17a, smaller notch radii cause a faster crack growth along the free boundary which is responsible for different stable crack shapes. Accordingly, the resultant stress triaxiality values are also different. The effect of the stress concentration on the h-curves is even more evident by comparing the results of stress triaxiality of unnotched (case 61 of Table 4.7) and notched plates. It makes clear that the h values are significantly smaller in the former case, particularly in the depth direction. Therefore, there is a strong relation between stress concentration and stress triaxiality.

The effect of the specimen size on the stress triaxiality is exhibited in Figure 6.23c. Three different values of thickness (t) are analysed (cases 04-06 of Table 4.6) in a notched plate with through crack. The crack configuration remained unaltered. The main differences occur near the free surface where high slopes of the h-curves are observed for the larger thicknesses. In the depth direction, the curves are nearly overlapped and therefore the differences are not remarkable.

The effect of the notch depth (n) on the h-curves is displayed in Figure 6.23d. Three different values of notch depth (cases 01, 04 and 13 of Table 4.7) are examined in a notched plate with through crack. Although not obvious at the first sight, the stress triaxiality rises along the whole crack front. The increase in the h values is more evident in the depth direction than that in the region surrounding the free surface. Besides, it is important to refer that the gain in the h-curves due to the notch depth is very slightly and tends to zero as the notch depth increases.

The effect of the crack length on the h-curves is presented in Figure 6.23e. Particularly in this case, the h-curves computed have different dimensionless crack lengths ($a/W=0.14$, $a/W=0.19$ and $a/W=0.24$) and resulted from a single propagation (case 02 of Table 4.6) in a notched round bar subjected to tension. As observed, the stress triaxiality near the surface decreases with the crack length but tends to be similar in the depth direction. This situation occurs in the notched and unnotched geometries with corner and surfaces cracks. In these cases, the crack front perimeter increases continuously during the propagation which explains the different h-curves obtained. In the notched and unnotched geometries with through cracks, the crack propagation is quite different. As noted in Figures 6.18 and 6.19, the crack front maintains similar profiles after a short initial period of propagation, which leads to h-curves practically independent of the crack length.

The effect of the exponent of the Paris law (m) on the h-curves is plotted in Figure 6.23e. Three different values of m are studied (cases 01, 11 and 12 of Table 4.6) in a notched round bar subjected to tension. As

can be seen, the curves have similar trends without relevant differences. However, a careful analysis of the data shows that the higher is the m value, the higher is the stress triaxiality.

The effect of the crack closure on the h-curves is shown in Figure 6.23f. This study comprised no crack closure (case 04 of Table 4.7), crack closure (case 58 of Table 4.7) and more intense crack closure (case 59 of Table 4.7). The geometry selected was a notched plate with through crack. The two first situations have almost similar crack shapes (as shown in Figure 6.17d) and therefore the stress triaxiality is equivalent. Nevertheless, the increase in the crack closure level produces higher crack shape changes which have repercussions on the h-curves.

The effect of the loading on the h-curves is depicted in Figure 6.23g. Three different loading situations corresponding to tension, bending and both simultaneously (cases 01, 04, 05 of Table 4.7) were studied in a notched round bar with surface crack. As can be seen, the h-curves are slightly different. The effect of the loading acts throughout the crack front. These facts are in agreement with the conclusions mentioned in relation to Figure 6.17b, i.e. different loading types produce different crack shape developments.

The effect of the Poisson's ratio (ν) on the h-curves can be seen in Figure 6.23h. Three different values of ν (cases 04, 11, 12 of Table 4.8) are analysed in a notched plate with through crack. In the range analysed, the differences are not clear but it is possible to conclude that the higher is the Poisson's ratio, the lower is the h-curve. This influence on the crack shape, as well as on the h-curves, can be explained by the corner singularity near the free surface of the round bar, which is a function of the Poisson's ratio. With regard to the Young's modulus, its effect on the h-curves is not relevant (Branco, 2013).

6.2.4. Evaluation of the extent of the surface region

The analysis of Figure 6.23 makes clear that a generic h-curve can be divided into three main regions (see Figure 6.24): a surface region, relatively small, characterised by high stress gradients; a near-surface

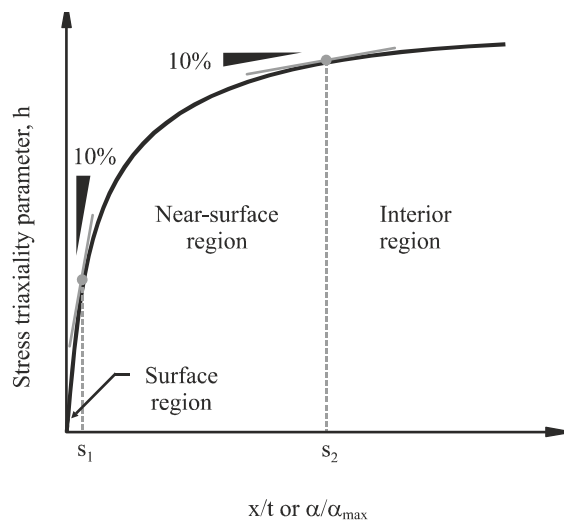


Figure 6.24. Definitions of surface, near-surface and interior regions (Branco, 2012a).

region, in which the stress gradients decrease progressively to asymptotic values near unity; and an interior region without significant stress gradients with a dominant extent relatively to the others.

A global criterion based on the slope of the h-curves was proposed to objectively quantify the extent of the above-mentioned regions. Briefly, as depicted in Figure 6.24, the transition between the surface and near-surface regions occurs when the slope of the h-curve is less than 90% and is represented by the dimensionless variable S_1 ; the transition between the near-surface and interior regions takes place when the slope of the h-curve is less than 10% and is represented by the dimensionless variable S_2 .

In order to apply the proposed criterion, each h-curve was fitted to a fifth order logarithm function

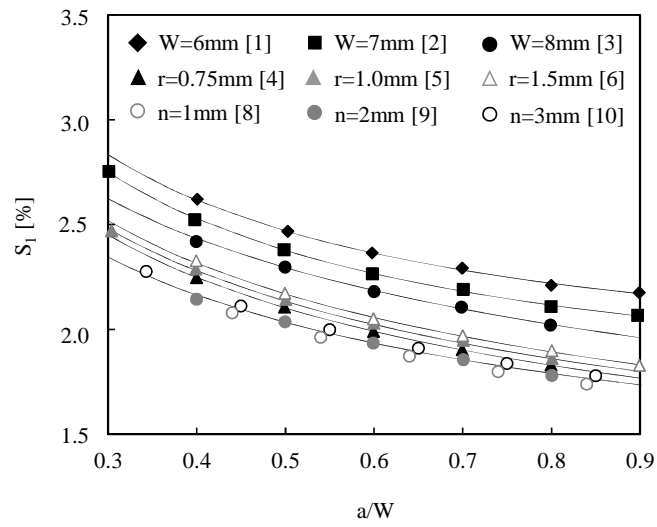
$$h(\chi) = a_0 + a_1 \ln(\chi) + a_2 \ln(\chi)^2 + a_3 \ln(\chi)^3 + a_4 \ln(\chi)^4 + a_5 \ln(\chi)^5 \quad (6.4)$$

being a_0 - a_5 fitting constants and χ the dimensionless variable x/t or α/α_{\max} . This type of function was adequate and led to correlation coefficients extremely high ($r > 0.999$). In a second stage, the derivatives of these functions were computed. Then, the values of S_1 and S_2 were calculated numerically using a specific subroutine written in VBA programming language. In order to define upper bounds for the surface and near-surface regions, the variables affecting the h stress triaxiality were examined.

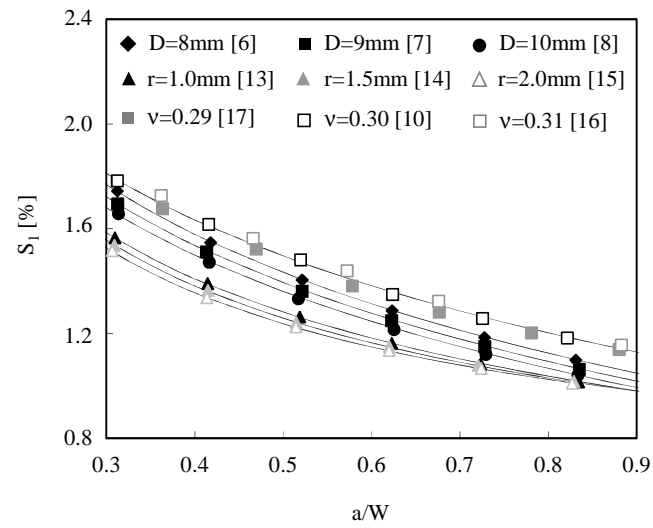
The main conclusions with respect to S_1 are reported in Figures 6.25a-c. These three figures plot the extent of the surface region (S_1) against the dimensionless crack length (a/W) in notched rectangular bars with corner cracks, notched round bars with surface cracks and notched plates with through cracks, respectively. The variables studied were the specimen size, notch radius, notch depth, crack length, Poisson's ratio and exponent of the Paris law. The numbers in brackets refer the FCG simulations performed which are listed in Tables 4.5-4.7, respectively.

The results of Figures 6.25a-b show that the extent of the surface region is a decreasing function of the dimensionless crack length. Regarding the notched plates with through cracks (Figure 6.25c), S_1 is independent of a/W . These two types of behaviour are expected and are in agreement with the conclusions stated in the previous subsection. In notched plates with through cracks, the crack front profiles stabilise after a short initial propagation period leading to identical h-curves and identical S_1 values. However, the fatigue crack growth process in the other cases is substantially different. The crack aspect ratio progressively changes during the propagation which has repercussions on the h-curves and on the extent of the surface region.

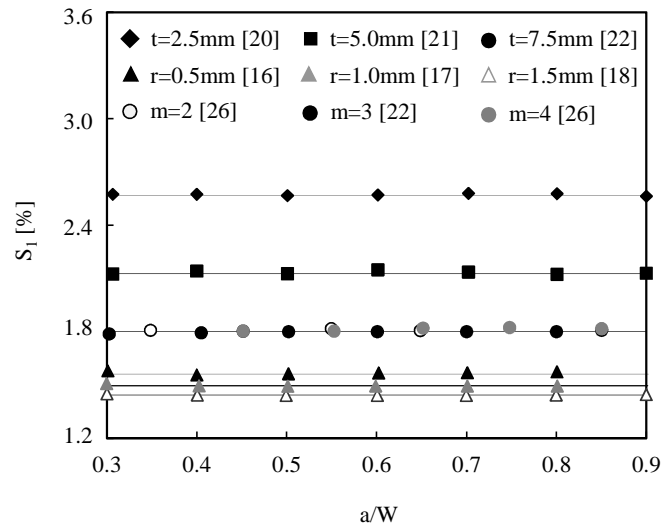
The effect of the specimen size on the extent of the surface region can be analysed by comparing the series of filled black diamonds, squares and circles (Figures 6.25a-c). The variables analysed were the width (W), diameter (D) and thickness (t) for notched rectangular bars with corner cracks, notched round bars with surface cracks and notched plates with through cracks, respectively. The results obtained show



a)



b)



c)

Figure 6.25. Evolution of S_1 with a/W : a) notched rectangular bars with corner cracks; b) notched round bars with surface cracks; c) notched plates with through cracks (Branco, 2012a).

that the increase in the specimen size decreases the extent of the surface region. A thicker specimen has a greater percentage of the crack front predominantly under plane strain state and therefore the relative size of the surface region is necessarily lower.

The effect of the notch radius on S_1 can be seen by comparing the series of filled black, grey and white triangles (Figures 6.25a-c). Regardless of the geometry, the decrease of the notch radius results in higher S_1 values. Smaller notch radii increase the stress concentration factors which originate more pronounced slopes of the h-curves near the free surface (see Figure 6.23b). As a consequence, the high stress gradients exist in a larger region.

The effect of the notch depth on the extent of the surface region is presented in Figure 6.25a. Three different values of n ($n=0.75\text{mm}$, $n=1\text{mm}$, $n=2\text{mm}$) were examined for a notched rectangular bar with corner crack. The results show that the higher is the notch depth, the higher is S_1 . However, the differences of the curves are not significant. This fact is due to the small influence of the notch depth on the h-curves, as already observed in Figure 6.23d.

The effect of the Poisson's ratio on S_1 is displayed in Figure 6.25b. Three different values of ν ($\nu=0.29$, $\nu=0.30$, $\nu=0.31$) were studied for a notched round bar with surface crack. The decrease in ν leads to smaller S_1 values. Besides, it is important to note that the Poisson's ratio has a significant influence on the extent of the surface region. Even in this small range, the final values of S_1 are clearly different.

The effect of the Paris law exponent on the extent of the surface region can be seen in Figure 6.25c. Three different values of m ($m=2$, $m=3$, $m=4$) were studied for a notched plate with through crack. Based on the results achieved, it is evident that the Paris law exponent has a limited influence on the S_1 values. This is in line with the conclusions stated in Figure 6.23e. As already said, the h-curves are not remarkably affected by this variable.

Apart from the previous analysis based on stable crack shapes, the values of S_1 for unstable crack shapes were also calculated. Figure 6.26 presents the evolution of the extent of the surface region with the dimensionless crack length considering both unstable crack shapes ($a/W < 0.2$) and stable crack shapes ($a/W > 0.2$). This analysis was conducted in notched rectangular bars with corner cracks, notched round bars with surface cracks, and notched plates with through cracks. The full lines were plotted only based on stable crack shapes. The symbols (squares, triangles and circles) refer to the entire propagation.

As can be seen, in the first part of the propagation, due to the significant crack shape changes already reported, the extent of the surface region does not fit the trends and is clearly unstable. Nevertheless, as the crack grows, this instability diminishes progressively and the values of S_1 fit the trends. However, it is possible to conclude that the values of S_1 in both the unstable and stable periods have approximately the same order of magnitude.

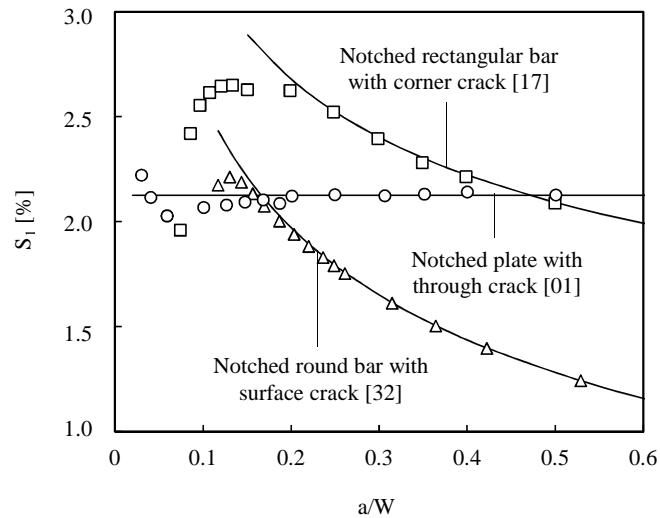


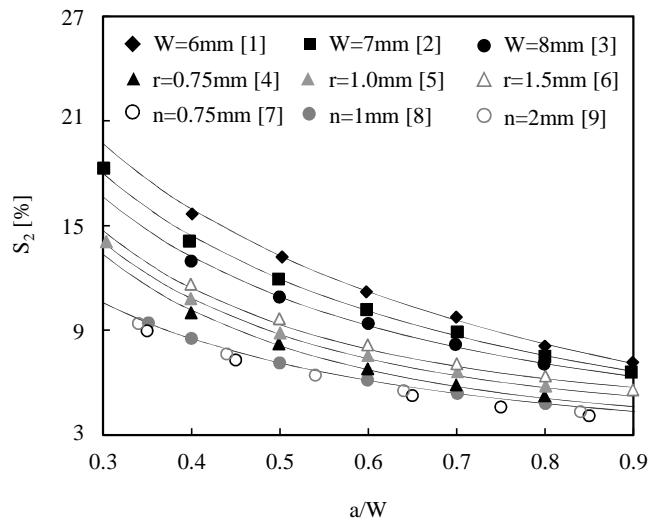
Figure 6.26. Evolution of S_1 with a/W for unstable crack shapes (Branco, 2012a).

The analysis of S_2 was performed in a similar manner. Figures 6.27a-c exhibit the evolution of the extent of the near-surface region with the dimensionless crack length in notched rectangular bars with corner cracks, notched round bars with surface cracks and notched plates with through cracks, respectively. The variables examined were the specimen size, notch radius, notch depth, crack length, Poisson's ratio and exponent of the Paris law. The numbers in brackets refer to the FCG simulations performed which are listed in Tables 4.5-4.7, respectively.

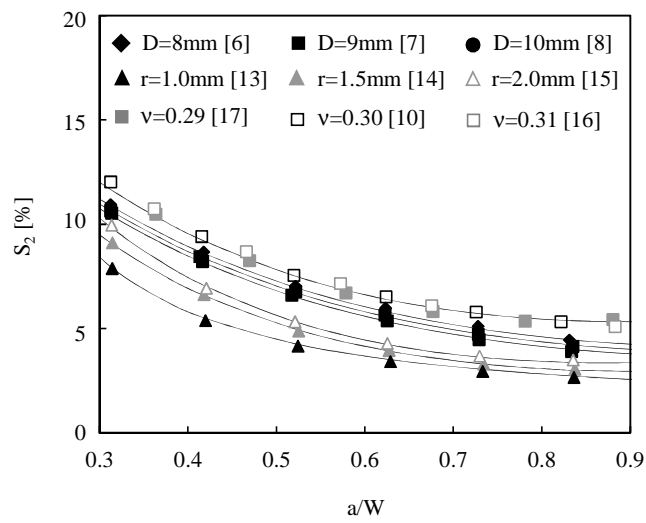
According to the results of Figures 6.27a-b, the extent of the near-surface region is a decreasing function of the dimensionless crack length. However, in the case of Figure 6.27c, S_2 is independent of a/W . As already said, the differences are due to different fatigue crack growth processes. In the latter case, the crack tends to stabilise after a short initial period of propagation which leads to identical crack front profiles, h-curves and S_2 values. In the former cases, the progressive change in the crack aspect ratio causes different crack front profiles, h-curves and S_2 values.

The effect of the specimen size on S_2 can be analysed by comparing the series of filled black diamonds, squares and circles (Figures 6.27a-c). The variables analysed were the width (W), diameter (D) and thickness (t) for notched rectangular bars with corner cracks, notched round bars with surface cracks and notched plates with through cracks, respectively. As can be seen, the higher is the size of the specimen, the lower is the extent of the near-surface region. Due to the increase in the specimen size, the portion of the crack front predominantly under plane strain state tends to increase. In this sense, the extent of the near-surface region is successively lower.

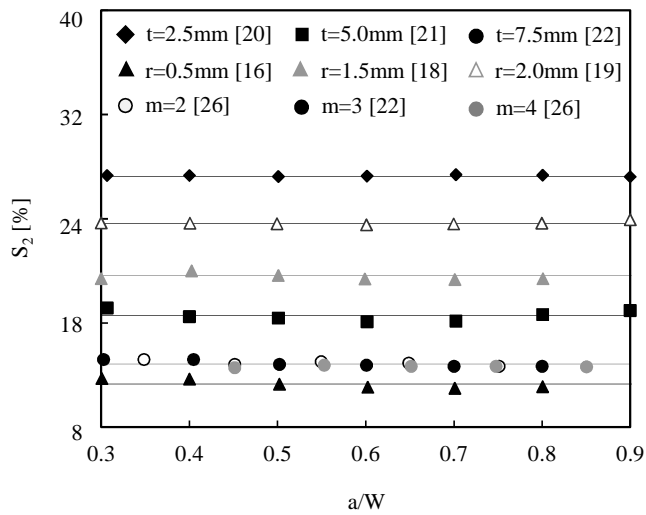
The effect of the notch radius on the extent of the near-surface region can be inferred by comparing the series of filled black, grey and white triangles (Figures 6.27a-c). The decrease in the notch radius results in smaller values of S_2 . Lower notch radii cause higher stress concentration factors and higher slopes in



a)



b)



c)

Figure 6.27. Evolution of S_2 with a/W : a) notched rectangular bars with corner cracks; b) notched round bars with surface cracks; c) notched plates with through cracks (Branco, 2012a).

the h-curves (see Figure 6.23b). As a consequence, the curves of higher slopes tend to become horizontal more rapidly which reduces the extent of the near-surface region.

The effect of the notch depth on S_2 is presented in Figure 6.27a. Three different values of n ($n = 1\text{mm}$, $n = 2\text{mm}$, $n = 3\text{mm}$) were examined for a notched rectangular bar with corner crack. The higher is the notch depth, the higher is the extent of the near-surface region. The increase in b produces slightly higher stress triaxiality values and slightly higher slopes of the h-curves at interior regions. In this way, the lower slopes of the h-curves are achieved more slowly, which means that S_2 tends to increase.

The effect of the Poisson's ratio on the extent of the near-surface region is exhibited in Figure 6.27b. Three different values of ν ($\nu = 0.29$, $\nu = 0.30$, $\nu = 0.31$) were studied for a notched round bar with surface crack. The differences are not significant in this range but it is perceptible that the increase in ν rises S_2 .

The effect of the Paris law exponent on S_2 can be seen in Figure 6.27c. Three different values of m ($m = 2$, $m = 3$, $m = 4$) were studied for a notched plate with through crack. Due to the low influence of this variable on the h-curves, the extent of the near-surface region is not particularly affected by the m values. As can be distinguished, the results of the three situations are practically overlapped.

The calculation of S_2 for unstable crack shapes was also carried out. Figure 6.28 plots the extent of the near-surface region against the dimensionless crack length for unstable ($a/W < 0.2$) and stable crack shapes ($a/W > 0.2$). The analysis comprised notched rectangular bars with corner cracks, notched round bars with surface cracks and notched plates with through cracks. The full lines were plotted from stable crack shapes. The symbols (squares, triangles and circles) refer to the entire propagation.

In the first part of the propagation, the values of S_2 oscillate considerably, which is a reflex of the intense

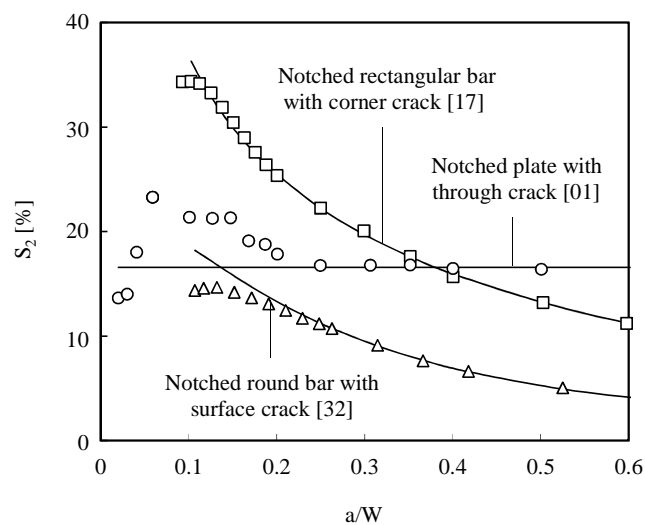


Figure 6.28. Evolution of S_2 with a/W for unstable crack shapes (Branco, 2012a).

crack shape changes that occur in this period. As a result of that, the resultant S_2 values do not fit the trends of the stable propagation. However, as the crack grows, the fluctuations disappear and S_2 follows the trends. Furthermore, it is important to note that the S_2 values have the same order of magnitude, either in the unstable period or in the stable period.

In a second stage, S_1 and S_2 were computed for a wide range of situations. The detailed information about the fatigue crack growth simulations performed in this research is given in Table 4.5 (cases 18-45) for notched rectangular bars with corner cracks; in Table 4.6 (cases 18-45) for notched round bars with surface cracks; and in Table 4.7 (cases 30-57) for notched plates with through cracks. This exhaustive analysis focused on the notch radius and specimen size. The other variables remained unchanged due to their smaller influence on the extents of the surface and near-surface regions. These calculations, as already stated in Chapter 4, were carried out from stable crack shapes.

Figures 6.29a-c exhibit the evolution of S_1 and S_2 with the specimen size and notch radius for notched rectangular bars with corner cracks, notched round bars with surface cracks and notched plates with through cracks, respectively. As can be seen, the S_1 values (grey symbols) tend to decrease with the notch radius whilst the S_2 values (black symbols) tend to increase. On the other hand, it is clear that both variables tend to asymptotic values. As referred to above, this behaviour is explained by the stress concentration factors resultant from each notch radius. Lower stress concentration factors are the reflex of higher notch radii and result in less intense stress triaxialities near the free boundary (i.e. smaller S_1 values) and in greater S_2 values since the transition to a predominant plane strain state is slower.

In relation to the specimen size, its effect on S_1 and S_2 is similar. Both variables tend to decrease with this variable. This fact is in line with the conclusions postulated before. The perimeter of the crack increases which reduces the relative size of the surface and near-surface regions. A six parameter Taylor series polynomial (Equation 6.5) was used to fit both the S_1 and S_2 curves. Table 6.2 presents the x_i constants found here. Besides, correlation coefficients relatively high ($r > 0.997$) were achieved. As can be seen, the

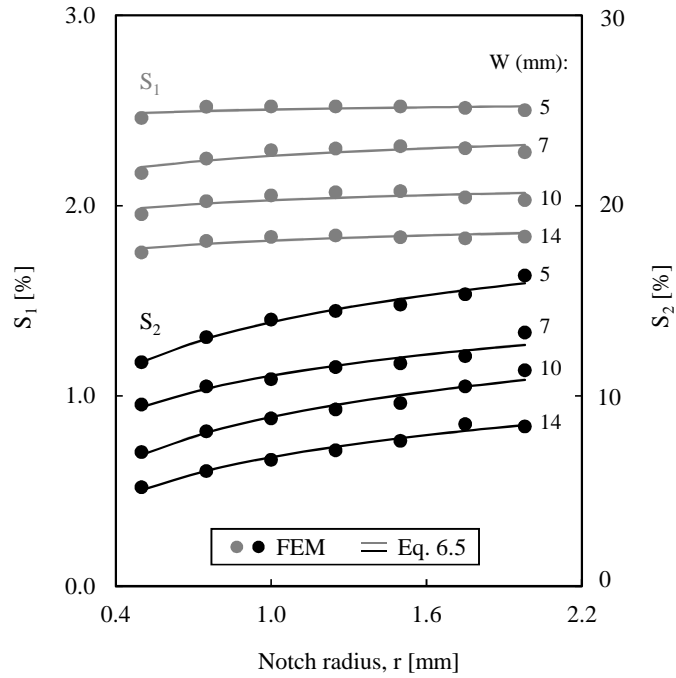
$$S_i(t, r) = x_1 + x_2 \ln(t) + x_3 \ln(r) + x_4 \ln(t)^2 + x_5 \ln(r)^2 + x_6 \ln(t) \ln(r) \quad (6.5)$$

Table 6.2. Constants of Equation 6.5 (Branco, 2012a).

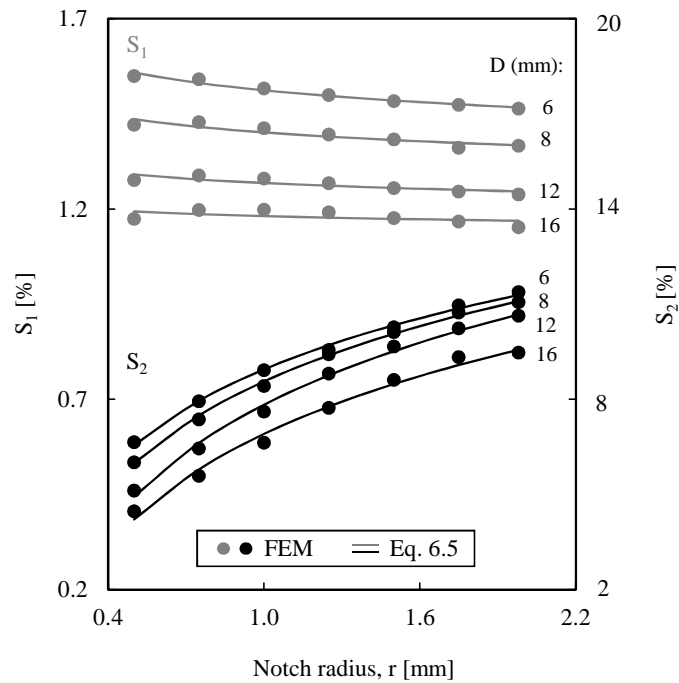
	x_1	x_2	x_3	x_4	x_5	x_6
Notched rectangular bar with corner crack						
S_1	3.7980×10^{-2}	-8.8866×10^{-3}	1.3042×10^{-4}	5.2009×10^{-4}	-4.5836×10^{-10}	2.0394×10^{-4}
S_2	3.1470×10^{-1}	-1.3489×10^{-1}	3.3428×10^{-2}	1.5725×10^{-2}	-2.6812×10^{-10}	-3.1079×10^{-3}
Notched round bar with surface crack						
S_1	2.4045×10^{-2}	-6.0341×10^{-3}	-1.5246×10^{-3}	5.8593×10^{-4}	6.0026×10^{-10}	4.8631×10^{-4}
S_2	4.9496×10^{-2}	4.9488×10^{-2}	2.5333×10^{-2}	-1.5304×10^{-2}	1.9302×10^{-10}	5.5585×10^{-3}
Notched plate with through crack						
S_1	2.6859×10^{-2}	-3.2684×10^{-3}	-4.8632×10^{-3}	-7.5458×10^{-4}	-5.2562×10^{-11}	1.5800×10^{-3}
S_2	5.2652×10^{-1}	-2.2482×10^{-1}	8.1154×10^{-2}	3.0394×10^{-2}	1.6026×10^{-10}	9.7227×10^{-3}

black and grey lines, plotted using the proposed equation, are very close to the FEM results.

The analysis of the results shows that S_1 is typically less than 3% of x/t or α/α_{\max} ; and S_2 varies from 3% to 30% of x/t or α/α_{\max} . Besides, it is also evident that S_1 is an order of magnitude lower than S_2 . Taking

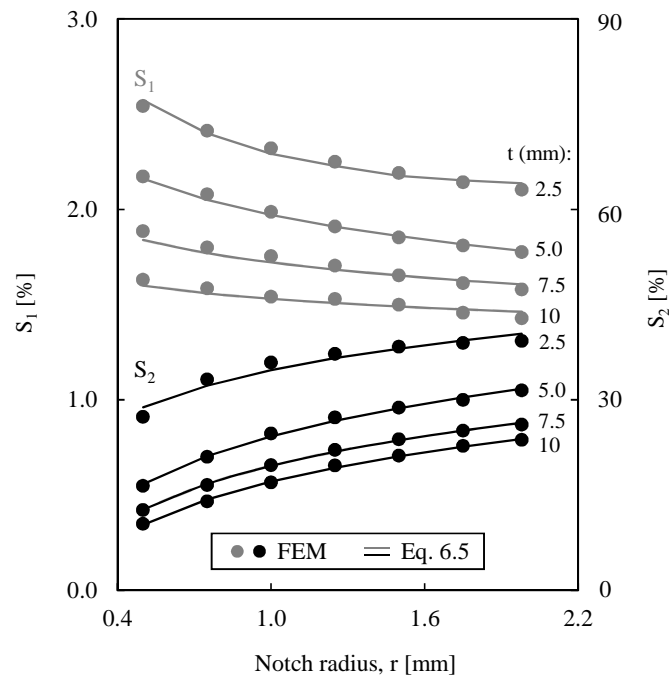


a)



b)

Figure 6.29. Evolution of S_1 and S_2 : a) notched rectangular bars with corner cracks; b) notched round bars with surface cracks (Branco, 2012a).



c)

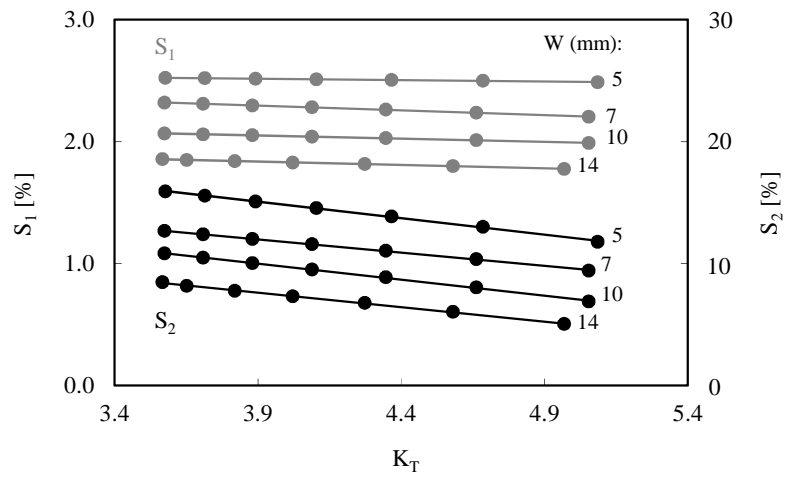
Figure 6.29 (continued). Evolution of S_1 and S_2 : c) notched plates with through cracks (Branco, 2012a).

into account that the three situations studied are substantially different, either in terms of type of geometries or in terms of crack families, the results achieved are expected to be generic and valid for a broad range of cases. Nevertheless, for smaller sizes of the specimens, it is important to note that S_1 and S_2 tend to increase and therefore the bounds proposed must be used with caution.

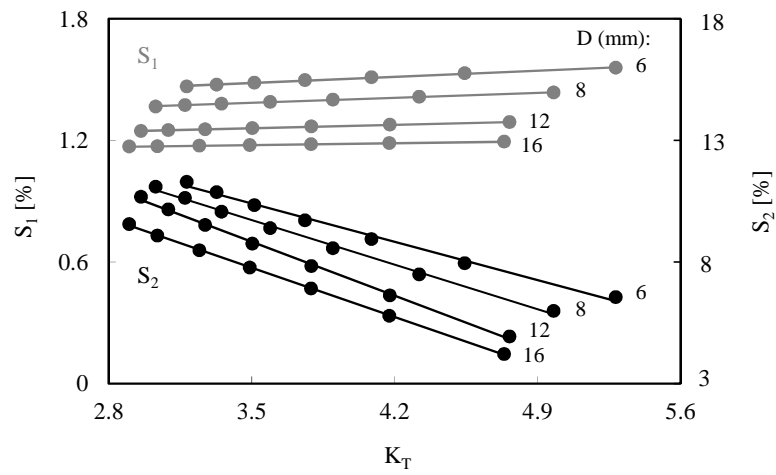
6.2.5. Relations S_1-K_T and S_2-K_T

In the previous subsections, the stress concentration factor (K_T) was used to explain the behaviour of the S_1 and S_2 values. In this subsection, the links between S_1-K_T and S_2-K_T are examined in detail. The cases studied before (i.e. cases 18-45 of Table 4.5 for notched rectangular bars with corner cracks; cases 18-45 of Table 4.6 for notched round bars with surface cracks; and cases 30-57 of Table 4.7 for notched plates with through cracks) were analysed in terms of stress concentration factor. This factor was defined as the ratio of the maximum stress to the corresponding remote nominal stress calculated from the gross cross-sectional area (see Equation 2.34). Such analyses, as in the previous subsection, focused on the effect of the specimen size and on the notch radius. The other variables remained unchanged ($n = 2\text{mm}$, $m = 3$, $\nu = 0.3$ and tension loading).

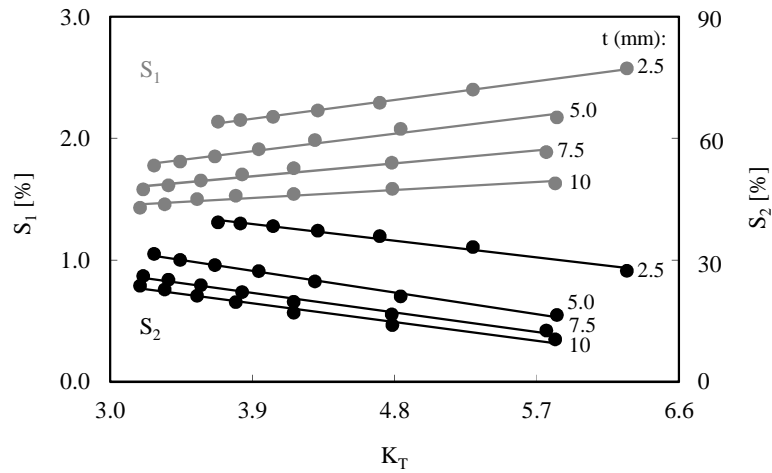
Figures 6.30a-c present the evolution of S_1 with K_T (grey symbols) and S_2 with K_T (black symbols) for notched rectangular bars with corner cracks; notched round bars with surface cracks; and notched plates with through cracks, respectively. As can be seen, linear equations can be used to describe the relations



a)



b)



c)

Figure 6.30. Evolution of S_1 and S_2 with K_T : a) notched rectangular bars with corner cracks; b) notched round bars with surface cracks; c) notched plates with through cracks (Branco, 2012a).

S_1 - K_T and S_2 - K_T . The correlation coefficients found were relatively high ($r > 0.990$). The slopes of the full lines seem to depend on the geometry but not on the size of the specimen. Besides, not surprisingly, the

increase in K_T results in greater S_1 values and lower S_2 values. These facts are in agreement with the conclusions referred to in the previous subsections. On the one hand, higher K_T values are responsible for higher stress triaxialities and higher slopes of the h-curves near the free boundary of the specimen which leads to greater extents of the surface region. On the other hand, higher K_T values promote a faster transition from a predominant plane stress state near the surface to a predominant plane strain state in the depth direction which means that the extent of the near-surface region tends to diminish.

Based on the results of Figures 6.30a-c, two empirical functions that relate the stress concentration factor, the notch radius and the size of the specimen to S_1 (Eq. 6.6) and S_2 (Eq. 6.7) were developed, i.e.

$$S_1(K_T, r, q) = Ln(K_T) \times 1.5^{\text{Log}(r)} \times [x_7(x_8 - q)] \quad (6.6)$$

$$S_2(K_T, r, q) = Ln\left(\frac{1}{K_T}\right) \times 1.5^{\text{Log}(r)} \times e^{x_9 \cdot q + x_{10}} \quad (6.7)$$

where q is the size of the specimen (W for notched rectangular bars with corner cracks; D for notched round bars with surface cracks; and t for notched plates with through cracks) and x_i are fitting constants given in Table 6.3. These equations proved to be independent of the geometry. Besides, this formulation is particularly interesting because it is based on three known variables, namely the stress concentration factor, notch radius and size of the specimen, and only on two unknown constants. These equations are valid in the ranges (dimensions in millimetres): $W \in [5-14]$, $D \in [8-16]$, $t \in [2.5-10]$ and $r \in [0.5-2]$. Note that the maximum errors between the proposed expressions (full lines) and the FEM results (circle symbols) are lower than 5%.

Finally, the effect of the crack length on S_1 and S_2 was examined. This study was carried out for the notched rectangular bar with corner crack and for the notched round bar with surface crack. As mentioned before, the notched plate with through crack is not affected by the crack length (see Figure 6.25c and Figure 6.27c) and therefore no corrections regarding the values of Equation 6.6 and Equation 6.7 are required. The correction function for the other two geometries is given by

$$S_i^g(K_T, r, q, a/W) = S_i(K_T, r, q) \times x_{11} (a/W)^{x_{12}} \quad (6.8)$$

being x_i the fitting constants listed in Table 6.4. This equation is valid in the range $0.3 \leq a/W \leq 0.85$. In this interval, the fitting error is lower than 4%.

Table 6.3. Constants of Equation 6.6 and Equation 6.7 (Branco, 2012a).

Geometry	x_7	x_8	x_9	x_{10}
Notched rectangular bar with corner crack	-4.9891×10^{-4}	1.9265×10^{-2}	6.2868×10^{-1}	-6.9932×10^{-1}
Notched round bar with surface crack	1.6729×10^{-4}	1.1822×10^{-2}	2.0363×10^{-1}	-2.8655×10^{-1}
Notched plate with through crack	-5.8200×10^{-4}	1.6650×10^{-2}	8.9323×10^{-1}	-6.0126×10^{-1}

Table 6.4. Constants of Equation 6.8 (Branco, 2012a).

Geometry	x_{11}	x_{12}
Notched rectangular bar with corner crack		
S_1	8.3578×10^{-1}	-2.6374×10^{-1}
S_2	5.5487×10^{-1}	-8.2373×10^{-1}
Notched round bar with surface crack		
S_1	7.4890×10^{-1}	-3.9501×10^{-1}
S_2	5.1319×10^{-1}	-9.9368×10^{-1}

6.3. Definition of a plane strain specimen for fatigue and fracture studies

Stress state has a major influence on different phenomena, namely those involving diffusion (hydrogen embrittlement, high temperature fatigue crack growth), plastic deformation (ductile fracture, plasticity induced crack closure), and brittle fracture:

- hydrogen induced cracking is susceptible to stress triaxiality (Cayón, 2003). The zones of the component more critical for hydrogen induced cracking are those submitted to triaxial stress states, since the volumetric deformation is favourable for hydrogen accumulation;
- high temperature fatigue crack growth in nickel-base superalloys has been found to be greatly influenced by the stress triaxiality. Significant tunnelling effect has been observed in C(T) and Corner Crack (CC) specimens, as a result of the influence of the stress state on the oxidation mechanism (Webster, 1994; Tong, 1997). At the surface, the plane stress state promotes cyclic plastic deformation and propagation is predominantly transgranular (Antunes, 2001). Inside, the triaxiality associated with plane strain states promotes diffusion of oxygen. Therefore, propagation tends to be intergranular and time-dependent;
- ductile fracture in metallic alloys usually follows a multi-step failure process involving several mechanisms: nucleation of microscopic voids by fracture or decohesion of second-phase inclusions, growth of voids induced by plastic straining, localisation of plastic flow between the enlarged voids and final tearing of the ligaments between enlarged voids (Van Stone, 1985). These mechanisms are greatly affected by the stress state (Clausmeyer, 1991; Kim, 2004a);
- plasticity induced crack closure (PICC) is an extrinsic micromechanism affecting fatigue crack growth (FCG), which also depends on crack tip plastic deformation. There is a general agreement that plane stress state has significantly larger levels of crack closure compared with plane strain loading conditions. However, the level and even the existence of PICC under plane strain conditions still are controversial (Newman, 1981a; Fleck, 1982; Sehitoglu, 1991; Pippan, 1994; Costa, 1998; Pommier, 2002; Antunes, 2010; Antunes, 2011);
- brittle fracture toughness is known to reduce with the increase of the thickness. A minimum thickness is defined in order to obtain the plane strain fracture toughness (K_{IC}). In fact, in standard fracture toughness testing of deeply cracked C(T) specimens or single edge cracked bars in three-point-bend, the thickness of the specimen is recommended to be either half of, or equal to the width of the specimen (ASTM E399, 2009).

The isolated analysis of plane stress and plane strain states is important in fundamental studies of material behaviour. In general, as discussed in Section 4.5, the plane stress state is obtained with thin specimens, while the plane strain state is achieved with thick specimens or introducing lateral side grooves. However, the plane stress state still exists at the surface and additionally the experimental procedure requires more material and higher loads. Besides, since there are no standards defining the specimen, or the lateral side grooves or the thickness, all of these aspects have been defined empirically without an objective measure of the resultant stress triaxiality state.

The development of a plane strain specimen would be useful to study all phenomena affected by stress triaxiality states. The approach followed here, as discussed in detail in Section 4.5, consists of a standard M(T) specimen modified with lateral side grooves. The lateral side grooves are introduced in order to reduce the size of the plane stress surface regions. This solution combines easiness of production, high groove reproducibility and comparability of results with standard geometries, which are very important features from an experimental point of view.

6.3.1. Selection of representative crack shapes

As stated in Section 4.5, the plane strain specimen was developed using realistic crack shapes. The crack growth simulations performed are summarised in Table 4.8. These simulations aimed at studying the main parameters affecting the crack shape, such as notch radius, notch depth, notch angle, thickness, fatigue crack growth rate and elastic constants.

The typical crack front developments obtained for the standard M(T) and modified M(T) specimens are presented in Figure 6.31. Many crack front profiles were intentionally omitted to avoid overlapping. This figure can also be used to understand the effects of some of the above-mentioned variables on the crack shape profiles. Figure 6.31a compares the crack shape evolution in both standard M(T) and modified

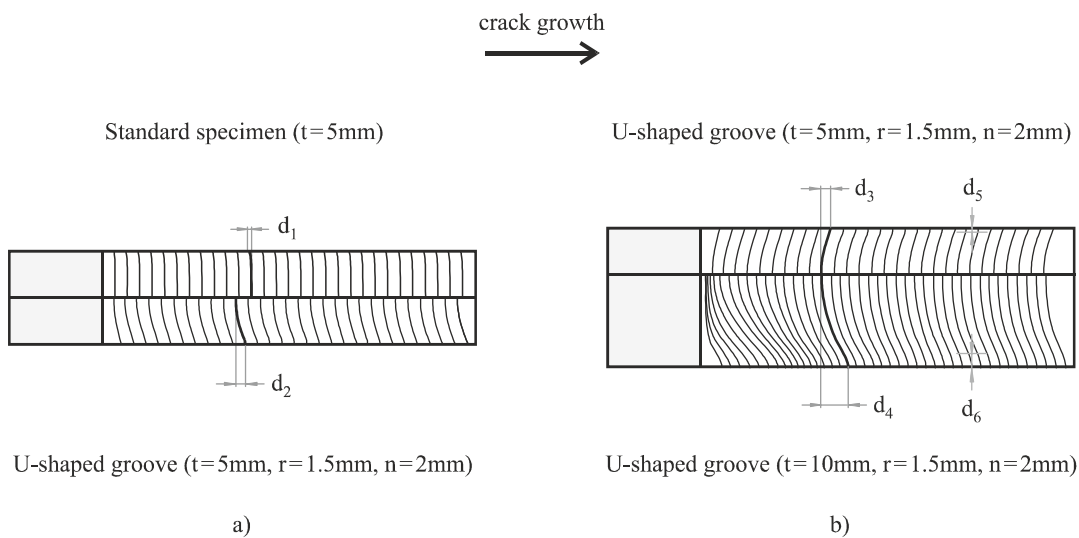


Figure 6.31. Effect of: a) groove; b) thickness on fatigue crack shape developments ($L=200\text{mm}$, $2W=50\text{mm}$, $a_0/W=0.2$) obtained in standard M(T) and notched M(T) specimens (Branco, 2013a).

M(T) specimens with the same reduced thickness. The evident differences in shape are, therefore, due to the presence of the groove. In the unnotched case, the crack shape is almost straight, except near the surface where a delay is observed which is depicted by the d_1 variable. In the other case, the crack growth along the boundary of the specimen is faster than in depth due to the increase of the stress concentration factor caused by the U-shaped groove, as can be distinguished by the d_2 variable.

Figure 6.31b compares the crack shape evolution in two modified M(T) specimens for two different values of thickness ($t = 5\text{mm}$ and $t = 10\text{mm}$). In both cases, the crack growth along the boundary of the specimen is faster than in the thickness direction. Nevertheless, the decrease in thickness results in a delay near the surface, as evidenced by the d_3 and d_4 variables. Besides, it is also clear that the sizes of these regions in the depth direction, evaluated by the d_5 and d_6 variables, are different and tend to be greater for higher values of thickness.

The analysis of this figure also makes clear that the crack front profiles, although different from case to case, tend to be similar after a short initial period of propagation in which high shape changes occur. As already analysed in Section 6.2, in particular in Figures 6.18 and 6.19, the transient part of propagation in M(T) specimens is relatively small; besides, the crack front maintains its shape during the stable phase of propagation. Based on these two premises, the 3D-FE refined models developed to compute the stress triaxiality were created from stable crack shapes. This was achieved by propagating the crack from a very small initial length ($a_0/W = 0.02$) up to $a/W = 0.5$. Consequently, unless stated otherwise, the analysis of stress triaxiality along the crack front in the following subsections is performed using stable crack shapes with dimensionless crack length equal to $a/W = 0.5$.

6.3.2. Stress triaxiality at the crack front

As already observed in Section 6.2, a close relationship between crack shape and stress triaxiality can be established. In this sense, all the variables affecting the stable crack shape, namely geometrical parameters and material properties, are important in terms of stress triaxiality. In this context, the former group (particularly the thickness, groove radius and groove depth) play a major role since they can be controlled by the user; unlike the others which are intrinsic characteristics of the materials. Accordingly, it is important to understand the effect of the geometrical variables on the stress triaxiality level of the modified M(T) specimen.

The relation between the stress triaxiality and the different variables studied here was carried out using the h stress triaxiality parameter (see Equation 4.17). This parameter, as observed in the study of the extent of the surface region (Section 6.2), is an easy and powerful way to establish a link between those variables and the resultant stress triaxiality state.

Figure 6.32 shows the effects of different variables on the stress triaxiality. This figure presents the evolution of the h stress triaxiality parameter with the dimensionless position along the thickness (x/t). In

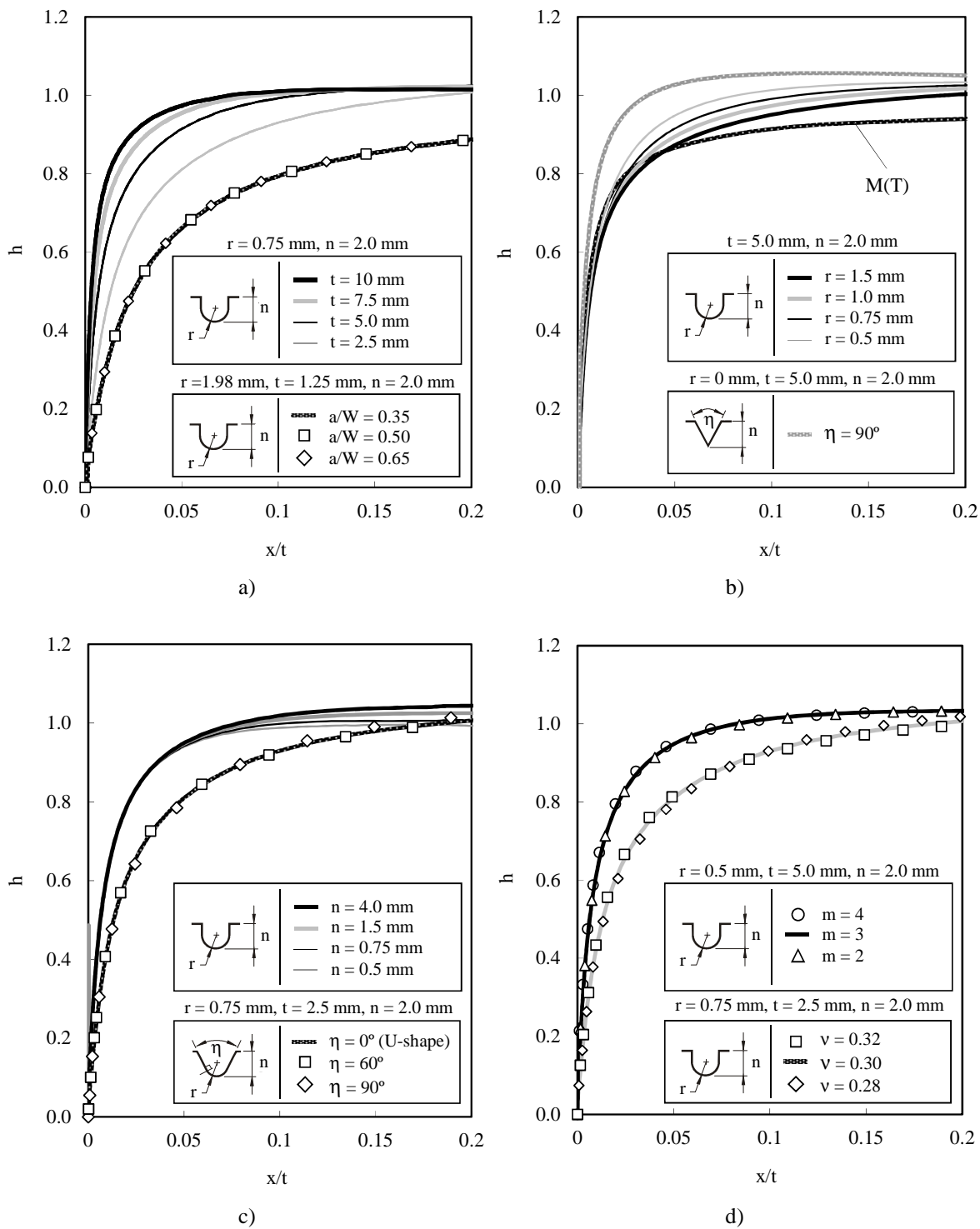


Figure 6.32. Effect of the: a) thickness and crack length; b) groove radius; c) groove depth and groove angle; d) exponent of the Paris law and Poisson's ratio on the h-curves (Branco, 2013).

general, the h-curves start from zero near the surface (plane stress state) and tend to unity (plane strain state) in the depth direction. Nevertheless, the transition between these two states varies considerably from case to case, in particular the slope of the curves near the surface. Therefore, the systematic quantification of these differences is necessary to develop a pure plane strain specimen.

Figure 6.32a shows the effect of the thickness on the h -curves (cases 01-04 of Table 4.8). The most significant differences are observed near the surface. The slope of the h -curves increases with the thickness which means that the curves computed for higher thicknesses lay above the others. As a result, stress triaxiality states are higher for greater thicknesses. However, it is also clear that the differences between the h -curves tend to decrease as the thickness increases.

Figure 6.32b presents the effect of the groove radius on the h -curves (cases 05-08 of Table 4.8). These results show that the stress triaxiality is extremely influenced by this variable. The decrease in the groove radius leads to higher h values in the whole domain of the curves. This can be explained by different stress concentration factors near the groove root. Smaller groove radii increase the stress concentration factor along the free boundary of the specimen which promotes a faster crack growth near the surface as well as high stress triaxiality levels. The effect of the stress concentration factor on the h -curves is even more visible by comparing the two extreme curves corresponding to the standard M(T) specimen (case 09 of Table 4.8) and the modified M(T) specimen with sharp V-shaped grooves (case 10 of Table 4.8). Not surprisingly, the curve of the latter case clearly lies above the other in consequence of its higher stress concentration factor. The nature of the M(T) specimen can explain the differences, i.e. a rectangular plate with constant cross-section cannot compete with a grooved geometry in terms of stress triaxiality.

Figure 6.32c exhibits the effect of the groove depth on the h -curves (cases 11-14 of Table 4.8). Near the surface, the influence of this variable on the stress triaxiality level is not relevant since the curves are practically overlapped. However, a notorious difference is observed in the in-depth direction. Therefore, the higher is the groove depth, the greater is the stress triaxiality value.

The effect of the groove angle on the h -curves can also be seen in Figure 6.32c (cases 15-17 of Table 4.8). Three groove angles ($\eta=0^\circ$, $\eta=60^\circ$, $\eta=90^\circ$) with the same groove radius ($r=0.75\text{mm}$) and the same groove depth ($n=2.0\text{mm}$) were examined. The results achieved show that the stress triaxiality levels are quite similar in the three curves which indicates that the groove shape is not relevant, provided that the groove radius and the groove depth are maintained.

Apart from the geometrical effects, the influences of the material properties on the stress triaxiality level were also studied. Figure 6.32d displays the effect of the exponent of the Paris law (m) on the h -curves (cases 05, 18, 19 of Table 4.8). The influence of this parameter on the stress triaxiality level is very slight. As can be seen, the three curves have the same behaviour in the whole domain. Although not obvious at the first sight, it is possible to conclude that an increase in the exponent of the Paris law is responsible for higher h values. Figure 6.32d also exhibits the effect of the Poisson's ratio on the h -curves (cases 01, 20, 21 of Table 4.8). The differences in the range represented ($\nu=0.28$, $\nu=0.30$, $\nu=0.32$) are relatively small. Nevertheless, this elastic property has a strong effect on the stress triaxiality. The results demonstrate that the h values increase with ν . This fact can be explained by the corner singularity existing near the surface of the specimen, which is a function of the Poisson's ratio (Heyder, 2005; Ševčík, 2012). With respect to the influence of the Young's modulus on the stress triaxiality, an extremely weak effect was observed.

After a careful analysis, it is possible to infer that the lower is the Young's modulus, the higher is the h-curve (Branco, 2013).

The effect of the crack length on the h-curves was also examined. Figure 6.32a shows the h-curves obtained for the same propagation (case 22 of Table 4.8) considering three crack fronts with different dimensionless crack lengths ($a/W=0.35$, $a/W=0.50$, $a/W=0.65$). As can be distinguished, there are no perceptible differences between the values of stress triaxiality. This is an expected result which demonstrates again that a single crack front profile can be used to evaluate the stress triaxiality in the stable phase of propagation.

In conclusion, higher stress triaxiality levels can be achieved by using thick specimens with small groove radii and long groove depths. The ideal situation ($r=0\text{mm}$) is not technologically feasible. In this way, a trade-off between groove radius and technology is required.

6.3.3. Definition of a plane strain specimen

The plane strain specimen was defined using the h-curves. This was a logical decision since these curves have revealed a high sensitivity to the variables that affect the stress triaxiality. In this sense, it was possible to quantitatively relate the stress triaxiality with the main geometrical variables.

The strategy adopted here is depicted in Figure 6.33. In a first stage, the resultant h-curves of the stable crack shapes obtained in the FCG simulations are computed. Then, the geometrical variables of the specimen that meet the plane strain state criterion are determined.

The plane strain state criterion applied is based on two independent limits (see Figure 6.33). The first one, the h-limit (β), defines the minimum intensity of the plane strain state (represented in the vertical plane of the figure below). The second one, the p_β -limit (ζ), defines the amount of the specimen in which there is a

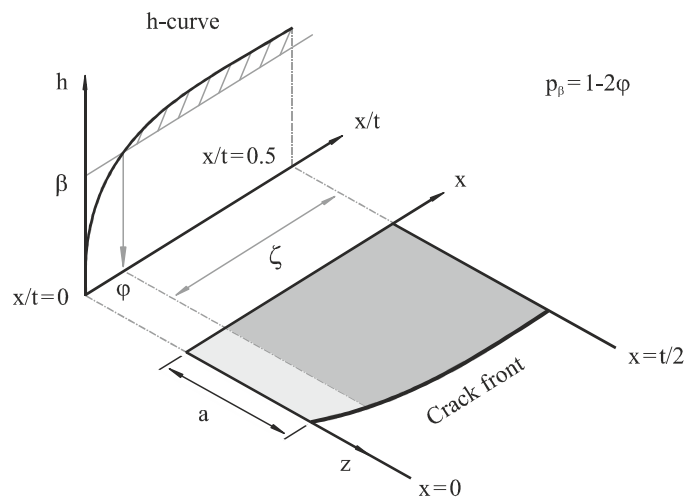


Figure 6.33. Scheme of the strategy adopted to define the plane strain specimen (Branco, 2013).

value greater or equal to the minimum intensity defined (dark grey region of the horizontal plane). The higher is β , the more intense is the plane strain state. The higher is ζ , the greater is the amount of the specimen under plane strain state. Therefore, the increase of the h -limit or of the p_β -limit results in more pure plane strain states and thicker specimens.

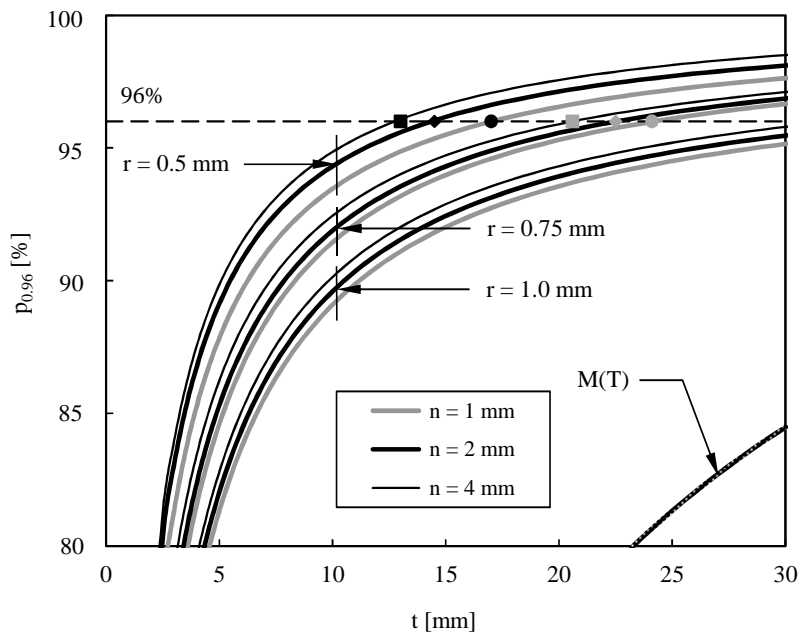
This concept is particularly interesting because it allows an effective comparison of different geometrical solutions in terms of stress triaxiality. Besides, this approach enables a balance between intensity and extent of plane strain state. In other words, the plane strain state (ps_β^ζ) is assumed to exist when a percentage of the thickness greater or equal to ζ has h stress triaxiality values greater or equal to β .

The h -limits considered here were $\beta=0.96$, $\beta=0.95$, $\beta=0.94$ and $\beta=0.93$. For each of them, the percentage of the thickness (p_β) in which the stress triaxiality parameter was greater or equal to the h -limit (β) was calculated. The calculations of p_β were exhaustively repeated for different geometrical variables. The cases studied here comprised groove radii in the range [0.5-1] mm; groove depths in the range [1-4] mm; and thicknesses in the range [2.5-40] mm. Table 4.8 summarises the main variables defined in the fatigue crack growth simulations performed to obtain the stable crack shapes necessary to compute the h -curves (cases 23-98). The standard M(T) specimen was also examined (cases 99-103 of Table 4.8).

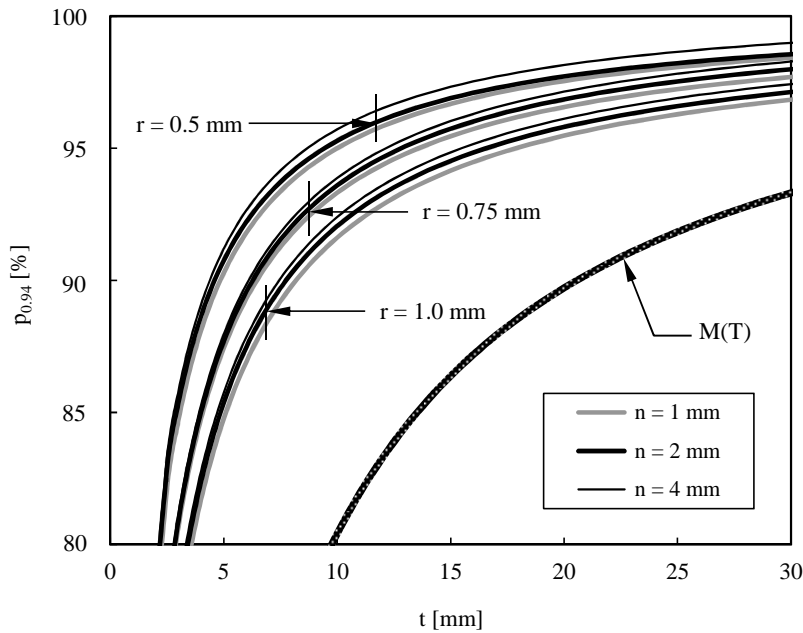
Figures 6.34a and 6.34b plot the p_β values against the thickness for two h -limits, respectively $\beta=0.96$ and $\beta=0.94$. Apart from the effect of the thickness, it is also possible to analyse the effect of the groove radius ($r=0.5\text{mm}$, $r=0.75\text{mm}$, $r=1.0\text{mm}$) and the effect of the groove depth ($n=1\text{mm}$, $n=2\text{mm}$, $n=3\text{mm}$). The evolution of p_β with the thickness for the standard M(T) specimen is also displayed in both figures.

The resultant curves, termed β -curves, are well-defined and have identical trends. The effect of the thickness is evident. For smaller thicknesses, the slopes are very steep whilst for greater thicknesses the curves tend to asymptotic values which depend on the groove geometry and on the h -limit. In relation to the groove radius, it is also clear that the greater is the value of r , the lower is the value of p_β . Regarding the groove depth, although its effect on the β -curves is less pronounced, it is visible that higher groove depths lead to greater values of p_β . These results are in line with the conclusions enunciated in Figure 6.32, i.e. higher thicknesses, higher groove depths and smaller groove radii result in increased stress triaxiality levels. Accordingly, the combination of these three factors can contribute to minimise the plane stress surface regions.

On the other hand, it is important to bear in mind that the β -curves of the standard M(T) specimens, in both cases, are well below the values obtained for the modified M(T) geometries. It means that the thickness necessary to achieve a given value of p_β is much higher in the standard M(T) specimen. So, as stated before, the introduction of lateral side grooves into the geometry is extremely beneficial to obtain thinner specimens with the same stress triaxiality level.



a)



b)

Figure 6.34. Evolution of p_{β} for: a) $\beta = 0.96$; b) $\beta = 0.94$ in standard and modified M(T) specimens (Branco, 2013).

Here, the pure plane strain state is assumed to exist when the limits $\beta = 0.96$ and $\zeta = 96\%$ are simultaneously met ($ps_{0.96}^{96\%}$), i.e. the specimen is considered under predominant plane strain condition when, at least, 96% of its thickness has values of the h stress triaxiality parameter greater or equal to 0.96. This is a very restrictive criterion because it combines a high intensity of plane strain state with a large amount of specimen that comply the condition. The dashed line of Figure 6.34a presents different geometrical solutions that meet this criterion (black and grey symbols). Table 6.5 summarises the values of the reduced thickness (t), groove radius (r) and groove depth (n) for each of those cases.

Table 6.5. Main geometrical variables of the plane strain specimens (Branco, 2013).

Geometry	Reduced thickness, t	Original thickness, T	Groove radius, r	Groove depth, n
1	13.0	21.0	0.5	4.0
2	14.5	18.5	0.5	2.0
3	17.0	19.0	0.5	1.0
4	20.6	28.6	0.75	4.0
5	22.5	26.5	0.75	2.0
6	24.9	26.9	0.75	1.0

Geometry 2 (of Table 6.5) is a balanced solution since it reduces the material and production costs. The groove radius ($r = 0.5\text{mm}$) is technically feasible. The groove depth ($n = 2\text{mm}$) is a reasonable value, avoiding excessive machining time. The amount of material is minimal because it has the smallest original thickness ($T = 18.5\text{mm}$). Besides, the proposed plane strain geometry can be made using current machining technology which simplifies the manufacturing process and reduces costs. Moreover, due to its small cross-section, tests can be performed using typical laboratory equipment. This simplifies the apparatus and ensures a good reproducibility. In order to avoid non-planar crack propagation, a perfect alignment of the opposite lateral side grooves is fundamental.

The remaining geometrical variables and the other aspects of the tests, namely the width-to-height ratio, specimen preparation, apparatus, data analysis, validation of results, etc., are similar to those proposed by the fatigue testing standards for the M(T) specimen. In this sense, the comparability of results between standard and modified geometries is possible, which is very interesting and highly desirable.

It is important to stress that a plane strain geometry defined from the standard M(T) specimen based on the same criterion would require a thickness of 78.9mm. On the other hand, a standard specimen with the same thickness to the proposed plane strain specimen would have plane stress surface regions equal to 15% (i.e. only 70% of the thickness with $h > 0.96$) against the 2% (96% of the thickness with $h > 0.96$) of the proposed solution. Therefore, the plane stress surface regions would be 7.5 times higher in the former specimen. The contrast between the two cases is remarkable. This is clear evidence that the introduction of lateral side grooves is an effective and straightforward approach to reduce the extent of the plane stress surface regions.

Figure 6.35 presents a versatile way to find alternative combinations of the geometrical variables that meet the plane strain criterion proposed which can be useful when the solutions of Table 6.5 are not viable, due to, for example, thickness constraints. In addition, solutions for less severe plane strain state criteria are also exhibited. The new criteria were defined in a similar manner but with lower h -limits and lower p_{β} -limits, i.e. 95% of the thickness with $h \geq 0.95$ ($ps_{0.95}^{95\%}$); 94% of the thickness with $h \geq 0.94$ ($ps_{0.94}^{94\%}$); and 93% of the thickness with $h \geq 0.93$ ($ps_{0.93}^{93\%}$). In this manner, the balance between intensity and extent of plane strain state is maintained but with a less intense degree. The plane strain state criterion should be defined in accordance with the severity of the phenomenon under study and the objectives of the research.

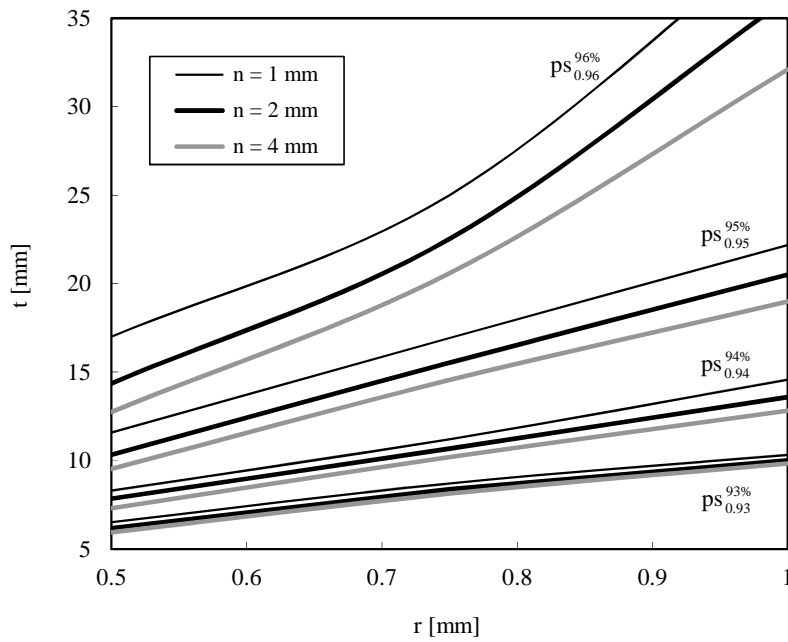


Figure 6.35. Different combinations of r , t and n for different plane strain state criteria (Branco, 2013).

As can be seen, the plane strain state criterion has a significant influence on the results. The decrease in the h -limit, which means less severe plane strain state criteria, leads to smaller thicknesses. Furthermore, the higher is the h -limit, the greater is the influence of the groove depth on the results, since the curves tend to be more distant from each other.

As referred to in Section 4.5, a parallel study aiming at defining a plane strain specimen using straight crack shapes was conducted. The first step, as for the study based on realistic crack shapes, was to understand the link between geometrical variables and stress triaxiality state. In the same way, the straight crack fronts had a dimensionless crack length equal to $a/W = 0.5$. The h stress triaxiality parameter was also used to examine the effects of the geometrical variables.

Not surprisingly, the h -curves behave in the same way. Figure 6.36a exhibits the effect of the thickness on the h -curves. As can be seen again, the slope of the h -curves increases with the thickness which means that the curves computed for higher t values lay above the others. Besides, it also clear that the differences between the h -curves tend to decrease as the thickness increases. In the direction of the thickness, the curves are overlapped which is not totally observed for the curved cracks (Figure 6.32a). The different behaviour is a consequence of the different stable crack shapes that result for each value of thickness. As mentioned with respect to Figure 6.17, the increase in the thickness affects the delay near the free surface, either in terms of tunnelling effect or size of the surface region.

Figure 6.36b presents the effect of the groove radius on the h -curves. As expected, the stress triaxiality is strongly affected by this variable. The increase of the groove radius results in lower h values near the surface. In the direction of the thickness, the curves converge to unity. Nevertheless, the convergence is

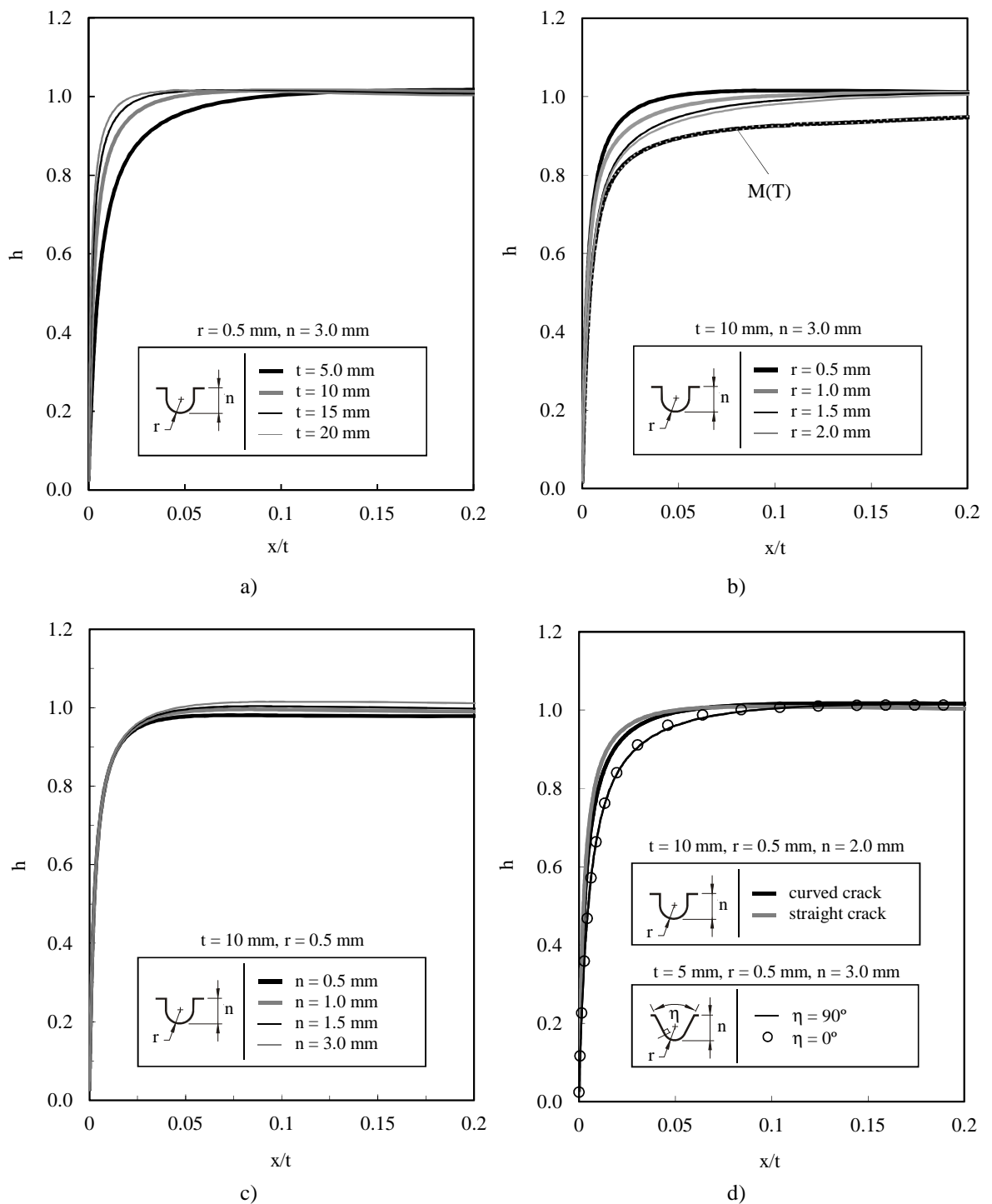


Figure 6.36. Effect of: a) thickness; b) groove radius; c) groove depth; d) groove angle and crack shape on the h-curves (Branco, 2010a).

faster for curved cracks (see Figure 6.32b). This is comprehensible because the crack fronts are straight which is not necessarily true in the case of realistic crack shapes obtained from different notch radii (Figure 6.31b). Besides, it is also evident that the standard M(T) specimen produces lower stress triaxiality states than the grooved geometries which is associated with its lower stress concentration factor due to the non-existence of any notch. As a consequence, the h-curves of geometrical configurations with higher stress concentration factors (i.e. lower groove radii) clearly lay above the others.

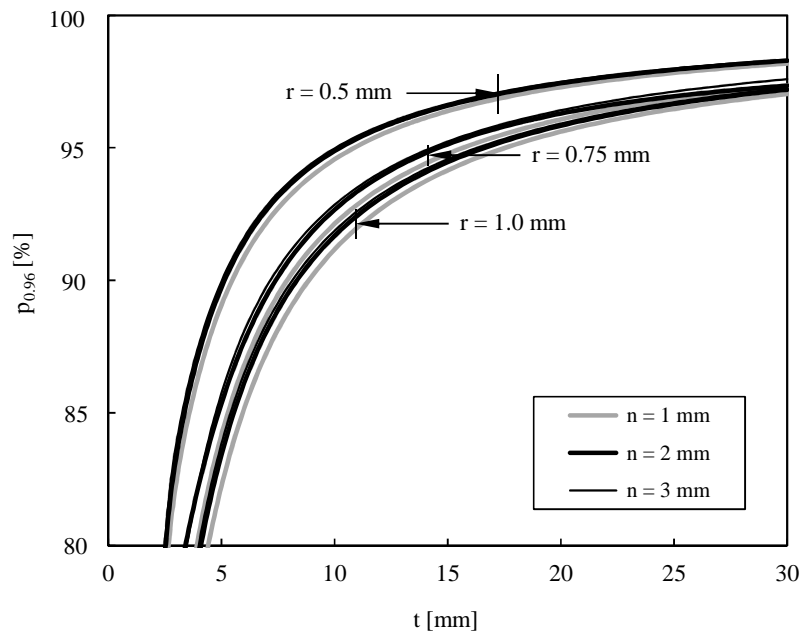
Figure 6.36c shows the effect of the groove depth (n) on the h-curves. As noted above, near the surface there are no relevant differences since the h-curves are perfectly overlapped (Figure 6.32c). In that region, the groove radius seems to be preponderant. Nevertheless, in the direction of the thickness, the h-curves tend to increase with longer grooves.

Figure 6.36d displays the effect of the groove angle on the h-curves. Similarly to the conclusions stated for the curved cracks (Figure 6.32c), the results achieved show that the stress triaxiality values are quite similar which is a strong sign that the groove shape is not relevant, provided that the groove radius and the groove depth are maintained.

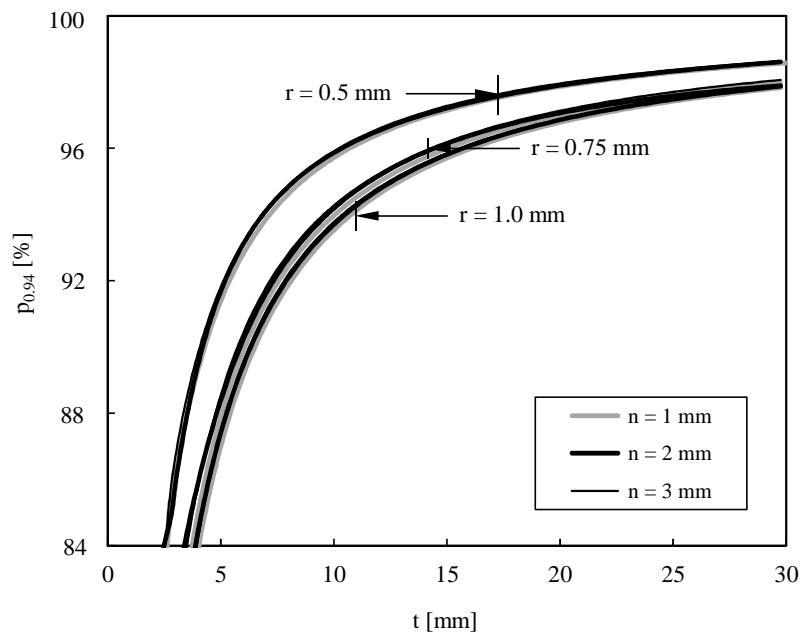
As postulated earlier, the h-curves are very sensitive to the crack shape. This can be seen in Figure 6.36d by comparing the h-curves of a realistic crack front obtained with the 3D-FE FCG technique (case 34 of Table 4.8) and of a straight crack shape with the same geometrical details and material properties. The h-curves behave differently in the whole domain represented. On the one hand, the slopes of the h-curves are clearly different, being higher for the straight crack front. On the other hand, the upper limits obtained are also different and tend to be greater in the case of the curved crack front. The higher slope of the straight crack front indicates that the transition from a predominant plane stress state to a predominant plane strain state is achieved faster. On the basis of these results, the plane strain specimen obtained from straight crack shapes is expected to be thinner than that obtained with curved crack shapes.

After this study, the β -curves were obtained. As before, the analysis comprised different thicknesses, groove radii and groove depths. The same h-limits were examined, namely $\beta=0.96$, $\beta=0.95$, $\beta=0.94$ and $\beta=0.93$. Figures 6.37a-b exhibit the p_β values for the cases $\beta=0.96$ and $\beta=0.94$, respectively. At first glance, the trends of the β -curves are similar to those achieved with fatigue crack growth modelling (see Figures 6.34a-b). In a similar way, the p_β values tend rapidly to zero as the thickness decreases; and converge to asymptotic values for thicker specimens. The asymptotic values increase with smaller notch radii and with greater notch depths. In fact, the same behaviour is observed in the whole domain of the curves, i.e. the p_β values are higher for smaller r values and higher h values. Nevertheless, the effect of the groove depth tends to be less effective as the notch radius decreases. On the other hand, the β -curves tend to be closer to each other as the notch radius diminishes.

The effect of the h-limit is also evident. The reduction of the β values results in an almost negligible influence of the notch depth on the p_β values (in Figure 6.37b the differences between the β -curves are much more mitigated than in Figure 6.37a). Moreover, the influence of the notch radius on the p_β values is also attenuated since the β -curves computed for the same notch radius tend to be closer in Figure 6.37b than in Figure 6.37a. These conclusions are not surprising. Indeed, they are in line with the trends observed in Figures 6.34a-b. However, the β -curves obtained with fatigue crack growth modelling are more sensitive to the notch radius and to the notch depth than with straight crack fronts. As can be seen in Figures 6.34a-b, the curves are furthest from each other.



a)



b)

Figure 6.37. Evolution of p_{β} for: a) $\beta=0.96$; b) $\beta=0.94$ in an analysis based on straight crack fronts.

Figure 6.38 compares the p_{β} values obtained with fatigue crack growth modelling (full lines) and with straight crack fronts (dashed lines) for $\beta=0.96$ ($p_{0.96}$) considering different notch radii ($r=0.5$ mm and $r=1.0$ mm) and different notch depths ($n=1$ mm and $n=2$ mm). As can be seen, the β -curves for straight crack fronts lay always above the others. This shows that the plane strain specimens obtained in this case are thinner than those obtained using stable crack shapes, as already observed in Figure 6.36d. Therefore,

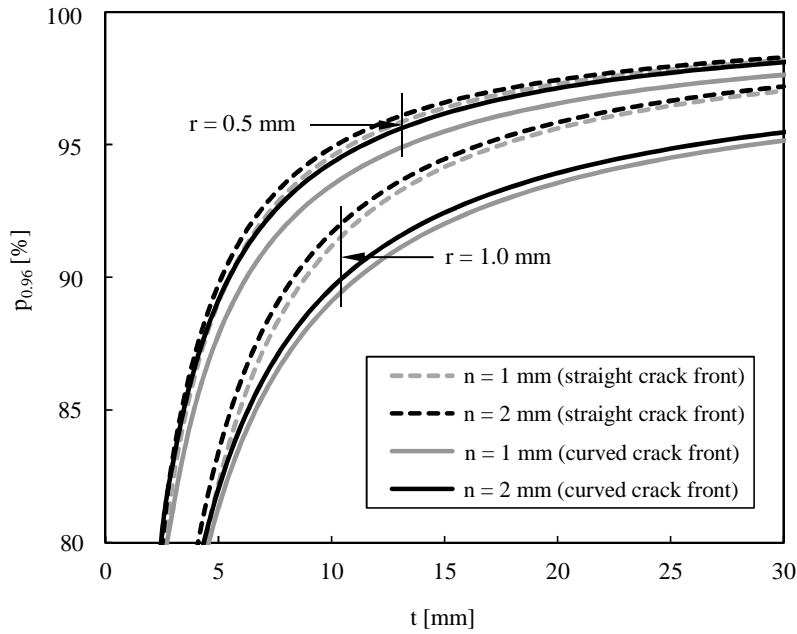


Figure 6.38. Comparison of p_{β} values considering stable crack fronts and straight crack fronts.

the plane strain specimen proposed (Geometry 2 of Table 6.5) continues to meet the pure plane strain state criterion (i.e. at least 96% of the thickness with h values greater than 0.96) but is, naturally, a more conservative solution than the one achieved from straight crack fronts.

6.3.4. Stress intensity factor solution

The stress intensity factor solution (K) for the proposed plane strain specimen was obtained by applying the finite element method. The relationship found can be expressed in the form

$$K = \left[1 + 0.17689 (a/W)^3 - 0.19230 \frac{(a/W)}{\ln(a/W)} \right] \sigma \sqrt{\pi a} \quad (6.9)$$

being a/W the dimensionless crack length, σ the remote stress, and a the half-crack length. The numerical results were fitted by the least square method. The fitting error of the proposed solution, in the range $0.1 \leq a/W \leq 0.9$, is less than 2%.

Figure 6.39 plots the geometric factor (Y) against the dimensionless crack length (a/W). The triangle symbols represent the results obtained from the FEM and the black full line represents the fitted curve. As exhibited in the figure, the proposed function is adequate to fit the data obtained here.

Figure 6.39 also presents the evolution of the geometric factor with the dimensionless crack length for the standard M(T) specimen. The dashed line corresponds to the numerical results of the present study whilst the circle symbols are the geometric factor derived from the solution proposed by Tada *et al.* (1973). As can be observed, the differences between these two sources are quite small, since the results are in excellent agreement. In the range $0.2 \leq a/W \leq 0.9$, the maximum differences are lower than 3%. The values

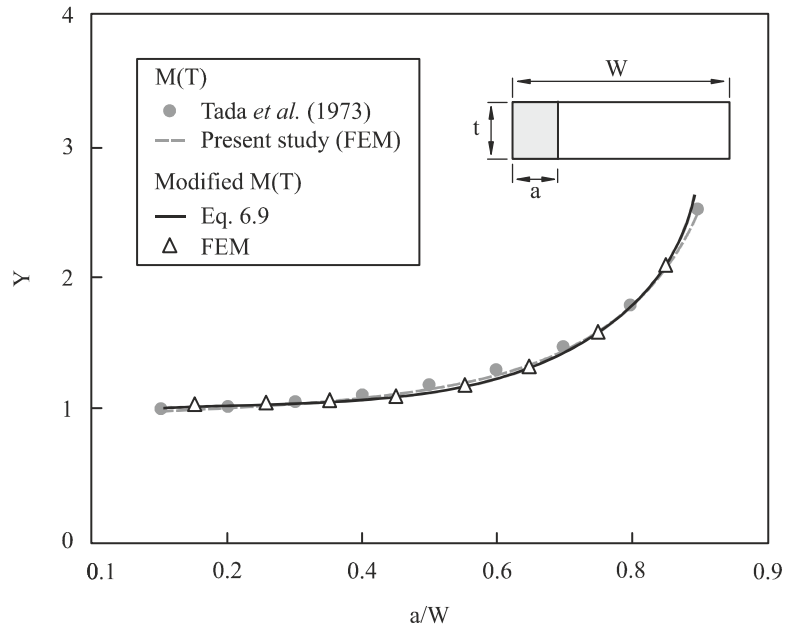


Figure 6.39. Stress intensity factor solution for the plane strain specimen.

of Tada *et al.* (1973) are, in general, slightly higher which means that such a solution is more conservative.

6.3.5. Sensitivity analysis

The plane strain specimen was subjected to a careful sensitivity analysis. The sensitivities were calculated analytically and in a dimensionless form to facilitate the comparison of results (see Equation 4.1). This study aimed at understanding the effect of the main variables that affect the crack shape on the p_β values. Thus, the independent variables analysed were the main geometrical variables (reduced thickness, groove radius and groove depth) and material properties (Poisson's ratio, Young's modulus and exponent of the Paris law).

Each sensitivity was calculated from three distinct analyses which were carried out using three different values of the independent variable, i.e. an independent variable with no perturbation; with a perturbation of -1%; and with a perturbation of +1%. Therefore, in order to obtain the stable crack shapes required to compute the h-curves necessary to calculate the p_β values, new fatigue crack growth simulations were performed. The new simulations were conducted in the plane strain geometry proposed (Geometry 2 of Table 6.5). For each independent variable (γ), three h-curves were established and the resultant values of p_β were computed. The three pairs of points p_β - γ were fitted to a second order polynomial function which was used to obtain the $\partial p_\beta / \partial \gamma$ derivative. After that, the dimensionless sensitivity was calculated.

Figure 6.40 presents the dimensionless sensitivities of the p_β to the independent variables for two different h-limits ($\beta=0.96$ and $\beta=0.94$). Regardless of the h-limit considered, the trends are similar. However, it is clear that the higher is the h-limit, the higher are the dimensionless sensitivities.

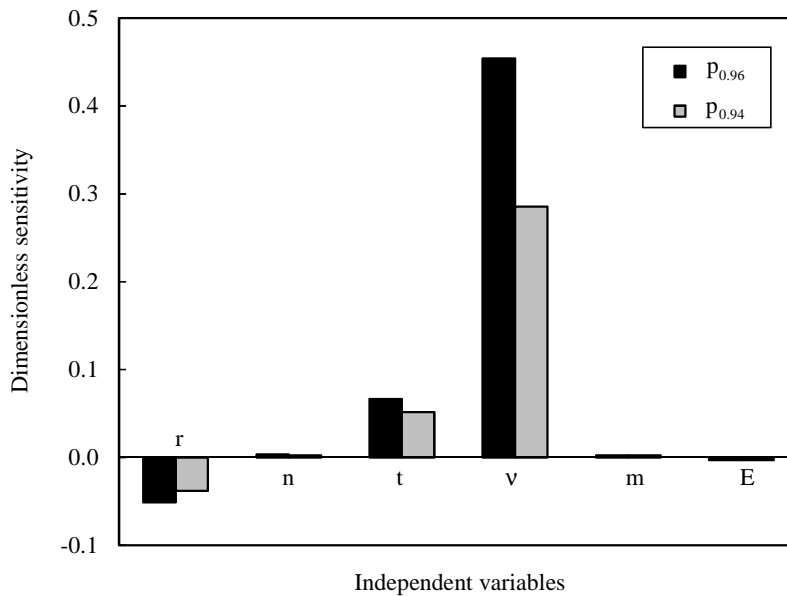


Figure 6.40. Sensitivity analysis of the main independent variables.

In relation to the geometrical variables, the most significant effects are caused by the thickness and groove radius. The groove depth has a limited influence on the p_{β} values. These results are in accordance with the conclusions stated before.

Regarding the Poisson's ratio and the Young's modulus, they behave differently. The former is responsible for the highest dimensionless sensitivities, whilst the latter has a negligible effect on this variable. In relation to the exponent of the Paris law, no significant dimensionless sensitivities were observed. These results are also in agreement with the previous conclusions.

6.4. Determination of the Paris law constants from fatigue crack front marks

Reliable fatigue crack propagation properties are essential for accurate life predictions. These properties are commonly evaluated using a standard procedure (BS ISO 12108; ASTM 647) that incorporates the use of standard specimens. The geometries employed (M(T) and C(T) specimens) are characterised by through cracks, nearly straight, and with no significant shape changes during the propagation.

In small circular shaped components, the application of this procedure is not recommended. On the one hand, the production of standard specimens is not easy; on the other hand, the use of miniature specimens has led to slower fatigue crack growth rates than in standard specimens (Shin, 2012). In view of these facts, alternative procedures are desirable.

In round bars, the crack suffers significant shape changes during the propagation. Under mode I, either numerically or experimentally, it has been demonstrated that small cracks are nearly part-elliptical whilst longer cracks tend to be flat (Carpinteri, 1993; Lin, 1997; Shin, 2004). Figure 6.41 presents the fatigue

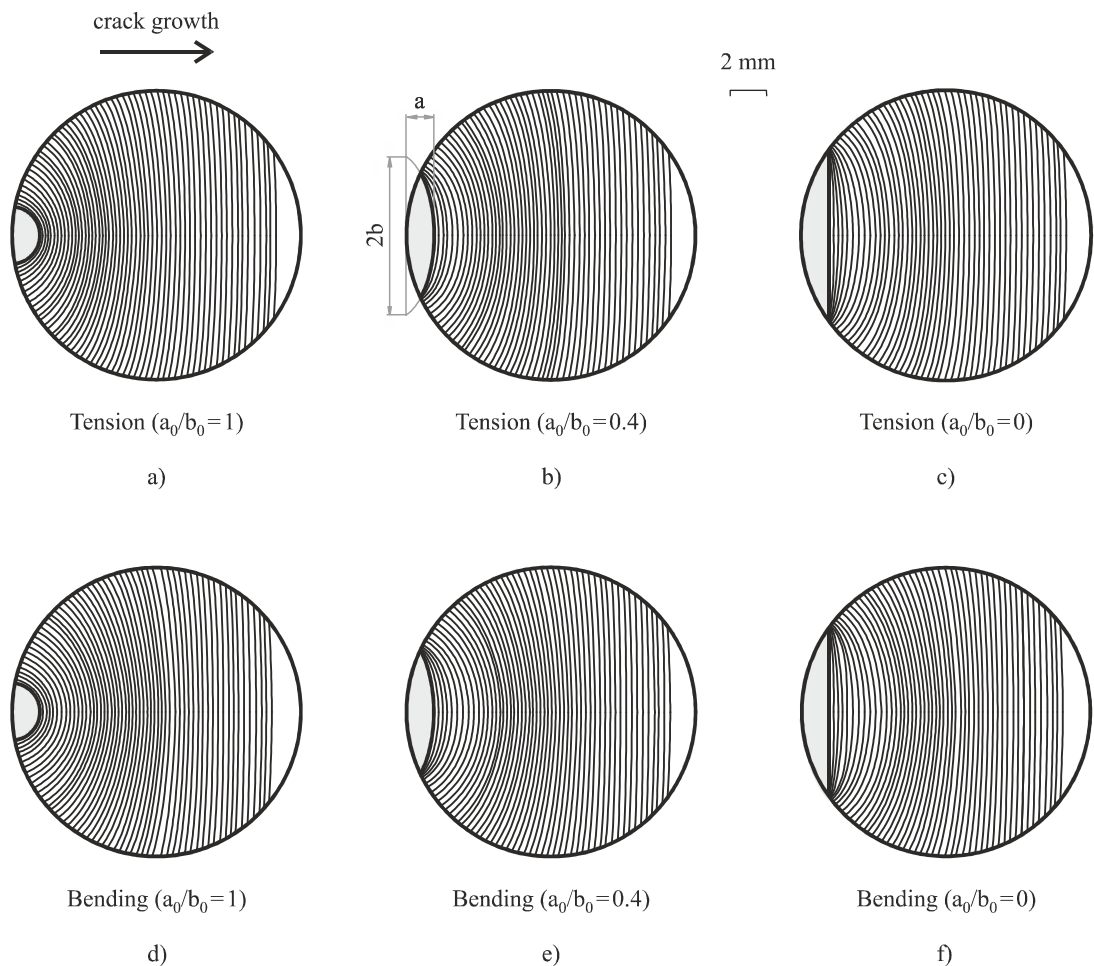


Figure 6.41. Fatigue crack shape developments of different initial surface cracks in round bars subjected to tension and bending (Branco, 2012c).

shape evolution of three different initial surface cracks ($a_0/b_0 = 1$, $a_0/b_0 = 0.4$, $a_0/b_0 = 0$) in round bars subjected to tension (Figures 6.41a-c) and bending (Figures 6.41d-f). It can be seen that at the early stage of crack growth, the shape development strongly depends on the initial crack configuration. It is clear that for the initial straight shape ($a_0/b_0 = 0$), the crack grows much more rapidly in depth than along the free surface whilst for the initial part-circular ($a_0/b_0 = 1$) and part-elliptical ($a_0/b_0 = 0.4$) shapes the growing is more balanced along the whole crack front. However, the importance of the initial crack configuration gradually disappears as the crack extends. As a consequence, the crack fronts tend to be similar. The amount of crack growth needed to achieve this part of propagation also depends on the initial crack configuration, as already discussed in Figure 6.16a, and therefore the shapes closer to the preferred propagation path reach it faster than the others.

The effect of the loading type on the crack profiles is not totally clear in the previous figure. Nevertheless, as has been reported in the literature (Carpinteri, 1993; Couroneau, 1998), the fatigue propagation paths are distinct for tension and bending. Figure 6.42 plots the crack aspect ratio (a/b) against the dimensionless crack length (a/D) for different initial crack fronts ($a_0/b_0 = 1$, $a_0/b_0 = 0.8$, $a_0/b_0 = 0.6$,

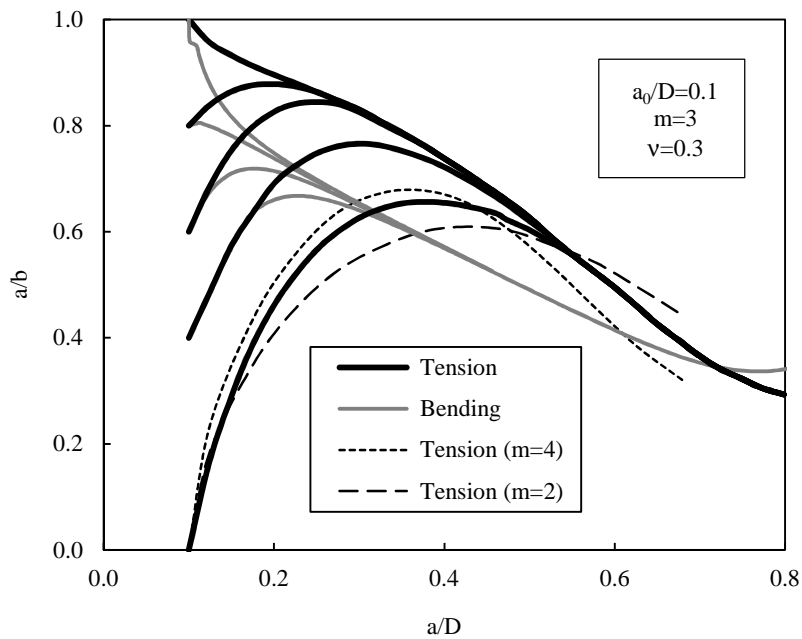


Figure 6.42. Fatigue propagation paths of different initial configurations in round bars subjected to tension and bending (Branco, 2012c; Branco, 2012d).

$a_0/b_0=0.4$, $a_0/b_0=0$) in round bars subjected to tension and bending. As can be seen, at the early stage of propagation, the crack paths are practically overlapped either for tension or for bending and seem to be controlled by the initial crack configuration. After this period, the trajectories drawn by the cracks are different and the results indicate that the cracks are more flat for bending than for tension. Besides, there is no doubt that the preferred propagation paths strongly depend on the loading type. Furthermore, the convergence to the preferred propagation paths is faster for bending than for tension.

The effect of the Paris law exponent on the crack aspect ratio is also exhibited in Figure 6.42. Three different fatigue propagation paths obtained from an initial straight crack shape ($a_0/b_0 = 0$, $a_0/D = 0.1$) subjected to tension are examined. At the early stage of propagation, there are no relevant changes. However, as the crack grows, different propagation paths are observed. Besides, it is notorious that the propagation paths crossover for dimensionless crack lengths in the range $0.47 \leq a/D \leq 0.50$. After that instant, the trajectories diverge. The crossover point depends on several variables, in particular the exponent of the Paris law, loading type and initial crack shape (Carpinteri, 1993; Lin, 1997; Couroneau, 1998; Shin, 2007; Toribio, 2009).

Such a study can be used to identify the region more sensitive to the m constant. Ideally, the experimental crack shapes used in the evaluation of the Paris law constants must be selected in this region. On the contrary, crack shapes in the early period of propagation are not recommended because the shape changes are not yet obvious which results in less accurate predictions. For example, in the case of Figure 6.42, the three curves tend to follow unequivocal paths for values of $a/D \geq 0.2$. In view of this fact, the experimental crack shapes should be selected from this point on. In this research, as summarised in Table 3.14, the experimental crack shapes used are in the above-mentioned range.

The first step encompassed the determination of the m exponent. A set of numerical simulations was performed using values of m contained in the interval 2.6 to 3.6 (da/dN [mm/cycle], ΔK [MPa·m^{0.5}]). Each numerical simulation was started from the crack shape 1 (Figure 3.19b) and was interrupted when the first node of the crack front (node at the symmetry line identified in Figure 4.23b) reached the length of the crack shape 2 (Figure 3.19b). Then, for each case, the values of the accumulated difference (ad) between the numerical and experimental crack shapes were computed using Equation 4.18.

Figure 6.43 plots the values of accumulated difference (ad) against the Paris law exponent. The proposed parameter has proved to be very sensitive to any crack shape changes. As can be seen, a well-defined tendency emerges from the results. This is clear evidence of the suitability of the selected dependent parameter for this purpose. The ad values were fitted to a second order polynomial function (Equation 6.10). A high correlation coefficient was achieved ($r=0.997$).

$$ad(m) = 9.021 \times 10^{-2} m^2 - 5.597 \times 10^{-1} m + 8.940 \times 10^{-1} \quad (6.10)$$

In theory, the correct value of m can be found by minimising the value of the accumulated difference. So, it means that the derivative of the previous function must be equal to zero. Therefore, solving this equation, the value of m is given by

$$\frac{d}{dm} [ad(m)] = 0 \Leftrightarrow 2 \times 9.021 \times 10^{-2} m - 5.597 \times 10^{-1} = 0 \Leftrightarrow m = 3.102 \quad (6.11)$$

being da/dN in mm/cycle and ΔK in MPa·m^{0.5}. The error involved in the prediction of m , relatively to the experimental value, is of 4.73%. This is clearly acceptable in this context. Note that due to the low stress

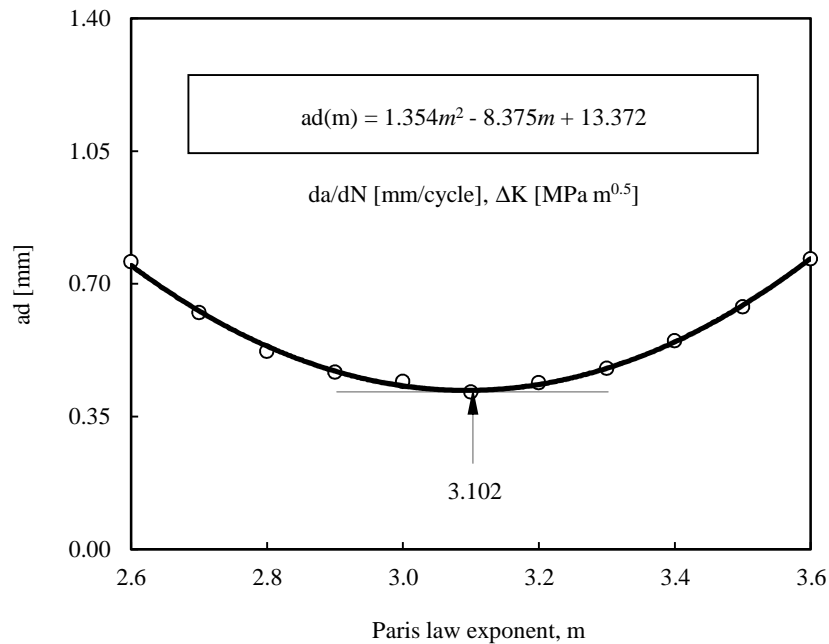


Figure 6.43. Determination of the Paris law exponent (Branco, 2012d).

ratio ($R=0.1$) used, crack closure can exist. This can affect both the crack shape and the m prediction. In order to avoid such a risk, higher stress ratios are preferable.

The second step comprised the determination of the C constant. The value of m predicted previously was fixed. Then, a new set of numerical simulations was performed using C values within the range of 7×10^{-9} to 2.4×10^{-9} (da/dN [mm/cycle], ΔK [MPa·m^{0.5}]). Each numerical simulation was started from the crack shape 1 (Figure 3.19b) and was interrupted when the first node of the crack front (node at the symmetry line identified in Figure 4.23b) reached the length of the crack shape 2 (Figure 3.19b). A maximum crack growth increment equal to $D/2000$ was used. The number of loading cycles between these two prescribed crack fronts, computed using Equation 4.13, was the result of each simulation.

Figure 6.44 plots the number of cycles predicted against the Paris law constant. The number of cycles obtained between the two experimental crack shapes is also exhibited. An exponential function was fitted to the results by employing the least square method (Equation 6.12). A relatively high correlation coefficient was achieved ($r=0.995$).

$$N(C) = 85.895 C^{-1.006} \quad (6.12)$$

Theoretically, the C constant can be calculated by equalising the previous function to the experimental number of cycles, i.e. solving the following equation

$$N(C) = 46523 \Leftrightarrow 85.895 C^{-1.006} = 46523 \Leftrightarrow C = 1.849 \times 10^{-9} \quad (6.13)$$

being da/dN in mm/cycle and ΔK in MPa·m^{0.5}. The numerical and experimental results are in good agreement. Note that the difference between both values is less than 2.87%. Naturally, this error can be considered acceptable.

In order to evaluate the robustness of the proposed technique, the procedure was carefully repeated for other combinations of the experimental crack shapes exhibited in Figure 3.19b. Two different situations, corresponding to the combinations 1 to B (1-B) and A to 2 (A-2), were studied. For each of them, as described previously, the accumulated difference parameter (ad) was computed through Equation 4.18 for various values of m . From the values of ad , a second order polynomial function was fitted. Then, the Paris law exponent was achieved by minimising this function. Next, with the predicted value of m , new numerical simulations were performed for different C constants aiming at obtaining the numerical number of cycles between both crack shapes. These results were fitted to an exponential function. Equalising the function achieved to the corresponding experimental number of cycles (see Table 3.15), the C constant was calculated. Finally, the predicted constants were compared with the experimental values. Table 6.6 presents the C and m constants predicted in each case as well as the errors relatively to the experimental results. Regardless of the combinations examined, the errors are similar. For example, in the combination

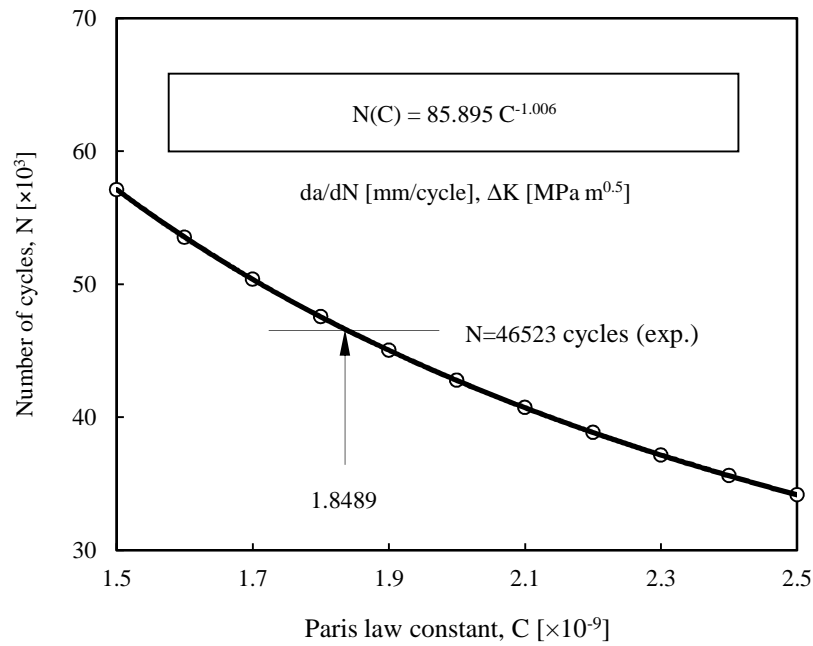


Figure 6.44. Determination of the Paris law constant (Branco, 2012d).

Table 6.6. Predicted C and m constants for different combinations of the experimental crack shapes used.

Crack shape combination	C	m	Error of C relatively to the experimental value [%]	Error of m relatively to the experimental value [%]
			$\frac{C_{\text{exp}} - C_{\text{num}}}{C_{\text{exp}}}$	$\frac{m_{\text{exp}} - m_{\text{num}}}{m_{\text{exp}}}$
1-2	1.8489×10^{-9}	3.102	2.87%	4.73%
1-B	1.8983×10^{-9}	3.101	2.19%	4.76%
A-2	1.8615×10^{-9}	3.099	1.35%	4.82%

da/dN in mm/cycle and ΔK in $\text{MPa} \cdot \text{m}^{0.5}$

1-B, no significant effects were introduced due to use of a different first visible crack shape; in the combination B-2, the influence of a different second visible crack shape was not relevant. These results reinforce the robustness of the proposed approach. The average values of C and m ($C = 1.8629 \times 10^{-9}$ and $m = 3.101$) were considered the final predictions of the Paris law constants.

The final numerical values of C and m were used to carry out an entire simulation from the initial straight crack shape used in the experimental tests. Then, the numerical and experimental crack shapes were compared. This comparison was done through the difference d_i (depicted in Figure 4.24) which was calculated assuming that both crack shapes were overlapped at the symmetry line of the cross-section of the specimen. Figure 6.45 shows the evolution of the dimensionless variable d_i/r_i with the angle θ_i (being r_i the experimental radius) for the crack fronts X , 1, A, B, 2 and Y schematised in Figure 3.19b. As can be

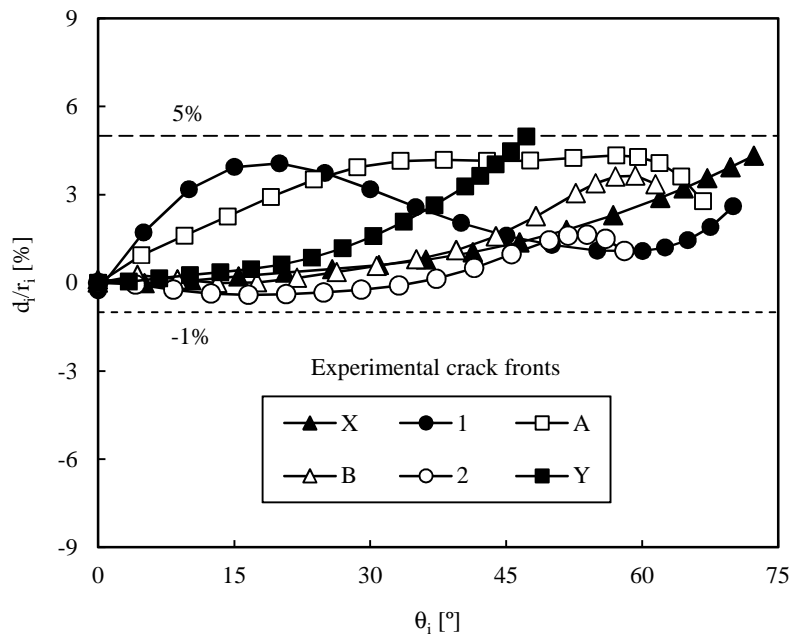


Figure 6.45. Evolution of d_i/r_i with θ_i for several experimental crack fronts (Branco, 2012d).

seen, the results obtained have well-defined limits that vary between -1% and 5%. Besides, although some exceptions are observed, it is possible to distinguish a dominant tendency for the curves in which the differences increase progressively towards the surface. Such results found in this study demonstrate that the mixed numerical-experimental technique proposed here is able to obtain the Paris law constants from materials in the form of round bars.

CHAPTER 7

CONCLUSIONS AND FUTURE RESEARCH

This chapter presents the main conclusions of the thesis and identifies some relevant topics that merit additional research.

NOMENCLATURE

ASTM	American Society of Testing and Materials
a	crack length
B	bending moment
C	Paris law constant
CM	Coffin-Manson
C(T)	compact tension specimen
FE	finite element
FEM	finite element method
IIW	International Institute of Welding
N	number of loading cycles
N_f	number of cycles to failure
$N_{0.5}$	number of cycles in which at the first time the crack reached a surface length of 0.5mm
m	Paris law exponent
M(T)	middle-crack tension specimen
R	stress ratio
S	applied stress
SEM	scanning electron microscopy
SWT	Smith, Watson and Topper
T	torsion moment

7.1. Conclusions

As outlined in the previous chapters, the present research aimed at studying the fatigue phenomenon from two different perspectives, i.e. by following experimental and numerical approaches. The experimental work consisted firstly of a full characterisation of the material in terms of microstructure, monotonic and cyclic stress-strain responses as well as in terms of fatigue ductility and fatigue strength properties. After that, the fatigue behaviour of severely notched specimens made of DIN 34CrNiMo6 high strength steel subjected to in-phase constant amplitude bending-torsion loading was tackled. The numerical work encompassed the development of fatigue crack growth software which was subsequently used to address different problems, such as the evaluation of the surface region in cracked bodies, the definition of a plane strain specimen for fatigue and fracture studies, and the determination of the Paris law constants from the analysis of crack front marks on fracture surfaces of small cross-section round bars.

Regarding the experimental work, the following conclusions can be drawn:

- The material exhibited a fine microstructure mainly composed of martensite and lower bainite. The average grain size obtained from the procedure described by the ASTM E112 standard (2010) was about 8 μm . As usual in this high strength steel, relatively high inclusions with sizes ranging from 2 to 30 μm were found;
- The monotonic response of the material was investigated from uniaxial tensile tests which were conducted according to the procedure described in the ASTM E8 (2011) standard. The stress-strain curve was characterised by a yield point elongation and considerable plastic deformation before fracture. The fracture surfaces revealed a mixed mechanism involving microvoid coalescence and cleavage;
- The elastic properties were evaluated using a mixed numerical-experimental technique. The first step encompassed the calculation of the experimental resonant frequencies, which were obtained applying the protocol described in the ASTM E1876 (2009) standard. After that, a finite element model relating the elastic constants to the resonant frequencies was developed from which the values of the Young's modulus and the Poisson's ratio were successfully determined;
- The low-cycle fatigue behaviour of the material was studied under fully-reversed strain-controlled conditions. The tests were conducted according to the procedure described in the ASTM E606 (2004) standard and aimed at obtaining the fatigue ductility and fatigue strength properties of the steel. A strain-softening phenomenon was observed throughout the entire life. The shape of the hysteresis loops exhibited an almost ideal Masing-type behaviour. The SEM micrographs evidenced transgranular crack propagation. At lower strain amplitudes, the initiation sites were dominated by cleavage-like facets whilst at higher strain amplitudes the initiation sites revealed a mixed of cleavage-like facets and ductile dimples;
- The fatigue behaviour of severely notched specimens subjected to different constant amplitude proportional loading paths was studied. The tests encompassed single bending, single torsion and in-phase combined bending-torsion loading and were performed under constant amplitude at stress

ratios close to zero. With respect to the last type of loading, three ratios of the bending moment (B) to the torsion moment (T) were defined, namely $B=2T$, $B=T$ and $B=2T/3$. The specimen geometries consisted of round bars with lateral U-shaped notches. The detection of crack initiation was carried out *in situ* with a digital monitoring system;

- A significant influence of the loading path on the surface crack trajectories was observed. In the absence of shear stress, the crack grows in a direction normal to the axis of the specimen. When the ratio of the shear stress to the normal stress increases, the surface crack trajectories tend to be more curved. These trajectories seem to be controlled by the distribution of the principal stresses at the notch. The numerical predictions based on this variable were very similar to those observed experimentally;
- Regarding the initiation sites, a strong effect of the loading path was also distinguished. In the presence of shear stresses, the crack tends to initiate closer to the curved edge of the notch, whilst in the absence of shear stresses or reduced levels of the ratio of the shear stress to the normal stress, the crack initiates in the centre of the notch. The most susceptible regions to crack initiation are those where the first principal stress achieves the maximum value. The predictions obtained with the FEM were very close to those observed in the experiments;
- The angle of the surface crack orientations at the initial stage of crack growth was also affected by the loading path. For single bending, it was normal to the specimen axis. In the other cases, it increased with the increase of the ratio of the shear stress to the normal stress. This angle orientation can be anticipated by the principal stress direction at the initiation site. The numerical predictions were practically the same to those found in the experimental tests;
- The fracture surfaces revealed a mechanism of multi-crack initiation. The cracks were nucleated from surface irregularities or surface defects that acted as local stress raisers making easier the fatigue crack initiation process. Due to the coalescence of neighbouring cracks, it was possible to distinguish several steps at the fracture surfaces. The SEM analysis denoted essentially ductile failure modes with evidence of local plastic deformation and transgranular fracture;
- A significant effect of the shear stress on the a-N curves (i.e. crack length versus fatigue life) and on the S-N curves (i.e. applied stress versus fatigue life) was found. Both curves show a significant reduction of the fatigue life with the shear stress amplitude. In relation to the a-N curves, derived in terms of surface crack length versus number of loading cycles, their slopes increased with the shear stress. With respect to the S-N curves, an opposite behaviour was distinguished;
- The local von Mises equivalent stress was adequate to correlate the resultant stress-strain states with the fatigue life. A very satisfactory linear correlation was found in a log-log scale between the equivalent stress and the fatigue life, regardless of the loading path. The design curve was created from the experimental data by applying the procedure recommended by the International Institute of Welding (IIW);
- The ratio of the number of cycles in which at the first time the crack reached a surface length of 0.5mm to the number of cycles to failure ($N_{0.5}/N_f$) varied between 42-75%. Such a ratio was similar for the various loading paths and ranged from 42-55% in about 70% of the cases studied;

- The fatigue life predictions were obtained using the well-known Coffin-Manson (CM) and Smith, Watson and Topper (SWT) models. The initiation lives were defined based on the El Haddad parameter. In a first stage, the theory of critical distances was applied. For higher lives, the two models gave very satisfactory results. However, for lower lives, both approaches were too conservative due to an unrealistic simulation of the stress-strain response at the notch tip. In a second stage, the strain energy density model was used to correct the stress-strain response at the notch tip. In both cases, the predictions for lower lives were considerably improved. Nonetheless, the predictions were on average conservative. In general, the SWT was more conservative than the CM model.

Regarding the numerical work, the main conclusions are the following:

- A new computer tool able to address in-plane fatigue crack growth propagation problems was developed. The software, named *Lynx*, incorporates an extensive range of situations, such as notched and unnotched rectangular bars with corner cracks, notched and unnotched round bars with surface cracks, notched and unnotched plates with surface cracks, and notched and unnotched plates with through cracks. Besides, this tool is able to compute automatically the transition from corner and surface cracks to through cracks;
- The calculation procedure consists of five steps cyclically repeated, i.e. generation of the FE mesh of the cracked body, calculation of the displacement field, calculation of the stress intensity factors at the crack front, calculation of the crack front advances and the resultant number of loading cycles, and definition of a new crack front. The main independent variables affecting the above-mentioned procedure were identified and optimised. After that, the procedure was successfully validated by comparing the predictions with results published by other authors. The crack front profiles and the stress intensity factors predicted here were in excellent agreement with those found in the literature;
- The extent of the surface region in cracked bodies was analysed using realistic crack shapes and stress triaxiality parameters. The main effects were caused by the specimen geometry, notch geometry and crack length. An intimate relation between crack shape and stress triaxiality was found. Based on the stress triaxiality curves, the crack front was divided into a surface region, a near-surface region and an interior region. According to the data collected, the surface region was lower than 3% of the crack front perimeter whilst the near-surface region varied from 3% to 30% of the crack front perimeter. The former is on average one order of magnitude lower than the latter. These two regions were successfully related to the stress concentration factors of the corresponding uncracked bodies by linear functions. Empirical two-constant equations were formulated to evaluate the extents of the surface and near-surface regions from the stress concentration factor, notch radius and specimen size;
- A plane strain specimen able to study different phenomena affected by the stress state was developed. The methodology adopted here was based on stress triaxiality parameters and on realistic crack shapes. The geometry consisted of a standard M(T) specimen with U-shaped grooves. The grooves were introduced to reduce the size of the plane stress surface regions. Since it is based on a standard geometry, the comparability of results is possible, which is an interesting aspect. Besides, it ensures

easiness of production and high reproducibility. A stress intensity factor solution obtained numerically using the FEM was proposed;

- A parallel study to define a plane strain specimen from straight crack shapes was conducted. The results demonstrated that without crack shape modelling the specimen required is thinner. Therefore, the geometry proposed based on realistic crack shapes is more conservative and remains appropriate to meet the pure plane strain state criterion in both cases;
- A mixed numerical-experimental technique capable of determining the Paris law constants from the analysis of crack fronts marks on fracture surfaces of small cross-section round bars was proposed. The technique comprises three main tasks. Firstly, an experimental test is performed in order to obtain, at least, two crack front profiles marked on the fracture surfaces and the number of cycles between them. Secondly, a 3D-FE fatigue crack growth technique able to predict the crack shape and fatigue life is created. Finally, the experimental data and the numerical predictions are compared to obtain the C and m constants. The former constant is determined by minimising the shape difference between the experimental and the predicted crack fronts. The latter constant is found by equalising both the experimental and numerical fatigue lives. The technique was successfully applied to 12mm-diameter and 190mm-long circular cross-section specimens made of S45 steel subjected to tension. The differences between the experimental and predicted C and m constants were less than 5% and 3%, respectively.

7.2. Future research

During the course of the present investigation, several issues were addressed. Nevertheless, there are a number of areas in which further research might be conducted. As in the previous section, the topics that merit additional research are divided into experimental and numerical work.

Regarding the experimental work, the suggestions are outlined below:

- The experimental tests carried out in this study were conducted under constant amplitude loading and at stress ratios close to zero. In order to better understand the damage accumulation process, it would be interesting to perform tests under variable amplitude loading as well as to use different stress ratios either under constant amplitude or variable amplitude loading;
- Although there have been used two geometries, for each loading path only a single specimen was tested. Thus, in order to better understand the stress concentration effect on the stress-strain response of the material at the notch tip, it would be interesting to conduct additional tests for specimens having different stress concentration factors or having alternative notch geometries;
- The El Haddad parameter (El Haddad, 1979) was calculated using reference values. The threshold stress intensity factor range was estimated from data available in the literature; the fatigue limit of the unnotched specimen was extrapolated from the results obtained experimentally at $R = -1$. In this sense, it would be interesting to perform specific tests to define these two material properties for the stress ratio used here;

- The stress-strain response at the notch tip used to predict the fatigue life was obtained using a simplified method based on linear elastic finite element analyses. Although the results obtained have been consistent, it would be preferable to develop a non-linear elastic-plastic model with isotropic and kinematic hardening to obtain more accurate stress-strain results. In fact, such a model has been already developed and all simulations have been already computed. Unfortunately, the analysis of results is taking place at the present moment and therefore the fatigue life predictions are not yet finished.

Concerning the numerical work, the possible future research is presented below:

- To date, *Lynx* was essentially designed to address in-plane fatigue crack growth problems. Therefore, a natural upgrade is to extend it to out-of-plane propagation. On the other hand, it is also desirable to include new in-plane problems, such as welded joints, pipes, pressure vessels, among others. In addition, new methods to estimate the stress intensity factor at the crack front can be implemented (in particular, energy-based methods). Besides, the development of other plug-in programs would be also interesting to make it compatible with more commercial FEM packages;
- Although the extent of the surface region in cracked bodies has been studied for a wide range of situations, a follow-up study is required to define the density of layers near the surface region to be incorporated into the fatigue crack growth models. Moreover, in order to broaden the scope of this study, it is recommended to analyse such a problem considering non-linear elastic-plastic models;
- In relation to the plane strain specimen and in order to better relate the different plane state criteria with the various phenomena affected by the stress state, it would be interesting to perform some experimental work to evaluate the performance of the proposed notched geometries in different circumstances;
- Regarding the determination of the Paris law constants, the fatigue crack front marks used in the calculations were performed for a stress ratio $R=0.1$. Therefore, crack closure is likely to exist at this stress ratio. In view of this fact, a numerical evaluation of the crack closure level would be interesting in order to be included into the fatigue crack growth models. In addition, it would be also interesting to test the proposed methodology with other materials and diameters as well as to extend it to other situations in which the standard procedure based on the well-known M(T) and C(T) specimens is not adequate.

REFERENCES

A

- Abreu L, Costa JD, Ferreira J (2007). Fatigue behaviour of AlMgSi tubular specimens subjected to bending-torsion loading. *International Journal of Fatigue* 31, 1327-1336.
- AHSS (Advanced High Strength Steel) Application Guidelines (2009). World Auto Steel, version 4.1.
- Andrews R, Brown M (1989). Elevated temperature out-of-phase fatigue behaviour of a stainless steel. *Biaxial and multiaxial fatigue*, EGF 3, Mechanical Engineering Publications, London, 641-658.
- Andrews J, Ellison E (1973). A testing rig for cycling at high biaxial strains. *Journal of Strain Analysis for Engineering Design* 8, 165-175.
- Antunes FV (1993). Use of finite element method in the calculation of stress intensity factors, Master Thesis, Department of Mechanical Engineering, University de Coimbra [in Portuguese].
- Antunes FV (1999). Influence of frequency, stress ratio and stress state on fatigue crack growth in nickel base superalloys at elevated temperature. PhD thesis, Department of Mechanical and Manufacturing Engineering, University of Portsmouth, United Kingdom.
- Antunes FV, Ferreira JAM, Branco CM, Byrne J (2000). Stress intensity factor solutions for corner cracks under mode I loading. *Fatigue and Fracture of Engineering Materials and Structures* 23, 81-90.
- Antunes FV, Ferreira JM, Branco CM, Byrne J (2001). Influence of stress state on high temperature fatigue crack growth in Inconel 718. *Fatigue and Fracture of Engineering Materials and Structures* 24, 127-135.
- Antunes FV, Ferreira JM, Costa JD, Capela C (2002). Fatigue life predictions in polymer particle composites. *International Journal of Fatigue* 24, 1095-1105.
- Antunes FV, Ramalho AL, Ferreira JM, Capela C, Reis P (2008). Determination of elastic constants by resonant technique: a sensitivity analysis. *Journal of Testing and Evaluation* 36, 89-99.
- Antunes FV, Branco R, Costa JD, Rodrigues D (2010). Plasticity induced crack closure in MT specimen: Numerical versus experimental. *Fatigue and Fracture of Engineering Materials and Structures* 33, 673-686.
- Antunes FV, Branco R, Rodrigues D (2011). Plasticity induced crack closure under plane strain conditions. *Key Engineering Materials* 465, 548-551.
- Anvari M, Scheider I, Thaulow C (2006). Simulation of dynamic ductile crack growth using strain-rate and triaxiality-dependent cohesive elements. *Engineering Fracture Mechanics* 73, 2210-2228.

- Armstrong P (1971). Measurement of Mechanical Properties, Techniques of Metals Research, Volume 5 (Part 2), Wiley, New York, 1971, 103.
- Armstrong P, Frederick C (1966). A mathematical representation of the multiaxial Bauschinger effect. CEGB Report RD/B/N731, Berkeley Nuclear Laboratories.
- ASM Handbook (2000). Properties and selection: irons, steels and high-performance alloys: high-strength structural and high-strength low-alloy steels. Volume 1, 391-446, ISBN: 0871703890.
- ASM Handbook (2000a). Properties and selection: irons, steels and high-performance alloys: Fatigue resistance of steels. Volume 1, 673-688, ISBN: 0871703890.
- ASTM E3 (2011). Standard guide for preparation of metallographic specimens. ASTM International, West Conshohocken, PA, DOI: 10.1520/E0003-11.
- ASTM E8 (2011). Standard test methods for tension testing of metallic materials. ASTM International, West Conshohocken, PA, DOI: 10.1520/E0008_E0008M-11.
- ASTM E112 (2010). Standard test methods for determining average grain size. ASTM International, West Conshohocken, PA, DOI: 10.1520/E0112-10.
- ASTM E399 (2009). Standard test method for linear-elastic plane-strain fracture toughness K_{IC} of metallic materials. ASTM International, West Conshohocken, PA, DOI: 10.1520/E0399-09E02.
- ASTM E606 (2004). Standard practice for strain-controlled fatigue testing. ASTM International, West Conshohocken, PA, DOI: 10.1520/E0606-04E01.
- ASTM E647 (2011). Standard test method for measurement of fatigue crack growth rates, ASTM International, West Conshohocken, PA, DOI: 10.1520/E0647-11E01.
- ASTM E739 (1998). Standard practice for statistical analysis of linear or linearized stress-life (S-N) and strain-life (ϵ -n) fatigue data, ASTM International, PA, DOI: 10.1520/E0739-91R98.
- ASTM E1049 (2011). Standard practices for cycle counting in fatigue analysis. ASTM International, West Conshohocken, PA, DOI: 10.1520/E1049-85R11E01.
- ASTM E1876 (2009). Standard test method for dynamic Young's modulus, shear modulus, and Poisson's ratio by impulse excitation of vibration, ASTM International, PA, DOI: 10.1520/E1876-09.
- Ayhan A (2011). Three-dimensional fracture analysis using tetrahedral enriched elements and fully unstructured mesh. International Journal of Solids and Structures 48, 492-505.

Ayorinde EO, Gibson RF (1993). Elastic constants of orthotropic composite materials using plate resonance frequencies classical lamination theory and an optimized three-mode Rayleigh formulation. *Composites Engineering* 3, 395-407.

B

Backstrom M, Marquis G (2001). A review of multiaxial fatigue of weldments: experimental results, design code and critical plane approaches. *Fatigue of Engineering Materials and Structures* 24, 279-291.

Baird L (1910). The elastic limits of iron and steel under cyclic variation of stress. *Philosophical Transactions of the Royal Society A* 210, 35-55.

Bakker A (1992). Three-dimensional constraint effects on stress intensity distributions in plate geometries with through-thickness cracks. *Fatigue and Fracture of Engineering Materials and Structures* 15, 1051-1069.

Ballard P, Dang Van K, Deperrois A, Papadopoulos IV (1995). High cycle fatigue and a finite element analysis. *Fatigue and Fracture of Engineering Materials and Structures* 18, 397-411.

Balthazar J, Malcher L (2007). A review on the main approaches for determination of the multiaxial high cycle fatigue strength. *Mechanics of Solids in Brazil*, Edited by Alves M and Mattos H, Brazilian Society of Mechanical Sciences and Engineering 63-80, ISBN 978-85-85769-30-7.

Bartlett M, Hudak Jr J (1990). The influence of frequency-dependent crack closure on corrosion fatigue crack growth. *Materials and Components Engineering*, Edited by Kitagawa H and Tanaka T, Volume III, 1783-1788.

Basquin OH (1910). The exponential law of endurance tests. *American Society for Testing and Materials, ASTM 10 (II)*, 625-630.

Bazant ZP, Estenssoro LF (1979). Surface singularity and crack propagation. *International Journal of Solids and Structures* 15, 405-426.

Benallal A, Marquis D (1987). Constitutive equations for nonproportional cyclic elasto-plastic viscoplasticity. *Transactions of the American Society of Mechanical Engineers, Journal of Engineering Materials and Technology* 109, 326-336.

Bentachfine S, Pluvinaige G, Gilgert J, Azari Z, Bouami D (1999). Notch effect in low cycle fatigue. *International Journal of Fatigue* 21, 421-430.

- Benthem JB (1977). State of stress at the vertex of a quarter-infinite crack in a half-space. *International Journal of Solids and Structures* 13, 479-492.
- Bernasconi A, Foletti S, Papadopoulos I (2008). A study on combined torsion and axial load fatigue limit tests with stresses of different frequencies. *International Journal of Fatigue* 30, 1430-1440.
- Berto F, Lazzarin P, Wang C (2004) Three-dimensional linear elastic distributions of stress and strain energy density ahead of V-shaped notched in plates of arbitrary thickness. *International Journal of Fracture* 127, 265-282.
- Borrego LP (2001). Fatigue crack growth under variable amplitude load in an AlMgSi alloy. PhD thesis, Department of Mechanical Engineering, University of Coimbra [in Portuguese].
- Boyer H (1986). Atlas of fatigue curves. ASM International, ISBN: 978-0-87170-214-2.
- Branco CM, Baptista J, Byrne J (1999). Crack growth under constant sustained load at elevated temperature in IN718 superalloy. *Materials at High Temperature* 16, 27-35.
- Branco R (2006). Numerical study of fatigue crack growth in M(T) specimens. MSc thesis, Department of Mechanical Engineering, University of Coimbra [in Portuguese].
- Branco R, Antunes FV (2008). Finite element modelling and analysis of crack shape evolution in mode-I fatigue Middle Cracked Tension specimens, *Engineering Fracture Mechanics* 75, 3020-3037.
- Branco R, Antunes FV, Martins RF (2008a). Modelling fatigue crack propagation in CT specimens, *Fatigue and Fracture of Engineering Materials and Structures* 31, 452-465.
- Branco R, Antunes FV, Rodrigues DM (2008b). Influence of through-thickness crack shape on plasticity induced crack closure. *Fatigue and Fracture of Engineering Materials and Structures* 31, 209-220.
- Branco R, Antunes FV, Martins Ferreira JA, Silva JM (2009). Determination of Paris Law constants with a reverse engineering technique, *Engineering Failure Analysis*, 16, 631-638.
- Branco R, Antunes FV, Costa JD, Barbosa J (2009b). Numerical modelling of fatigue crack growth in shafts under tension and bending. 3rd International Conference on Integrity Reliability and Failure (IRF'2009), University of Porto, FEUP, 20-24 July, Portugal.
- Branco R, Antunes FV, Costa JD (2009c). Influence of elastic constants on crack shape evolution in axles. 3rd International Conference on Integrity Reliability and Failure (IRF'2009), University of Porto, FEUP, 20-24 July, Portugal.

- Branco R, Silva JM, Infante V, Antunes F, Ferreira F (2010a). Using a standard specimen for crack propagation under plain strain conditions. *International Journal of Structural Integrity* 1, 332-343.
- Branco R, Antunes FV, Costa JD, Yang F, Kuang Z (2010b). Determination of the Paris law constants from crack shapes on fracture surfaces in round bars, *Advances in Mechanical Engineering Research*. Volume 1, Edited by David Malach, Nova Science Publishers, 1-14, USA, ISBN: 978-1-61761-111-0.
- Branco R, Antunes FV, Martins Ferreira JA, Silva JM (2011). Effect of residual stresses on crack shape of corner cracks at holes in nickel base superalloys. *Superalloys: Production, Properties and Applications*, Edited by Jeremy E. Watson, 1-24, Nova Science Publishers, USA, ISBN: 978-1-61209-536-3.
- Branco R, Antunes FV, Costa JD (2011a). Lynx: a user-friendly computer application for simulating fatigue growth of planar cracks using FEM. *Computer Applications in Engineering Education*, DOI:10.1002/cae.20578 (in press).
- Branco R, Antunes FV, Costa JD (2011b). Extent of surface region near corner points. 28th Meeting of Spanish Group of Fracture, 26, 637-642, 6-8 April, Gijón, Spain.
- Branco R, Antunes FV, Ricardo LCH, Costa JD (2012a). Extent of surface regions near corner points of notched cracked bodies subjected to mode-I loading. *Finite Elements in Analysis and Design* 50, 147-160.
- Branco R, Costa JD, Antunes FV (2012b). Low-cycle fatigue behaviour of 34CrNiMo6 high strength steel. *Theoretical and Applied Fracture Mechanics* 58, 28-34.
- Branco R, Antunes FV, Costa JD (2012c). Lynx: new tool to model mode-I fatigue crack propagation, 4th International Conference on Crack Paths (CP2012), 19-21 September, Gaeta, Italy.
- Branco R, Antunes FV, Costa JD, Yang F, Kuang Z (2012d). Determination of the Paris law constants in round bars from beach marks on fracture surfaces. *Engineering Fracture Mechanics* 96, 96-106.
- Branco R, Costa JD, Antunes FV (2012e). Multiaxial fatigue life prediction for lateral notched round bars made of 34CrNiMo6 high strength steel. *Fatigue Crack Growth: Mechanisms, Behavior and Analysis*. Edited by Ping Tang and Jim Leor Zhang, Nova Science Publishers, 273-292, USA, ISBN: 978-1-62081-599-1.
- Branco R, Antunes FV, Costa JD (2013). Notched M(T) specimen for plane strain studies. *International Journal of Fatigue*, DOI: 10.1016/j.ijfatigue.2013.01.011 (in press).

- Branco R, Antunes FV, Costa JD (2013a). Extent of the surface region in notched Middle Cracked Tension specimens. *Key Engineering Materials. Special Issue on Crack Growth Modelling*. Edited by M. H. Alibadi, pages 1-21 (accepted for publication).
- Bremberg D, Dhondt G (2008). Automatic crack insertion for arbitrary crack growth. *Engineering Fracture Mechanic* 75, 404-416.
- Brighenti R (2000). Axially-cracked pipes under pulsating internal pressure. *International Journal of Fatigue* 22, 559-567.
- Brown M, Miller K (1973). A theory for fatigue failure under multiaxial stress-strain conditions. *Proceedings of the Institute of Mechanical Engineers* 187, 745-755.
- Brown M, Miller K (1979). Initiation and growth of cracks in biaxial fatigue. *Fatigue of Engineering Materials and Structures* 1, 231-246.
- Brown M, Miller K (1982). Two decades of progress in the assessment of multiaxial low-cycle fatigue life. *Low-cycle fatigue and life prediction, ASTM STP 770*, 482-99.
- BS ISO 12108 (2002). *Metallic materials. Fatigue testing. Fatigue crack growth method*. British Standards Institution, London, ISBN 0-580-42962-8.
- Buch A (1974). Analytical approach to size and notch-size effects in fatigue of aircraft material specimens. *Materials Science and Engineering* 15, 75-85.
- Burande S, Sethuraman R (1999). Computational simulation of fatigue crack growth and demonstration of leak before break criterion. *International Journal of Pressure Vessels and Piping* 76, 331-338.
- Burton WS, Sinclair GB, Solecki JS, Swedlow JL (1984). On the implications for LEFM of the three-dimensional aspects in some crack/surface intersection problems. *International Journal of Fracture* 25, 3-32.

C

- Cailletaud G, Doquet V, Pineau A (1991). Cyclic multiaxial behaviour of an austenitic stainless steel: Microstructural observations and micromechanical modelling. *Fatigue Under Biaxial and Multiaxial loading*. European Structural Integrity Society, ESIS publication 10, 131-149.
- Camas D, Garcia-Manrique J, Gonzalez-Herrera A (2011). Numerical study of the thickness transition in bi-dimensional specimen cracks. *International Journal of Fatigue* 33, 921-928.

- Camas D, Garcia-Manrique J, Gonzalez-Herrera A (2012). Crack front curvature: Influence and effects on the crack tip fields in bi-dimensional specimens. *International Journal of Fatigue* 44, 41-50.
- Cao Y (2002). Three-dimensional finite element modelling of subsurface median crack in trilayer sandwiches due to contact loading. *Engineering Fracture Mechanics* 69, 729-743.
- Carpinteri A (1992). Elliptical-arc surface cracks in round bars. *Fatigue and Fracture of Engineering Materials and Structures* 15, 1141-1153.
- Carpinteri A (1993). Shape change of surface cracks in round bars under cyclic axial loading. *International Journal of Fatigue* 15, 21-26.
- Carpinteri A, Brighenti R (1996a). Part-through cracks in round bars under cyclic combined axial and bending loading. *International Journal of Fatigue* 18, 33-39.
- Carpinteri A, Brighenti R (1996b). Fatigue propagation of surface flaws in round bars: a three-parameter theoretical model. *Fatigue and Fracture of Engineering Materials and Structures* 19, 1471-1480.
- Carpinteri A, Brighenti R (1998). Circumferential surface flaws in pipes under cyclic axial loading. *Engineering Fracture Mechanics* 60, 383-396.
- Carpinteri A, Brighenti R, Spagnoli A (1998a). Part-through cracks in pipes under cyclic bending. *Nuclear Engineering and Design* 185, 1-10.
- Carpinteri A, Brighenti R, Spagnoli A (2000). Fatigue growth simulation of part-through flaws in thick-walled pipes under rotary bending. *International Journal of Fatigue* 22, 1-9.
- Carpinteri A, Brighenti R (2000a). A three-parameter model for fatigue behaviour of circumferential surface flaws in pipes. *International Journal of Mechanical Sciences* 42, 1255-1269.
- Carpinteri A, Brighenti R, Vantadori S (2003). Circumferential notched pipe with an external surface crack under complex loading. *International Journal of Mechanical Sciences* 45, 1929-1947.
- Carpinteri A, Brighenti R, Vantadori S (2004). A numerical analysis on the interaction of twin coplanar flaws. *Engineering Fracture Mechanics* 71, 485-499.
- Carpinteri A, Brighenti R, Huth H, Vantadori S (2005). Fatigue growth of a surface crack in a welded T-joint. *International Journal of Fatigue* 27, 59-69.
- Carpinteri A, Brighenti R, Vantadori S (2006). Notched shells with surface cracks under complex loading. *International Journal of Mechanical Sciences* 48, 638-649.

- Carpinteri A, Brighenti R, Vantadori S (2006a). Surface cracks in notched round bars under cyclic tension and bending. *International Journal of Fatigue* 28, 251-260.
- Carpinteri A, Brighenti R, Vantadori S, Viappiani D (2007). Sickle-shaped cracks in a round bar under complex mode-I loading. *Fatigue and Fracture of Engineering Materials and Structures* 30, 524-534.
- Carpinteri A, Vantadori S (2009). Sickle-shaped cracks in metallic round bars under cyclic eccentric axial loading, *International Journal of Fatigue* 31, 759-765.
- Carpinteri A, Brighenti R, Vantadori S (2010). Influence of the cold-drawing process on fatigue crack growth of a V-notched round bar, *International Journal of Fatigue* 32, 1136-1145.
- Caspers M, Mattheck C, Munz D (1990). Propagation of surface cracks in notched and unnotched rods. In: *Surface-crack growth: Models, experiments and structures*, ASTM STP 1060, American Society of Testing and Materials, 365-389.
- Cayón A, Alvarez JA, Gutiérrez-Solana F (2003). Influence of microstructure and triaxial stress states on hydrogen induced cracking. *Anales de Mecanica de la Fractura* 20, 273-278.
- Castro JT, Meggiolaro MA, Miranda AC, Wu H, Imad A, Benseddiq N (2012). Prediction of fatigue crack initiation lives at elongated notch roots using short crack concepts. *International Journal of Fatigue* 42, 172-182.
- Cazaud R (1953). *Fatigue of metals*. Chapman and Hall, London.
- Chaboche J, Dang Van K, Cordier G (1979). Modelization of the strain memory effect on the cyclic hardening of 316 stainless steel. SMIRT-5, Division L, Berlin.
- Chaboche J (2008). A review of some plasticity and viscoplasticity constitutive theories. *International Journal of Plasticity* 24, 1642-1693.
- Chan SK, Tuba IS, Wilson WK (1970). On the finite element method in linear fracture mechanics. *Engineering Fracture Mechanics* 2, 1-17.
- Chandrakanth, S, Pandey PC (1995). An isotropic damage model for ductile material. *Engineering Fracture Mechanics* 50, 457-465.
- Chen CR, Kolednik O, Heerens J, Fischer FD (2005). Three-dimensional modeling of ductile crack growth: Cohesive zone parameters and crack tip triaxiality. *Engineering Fracture Mechanics* 72, 2072-2094.

- Chen X, Gao Q, Sun X (1996). Low-cycle fatigue under non-proportional loading. *Fatigue and Fracture of Engineering Materials and Structures* 19, 839-854.
- Chu C, Conle F, Bonnen J (1993). Multiaxial stress-strain modeling and fatigue life prediction of SAE axle shafts. *Advances in Multiaxial Fatigue*, ASTM STP 1191, American Society for Testing and Materials, USA, 37-54.
- Chu C (1995). Fatigue damage calculation using the critical plane approach. *Journal of Engineering Materials and Technology* 117, 41-49.
- Citarella R, Cricrì G (2010). Comparison of DBEM and FEM crack path predictions in a notched shaft under torsion, *Engineering Fracture Mechanics* 77, 1730-1749.
- Clausmeyer H, Kussmaul K, Roos E (1991). Influence of stress state on the failure behaviour of cracked components made of steel. *Applied Mechanics Review* 44, 77-92.
- Coffin LF (1954). A study effects of cyclic thermal stresses on ductile metal. *Transactions of ASME* 76, 931-950.
- Cosmos/M (2001). User's manual, Cosmos/M 2.7, Structural Research and Analysis Corporation, 1st Edition, December.
- Costa JD, Ferreira JM, Ramalho AL (2001). Fatigue and fretting fatigue of ion-nitrided 34CrNiMo6 steel. *Theoretical and Applied Fracture Mechanics* 35, 69-79.
- Costa JD, Ferreira JM (1998). Effect of stress ratio and specimen thickness on fatigue crack growth of CK45. *Theoretical and Applied Fracture Mechanics* 30, 65-73.
- Costa JD (1991). Analysis of defect tolerance in aluminum alloys. PhD thesis. Department of Mechanical Engineering. University of Coimbra [in Portuguese].
- Couroneau N, Royer J (1998). Simplified model for the fatigue crack growth analysis of surface cracks in round bars under mode I. *International Journal of Fatigue* 20, 711-718.
- Couroneau N, Royer J (2000). Simplifying hypotheses for fatigue growth analysis of surface cracks in round bars under mode I. *Computers and Structures* 77, 381-389.
- Crossland B (1956). Effect of large hydrostatic pressures on torsional fatigue strength of an alloy steel. *International Conference on Fatigue Metals*. Institution of Mechanical Engineers, London, 138-149.

D

- Dang Van K (1973). Sur la résistance à la fatigue des métaux. Thèse de doctorat. Scientifique et Technologique l'Armement 47, 643 [in French].
- Dang Van K, Griveau B, Message O (1989). On a new multiaxial fatigue limit criterion: theory and application. *Biaxial and Multiaxial Fatigue*, EGF 3, Mechanical Engineering Publications, London, 479-496.
- Dang Van K, Cailletaud J, Douaron A, Lieurade H (1989a). Criterion for high-cycle fatigue failure under multiaxial loading. *Biaxial and Multiaxial Fatigue*, EGF 3, Mechanical Engineering Publications, London, 459-478.
- Dang Van K (1993). Macro-micro approach in high-cycle multiaxial fatigue. *Advances in Multiaxial Fatigue*, ASTM STP 1191, American Society for Testing and Materials, Palo Alto, USA, 120-130.
- Dang Van K (1999). Introduction to fatigue analysis in mechanical design by the multiscale approach. *High-Cycle Metal Fatigue in the Context of Mechanical Design*, Springer-Verlag, Vienna, 57-88.
- DeLorenzi H (1982). On the energy release rate and the J-Integral for 3-D crack configurations. *International Journal of Fracture* 19, 183-193.
- DeLorenzi H (1985). Energy release rate calculations by the finite element method. *Engineering Fracture Mechanics* 21, 129-143.
- Deobald LR, Gibson RF (1988). Determination of elastic constants of orthotropic plates by a modal analysis Rayleigh-Ritz technique. *Journal of Sound and Vibration* 124, 269-283.
- Deperrois A (1991). Sur le calcul de limites d'endurance des aciers. Thèse de Doctorat. Ecole Polytechnique, Paris [in French].
- Dhondt G (2005). Cyclic crack propagation at corners and holes. *Fatigue and Fracture of Engineering Materials and Structures* 28, 25-30.
- Díaz JA, Passarelli M, Berríos JA, Puchi-Cabrera ES (2002). Fatigue behavior of a 4340 steel coated with an electroless Ni-P deposit. *Surface and Coatings Technology* 49, 45-56.
- Ding X, He G, Chen C, Zhu Z, Liu X, Crepeau P (2007). A brief review of multiaxial high-cycle fatigue. *Metallurgical and Materials Transactions* 38B, 591-599.

Doong S, Socie D, Robertson I (1990). Dislocation substructures and non-proportional hardening. *Journal of Engineering Materials and Technology* 112, 456-464.

Doong S, Socie, D (1991). Constitutive modeling of metals under nonproportional cyclic loading. *Journal of Engineering Materials and Technology* 113, 23-30.

E

El Haddad MH, Topper TH, Smith KN (1979). Prediction of non propagating cracks. *Engineering Fracture Mechanics* 11, 573-584.

El Haddad MH, Dowling NF, Topper TH, Smith KN (1980). J-integral applications for short fatigue cracks at notches. *International Journal of Fracture* 16, 15-24.

Eliaz N, Sheinkopf H, Shemesh G, Artzi H (2005). Cracking in cargo aircraft main landing gear truck beams due to abusive grinding following chromium plating. *Engineering Failure Analysis* 12, 337-347.

Ellyin F, Valaire B (1982). High strain multiaxial fatigue. *Journal of Engineering Materials and Technology* 104, 165-173.

Ellyin F (1985). Effect of tensile-mean-strain on plastic strain energy and cyclic response. *Journal of Engineering Materials and Technology* 107, 119-125.

Ellyin F, Kujawski D (1987). Notch stress-strain prediction for elastic-plastic loading. *Res. Mechanica* 20, 177-190.

Ellyin F, Golos K, Xia Z (1988). Multiaxial fatigue damage criterion. *Journal of Engineering Materials and Technology* 110, 63-68.

Ellyin F, Kujawski (1989). Generalization of notch analysis and its extension to cyclic loading. *Engineering Fracture Mechanics* 32, 819-826.

Ellyin F, Golos K, Xia Z (1991). In-phase and out-of-phase multiaxial fatigue. *Journal of Engineering Materials and Technology* 113, 112-118.

Ellyin F, Xia Z (1993). A general theory of fatigue with application to out-of-phase cyclic loading. *Journal of Engineering Materials and Technology* 115, 411-416.

Ellyin F (1997). *Fatigue damage, crack growth and life prediction*. Chapman & Hall, First edition, ISBN 0-412-59600- 8.

Endo T, Morrow J (1969). Cyclic stress-strain and fatigue behavior of representative aircraft metals. *Journal of Materials* 4, 159-175.

ESA v4.0 (2000). ESACRACK user's manual. TOS-MCS/2000/41/In.

Espadafor F, Villanueva J, García M (2009). Analysis of a diesel generator crankshaft failure. *Engineering Failure Analysis* 16, 2333-2341.

Ewing JA, Humfrey JC (1903). The fracture of metals under repeated alternations of stress. *Philosophical Transactions of the Royal Society A* 200, 241-250.

F

Fallstrom K, Jonsson M (1991). A nondestructive method to determine material properties in anisotropic plates. *Polymer Composites* 12, 293-305.

Fan J, Peng X (1991). A physically based constitutive description for nonproportional cyclic plasticity. *Journal of Engineering Materials and Technology* 113, 254-262.

Farahmand B, Bockrath G, Glassco J (1997). *Fatigue and Fracture Mechanics of High Risk Parts: Application of LEFM & FMDM theory*. Chapman & Hall, ISBN: 0-412-12991-4.

Fatemi A, Socie D (1988). A critical plane approach to multiaxial fatigue damage including out-of-phase loading. *Fatigue and Fracture of Engineering Materials and Structures* 11, 149-165.

Fatemi A, Socie D (1989). *Damage mechanisms and life predictions*. Advances in Fatigue Science and Technology, NATO Advanced Study Institute, Series E: Applied Sciences, Klumer Academic Publishers 159, 877-890.

Fatemi A, Yang L (1998). Cumulative fatigue damage and life prediction theories: a survey of the state of the art for homogeneous materials. *International Journal of Fatigue* 20, 9-34.

Fatemi A, Shamsaei N (2011). Multiaxial fatigue: An overview and some approximation models for life estimation. *International Journal of Fatigue* 33, 948-958.

Favier E, Lazarus V, Leblond J (2006). Coplanar propagation paths of 3D cracks in infinite bodies loaded in shear, *International Journal of Solids and Structures* 43, 2091-2109.

Findley W (1958). *A theory for the effect of mean stress on fatigue of metals under combined torsion and axial load or bending*. Engineering Materials Research Laboratory, Division of Engineering, Brown University.

Fleck NA, Smith RA (1982). Crack closure - is it just a surface phenomenon? *International Journal of Fracture* 4, 157-159.

FRANC3D v1.14 (1999). Concepts and users guide. Cornell University.

FRANC3D v1.14 (1999b). Menu and dialog reference. Cornell University

Frederiksen PS (1995). Single-layer plate theories applied to the flexural vibration of completely free thick laminates. *Journal of Sound and Vibration* 186, 743-759.

Freed C.N., Krafft J.M. (1966). Effect of side grooving on measurements of plane strain fracture toughness. *Journal of Materials* 1, 770-790.

Freitas M, Li B, Santos J (2000). *Multiaxial Fatigue and Deformation: Testing and Prediction*. ASTM STP 1387, 139-156.

Fricke W (2003). Fatigue analysis of welded joints: state of development. *Marine Structures* 16, 185-200.

Frost N, Denton K (1962). Surface layer effects when comparing reversed direct stress and rotating bending fatigue limits of mild steel. *Metallurgia* 65, 287-290.

Frost NE, Marsh KJ, Pook LP (1999). *Metal Fatigue*. Oxford Engineering Science Series, Oxford University Press, ISBN 0-486-40927-9.

Fulland M, Sander M, Kullmer G, Richard HA (2008). Analysis of fatigue crack propagation in the frame of hydraulic press. *Engineering Fracture Mechanics* 75, 892-900.

G

Gadd C, Zmuda A, Ochiltree N (1945). Correlation of stress concentration with fatigue strength of engine components. Society of Automotive Engineers, Technical Paper 450227 53.

Garcés Y, Sánchez H, Berríos J, Pertuz A, Chitty J, Hintermann H, Puchi ES (1999). Fatigue behavior of a quenched and tempered AISI 4340 steel coated with an electroless Ni-P deposit. *Thin Solid Films* 355-356, 487-493.

Gardin C, Courtin S, Bézine G, Bertheau D, Ben Hadj Hamouda H (2007). Numerical simulation of fatigue crack propagation in compressive residual stress fields of notched round bars. *Fatigue and Fracture of Engineering Materials and Structures* 30, 231-242.

Garud YS (1981). Multiaxial fatigue: a survey of the state-of-the-art. *Journal of Testing and Evaluation* 9, 165-178.

- Garud YS (1981b). A new approach to the evaluation of fatigue under multiaxial loadings. *Journal of Engineering Materials and Technology* 103, 118-126.
- Gavete L, Michavila F, Díez, F (1989). A new singularity finite element in linear elasticity. *Computational Mechanics* 4, 361-371.
- Gerber WZ (1874). Calculation of the allowable stresses in iron structures (Bestimmung der zulässigen spannungen in eisen-constructionen). *Bayer Archit. Ing. Ver.* 6, 101-110.
- Gilchrist MD, Smith RA (1991). Finite element modelling of fatigue crack shapes. *Fatigue and Fracture of Engineering Materials and Structures* 6, 617-626.
- Glinka G (1985). Calculation of inelastic notch-tip strain-stress histories under cyclic loading. *Engineering Fracture Mechanics* 22, 839-854.
- Glinka G, Wang G, Plumtree A (1995). Mean stress effects in multiaxial fatigue. *Fatigue and Fracture of Engineering Materials and Structures* 18, 755-764.
- Golos K, Ellyin F (1987). Generalization of cumulative damage criterion to multilevel cyclic loading. *Theoretical and Applied Fracture Mechanics* 7, 169-176.
- Golos K, Ellyin F (1988). A total strain energy density theory for cumulative damage. *Journal of Pressure Vessel Technology* 110, 36-41.
- Goodman J (1899). *Journal of Mechanics Applied to Engineering*, 1st edition, Longman, London.
- Gough HJ (1924). *The fatigue of metals*. Scott, Greenwood & Son, London.
- Gough HJ, Pollard HV (1935). The strength of metals under combined alternating stress. *Proceedings of the Institute of Mechanical Engineers* 131, 3-18.
- Gough HJ, Pollard HV (1937). Properties of some materials for cast crankshafts, with special reference to combined alternating stresses. *Proceedings of the Institute of Automobile Engineers* 31, 821-893.
- Gough H, Pollard H, Clenshaw W (1951). Some experiments on the resistance of metals to fatigue under combined stresses. *Aero Research Council, R&M* 2522.
- Grange RA, Hribal CR, Porter LF (1977). Hardness of tempered martensite in carbon and low-alloys steels, *Metallurgical Transactions* 8A, 1775-1785.
- Griza S, Bertoni F, Zanon G, Reguly A, Strohaecker T (2009). Fatigue in engine connecting rod bolt due to forming laps. *Engineering Failure Analysis* 16, 1542-1548.

Grubisic V, Simbürger A (1976). Fatigue under combined out-of-phase multiaxial stresses. International Conference on Fatigue, Testing and Design. Society of Environmental Engineers, London, 27.1-27.8.

Guinea GV, Planas J, Elices M (2000). K_I evaluation by the displacement extrapolation technique. Engineering Fracture Mechanics 66, 243-255.

Guo W (1993) Elastoplastic three-dimensional crack border field I - Singular structure of the field. Engineering Fracture Mechanics 46, 93-104.

Guo W (1999). Three-dimensional analyses of plastic constraint for through-thickness cracked bodies. Engineering Fracture Mechanics 62, 383-407.

Guzmán C, Díaz N, Berríos JA, Pertuz A, Puchi Cabrera ES (2000). Fatigue properties of a SAE 4340 steel coated with a Nimet HP autocatalytic nickel deposit. Surface and Coatings Technology 133-134, 561-571.

H

Haddadi H, Bouvier S, Banu M, Maier C, Teodosiu C (2006). Towards an accurate description of the anisotropic behaviour of sheet metals under large plastic deformations: modelling, numerical analysis and identification. International Journal of Plasticity 22, 2226-2271.

Haigh B (1923). The thermodynamic theory of mechanical fatigue and hysteresis in metals. Report of the British Association for the Advancement of Science 358-368.

Hamada N, Sakane M (1997). High temperature nonproportional low cycle fatigue using fifteen loading paths. 5th International Conference on Biaxial/Multiaxial Fatigue. Edited by Macha E and Mróz Z, Technical University of Opole, Poland, 251-266.

Hardrath F, Ohman L (1953). A study of elastic and plastic stress concentration factors due to notches and fillets in flat plates, NASA TC1117.

Hardy S, Malik N (1992). A survey of post-Peterson stress concentration factor data. International Journal of Fatigue 14, 147

Harrop LP (1982). The optimum size of quarter-point crack tip elements. International Journal for Numerical Methods in Engineering 17, 1101-1103.

Harter JA (2002). AFGROW users guide and technical manual. Ohio: Air Vehicles Directorate, Air Force Laboratory, Wright-Patterson Air Force Base.

- Hellen TK (1975). On the method of virtual crack extension, *International Journal for Numerical Methods in Engineering* 9,187-207.
- Henry BS, Luxmoore AR (1997). The stress triaxiality constraint and the Q-value, as a ductile fracture parameter. *Engineering Fracture Mechanics* 57, 375-390.
- Heyder M, Kolk K, Kuhn G (2005). Numerical and experimental investigations of the influence of corner singularities on 3D fatigue crack propagation. *Engineering Fracture Mechanics* 72, 2095-2105.
- Heywood R (1962). *Designing against fatigue of metals*. Reinhold Publishing Corporation, New York.
- Hobbacher A (1996). *Recommendations for fatigue design of welded joints and components*. Abington Publishing [IIW Document XII-1966-03/XV-1127-03].
- Hosseini A, Mahmoud MA (1985). Evaluation of stress intensity factor and fatigue crack growth of surface cracks in bending plates. *Engineering Fracture Mechanics* 22, 957-974.
- Hou Chien-Yuan (2008). Simultaneous simulation of closure behaviour and shape development of fatigue surface cracks. *International Journal of Fatigue* 30, 1036-1046.
- Hou Chien-Yuan (2011). Simulation of surface crack shape evolution using the finite element technique and considering the crack closure effects. *International Journal of Fatigue* 33, 719-726.
- Hou J, Goldstraw M, Maan S, Knop M (2001). An evaluation of 3D crack growth using ZENCRACK. Department of Defence, Defence Science & Technology Organisation, DSTO Technical Report (DSTO-TR-1158).
- Huang DH, Thomas G (1971). Structure and mechanical properties of tempered martensite and lower bainite in Fe-Ni-Mn-C steels, *Metallurgical Transactions* 2, 1587-1598.
- Hutchinson J (1968). Singular behaviour at the end of a tensile crack in a hardening material. *International Journal of Physics and Solids* 16, 13-31.
- Hwang SF, Chang CS (2000). Determination of elastic constants of materials by vibration testing. *Composite Structures* 49, 183-190.

I

- Ince A, Glinka G (2011). A modification of Morrow and Smith-Watson-Topper mean stress correction models. *Fatigue and Fracture of Engineering Materials and Structures* 34, 854-867.

Ingraffea AR, Manu C (1980). Stress-intensity factor computation in three dimensions with quarter-point elements, *International Journal for Numerical Methods in Engineering* 15, 1427-1445.

Ioth T, Sakane M, Ohnami M, Socie D (1995). Nonproportional low-cycle fatigue criterion for type 304 stainless steel. *Transaction of the American Society of Mechanical Engineers, Journal of Engineering Materials and Technology* 117, 285-292.

Ioth T, Nakata T, Sakane M, Ohnami M (1997). Nonproportional low cycle fatigue of 6061 aluminum alloy under 14 strain paths. *Proceedings of 5th International Conference on Biaxial/Multiaxial Fatigue*. Edited by Macha E and Mróz Z, Technical University of Opole, Poland, 173-187.

Itoh T, Kameoka, M, Obataya Y (2004). A new model for describing a stable cyclic stress-strain relationship under non-proportional loading based on activation state of slip systems. *Fatigue and Fracture of Engineering Materials and Structures* 27, 957-966.

Iranpour M, Taheri F (2006) A study on crack front shape and the correlation between the stress intensity factors of a pipe subject to bending and a plate subject to tension. *Marine Structures* 19, 193-216.

Irwin G (1957). *Fracture*. Encyclopedia of Physics 4, Springer, Berlin.

J

Javidi A, Rieger U, Eichlseder W (2008). The effect of machining on the surface integrity and fatigue life, *International Journal of Fatigue* 30, 2050-2055.

Jiang Y, Kurath P (1997). Nonproportional cyclic deformation: critical experiments and analytical modelling. *International Journal of Plasticity* 13, 743-763.

Josefson B, Svensson T, Ringsberg J, Gustafsson T, Maré J (2000). Fatigue life and crack closure in specimens subjected to variable amplitude loads under plane strain conditions. *Engineering Fracture Mechanics* 66, 587-600.

K

Kakuno H, Kawada Y (1979). A new criterion of fatigue strength of a round bar subjected to combined static and repeated bending torsion. *Fatigue and Fracture of Engineering Materials and Structures* 2, 229-236.

Kanazawa K, Miller KJ, Brown MW (1977). Low-cycle fatigue under out-of phase loading conditions. *Journal of Engineering Materials and Technology* 99, 222-228.

- Kanazawa K, Miller KJ, Brown MW (1979). Cyclic deformation of 1% Cr-Mo-V steel under out-of-phase loads. *Fatigue of Engineering Materials and Structures* 2, 217-228.
- Kandil F, Brown (1982). Biaxial low-cycle fatigue fracture of 316 stainless steel at elevated temperatures. Book 280, The Metals Society, London, 213-210.
- Karolczuk A, Macha E (2005). A review of critical plane orientations in multiaxial fatigue failure criteria of metallic materials. *International Journal of Fracture* 134, 267-304.
- Kenmeugne B, Fotsing B, Anago G, Fogue M, Robert J, Kenne J (2012). On the evolution and comparison of multiaxial fatigue criteria. *International Journal of Engineering and Technology* 4, 37-46
- Kim Y-J, Kim J-S, Cho S-M (2004). 3-D constraint effects on J testing and crack tip constraint in M(T), SE(B), SE(T) and C(T) specimens: numerical study. *Engineering Fracture Mechanics* 71, 1203-1218.
- Kim J, Gao X, Srivatsan S (2004a). Modelling of void growth in ductile solids: effects of stress triaxiality and initial porosity. *Engineering Fracture Mechanics* 71, 379- 400.
- Kim K, Park J, Lee J (1999) Multiaxial fatigue under variable amplitude loads. *Transactions of the American Society of Mechanical Engineers, Journal of Engineering Materials and Technology* 121, 286-293.
- Kirkby WT, Forsyth PJE, Maxwell RJ (1980). Design against fatigue - current trends. *Aeronautical Journal* 84, 1-12.
- Kitagawa H, Takahashi S (1976). Applicability of fracture mechanics to very small cracks or the cracks in the early stage. 2nd International Conference on Mechanical Behaviour of Materials, Boston, 627-631.
- Klesnil M, Lukas P (1972). Effect of stress cycle asymmetry on fatigue crack growth. *Materials Science and Engineering* 9, 231-240.
- Koh SK (2002). Fatigue damage evaluation of a high pressure tube steel using cyclic strain energy density. *Pressure Vessels and Piping* 79, 791-798.
- Koh SK, Stephens RI (1991). Mean stress effect on low-cycle fatigue for high strength steel. *Fatigue and Fracture of Engineering Materials and Structures* 14, 413-428.
- Kolk K, Kuhn G (2006). The advanced simulation of fatigue crack growth in complex 3D structures. *Archive of Applied Mechanics* 76, 699-709.

Kotousov A, Wang CH (2002). Three dimensional stress constraint in an elastic plate with a notch. *International Journal of Solids and Structures* 39, 4311-4326.

Kotousov A, Lazzarin P, Berto F, Hardinga S (2010). Effect of the thickness on elastic deformation and quasi-brittle fracture of plate components. *Engineering Fracture Mechanics* 77, 1665-1681.

Krempf E, Lu H (1984). The hardening and rate dependence behavior of fully annealed AISI type 304 stainless steel under biaxial in-phase and out-of-phase strain cycling at room temperature. *Transactions of the American Society of Mechanical Engineers, Journal of Engineering Materials and Technology* 106, 376-382.

Krouse GN (1934). A high-speed fatigue testing machine and some tests of speed effect on endurance limit. *Proceedings of American Society for Testing and Materials* 34, 156-164.

Kuhn P, Hardraht H (1952). An engineering method for estimating the notch-size effect in fatigue tests on steel. NACA TN2805, Langley Aeronautical Laboratory, Washington.

Kujawski D, Ellyin F (1988). On the concept of cumulative fatigue damage. *International Journal of Fracture* 37, 263-278.

L

Landgraf R (1970). Achievement of high fatigue resistance in metals and alloys. American Society for Testing and Materials, ASTM STP-467, 3-36.

Landgraf R, Morrow JD, Endo J (1969). Determination of the cyclic stress-strain curve. American Society for Testing and Materials, *Journal of Materials* 4, 176-188.

Lanza G (1886). Strength of shafting subjected to both twisting and bending. *Transactions of American Society of Mechanical Engineers* 8, 130-144.

Lauwagie T, Sol H, Heylen W, Roebben G (2004). Determination of the in-plane elastic properties of the different layers of laminated plates by means of vibration testing and model updating. *Journal of Sound and Vibration* 274, 529-546.

Lazarus V (1999) Fatigue propagation path of 3D plane cracks under mode I loading. *Comptes Rendus de l'Académie des Sciences Paris, T327, Série IIb: 1319-1324.*

Lazarus V (2003). Brittle fracture and fatigue propagation paths of 3D plane cracks under uniform remote tensile loading. *International Journal of Fracture* 122, 23-46.

- Lazzarin P, Tovo R, Meneghetti G (1997). Fatigue crack initiation and propagation phases near notches in metals with low notch sensitivity. *International Journal of Fatigue* 19, 647-657.
- Le HN, Gardin C (2011). Analytical prediction of crack propagation under thermal cyclic loading inducing a thermal gradient in the specimen thickness - Comparison with experiments and numerical approach. *Engineering Fracture Mechanics* 78, 638–652
- Lee S (1985). A criterion for fully-reversed out-of-phase torsion and bending. *Multiaxial Fatigue*. American Society for Testing and Materials, ASTM STP 853, 553-568.
- Lee S (1989). Out-of-phase, combined bending and torsion fatigue of steels. *Biaxial and multiaxial fatigue*, EGF 3, Mechanical Engineering Publications, London, 621-634.
- Lee WS, Su TT (1999). Mechanical properties and microstructural features of AISI 4340 high-strength alloy steel under quenched and tempered conditions. *Journal of Materials Processing Technology* 87, 198-206.
- Lee WY, Lee JJ (2004) Successive 3D analysis technique for characterization of fatigue crack growth behaviour in composite-repaired aluminum plate. *Composite Structures* 66, 513-520.
- Lefebvre D, Ellyin F (1984). Cyclic response and inelastic strain energy in low cycle fatigue, *International Journal of Fatigue* 6, 9-15.
- Lemaitre J (1996). *A course on damage mechanics*. Springer, New York.
- Li F, Shih CF, Needleman A (1985). A comparison of methods for calculating energy release rates. *Engineering Fracture Mechanics* 21, 405-421.
- Li B, Reis M, Freitas M (2009). Comparative study of multiaxial fatigue damage models for ductile structural steels and brittle materials. *International Journal of Fatigue* 31, 1895-1906.
- Li B, Santos J, Freitas M (2000). A unified numerical approach for multiaxial. fatigue limit evaluation. *Mechanics of Structures and Machines* 28, 85-103.
- Li M, Stubbins JF (2002). Subsize specimens for fatigue crack growth rate testing of metallic materials. In: Sokolov MA, Landes JD, Lucas GE, editors. *Small specimen test techniques: fourth volume*, ASTM STP 1418. West Conshohocken, PA, ASTM International 321-335.
- Lin XB, Smith RA (1997). Shape growth simulation of surface cracks in tension fatigued round bars. *International Journal of Fatigue* 19, 461-469.

- Lin XB, Smith RA (1997a). An improved numerical technique for simulating the growth of planar fatigue cracks. *Fatigue and Fracture of Engineering Materials and Structures* 20, 1363-1373.
- Lin XB, Smith RA (1997b). Numerical analysis of fatigue growth of external surface cracks in pressurised cylinders, *International Journal of Pressure Vessels* 71, 293-300.
- Lin XB, Smith RA (1997c). Fatigue growth analysis of interacting and coalescing surface defects. *International Journal Fracture* 85, 283-299.
- Lin XB, Smith RA (1998). Fatigue shape analysis for corner cracks at fastener holes. *Engineering Fracture Mechanics* 59, 73-87.
- Lin XB, Smith RA (1998a). Fatigue growth simulation for cracks in notched and unnotched round bars. *International Journal of Mechanical Sciences* 5, 405-419.
- Lin XB, Smith RA (1999). Finite element modelling of fatigue crack growth of surface cracked plates. Part I: The numerical technique. *Engineering Fracture Mechanics* 63, 503-522.
- Lin XB, Smith RA (1999a). Finite element modelling of fatigue crack growth of surface cracked plates. Part II: Crack shape change. *Engineering Fracture Mechanics* 63, 523-540.
- Lin XB, Smith RA (1999b). Finite element modelling of fatigue crack growth of surface cracked plates. Part III: stress intensity factor and fatigue crack growth. *Engineering Fracture Mechanics* 63, 541-556.
- Lin XB, Smith RA (1999c). Shape evolution of surface cracks in fatigued round bars with a semicircular circumferential notch. *International Journal of Fatigue* 21, 965-973.
- Lin XB, Smith RA (2001). Numerical simulation of fatigue crack growth for corner cracks emanating from fastener holes. *Notch Effects in Fatigue and Fracture*, 271-287.
- Liu GR, Lam KY, Han X (2002). Determination of elastic constants of anisotropic laminated plates using elastic waves and a progressive neural network, *Journal of Sound and Vibration* 52, 239-259.
- Liu J (1999). Weakest link theory and multiaxial criteria. *European Structural Integrity Society* 25, 55-68.
- Liu K (1993). A method based on virtual strain-energy parameters for multiaxial fatigue life prediction. *Advances in Multiaxial Fatigue*. Edited by McDowell D and Ellis R. American Society for Testing and Materials STP 1191, Philadelphia, 67-84.
- Liu Y, Mahadevan S (2005). Strain-based multiaxial fatigue damage modelling. *Fatigue and Fracture of Engineering Materials and Structures* 28, 1177-1189.

Luke M, Varfolomeev I, Lütkepohl K, Esderts A (2011). Fatigue crack growth in railway axles: Assessment concept and validation tests. *Engineering Fracture Mechanics* 78, 714-730.

Lynch SP (2007). Progression markings, striations, and crack-arrest markings on fracture surfaces. *Materials Science and Engineering A*, 468–470, 74-80.

M

MacDonald BD, Pajot JJ (1990). Stress intensity factors for side-grooved fracture specimens. *Journal of Testing and Evaluation* 18, 281-285.

Macha E (1988). Generalization of strain criteria of multiaxial cyclic fatigue to random loadings. *Technical University of Opole* 23, 89-123.

Macha E (2001). A review on energy-based multiaxial fatigue failure criteria. *The Archive of Mechanical Engineering* 48, 71-101.

Macha E, Sonsino CM (1999). Energy criteria of multiaxial fatigue failure. *Fatigue and Fracture of Engineering Materials and Structures* 22, 1053-1070.

Mahmoud MA, Hosseini A (1986). Assessment of stress intensity factor and aspect ratio variability of surface cracks in bending plates. *Engineering Fracture Mechanics* 24, 897-913.

Maligno AR, Sajaratnam R, Leen SB, Williams EJ (2010). A three-dimensional (3D) numerical study of fatigue crack growth using remeshing techniques, *Engineering Fracture Mechanics* 77, 94-111.

Mamiya EN, Araújo JA (2002). Fatigue limit under multiaxial loadings: on the definition of the equivalent shear stress. *Mechanics Research Communications* 29, 141-151.

Manson SS (1954). Behaviour of materials under conditions of thermal stress. NACA TN-2933, National Advisory Committee for Aeronautics.

Mason W (1917). Alternating stress experiments. *Proceedings of Institution of Mechanical Engineers*, 121- 196.

Marder AR (1986). Heat-treated alloy steels, *Encyclopedia of Materials Science*. Pergamon Press and MIT Press, 2111-2116.

Masing G (1926). *Eigenspannungen und verfestigung beim messing*. 2nd International Congress of Applied Mechanics. Zurich: Orell Fussli Verlag, 332-335.

- Matake T (1977). An explanation on fatigue limit under combined stress. *Bulletin of The Japan Society of Mechanical Engineers* 20, 257-263.
- Matsuishi M, Endo T (1968). Fatigue of metals subjected to varying stress. *Preliminary Proceedings of the Kyushu District Meeting. The Japan Society of Mechanical Engineers* 37-40 [in Japanese].
- McDiarmid D (1991). A general criterion for high cycle multiaxial fatigue failure. *Fatigue and Fracture of Engineering Materials and Structures* 14, 429-453.
- McDiarmid D (1994). A shear stress based critical plane criterion of multiaxial fatigue failure for design and life prediction. *Fatigue and Fracture of Engineering Materials and Structures* 17, 1475-1485.
- McDowell DL (1985). A two surface model for transient nonproportional cyclic plasticity. Part I: development of appropriate equations. *Journal of Applied Mechanics* 52, 298-302.
- McIntyre ME, Woodhouse J (1988). On measuring the elastic and damping constants of orthotropic sheet materials. *Acta Metallurgica* 36, 1397-1416.
- Meggiolaro M, Castro J (2009). Evaluation of multiaxial stress-strain models and fatigue life prediction methods under proportional loading. *Mechanics of Solids in Brazil*, Edited by Mattos H and Alves M, *Brazilian Society of Mechanical Sciences and Engineering* 365-384, ISBN: 978-85-85769-43-7.
- Mejía I, Bedolla-Jacuinde A, Maldonado C, Cabrera JM (2011). Hot ductility behavior of a low carbon advanced high strength steel (AHSS) microalloyed with boron. *Materials Science and Engineering* 528A, 4468-4474.
- Melcon MA, Crichlow WJ, McCulloch AJ (1962). An engineering evaluation of methods for the prediction of fatigue life in airframe structures. *Technical Report ASD-TR-61-134*, Lockheed California Company.
- Mi Y, Aliabadi MH (1994). Three-dimensional crack growth simulation using BEM. *Computers and Structures* 52, 871-878.
- MIL-HDBK-5H (1988). *Military Handbook: Metallic materials and elements for aerospace vehicle structures*. Military Standardisation Handbook, Department of Defense, USA.
- Minner MA (1945). Cumulative damage in fatigue. *Journal of Applied Mechanics* 12, A159-A164.
- Mirone G (2007). Role of stress triaxiality in elastoplastic characterization and ductile failure prediction. *Engineering Fracture Mechanics* 74, 1203-1221.

- Molski K, Glinka G (1981). A method of elastic-plastic stress and strain calculation at a notch root. *Materials Science and Engineering* 50, 93-100.
- Moore HF, Jordan RL (1939). 5th International Congress for Applied Mechanics 188.
- Moore HF, Kommers JB (1927). *The fatigue of metals*. McGraw-Hill, New York.
- Morkovin D, Moore HF (1944). Third progress report on the effect of size of specimen on fatigue strength of three types of steel. *Proceedings of American Society for Testing and Materials* 42, 137-155.
- Morrow JD (1965). Cyclic plastic strain energy and fatigue of metals. *International Friction, Damping and Cyclic Plasticity*, American Society for Testing and Materials, ASTM STP 378, Philadelphia, 45-87.
- Moslemi H, Khoei A (2009). 3D adaptive finite element modeling of non-planar curved crack growth using the weighted superconvergent patch recovery method. *Engineering Fracture Mechanics* 76, 1703-1728.
- Mostovoy S., Crosley P.B., Ripling E.J. (1967). Use of crack-line-loaded specimens for measuring plane-strain fracture toughness. *Journal of Materials* 2, 661-681.
- Mowbray D (1980). A hydrostatic stress-sensitive relationship for fatigue under biaxial stress conditions. *Journal of Testing and Evaluation* 8, 3-8.
- Mroz Z (1967). On the description of anisotropic work hardening. *Journal of the Mechanics and Physics of Solids*. 15, 163-175.
- Murakami Y, Endo M (1994) Effects of defects, inclusions and in homogeneities on fatigue strength. *International Journal of Fatigue* 16, 163-182.
- Murakami T, Sato T (1983). Three-dimensional J-Integral calculation of part-through surface crack problems. *Computers and Structures* 17, 731-736.
- Murti V, Valliappan S (1986). A universal optimum quarter point element. *Engineering Fracture Mechanics* 25, 237-258.
- Murty YV, Morral JE, Kattamis TZ, Mehrabian R (1975). Initial coarsening of manganese sulfide inclusions. *Metallurgical and Materials Transactions* 6A, 2031-2039.

N

Narayana KB, Dattaguru B, Ramamurthy TS, Vijayakumar K (1994). A General procedure for modified crack closure integral in 3D problems with cracks. *Engineering Fracture Mechanics* 48, 167-176.

NASCRAC (1989). Manual. Failure Analysis Associates, Palo Alto, California, USA.

NASCRAC (1989b). Theory Manual, Failure Analysis Associates, Palo Alto, California, USA.

NASGRO v6.0 (2009). Fracture mechanics and fatigue crack growth analysis software. Reference manual.

Neuber (1968). Theory of stress concentration for shear-strained prismatical bodies with arbitrary non-linear stress-strain law. *Journal of Applied Mechanics* 28, 544-551

Neuber H (1958). *Theory of Notch Stresses: Principles for Exact Calculation of Strength with Reference to Structural form and Material*, Springer, Berlin, Germany, 1958.

Newman Jr JC, Raju IS (1981). An empirical stress intensity factor equation for the surface crack. *Engineering Fracture Mechanics* 15,185-192.

Newman Jr JC (1981a). A crack-closure model for predicting fatigue crack propagation under aircraft spectrum loading. *Methods and models for prediction of crack growth under random loading*, ASTM STP 748, 53-84.

Newman Jr JC, Raju IS (1984). Prediction of fatigue crack growth patterns and lives in three-dimensional cracked bodies. 6th International Conference on Fracture, New Delhi, India, December 4-10.

Nishiara T, Kawamoto M (1941). *The strength of metals under combined alternating bending and torsion*. College of Engineering, Volume 10, Kyoto Imperial University, Japan.

Nykänen TJ (1996). Fatigue crack growth simulations based on free front shape development. *Fatigue and Fracture of Engineering Materials and Structures* 19, 99-109.

O

O'dowd NP, Shih CF (1991). Family of crack-tip fields characterized by a triaxiality parameter - I: Structure of fields. *Journal of Mechanics and Physics of Solids* 39, 989-1015.

O'dowd NP, Shih CF (1992). Family of crack-tip fields characterized by a triaxiality parameter - II: Fracture Applications. *Journal of Mechanics and Physics of Solids* 40, 939-963.

O'Neil MJ (1970). A review of some cumulative damage theories. Australian Defence Scientific Service, Aeronautical Research Laboratories, Report 326, Melbourne, Australia.

Ohashi Y, Kawai M, Kaito M (1985). Inelastic behavior of type 316 stainless steel under non-proportional cyclic stressings at elevated temperature. Transactions of the American Society of Mechanical Engineers, Journal of Engineering Materials and Technology 107, 101-109.

Ohno N (1982). Constitutive model of cyclic plasticity with a nonhardening strain region. Transactions of the American Society of Mechanical Engineers, Journal of Applied Mechanics 49, 721-726.

Ostash O, Panasyuk V (2001). Fatigue process zone at notches. International Journal of Fatigue 23, 627-636.

P

Palmgren A (1945). Ball and roller bearing engineering. Translated by G. Palmgren and B. Ruley. SKF Industries, Philadelphia, 82-83.

Pang H (1993). Fatigue crack growth and coalescence of surface cracks. 12th conference offshore mechanics arctic engineering, 485-491.

Pantano M, Espinosa H, Pagnotta L (2012) Mechanical characterization of materials at small length scales. Journal of Mechanical Science and Technology 26, 545-561.

Papadopoulos I (1987). Fatigue polycyclique des métaux: une nouvelle approche. Thèse de doctorat. Ecole Nationale des Ponts et Chaussées, Paris, France.

Papadopoulos I, Dang Van K (1988). Sur la nucleation des fissures en fatigue polycyclique sous chargement multiaxial. Archives of Mechanics 40, 759-774.

Papadopoulos I (1995). A high-cycle fatigue criterion applied in biaxial and triaxial out-of-phase stress conditions. Fatigue and Fracture of Engineering Materials and Structures 18, 79-91.

Papadopoulos I, Davoli P, Gorla C, Filippini M, Bernasconi A (1997). A comparative study of multiaxial high-cycle fatigue criteria for metals. International Journal of Fatigue 19, 219-235.

Papadopoulos I (1998). Critical plane approaches in high-cycle fatigue: on the definition of the amplitude and mean value of shear stress acting on the critical plane. Fatigue and Fracture of Engineering Materials and Structures 21, 269-285.

Papadopoulos I (2001). Long life fatigue under multiaxial loading. International Journal of Fatigue 23, 831-849.

- Pape J, Neu R (2007). A comparative study of the fretting fatigue behavior of 4340 steel and PH 13-8 Mo stainless steel. *International Journal of Fatigue* 29, 2219-2229.
- Park J, Nelson D (2000). Evaluation of an energy-based approach and a critical plane approach for predicting constant amplitude multiaxial fatigue life. *International Journal of Fatigue* 22, 23-39.
- Parks D (1974). A stiffness derivative finite element technique for determination of crack tip stress intensity factors. *International Journal of Fracture* 10, 487-502.
- Peterson R (1959). *Metal Fatigue*, Edited by Sines G and Waisman J, McGraw-Hill, New York.
- Pippan R, Kolednik O, Lang M (1994). A mechanism for plasticity-induced crack closure under plane strain conditions. *Fatigue and Fracture of Engineering Materials and Structures* 17, 721-726.
- Pluvinage G (1997). Notch effect in high cycle fatigue. *Advances in fracture research. Fatigue of metallic and non-metallic materials and structures. 9th International Conference on Fracture (ICF9)* 3, 1239-1250.
- Pluvinage G (1997a). Application of notch fracture mechanics to fracture emanating from stress concentrators. *Advances in Computational Engineering Congress of Computational Engineering Sciences*, 213-218.
- Pluvinage G (1998). Fatigue and fracture emanating from notch; the use of the notch stress intensity factor. *Nuclear Engineering and Design* 185, 173-184.
- Pommier S (2002). Plain strain crack closure and cyclic hardening. *Engineering Fracture Mechanics* 69, 25-44.
- Pook LP (1994). Some implications of corner point singularities. *Engineering Fracture Mechanics* 48, 367-378.
- Poursaeidi E, Salavatian M (2009). Fatigue crack growth simulation in a generator fan blade. *Engineering Failure Analysis* 16, 888-898.
- Puchi-Cabrera ES, Staia H, Quinto DT, Villalobos-Gutiérrez C, Ochoa-Pérez E (2007). Fatigue properties of a SAE 4340 steel coated with TiCN by PAPVD. *International Journal of Fatigue* 29, 471-480.
- Puigh RJ, Bauer RE, Ermi AM, Chin BA (1981). Miniaturized fatigue crack growth specimen technology and results. *Journal of Nuclear Materials* 103-104, 1501-1504.

Q

Qylafku G, Azari Z, Gjonaj M, Pluvinage G (1998). On the fatigue failure and life prediction for notched specimens. *Materials Science* 34, 604-618.

Qylafku G, Azari Z, Kadi N, Gjonaj M, Pluvinage G (1999). Application of a new model proposal for fatigue life prediction on notches and key-seats. *International Journal of Fatigue* 21, 753-760.

R

Rabb R (1996). Fatigue failure of a connecting rod. *Engineering Failure Analysis* 3, 13-28.

Radovic M. (2004). Comparison of different experimental techniques for determination of elastic properties of solids, *Materials Science and Engineering* 368A, 56-70.

Ramberg W, Osgood WR (1943). Description of stress-strain curves by three parameters. NACA TN 902, National Advisory Committee for Aeronautics.

Ransom, JT (1954). The effect of inclusions on the fatigue strength of SAE 4340 steels. *Transactions of the American Society of Metals* 46, 1254-1269.

Ranson JT, Mehl RF (1952). The anisotropy of the fatigue properties of SAE 4340 steel forgings. *Proceedings of American Society for Testing and Materials* 52, 779-786.

Rébillat M, Boutillon X (2011). Measurement of relevant elastic and damping material properties in sandwich thick plates. *Journal of Sound and Vibration* 330, 6098-6121.

Rice J (1968). A path independent integral and approximate analysis of strain concentration by notches and cracks. *Journal of Applied Mechanics* 10, 487-502.

Richard HA, Fulland M, Sander M, Kullmer G (2005). Fracture in a rubber-sprung railway wheel, *Engineering Failure Analysis* 12, 986-999.

Richard HA, Sander M, Fulland M, Kullmer G (2008). Development of fatigue crack growth in real structures, *Engineering Fracture Mechanics* 75, 331-340.

Richard HA, Sander M, Schramm B, Kullmer G, Wirxel M (2012). Fatigue crack growth in real structures. *International Journal of Fatigue* (in press).

Roeck G, Wahab M (1995). Strain energy release rate formulae for 3D finite elements. *Engineering Fracture Mechanics* 50, 569-580.

Roy M, Sumpter J, Timbrell C, Wiehahn M (2005). Stress intensity factors for cracked plates under out-of-plane bending, 18th Annual Worldwide ABAQUS Users' Conference, Stockholm, Sweden, May 18-20.

Rozumek D, Lachowicz C, Macha E (2010). Analytical and numerical evaluation of stress intensity factor along crack paths in the cruciform specimens under out-of-phase cyclic loading. *Engineering Fracture Mechanics* 77, 1808-1821.

Rybicki E, Kanninen M (1977). A finite element calculation of stress intensity factors by modified crack closure integral. *Engineering Fracture Mechanics* 9, 931-938.

S

Savković M, Gašić M, Petrović D, Zdravković N, Pljakić R (2012). Analysis of the drive shaft fracture of the bucket wheel excavator. *Engineering Failure Analysis* 20, 105-117.

Schijve J (1980). Stress gradients around notches. *Fatigue and Fracture of Engineering Materials and Structures* 3, 325-338.

Schijve J (1998). Fatigue specimens for sheet and plate material. *Fatigue and Fracture of Engineering Materials and Structures* 21, 347-357.

Schöllmann M, Richard HA (1999). FRANC/FAM - a software system for the prediction of crack propagation. *Journal of Structural Engineering* 26, 39-48.

Schöllmann M, Fulland M, Richard HA (2003). Development of a new software for adaptive crack growth simulations in 3D structures. *Engineering Fracture Mechanics* 70, 249-268.

Sedmak A, Savovic N, Pavisic M (1992) ESIS Recommendations for use of finite element method in fracture mechanics. 9th European Conference on Fracture (ECF9), Bulgaria, Reliability and Structural Integrity of Advanced Materials, Ed. by Sedmak S, Sedmak A, Ruzić A, EMAS.

Sehitoglu H, Sun W (1991). Modelling of plane strain fatigue crack closure. *ASME Journal of Engineering Materials and Technology* 113, 31-40.

Sekine H, Yan B, Yasuho T (2005). Numerical simulation study of fatigue crack growth behaviour of cracked aluminum panels repaired with a FRP composite patch using combined BEM/FEM. *Engineering Fracture Mechanics* 75, 2549-2563.

Ševčík M, Hutař P, Zouhara M, Náhlík L (2012). Numerical estimation of the fatigue crack front shape for a specimen with finite thickness. *International Journal of Fatigue* 39, 75-80.

- Serra A, Branco R, Costa JD, Antunes FV (2012). Fatigue behaviour of lateral notched round bars under torsion-bending loading. 13th Portuguese Conference on Fracture, 2-3 February, 107-112, Coimbra, Portugal.
- Ševčík M, Hutar P, Zouhar M, Náhlík L (2012). Numerical estimation of the fatigue crack front shape for a specimen with finite thickness. *International Journal of Fatigue* 39, 75-80.
- Shang D, Wang D, Li M, Yao W (2001). Local stress-strain field intensity approach to fatigue life prediction under random cyclic loading. *International Journal of Fatigue* 23, 903-910.
- She C, Guo W (2007). The out-of-plane constraint of mixed-mode cracks in thin elastic plates. *International Journal of Solids and Structures* 44, 3021-3034.
- Shi J, Chopp D, Lua J, Sukumar N, Belytschko T (2010). Abaqus implementation of extended finite element method using a level set representation for three-dimensional fatigue crack growth and life predictions, *Engineering Fracture Mechanics* 77, 2840-2863.
- Shih CF, Moran B, Nakamura T (1986). Energy release rate along a three-dimensional crack front in a thermally stressed body. *International Journal of Fracture* 30, 79-102.
- Shih Y, Chen J (1997). Analysis of fatigue crack growth on a cracked shaft. *International Journal of Fatigue* 19, 477-485.
- Shin CS, Cai CQ (2004). Experimental and finite element analyses on stress intensity factors of an elliptical surface cracks in a circular shaft under tension and bending. *International Journal of Fracture* 129, 239-264.
- Shin CS, Cai CQ (2007). Evaluating fatigue crack propagation properties using a cylindrical rod specimen. *International Journal of Fatigue* 29, 397-405.
- Shin CS, Liu SW CQ (2012). Evaluating fatigue crack propagation properties using miniature specimens. *International Journal of Fatigue* 43, 105-110.
- Shivakumar K, Tan P, Newman Jr J (1988). A virtual crack-closure technique for calculating stress intensity factors for cracked three dimensional bodies. *International Journal of Fracture* 36, R43-R50.
- Siebel E, Stieler M (1955). Significance of dissimilar stress distributions for cycling loading. *VDI-Zeitschrift* 97, 121-126 [in German].

- Sih GC, Jeong DY (2004). Hysteresis loops predicted by isoenergy density theory for Polycrystals. Part I: Fundamentals of non-equilibrium thermal–mechanical coupling effects. *Theoretical and Applied Fracture Mechanics* 41, 233-266.
- Sih GC, Jeong DY (2004a). Hysteresis loops predicted by isoenergy density theory for Polycrystals. Part II: Cyclic heating and cooling effects predicted from nonequilibrium theory for 6061-T6 aluminum, SAE 4340 steel and Ti–8Al–1Mo–1V titanium cylindrical bars. *Theoretical and Applied Fracture Mechanics* 41, 267-289.
- Sines G (1959). Behavior of metals under complex static and alternating stresses. *Metal Fatigue*, Edited by Sines G and Waisman J, McGraw-Hill, New York, 145-169.
- Sines G, Ohgi G (1981). Fatigue criteria under combined stresses or strains. *Journal of Engineering Materials and Technology* 103, 82-90.
- Sirin SY, Sirin K, Kaluc E (2008) Effect of the ion nitriding surface hardening process on fatigue behavior of AISI 4340 steel. *Materials Characterization* 59, 351-358.
- Smith RA, Miller K (1977). Fatigue cracks at notches. *International Journal of Mechanical Sciences* 19, 11-22.
- Smith RA, Cooper JF (1989). A finite element model for the shape development of irregular planar cracks. *International Journal of Pressure Vessels and Piping* 36, 315-326.
- Smith RW, Hirschberg MH, Manson SS (1963). Fatigue behaviour of materials under strain cycling in low and intermediate life range, NACA TN D-1574, National Advisory Committee for Aeronautics.
- Smith R, Watson P, Topper T (1970). A stress-strain parameter for the fatigue of metals. *Journal of Materials* 5, 767-778.
- Sneddon IN (1946). The distribution of stress in the neighbourhood of a crack in an elastic solid. *Proceedings of the Royal Society of London. Series A* 187, 229-260.
- Socie D.F (1980). Fatigue life estimation techniques. Technical Report, 145, Electro General Corporation.
- Socie, D (1987). Multiaxial fatigue damage models. *Journal of Engineering, Materials and Technology* 109, 293-298.
- Socie D, Marquis G (2000). *Multiaxial Fatigue*. Society of Automotive Engineers, ISBN: 0-7680-0453-5.
- Sokolnikoff IS (1956). *Mathematical Theory of Elasticity*, McGraw-Hill.

Spievak L, Wawrzynek P, Ingraffea A, Lewicki G (2001). Simulating fatigue crack growth in spiral bevel gears. *Engineering Fracture Mechanics* 68, 53-76.

Sriharsha HK, Pandey RK, Chatterjee S (1999). Towards standardizing a sub-size specimen for fatigue crack propagation behaviour of a nuclear pressure vessel steel. *Engineering Fracture Mechanics* 64, 607-624.

Suresh S, Ritchie RO (1982). Mechanistic dissimilarities between environmentally influenced fatigue-crack rates in lower strength steels, *Metal Science* 16, 592-538.

Suresh S (1998). *Fatigue of Materials*. Cambridge University Press, 2nd Edition, ISBN: 9780521578479.

Susmel S, Taylor D (2011). The Theory of Critical Distances to estimate lifetime of notched components subjected to variable amplitude uniaxial fatigue loading. *International Journal of Fatigue* 33, 900-911.

Swift HW (1952). Plastic instability under plane stress. *Journal of Mechanical and Physics of Solids* 1, 1-18.

T

Tada H, Paris PC, Irwin G (1973). *The stress analysis of cracks handbook*. Del Research Corporation, Missouri, USA.

Taleb L, Hauet A (2009). Multiscale experimental investigations about the cyclic behavior of the 304L SS. *International Journal of Plasticity* 25, 1359-1385.

Tanaka K (1983). Engineering formulate for fatigue strength reduction due to crack-line notches. *International Journal of Fracture* 22, 39-45.

Tanaka E (1994). A nonproportionality parameter and a cyclic viscoplastic constitutive model taking into account amplitude dependence and memory effects of isotropic hardening. *European Journal of Mechanics, A/Solids* 13, 155-173.

Tanaka E, Murakami S, Ooka M (1985a). Effects of plastic strain amplitudes on non-proportional cyclic plasticity. *Acta Mechanica* 57, 167-182.

Tanaka E, Murakami S, Ooka M (1985b). Effects of strain path shapes on nonproportional cyclic plasticity. *Journal of Mechanics of Physics and Structures* 33, 559-575.

Tartaglia J, Hayrynen K (2012). A Comparison of fatigue properties of austempered versus quenched and tempered 4340 steel, *Journal of Materials Engineering and Performance* 21, 1008-1024.

Tartaglia J, Lazzari K, Hui G, Hayrynen K (2008). A comparison of mechanical properties and hydrogen embrittlement resistance of austempered vs quenched and tempered 4340 steel. *Metallurgical and Materials Transactions* 39A, 559-576.

Taylor D (1999). Geometrical effects in fatigue: a unifying theoretical model. *International Journal of Fatigue* 21, 413-420.

Taylor D (2008). The theory of critical distances. *Engineering Fracture Mechanics* 75, 1696-1705

Timbrell C, Cook G. 3D FE fracture mechanics analysis for industrial applications. Zentech International Limited, UK.

Ting J, Lawrence F (1993). A crack closure model for predicting the threshold stresses of notches. *Fatigue and Fracture of Engineering Materials and Structures* 16, 93-114.

Tong J, Byrne J, Hall R, Aliabadi MH (1997). A comparison of corner notched and compact tension specimens for high temperature fatigue testing. In: *Proc. Conference Engineering Against Fatigue*, 17-21 March, University of Sheffield, United Kingdom.

Topper TH, Sandor BI, Morrow J (1969). Cumulative damage under cyclic plastic strain control. *Journal of Materials* 4, 189-99.

Toribio J, Matos JC, González B, Escuadra J (2009). Numerical modelling of crack shape evolution for surface flaws in round bars under tensile loading. *Engineering Failure Analysis* 16, 618-630.

Toribio J, Matos JC, González B, Escuadra J (2011). Compliance evolution in round cracked bars under tensile fatigue. *Engineering Fracture Mechanics* 78, 3243-3252.

Trattnig G, Antretter T, Pippan R (2008). Fracture of austenitic steel subject to a wide range of stress triaxiality ratios and crack deformation modes. *Engineering Fracture Mechanics* 75, 223-235.

U

Ural A, Heber G, Wawrzynek P, Ingraffea A, Lewicki D, Neto J (2005). Three-dimensional, parallel, finite element simulation of fatigue crack growth in a spiral bevel pinion gear. *Engineering Fracture Mechanics* 72, 1148-1170.

V

Van Stone RH, Cox TB, Low JR, Psioda JA (1985). Microstructural aspects of fracture by dimple rupture. *International Materials Reviews* 30, 157-179.

Vosikivsky O (1979). The effect of stress ratio on fatigue crack growth rates in steels. *Engineering Fracture Mechanics* 11, 595-602.

W

Wang C, Brown M (1993). A path-independent parameter for fatigue under proportional and nonproportional loading. *Fatigue and Fracture of Engineering Materials and Structures* 16, 1285-1298.

Wang C, Brown M (1996). Life prediction techniques for variable amplitude multiaxial fatigue. Part 1: theories. *Journal of Engineering Materials and Technology* 118, 367-370.

Wang B, Hu N, Kurobane Y, Makino Y, Lie ST (2000). Damage criterion and safety assessment approach to tubular joints. *Engineering Structures* 22, 424-434.

Wang Z, Zhao S (1992). *Fatigue design*, Mechanical Industry Publisher.

Wang Y, Yao W (2004). Evaluation and comparison of several multiaxial fatigue criteria. *International Journal of Fatigue* 26, 17–25.

Weber W, Steinmann P, Kuhn G (2008). Precise 3D crack growth simulations. *International Journal of Fracture* 149, 175-192.

Webster GA, Ainsworth RA (1994). *High temperature component life assessment*. Ed. Chapman Hall, United Kingdom.

Witek L (2006). Failure analysis of the wing-fuselage connector of an agricultural aircraft. *Engineering Failure Analysis* 13, 572-581.

Wöhler A (1871). Tests to determine the forces acting on railway carriage axles and the capacity of resistance of the axles. *Engineering*, 11.

Wu Z (2006). The shape of a surface crack in a plate based on a given stress intensity factor distribution. *Pressure Vessels and Piping* 83, 168-180.

Wu Z (2006a). On the through-thickness crack with a curve front in center-cracked tension specimens. *Engineering Fracture Mechanics* 73, 2600-2613.

Y

Yang FP, Kuang Z., Shlyannikov VN (2006). Fatigue crack growth for straight-fronted edge crack in a round bar, *International Journal of Fatigue* 28, 431-437.

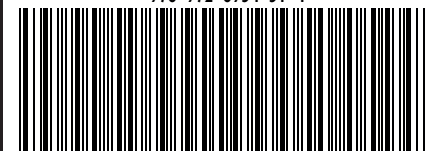
- Yang Z (2009). Stress and strain concentration factors for tension bars of circular cross-section with semicircular groove. *Engineering Fracture Mechanics* 76, 1683-1690.
- Yao W (1993). Stress field intensity approach for predicting fatigue life. *International Journal of Fatigue* 15, 243-245.
- Yao W, Kaiquan X, Gu Y (1995). On the fatigue notch factor, K_f . *International Journal of Fatigue* 17, 245-251.
- Yngvesson M, Nilsson F (1999). Fatigue crack growth of surface cracks under non-symmetric loading. *Engineering Fracture Mechanics* 63, 375-393.
- Yokobori Y, Yamanouchi H, Yamamoto S (1965). Low cycle fatigue of thin-walled hollow cylinder specimens of mild in uniaxial and torsional tests at constant strain amplitude. *International Journal of Fracture Mechanics* 1, 3-13.
- You B, Lee S (1996). A critical review on multiaxial fatigue assessments of metals. *International Journal of Fatigue* 18, 235-244.
- Yu M, DuQuesnay D, Topper T (1988). Notch fatigue behaviour of SAE1045 steel. *International Journal of Fatigue* 10, 109-116.
- Yu P, She C, Guo W (2010). Equivalent thickness conception for corner cracks. *International Journal of Solids and Structures* 47, 2123-2130.
- Yu P, Guo W (2012). An equivalent thickness conception for prediction of surface fatigue crack growth life and shape evolution. *Engineering Fracture Mechanics* 93, 65-74.
- Yu Z, Xu X (2008). Failure analysis of connecting bolts and location pins assembled on the plate of main-shaft used in a locomotive turbocharger. *Engineering Failure Analysis* 15, 471-479.
- Yu Z, Xu X (2009). Failure analysis of a locomotive turbocharger main-shaft. *Engineering Failure Analysis* 16, 495-502.

Z

- Zencrack User's Manual v7.5 (2007). Zentech International Limited, United Kingdom.
- Zenner H (2004). Multiaxial fatigue methods, hypotheses and applications an overview. 7th International Conference on Biaxial/Multiaxial Fatigue and Fracture, Berlin, Germany, 3-16.

- Zenner H, Simbürger A, Liu J (2000). On the fatigue limit of ductile metals under complex multiaxial loading, *International Journal of Fatigue* 22, 2000.
- Zhang B, Guo W (2007). Three-dimensional stress state around quarter-elliptical corner cracks in elastic plates subjected to uniform tension loading. *Engineering Fracture Mechanics* 74, 386-398.
- Zhang X, Wang Z (2003). Fatigue life improvement in fatigue-aged fastener holes using the cold expansion technique. *International Journal of Fatigue* 25, 1249-1257.
- Zhao J, Guo W, She C (2007). The in-plane and out-of-plane stress constraint factors and K-T-Tz description of stress field near the border of a semi-elliptical surface crack. *International Journal of Fatigue* 29, 435-443.
- Zhiqiang X, Yujiu S, Mingjing T (1991). Crack closure induced by corrosion products and its effect in corrosion fatigue. *International Journal of Fatigue* 13, 69-72.

978-972-8954-31-4



ISBN 978-972-8954-31-4